Insights into the mechanism of action of quinoline antimalarials against *Plasmodium falciparum* revealed by novel fluorescent analogues and chemical proteomics

Thesis presented for the degree of

DOCTOR OF PHILOSOPHY

in the Department of Chemistry

UNIVERSITY OF CAPE TOWN

JOHN GEOFFREY WOODLAND

SUPERVISORS

Professor Timothy Egan and Professor Roger Hunter

AUGUST 2016

Declaration

Insights into the mechanisms of action of quinoline antimalarials against *Plasmodium falciparum* revealed by novel fluorescent analogues and chemical proteomics

I, John Geoffrey Woodland, declare the following:

1. That the above-titled report is my own work, both in concept and execution, apart from the normal guidance of my supervisors;
2. That in cases where others' work has been cited, this has been acknowledged and referenced;
3. That no part of this work has been, is being, or is to be submitted for another degree at this or any other university;
4. That I grant the University of Cape Town free licence to reproduce this work, in whole or in part, for the purpose of research.

I hereby present this report in fulfilment of the requirements for the degree of Doctor of Philosophy in the Department of Chemistry at the University of Cape Town.

Signature removed

Signed by candidate

August 2016

Abstract

For centuries, quinoline-based drugs have formed the cornerstone of antimalarial treatment. Despite recent challenges posed by resistance, interest in these molecules persists. It is thus surprising that crucial details of their mechanism of action against the most virulent malaria parasite, *Plasmodium falciparum*, remain unresolved. This thesis develops new tools to generate deeper insights into the modes of action of the two major classes of the quinoline antimalarials against *P. falciparum*. These are the quinoline methanols, represented by the diastereomeric *Cinchona* alkaloids quinine and quinidine, and the 4-aminoquinolines, represented by chloroquine.

Mechanistic studies of these antimalarials have typically focused on the inhibition of haemozoin biocrystallisation within the acidic digestive vacuole of *P. falciparum*. In order to conduct a comprehensive survey of the subcellular localisation of these antimalarials across the entire infected erythrocyte, a suite of novel fluorescent derivatives was designed and synthesised. Key physicochemical properties of these antimalarials were retained in order to preserve the interactions of these drugs with their putative target, ferriprotoporphyrin IX or Fe(III)PPIX. Versatile derivatisation of the alkaloids was enabled by a regioselective radical-mediated thiol-ene click reduction. 7-Nitrobenz-2-oxa-1,3-diazole (NBD) was identified as a suitable reporter fluorophore and was attached to the quinoline core by nucleophilic aromatic substitution. The length of the spacer chain between the quinoline and the fluorophore was varied by preparing NBD-labelled amino acids and their corresponding succinimidyl esters. A novel NBD-labelled chloroquine derivative was prepared by using its *N*-dealkylated analogue as a key intermediate. A single quinine derivative with an alternative fluorophore, bimane, was also prepared.

In order to determine whether these fluorescent derivatives were suitable analogues of the parent antimalarials, their photophysical and physicochemical properties were thoroughly evaluated. Spectrophotometric titrations revealed that characteristic features of association with Fe(III)PPIX were retained for most of the NBD-labelled alkaloids, vindicating the design choice to functionalise their vinyl groups. For chloroquine and its NBD-labelled derivative, μ-oxo dimerisation of Fe(III)PPIX was conserved. A detergent-mediated assay indicated that all fluorescently-labelled derivatives possessed improved activity against β-haematin formation compared to their parent antimalarials. Crucially, all fluorescent derivatives, with the exception of the bimane-labelled alkaloid, exhibited low to moderate nanomolar activities against a chloroquine-sensitive strain of *P. falciparum*. Taken together, these results showed that some of

the fluorescent-labelled derivatives were suitable analogues of the parent molecules and were thus appropriate for use in microscopy studies.

Live-cell imaging revealed selective accumulation of the fluorescently-labelled analogues within *P. falciparum*-infected erythrocytes. All three analogues were found in close proximity to haemozoin and hence the region corresponding to the digestive vacuole, especially in the case of chloroquine, consistent with haemozoin inhibition as their primary mechanism of action. Quantitative analysis of cells co-stained with the alkaloid analogues and LysoTracker Red demonstrated extensive colocalisation between these signals, indicating a preference of these analogues for phospholipid bilayers in acidic environments. Quantitative analysis also revealed that these analogues did not localise to the nucleus. This observation makes the claims that these molecules disrupt DNA replication in *P. falciparum* very unlikely. To overcome resolution limitations, super-resolution structured-illumination microscopy (SR-SIM) was employed. This indicated clear colocalisation between the analogues of all three quinoline antimalarials with the endoplasmic reticulum in *P. falciparum*. Colocalisation between these analogues and the mitochondrion was also evident but less conclusive. These observations corroborate previous ultrastructural studies implicating these organelles in the modes of action of these quinolines.

Chemical proteomics was used to investigate whether the observed accumulation in *P. falciparum* corresponded to the binding of these antimalarials to protein targets. Drug-labelled matrices were used to capture binding targets of the quinoline antimalarials from uninfected erythrocytes and *P. falciparum*. Several binding targets specific for these drugs were detected from human erythrocytes, especially from the chloroquine-labelled beads. On the other hand, SDS-Page revealed only a single prominent band between 200-250 kDa from the membrane-associated fraction recovered from *P. falciparum* lysate. Proteomic analysis revealed that this band corresponded to *P. falciparum* multidrug resistance-associated protein (PfMRP1). This is intriguing as PfMRP1 has been implicated in resistance mechanisms of chloroquine and quinine. Disrupting this gene has previously been shown to make cells more susceptible to these drugs, indicating that this protein plays a role in transport and hence must bind these substrates. That PfMRP1 was detected in the binding sub-proteomes corresponding to each of the drug-labelled matrices shows that this protein dynamically binds to all three of the quinoline antimalarials investigated in this study.

Taken together, these results support haemozoin inhibition by accumulation in the digestive vacuole as the primary mechanism of action of these quinoline antimalarials, with Fe(III)PPIX as their primary target. Only a single protein binding target of these quinoline antimalarials, PfMRP1, was identified in *P. falciparum*. PfMRP1 is unlikely to be a drug target and instead may

be responsible for modulating the activity of these compounds as a transporter. It may be speculated that secondary effects due to association with organelles such as the endoplasmic reticulum, the mitochondrion and membranous structures such as phospholipid bilayers may be responsible for additional metabolic disruption caused by these antimalarials. Overall, this thesis has developed new tools for generating deeper insights into the mechanistic details of these prototypical antimalarials. The observations described herein and subsequent studies using these novel tools may facilitate the identification of hitherto unexplored targets for new antimalarials to treat this devastating infectious disease.

Publications and Conference Proceedings

Parts of this work have featured in the following publications:

- J. G. Woodland, R. Hunter, P. J. Smith and T. J. Egan, *Org. Biomol. Chem.*, 2016, "Shining new light on ancient drugs: Preparation and subcellular localisation of novel fluorescent analogues of *Cinchona* alkaloids in intraerythrocytic *Plasmodium falciparum*", DOI: 10.1039/C6OB02110G.
- Provisional Patent Application South Africa 2013/05171. T. J. Egan, R. Hunter and J. G. Woodland, "Fluorescent Sensors for Haem".

Parts of this work have been presented at the following scientific meetings:

- **2015:** "Seeing is Believing – Imaging the Processes of Life" EMBL Symposium, Heidelberg, Germany (poster presentation)
- **2015:** Single-Molecule Spectroscopy and Microscopy: Faraday Discussion, London, United Kingdom (poster and flash oral presentations)
- **2015:** South African Chemical Institute (SACI) Inorganic Chemistry Conference, Rhodes University (poster and flash oral presentations)
- **2015:** Postgraduate Research Expo, University of Cape Town (poster presentation) – *First Prize (Science Faculty Category)*
- **2015:** South African Spectroscopic Society (SASS) Young Spectroscopists' Symposium, Stellenbosch University (oral presentation) – *National Winner*
- **2014:** SACI-ACS Binational Organic Chemistry Conference, Stellenbosch University (poster and flash oral presentation) – *First Prize (Flash Oral Category)*
- **2013:** SACI Young Chemists' Symposium, Stellenbosch University (poster presentation) – *Best Poster Prize*
- **2013:** Falling Walls Conference, "The International Conference on Future Breakthroughs in Science and Society" (oral presentation) – *Third Place in the Falling Walls Young Innovator of the Year Competition 2013*
- **2013:** International Conference on Bioinorganic Chemistry, Grenoble, France (poster presentation)
- **2012:** H3-D Symposium on New Paradigms in Drug Discovery, Newlands, Cape Town (poster presentation)

Poets say science takes away from the beauty of the stars – mere globs of gas atoms. Nothing is "mere". I too can see the stars on a desert night, and feel them. But do I see less or more? The vastness of the heavens stretches my imagination – stuck on this carousel my little eye can catch one-million-year-old light. A vast pattern – of which I am a part… What is the pattern, or the meaning, or the why*? It does not do harm to the mystery to know a little about it. For far more marvellous is the truth than any artists of the past imagined! Why do the poets of the present not speak of it? What men are poets who can speak of Jupiter if he were like a man, but if he is an immense spinning sphere of methane and ammonia must be silent?*

…

A poet once said, "The whole universe is in a glass of wine." We will probably never know in what sense he meant that, for poets do not write to be understood. But it is true that if we look at a glass of wine closely enough we see the entire universe. There are the things of physics: the twisting liquid which evaporates depending on the wind and weather, the reflections in the glass, and our imagination adds the atoms. The glass is a distillation of the Earth's rocks, and in its composition we see the secrets of the universe's age, and the evolution of stars. What strange arrays of chemicals are in the wine? How did they come to be? There are the ferments, the enzymes, the substrates, and the products. There in wine is found the great generalisation: all life is fermentation. Nobody can discover the chemistry of wine without discovering, as did Louis Pasteur, the cause of much disease. How vivid is the claret, pressing its existence into the consciousness that watches it! If our small minds, for some convenience, divide this glass of wine, this universe, into parts – physics, biology, geology, astronomy, psychology, and so on – remember that nature does not know it! So let us put it all back together, not forgetting ultimately what it is for. Let it give us one more final pleasure: drink it and forget it all!

R. P. Feynman, *The Feynman Lectures on Physics*, 1964, Vol. 1, Lecture 3.

Acknowledgements

Of principal importance in this research have been my supervisors. I am indebted to them for the rigorous scientific training, guidance and inspiration they have provided. First and foremost, my thanks go to Professor Tim Egan for providing so many resources, both material and intellectual, for this project. I have benefited enormously from his broad knowledge, his attention to detail and his ability to see the "bright side" of any experimental result, no matter how unexpected or discouraging. I am also extremely grateful to Professor Roger Hunter for his passion, advice and commitment and for not forgetting the toll that the scientific endeavour occasionally takes on one's soul.

Members of the Egan research group ("The Haem Team") have been generous with their time and expertise. These include Dr Katherine de Villiers, Dr David Kuter, Dr Melvin Ambele, Dr Kathryn Wicht, Jill Combrinck, Fabrizio L'abbate, Nomakhwezi Mvumvu, Stefan Benjamin, Nikki Kuter, John Okombo and Roxanne Openshaw. Roxanne Mohunlal provided endless smiles and advice, especially concerning parasite work. Special thanks go to Dr Aneesa Omar, with whom I shared this journey as a close colleague. Her enthusiasm, cheerfulness and our many conversations contributed immensely to creating a beneficial working environment.

I am also grateful to members of the Hunter research group, especially Dr Sophie Rees-Jones for willingly sharing her vast expertise and for always presenting a friendly face when it was most needed. Thanks also go to Dr Wade Peterson, Dr Athi Msutu, Dr Cathryn Driver, Dr Rudy Cozett, Ana Andrijevic, James Biwi, Daniel Kusza, Mandla Mabunda, Thobela Bixa and Shankari Nair.

I am grateful to Professor Pete Smith at the UCT Division of Pharmacology for overseeing the in vitro testing of derivatives against *P. falciparum*. Jill Combrinck, Sumaya Salie and Virgil Verhoog generously donated parasites for imaging purposes. Our friendly chats eased the logistical challenges of working on two separate university campuses.

At the UCT Confocal and Light Microscope Imaging Facility, Associate Professor Dirk Lang and Susan Cooper were instrumental in igniting my passion for microscopy. I am grateful for their advice and combined hours of assistance. Super-resolution imaging was carried out at the CAF Fluorescence Microscopy Unit at Stellenbosch University. There I was always enthusiastically assisted by Dr Ben Loos, Lize Engelbrecht and Rozanne Adams.

For analytical work, thanks go to the NMR and mass spectrometry staff at UCT and Stellenbosch University. Dr Maré Vlok from the CAF Proteomics Unit at Stellenbosch University delivered results under time constraints and patiently answered my many questions. Madhu Chauhan from the UCT Molecular and Cell Biology Department assisted with ultracentrifugation.

Many others in the Chemistry Department contributed to creating an exceptionally pleasant space in which to work. Associate Professor Neil Ravenscroft provided much helpful advice and our occasional coffee outings were welcome breaks from the lab bench. Associate Professors Alan Hutton and David Gammon and Professors Susan Bourne and Luigi Nassimbeni all played important roles as colleagues, role models and friends. I am grateful to the teams who assisted in the teaching laboratories as well as with the annual Jack Elsworth lecture-demonstrations. Administrative assistance from Deirdre Brooks and Zaeem Najaar was much appreciated.

Thanks are due to the National Research Foundation (NRF) of South Africa for financial support. Travel grants were generously provided by the NRF and the Royal Society of Chemistry.

Several close friends have shared parallel scientific journeys with me at UCT: Dr Kathryn Wicht, Dr Raissa Philibert, Timothy Povall, Dr Taigh Anderson, Stephen Fienberg and Stuart Hall. Others have played important supportive roles throughout this journey: Emily Hallinan, Matthew Golesworthy, Margaret Barrie, Caitlin Melidonis and James Rink.

Very special thanks to my parents, Kristin and Gavin Woodland, who have always been so enthusiastic and supportive of me and all my endeavours. Finally, I am deeply grateful to Kyle Paulssen for sharing this journey alongside me and for reminding me of the importance, even in the scientific realm, of suspending my disbelief.

Brief Contents

Detailed Contents

Chapter One: Introduction and Literature Review

Chapter Two: Principles of Fluorescence and Applications in Spectroscopy and Microscopy

Chapter Four: Photophysical and Physicochemical Characterisation of Novel Fluorescent Derivatives

Chapter Five: Live-Cell Fluorescence Microscopy of Novel Analogues of the Quinoline Antimalarials

Chapter Six: Affinity Detection and Identification of Quinoline Antimalarial Binding Proteins

Chapter Seven: Overall Conclusions and Further Work

Appendix: Experimental Methods and Characterisation of Organic Compounds

Chapter One

Introduction and Literature Review

1.1. Overview

Malaria is a devastating infectious disease that places a large proportion of the population at risk and impedes economic development, especially in the developing world. For centuries, quinoline-based antimalarials have formed the cornerstone of treatment regimes. Despite challenges posed by resistance, interest in these molecules remains. Surprisingly, their modes of action against the malaria parasite remain incompletely resolved and, indeed, may differ in their details.

This study aims to develop novel tools to generate deeper insights into the mechanism of action of the two most important classes of these antimalarials, the quinoline methanols and the 4-aminoquinolines, represented by the diastereomeric *Cinchona* alkaloids, quinine and quinidine, and a synthetic analogue, chloroquine, respectively (Figure 1.1).

This chapter will outline the broader context of this study. The disease burden posed by malaria as well as the life cycle of its most virulent parasite, *Plasmodium falciparum*, will be discussed with an emphasis on its pathogenic intraerythrocytic stage. During this period of its life cycle, the parasite faces several metabolic challenges that are relevant to work contained herein. These include haemoglobin catabolism and the challenge faced by the disposal of the cytotoxic

iron species ferriprotoporphyrin IX. The structure of malaria pigment (haemozoin) and recent progress in understanding its formation will be discussed. Lipid metabolism during the intraerythrocytic cycle and mechanisms of intracellular pH regulation will be described.

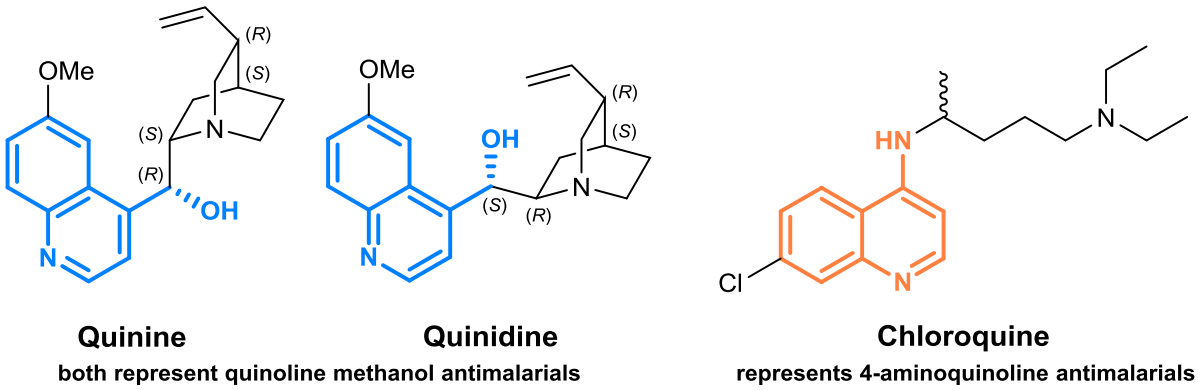

Figure 1.1. *The structures of the representative quinoline antimalarials investigated in this study. The quinoline methanol and 4-aminoquinoline motifs are highlighted in blue and orange, respectively.*

The origins of the quinoline antimalarials and the development of their synthetic derivatives will be discussed in the context of current antimalarial treatment strategies. Challenges posed by membrane transporter proteins in facilitating drug resistance in *P. falciparum* will be highlighted. Various aspects of contemporary antimalarial drug discovery will be presented including efforts to identify novel β-haematin inhibitors.

As the inhibition of haemozoin formation is suspected to be the primary target of many quinoline antimalarials, there is much interest in understanding the mechanism of this process. A central aspect of this process is the interaction of these drugs with ferriprotoporphyrin IX. Recent advances in understanding these interactions both in solution and the solid state will be presented. Brief reference will also be made to alternative hypotheses that have been presented to account for the activity of the quinoline antimalarials.

Although similar in some respects, the quinoline methanol alkaloids and chloroquine possess considerable physicochemical differences that are highlighted by differences in accumulation within *P. falciparum*. They have also been found to elicit differential morphological effects on the parasite such as modulation of endocytosis and vesicle trafficking. Various efforts to identify proteinaceous binding targets will be presented. This chapter concludes with an outline of the major objectives of this study in line with the aim of developing new tools to generate novel insights into the modes of action of these two classes of antimalarials within *P. falciparum*.

1.2. The global disease burden and life cycle of the malaria parasite

1.2.1. The scourge of malaria

Malaria imposes an intolerable burden on global health. According to the most recent report by the World Health Organisation, the disease is responsible for nearly half a million deaths every year of which approximately 90% occur in Africa.[1] Infants and children are most affected by the disease which is thought to account for one in every ten child deaths.[1] Furthermore, malaria is recognised as a cause of poverty and poses a major hindrance to economic development in affected regions: "Where malaria prospers most, human societies have prospered least."[2]

In 2008, as one of its Millennium Development Goals, the United Nations called for a concerted international effort to halt and reverse the global incidence of malaria by 2015. While this target has unquestionably been achieved, much remains to be done and ambitious new goals have been set for 2030 to reduce global incidence and mortality by at least 90%.[1]

Malaria is an infectious disease caused by protozoan parasites belonging to the genus *Plasmodium*. Four species of *Plasmodium* are chiefly responsible for infection in humans, namely *P. falciparum*, *P. malariae*, *P. ovale* and *P. vivax*. Of these, *P. falciparum* is the most virulent, especially in Africa where it is also the most prevalent species.[1] Common symptoms of malaria include recurrent fever and headaches. In serious cases, infection can lead to long-term liver damage, neurological damage, coma and death.

The primary hosts and transmission vectors of the malaria parasites are female *Anopheles* mosquitoes. For this reason, the prevalence of the disease varies across the globe according to exposure to the mosquito. Hence malaria is typically endemic to the tropical and subtropical regions of sub-Saharan Africa, Asia and the Americas.

1.2.2. The life cycle of the malaria parasite, *Plasmodium falciparum*

While the four species of *Plasmodium* mainly responsible for malaria in humans all share similar life cycles, only the life cycle of *P. falciparum* will be described in detail.

Human infection begins with the injection of sporozoites into the bloodstream by an infected female *Anopheles* mosquito during a blood meal. The sporozoites travel to the liver and invade hepatocytes where they multiply asexually to form liver schizonts over the course of approximately one week.[3] This is followed by the release of merozoites into the bloodstream.

Merozoite release is followed by the rapid invasion of red blood cells, or erythrocytes, initiating the intraerythrocytic cycle (Figure 1.2). This asexual development phase is complex and comprises three successive morphological stages. During the ring stage, the expression of parasite proteins exported into the host erythrocyte peaks, suggesting that host cell modifications are a major task of this stage.[4,5] The trophozoite stage is characterised by rapid parasite growth and the distinct appearance of malaria pigment, the remnant of catabolised haemoglobin. Finally, the parasite enters the schizont stage during which it generates up to 32 daughter merozoites. After rupture of the host cell, these merozoites invade new erythrocytes.

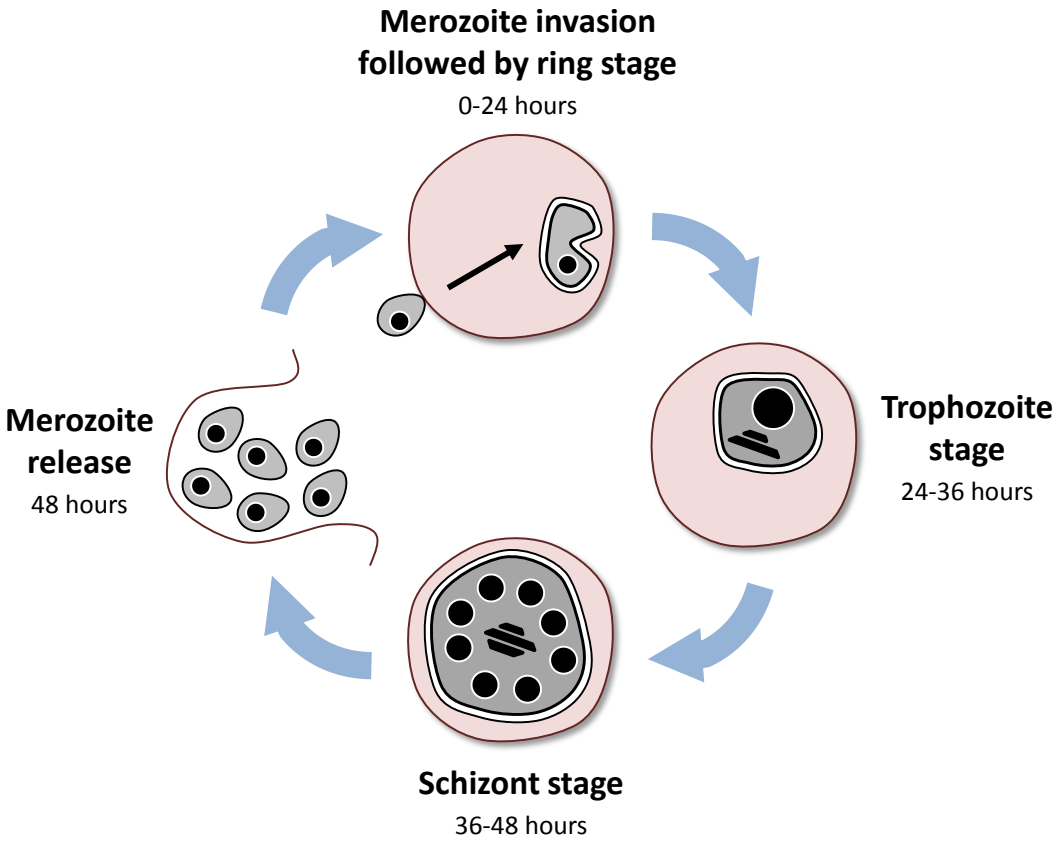

Figure 1.2. *An illustration of the main stages of the intraerythrocytic life cycle of* P. falciparum*. Merozoite invasion of erythrocytes is followed by the ring, trophozoite and schizont stages, after which the host cell ruptures to release further populations of merozoites.*

It is during the 48-hour intervals of this cycle that the periodic chills and fevers, characteristic of malaria, are experienced. This is triggered by the rupture of mature schizonts and the release of cell debris, both of which stimulate the host's innate immune response. This cycle also produces the disease pathology associated with malaria. Most deaths occur due to complications arising from *P. falciparum* infections whereby infected erythrocytes adhere to the endothelium of capillaries and venules, particularly in the brain. This vascular occlusion may lead to coma, after

which the patient has little chance of survival even with optimal care.[6] Although the blood stages of the parasite cause most of the pathology related to the disease, they are also the stages that are the most susceptible to treatment by antimalarial agents.

A fraction of merozoites form sexual gametocytes, the only form of the parasite that is capable of transmission from humans to the mosquito vector. Immature gametocytes are sequestered in the bone marrow but, once mature, they circulate in peripheral blood. At this point, when an *Anopheles* mosquito feeds on an infected human, *P. falciparum* gametocytes are ingested along with the blood and the mosquito itself becomes infected.[3] Following maturation of a gametocyte into a gamete within the mosquito midgut, gamete fusion produces ookinetes which penetrate the midgut wall and form oocysts. These enlarge over time and burst to release sporozoites that migrate to the salivary gland of the mosquito, from where they can infect humans during the mosquito's next blood meal.[3]

1.2.3. Ultrastructural features of the intraerythrocytic life cycle

It was only after continuous in vitro cultures of *P. falciparum* were established in 1976 that a definitive ultrastructural description of the parasite could be given.[7] Since then, immunolabelling, serial electron tomography and other imaging techniques have vastly improved our understanding of the ultrastructure of *P. falciparum*. However, extensive sample preparation and the harsh conditions required for transmission electron microscopy mean that dynamic information is lost and imaging artefacts are easily introduced.

As described above, the intraerythrocytic stage of the *P. falciparum* life cycle commences with merozoite invasion of host erythrocytes, signalling the beginning of a continuous and dynamic process which takes approximately 48 hours. The merozoites are ellipsoid with an apical prominence and are similar in dimension to a large bacterium.[8] They contain the equipment needed for invasion of the erythrocytes; these are the "apical organelles" which comprise rhoptries, micronemes, mononemes and dense granules (Figure 1.3A).[9] Merozoites also possess other organelles including ribosomes, a single acrystate mitochondrion, a non-photosynthetic plastid called an apicoplast and a nucleus.

After adhesion to the erythrocyte the parasite re-orientates itself so that the apical prominence is in contact with the erythrocyte membrane. The complex mechanism of this invasion has been thoroughly investigated using super-resolution fluorescence and immunoelectron microscopy.[10] Once inside the erythrocyte, the parasite encloses itself in its own compartment, separate from the erythrocyte cytosol. This compartment is bounded by the parasitophorous vacuolar membrane which is in close proximity to the parasite plasma membrane.

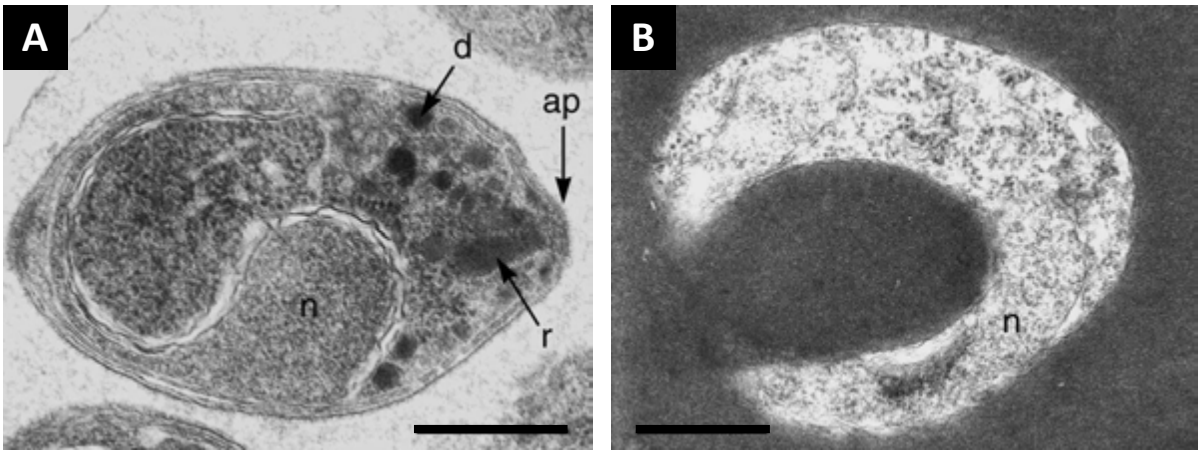

Figure 1.3. *Electron micrographs of the merozoite and ring stages of the intraerythrocytic* P. falciparum*. (A) A merozoite showing the apical prominence (ap) with a rhoptry (r), dense granules (d) and an indented nucleus (n). (B) A ring stage parasite exhibiting the nucleus (n), surrounded by ribosomes and endoplasmic reticulum. Scale bars represent 0.5 µm. Reproduced from Bannister et al.,* Parasitol. Today*, 2000, **16**, 427 with permission from Elsevier.*

In the early ring stage, the central region is thin while the peripheral region, containing the nucleus and other organelles, is thicker (Figure 1.3B). Giemsa-stained smears depict a signet ring-shaped structure which gives this stage its name.[8] The mid-ring stage, about 10-15 hours after invasion, was originally thought to be a metabolically-nondescript phase. However, there is now evidence that haemoglobin ingestion and catabolism begin at this stage as well as the synthesis of proteins for export to the host cell.[5,11] The parasite feeds on the erythrocyte cytosol via a cytostome ("cell mouth") and haemoglobin catabolism most likely commences in small acidic vesicles. An increase in protein synthesis is indicated via a proliferation of ribosomes and an extensive endoplasmic reticulum.[8] The erythrocyte is gradually altered by proteins exported from the parasite, many of which are incorporated into the surface of the host cell. This increases the adhesiveness of the erythrocyte membrane and is eventually responsible for the pathogenic obstruction of the vasculature characteristic of severe malaria.[8]

The trophozoite stage occurs approximately 20-38 hours after invasion and is the most active metabolic stage (Figure 1.4A). During this stage the cell increases the most in size. The enlarged Golgi complex is located close to the nucleus which is already involved in the first rounds of nuclear division.[8] The mitochondrion is surrounded by a double membrane while the apicoplast is observed to be contained within four membranes. These organelles are elongated and branched but remain in close apposition at a number of points.[9] The mature digestive vacuole is readily distinguishable by the crystals of malaria pigment (haemozoin), a by-product of haemoglobin catabolism. During this stage, haemoglobin metabolism continues in earnest.

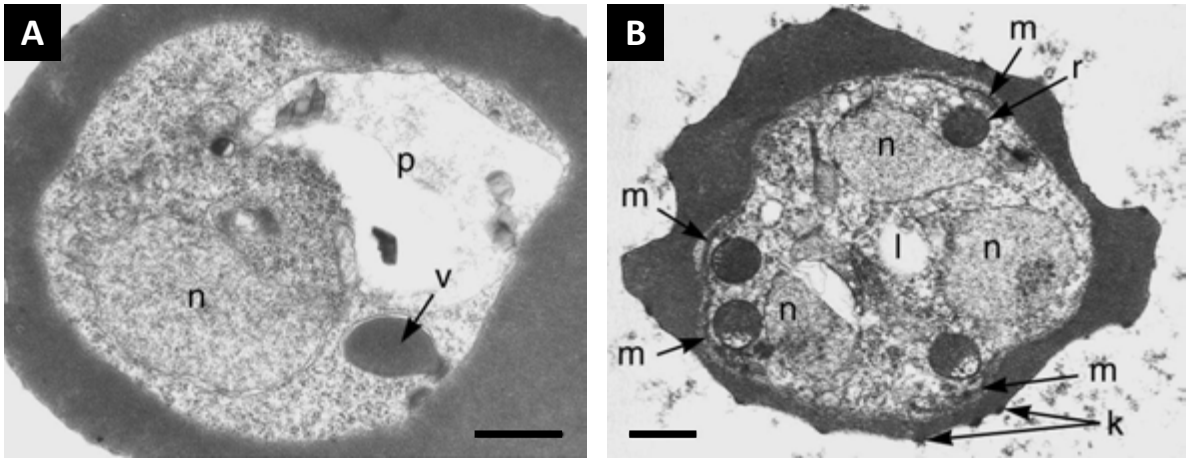

Figure 1.4. *Electron micrographs of the trophozoite and schizont stages of intraerythrocytic* P. falciparum*. (A) Mid-trophozoite stage showing the nucleus (n), digestive vacuole (p) and a cytostome with a forming food vacuole (v). (B) A schizont showing a series of nuclei (n) and developing merozoites (m). Note the irregular appearance of the host cell surface and the presence of knobs (k). Scale bars represent 0.5 µm. Reproduced from Bannister et al.,* Parasitol. Today*, 2000, **16**, 427 with permission from Elsevier.*

During the trophozoite stage a number of dramatic modifications to the host erythrocyte take place. Proteins continue to be secreted by the parasite across the parasitophorous vacuolar membrane to the erythrocyte cytoplasm. Destinations include the Maurer's clefts which are compartments that concentrate virulence proteins for delivery to the host membrane.[9] Knobs, self-associated clusters which represent the major adhesive proteins, distort the appearance of the host cell.[9] The parasite also constructs an extensive exomembrane system called the tubovesicular network which extends from the parasite plasma membrane to the erythrocyte cytoplasm, and possibly to the external milieu, and is used to traffic lipids and nutrients.[9]

Finally, during the schizont phase, further mitotic nuclear division occurs to generate between 16 and 32 daughter merozoites (Figure 1.4B). Ingestion of almost all the host cell haemoglobin means that the parasite takes up the complete erythrocyte. The digestive vacuole is compacted into a round, single, dense mass.[8] Merozoite-forming foci are spaced around the circumference of the parasite. There is proliferation of the rough endoplasmic reticulum and ribosomes, and multiplication of the mitochondrion and plastid means that a copy of each of these organelles is inherited by a daughter merozoite. Eventually the parasite plasma, parasitophorous vacuolar and the erythrocyte plasma membranes are breached as the merozoites are released into the bloodstream of the host at the end of this stage of the life cycle.

1.3. Metabolic challenges faced by the intraerythrocytic parasite

1.3.1. Haemoglobin ingestion and catabolism

The human erythrocyte provides a convenient niche for the malaria parasite and provides excellent protection from the host immune system. Apart from lacking almost any organelles, this blood cell provides vast quantities of haemoglobin, some of which is exploited by the parasite as a nutrient source.[12] This also poses several metabolic challenges for the parasite that needs to make space for itself in the erythrocyte in order to grow. Furthermore, it needs to detoxify the cytotoxic iron-containing prosthetic groups of haemoglobin which are released following catabolism. Hence, *P. falciparum* has evolved an efficient pathway that catabolises haemoglobin to amino acids with the concomitant biocrystallisation of ferriprotoporphyrin IX into a remarkable structure called haemozoin.

Haemoglobin degradation occurs in the acidic digestive vacuole, a lysosomal compartment unique to *Plasmodium*. Unlike most other organelles, this vacuole does not persist throughout the entire intraerythrocytic life cycle but instead is discarded at the end of each cycle of the blood stage. Although there are several competing models that attempt to explain the biogenesis of the digestive vacuole,[11,13,14] each one relies on cytsostomal invagination of the double membrane between the erythrocyte and parasite cytoplasm (Figure 1.5). In this endocytosis-like process, haemoglobin-containing vesicles are pinched off by the cytostome and travel to the digestive vacuole where haemoglobin is broken down. Recent evidence suggests that haemoglobin catabolism probably already commences in the acidified transport vesicles.[11]

During the semi-ordered process of haemoglobin degradation, two families of proteases play prominent roles. Four aspartic acid proteases called plasmepsins and three cysteine proteases called falcipains are found in the digestive vacuole.[15,16] Digestion into smaller peptides is facilitated by the zinc metalloprotease falcilysin after which a dipeptidyl aminopeptidase generates dipeptides, some of which are exported to the cytosol for catabolism into free amino acids by aminopeptidases.[17,18]

Haemoglobin degradation is necessary for parasite survival as it has been found that parasite development is interrupted when haemoglobin proteolysis is blocked by protease inhibitors.[19] Catabolised haemoglobin forms the main amino acid source for the parasite and the proportions of free amino acids which are generated by *P. falciparum* resemble the amino acid composition of globin.[20,21] While 25-75% of the host cell protein may be degraded, only a small amount of this is utilised for parasite protein synthesis. This is typically around 16% but does not exceed

25%.[12] The majority of amino acids are simply released from the infected cell into the external medium. It has been suggested that the reason for this lies in the need to limit the swelling of the host erythrocyte and thereby prevent its premature lysis.[21-24]

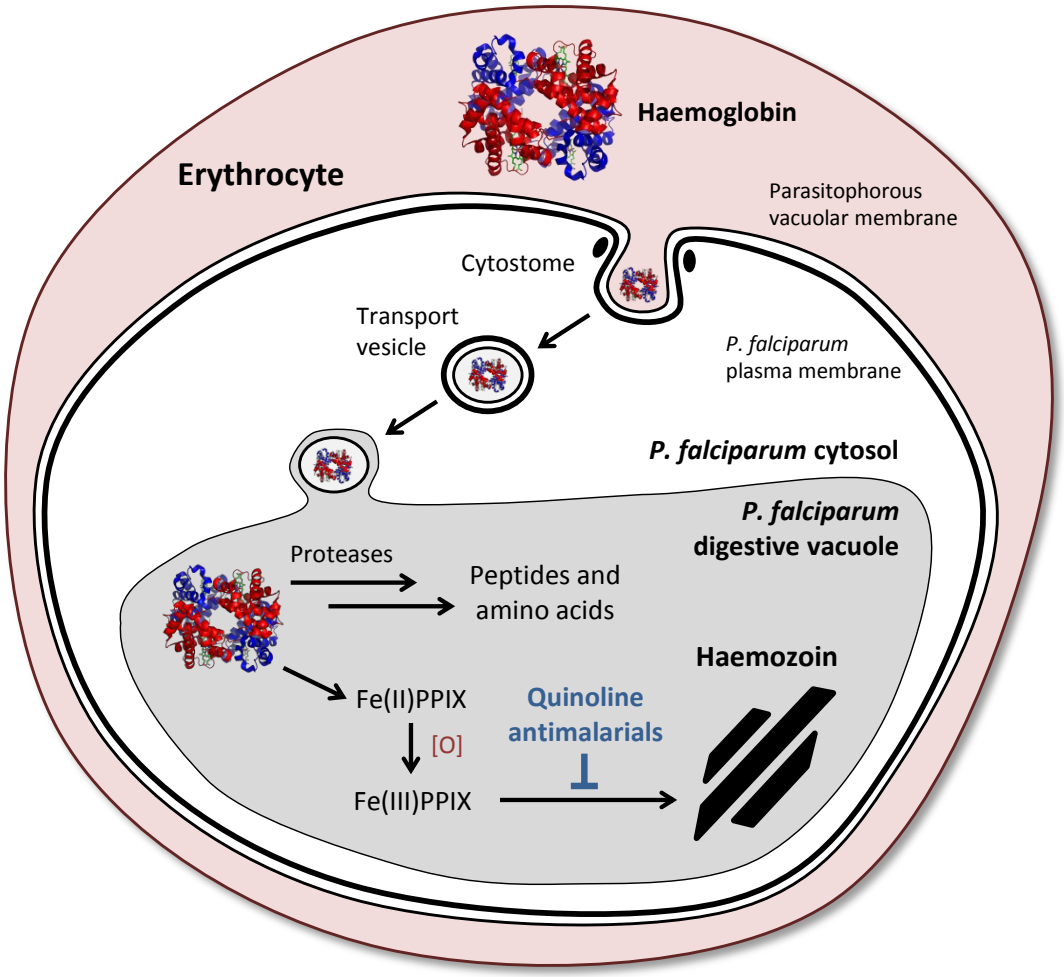

Figure 1.5. *Representation of haemoglobin ingestion and catabolism by* P. falciparum *in the host cell.*

1.3.2. Ferriprotoporphyrin IX detoxification and haemozoin formation

Haemoglobin comprises four globular protein subunits, each of which is composed of a globin chain tightly associated with an iron-containing prosthetic group called haem. Hence, four haem groups are liberated for every molecule of haemoglobin catabolised. Upon release, haem is rapidly and irreversibly oxidised to its ferric form, ferriprotoporphyrin IX or Fe(III)PPIX (Figure 1.6), with concomitant production of hydrogen peroxide. The iron atom is coordinated to a fifth axial ligand which is typically water, in which case the molecule is referred to as haematin.

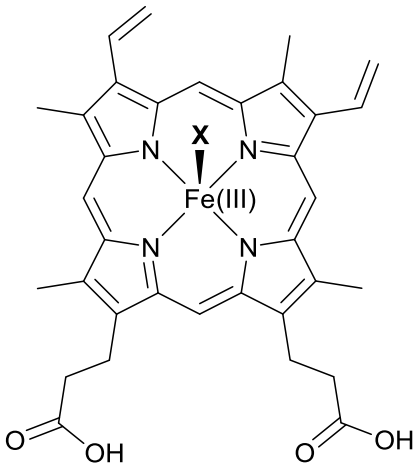

Figure 1.6. *The structure of an oxidised haem molecule following release from a globin subunit, referred to as ferriprotoporphyrin IX or Fe(III)PPIX. When the axial ligand "X" is a water molecule or a hydroxide ion, the entity is called haematin. The former species is dominant in the digestive vacuole.*

Free Fe(III)PPIX is poisonous to the parasite due to its cytotoxic, pro-oxidant activity. At high concentrations, free Fe(III)PPIX can inhibit protein function and partition into and disrupt lipid bilayers.[25] It can also undergo electron transfer reactions with molecular oxygen to produce diverse and damaging reactive oxygen species that can destroy the integrity of the cell.[25] In mammalian cells, levels of dissociated Fe(III)PPIX are strictly regulated by haem oxygenase enzymes. However, the malaria parasite lacks a functional haem oxygenase and hence faces a unique challenge as it cannot degrade Fe(III)PPIX enzymatically.[26] (Incidentally, enzymatic degradation of Fe(III)PPIX would also be problematic for the parasite as it would produce massive quantities of free iron which are equally toxic.) Instead, Fe(III)PPIX is efficiently biocrystallised to relatively inert and insoluble haemozoin, historically known as malaria pigment, within the acidic digestive vacuole.

Haemozoin is a crystalline cyclic dimer of Fe(III)PPIX in which the propionate group of one porphyrin moiety coordinates to the iron centre of its partner and vice versa, while the second propionic acid group of each Fe(III)PPIX hydrogen bonds to a neighbouring dimer in the crystal (Figure 1.7). The synthetic counterpart of haemozoin is called β-haematin and the two species are chemically, spectroscopically and crystallographically identical.[27]

It was first suspected by Fitch and Kanjananggulpan that haemozoin was probably identical to β-haematin, an insoluble Fe(III)PPIX precipitate first described in the 1930s.[28] Subsequently, Slater et al. demonstrated by X-ray diffraction, infrared spectroscopy and solubilisation studies that haemozoin is indeed identical to β-haematin. They showed that both species possess bonds between the propionate group of one porphyrin and the Fe(III) centre of its neighbour.[29]

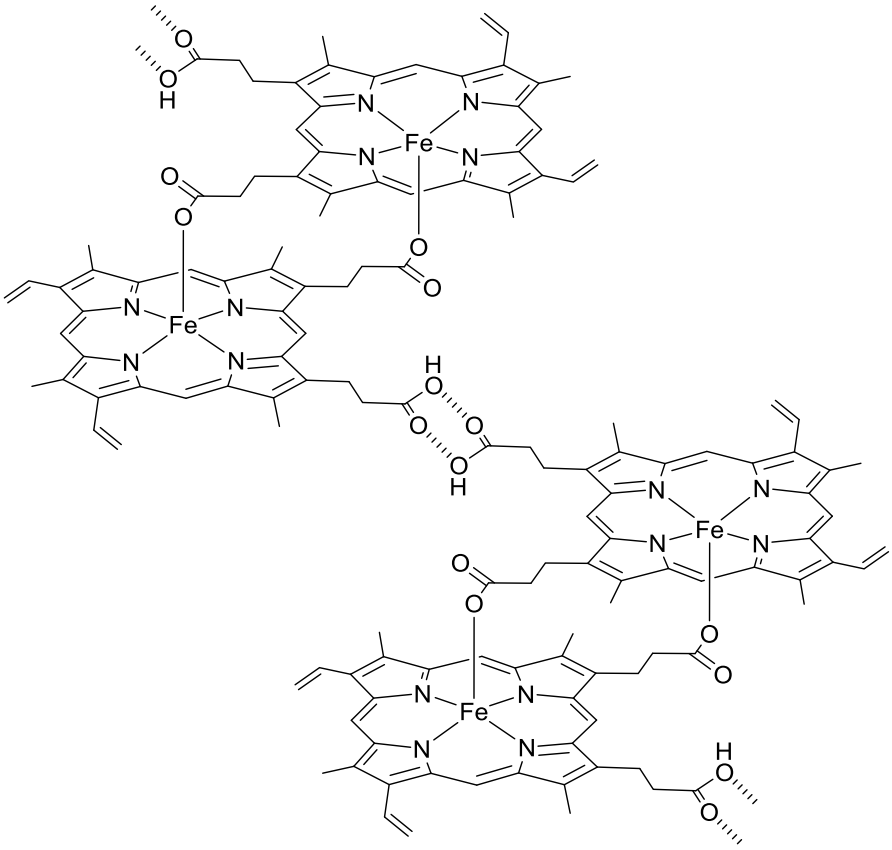

Figure 1.7. *The structure of haemozoin. Two hydrogen-bonded μ-propionato dimers of Fe(III)PPIX are represented, each of which forms the symmetrical repeating unit of the crystal.*

Bohle et al. further demonstrated by synchrotron X-ray diffraction that identical diffraction patterns are obtained from lyophilised parasitised erythrocytes and β-haematin, showing that haemozoin and β-haematin are identical.[30,31] In 2000, Pagola et al. determined the structure of β-haematin from its X-ray powder diffraction pattern by Rietveld refinement.[27] Eventually, the single crystal X-ray structure of the DMSO solvate of β-haematin was presented, providing irrefutable evidence of its structure (Figure 1.8).[32]

Haemozoin formation represents the overwhelming fate of Fe(III)PPIX released in the parasite, accounting for at least 95% of the total iron in *P. falciparum*.[33] Most quinoline antimalarials are suspected to inhibit this pathway, leading to a deleterious accumulation of Fe(III)PPIX. Amongst other manifestations, this is suspected to generate reactive oxygen species and destabilise the vacuolar membrane.[25] However, the mechanism whereby Fe(III)PPIX is sequestered into crystalline haemozoin and, consequently, the mechanism of its inhibition by quinoline antimalarials, remains unclear. Theories of haemozoin formation have variously included protein-mediated or enzyme-catalysed mechanisms, autocatalysis and lipid-mediated processes.[34-38]

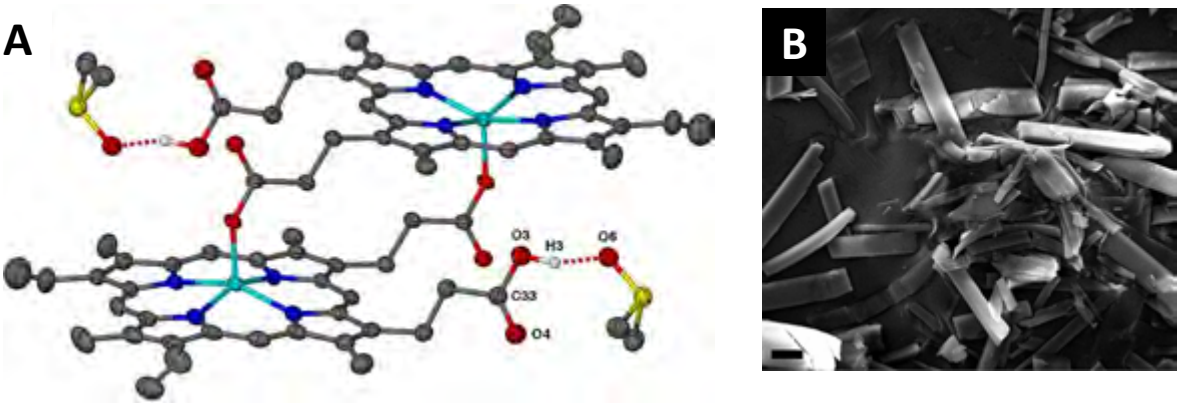

Figure 1.8. *(A) The μ-propionato dimer reported by Gildenhuys et al. as the symmetrical repeating unit of β-haematin as a DMSO solvate. Ellipsoids have been drawn at 50% probability. Atom colours are grey (C), white (H), blue (N), red (O), cyan (Fe) and yellow (S). All other hydrogen atoms as well as the included DMSO molecules that do not participate in hydrogen bonding have been removed for clarity. (B) SEM micrograph of crystals of the β-haematin DMSO solvate grown in the presence of chloroquine. The scale bar (bottom left) represents 20 μm. Reproduced with permission from Gildenhuys et al.,* J. Am. Chem. Soc.*, 2013,* ***135****, 1037. Copyright 2013 American Chemical Society.*

Lipid-mediated theories of haemozoin formation have enjoyed recent success. It was first suggested in 1995 that phospholipids may be associated with haemozoin formation and that contaminating phospholipids were most likely the source of the heat-stable, protease-resistant "autocatalytic" behaviour of the haemozoin extracts previously observed.[39,40] It was later shown that chloroform extracts of parasite-infected erythrocyte lysates showed approximately 70% of the proposed Fe(III)PPIX "polymerising activity" and this activity was chiefly attributed to cholesterol, neutral lipids (glycerolipids) and fatty acids.[41] Fitch et al. suggested that the lipids act by solubilising Fe(III)PPIX to facilitate haemozoin formation.[41]

Subsequently, Jackson et al. used fluorescence and electron microscopy to identify particles ranging over a few hundred nanometres in size that were in intimate association with the digestive vacuole and were shown to be composed of diacylglycerols and triacylglycerols (Figure 1.9A).[42] Further evidence was provided by Coppens and Vielemeyer who discovered haemozoin crystals enveloped by these "neutral lipid bodies" inside the digestive vacuole of *P. falciparum* (Figure 1.9B).[43] Following purification of haemozoin, Pisciotta et al. identified mono- and diacylglycerols as well as various polar lipids in close association with the crystals.[44] The authors proposed a "reconstituted neutral lipid blend" which was found to be an efficient mediator of β-haematin.[44] They suggested that neutral lipid bodies are transient repositories of lipophilic free Fe(III)PPIX, concentrating it while promoting haemozoin formation at the surface where acidic conditions favour lipid-mediated biocrystallisation.[44]

Taken together, these observations have shifted the focus of the intracellular microenvironment of Fe(III)PPIX biocrystallisation and its concomitant inhibition by quinoline antimalarials from a polar aqueous to a non-polar neutral lipid environment that is able to lower the activation energy required for efficient haemozoin formation.[45]

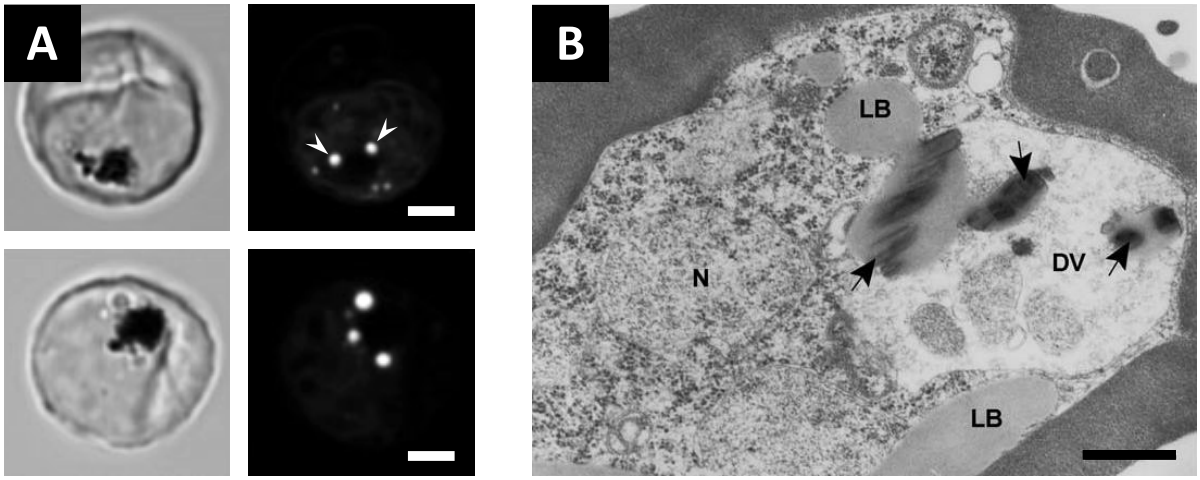

Figure 1.9. *Micrographs showing the association between lipid bodies and haemozoin in* P. falciparum*. (A) Schizont-infected erythrocytes examined by confocal microscopy, with Nile Red-illuminated images on the right. The most intense spots of fluorescence intensity are indicated by arrow heads in the upper image. Scale bars represent 2 µm. Reproduced from Jackson et al.,* Mol. Microbiol.*, 2004, **54**, 109 with permission from John Wiley & Sons. (B) Formation of haemozoin within lipid bodies (marked by black arrows) is evident when samples are fixed with malachite green. The scale bar represents 0.5 µm. Reproduced from Coppens et al.,* Int. J. Parasitol.*, 2005, **35**, 597 with permission from Elsevier.*

Most recently, Kapishnikov et al. have applied cryogenic soft X-ray tomography and three-dimensional electron microscopy to address the location and orientation of haemozoin within the digestive vacuole. They have shown that haemozoin crystals nucleate in a specific manner at the inner surface of the digestive vacuole, with crystallisation occurring in the aqueous rather than in the lipid phase. They argue that their data rule out the possibility of haemozoin crystals being nucleated within, or on the surfaces of, lipid nanospheres.[46,47]

1.3.3. Lipid metabolism during the intraerythrocytic life cycle

A significant feature of intraerythrocytic *P. falciparum* is the dramatic increase in the total lipid content of the infected erythrocyte over the 48-hour life cycle, despite the fact that lipid metabolism in the uninfected erythrocyte is almost non-existent.[48-50] This reflects the parasite's ability to orchestrate a vast array of lipid-dependent processes in a stage-dependent manner, ranging from intracellular signalling and protein trafficking to membrane biogenesis.[51]

Recently, Gulati et al. surveyed lipid species and abundances over the 48-hour intraerythrocytic life cycle.[51] Phospholipids were the major class detected, with phosphatidylcholine and phosphatidylethanolamine together accounting for half of the total lipid content in the infected erythrocyte.[51] These phospholipids mainly serve a structural role, especially as the chief constituents of membranes. Over the 48-hour developmental cycle, the total amount of phospholipid remained relatively constant.[51]

The remaining half of the lipid content was divided between sphingolipids and glycerolipids (neutral lipids).[51] Sphingolipid levels decreased over the course of intraerythrocytic development. However, the amount of sphingomyelin, the third most abundant lipid in the parasitised erythrocyte which aids in the biogenesis and maintenance of the tubovesicular network, remained static throughout the cycle. Sphingomyelin can also serve as a reservoir for the production of ceramides via its hydrolysis, with ceramides serving as potent second messengers that regulate a host of diverse processes within *P. falciparum*.[51]

Intraerythrocytic parasites possess two major neutral lipid species, both of which are virtually non-existent in the uninfected erythrocyte and which showed a dramatic increase in abundance over the 48 hours.[51] Diacylglycerols are potent second messengers and serve as a precursor for phospholipids and triacylglycerols. Triacylglycerols are themselves packaged into lipid bodies that may be responsible for sequestering free fatty acids.[51]

In mammalian cells lipid bodies typically serve as highly reduced stores of oxidisable energy.[43] However, malaria parasites have little to no capacity for the oxidative degradation of fatty acids, implying that triacylglycerols must be used for purposes other than energy storage during intraerythrocytic growth.[52] It is unlikely that *P. falciparum* uses triacylglycerols as a reservoir of fatty acids for phospholipid synthesis since lipid bodies are not observed in ring-stage parasites which themselves undergo massive membrane biogenesis.[52] It has been observed that triacylglycerol degradation becomes active during the late schizont phase, suggesting that triacylglycerol metabolism facilitates merozoite maturation[51] or that it is involved in parasite egress from the host cell.[43] As described in Section 1.3.2, these lipid bodies have been observed in intimate contact with the digestive vacuole and haemozoin; hence, they may play a role in Fe(III)PPIX detoxification.[42,44]

Finally, during intraerythrocytic development of *P. falciparum*, the composition of the erythrocyte plasma membrane is also strikingly altered.[53] Since erythrocytes have a limited capacity for lipid synthesis and metabolism, these alterations must occur as a result of parasite-directed metabolism of erythrocyte lipids and/or trafficking of lipids between the parasite and the erythrocyte membrane.[53]

1.3.4. Regulation of pH within the malaria parasite

The regulation of pH plays an important role in the pathophysiology of *P. falciparum*, both in the exploitation of the host erythrocyte and in the response to various antimalarials (Section 1.6.1.). Two proton pumps are responsible for the acidification of the digestive vacuole. These are located on the digestive vacuole membrane and comprise a V-type H^+-ATPase and a H^+-pyrophosphatase, the latter of which couples the hydrolysis of the phosphoanhydride bond of pyrophosphate to the influx of protons into the vacuole.[54] These proton pumps act concurrently to maintain a low internal pH in the digestive vacuole.[54]

The pH of the digestive vacuole and the cytosol in *P. falciparum* have been of great interest; however, these measurements have not been straightforward and have been the subject of much controversy.[55] Most estimates of steady-state vacuolar and cytosolic pH values of *P. falciparum* have relied on quantitative fluorimetric techniques. Only recently have more reliable pH determinations in *P. falciparum* been achieved. These employed parasite expression of the ratiometric pH-dependent fluorescent protein pHluorin, which was localised to the digestive vacuole.[56] Single-cell confocal measurements gave pH 5.18 ± 0.05 with no significant difference recorded between chloroquine-sensitive and chloroquine-resistant strains.[56] These were corroborated by a thorough study involving dextran-linked, pH sensitive fluorescent dyes which also concluded that digestive vacuole pH does not play a primary role in chloroquine resistance.[57]

Metabolic and biosynthetic activity at the trophozoite stage is particularly vigorous. The parasite is wholly reliant on glycolysis as its energy source and generates a substantial intracellular lactic acid load.[58] Thus the parasite requires an effective means of extruding H^+ to maintain its cytosolic pH. There is compelling evidence for another V-type H^+-ATPase in the parasite's plasma membrane which serves as the major route for the efflux of H^+ ions.[58] The same investigators measured the cytosolic pH of *P. falciparum* with pHluorin and recorded a steady-state pH of 7.15 ± 0.07 for trophozoites, again with no significant difference between chloroquine-sensitive and chloroquine-resistant strains.[58]

Hydrogen peroxide released during haemoglobin degradation has been shown to inhibit the digestive vacuolar H^+-ATPase, disrupting pH regulation in the parasite.[59] Furthermore, it has been observed that moderate exposure to light causes irreversible acidification of the parasite cytosol by as much as a whole pH unit.[60] The implications of these observations are important in the context of live-cell imaging of *P. falciparum* which will form an important part of this work.

1.4. Antimalarial chemotherapy, resistance and drug discovery

1.4.1. Current efforts to prevent and treat malaria

There are a number of strategies to prevent the transmission of malaria. Eradicating mosquito populations and preventing mosquito bites by using insecticide-treated nets have been highly effective.[1,2] The use of sterile male insects has emerged as an alternative vector control method although this has not yet been used in the field.[61] Malaria vaccines, which ensure a high level of protection for a sustained period, are an area of intensive research.[62]

Prophylactic drugs are able to prevent infection in travellers to malaria-endemic areas. In areas of chloroquine resistance, chemoprophylactics such as doxycycline and atovaquone-proguanil are generally well-tolerated and may be used.[63] Unfortunately, the use of prophylaxis is not practical for residents of these areas due to the cost of the drugs as well as negative side-effects resulting from long-term use. Furthermore, extensive use of prophylactic drugs may encourage the development of drug tolerance and ultimately drug resistance in the parasite.

Once infected with malaria, however, patients can expect to make a full recovery if treated properly. As a result, antimalarials are widely used as curative agents. The alkaloid quinine has been used for centuries and was the first effective drug used in the treatment of malaria. Since the 1940s, quinine has been replaced by alternative drugs such as chloroquine, mefloquine and amodiaquine, many of which are inexpensive. Unfortunately, resistance to these drugs has developed, or is developing rapidly, resulting in increased morbidity.

Currently, the World Health Organisation recommends artemisinin-based combination therapies as the preferred treatment for malaria.[1] These usually comprise a derivative of the sesquiterpene endoperoxide artemisinin in conjunction with another non-artemisinin-based antimalarial such as amodiaquine, mefloquine or lumefantrine. These “cocktails” are generally effective and well-tolerated in patients. However, resistance to artemisinins has now been reported in five countries in Southeast Asia.[1]

1.4.2. A brief history of the quinoline antimalarials

It is remarkable that two natural products, quinine and artemisinin (Figure 1.10), which were used to treat malaria for centuries before the aetiology or the pathogenesis of the disease was understood, remain cornerstones of contemporary antimalarial treatment. Following the isolation of quinine, malaria was probably the first disease treated by a pure compound.[64]

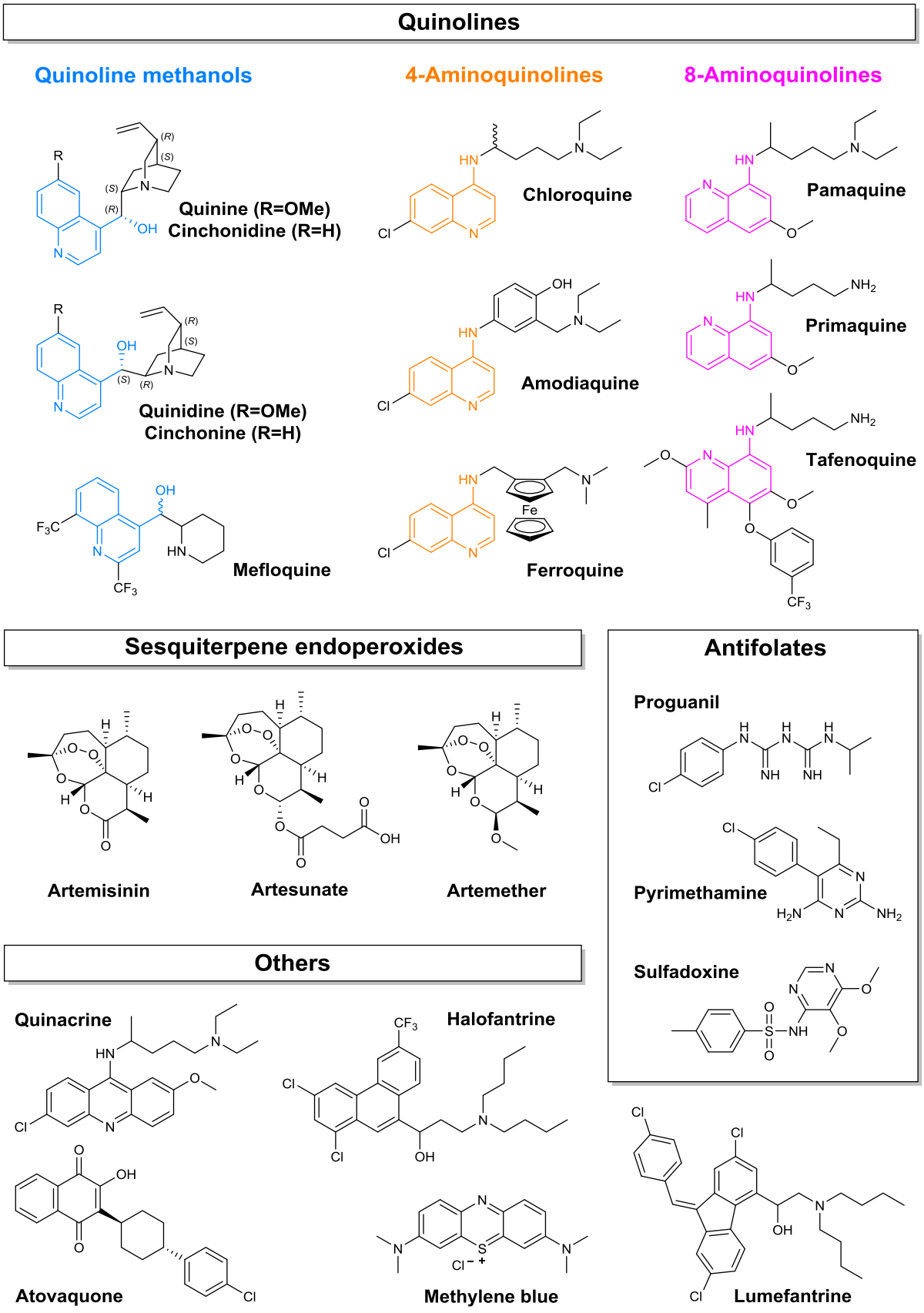

Figure 1.10. *Representative compounds of the most important classes of antimalarial agents.*

Malaria-like febrile illnesses have been described since the time of Hippocrates and were associated with marshes and swamps. It was not until 1880 that the French physician, Charles Louis Alphonse Laveran, discovered that the cause of malaria is a protozoan, having observed the parasites in a blood smear taken from a patient who had just died of malaria.[65] Mosquitoes were incriminated as the vectors of the disease, first for avian malaria by Ronald Ross in 1897 and then for human malaria by Giovanni Battista Grassi and others between 1898 and 1900.[65]

Quinine occurs naturally in the bark of trees belonging to the genus *Cinchona*, originally found in the high altitudes of South America. According to one account, the Native Peruvians used it while working in the cold streams in Spanish-owned mines to stop shivering. This effect was probably the result of quinine's direct effect on skeletal muscle and neuromuscular junctions.[64] Some physicians and Jesuit priests in Peru suspected that concoctions of the bark might be able to stop the shivering associated with attacks of febrile illnesses. They tried the bark of the "fever tree" on malarial patients and found that their feverish symptoms were miraculously relieved.[64]

Prior to the isolation of quinine, the bark was administered as a suspension in wine or spirits to offset its bitterness; this recipe probably evolved into the gin and tonic drink.[64] In 1820, two French chemists, Pierre Pelletier and Joseph Caventou, isolated the major alkaloids quinine and cinchonine from *Cinchona* bark.[66] Their respective diastereomers, quinidine and cinchonine, are present in smaller proportions. The term quinine comes from "quina-quina", the name which the Native Peruvians gave to the bark which means "medicine of medicines" or "bark of barks".[67] Within a year, French physicians were using pure quinine to treat patients with intermittent fever and, from the mid-19th century to the 1940s, quinine became the standard treatment for such fevers throughout the world.[64] Consequently, it has been described as "a drug that has probably benefited more people than any other in the combat of infectious disease".[68]

These early investigations into the chemistry of quinine coincided with a revolution in synthetic organic chemistry. In 1856, William Henry Perkin, a young English chemist, set out to synthesise quinine but instead serendipitously created mauveine, the first synthetic textile dye that did not wash off in water.[64] The new dye industry promoted advancement in medicine as some of these dyes were used to stain microbes under the microscope. Paul Ehrlich (1854-1915), a German physician and scientist, noticed that methylene blue (Figure 1.10) was particularly effective in staining malaria parasites. Reasoning that the parasite might be poisoned by the uptake of the dye, he used this molecule to cure two patients of malaria in 1891.[64]

Subsequently, Bayer, a leading dye company, assembled a team to develop new antimalarials using methylene blue as a prototype. In 1925 they developed pamaquine, an 8-aminoquinoline, and, later, quinacrine, an acridine derivative (Figure 1.10).[69] In 1934, a compound called

"resochin" was developed but it was thought to be too toxic. During World War II, the Japanese took over the Indonesian island of Java and cut off the world's main source of quinine, the *Cinchona* plantations on the island which had been cultivated by Dutch colonials. As part of the war effort, American, British and Australian scientists cooperated in a large-scale attempt to develop new synthetic antimalarials. Interest was rekindled in resochin, which was renamed chloroquine.[64]

Chloroquine has since proved to be the most effective, and arguably the most important, antimalarial in history. It was initially highly effective with only few adverse side-effects and was relatively inexpensive, making it an ideal chemotherapeutic drug. Consequently, it was the main antimalarial in the World Health Organisation's Global Malaria Eradication Programme between the 1950s and 1960s and, although somewhat overshadowed by the widespread spraying of the insecticide DDT, chemoprophylaxis with chloroquine tablets or chloroquine-medicated salt (introduced in the 1950s in Brazil) was an important supplementary component of eradication and control programmes.[70] However, this extensive use of chloroquine probably contributed to the advent of resistance in *P. falciparum* in the 1960s.

Despite challenges posed by resistance, the quinolines have formed the cornerstone of antimalarial chemotherapeutic development. Most of the quinolines are believed to target the intraerythrocytic stage of the parasite's life cycle by inhibiting haemozoin formation, leading to a toxic accumulation of Fe(III)PPIX that eventually poisons the parasite (Section 1.5).

1.4.3. Involvement of membrane transporters in *P. falciparum* resistance

For several decades, chloroquine remained the gold standard for the treatment of malaria. Unfortunately, massive worldwide use beginning in the late 1940s was followed two decades later by reports of chloroquine-resistant strains of *P. falciparum* in Southeast Asia and South America. Today, chloroquine resistance has spread to the vast majority of malaria-endemic areas, rendering this drug increasingly ineffective. The fact that chloroquine resistance took over two decades to develop, despite extensive use of the drug, suggests that mutations in several genes of the parasite are required to produce the resistant phenotype.[71] Varying clinical responsiveness also affects many other antimalarials such as quinine and mefloquine which are sometimes used as a second-line treatment for chloroquine-resistant strains. Disturbingly, resistance to artemisinin-combination therapies has now been reported, lending even more urgency to the search for novel antimalarials.[71]

It was soon identified that chloroquine resistance was associated with an efflux of the drug in resistant phenotypes. Consequently, research in the resistance mechanisms has centred on

parasite membrane transporters as they are responsible for trafficking diverse substrates in and out of the parasite and the host cell.[72] In particular, the *P. falciparum* chloroquine-resistance transporter (PfCRT) and *P. falciparum* multidrug resistance transporter (PfMDR1) have been implicated. More recently, the multidrug resistance-associated protein (PfMRP1) has also been associated with changes in susceptibility to chloroquine and quinine.[71]

In 1987 Krogstad and colleagues identified that chloroquine flows out of chloroquine-resistant parasites much faster than chloroquine-sensitive parasites by a route that can be blocked by verapamil, a general efflux pump inhibitor.[73] This suggested the existence of a membrane protein that acts as either a channel or a carrier for chloroquine. In pioneering work reported in 2000, PfCRT was identified as the main determinant of chloroquine resistance.[74]

PfCRT comprises 424 amino acids and ten predicted trans-membrane domains and is localised in the digestive vacuole membrane (Figure 1.11).[71] As mentioned above, the digestive vacuole is suspected to be the site of action for several antimalarials including chloroquine, quinine and quinidine where they are thought to interfere with haemozoin biocrystallisation.

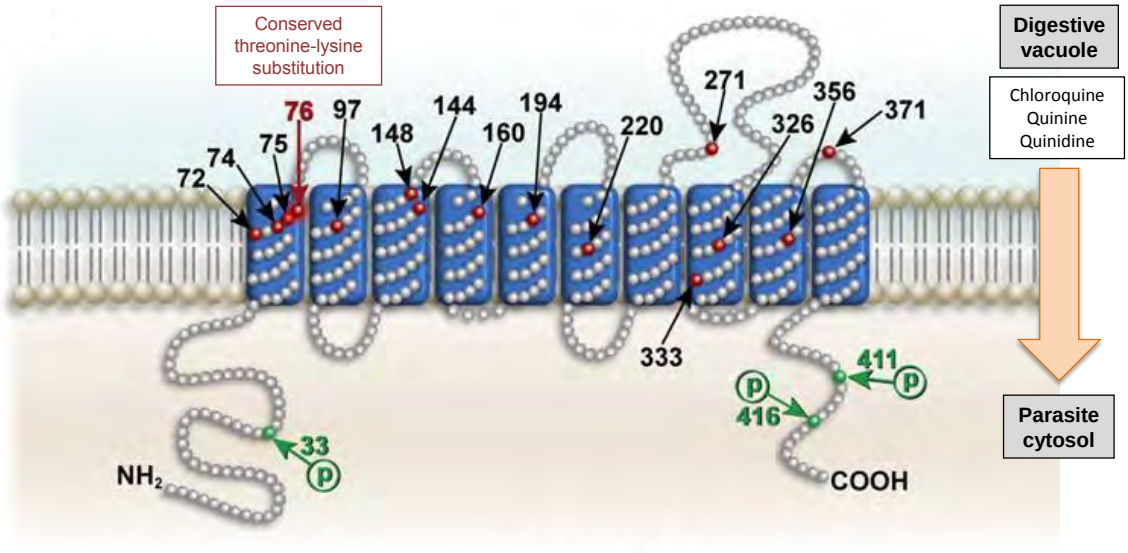

Figure 1.11. *Topology and function of PfCRT. Black arrows highlight polymorphic amino acids. The conserved threonine-lysine substitution at position 76, found in chloroquine-resistant parasites, is indicated in red. Residues that can be phosphorylated are highlighted in green. The orange arrow indicates that PfCRT transports a variety of quinoline drugs out of the digestive vacuole. Verapamil inhibits PfCRT-mediated drug transport. Reproduced from Sanchez et al.,* Int. J. Parasitol.*, 2010, **40**, 1109 with permission from Elsevier.*

Chloroquine-resistant strains have originated in at least six different geographic regions with different sets of polymorphisms in the *pfcrt* gene of *P. falciparum*. All alleles feature the replacement of a lysine residue by a threonine residue at position 76.[74] Since reduced chloroquine accumulation is linked with PfCRT polymorphisms in resistant strains, it is suspected that PfCRT controls the access of chloroquine to its target. There has been debate as to the nature of the natural substrate for PfCRT which is thought to be small amino acids, possibly those from haemoglobin catabolism.[71] Recently, PfCRT has been characterised as a H^+-coupled polyspecific nutrient and drug exporter.[75] However, there is a fitness cost associated with the mutations and chloroquine-sensitive strains eventually outcompete resistant phenotypes in the field.[71]

The other transporter protein implicated in chloroquine resistance is the *P. falciparum* multidrug resistance transporter (PfMDR1, Figure 1.12). In mammalian cancer cells, drug resistance frequently arises from the presence of an overexpressed P-glycoprotein. This is an ATP-binding cassette (ABC) transporter capable of expelling a wide range of structurally and functionally diverse substrates, also in a verapamil-dependent manner.[71] Consequently, it was thought that polymorphisms in the *P. falciparum* homologues, later termed PfMDR1 or Pgh-1, may be linked to chloroquine resistance as well as to susceptibility to other quinolines.[71]

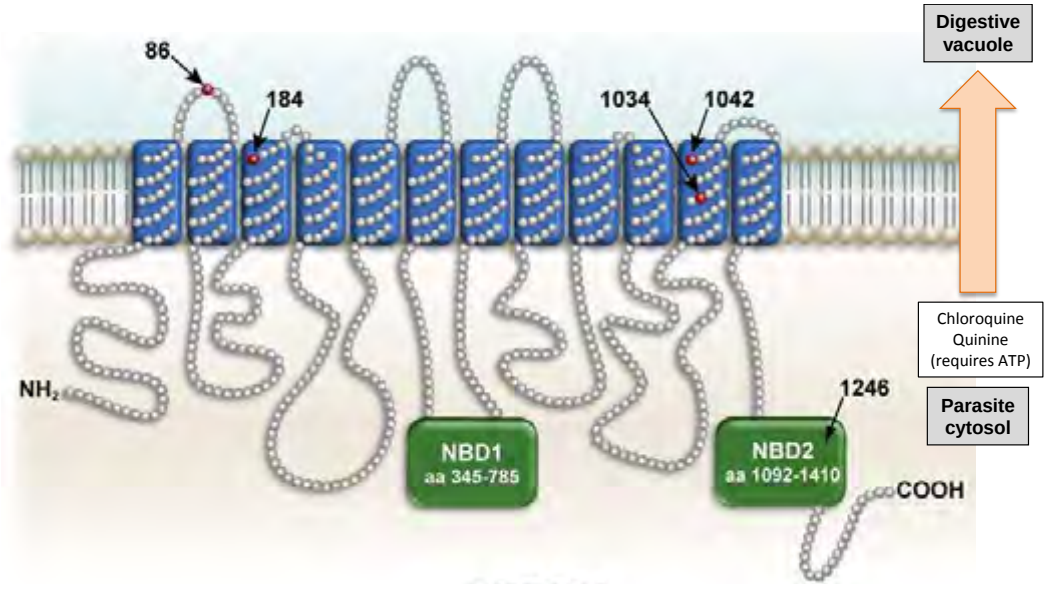

Figure 1.12. *Topology and function of PfMDR1. Black arrows highlight polymorphic amino acids with altered drug responsiveness in* P. falciparum*. The orange arrow indicates the direction of transport of substrates including chloroquine, quinine, mefloquine and artemisinin from cytoplasm* towards *the digestive vacuole. Nucleotide binding domains, represented by NBD1 and NBD2, are the sites of ATP binding. Reproduced from Sanchez et al.,* Int. J. Parasitol.*, 2010, **40**, 1109 with permission from Elsevier.*

Amplification of the gene is indeed associated with in vitro resistance to quinine, mefloquine and halofantrine in *P. falciparum*.[76] However, PfMDR1 is found in the digestive vacuole membrane with its ATP-binding domains facing the cytoplasm (NBD1 and NBD2 in Figure 1.12), meaning that transport is directed *inwards* to the digestive vacuole.[77] This counterintuitive observation is the opposite of mammalian cells in which P-glycoprotein-mediated export is directed out of the cell.[77] In comparison to mammalian cells, little PfMDR1 is expressed in the parasite plasma membrane. While polymorphisms within PfMDR1 can contribute to resistance to chloroquine and related antimalarials depending on the genetic background of the parasite strain, the mechanism of action of this membrane transporter remains unclear.[71]

P. falciparum multidrug resistance-associated protein (PfMRP1) was first identified in 2004 (Figure 1.13).[78] PfMRP1 has been shown to localise to the parasite plasma membrane and to membrane-bound vesicles during intraerythrocytic stages.[79,80] Disrupting PfMRP1 expression in *P. falciparum* under normal culture conditions resulted in parasites that could not grow to a parasitaemia higher than 5%, possibly because of lower efficiency in removing toxic metabolites.[80] These parasites also accumulated more radiolabelled glutathione, chloroquine and quinine and became more sensitive to several antimalarials, including chloroquine, quinine and artemisinin.[80] This indicates that PfMRP1 most likely plays a role in the efflux of glutathione, chloroquine and quinine from the parasite.[81]

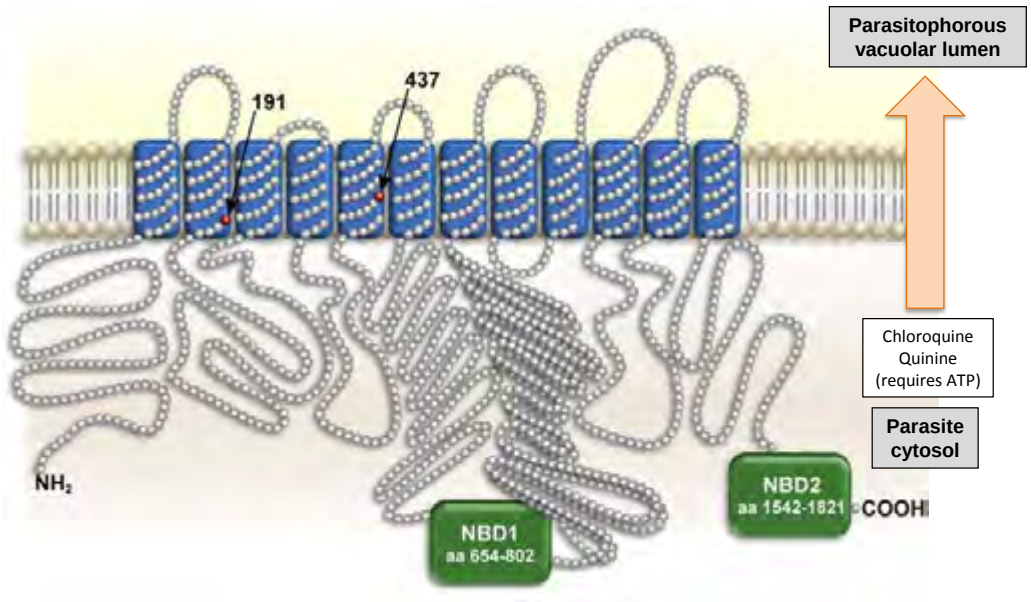

Figure 1.13. *Topology and function of PfMRP1. Black arrows highlight polymorphic amino acids. The orange arrow indicates the direction of transport of substrates including chloroquine and quinine out of the parasite cytosol. Nucleotide binding domains, represented by NBD1 and NBD2, are the sites of ATP binding. Reproduced from Sanchez et al.,* Int. J. Parasitol.*, 2010, **40**, 1109 with permission from Elsevier.*

1.4.4. Aspects of contemporary antimalarial drug discovery

While improved measures in the prevention and treatment of malaria have led to decreased mortality in recent years, the resistance of *P. falciparum* to quinoline antimalarials and newer artemisinin-combination therapies provides an urgent stimulus to develop novel antimalarial chemotherapies. Typically, antimalarial drug discovery takes two forms. A screening method, in which hit compounds are identified, usually results in the synthesis of libraries of derivatives which are tested for their activity against *P. falciparum* in order to develop structure-activity relationship models. Alternatively, rational drug design requires a detailed understanding of both the drug target and the antimalarial pharmacophore. This latter method is particularly challenging. Indeed, most current antimalarial agents were not developed by rational design but followed the serendipitous discovery of natural products (quinine and artemisinin) or structural analogues of these molecules (chloroquine).

Antimalarial drug discovery has been greatly aided by the development of in vitro culturing techniques for *P. falciparum* in human erythrocytes. This has become a vital method to determine the activities of potentially therapeutic compounds. First developed by Trager and Jensen in 1976, it has since been refined to optimise oxygen pressure, nutrient availability and temperature.[82] In order to determine dose-response curves to generate a 50% inhibitory concentration (IC_{50}) of a potentially therapeutic compound, parasite viability is commonly quantified using the lactate dehydrogenase assay which was developed by Makler and colleagues. This enzyme assay exploits a correlation between parasite lactate dehydrogenase activity and parasitaemia.[83]

Despite these techniques, the challenges associated with antimalarial drug discovery and development mean that there have been no new classes of antimalarials introduced for two decades. This has motivated the development of improved methods for identifying active compounds. The construction of large compound libraries and increased knowledge of drug targets have encouraged parallel advances in high-throughput screening. On the one hand, phenotypic-based screening methods measure the effects of a compound on cell or tissue, such as cell viability. On the other hand, target-based approaches include screening compounds for their ability to inhibit β-haematin formation, for example.

Determining β-haematin inhibition demands assays which are efficient and mimic biological environments appropriately. The first β-haematin inhibition assay was reported in 1994.[84] It was a qualitative, acetate-based assay which exploited infrared spectroscopy to determine the presence of crystallised Fe(III)PPIX via characteristic peaks, i.e. 1660 cm^{-1} and 1207 cm^{-1}.[84]

Other investigators developed quantitative techniques using radiolabelled haematin. However, this is not ideal as it requires special materials and skills and is often expensive.[85]

The acetate-based assay described above was improved when the amount of β-haematin formed was quantified by reacting the remaining Fe(III)PPIX with aqueous pyridine. This selectively forms a low-spin bis-pyridyl complex with unreacted Fe(III)PPIX but not with β-haematin. (Figure 1.14).[86] In the presence of pyridine, the Soret band of Fe(III)PPIX increases in intensity which is indicative of monomerisation and shifts from 389 to 404 nm as a result of the change in spin state. The absorbance is thus directly proportional to the concentration of uncrystallised haematin. Pyridine is also likely to displace other coordinating substances, reducing interference in this system.

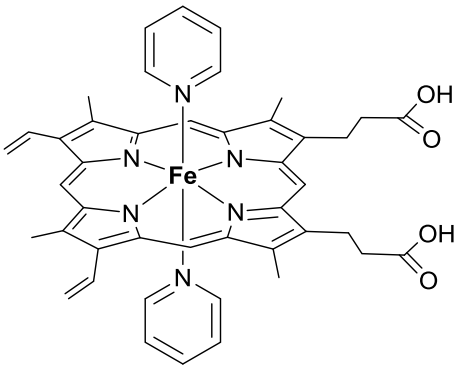

Figure 1.14. *The low-spin bis-pyridyl complex used to quantify the amount of unreacted Fe(III)PPIX in colourimetric β-haematin inhibition assays.*

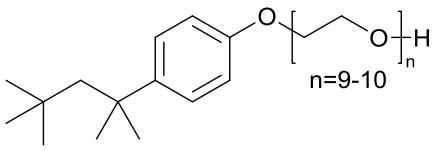

Figure 1.15. *The structure of NP-40, the detergent used in an assay for β-haematin inhibition.*

As described in Section 1.3.2, it has been shown that lipids are implicated in haemozoin formation. Replacing the high concentrations of acetate with lipids as mediators of β-haematin formation meant that milder conditions that were more biologically-relevant could be used. However, lipids are not ideal for high-throughput screening approaches and so studies were done to find suitable, inexpensive substitutes. Detergents are surfactants that mimic the amphiphilic nature of lipids; that is, they are molecules with both hydrophilic and hydrophobic regions. Consequently, a number of detergents were screened for their capacity to mediate β-haematin formation and, in 2010, a detergent-mediated assay was reported in which NP-40, a neutral non-denaturing detergent (Figure 1.15), was determined to be the best mimic.[87] NP-40 not only generated comparable yields of β-haematin compared to a neutral lipid blend, but also yielded similar IC_{50} values for β-haematin inhibition in the presence of chloroquine and amodiaquine. This NP-40 detergent-mediated assay for β-haematin inhibition has formed the basis of several high-throughput screening efforts to find novel antimalarial chemotypes.[88,89]

1.5. Interactions between the quinoline antimalarials and Fe(III)PPIX

1.5.1. Recent developments in understanding haemozoin inhibition

It was first proposed by Macomber and colleagues in 1967,[90] and later elaborated upon by Chou et al. in 1980,[91] that Fe(III)PPIX is the molecular drug target of various quinoline antimalarials. Since then, increasing evidence has shown that the interactions of these drugs with Fe(III)PPIX indeed lie at the heart of their antimalarial activity.[92] This appears to involve inhibition of the incorporation of Fe(III)PPIX into haemozoin as it has been shown that these drugs inhibit β-haematin formation under abiotic conditions.[84] This means that inhibition must occur by direct interaction between the drugs and Fe(III)PPIX, verifying that the haemozoin biocrystallisation pathway is indeed the likely target of these drugs.

There are two prevailing theories of haemozoin inhibition. The first is that the quinoline antimalarials adsorb to the fastest-growing face of the haemozoin crystal, "capping" it and preventing further crystal growth. The second theory relies on the formation of stable complexes between the quinoline antimalarials and free Fe(III)PPIX that also prevents the incorporation of the metalloporphyrin into the growing crystal.

Pagola et al. were the first to propose that chloroquine adsorbs to the fastest-growing faces of haemozoin crystals.[27] The fast-growing face of the crystals exhibit grooves that expose the unligated porphyrin face and propionic acid side chains of Fe(III)PPIX molecules. The structure of the adsorbed chloroquine-haemozoin complex was subsequently proposed by Buller et al. in which four specific intermolecular interactions between chloroquine and Fe(III)PPIX molecules were identified to stabilise the complex.[93] Gildenhuys et al. have recently provided kinetic evidence that supports the adsorption of chloroquine and quinidine onto the surface of haemozoin crystals.[32] They found that the reduced rate of formation of β-haematin in the presence of low drug concentrations was consistent with a drug adsorption process. At higher drug concentrations, precipitation of quinoline-Fe(III)PPIX complexes caused a reduction in the yield of β-haematin.[35] Most recently, Olafson et al. have directly imaged inhibition of β-haematin crystal growth by chloroquine using atomic-force microscopy.[94]

The second proposed mechanism of inhibition by quinoline antimalarials is that of drug-Fe(III)PPIX complex formation. These complexes have been suggested to bind to Fe(III)PPIX in a form that no longer allows its incorporation into haemozoin, probably by increasing the solubility of the metalloporphyrin. Additionally, these complexes cause deleterious effects on *P. falciparum*. The complex between chloroquine and Fe(III)PPIX enhances the lytic effects on

cells that have been observed with Fe(III)PPIX alone.[95,96] Quinine, quinidine and chloroquine all form stable complexes with Fe(III)PPIX in the solution phase, lending support to this hypothesis (Section 1.5.2). Furthermore, the single crystal structures of Fe(III)PPIX complexes have been elucidated for quinine and quinidine, as well as for the related antimalarials mefloquine and halofantrine (Section 1.5.3).

Regardless of which mechanism is responsible for the inhibition of haemozoin formation by these antimalarials, a recent study reported that a dose-dependent increase in free Fe(III)PPIX in *P. falciparum* was measured upon chloroquine treatment that was found to correlate with a decrease in parasite growth.[97] Indeed, the curve representing the percentage of "free" Fe(III)PPIX was found to cross the parasite survival curve at approximately the IC_{50} of chloroquine (Figure 1.16).

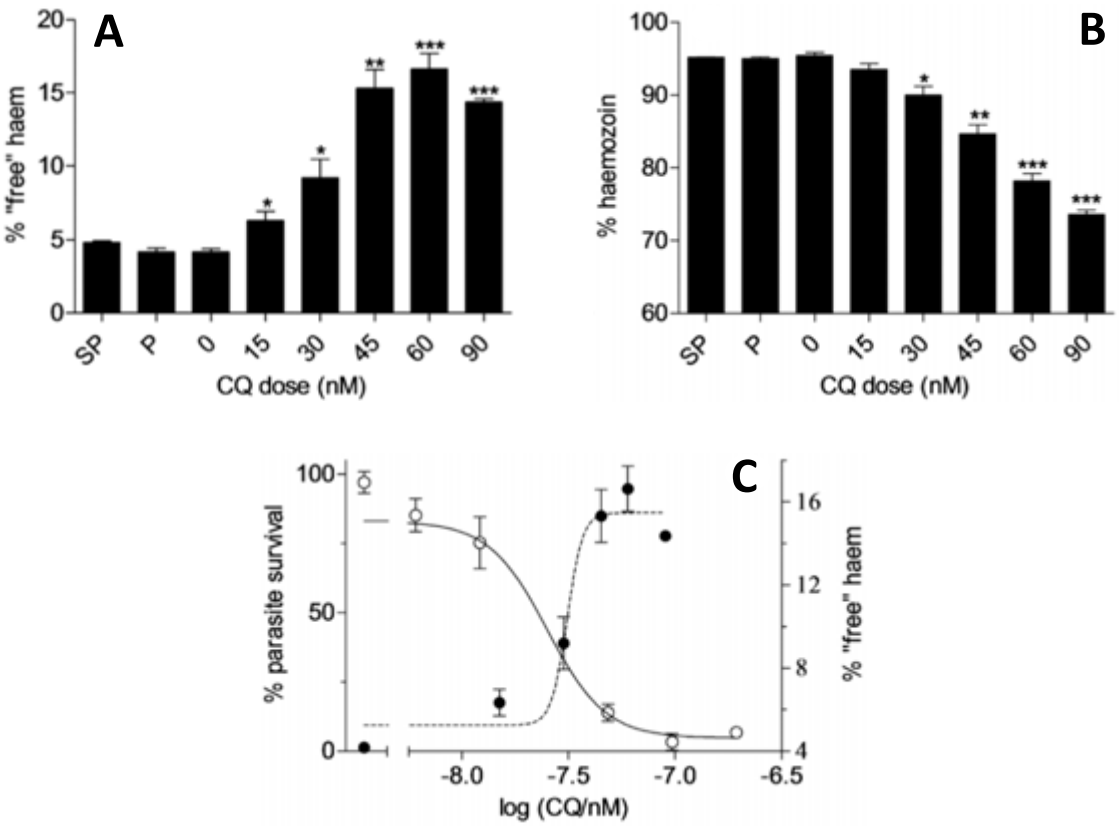

Figure 1.16. *Fraction of total Fe(III)PPIX present as (A) "free" Fe(III)PPIX and (B) haemozoin. Asterisks indicate statistical significance relative to the control: *P < 0.05; **P < 0.01; ***P < 0.001, n = 3. "P" represents pyrimethamine and "SP" represents sulfadoxine/pyrimethamine. (C) Parasite survival curve (open circles, left axis) determined using the lactate dehydrogenase assay and percentage free Fe(III)PPIX (closed circles, right axis) as a function of chloroquine (CQ) dose. Adapted from Combrinck et al.,* ACS Chem. Biol.*, 2013, **8**, 133. Copyright 2013 American Chemical Society.*

Furthermore, a single-dose treatment of quinine as well as mefloquine, amodiaquine, artesunate and lumefantrine, well above their IC_{50} concentrations, were all shown to correspond to an increase in free Fe(III)PPIX and a decrease in the amount of haemozoin formed.[97] On the other hand, this was shown not to be the case for pyrimethamine and sulfadoxine which are known to target the folate synthesis pathway.[97] This study provides direct evidence in support of the haemozoin inhibition hypothesis for the mechanism of action of chloroquine and other quinoline antimalarials, including quinine.

The cytotoxic effects of free Fe(III)PPIX are likely compounded by the high concentrations of quinoline antimalarials that accumulate in the parasite. It has been shown that degradation of Fe(III)PPIX by both glutathione[98] and hydrogen peroxide[99] are inhibited by chloroquine, although this has not been established in vivo. It has consequently been proposed that these large concentrations of free Fe(III)PPIX associate with membranes, increasing their permeability and damaging the integrity of the parasite.[98,99] A redistribution of Fe(III)PPIX iron has been detected in the cytoplasm of *P. falciparum* following treatment with chloroquine, in a region possibly corresponding to the endoplasmic reticulum.[97]

1.5.2. Interactions of the quinoline antimalarials with Fe(III)PPIX in solution

The differences between the quinoline methanol and 4-aminoquinoline antimalarials that are examined in this study are possibly best exemplified by their respective interactions with Fe(III)PPIX in solution. Despite structural similarities, the quinoline methanols and the 4-aminoquinolines share very different modes of association with Fe(III)PPIX.

Formation of a complex between the archetypal 4-aminoquinoline, chloroquine, and Fe(III)PPIX was first reported in the 1960s by Cohen, Phifer and Yielding.[100] This observation was based on changes in the absorption spectrum of Fe(III)PPIX upon addition of chloroquine. In aqueous solution, such as the phosphate buffer used in their study, significant changes are seen in the shape of the Soret band of the porphyrin with only minor changes in its intensity. These can be interpreted to give useful information about the interaction between the two molecules.

However, in mixed aqueous solution and, to a lesser extent, in pure organic solvents, the Soret band of Fe(III)PPIX exhibits a considerable hypochromic effect (that is, a decrease in absorbance) upon interaction with chloroquine, quinine and related antimalarials (Figure 1.17).[92] This hypochromic effect is not accompanied by a shift in wavelength and appears to be largely masked in purely aqueous medium on account of the fact that Fe(III)PPIX is essentially dimeric under these conditions which itself gives rise to a large hypochromic effect.[92] Further changes in the spectrum include the apparent disappearance of the Q-band and shifts in the

charge-transfer bands with a significant hyperchromism (that is, an increase in absorbance) at about 600 nm which can also be extremely valuable in detecting and monitoring the interactions. Indeed, in aqueous DMSO and in pure organic solvents, where Fe(III)PPIX is monomeric, the strong quenching of the Soret band can be used to determine association constants.

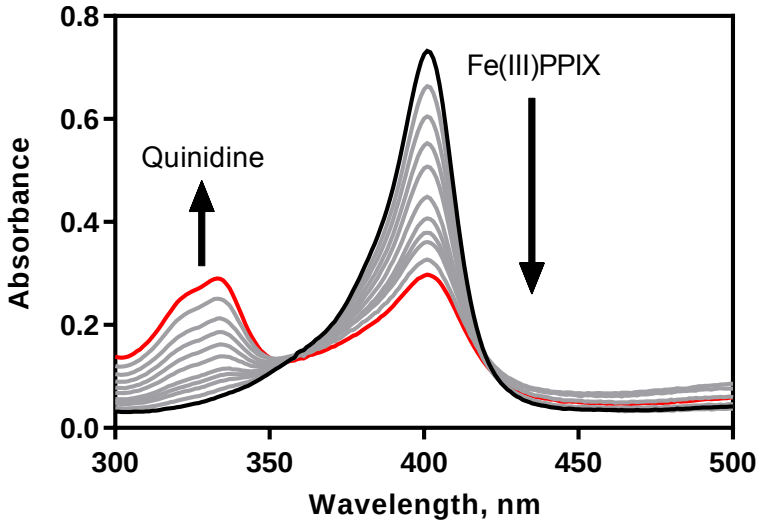

Figure 1.17. *The effects of increasing concentrations of quinidine on the absorption spectrum of Fe(III)PPIX in 40% (v/v) DMSO in 20 mM Hepes, pH 7.5 (25°C). The black trace represents Fe(III)PPIX alone and the red trace indicates the final spectrum after several additions of quinidine (indicated in grey).*

Consequently, 40% DMSO (v/v) buffered at pH 7.5 has proved to be a useful medium for measuring the strength of quinoline-Fe(III)PPIX interactions and for exploring relationships between structure and strength of association with Fe(III)PPIX (Table 1.1).[92] The solvent environment in 40% (v/v) DMSO comprises about 86% water (by mole fraction) and is thus still a reasonable approximation of pure aqueous solution. Association constants between Fe(III)PPIX and some of the quinoline antimalarials relevant to this study are listed in Table 1.1.

Table 1.1. *Association constants with Fe(III)PPIX determined from spectrophotometric titrations in 40% (v/v) DMSO in 20 mM Hepes, pH 7.5 (25°C). Association constants were fitted using a 1:1 binding model and were taken from De Villiers et al.*[101]

Compound	Log *K*
Quinine	4.10 ± 0.02
Quinidine	5.02 ± 0.03
Epiquinine	4.04 ± 0.03
Epiquinidine	4.37 ± 0.02

In mixed aqueous solution these association constants are almost invariably weaker than in pure aqueous solution, while in pure organic solvents they are weaker still.[102] The fact that the strength of the interaction increases enormously with increasing solvent polarity indicates that the hydrophobic effect plays a major role in determining the stability of these complexes.[102] Measured thermodynamic parameters suggest a large loss in flexibility and a high degree of desolvation upon complex formation.[102,103] Free energies of association are largely insensitive to salt concentrations, demonstrating that electrostatic interactions play only a minor role in the stability of these complexes under these conditions.[102]

What evidence is there for the binding stoichiometries of these complexes in the solution state? Previous studies in mixed aqueous solution show that spectrophotometric titrations of quinine and Fe(III)PPIX conform very well to a 1:1 binding model.[103] Casabianca et al. used magnetic susceptibility measurements to show that quinine promotes monomerisation of Fe(III)PPIX while chloroquine promotes the formation of its μ-oxo dimer.[104] In support of the former conclusion, Gildenhuys et al. were able to show coordination of the alkoxide group of quinine and quinidine to the iron centre of Fe(III)PPIX by measuring the bond length by extended X-ray absorption fine structure (EXAFS) spectroscopy.[105] This unequivocally confirmed that coordination of the quinoline methanol compounds to Fe(III)PPIX occurs in non-aqueous aprotic medium via their benzylic alkoxide groups. Existence of the 1:1 complexes was also confirmed by mass spectrometry.[105] While these measurements were made in a non-aqueous medium, this may more closely mimic the site of haemozoin formation in *P. falciparum* which is likely to be associated with a neutral lipid environment.

Meanwhile, for chloroquine, a recent comprehensive study using multiple spectroscopic techniques showed that it does indeed induce μ-oxo dimerisation of Fe(III)PPIX.[106] It was confirmed that chloroquine binds to Fe(III)PPIX with a 1:2 stoichiometry with an aqueous association constant (log K_{obs}) of 13.3 ± 0.2.[106] Furthermore, the interaction of chloroquine and the μ-oxo dimer of Fe(III)PPIX in aqueous solution was modelled using molecular dynamics simulations. Two models of the complex were investigated, one involving chloroquine π-stacked with an unligated porphyrin face of μ-oxo Fe(III)PPIX and the other in which chloroquine was docked between the two porphyrin rings. The feasibility of both models was tested by fitting predicted structures to the observed EXAFS spectrum of the CQ-(μ-oxo Fe(III)PPIX) complex in frozen aqueous solution. The docked model produced better agreement with experimental data, suggesting that this is the more likely structure in aqueous solution (Figure 1.18).[107]

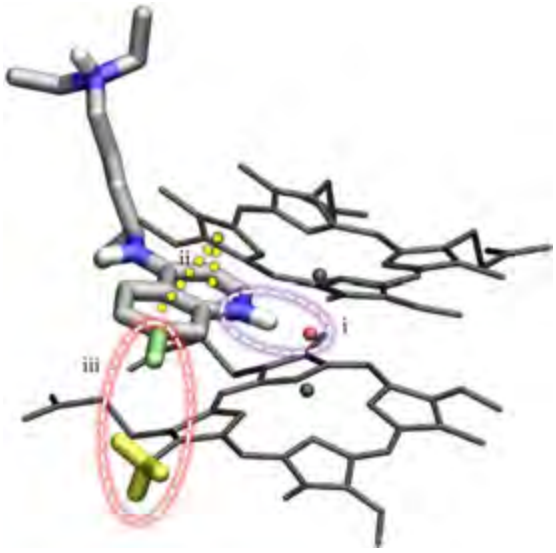

Figure 1.18. *Important interactions identified between chloroquine and μ-oxo Fe(III)PPIX in the docked model of the CQ-(μ-oxo Fe(III)PPIX) complex include (i) an intermolecular hydrogen bond between the oxide bridge of μ-oxo Fe(III)PPIX and protonated quinolinium nitrogen atom of chloroquine, (ii) π-stacking interactions between the quinoline ring of chloroquine and porphyrin ring system of Fe(III)PPIX and (iii) contact between the 7-chloro substituent of chloroquine and the methyl hydrogen atoms of the porphyrin. Reproduced from Kuter et al.,* J. Inorg. Biochem.*, 2016, **154**, 114 with permission from Elsevier.*

1.5.3. Crystal structures of the quinoline antimalarials with Fe(III)PPIX

The first example of a crystal structure of a complex of Fe(III)PPIX with an antimalarial was that with the aryl methanol halofantrine reported by De Villiers et al. in 2008.[101] This structure showed that halofantrine forms a five-coordinate complex with Fe(III)PPIX via its deprotonated hydroxyl group in addition to a π-stacking interaction of the phenanthrene ring over the porphyrin.[101] An intermolecular hydrogen bond was observed between the protonated nitrogen of halofantrine and the propionate group of a neighbouring Fe(III)PPIX-halofantrine complex.[101]

Using these interactions as a model, the authors attempted to rationalise the antimalarial activities of quinine and quinidine compared to their epimers, which are neither active antimalarials nor active β-haematin inhibitors. Surprisingly, all four stereoisomers exhibit similar association constants (Table 1.1) while, structurally, they all have the capacity to π-stack and coordinate to the iron centre through their oxygen atoms. Molecular mechanics modelling showed that the energy required to maintain a proposed conformation in which the Fe(III)PPIX propionate can form an intramolecular hydrogen bond to the protonated quinuclidine nitrogen of quinine and quinidine as well as their epimers was directly correlated to their corresponding

IC_{50} values.[101] This suggested that the comparative ease of forming hydrogen bonds with the propionate side chain of Fe(III)PPIX was important for antimalarial activity.

That the quinine- and quinidine-Fe(III)PPIX complexes actually adopt this conformation with the proposed intramolecular hydrogen bond was subsequently confirmed by their crystal structures (Figure 1.19).[108] It is interesting that this hydrogen bond was present despite a crystallisation medium rich in other hydrogen-bonding partners, i.e. 3:7 (v/v) DMSO:methanol.

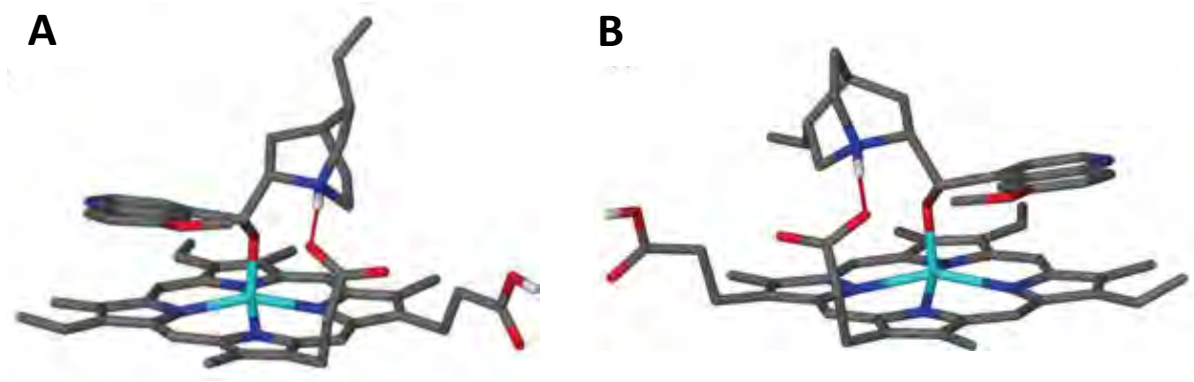

Figure 1.19. *The crystal structures of the Fe(III)PPIX complexes of (A) quinine and (B) quinidine. Hydrogen bonds are shown as broad dashed lines (red). Solvent and hydrogen atoms not involved in bonding have been removed for clarity. Atom colours are grey (C), white (H), blue (N), red (O) and cyan (Fe). Reproduced with permission from De Villiers et al.,* ACS Chem. Biol.*, 2012, **7**, 666. Copyright 2012 American Chemical Society.*

Single crystal X-ray diffraction confirmed that monomeric Fe(III)PPIX interacted with quinidine and quinine in three specific ways analogous to the interaction with halofantrine; namely, coordination of the alkoxide to the iron centre of Fe(III)PPIX, a π-stacking interaction between the quinoline ring systems of the alkaloid and the porphyrin of Fe(III)PPIX, and hydrogen bonding to propionate side chains on the same porphyrin (not to a neighbouring complex, as in the case of halofantrine).[108] Most recently, the mefloquine-Fe(III)PPIX complex has also been crystallised confirming that alkoxide coordination is a key feature of these solid-state interactions.[105]

The crystal structure of a complex between a 4-aminoquinoline antimalarial and Fe(III)PPIX has not yet been published. Solid-state characterisation of the precipitated CQ-Fe(III)PPIX complex has yielded conflicting reports of Fe(III)PPIX speciation, with solid-state NMR studies leading to a proposed covalent chloroquine-Fe(III)PPIX complex.[109] This 1:1 stoichiometry was corroborated via mass spectrometry on an isolated Fe(III)PPIX adduct with a chloroquine analogue while a corresponding vibrational study also indicated a 1:1 stoichiometry.[110,111] These

results contrast with those obtained from Mössbauer measurements of isolated chloroquine and quinine complexes with Fe(III)PPIX, respectively, where the former produced a distinctly different spectrum which corresponds to the μ-oxo dimer while the latter was subsequently shown to correspond to a 1:1 complex.[112]

Spectroscopic evidence leaves little doubt that quinoline antimalarials are privileged scaffolds that are able to form stable complexes with Fe(III)PPIX in solution and in the solid-state. Although several crystal structures of quinoline-Fe(III)PPIX complexes are available, there is no guarantee that such structures resemble the species present in solution, especially given that these complexes tend to interact non-covalently and in a solvent-dependent manner. Hence solution-state and solid-state interactions must be dealt with in a complementary manner.

1.5.4. Other possible mechanisms of action of the quinoline antimalarials

Despite convincing evidence that the quinoline antimalarials exert their mechanism of action by the inhibition of haemozoin biocrystallisation, most likely as a consequence of their selective interactions with Fe(III)PPIX, alternative modes of action have been proposed which, although less likely, are mentioned here for completeness.

The original observations in 1949 that quinoline and acridine antimalarial compounds interact with nucleic acids suggested a possible mechanism by which these agents might interfere with cellular processes in malarial parasites.[113] At physiological pH, chloroquine and quinine are positively-charged cations that are able to bind to DNA, RNA and other anions.[114,115] Subsequently, a number of investigators have shown that these quinoline antimalarials inhibit nucleic acid synthesis in bacterial and mammalian cells.[116,117]

It has been proposed that chloroquine might exert its antimalarial effect by intercalation with parasite DNA and that the activity of similar compounds might be proportional to the stability of their complexes with DNA.[118,119] However, the chloroquine concentrations required to inhibit nucleic acid synthesis are much larger than those that inhibit the growth of chloroquine-susceptible strains of *P. falciparum* (millimolar versus nanomolar, respectively).[120] Although parasitised cells accumulate chloroquine several thousand-fold, even these concentrations are too low. Thus, for this mechanism to be important, the parasite would need to concentrate chloroquine a further hundred-fold in the nucleus, for which there is no evidence. Also, while quinine can also interact with DNA, albeit more weakly than chloroquine, mefloquine does not measurably bind to DNA.[121,122] Furthermore, binding to DNA is greatly reduced at physiological salt concentrations.[123] A final problem with this proposed mechanism of action is that chloroquine has a higher affinity for GC-rich DNA.[115,116,124,125] However, the genome of

P. falciparum is AT-rich (approximately 82%) which predicts that the affinity for chloroquine will be lower for the parasite genome compared to GC-rich mammalian DNA.[126] All this evidence taken together makes it very unlikely that DNA binding accounts for the antimalarial activity of chloroquine. Surprisingly, this theory is still reported,[127] especially in textbooks,[128,129] and is occasionally resurrected.[130-132]

It has also been shown that several quinoline antimalarials directly inhibit the activity of partially-purified haemoglobin-degrading proteases. For example, Gyang et al. partly purified an aspartic protease from *P. falciparum* and found that 33 mM chloroquine was required to inhibit its activity by 60%.[133] Vander Jagt et al. also isolated a low-molecular weight aspartic protease and detected approximately 10% inhibition at 1 mM chloroquine.[134] However, it is extremely unlikely that the concentration of chloroquine in the digestive vacuole ever reaches these levels which are several orders of magnitude higher than the micromolar concentrations required for haemozoin inhibition. It is therefore very unlikely that inhibition of the proteases described above is sufficient to account for the specific antimalarial activity of these drugs.

Nevertheless it is worth noting that Vander Jagt et al. found that Fe(III)PPIX was a much better inhibitor of their partially purified aspartic protease than chloroquine and that this inhibition was unchanged in the presence of chloroquine.[134,135] Therefore, if chloroquine indeed inhibits haemozoin biocrystallisation following haemoglobin catabolism, it is possible that free Fe(III)PPIX may accumulate to concentrations which may inhibit further proteolysis. While protease inhibition has been found to be reversible following removal of the inhibitor,[19] the inhibition of parasite growth by quinoline antimalarials is irreversible.[136] This observation was critical for concluding that the quinoline antimalarials must have more specific, irreversible effects on the parasite.

1.6. Differential effects of the quinoline antimalarials on *P. falciparum*

1.6.1. Physicochemical considerations and accumulation in *P. falciparum*

There is convincing evidence that the interaction of the quinoline antimalarials with Fe(III)PPIX is central to their activity against *P. falciparum*. However, this alone is unlikely to account for their differences in parasite accumulation as well as differential morphological effects that are observed in parasites following drug treatment (Section 1.6.2). These effects may instead be closely related to differences in their physicochemical properties which belie the superficial structural similarities of the quinoline methanol and 4-aminoquinoline archetypes.

Quinine and quinidine are typically described as monoprotic weak bases at physiological pH. Their rigid quinuclidine systems (pK_a 8.58) are connected to quinoline cores via benzylic hydroxyl groups (Figure 1.20). All three structural motifs are important for the antimalarial activity of these compounds.[137,138] The quinolinic pK_a values of quinine and quinidine are approximately 4.14 and 4.42, respectively.[137] Mesomeric donation of the methoxy group into the quinoline system increases its electron density which may encourage π-stacking interactions with the relatively electron-poor metal centre of Fe(III)PPIX.[139]

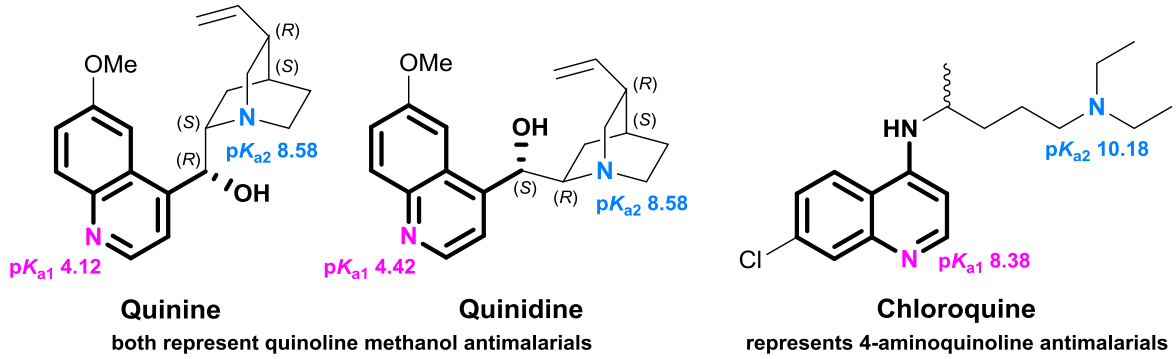

Figure 1.20. *The structures of the quinoline antimalarials examined in this study. The quinoline methanol and 4-aminoquinoline motifs are highlighted.* pK_a *values are taken from Warhurst et al.*[137]

Chloroquine, on the other hand, is a diprotic weak base at physiological pH. The pK_a of its quinolinic nitrogen is higher (8.38) relative to the quinoline methanols due to mesomeric stabilisation of the conjugate acid by the 4-amino group.[137] The tertiary amine (pK_a 10.18) is also more basic than the corresponding quinuclidine of the quinoline methanols.[137] Consequently, chloroquine is expected to accumulate far more efficiently in the acidic digestive vacuole of *P. falciparum* due to the weak base effect, also known as pH trapping.

Weakly-basic compounds such as the quinoline antimalarials are able to exist in both charged (protonated) and uncharged (unprotonated) forms. The latter (neutral) form of the molecule is highly membrane permeable and can diffuse rapidly across biological membranes. On the other hand, mono- or diprotonated forms of the molecule are substantially less membrane permeable and so diffuse across membranes at a much reduced rate, if at all. Therefore, if the unprotonated form of the drug diffuses across a membrane into the acidic digestive vacuole of *P. falciparum*, it will become protonated and thus unable to diffuse back out again.

This idea was formulated by Belgian biologist Christian de Duve who discovered the lysosome and was later awarded the Nobel Prize in Medicine or Physiology in 1974.[140] The concentration of weakly-basic compounds in acidic compartments is, in principle, predictable and Krogstad and Schlesinger proposed a model for accumulation based on the Henderson-Hasselbalch equation.[120] This takes into account the pK_a values of the molecules and the pH values of the cellular compartments. Assuming that protonated drugs are membrane-impermeable, it is possible to predict the digestive vacuolar accumulation ratio (VAR) using Equation 1.1:[120]

$$\text{Vacuolar accumulation ratio (VAR)} = \frac{[\text{Drug}]_v}{[\text{Drug}]_c} = \frac{1 + 10^{(\text{p}K_{\text{a}1} - \text{pH}_v)} + 10^{(\text{p}K_{\text{a}1} + \text{p}K_{\text{a}2} - 2\text{pH}_v)}}{1 + 10^{(\text{p}K_{\text{a}1} - \text{pH}_c)} + 10^{(\text{p}K_{\text{a}1} + \text{p}K_{\text{a}2} - 2\text{pH}_c)}}$$

Equation 1.1

In this equation, the pK_a values refer to the weakly-basic sites of the molecule of interest while pH_v and pH_c represent the pH of the acidic digestive vacuole and the cytosol of *P. falciparum*, respectively. The pH measurements provided by Kuhn et al. were used as the limits in these calculations; that is, pH 7.15 ± 0.07 for the cytosol and pH 5.18 ± 0.05 for the digestive vacuole with no significant difference between chloroquine-sensitive and -resistant strains.[55]

The cellular accumulation ratio (CAR) in the parasitised erythrocyte may also be calculated by multiplying the VAR by the fraction of the infected erythrocyte that is occupied by the digestive vacuole. The digestive vacuole of the parasite occupies approximately 3.25 fL (the average of two previous measurements)[141,142] of the total erythrocyte volume which is about 75 fL.[143]

Taking all of this into account, accumulation values for quinine, quinidine and chloroquine may be estimated. These are listed in Table 1.2. In the absence of additional accumulating forces, these calculations suggest that the quinoline methanols should accumulate approximately three- to six-fold in the infected erythrocyte relative to the serum concentration. Given its higher pK_a values, chloroquine is predicted to have a higher overall cellular accumulation in the parasitised cell, approximately 200- to 600-fold.

Table 1.2. *Predicted vacuolar and cellular accumulations of the quinoline antimalarials taking into account the various assumptions listed in the text.*

	pK_{a1}	pK_{a2}	Predicted vacuolar accumulation ratio (VAR)	Predicted cellular accumulation ratio (CAR)
Quinine	8.58	4.12	75-130	3.4-6.0
Quinidine	8.58	4.42	80-140	3.7-6.6
Chloroquine	10.18	8.14	4 600-13 500	215-630

It was previously thought that a consequence of this accumulation might be a drug-induced alkalinisation effect on the pH of the digestive vacuole. This was thought to play a role in the antimalarial activities of the molecules; for example, by raising the pH of the digestive vacuole above the optimal range for protease action.[143] However, any alkalinising effects of these drugs were only observed at concentrations very much larger than their IC_{50} values, meaning that vacuolar alkalinisation is not their primary effect.[144]

Despite this large predicted accumulation of chloroquine, these calculations only account for approximately 10% of the total amount of chloroquine that has been observed to accumulate in sensitive strains of *P. falciparum*.[145,146] This "non-saturable" predicted accumulation due to the weak base effect is exceeded by an additional "saturable" effect.[147,148] This second component has been suggested to be due to the binding of chloroquine to Fe(III)PPIX in the digestive vacuole.

Convincing evidence for the two-component model of accumulation comes from the observation that chloroquine uptake was reduced by up to 90% in parasitised erythrocytes by interrupting haemoglobin degradation with a plasmepsin inhibitor, reducing the availability of Fe(III)PPIX.[147] Furthermore, the model can account for the saturable uptake of chloroquine in susceptible and resistant strains in the presence and absence of verapamil (Figure 1.21).[147] Finally, erythrocyte "ghost" cells (erythrocytes no longer containing haemoglobin) loaded with Fe(III)PPIX also exhibited this saturable chloroquine binding in a manner dependent on the concentration of Fe(III)PPIX.[148]

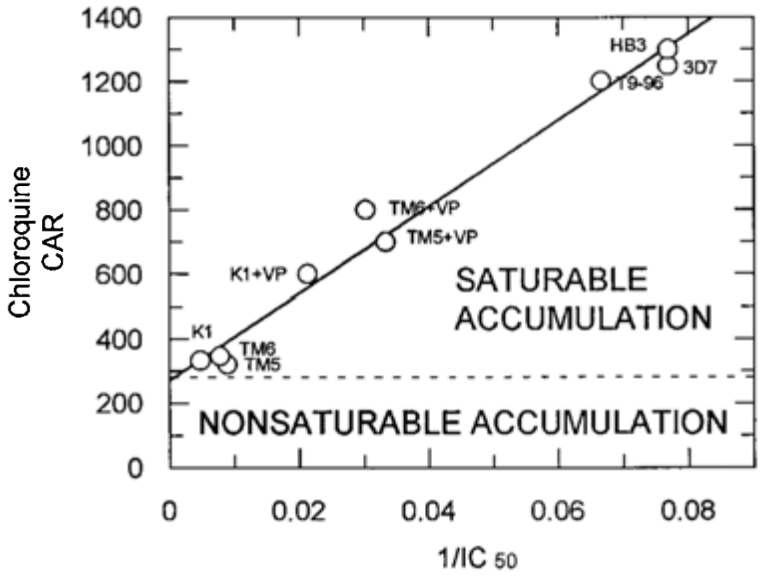

Figure 1.21. *The cellular accumulation ratio (CAR) of chloroquine in* P. falciparum*-infected erythrocytes as a function of IC_{50}, validating the two-component accumulation model of Bray et al.*[147] *Data from three chloroquine-sensitive strains (HB3, 3D7 and T9-96) and three chloroquine-resistance strains (K1, TMS5 and TMS6) are shown in the absence and presence of verapamil (VP). Reproduced with permission from P. G. Bray et al.,* Mol. Pharm.*, 1998, **54**, 170.*

Although it only accounts for a small proportion of the overall accumulation, the non-saturable component is crucial. In the absence of weak base trapping and hence a low intravacuolar concentration of chloroquine, only a very small amount of the complex would form based on the binding constant of the complex. Therefore, in order to permit binding to Fe(III)PPIX which forms the majority of chloroquine accumulation, weak base trapping is required to achieve sufficient free drug concentrations to form a complex in the digestive vacuole.[149]

The accumulation of the two quinoline methanol antimalarials, quinine and quinidine, in *P. falciparum* is rather different. Although a three- to six-fold cellular accumulation ratio is predicted on the basis of the equation above, a 300-fold cellular accumulation ratio of quinine is actually observed for some strains of *P. falciparum* (Figure 1.22).[150] Sanchez et al. argue that non-saturable passive distribution, in accordance with the weak base effect, and saturable intracellular binding to Fe(III)PPIX can account only for a small fraction of this accumulation.[150]

The results of *trans*-stimulation kinetic studies suggest that the unusually high accumulation of quinine is brought about by a carrier-mediated import system. This import system is weakened in parasites with reduced quinine susceptibility. This may be related to polymorphisms within PfCRT but not to polymorphisms within PfMDR1.[151] Interestingly, a K76I mutation in PfCRT reversed the normal potency order of quinine and quinidine toward *P. falciparum*.[151,152]

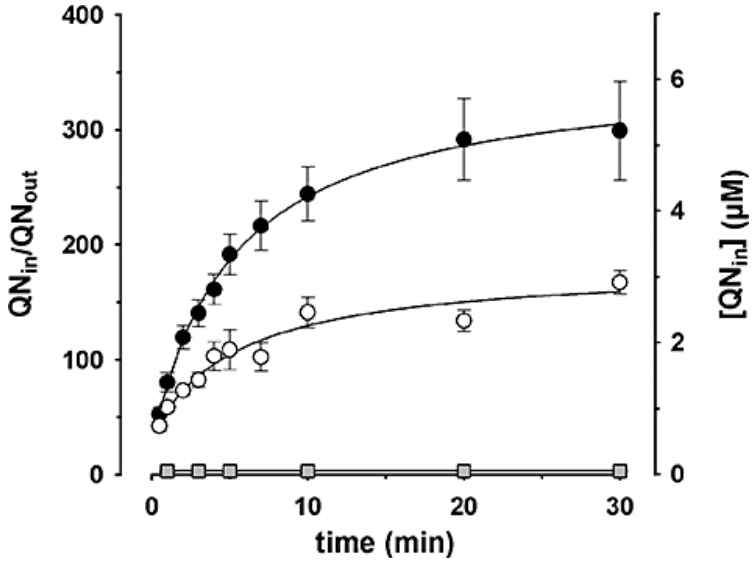

Figure 1.22. *Time courses of [³H]-quinine accumulation. The CAR is expressed as the ratio of the intracellular to the extracellular quinine concentration (QN_{in}/QN_{out}) and as the total intracellular quinine concentration [QN_{in}]. The chloroquine-sensitive HB3 strain (closed circles) is compared to the chloroquine-resistant Dd2 strain (open circles) and uninfected erythrocytes (grey squares). Reproduced with permission from C. P. Sanchez et al.,* Mol. Microbiol.*, 2008, **67**, 1081.*

Figure 1.22 demonstrates the minimal accumulation of quinine in uninfected erythrocytes (grey squares). While the specificity of accumulation of quinine, quinidine and chloroquine for *P. falciparum* over uninfected erythrocytes is now beyond doubt, further visual evidence has been provided by high-resolution electron autoradiography.

In this technique, tritium (^3H) is typically used as a radioactive tracer and is incorporated into a drug molecule. Following incubation with live cells, these are placed in contact with an emulsion. As ionising radiation is emitted during decay, silver ions in the emulsion become reduced to metallic silver grains.[153] Low-energy beta particles, emitted by ^3H, produce silver grains within a few microns of their disintegration site and so provide satisfactory resolution for electron autoradiography.[153] Consequently, the number and distribution of these silver grains can be used to provide information about cellular distribution.

Aikawa showed [^3H]-chloroquine accumulation in the digestive vacuole in *P. berghei*.[154] In 1996, Sullivan et al. reported [^3H]-chloroquine and [^3H]-quinidine accumulation in *P. falciparum* using electron autoradiography and found that the radiolabelled signals were associated with haemozoin (Figure 1.23).[142] Furthermore, intracellular chloroquine-Fe(III)PPIX interactions have been detected by non-invasive photoacoustic spectroscopy in situ.[155]

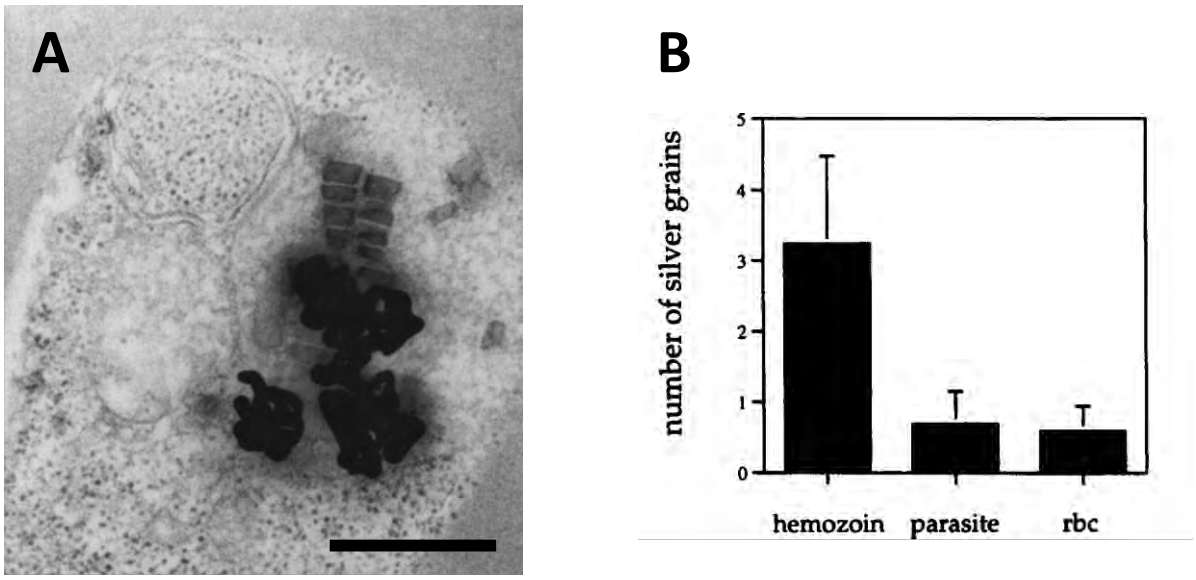

Figure 1.23. *Evidence of chloroquine-haemozoin association in cultured* P. falciparum*. (A) [^{3}H]-Chloroquine is located over the haemozoin crystals situated in the digestive vacuole. In this example, three silver grains are observed. The scale bar represents 0.5 µm. (B) The majority of [^{3}H]-chloroquine signal is measured directly over the crystals. Fifty parasitized erythrocytes were scored for signal distribution. The parasite bar denotes grains located in the parasite but not haemozoin-associated. Data represent the mean ± SEM. Reproduced from D. J. Sullivan et al.,* Proc. Natl. Acad. Sci. USA*, 1996, **93**, 11865.*

Finally, the differences in the interactions of these two classes of drugs with biological membranes have been investigated. Model dipalmitoylphosphatidylcholine bilayers and membranes reformed from lipids extracted from uninfected human erythrocytes were studied using ^{2}H- and ^{31}P-NMR.[156,157] The results showed no significant perturbation of the bilayer structure by chloroquine up to a molar ratio of 1:2 of drug to lipid. In contrast, quinine exhibited stronger interactions with the bilayers, causing significant disordering of the lipid side chains.[156,157] Such behaviour is consistent with the penetration of quinine, rather than chloroquine, into the interior of the bilayers and this may contribute to the differential morphological effects elicited by the quinoline antimalarials on *P. falciparum* as described in the next subsection.

1.6.2. Ultrastructural and morphological effects of the quinoline antimalarials

As a result of the vast accumulation of these drugs in the digestive vacuole, the osmotic gradient between the cytosol and vacuole is predicted to increase resulting in the diffusion of water into the digestive vacuole with concomitant swelling and/or membrane leakiness of the vacuole. Indeed, swelling of the digestive vacuole following drug treatment has been described by a

number of investigators in chloroquine-sensitive *Plasmodium* species and these ultrastructural observations were amongst the first indications that this may be the primary site of action of the quinoline antimalarials.[92,158-160] These and other morphological effects on *P. falciparum*, before and after drug treatment, have been recorded using different microscopies.

When exposed to therapeutic plasma concentrations of chloroquine, chloroquine-sensitive *P. falciparum* show enlargement of the digestive vacuole with increased granular matrix material (Figure 1.24A).[160] Significant clumping is seen amongst the haemozoin crystals. In some parasites, the digestive vacuole and plasma membrane disintegrate. Pigment granules and empty vesicles lie within the cytoplasm. Some nuclei become more densely stained and coarsely clumped with the cytoplasm showing ribosomal aggregation as well as patchy loss.[160] The mitochondrion appears swollen and rough endoplasmic reticulum becomes difficult to identify.[160]

Electron microscopy of a chloroquine-resistant strain of *P. falciparum* treated with chloroquine did not reveal the above changes and instead resembled the control cultures (Figure 1.24B).[160] Digestive vacuoles were only minimally enlarged (if at all), consistent with the mechanism of chloroquine efflux from the digestive vacuole of chloroquine-resistant strains.[160] Other cell constituents appeared normal.

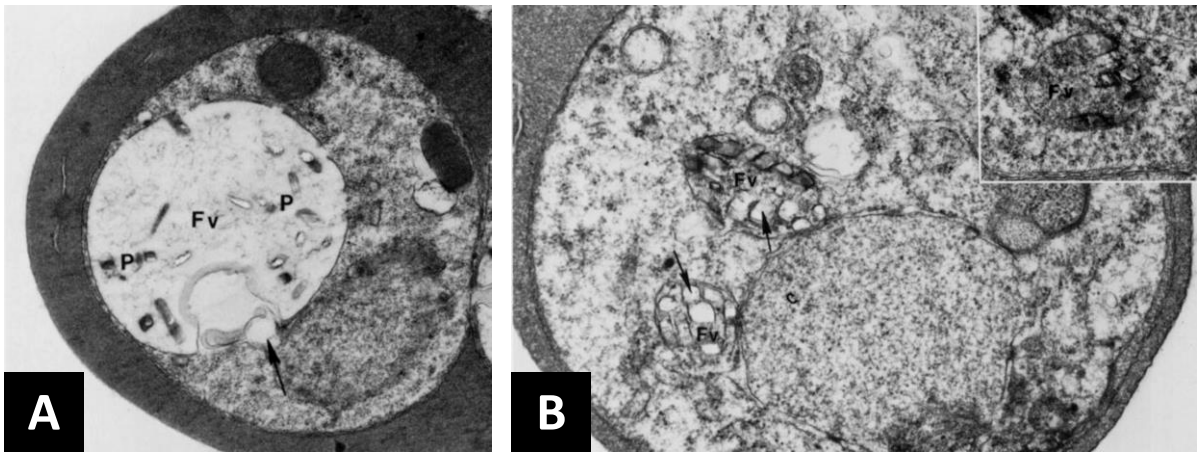

Figure 1.24. *Transmission electron micrographs of chloroquine-treated* P. falciparum *strains. (A) Chloroquine-sensitive strain treated with chloroquine alone (x 21 000). Marked enlargement of digestive vacuoles (Fv) containing pigment (P) granules and granular matrix material is present. Degenerative membranous changes are also seen (arrow). (B) Digestive vacuoles (Fv) in chloroquine-resistant strains appear compact with no evidence of swelling (x 33 000). Inset: Normal digestive vacuole (Fv) of control cells (x 26 000). Reproduced from Jacobs et al.,* Am. J. Trop. Med. Hyg.*, 1988, **39**, 15, published by the American Society of Tropical Medicine and Hygiene.*

In quinine-exposed *P. falciparum* parasites, there was an extensive depletion of free ribosomes in the cytoplasm (Figure 1.25).[161] Haemozoin in digestive vacuoles was decreased or almost absent and mitochondria showed marked swelling with a more electron-lucent matrix.[161] These observations are similar to those of quinine-treated parasites of *P. berghei*.[158] In this species, the first observation was an increase in "the space between outer and inner parasite limiting membranes" (presumably the parasitophorous vacuolar and parasite plasma membranes, respectively). Quinine also appeared to affect the integrity of the digestive vacuole membrane, followed by swelling of the vacuole and a decrease in electron density of the haemozoin. Clumping of the ribosomes, a reduction in their number and blebbing of the nuclear membrane was also observed.[158]

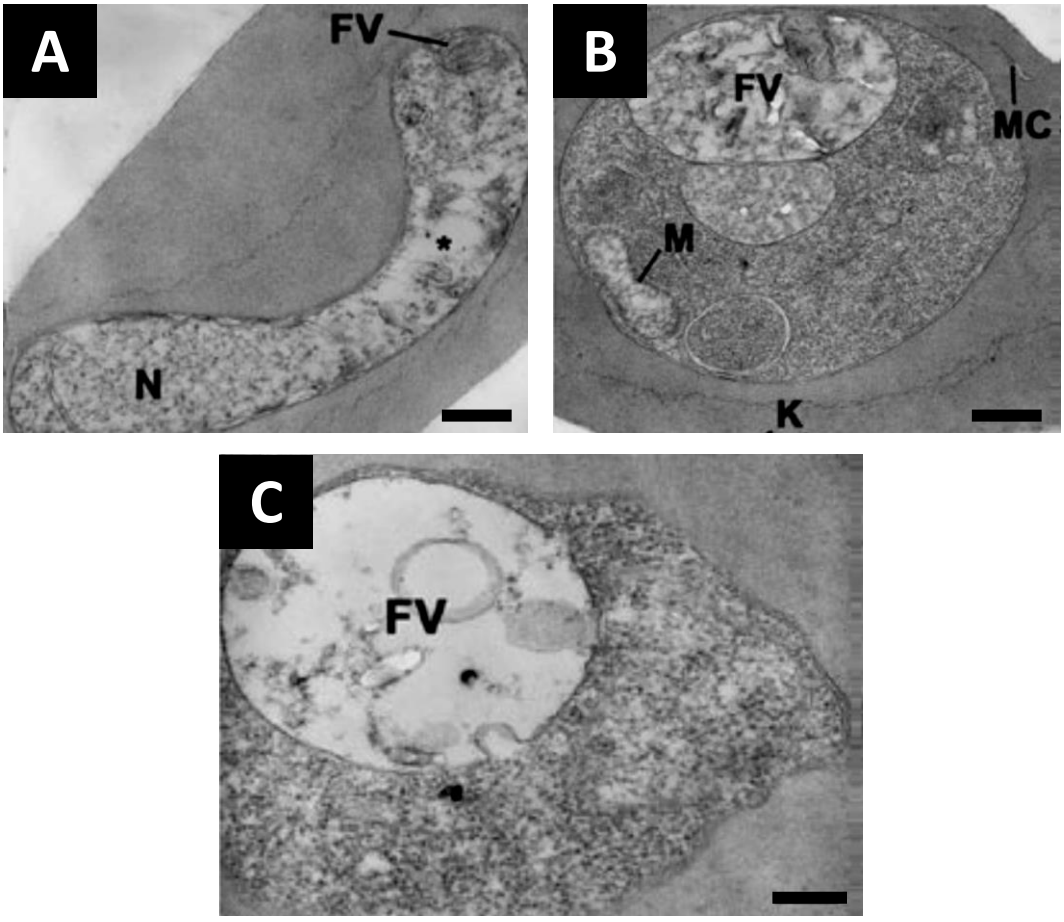

Figure 1.25. *Transmission electron micrographs of quinine-treated* P. falciparum *parasites. (A) An early ring, one hour after exposure, shows the depletion of ribosomes (*) in the cytoplasm and a small digestive vacuole (FV). (B) A parasite, four hours after exposure, shows a swollen mitochondrion (M) and a digestive vacuole (FV) containing few haemozoin crystals. (MC) represents a Maurer's cleft. (C) At eight hours after exposure the parasite exhibits a digestive vacuole (FV) containing abnormally few haemozoin crystals. Scale bars represent 200 nm. Reproduced from Sachanonta et al.,* Ultrastruct. Pathol.*, 2011, **35**, 214 with permission from Taylor & Francis.*

Although many of the effects on the ultrastructure of *P. falciparum* following drug treatment are shared by chloroquine and quinine, there are some differences which suggest that the modes of action of these antimalarials may differ in other mechanistic details.

It has now been extensively shown that these antimalarials modulate endocytosis and vesicle trafficking in the malaria parasite in different ways.[162-164] Endocytosis is a fundamental process in eukaryotic cells and fulfils numerous functions, most notably that of macromolecular nutrient uptake. As described in Section 1.3.1, during its intracellular development *P. falciparum* ingests large amounts of host cytoplasm by cytostomal-mediated endocytosis. These vesicles are then trafficked to the digestive vacuole where catabolism of haemoglobin is accomplished.

In order to investigate the effects of antimalarials on the endocytic pathway, early trophozoite stage cultures were incubated for eight hours with quinoline antimalarials at five times their IC_{50} values. Following release from the infected erythrocytes by saponin lysis, haemoglobin levels were determined by Western blots. Quinine and related antimalarials mefloquine and halofantrine reduced haemoglobin content significantly, showing that they inhibit parasite ingestion of haemoglobin by endocytosis (Figure 1.26A).[162] By contrast, haemoglobin levels in chloroquine-treated parasites increased compared to those in untreated parasites.[162]

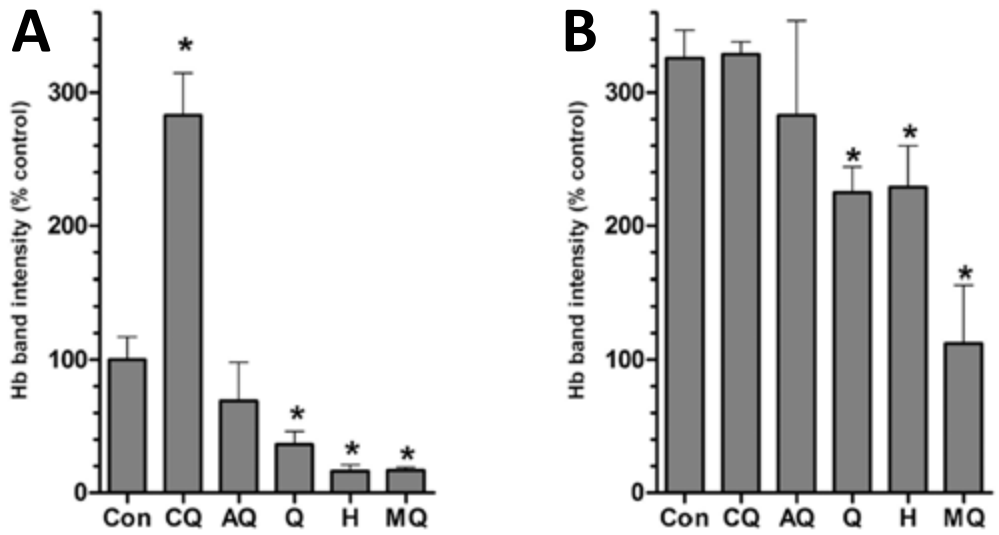

Figure 1.26. *Haemoglobin levels in drug-treated parasites. (A) Parasite cultures were untreated (Con) or incubated with chloroquine (CQ), amodiaquine (AQ), quinine (Q), halofantrine (H) or mefloquine (MQ). (B) In parallel cultures, the quinoline drugs were added in combination with two protease inhibitors. The intensities of the haemoglobin bands on the Western blots were normalised. Error bars indicate standard deviations. An asterisk (*) indicates a significant change from the results for the controls (P < 0.05). Reproduced from Roberts et al.,* Antimicrob. Agents Chemother.*, 2008, **52**, 1840 with permission.*

This latter finding corroborates previous observations by Famin et al.[163] A previous study also showed that chloroquine inhibited haemoglobin digestion but had no other significant effect on the endocytic pathway of the parasite as assessed by electron microscopy, haemoglobin immunofluorescence and the distribution of fluorescent and biotinylated dextran tracers.[164]

By contrast, protease inhibitors moderated haemoglobin perturbations, suggesting a common role for Fe(III)PPIX binding.[162] Parasites were incubated with the quinoline antimalarials in combination with protease inhibitors to halt haemoglobin digestion. Predictably, these inhibitors increased the concentration of haemoglobin in control parasites more than three-fold (Figure 1.26B). Chloroquine did not significantly affect haemoglobin levels in the presence of protease inhibitors while a reduction in haemoglobin levels was still found in quinine-treated cultures, although less severe than previously observed (Figure 1.26A).[164]

This agrees with reports that inhibition of haemoglobin digestion antagonises quinoline action[165] and supports the notion that quinolines share Fe(III)PPIX binding as a common mode of action. Consequently, their differential effects on the haemoglobin endocytic pathway are most likely manifestations of their physicochemical differences.

Finally, it was shown, following quinoline treatment, that there is an accumulation of transport vesicles in the parasite cytosol as identified by immunofluorescence microscopy using anti-haemoglobin antibodies.[162] While the majority of the haemoglobin colocalised with haemozoin in the digestive vacuole, additional fluorescent puncta representing transport vesicles were observed in the parasite cytoplasm.[162] Enumeration of the vesicles showed that quinine caused a reduction in endocytic vesicle content per parasite (0.66 ± 0.09) compared to control parasites (1.2 ± 0.12). This proves that quinine inhibits endocytosis and, consequently, endocytic vesicle formation.[162] On the other hand, chloroquine treatment markedly increased the vesicle content (6.1 ± 0.10), consistent with a disruption of normal vesicle trafficking.[162]

1.6.3. Previous efforts to investigate protein targets of the quinoline antimalarials

Enduring interest in the quinoline antimalarials, as well as unresolved details regarding their mechanisms of action, has resulted in several attempts to identify proteinaceous binding targets within uninfected erythrocytes and *P. falciparum*. These efforts have almost exclusively exploited photoaffinity labelling strategies. In this technique, a molecular probe (in this case, a photoreactive derivative of the quinoline antimalarial) is activated by light to form a covalent bond to its target.[166] The advantage of this technique is that it tends to label proteins with high specificity.

Typically, the photoreactive group is an aromatic azide group. When exposed to ultraviolet light, photodecomposition of the azide produces a highly reactive, short-lived nitrene intermediate that covalently labels proteins in close proximity. A common photoreactive azide group is the azidosalicylate moiety, highlighted in Figure 1.27, which may be additionally labelled by a radioisotope (often ^{125}I) to facilitate detection by sensitive phosphorimage analysis.

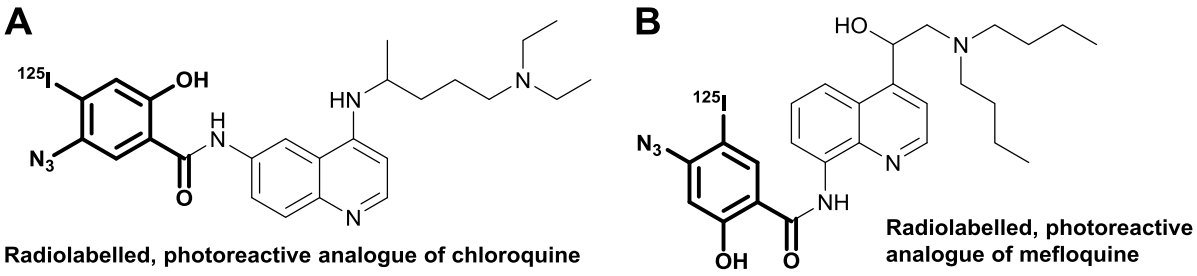

Figure 1.27. *Representative analogues of quinoline antimalarials used in protein-binding studies. The radiolabelled, photoreactive azidosalicylate is highlighted.*

Foley and colleagues synthesised a photoreactive chloroquine analogue (Figure 1.27A) that was comprehensively validated against *P. falciparum*.[167] The analogue was active against a chloroquine-sensitive strain of *P. falciparum* but was less effective at killing a chloroquine-resistant strain; these effects could be modulated using verapamil. (It is now known that these observations can be rationalised in terms of PfCRT-mediated efflux.) Following radiolabelling with $Na^{125}I$, two proteins with masses of 42 kDa and 33 kDa were retrieved. Incubation with chloroquine competitively inhibited the photolabelling, suggesting a specific interaction.[167]

A follow-up study found that the 42 kDa protein was present in unlabelled erythrocytes as well as *P. falciparum*-infected erythrocytes, while the 33 kDa chloroquine-binding protein was found exclusively in infected erythrocytes (Figure 1.28).[168] Consequently, the investigators decided to pursue the characterisation of the 33 kDa protein. This protein was purified and identified as *P. falciparum* lactate dehydrogenase (PfLDH), one of the most ubiquitous enzymes in the parasite proteome.[168] The enzyme was cloned and expressed in *E. coli* and the recombinant protein was used to produce an antiserum, after which immunoprecipitation using affinity-purified anti-PfLDH antibodies confirmed the identity of the protein.[168] However, the enzyme activity of purified PfLDH was not significantly affected by chloroquine indicating that PfLDH is not a direct target of the quinoline. Instead, the authors found that PfLDH was "exquisitely sensitive" to inhibition by free Fe(III)PPIX. Chloroquine protected against this inhibitory effect.[168]

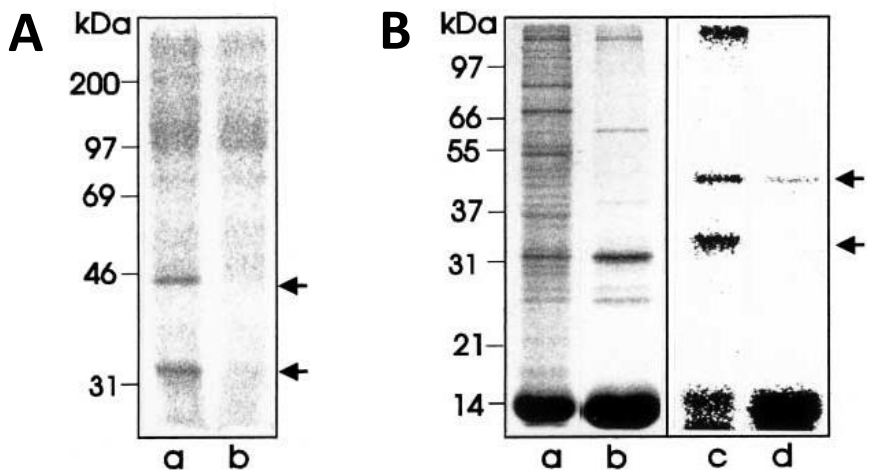

Figure 1.28. *Photoaffinity labelling of chloroquine-interacting proteins. (A) Erythrocytes infected with a chloroquine-sensitive strain of* P. falciparum *were incubated with the radiolabelled, photoreactive chloroquine analogue and exposed to ultraviolet illumination either alone (lane a) or in the presence of chloroquine (lane b). Samples were subjected to SDS-Page and visualised by phosphorimage analysis. (B) Parasite-infected erythrocytes or uninfected erythrocytes were washed, lysed and incubated with the probe. They were exposed to ultraviolet illumination and subjected to SDS-Page. Lanes (a) and (b) represent Coomassie-blue stained profiles of lanes (c) and (d) which themselves were visualised by phosphorimage analysis. The 33 kDa and 42 kDa chloroquine-binding proteins are marked with arrows. Reproduced from Menting et al.,* Mol. Biochem. Parasitol.*, 1997,* ***88****, 215 with permission from Elsevier.*

Finally, Read and colleagues determined the crystal structure of the complex between PfLDH and chloroquine (Figure 1.29).[169] This is the first structure of a complex between chloroquine and an enzyme. The bound chloroquine is observed within the NADH binding pocket of the enzyme, occupying a position similar to that of the adenyl ring of the cofactor, indicating that chloroquine acts as a competitive inhibitor of NADH for this critical glycolytic enzyme.[169] Specific interactions between the drug and amino acid residues unique to the malarial form of the enzyme suggest that the binding is mildly selective for the parasite enzyme over its human homologue.[169]

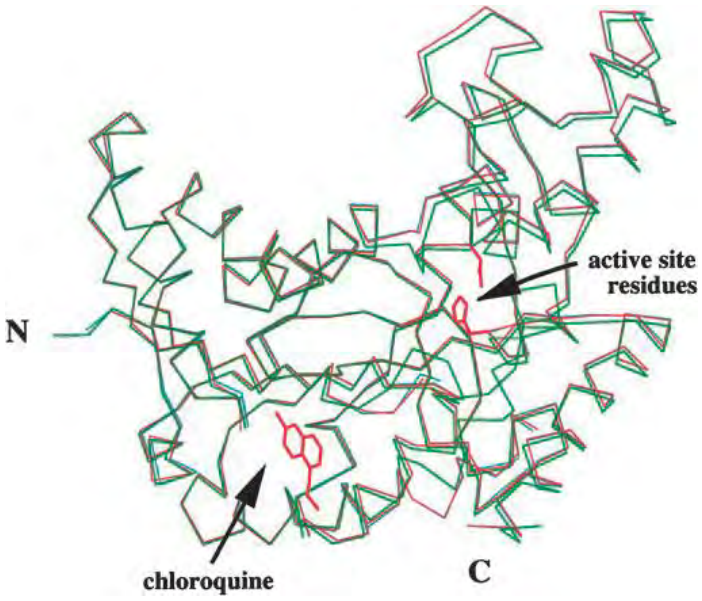

Figure 1.29. *Superimposed C_α traces for apo-PfLDH (blue), the chloroquine-PfLDH complex (red) and the ternary complex of PfLDH incorporating the NADH cofactor (green). The bound chloroquine is shown relative to the active site. Reproduced from Read et al.*, J. Biol. Chem.*, 1999, **274**, 10213 with permission.*

Meanwhile, Desneves and colleagues applied the same methodology to probe for mefloquine-binding proteins. They also synthesised a photoreactive azidosalicylate analogue that was subsequently radiolabelled (Figure 1.27B) and validated against mefloquine-sensitive and mefloquine-resistant strains of *P. falciparum*.[170] They showed that the mefloquine analogue interacts specifically with apolipoprotein Al, the major protein of serum high-density lipoproteins. In addition, the probe was shown to interact specifically with erythrocyte membrane protein, stomatin (31 kDa). A further two high affinity proteins with apparent molecular masses of 22 kDa and 36 kDa were observed in three different strains of *P. falciparum*.[170] These proteins have not subsequently been identified.

More recently, Graves et al. took a different approach.[171] Recognising that the heterocyclic quinoline ring shares common structural features with purine nucleotides and, considering that purine-interacting proteins represent a large proportion of the proteins in cells, they hypothesised that proteins that interact with purines might also interact with quinolines. As a result, they used a functional proteomics approach that exploited the structural similarities between the quinoline ring and the purine ring of adenosine triphosphate (ATP). Consequently, Graves et al. used a γ-phosphate-linked ATP-Sepharose affinity matrix to isolate the entire purine binding proteome from cell lysates in order to reduce the complexity of the protein mixtures.[171] Several quinoline drugs were screened by displacement affinity chromatography against the purine binding proteome captured by the ATP-Sepharose matrix. Screening of the

human erythrocyte purine-binding proteome identified two human proteins, aldehyde dehydrogenase 1 (ALDH1, 55 kDa) and quinone reductase 2 (QR2, 26 kDa). By contrast, no proteins were detected upon screening of the *P. falciparum* purine-binding proteome.[171]

In a complementary approach, the authors passed cell lysate from a mouse, uninfected erythrocytes and *P. falciparum* sequentially over hydroxychloroquine- or primaquine-linked Sepharose. Consistent with the displacement affinity chromatography screen, ALDH1 and QR2 were the only proteins recovered from the mouse and erythrocyte cell lysate. As before, no proteins were recovered from *P. falciparum.* Furthermore, the activity of QR2 was potently inhibited by several of the quinolines in vitro, confirming the selectivity of this target.[171]

In an even more recent development, Lekostaj and colleagues designed and synthesised novel perfluorophenylazido chloroquine analogues for photolabelling studies with the deliberate intention of being able to extract the PfCRT protein from *P. falciparum*.[172,173] Their probe places the photoreactive group at the terminal aliphatic nitrogen of chloroquine via a flexible four-carbon ester linker and includes a convenient biotin tag (Figure 1.30A). They found that this probe photolabels PfCRT in *P. falciparum* with high specificity.

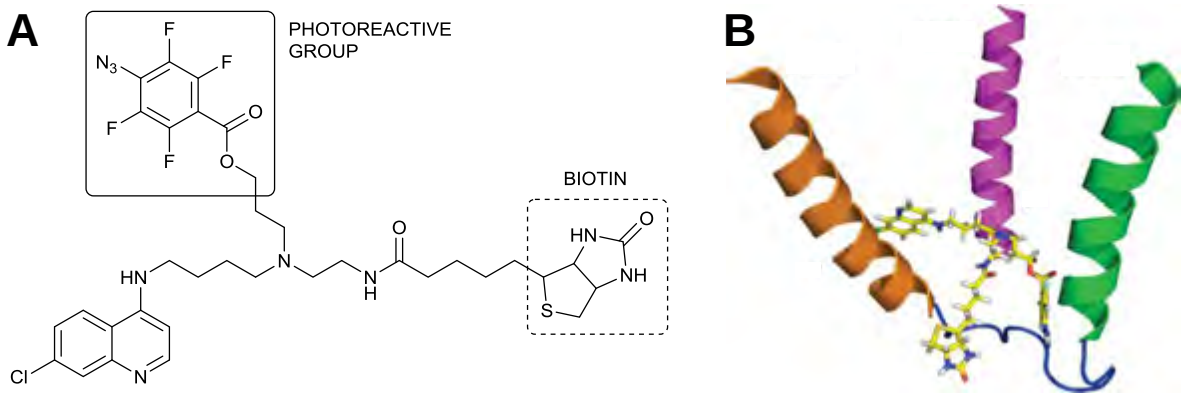

Figure 1.30. *(A) The biotinylated, photoreactive chloroquine analogue which was used to label PfCRT. (B) A cartoon showing the modelled interaction between the biotinylated, photoreactive chloroquine analogue and PfCRT. The authors propose that the 7-chloro-4-aminoquinoline pharmacophore binds within a cleft defined by three of the transmembrane helices. Reproduced from Lekostaj et al.,* Biochemistry*, 2008,* ***47****, 10394 with permission from the American Chemical Society. Copyright 2008 American Chemical Society.*

Using reconstituted proteoliposomes harbouring partially-purified recombinant PfCRT, they analysed the efficiency of photolabelling in the presence of chloroquine and other drugs, including verapamil, and various amino acid mutations in PfCRT. They were able to define a single attachment site to their chloroquine analogue lying within the digestive vacuolar-

disposed loop between putative helices 9 and 10 of PfCRT, allowing them to propose a model for a single chloroquine binding site in PfCRT (Figure 1.30B).[173] It is surprising to note that, in a later work, the same group demonstrated exogenous binding of this chloroquine analogue to PfMDR1.[174] However, they did not identify this latter protein in the photolabelling study described above.

The results from the photoaffinity labelling studies of quinoline antimalarials described above are summarised in Table 1.3. Protein binding targets of the *Cinchona* alkaloids in *P. falciparum* have not yet been probed. Hence, these will form a key part of this study as outlined in the next section.

Table 1.3. *A summary of the results of protein affinity studies of the quinoline antimalarials.*

Investigator	Probe	Protein(s) detected and/or identified
Foley et al. (1994)[167]	Radiolabelled, photoreactive chloroquine analogue	Two bands from infected erythrocytes were detected, 33 kDa and 42 kDa, the former of which was later identified as *P. falciparum* lactate dehydrogenase by Menting et al. (1997)[168]
Desneves et al. (1996)[170]	Radiolabelled, photoreactive mefloquine analogue	Several bands from uninfected erythrocytes were detected including an erythrocyte integral membrane protein stomatin (31 kDa). Two *P. falciparum* proteins of masses 22 kDa and 36 kDa were detected but not identified
Graves et al. (2002)[171]	γ-ATP-Sepharose to identify purine binders, followed by primaquine- and hydroxychloroquine-labelled affinity columns	In uninfected erythrocytes, two human proteins were identified: human aldehyde dehydrogenase 1 (ALDH1, 55 kDa) and quinone reductase 2 (QR2, 26 kDa). No *P. falciparum* proteins were detected
Lekostaj et al. (2008)[173]	Photoreactive chloroquine analogue with biotin tag	In *P. falciparum* trophozoites, PfCRT was labelled with high specificity

1.7. Aims and objectives of this study

Malaria is the most serious and widespread parasitic disease occurring in man. The quinoline antimalarials, which have provided the foundation of malaria treatment for centuries, remain of great interest to public health. However, mechanistic details of their modes of action remain unresolved, particularly between the two major classes of these antimalarials. These are the quinoline methanols, represented in this study by the diastereomeric *Cinchona* alkaloids quinine and quinidine, and the 4-aminoquinolines, represented by chloroquine.

Hence the aim of this work was to develop new tools with which to investigate the quinoline antimalarials and to use these tools to generate deeper insights into their mechanism of action against *P. falciparum*. The context of this research is to contribute to the development of antimalarial chemotherapies by elucidating novel mechanistic insights into the activities of these drugs on *P. falciparum*, the causative agent of a crippling but curable infectious disease.

Consequently, the broad aims of this project were three-fold: (1) To design and synthesise novel fluorescent analogues of quinine, quinidine and chloroquine suitable for live-cell fluorescence microscopy; (2) to investigate systematically their subcellular localisation in *P. falciparum*; and (3) to identify protein binding targets, if any, of these molecules within uninfected erythrocytes and *P. falciparum*.

Specific objectives relating to the aims of each chapter are given at the beginning of each relevant chapter. The following overarching objectives were envisaged for this work:

i. To use current structure-activity models of the antimalarials quinine, quinidine and chloroquine with Fe(III)PPIX to design and synthesise novel fluorescent derivatives of these molecules suitable for live-cell imaging;
ii. To fully characterise these novel derivatives photophysically and physicochemically, and to evaluate their activities against *P. falciparum* in vitro, in order to determine which of these derivatives were suitable fluorescent analogues of the parent antimalarials;
iii. To use these analogues with confocal and super-resolution microscopy in the presence of fluorescent dyes and organelle-specific trackers to identify patterns of accumulation across the mature stages of *P. falciparum*;
iv. To isolate protein binding targets of the quinoline antimalarials in uninfected erythrocytes and *P. falciparum* using matrix-based affinity chromatography and to identify these proteins using proteomic methods.

1.8. References

1. World Health Organisation, *World Malaria Report 2015*, WHO Press, Geneva, 2015.
2. J. Sachs and P. Malaney, *Nature*, 2002, **415**, 680.
3. T. Bousema, L. Okell, I. Felger and C. Drakeley, *Nature Rev. Microbiol.*, 2014, **12**, 833.
4. C. Guring, A. Heiber, F. Kruse, J. Ungefehr, T. Gilberger and T. Spielmann, *Nat. Commun.*, 2011, **2**, 165.
5. M. Marti, R. T. Good, M. Rug, E. Knuepfer and A. E. Cowman, *Science*, 2004, **306**, 1930.
6. M. Foley and L. Tilley, *Pharmacol. Ther.*, 1998, **79**, 55.
7. S. G. Langreth, J. B. Jensen, R. T. Reese and W. Trager, *J. Protozool.*, 1978, **25**, 443.
8. L. H. Bannister, J. M. Hopkins, R. E. Fowler, S. Krishna and G. H. Mitchell, *Parasitol. Today*, 2000, **16**, 427.
9. E. Hanssen, P. J. McMillan and L. Tilley, *Int. J. Parasitol.*, 2010, **40**, 1127.
10. D. T. Riglar, D. Richard, D. W. Wilson, M. J. Boyle, C. Dekiwadia, L. Turnbull, F. Angrisano, D. S. Marapana, K. L. Rogers, C. B. Whitchurch, J. G. Beeson, A. F. Cowman, S. A Ralph and J. Baum, *Cell Host Microbe*, 2011, **9**, 9.
11. N. Abu Bakar, N. Klonis, E. Hanssen, C. Chan and L. Tilley, *J. Cell Sci.*, 2010, **123**, 441.
12. M. Krugliak, J. Zhang and H. Ginsburg, *Mol. Biochem. Parasitol.*, 2002, **119**, 249.
13. D. A. Elliott, M. T. McIntosh, H. D. Hosgood III, S. Chen, G. Zhang, P. Baevova and K. A. Joiner, *Proc. Natl. Acad. Sci. USA*, 2008, **105**, 2463.
14. F. Ehlgen, J. S. Pham, T. de Koning-Ward, A. F. Cowman and S. A. Ralph, *PLOS ONE*, 2012, **7**, e38781.
15. R. Banerjee, J. Liu, W. Beatty, L. Pelosof, M. Klemba and D. E. Goldberg, *Proc. Natl. Acad. Sci. USA*, 2002, **99**, 990.
16. P. J. Rosenthal, *Int. J. Parasitol.*, 2004, **34**, 1489.
17. C. E. Murata and D. E. Goldberg, *J. Biol. Chem.*, 2003, **278**, 38022.
18. D. J. Sullivan, in *Malaria: Drugs, Disease and Post-Genomic Biology*, ed. D. J. Sullivan and S. Krishna, Springer-Verlag, Heidelberg, 2005, pp. 275-292.
19. P. J. Rosenthal, J. H. McKerrow, M. Aikawa, H. Nagasawa and J. H. Leech, *J. Clin. Invest.*, 1988, **82**, 1650.
20. S. Zarchin, M. Krugliak and H. Ginsburg, *Biochem. Pharmacol.*, 1986, **35**, 2435.
21. J. Liu, E. S. Istvan, I. Y. Gluzman, J. Gross and D. E. Goldberg, *Proc. Natl. Acad. Sci. USA*, 2006, **103**, 8840.
22. V. L. Lew, T. Tiffert and H. Ginsburg, *Blood*, 2003, **101**, 4189.
23. R. J. W. Allen and K. Kirk, *Trends Parasitol.*, 2004, **20**, 7.
24. V. L. Lew, T. Tiffert and H. Ginsburg, *Trends Parasitol.*, 2004, **20**, 10.
25. P. A. Sigala and D. E. Goldberg, *Annu. Rev. Microbiol.*, 2014, **68**, 259.

26. P. A. Sigala, J. R. Crowley, S. Hsieh, J. P. Henderson and D. E. Goldberg. *J. Biol. Chem.*, 2012, **287**, 37793.
27. S. Pagola, P. W. Stephens, D. S. Bohle, A. D. Kosar and S. K. Madsen, *Nature*, 2002, **404**, 307.
28. C. D. Fitch and P. Kanjananggulpan, *J. Biol. Chem.*, 1987, **262**, 15552.
29. A. F. G. Slater, W. J. Swiggard, B. R. Orton, W. D. Flitter, D. E. Goldberg, A. Cerami and G. B. Henderson, *Proc. Natl. Acad. Sci. USA*, 1991, **88**, 325.
30. D. S. Bohle, R. E. Dinnebier, S. K. Madsen and P. W. Stephens, 1997, *J. Biol. Chem.*, 1997, **272**, 713.
31. D. S. Bohle, P. Debrunner, P. A. Jordan, S. K. Madsen and C. E. Shulz, *J. Am. Chem. Soc.*, 1998, **120**, 8255.
32. J. Gildenhuys, T. le Roux, T. J. Egan and K. A. de Villiers, *J. Am. Chem. Soc.*, 2013, **135**, 1037.
33. T. J. Egan, J. M. Combrinck, J. Egan, G. R. Hearne, H. M. Marques, S. Ntenteni, B. T. Sewell, P. J. Smith, D. Taylor, D. A. van Schalkwyk and J. C. Walden, *Biochem. J.*, 2002, **365**, 343.
34. A. F. G. Slater and A. Cerami, *Nature*, 1992, **355**, 167.
35. A. Dorn, R. Stoffel, H. Matile, A. Bubendorf and R. G. Ridley, *Nature*, 1995, **374**, 269.
36. D. J. Sullivan, I. Y. Gluzman, D. E. Goldberg, *Science*, 1996, **271**, 219.
37. D. Jani, R. Nagarkatti, W. Beatty, R. Angel, C. Slebodnick, J. Andersen, S. Kumar and D. Rathore, *PLOS ONE*, 2008, **4**, e1000053.
38. M. Chugh, V. Sundararaman, S. Kumar, V. S. Reddy, W. A. Siddiqui, K. D. Stuart and P. Malhotra, *Proc. Natl. Acad. Sci. USA*, 2013, **110**, 5392.
39. K. Bendrat, B. J. Berger and A. Cerami, *Nature*, 1995, **378**, 138.
40. R. G. Ridley, A. Dorn, H. Matile and M. Kansy, *Nature*, 1995, **378**, 138.
41. C. D. Fitch, G. Cai, Y. Chen, J. D. Shoemaker, *Biochem. Biophys. Acta*, 1999, **1454**, 31.
42. K. E. Jackson, N. Klonis, D. J. P. Ferguson, A. Andisa, C. Dogovski and L. Tilley, *Mol. Microbiol.*, 2004, **54**, 109.
43. I. Coppens and O. Vielemeyer, *Int. J. Parasitol.*, 2005, **35**, 597.
44. J. M. Pisciotta, I. Coppens, A. K. Tripathi, P. F. Scholl, J. Shuman, S. Bajad, V. Shulaev and D. J. Sulliven, *Biochem. J.*, 2007, **402**, 197.
45. A. N. Hoang, R. D. Sandlin, A. Omar, T. J Egan and D. W. Wright, *Biochemistry*, 2010, **49**, 10107.
46. S. Kapishnikov, T. Berthing, L. Hviid, M. Dierolf, A. Menzel, F. Pfeiffer, J. Als-Nielsen and L. Leiserowitz, *Proc. Natl. Acad. Sci. USA*, 2012, **109**, 11184.
47. S. Kapishnikov, A. Weiner, E. Shimoni, P. Guttmann, G. Schneider, N. Dahan-Pasternak, R. Dzikowski, L. Leiserowitz and M. Elbaum, *Proc. Natl. Acad. Sci. USA*, 2012, **109**, 11188.
48. T. Mitamura and N. M. Q. Palacpac, *Microbes Infect.*, 2003, **5**, 545.
49. G. G. Holz, *Bull. World Health Organ.*, 1977, **55**, 237.
50. H. J. Vial, M. J. Thuet and J. R. Philippot, *J. Protozool.*, 1982, **29**, 258.

51. S. Gulati, E. H. Ekland, K. V. Ruggles, R. B. Chan, B. Jayabalasingham, B. Zhou, P. Mantel, M. C. S. Lee, N. Spottiswoode, O. Coburn-Flynn, D. Hjelmqvist, T. S. Worgall, M. Marti, G. D. Paolo and D. A. Fidock, *Cell Host Microbe*, 2015, **18**, 371.
52. N. M. Q. Palacpac, Y. Hiramine, F. Mi-ichi, M. Torii, K. Kita, R. Hiramatsu, T. Horii and T. Mitamura, *J. Cell Sci.*, 2004, **117**, 1469.
53. L. L. Hsao, R. J. Howard, M. Aikawa and T. F. Taraschi, *Biochem. J.*, 1991, **274**, 121.
54. K. J. Saliba, R. J. W. Allen, S. Zissis, P. G. Bray, S. A. Ward and K. Kirk, *J. Biol. Chem.*, 2003, **278**, 5606.
55. M. Lanzer and P. Rohrbach, *Curr. Sci.*, 2007, **92**, 1561.
56. Y. Kuhn, P. Rohrbach and M. Lanzer, *Cell. Microbiol.*, 2007, **9**, 1004.
57. R. Hayward, K. J. Saliba and K. Kirk, *J. Cell Sci.*, 2006, **119**, 1016.
58. K. J. Saliba and K. Kirk, *J. Biol. Chem.*, 1999, **274**, 33213.
59. D. A. van Schalkwyk, K. J. Saliba, G. A. Biagini, P. G. Bray and K. Kirk, *PLOS ONE*, 2013, **8**, e58933.
60. F. Wissing, C. Sanchez, P. Rohrbach, S. Ricken and M. Lanzer, *J. Biol. Chem.*, 2002, **277**, 37747.
61. J. Ito, A. Ghosh, L. A. Moreira, E. A. Wimmer and M. Jacobs-Lorena, *Nature*, 2002, **417**, 452.
62. A. Waters, *Cell*, 2006, **124**, 689.
63. F. A. Jacquerioz and A. M. Croft, *Drugs for preventing malaria in travellers (Review)*, John Wiley & Sons, 2010.
64. S. R. Meshnick and M. J. Dobson, Chapter 2 from *Antimalarial Chemotherapy: Mechanisms of Action, Resistance, and New Directions in Drug Discovery*. Ed. P. J. Rosenthal, Humana Press, Totowa, New Jersey, 2001.
65. L. J. Bruce-Chwatt, *J. R. Soc. Med.*, 1981, **74**, 531.
66. D. C. Smith, *J. Hist. Med. Allied Sci.*, 1976, **31**, 343.
67. T. S. Kaufman and E. A. Rúveda, *Angew. Chem. Int. Ed.*, 2005, **44**, 854.
68. P. Reiter, *Emerg. Infect. Dis.*, 2000, **6**, 1.
69. D. Greenwood, *J. Antimicrob. Chemother.*, 1995, **36**, 857.
70. J. A. Nájera, M. González-Silva and P. L. Alonso, *PLOS Med.*, 2011, **8**, e1000412.
71. C. P. Sanchez, A. Dave, W. D. Stein and M. Lanzer, *Int. J. Parasitol.*, 2010, **40**, 1109.
72. R. E. Martin, H. Ginsburg and K. Kirk, *Mol. Microbiol.*, 2009, **74**, 519.
73. D. J. Krogstad, I. Y. Gluzman, D. E. Kyle, A. M. J. Oduola, S. K. Martin, W. K. Milhous and P. H. Schlesinger, *Science*, 1987, **238**, 1283.
74. D. A. Fidock, T. Nomura, A. K. Talley, R. A. Cooper, S. M. Dzekunov, M. T. Ferdig, L. M. B. Ursos, A. S. Sidhu, B. Naude, K. W. Deitsch, X. Su, J. C. Wootton and P. D. Roepe, *Mol. Cell*, 2000, **6**, 861.
75. N. Juge, S. Moriyama, T. Miyaji, M. Kawakami, H. Iwai, T. Fukui, N. Nelson, H. Omote and Y. Moriyama, *Proc. Natl. Acad. Sci. USA*, 2015, **112**, 3356.

76. M. B. Reed, K. J. Saliba, S. R. Caruana, K. Kirk and A. F. Cowman, *Nature*, 2002, **403**, 906.
77. A. F. Cowman, S. Karcz, D. Galatis and J. G. Culvenor, *J. Cell Biol.*, 1991, **113**, 1033.
78. Klokouzas, T. Tiffert, D. van Schalkwyk, C. Wu, H. W. van Veen, M. A. Barrand and S. B. Hladky, *Biochem. Biophys. Res. Commun.*, 2004, **321**, 197.
79. R. A. Kavishe, J. M. W. van den Heuvel, M. van de Vegte-Bolmer, A. J. F. Luty, F. G. M. Russel and J. B. Koenderink, *Malaria J.*, 2009, **8**, 205.
80. D. K. Raj, J. Mu, H. Jiang, J. Kabat, S. Singh, M. Sullivan, M. P. Fay, T. F. McCutchan and X. Su, *J. Biol. Chem.*, 2009, **284**, 7686.
81. J. B. Koenderink, R. A. Kavishe, S. R. Rijpma and F. G. M. Russel, *Trends Parasitol.*, 2010, **26**, 440.
82. W. Trager and J. B. Jensen, *Science*, 1976, **193**, 673.
83. M. T. Makler, J. M. Ries, J. A. Williams, J. E. Bancroft, R. C. Piper, B. L. Gibbins and D. J. Hinrichs, *Am. J. Trop. Med. Hyg.*, 1993, **48**, 739.
84. T. J. Egan, D. C. Ross and P. A. Adams, *FEBS Lett.*, 1994, **352**, 54.
85. Y. Kurosawa, A. Dorn, M. Kitsuji-Shirane, H. Shimada, T. Satoh, H. Matile, W. Hofheinz, R. Masciadri, M. Kansy and R. G. Ridley, *Antimicrob. Agents Chemother.*, 2000, **44**, 2638.
86. K. K. Ncokazi and T. J. Egan, *Anal. Biochem.*, 2005, **338**, 306.
87. M. D. Carter, V. V. Phelan, R. D. Sandlin, B. O. Bachmann and D. W. Wright, *Comb. Chem. High Throughput Screen.*, 2010, **13**, 285.
88. R. D. Sandlin, M. D. Carter, P. J. Lee, J. M. Auschwitz, S. E. Leed, J. D. Johnson and D. W. Wright, *Antimicrob. Agents Chemother.*, 2011, **55**, 3363.
89. R. D. Sandlin, K. Y. Fong, K. J. Wicht, H. M. Carrell, T. J. Egan and D. W. Wright, *Int. J. Parasitol.*, 2014, **4**, 316.
90. P. B Macomber, H. Sprinz and A. J. Tousimis, *Nature*, 1967, **214**, 937.
91. A. C. Chou, R. Chevli and C. D. Fitch, *Biochemistry*, 1980, **19**, 1543.
92. T. J. Egan, *J. Inorg. Biochem.*, 2006, **100**, 916.
93. R. Buller, M. L. Peterson, O. Almarsson and L. Leiserowitz, *Cryst. Growth. Des.*, 2002, **2**, 553.
94. K. N. Olafson, M. A. Ketchum, J. D. Rimer and P. G. Vekilov, *Proc. Natl. Acad. Sci. USA*, 2015, **112**, 4946.
95. C. D. Fitch, R. Chevli, H. S. Banyal, G. Phillips, M. A. Pfaller and D. J. Krogstad, *Antimicrob. Agents Chemother.*, 1982, **21**, 819.
96. A. C. Chou and C. D. Fitch, *J. Clin. Invest.*, 1980, **66**, 856.
97. J. M. Combrinck, T. E. Mabotha, K. K. Ncokazi, M. A. Ambele, D. Taylor, P. J. Smith, H. C. Hoppe and T. J. Egan, *ACS Chem. Biol.*, 2013, **8**, 133.
98. H. Ginsburg, O. Famin, J. Zhang and M. Krugliak, *Biochem. Pharmacol.*, 1998, **56**, 1305.
99. P. Loria, S. Miller, M. Foley and L. Tilley, *Biochem. J.*, 1999, **339**, 363.
100. S. N. Cohen, K. O. Phifer and K. L. Yielding, *Nature*, 1964, **202**, 805.
101. K. A. de Villiers, H. M. Marques and T. J. Egan, *J. Inorg. Biochem.*, 2008, **102**, 1660.

102. T. J. Egan and K. K. Ncokazi, *J. Inorg. Biochem.*, 2004, **98**, 144.
103. T. J. Egan, W. W. Mavuso, D. C. Ross, H. M. Marques, 1997, *J. Inorg. Biochem*., 1997, **68**, 137.
104. L. B. Casabianca, D. An, J. K. Natarajan, J. N. Alumasa, P. D. Roepe, C. Wolf and A. C. de Dios, *Inorg. Chem.*, 2008, **47**, 6077.
105. J. Gildenhuys, C. J. Sammy, R. Muller, V. A. Streltsov, T. le Roux, D. Kuter and K. A. de Villiers, *Dalton Trans.*, 2015, **44**, 16767.
106. D. Kuter, S. Benjamin and T. J. Egan, *J. Inorg. Biochem.*, 2014, **133**, 40.
107. D. Kuter, V. Streltsov, N. Davydova, G. A. Venter, K. J. Naidoo and T. J. Egan, *J. Inorg. Biochem.*, 2016, **154**, 114.
108. K. A. de Villiers, J. Gildenhuys and T. le Roux, *ACS Chem. Biol.*, 2012, **7**, 666.
109. A. C. de Dios, R. Tycko, L. M. R. Ursos and P. D. Roepe, *J. Phys. Chem. A*, 2003, **107**, 5821.
110. M. J. Dascombe, M. G. B. Drew, H. Morris, P. Wilairat, S. Auparakkitanon, W. A. Moule, S. Alizadeh-Shekalgourabi, P. G. Evans, M. Lloyd, A. M. Dyas, P. Carr and F. M. D. Ismail, *J. Med. Chem.*, 2005, **48**, 5423.
111. M. Asghari-Khiavi, J. Vongsvivut, I. Perepichka, A. Mechler, B. R. Wood, D. McNaughton and D. S. Bohle, *J. Inorg. Biochem.*, 2011, **105**, 1662.
112. P. A. Adams, P. A. M. Berman, T. J. Egan, P. J. Marsh and J. Silver, *J. Inorg. Biochem.*, 1996, **63**, 69.
113. J. L. Irvin, E. M. Irvin and F. S. Parker, *Science*, 1949, **110**, 426.
114. S. N. Cohen and K. L. Yielding, *J. Biol. Chem.*, 1965, **240**, 3123.
115. J. L. Allison, R. L. O'Brien and F. E. Hahn, *Science*, 1965, **149**, 1111.
116. S. N. Cohen and K. L. Yielding, *Proc. Natl. Acad. Sci. USA*, 1965, **54**, 521.
117. R. L. O'Brien, J. G. Olenick and F. E. Hahn, *Proc. Natl. Acad. Sci. USA*, 1966, **55**, 1511.
118. R. L. O'Brien, J. L. Allison and F. E. Hahn, *Biochim. Biophys. Acta*, 1966, **129**, 622.
119. G. E. Bass, D. R. Hudson, J. E. Parker and W. P. Purcell, *J. Med. Chem.*, 1971, **14**, 275.
120. D. J. Krogstad and P. H. Schlesinger, *Biochem. Pharmacol.*, 1986, **35**, 547.
121. M. W. Davidson, B. G. Griggs, D. W. Boykin, W. D. Wilson, *Nature*, 1975, **254**, 632.
122. M. W. Davidson, B. G. Griggs, D. W. Boykin, W. D. Wilson, *J. Med. Chem.*, 1977, **20**, 1117.
123. F. Kwakye-Berko and S. R. Meshnick, *Mol. Biochem. Parasitol.*, 1989, **35**, 51.
124. A. F. G. Slater, *Pharmac. Ther.*, 1993, **57**, 203.
125. H. Ginsburg and M. Krugliak, *Biochem. Pharmacol.*, 1992, **43**, 63.
126. J. L. Weber, *Gene*, 1987, **52**, 103.
127. S. Percário, D. R. Moreira, B. A. Q. Gomes, M. E. S. Ferreira, A. C. M. Gonçalves, P. S. O. C. Laurindo, T. C. Vilhena, M. F. Dolabela and M. D. Green, *Int. J. Mol. Sci.*, 2012, **13**, 16346.
128. *Antimicrobial Drug Resistance*, ed. L. Bryan, Academic Press, Inc., London, 1984.
129. *Principles of Pharmacology: The Pathophysiological Basis of Drug Therapy*, ed. D. E. Golan, Lippincott Williams & Wilkins, China, 2012.

130. S. R. Meshnick, *Parasitol. Today*, 1990, **6**, 77.
131. H. Ginsburg, *Parasitol. Today*, 1990, **6**, 230.
132. S. R. Meshnick, *Parasitol. Today*, 1990, **6**, 230.
133. F. N. Gyang, B. Poole and W. Trager, *Mol. Biochem. Parasitol.*, 1982, **5**, 263.
134. D. L. Vander Jagt, L. A. Hunsaker and N. M. Campos, *Mol. Biochem. Parasitol.*, 1986, **18**, 389.
135. D. L. Vander Jagt, L. A. Hunsaker and N. M. Campos, *Biochem. Pharmacol*, 1987, **36**, 3285.
136. A. Yayon, J. A. Wande Waa, M. Yayon, T. G. Geary and J. B. Jensen, *J. Protozool.*, 1983, **30**, 642.
137. D. C. Warhurst, J. C. Craig, I. S. Adagu, D. J. Meyer and S. Y. Lee, *Malaria J.*, 2003, **2**, 26.
138. J. N. Alumasa, A. P. Gorka, L. B. Casabianca, E. Comstock, A. C. de Dios and P. D. Roepe, *J. Inorg. Biochem.*, 2011, **105**, 467.
139. C. R. Martinez and B. L. Iverson, *Chem. Sci.*, 2012, **3**, 2191.
140. C. de Duve, T. de Barsy, B. Poole, A. Trouet, P. Tulkens and F. van Hoof, *Biochem. Pharmacol.*, 1974, **23**, 2495.
141. A. Yayon, Z. I. Cabantchik and H. Ginsburg, *EMBO J.*, 1984, **3**, 2695.
142. D. J. Sullivan, I. Y. Gluzman, D. G. Russell and D. E. Goldberg, *Proc. Natl. Acad. Sci. USA*, 1996, **93**, 11865.
143. C. A. Homewood, D. C. Warhurst, W. Peters and V. C. Baggaley, *Nature*, 1972, **235**, 50.
144. H. Ginsburg, E. Nissani and M. Krugliak, *Biochem. Pharmacol.*, 1989, **38**, 2645.
145. S. R. Hawley, P. G. Bray, B. K. Park and S. A. Ward, *Mol. Biochem. Parasitol.*, 1996, **80**, 15.
146. S. R. Hawley, P. G. Bray, P. M. O'Neill, B. K. Park and S. W. Ward, *Biochem. Pharmacol.*, 1996, **52**, 723.
147. P. G. Bray, M. Mungthin, R. G. Ridley and S. A. Ward, *Mol. Pharm.*, 1998, **54**, 170.
148. P. G. Bray, O. Janneh, K. J. Raynes, M. Mungthin, H. Ginsburg and S. A. Ward, *J. Cell. Biol.*, 1999, **145**, 363.
149. T. J. Egan, *Mini. Rev. Med. Chem.*, 2001, **1**, 113.
150. C. Sanchez, W. D. Stein and M. Lanzer, *Mol. Microbiol.*, 2008, **67**, 1081.
151. R. A. Cooper, M. T. Ferdig, X. Su, L. M. B. Urbos, J. Mu, T. Nomura, H. Fujioka, D. A. Fidock, P. D. Roepe and T. E. Wellems, *Mol. Pharmacol.*, 2002, **61**, 35.
152. R. A. Cooper, K. D. Lane, B. Ding, J. Mu, J. J. Patel, T. E. Wellems, X. Su and M. T. Ferdig, *Mol. Microbiol.*, 2007, **63**, 270.
153. S. Harisha, *An Introduction to Practical Biotechnology*, Laximi Publications, New Delhi, 2006.
154. M. Aikawa, *Am. J. Path.*, 1972, **67**, 277.
155. D. Balasubramanian, C. Mohan Rao and B. Panijpan, *Science*, 1984, **223**, 828.
156. R. Zidovetzki, I. W. Sherman, A. Atiya and H. De Boeck, *Mol. Biochem. Parasitol.*, 1989, **35**, 199.

157. R. Zidovetzki, I. W. Sherman, P. A. Maguire and H. De Boeck, *Mol. Biochem. Parasitol.*, 1990, **38**, 33.
158. E. E. Davies, D. C. Warhurst and W. Peter, *Ann. Trop. Med. Parasitol.*, 1975, **69**, 147.
159. G. H. Jacobs, M. Aikawa, W. K. Milhous and J. R. Rabbege, *Am. J. Trop. Med. Hyg.*, 1987, **36**, 9.
160. G. H. Jacobs, A. Oduola, D. E. Kyle, W. K. Milhous, S. K. Martin and M. Aikawa, *Am. J. Trop. Med. Hyg.*, 1988, **39**, 15.
161. N. Sachanonta, K. Chotivanich, U. Chaisri, G. D. H. Turner, D. J. P. Ferguson, N. P. J. Day and E. Pongponratn, *Ultrastruct. Pathol.*, 2011, **35**, 214.
162. L. Roberts, T. J. Egan, K. A. Joiner and H. C. Hoppe, *Antimicrob. Agents Chemother.*, 2008, **52**, 1840.
163. O. Famin and H. Ginsburg, *Biochem. Pharmacol*., 2002, **63**, 393.
164. H. C. Hoppe, D. A. van Schalkwyk, U. I. M. Wiehart, S. A. Meredith, J. Egan and B. W. Weber, *Antimicrob. Agents Chemother.*, 2004, **48**, 2370.
165. M. Mungthin, P. G. Bray, R. G. Ridley and S. A. Ward, *Antimicrob. Agents Chemother.*, 1998, **42**, 2973.
166. E. Smith and I. Collins, *Future Med. Chem.*, 2015, **7**, 159.
167. M. Foley, L. W. Deady, K. Ng, A. F. Cowman and L. Tilley, *J. Biol. Chem.*, 1994, **269**, 6955.
168. J. G. Menting, L. Tilley, L. W. Deady, K. Ng, R. J. Simpson, A. F. Cowman and M. Foley, *Mol. Biochem. Parasitol.*, 1997, **88**, 215.
169. J. A. Read, K. W. Wilkinson, R. Tranter, R. B. Sessions and R. L. Brady, *J. Biol. Chem.*, 1999, **274**, 10213.
170. J. Desneves, G. Thorn, A. Berman, D. Galatis, N. La Greca, J. Sinding, M. Foley, L. W. Deady, A. F. Cowman and L. Tilley, *Mol. Biochem. Parasitol.*, 1996, **82**, 181.
171. P. R. Graves, J. J. Kwiek, P. Fadden, R. Ray, K. Hardeman, A. M. Coley, M. Foley and T. A. J. Haystead, *Mol. Pharm.*, 2002, **62**, 1364.
172. H. Zhang, M. Paguio and P. D. Roepe, *Biochemistry*, 2004, **43**, 8290.
173. J. K. Lekostaj, J. K. Natarajan, M. F. Paguio, C. Wolf and P. D. Roepe, *Biochemistry*, 2008, **47**, 10394.
174. P. Pleeter, J. K. Lekostaj and P. D. Roepe, *Mol. Biochem. Parasitol.*, 2010, **173**, 158.

Chapter Two

Principles of Fluorescence and Applications in Spectroscopy and Microscopy

2.1. Introduction

Fluorescence spectroscopy and microscopy form the basis of the investigations reported in Chapters 4 and 5 of this thesis, respectively. Hence, in order to provide a more meaningful discussion of the results in these chapters, theoretical aspects of fluorescence and their specific applications to these technologies are presented in this chapter.

Fluorescence-based techniques have recently enjoyed remarkable growth across many disciplines, culminating in the award of the 2014 Nobel Prize in Chemistry for the development of super-resolution fluorescence microscopy. This recognition represents the pinnacle of a century-and-a-half of investigation that now permits the imaging of single proteins inside living cells with exquisite precision.

Technologies exploiting fluorescence are characterised by rapid speeds of response, high spatial resolution and ultra-high sensitivity, making fluorescence the physical technique of choice for probing the structure and dynamics of biological systems. However, although modern instruments enjoy single parts-per-trillion sensitivity over large concentration ranges, the susceptibility of electronically-excited states to deactivation means that experiments must be planned carefully to avoid the pervasive effects of interference.

This chapter will describe the theoretical principles of fluorescence and their applications in spectroscopy and microscopy with specific relevance to this study. The historical context of fluorescence will be presented as well as detailed descriptions of the electronic events associated with fluorescence excitation and emission. Practical aspects of fluorescence spectroscopy will be described, noting the challenges posed by inner-filter effects. Applications in fluorescence microscopy will then be presented with specific reference to the diffraction limit and super-resolution structured-illumination microscopy (SR-SIM). Finally, various methods of quantitative image analysis by global statistical analysis of pixel intensity distributions will be explained.

2.2. Historical aspects of fluorescence

It is an interesting reflection in the context of this study that the history of fluorescence is intimately linked to the alkaloid quinine. Its reputation as a famous antimalarial meant that it was a molecule of intense interest amongst scientists. The alkaloid fluoresces strongly in aqueous solutions excited by ultraviolet light, so it is not surprising that modern investigations in fluorescence began with the observation of a quinine solution in sunlight.

Firstly, it is worth drawing attention to the origin of the term "fluorescence" which is not immediately clear. It is odd that the word contains "fluor" (fluorine) which is not a fluorescent element. In contrast, the etymologies of the related terms "phosphorescence" and "luminescence" are straightforward; both of these are preceded by the Greek and Latin words for "light", respectively.[1] Instead, the word "fluorescence" was invented by Sir George Stokes (1819-1903), a 19th century physicist and mathematician.

Stokes's observations of quinine sulfate in solution followed those of Sir John Herschel (1792-1871), the famous polymath, who was the first to observe the unusual blue phenomenon at the surface of an acidic solution of the alkaloid in sunlight:

> *Though perfectly transparent and colourless when held between the eye and the light …* [the quinine sulfate solution] *yet exhibits … under certain incidences of light an extremely vivid and beautiful celestial blue colour, which, from the circumstance of its occurrence, would seem to penetrate in those strata in which the light first penetrates in entering the liquid, and which … exert their peculiar power … only through a very small depth within the medium.*[2]

He called this phenomenon "epipolic dispersion" from the Greek word meaning "pertaining to the surface".[3] Herschel's description also reveals the first indirect observation of the inner-filter effect (Section 2.4.2). As relatively concentrated (millimolar) solutions of quinine were used, the fluorescence was only observed near the surface and "only through a very small depth" because the sunlight was entirely absorbed by the fluorophore within the first few millimetres before penetrating more deeply into the solution.

Later, it was Stokes who demonstrated that the phenomenon was an emission process following the absorption of light. In an elegant experiment, Stokes formed the solar spectrum by means of a prism.[1] When he moved the quinine sulfate solution through the visible part of the spectrum, the solution simply remained transparent. But beyond the violet portion of the spectrum (that is, in the region corresponding to ultraviolet radiation), the solution glowed with a blue light.[4] He wrote: "It was certainly a curious sight to see the tube instantaneously light up when plunged into the invisible rays; it was literally *darkness visible*."[5]

Stokes initially called this phenomenon "dispersive reflexion" but in a footnote he wrote: "I do not like this term. I am almost inclined to coin a word, and call the appearance *fluorescence*, from fluorspar, as the analogous term opalescence is derived from the name of a mineral."[6] It is now known that, while calcium fluoride (the major constituent of fluorspar) is not fluorescent, fluorspar *appears* fluorescent due to the presence of small amounts of fluorescent lanthanides.[4]

Together, these observations by Herschel and Stokes laid the foundations for a century-and-a-half of intense development in the field of fluorescence. Edmond Becquerel (1820-1891), a French physicist and father of Henri Becquerel who discovered radioactivity, described the apparent "fluorescence" of calcium sulfide and was the first to articulate that the emitted light is of longer wavelength than the incident light.[4] Calcium sulfide is, in fact, phosphorescent and the first theoretical distinction between these two processes was provided by Francis Perrin (1901-1992) who also worked on a quantitative model of fluorescence quenching and polarised fluorescence.[4] In 1948, Theodor Förster (1910-1974) published his quantum mechanical theory of dipole-dipole energy transfer (Section 2.3.5).

It was around this time that quinine was again to play an important role in the history of fluorescence.[7] During World War II, the United States Department of War was interested in developing fluorimetric techniques to monitor blood levels of antimalarials that were being tested in patients and volunteers, including quinine and chloroquine.[8] A programme at the National Institutes of Health led to the development of the first commercial spectrofluorimeters, the precursors to the instruments that are now ubiquitous in analytical research laboratories.

2.3. Characteristics of fluorescence excitation and emission

2.3.1. Electronic spin states

Luminescence is the emission of light by a substance that has not been heated and is thus a form of cold body radiation. Fluorescence and phosphorescence are alike in that they both involve the emission of light from an excited state brought about by the absorption of photons. Consequently, they are referred to as *photo*luminescent processes to distinguish them from other types of luminescence.

Fluorescence is the emission of light from a singlet excited state while phosphorescence is the emission of light from a triplet excited state. In the former state, the electron in the excited orbital is paired by opposite spin to the electron in the ground state orbital (Figure 2.1). Return to the ground state is spin-allowed and typically occurs within nanoseconds. Emission of light from a triplet excited state is spin-forbidden but it is still observed as a result of spin-orbit coupling. As a result, transitions to the ground state from the triplet excited state are much slower and typically occur within milliseconds or seconds.‡

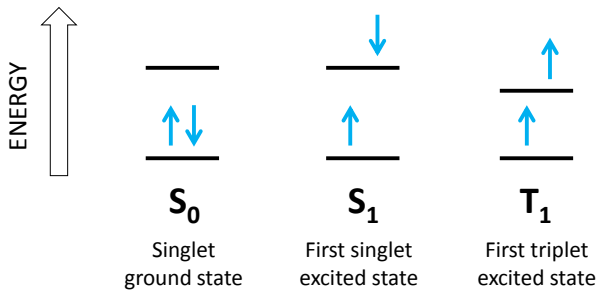

Figure 2.1. *An illustration of singlet and triplet electronic states. Note that the triplet excited state is less energetic than the corresponding singlet excited state.*

2.3.2. The Perrin-Jabłoński diagram

The Perrin-Jabłoński diagram is a partial energy-level diagram for a photoluminescent system and is a useful illustration of the photophysical processes that are relevant to fluorescence

‡ The nomenclature "singlet" and "triplet" derive from spectroscopic multiplicity considerations. Multiplicity is defined as $M = 2S + 1$, where S represents the total spin quantum number which is the sum of the individual spins of electrons which are either +½ or -½ depending on their direction. In a singlet state, for example, the total spin quantum number corresponds to $S = 0$. Consequently, the multiplicity equals one and the state is described as a singlet.

excitation and emission. The Polish physicist Alexander Jabłoński (1898-1950) is regarded as the "father" of fluorescence spectroscopy and the diagram is named after him along with Francis Perrin and his father, the physicist Jean Perrin (1872-1942).[4]

The singlet ground state and first and second excited states are depicted by $\mathbf{S_0}$, $\mathbf{S_1}$ and $\mathbf{S_2}$, respectively (Figure 2.2). At each of these electronic energy levels the molecules can exist in a number of vibrational states depicted by 0, 1, 2, etc. and further rotational energy levels which are not illustrated. Transitions between states are indicated by vertical lines to indicate the almost instantaneous nature of light absorption or emission. Dotted lines are used to indicate transitions between states resulting from internal conversion or non-radiative relaxation processes.

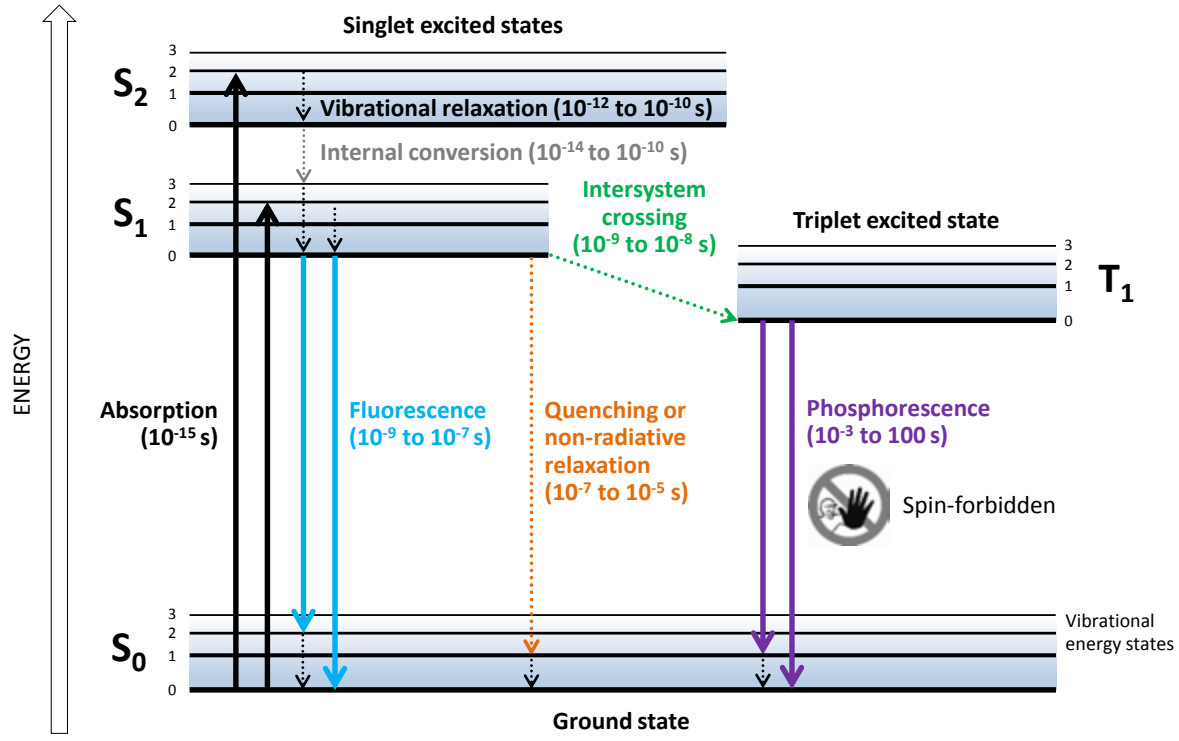

Figure 2.2. *A Perrin-Jabłoński diagram indicating energy levels and states leading to fluorescence, phosphorescence and non-radiative relaxation processes. Typical timescales for these events are indicated.*

At room temperature, thermal energy is not sufficient to populate excited vibrational states. At this temperature an even larger energy difference between ground and excited singlet states does not allow for thermal population of $\mathbf{S_1}$. Consequently, as absorption and emission typically occur from molecules in their lowest vibrational energy states, light is used to induce fluorescence and not heat.[7]

The fluorescence process is typically governed by three important events, all of which occur on timescales separated by several orders of magnitude. When a photon is rapidly absorbed by a susceptible molecule (a femtosecond event), the molecule is excited to a higher vibrational level of either of the electronically-excited singlet states, $\mathbf{S_1}$ or $\mathbf{S_2}$. These higher states then rapidly relax to the lowest vibrational level of $\mathbf{S_1}$ by the slower processes of vibrational relaxation or internal conversion which are together measured on the picosecond scale. The excess energy is dissipated to solvent molecules as heat.

The final process, emission of a photon and return to the ground state which typically manifests as fluorescence, is longer still on the order of nanoseconds. Fluorescence emission almost inevitably occurs from a thermally-equilibrated excited state, i.e. the lowest vibrational state of $\mathbf{S_1}$. Return to the ground state typically occurs to a higher vibrational level of $\mathbf{S_0}$ which then rapidly (10^{-12} s) reaches thermal equilibrium to the lowest vibrational level in the ground state. Consequently, the fluorescence emission spectrum is often a mirror-image of the absorbance spectrum of the $\mathbf{S_0 \rightarrow S_1}$ transition which reflects the manifold of closely-spaced vibrational modes of the ground state to which the fluorophore may return.

Although the entire fluorescence lifetime, from excitation to emission, is measured in billionths of a second, the phenomenon is a stunning manifestation of the interaction between light and matter which forms the foundation for the expansive fields of florescence spectroscopy and microscopy.[9] Most fluorophores repeat this excitation and emission cycle many hundreds of thousands of times before the highly-reactive excited state molecule is photobleached, resulting in destruction of the fluorophore.[9]

Several other excitation pathways with varying degrees of probability compete with the fluorescence emission process. The excited state can be dissipated non-radiatively as heat, either through a quenching mechanism or via energy transfer to a second molecule in another non-radiative process. These intermolecular deactivation processes are broadly termed external conversion.[10]

Alternatively, molecules in $\mathbf{S_1}$ can also undergo spin conversion to the first triplet state ($\mathbf{T_1}$) via intersystem crossing. As mentioned previously, emission from the triplet state is termed phosphorescence and generally occurs at longer wavelengths than fluorescence. As the transition to the singlet state is a forbidden process which violates the spin selection rule, these processes exhibit rate constants much lower than those for fluorescence and may occur on a timescale from milliseconds to dozens of seconds. However, phosphorescence is seldom observed in solution as it is outcompeted by non-radiative quenching processes.

The $\mathbf{T_1 \rightarrow S_0}$ transition is favoured by spin-orbit coupling and can therefore be increased in the presence of heavy atoms such as bromine and iodine. The efficiency of intersystem crossing increases according to the fourth power of the atomic number, indicating that these interactions are significantly larger for heavier atoms.[4] Fluorescence quenching by "heavy atom" effects are also explained by the rate enhancement of spin-forbidden processes due to the presence of an atom of high atomic number.

2.3.3. Other concepts associated with fluorescence

Three fundamental parameters are commonly used to describe and compare fluorophores: the molar absorption coefficient, the fluorescence quantum yield and the fluorescence lifetime.

The molar absorption coefficient (ε) is a direct measure of the molecule's ability to absorb light. Fluorophores with a large molar absorption coefficient typically have a high probability of fluorescence emission.

The fluorescence quantum yield (Φ) or quantum efficiency is defined as the ratio of the number of photons emitted as fluorescence to the number of photons absorbed. The brightest fluorophores have fluorescence quantum yields approaching unity. Experimentally, relative fluorescence quantum yields can be determined by comparing a fluorophore of known fluorescence quantum yield to a fluorophore of unknown fluorescence quantum yield while keeping the experimental parameters constant.

As the fluorescence quantum yield of a compound is determined by the relative rate constants of processes by which the lowest excited singlet state is deactivated, the fluorescence quantum yield is susceptible to a variety of other factors such as pH, solvent polarity and concentration. The most important processes to consider are the fluorescence itself (k_f), intersystem crossing (k_i), internal conversion (k_{ic}), external conversion (k_{ec}) and dissociation (k_d).[11] These relationships are expressed in Equation 2.1:

$$\text{Fluorescence quantum yield } (\Phi) = \frac{k_f}{k_f + k_i + k_{ic} + k_{ec} + k_d}$$

Equation 2.1

The reciprocal of the fluorescence decay rate constant (k_f) is called the intrinsic lifetime of a fluorophore (τ_0), which is defined as the lifetime of the excited state in the absence of all processes that compete for excited state deactivation.[9] In reality, the fluorescence excited state

lifetime is shortened by non-radiative processes resulting in a measured lifetime (τ_f) that is a combination of the intrinsic lifetime and competing non-fluorescent relaxation mechanisms. Because the measured lifetime is always less than the intrinsic lifetime, the fluorescence quantum yield never exceeds a value of unity. Thus the fluorescence quantum yield can also be defined in terms of lifetime values in Equation 2.2:

$$\text{Fluorescence quantum yield } (\Phi) = \frac{\tau_f}{\tau_0}$$

Equation 2.2

"Kasha's rule", named after the American spectroscopist Michael Kasha (1920-2013), states that the emission spectrum of a fluorophore is independent of the excitation wavelength. As previously described, despite a manifold of higher electronic and vibrational levels being reached upon excitation, the excess energy is quickly dissipated to the lowest vibrational level of the first singlet excited state ($\mathbf{S_1}$). This relaxation occurs irrespective of the excitation wavelength and, because of this rapid deactivation process, emission spectra appear to be independent of the excitation wavelength.

This effect is illustrated by the absorption and emission spectra of the quinine dication (Figure 2.3). Primary and secondary absorption peaks are observed at λ_{max} 345 nm and 320 nm, respectively. The lower-energy band corresponds to a transition to the first excited singlet state ($\mathbf{S_0 \rightarrow S_1}$) while the higher-energy band corresponds to the $\mathbf{S_0 \rightarrow S_2}$ transition which rapidly relaxes to $\mathbf{S_1}$. Hence fluorescence is observed only from $\mathbf{S_1}$ and not from the second singlet excited state. Consequently, the emission spectrum is a mirror image of only the $\mathbf{S_0 \rightarrow S_1}$ absorption spectrum. This general observation is called the "mirror-image rule".

Because the energy associated with the fluorescence emission transition ($\mathbf{S_1 \rightarrow S_0}$) is almost invariably less than that of the absorption process, the emitted photons have less energy and longer wavelengths. This gives rise to the "Stokes shift" which is the difference between the positions of the two band maxima of the absorption and emission spectra of the same electronic transition (Figure 2.3). An increase in the Stokes shift may also be observed due to solvent effects, with more polar solvents resulting in larger Stokes shifts than less polar solvents due to solvent-specific relaxation effects during the excited state (Section 2.3.6).

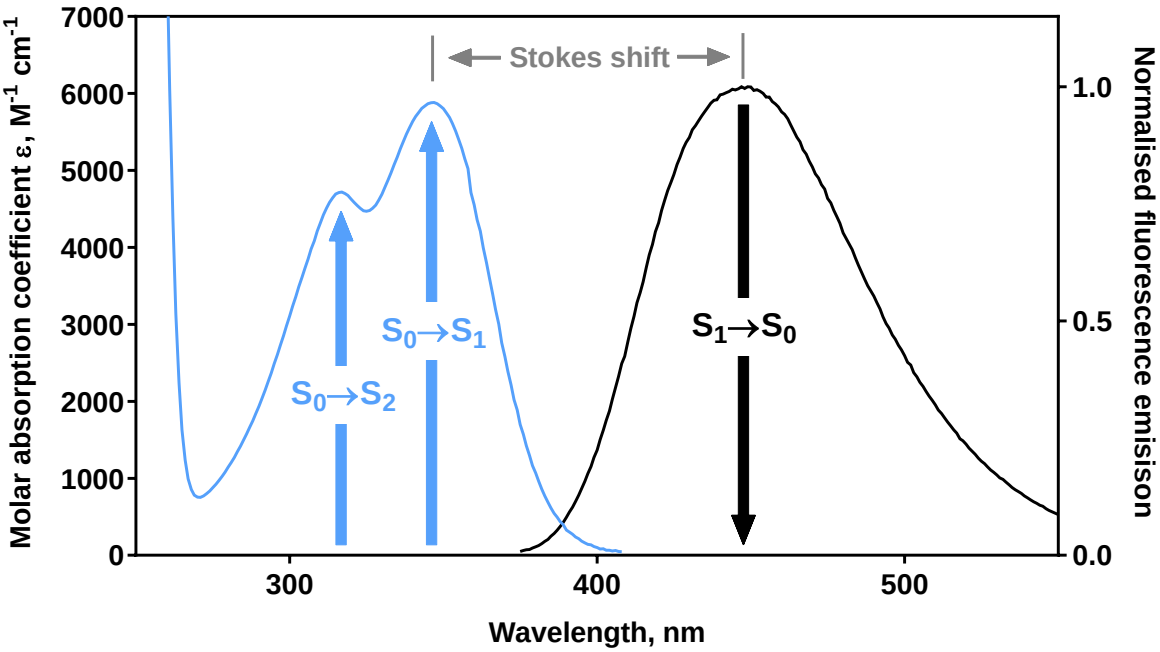

Figure 2.3. *The absorption spectrum of quinine in 0.5 M sulphuric acid and its corresponding fluorescence emission spectrum following excitation at 333 nm. Vertical arrows indicate electronic transitions and the horizontal arrows indicate a large Stokes shift between the absorption and emission maxima.*

2.3.4. Fluorescence quenching

The intensity of fluorescence emission is susceptible to changes in pH, temperature and solvent polarity. Perhaps the most important measurements of changes in the intensity of fluorescence emission are those caused by quenching. These are decreases in fluorescence intensity arising from competing *intermolecular* processes that induce non-radiative relaxation of excited state electrons to the ground state. The kinetics of these deactivation processes are typically described using the Stern-Volmer relationship that was developed at the beginning of the 20th century.[7]

While processes such as fluorescence and phosphorescence are examples of *intra*molecular deactivation processes, *inter*molecular deactivation processes usually fall into two groups. Static quenching (also referred to as contact quenching) arises from the formation of a non-fluorescent complex between the fluorophore and the quencher that serves to limit absorption by reducing the population of active, excitable molecules.[7] Static quenching occurs when the molecules form a complex in the ground state before excitation occurs. The complex has its own unique properties such as being non-fluorescent and having its own absorption spectrum. The

fluorescence emission is therefore reduced without altering the average lifetime of the excited state.[7]

On the other hand, collisional (or dynamic) quenching occurs when the excited state is deactivated upon interaction with another non-fluorescent molecule in solution.[7] Neither of the molecules is chemically altered in the collisional quenching process. Mechanisms for collisional quenching include electron transfer, spin-orbit coupling (usually in the presence of the heavier halogens) and intersystem crossing to the excited triplet state. Typically, higher temperatures and lower viscosities accelerate the quenching process as they lead to increased collisions between molecules and hence diminished fluorescence. A fluorophore in the excited state may also be quenched by a dipolar resonance energy transfer mechanism to an acceptor molecule in which the excited state energy can be transferred non-radiatively.

2.3.5. Förster resonance energy transfer

A fluorophore in the first singlet excited state can variously lose its excitation energy by conversion into light (fluorescence), via thermal equilibration (vibrational relaxation) or by formation of a non-fluorescent ground state complex with another molecule (static quenching).

Yet another mechanism, first described by Theodor Förster in 1948, is a non-radiative energy transfer process that is regarded as a dynamic quenching mechanism because energy transfer occurs while the donor is in the excited state.[12] Förster resonance energy transfer is a long-range electrodynamic phenomenon that has found countless applications, particularly in biological systems in which its distance-dependence means that it can be used as a "spectroscopic ruler".‡ The premise of Förster's theory is that the "donor" fluorophore can be treated as an oscillating dipole at a particular resonant frequency in a manner analogous to the behaviour of coupled oscillators.

Förster resonance energy transfer occurs between a donor in its excited state and an "acceptor" in its ground state. (The latter molecule does not have to be capable of fluorescence.) Energy transfer occurs without the appearance of a photon and is the result of long-range dipole-dipole interactions between the donor and acceptor.[7] The transfer of energy is manifested both by quenching of the donor fluorescence emission in the presence of the acceptor and increased (so-called "sensitised") fluorescence emission from the acceptor.[7]

‡ "FRET" is sometimes inappropriately called "fluorescence" resonance energy transfer. This is misleading because the resonance energy transfer associated with Förster resonance energy transfer does not necessarily involve fluorescence.

The rate of energy transfer depends on (i) the spectral overlap of the emission spectrum of the donor and the absorption spectrum of the acceptor, (ii) the quantum yield of the donor, (iii) the relative orientation of donor and acceptor transition dipoles and (iv) the distance between the two molecules. This distance-dependence allows quantitative distance measurements between the donor and acceptor.

The distance between a donor and acceptor pair (R) can be calculated from the efficiency of energy transfer (E) given by Equation 2.3 below:

$$E = 1/[1 + (R/R_0)^6]$$

Equation 2.3

R_0, the characteristic transfer distance for which I/I_0 = 0.5 and which is known as the Förster distance, is given by Equation 2.4:

$$R_0 = 9.79 \times 10^{-5} \, (J \, \kappa^2 \, n^{-4} \, \Phi_D)^{1/6}$$

Equation 2.4

In this equation, J is a measure of the spectral overlap between the donor fluorescence emission and acceptor absorption, κ is a geometric factor dependent on the relative orientations of the donor and acceptor, n is the refractive index of the medium and Φ_D is the donor fluorescence quantum yield. κ approaches two-thirds if the donor and acceptor are free to tumble rapidly on the timescale of the fluorescence emission and this value is usually used in such calculations.[13] The efficiency of Förster resonance energy transfer varies with the degree of spectral overlap but, most importantly, as the inverse of the sixth power of the distance separating the donor and acceptor. The value of the spectral overlap is calculated from Equation 2.5:

$$J = \int \varepsilon_A(\lambda) \, I_D(\lambda) \, \lambda^4 \, d\lambda \Big/ \int I_D(\lambda) \, d\lambda$$

Equation 2.5

Here, $\varepsilon_A(\lambda)$ is the extinction coefficient of the acceptor and $I_D(\lambda)$ is the normalised fluorescence intensity of the donor. Wavelengths (λ) are expressed in centimetres. Typically the fluorescence intensity is measured in arbitrary units (I) and normalisation is achieved using this equation.

2.3.6. Solvatochromism

It has been mentioned before that local environmental factors such as temperature, pH and solvent polarity have profound effects on the emission spectra of fluorophores. The effects of these parameters vary widely from one fluorophore to another. Solvatochromism is the shift in fluorescence emission maxima resulting from changes in solvent polarity.

Solvent molecules surrounding the ground state fluorophore also possess dipole moments that can interact with the dipole moment of the fluorophore. In the ground state, these arrange to form an ordered distribution of solvent molecules around the fluorophore (Figure 2.4). Following excitation, there is a change in the dipole moment of the fluorophore that ultimately induces a rearrangement of surrounding solvent molecules. However, the Franck-Condon principle dictates that, upon excitation of a fluorophore, the molecule is excited to a higher electronic level far more rapidly than it takes for the fluorophore and solvent molecules to rearrange. As a result, there is a delay between the excitation and the re-ordering of the solvent molecules around the solvated fluorophore, which generally has a much larger dipole moment in the excited state.

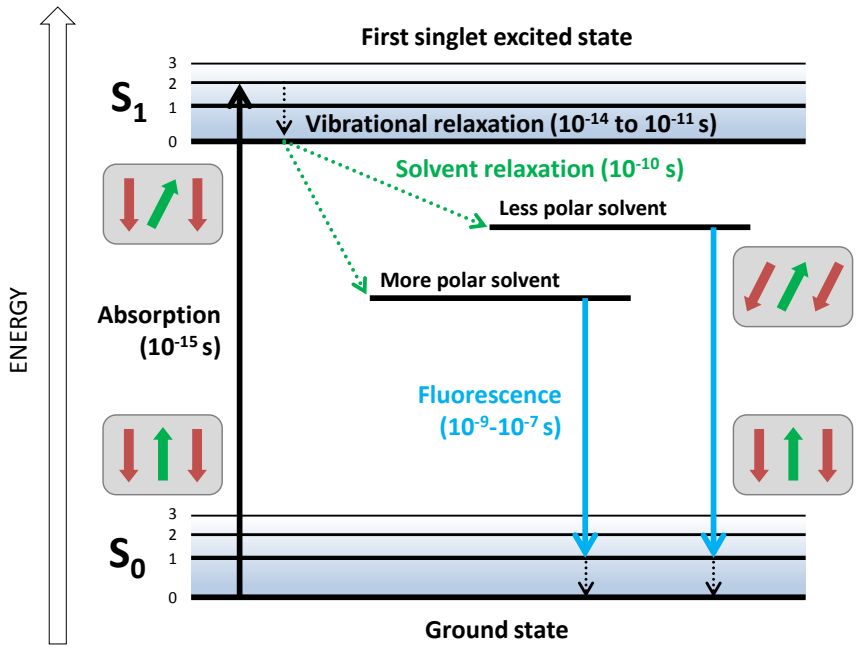

Figure 2.4. *A Perrin-Jabłoński diagram indicating energy levels and states involved in solvent relaxation. The grey boxes indicate the alignment of the dipole moments of the fluorophore (green) and solvent molecules (red) relative to one another in their ground and energetically-excited states.*

After the fluorophore has been excited to higher vibrational levels of the first excited singlet state ($\mathbf{S_1}$), excess vibrational energy is rapidly lost to the surrounding solvent molecules as the fluorophore slowly relaxes to the lowest vibrational energy level of that state. Solvent molecules assist in lowering the energy of the excited state by rearranging around the excited fluorophores in a slower process termed solvent relaxation. A more polar solvent produces a correspondingly larger reduction in the energy level of the excited state, while a less polar solvent reduces the stabilisation effects of the solvent on the excited state. Consequently, a larger Stokes shift is seen in polar solvents while a smaller Stokes shift is observed in non-polar solvents.

Because fluorescence lifetimes are much longer than the time required for solvent relaxation (on the order of picoseconds), fluorescence emission spectra are representative of the solvent-relaxed environment in which solvent molecules are oriented around the dipole moment of the excited state fluorophore. However, because absorption is so rapid (on the order of femtoseconds), absorption spectra are less affected by solvent polarity because the ground and excited states are exposed to the same local environments.

2.4. Fluorescence spectroscopy

2.4.1. Instrumentation

Spectrofluorimetry is most accurate at very low concentrations of the fluorophore. Under optically dilute or "ideal" conditions, the intensity of fluorescence $F_{\text{ideal}}(\lambda_{\text{ex}}, \lambda_{\text{em}})$ that is observed is related to the intensity of the incident radiation $I_0(\lambda_{\text{ex}})$ according to Equation 2.6:

$$F_{\text{ideal}}(\lambda_{\text{ex}}, \lambda_{\text{em}}) = 2.3 \times k(\lambda_{\text{ex}}, \lambda_{\text{em}}) \times I_0(\lambda_{\text{ex}}) \times \varepsilon(\lambda_{\text{ex}}) \times \Phi(\lambda_{\text{em}}) \times \Delta x \times c$$

Equation 2.6

Here, $k(\lambda_{\text{ex}}, \lambda_{\text{em}})$ is an instrument constant dependent on geometrical and optical factors and is a function of the excitation and emission wavelengths, $\varepsilon(\lambda_{\text{ex}})$ is the molar absorption coefficient at the excitation wavelength, c is the concentration of the fluorophore, Δx is the pathlength of the excitation beam and $\Phi(\lambda_{\text{em}})$ is the fluorescence quantum yield at the emission wavelength.[14]

This direct relationship between fluorescence intensity and the concentration of the fluorophore allows relatively simple electronics and optics to be used in a spectrofluorimeter (Figure 2.5). The light source is generally a xenon lamp that illuminates equally in all directions. Two monochromators are usually employed, the first of which selects the excitation wavelength. Radiation from the excitation monochromator is split with part of the radiation passing to a reference photomultiplier tube and part to the sample. After fluorescence emission occurs from the sample in all directions, the second monochromator determines the emission wavelengths to be transmitted to the detector. Following dispersion by the emission monochromator, the light is detected using a second sensitive photocell.[11,15]

Temperature control is required for accurate work as the intensity of fluorescence varies considerably over small temperature ranges. Furthermore, it is difficult to compare emission spectra quantitatively across instruments as the output depends not only on the fluorescence intensity but also on the characteristics of the lamp, transducer and monochromators. All of these components vary with wavelength and differ from instrument to instrument.[11]

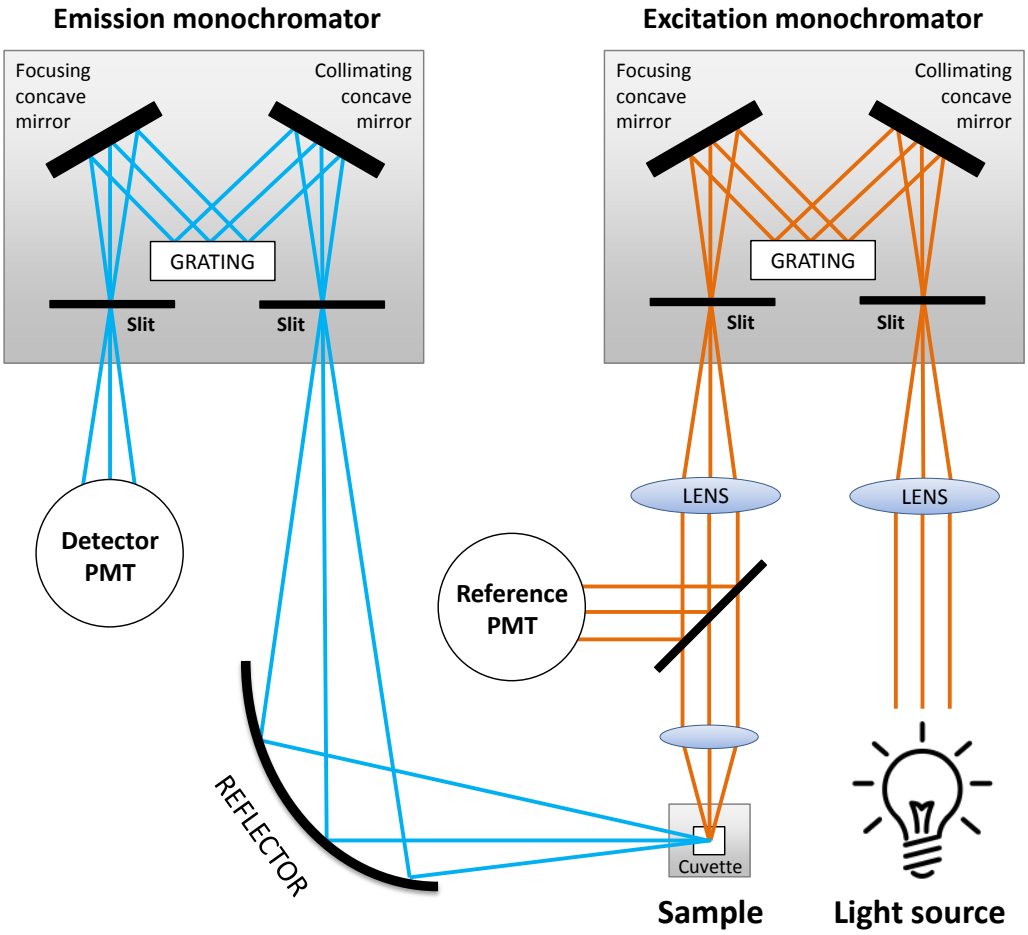

Figure 2.5. *Schematic of a typical spectrofluorimeter. Orange rays indicate incident radiation while blue rays indicate fluorescence leaving the sample following excitation.*

Two approaches are possible for the illumination of the sample. The simplest and most common configuration involves excitation and emission from the centre of the cuvette, at right angles to one another. An alternative and less common approach is front-face illumination which obviates inner-filter effects.

2.4.2. Inner-filter effects

As shown in Equation 2.6, fluorescence intensity is a linear function of the concentration of the fluorophore with zero intercept under "ideal" conditions. However, these conditions are met only when the attenuation of light at both excitation and emission wavelengths is negligible over the pathlengths of interest. Absorption of excitation and/or emission radiation by a sample reduces the fluorescence intensity and results in a nonlinear relationship between the observed

fluorescence intensity and the concentration of the fluorophore. This is called the inner-filter effect.

Usually, the optical arrangement of a commercial spectrofluorimeter focuses the exciting light and collects the fluorescence emission from the centre of the cuvette (Figure 2.6). Therefore, when absorption at the excitation wavelength is significant, less light reaches the centre of the sample and thus the fluorescence of the fluorophore is reduced. This is called the primary inner-filter effect (or pre-inner filter effect). Similarly, absorption at the emission wavelength reduces the emitted light that reaches the detector. This is the secondary inner-filter effect (or post-inner-filter effect). Such effects are particularly evident in concentrated solutions. An excellent example is Herschel's original observation of quinine fluorescence which was only seen to penetrate "through a very small depth" of the solution.[2]

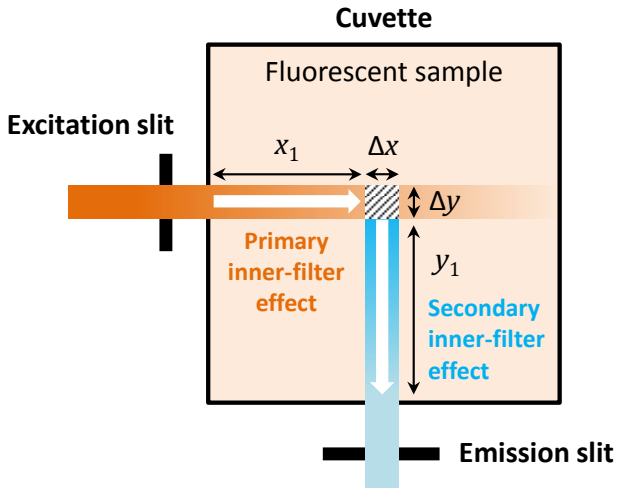

Figure 2.6. *Illustration of inner-filter effects within a cuvette showing the attenuation of both the excitation radiation and the emitted fluorescence. Instrument parameters relevant to Equation 2.8 are also indicated.*

Various correction factors have been proposed to reduce the impact of the inner-filter effect. If the geometry of the instrument is such that the collected intensity comes exactly from the centre of the cuvette, the inner-filter effect can be estimated from Equation 2.7:

$$F_{\text{corr}} = F_{\text{obs}} \times 10^{-\frac{A_{\text{ex}} \times d_{\text{ex}}}{2} - \frac{A_{\text{em}} \times d_{\text{em}}}{2}}$$

Equation 2.7

Here, F_{corr} is the corrected fluorescence intensity that would be measured in the absence of the inner-filter effect, F_{obs} is the observed (measured) fluorescence in the presence of the inner-filter effect, d_{ex} and d_{em} are the cuvette pathlengths in the excitation and emission direction, respectively, recorded in centimetres (these are typically 0.5 cm in a 1 cm pathlength cuvette), and A_{ex} and A_{em} are the measured *changes* in absorbance at the excitation and emission wavelengths, respectively, caused by the addition of the aliquot (in a 1 cm pathlength cuvette).[16]

In Equation 2.7 above, the fluorescence is assumed to originate exactly from the centre of the cuvette. This may be the case for some spectrometers, but certainly not all. A more sophisticated correction takes into account instrument-specific factors as well. In this case, the most common case of right-angle geometry is used and the excitation and emission beams are modelled as sharp-edged, uniform and collimated with rectangular cross-sections of known dimensions determined by the slit widths and heights of the excitation and emission monochromators.[14]

This results in a relationship between F_{ideal} and F_{obs} as described in the Equation 2.8:[14]

$$F_{\text{ideal}} = F_{\text{obs}} \times \frac{2.3a_{\text{ex}}\Delta x 10^{a_{\text{ex}}x_1}}{1-10^{-a_{\text{ex}}\Delta x}} \times \frac{2.3a_{\text{em}}\Delta y 10^{a_{\text{em}}y_1}}{1-10^{-a_{\text{em}}\Delta y}}$$

Equation 2.8

Here, a_{ex} and a_{em} are absorbances of the solution per centimetre at λ_{ex} and λ_{em}, respectively, and x_1 and y_1 are the distances from the edges of the beams to the cuvette wall towards the light source and towards the detector, respectively (Figure 2.6). The geometrical parameters Δx, x_1, Δy and y_1 are in units of centimetres. In this model, the fluorescence signal arises from molecules in the overlap volume of the excitation and emission beams (shown as the shaded square in Figure 2.6). Approximation of each of these correction factors as $10^{a_{ex}x_1}$ and $10^{a_{em}y_1}$, respectively, with $x_1 = y_1$ (approximately 0.5 cm for the typical 1 cm square cuvette), returns the simpler expression in Equation 2.7 above.[14]

Deviations from these more advanced correction methods may still occur, particularly at high absorbance values. Thus, rather than correcting the inner-filter effects, it may be more appropriate to minimise them by practical considerations such as reducing the pathlength by using a smaller cuvette or selecting excitation and emission wavelengths that minimise absorption.

2.5. Fluorescence microscopy

The purpose of microscopy is insight not images.

– R.W. Hamming

Fluorescence is arguably at its most powerful when it is used in biological imaging. Modern fluorescence microscopy offers one the possibility to probe the dynamics of living cells at high spatial resolution and in a manner that is minimally invasive. With the vast number of fluorescent stains that are readily available, fluorescence microscopy also allows for the rapid identification of subcellular components with a high degree of specificity.

An important technical consideration is the ability of the microscope to form an image in the focal plane with simultaneous suppression of out-of-plane emission. This is the advantage of confocal microscopy over traditional widefield methods, as detailed below. Meanwhile, the limit of spatial resolution in fluorescence microscopy is dictated by the wavelength of light that is used and is known as the "diffraction limit". The German physicist Ernst Abbe (1840-1905) defined this limit as the ability of a lens-based optical microscope to discern only those details that are longer than half the wavelength of the incident light. However, this limit has been surpassed by a suite of super-resolution techniques that has given rise to the field of "nanoscopy".

2.5.1. Widefield (epifluorescence) microscopy

Widefield microscopy is the most popular fluorescence microscopy technique. Although it is not used in this study, it is presented here for comparison with other techniques.

In this configuration, excitation and observation occurs from *above* the specimen (hence it is also known as "epifluorescence" microscopy). This is in contrast to common optical microscopes that collect light that is transmitted through the sample.[17]

The light source passes bright white light through a filter to produce the excitation beam (Figure 2.7). This is reflected by a dichroic mirror that passes the beam through the objective to interact with the sample. Fluorescence emission from the sample is passed back through the objective and the dichroic mirror transmits only the (weaker) fluorescence light. Finally, the fluorescence is passed through the emission filter and is captured with a detector.

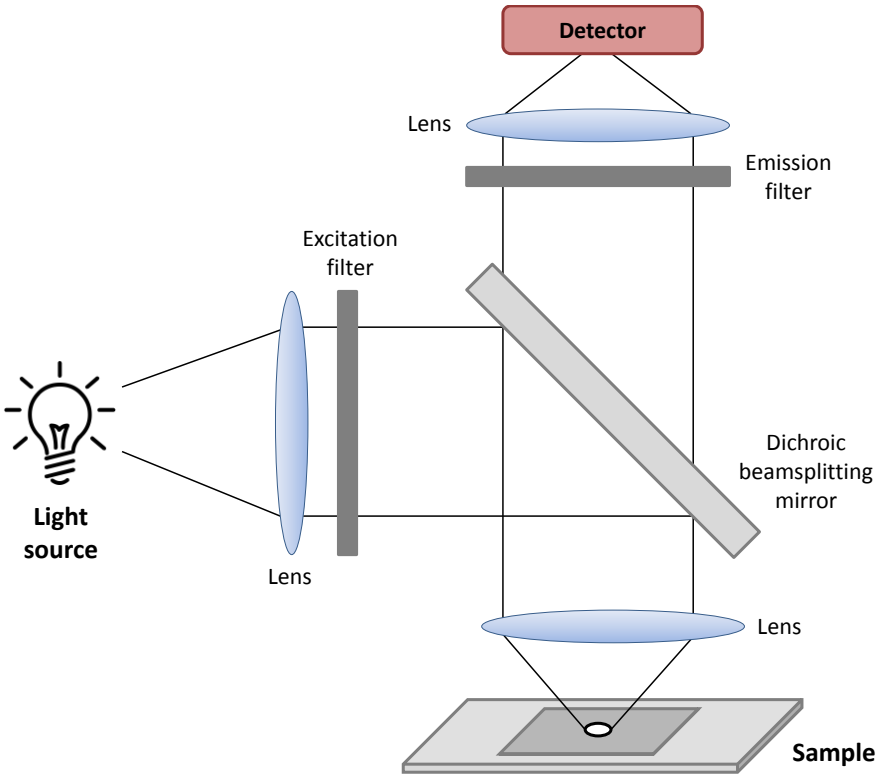

Figure 2.7. *Schematic of a simple widefield microscope. Excitation light, after passing through the first optical filter, is focused on the specimen from above. Fluorescence is directed to the detector after passing through the emission filter that rejects reflected and scattered excitation light.*

The epifluorescence microscope allows efficient collection of fluorescence arising from the sample. Filters match the excitation light that is used to illuminate the specimen and sort the (much weaker) emitted light from the scattered excitation light to make up the image. Hence the bright fluorescence areas are observed against a dark background with high contrast. The major disadvantage of this form of microscopy is that it collects the image of a specimen with three-dimensional emission of fluorescence as a two-dimensional image formed by in-focus and out-of-focus fluorescence emission. Thus is it sometimes difficult to judge what is "in front" and what is "behind". This spatial information has been lost.[17]

2.5.2. Confocal microscopy and two-photon excitation

Confocal microscopy offers a different principle for forming sharp images. While the excitation of out-of-focus fluorophores by the incident beam is not avoided, an optical configuration of the instrument allows the rejection of their emission by means of a confocal pinhole that provides geometric restriction to the transmission of this out-of-focus emission. The application of this

principle allows the rendering of sharp images due to a dramatically-improved signal-to-noise ratio.

A schematic of a typical confocal microscope is shown in Figure 2.8. Because a higher intensity of photons is required for excitation in comparison to widefield microscopes, lasers are employed. The beam enters the microscope and passes through the excitation filter and a dichroic mirror. Next, two scanning mirrors (not indicated in Figure 2.8) move the beam in a raster across the sample. Fluorescence emission then passes back through the objective and is de-scanned by reflecting off both of the scanning mirrors. The light is then reflected off the dichroic mirror. Importantly, only in-focus light is allowed to proceed through the pinhole and emission filter to the detector. Out-of-focus light is rejected by the pinhole and does not reach the detector.

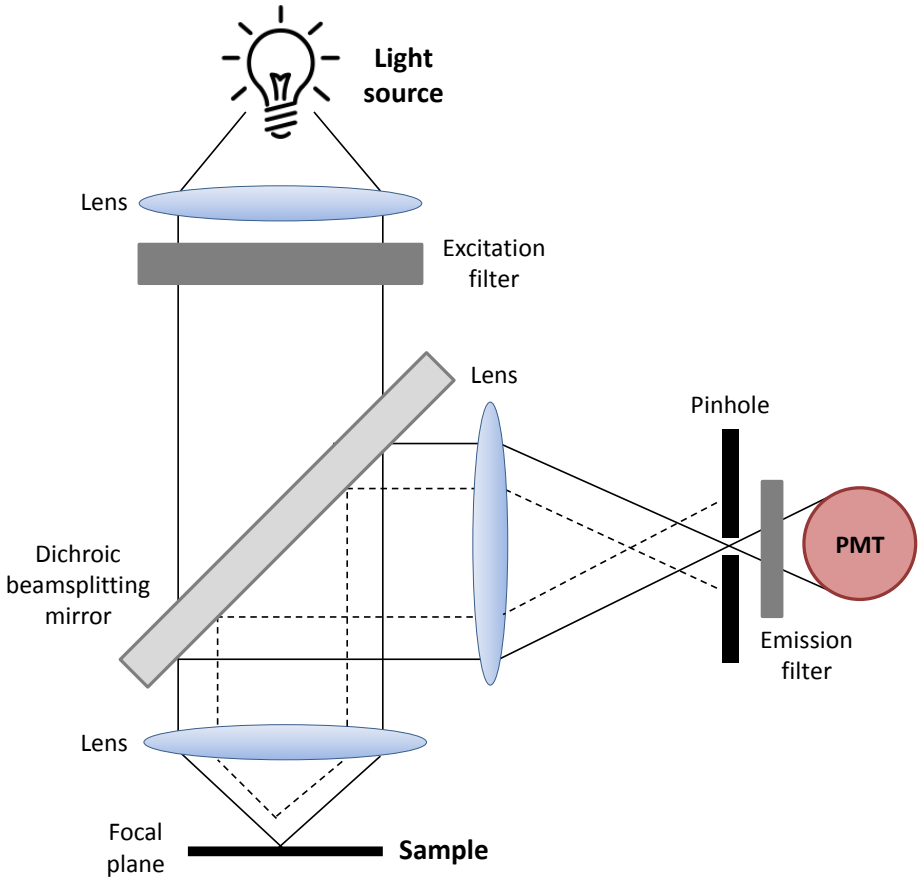

Figure 2.8. *Schematic of a typical confocal microscope showing the beam geometry that allows rejection of photons emitted from outside the focal plane. The sold lines indicate in-focus photons that pass through the pinhole while the dashed lines indicate out-of-focus photons that are rejected by the pinhole.*

The great advantage of confocal microscopy is the ability to adjust the focal plane. This enables one to scan the object at different z-levels so that cross-sections at various depths can be obtained. These two-dimensional sections can then be reconstructed to form a three-dimensional image of the object. The disadvantage of the confocal microscope is the need to use high intensity lasers for excitation and to illuminate the sample with a large volume of light, not only within the focal plane. As a result this increases the possibility of photobleaching and phototoxicity, especially when imaging live cells.[17]

This problem can be circumvented to some extent by utilising a two-photon excitation source. This takes advantage of a phenomenon that brings an electronic system to an excited state by the absorption of two photons simultaneously, the total energy of which corresponds to the energy of the required transition (Figure 2.9). For such summation of energies, these quanta should appear together in the right place at the right time and their simultaneous absorption should occur in a single event which is typically very rare. To increase this probability, a high photon flux is needed. In order to excite a dye that absorbs at 350 nm, a two-photon laser should emit at a wavelength of approximately 700 nm.[17]

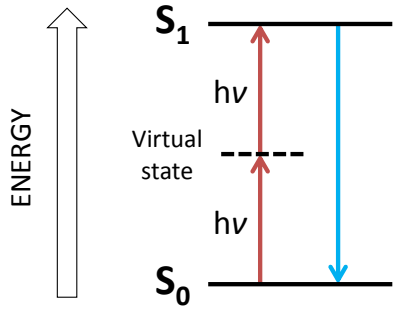

Figure 2.9. *Energy scheme for a two-photon up-conversion process.*

The major advantage of this technique, in contrast to single-photon excitation in which the emission changes linearly with the intensity of the excitation light, is that the fluorescence emission of two-photon excitation varies with the *square* of the excitation intensity. This quadratic relationship between excitation and emission allows the excitation power to be focused to a very small volume without observing emission outside this volume, achieving high spatial resolution.[17] Above and below the focal point, the photon density is not sufficiently high for two photons to pass at the same instant within the absorption cross-section of a single fluorophore. Only at the focal point is this density adequately high that two photons will be absorbed simultaneously with sufficient probability. This is especially valuable for DNA-specific

dyes such as Hoechst or DAPI that require ultraviolet excitation. This high-energy radiation is damaging to cells. A two-photon excitation system minimises this damage.

2.5.3. The diffraction limit and the advent of super-resolution microscopy

Towards the end of the 19th century, Ernst Abbe (1873)[18] and Lord Rayleigh (1896)[19] found that light of wavelength λ, travelling in a medium with refractive index n and converging with angle θ, will form a focal "spot" with radius d as described by Equation 2.9:‡

$$d = \frac{\lambda}{2\, n \sin\theta}$$

Equation 2.9

Consequently, widefield and confocal microscopes are constrained by this "diffraction limit". When light is focused by the objective of a microscope, the notion of light "rays" converging to an infinitely sharp focal point does not occur. Instead, the light forms a blurry focal "spot" with a finite size due to diffraction.

A single point emitter such as a fluorescent molecule therefore appears as a blurry "smudge" with a finite size when imaged through a microscope. The intensity profile of this smudge defines the point spread function of the microscope and has approximately the same width as the focal "spot" defined above. Consequently, two identical emitters separated by a distance less than the width of the point spread function will appear as a single object and are thus unresolvable from one another.[20]

Practically, this means that for green light of wavelength 500 nm passing through a microscope objective with a high numerical aperture (1.2-1.5), the Abbe limit is about 200 nm perpendicular to the direction of light propagation (laterally) and about 500 nm parallel to the direction of the light propagation (axially, or in the z-direction). These dimensions may be small compared to most cells (1-100 μm) but not viruses (100 nm) or proteins (10 nm). Structures as small as these are unresolvable by light microscopy.

Typically, electron microscopes have been used to overcome these resolution problems but they cannot be used for imaging live cells. Furthermore, electron microscopy typically requires

‡ In this equation, the term $n \sin\theta$ is sometimes abbreviated to "NA" which represents the numerical aperture of the objective. This quantity characterises the light-gathering ability of the objective.

extensive sample preparation and suffers from a lack of contrast in biological samples, making the identification of subcellular components extremely challenging.

For almost a century-and-a-half it was believed this limit of resolution could not be surpassed. However, a number of different techniques have subsequently been developed that overcome this limit. These technologies, with a resolving power exceeding the diffraction limit, are collectively known as super-resolution (SR) microscopy.

Stimulated emission depletion (STED) microscopy was developed and demonstrated by Stefan Hell in the 1990s. This method creates super-resolution images by the selective deactivation of fluorophores, minimising the area of illumination of the focal point and thus increasing the resolution. Two laser sources are used; one excites the fluorophores while the other quenches all the fluorophores except those surrounding the nanometre-sized region of interest. Quenching occurs by forcing these outer fluorophores into higher vibrational levels of the ground state without emission of fluorescence ("stimulated depletion"). The energy of the second laser is therefore lower than the excitation energy and is generally in the far-red region. However, the high intensities required for STED microscopy mean that photobleaching is problematic when working with live cells. Special fluorophores are typically required.

Eric Betzig and W. E. Moerner, who were awarded the 2014 Nobel Prize in Chemistry jointly with Hell, separately laid the foundations for a second way of performing super-resolution microscopy. Their method relies on photoswitchable fluorophores that alternate between "on" (fluorescent) and "off" (dark) states. Typically, only a few of these molecules are "on" during a single image acquisition. The center of each "spot" can be found by fitting the observed emission profile to a known geometrical function. Superimposing these partial fluorescent representations yields a dense, super-resolved image; essentially, this is a pointillist representation of the coordinates of all the localised molecules. The two most popular variations on this theme are photoactivated localisation microscopy (PALM) and stochastic optical reconstruction microscopy (STORM).

2.5.4. Super-resolution structured-illumination microscopy (SR-SIM)

A different kind of super-resolution technology, structured-illumination microscopy (SIM), is based upon the idea of patterning the excitation light. By allowing the patterned light (usually a fine grid) to interfere with the structures in the sample, a characteristic pattern is produced. By rotating the grid between the acquisition of each image set and transforming the images into

frequency space, additional spatial information may be retrieved. The reverse Fourier transform returns the reconstructed super-resolution image.

This process is best understood in terms of the moiré effect. If two fine patterns are superimposed multiplicatively, a beat pattern (moiré fringes) will appear in their product (Figure 2.10). In SIM, one of the patterns being superimposed is the unknown sample structure (specifically, the unknown spatial distribution of the fluorescent dye) and the other pattern is a purposely-structured excitation light intensity.[21] As the amount of light emitted from a point is proportional to the product of the dye intensity and the local excitation light intensity, the observed emission image is the product of the two patterns and will thus contain moiré fringes. As the moiré fringes contain information about the unknown structure and, because the illumination pattern is known, one can thus gain access to normally-unresolvable high-resolution information.

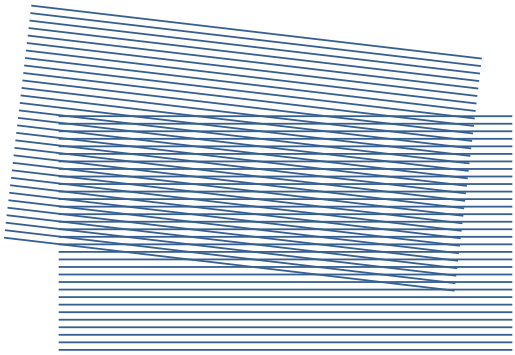

Figure 2.10. *A demonstration of moiré fringes, observed here as vertical stripes occurring in the region of overlap between two sets of parallel lines.*

In reciprocal space, low-resolution information resides close to the origin while higher-resolution information resides further away. In a conventional microscope hindered by diffraction, the set of low-resolution information it can detect defines a circular "observable region" of reciprocal space (Figure 2.11.1).[21]

Consider the Fourier transform of an illumination light structure that consists of a sinusoidal stripe pattern. This has only three non-zero points – one at the origin and the other two offset from the origin but contained within the circle defining the observable region (Figure 2.11.2).[21] If the sample is illuminated with the patterned light, moiré fringes will appear which represent information that has changed position in space. The observable region not only contains the usual information that itself resides there but information originating in the two offset regions

as well (Figure 2.11.3). From a sequence of such images with different orientations and phases of the pattern, it is possible to recover information from an area twice the size of the normally observable region, corresponding to twice the normal resolution (Figure 2.11.4).[21]

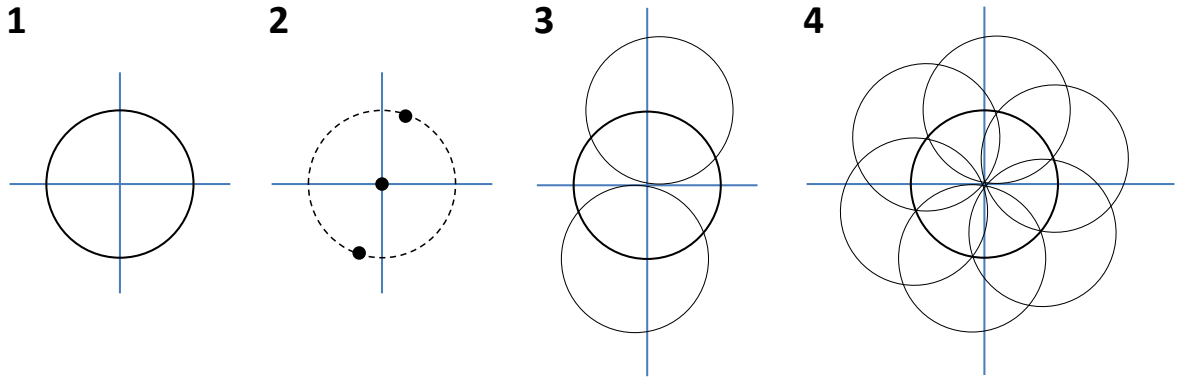

Figure 2.11. *A series of diagrams to explain the resolution enhancement possible by SIM.*[21] *See the text for details.*

Hence SIM is capable of doubling the conventional diffraction-limited resolution to 100 nm laterally and 300 nm axially. Furthermore, the technique does not rely on special photophysical properties of the fluorophores but purely on the optics of the microscope. Therefore any fluorescent probe used in a typical fluorescence microscope is compatible with SIM. It is regarded as a widefield technique as it does not make use of the confocal pinhole to reject out-of-focus emission light.

2.5.5. Quantitative image analysis

> *Beware of determining and declaring your opinion suddenly on any subject; for imagination often gets the start of judgement, and makes people believe they see things which better observations will convince them could not be seen: therefore assert nothing till after repeated experiments and examinations in all lights and in all positions. When you employ a microscope shake off all prejudice, nor harbour any favourite opinions.*
>
> **– Advice of an 18th century microscopist**

One of the most common applications of fluorescence microscopy is to compare the subcellular distributions of two fluorescent molecules. Often the goal is to probe the localisation of a

fluorescently-tagged substrate and thus the second fluorophore is usually a commercially-available tracker dye that is specific for a subcellular region or organelle.

"Colocalisation" is a term that has received much criticism but appears ubiquitously in the literature. The term refers to the general spatial overlap between two (or more) different fluorescence signals; however, even super-resolution images cannot identify the physical apposition of two molecules merely by comparing their fluorescence signals. Hence the term "codistribution" may be preferred in which it is asked whether the molecules tend to associate with the same structures.[22] This, in turn, may be thought of as a combination of "co-occurrence" (the spatial overlap of probes in a fluorescence image) and "correlation" (distribution in proportion to one another within and between structures).[22] Although it may be helpful to bear these nuances in mind, in this text "colocalisation" will be used to retain consistency with the rest of the literature.

Qualitative methods of image analysis rely on a comparison of separate fluorescence channels. Typically, images are displayed in different channels using pseudo-colouring (usually green and red) and regions of overlap are identified in a dual-channel image (in this case, regions of overlap would appear yellow). Quantitative methods, on the other hand, involve global statistical analysis of the pixel intensity distribution and are called intensity correlation coefficient-based analyses. This involves statistical analysis of the correlation of the intensity values of the pixels in the dual-channel image and is usually done using correlation coefficients that measure the strength of the linear relationship between two values.

2.5.5.1. Scatterplots and the Pearson correlation coefficient. A simple way of measuring the dependency of pixels in dual-coloured images is to plot the pixel intensity values of the two images against one another and to display the result in a pixel distribution diagram, also called a scatterplot or "cytofluorogram". If the intensities of both pixel distributions are proportional to one another and if detection has been carried out in the linear range, the resulting scatterplot should form a dot cloud in the shape of a line, the slope of which reflects the relative (unique) stoichiometry of both fluorophores. The spread of this distribution with respect to a fitted line, calculated by linear regression, may be estimated by calculating the Pearson correlation coefficient.

The Pearson correlation coefficient is a standard procedure in pattern recognition for matching one image with another and is used to describe the degree of overlap between two patterns. It provides information about the similarity of shape without regard to the average intensity of the signals. In the case of pixel scatterplots, the Pearson correlation coefficient quantifies the

spread of the dot cloud relative to the median line. Values may range from 1 (complete correlation) to -1 (negative correlation), while a value of zero indicates no correlation and results from a random distribution of pixels. A hypothetical data set, illustrating cases of positive and negative correlation, is depicted in Figure 2.12.

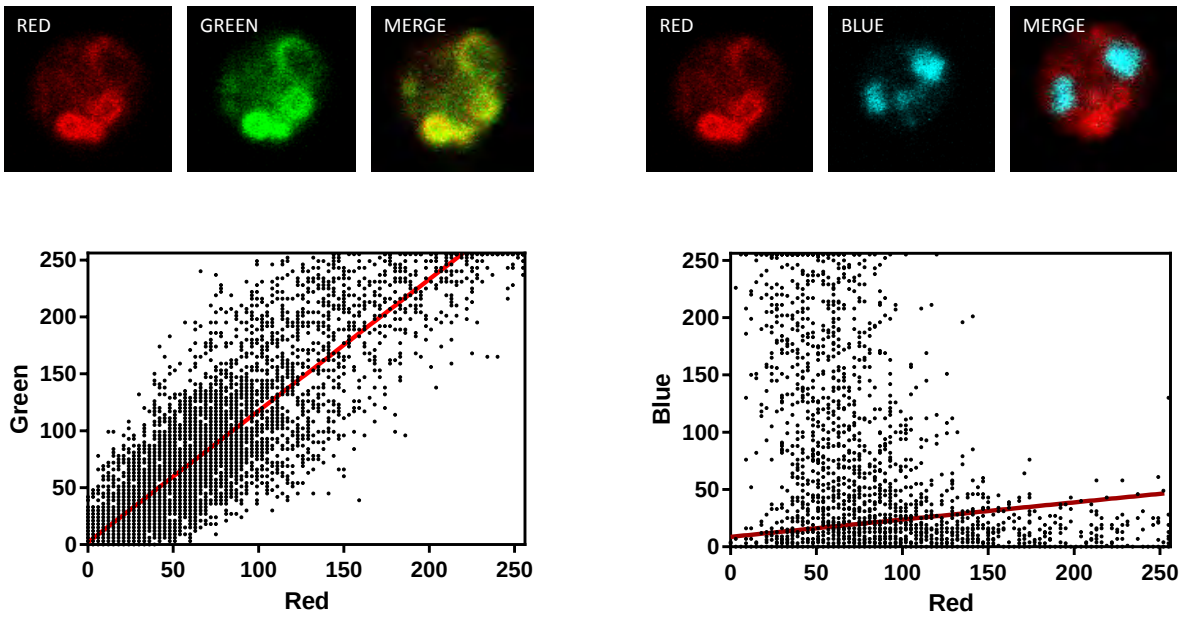

Figure 2.12. *Scatterplots for a hypothetical data set, showing positive colocalisation between the red and green data sets (left) but negative colocalisation between the red and blue data sets (right). Calculated Pearson correlation coefficients are 0.830 and -0.455, respectively.*

The Pearson correlation coefficient may be calculated from Equation 2.10:

$$r_P = \frac{\sum_i (A_i - a) \times (B_i - b)}{\sqrt{\sum_i (A_i - a)^2 \times \sum_i (B_i - b)^2}}$$

Equation 2.10

Here, A_i and B_i represent the intensities of pixel i of channels A and B of a dual-colour image, respectively, while a and b are the mean intensities of the two channels, respectively. In this equation, the average intensity values are subtracted from the original intensity values and hence the value of this coefficient ranges from -1 to 1.

Pearson correlation coefficients are highly dependent on noise, heterogeneity and variations in fluorescence intensity. Evaluation of colocalisation using the Pearson correlation coefficient

exclusively should be avoided. However, scatterplots and the Pearson correlation coefficient provide a useful first estimate of colocalisation.[23]

2.5.5.2. The Manders overlap coefficient. When the average intensity values of the pixels are not subtracted from the original intensity values in the Equation 2.10, a new coefficient may be defined (Equation 2.11). This is known as the Manders overlap coefficient (r_M).[24]

$$r_M = \frac{\sum_i A_i \times B_i}{\sqrt{\sum_i A_i^2 \times \sum_i B_i^2}}$$

Equation 2.11

This new coefficient ranges from zero (no overlap) to one (full colocalisation). The product in the numerator brings in a non-zero value only when the pixel intensities A_i or B_i belong to a pixel of one of the colocalising objects ($A_i > 0$ and $B_i > 0$). In other words, each added product is zero when one of the pixel values is zero (no fluorescence signal). Thus the numerator is proportional to the number of colocalising objects. In the same way, the denominator is proportional to the total number of (colocalising and not colocalising) objects in both components of an image.[24]

A major advantage of the Manders overlap coefficient over the Pearson correlation coefficient is that is it not sensitive to differences in signal intensities between the components of an image caused by different labelling with fluorophores, photobleaching or changes in gain settings during acquisition. A disadvantage of the Manders overlap coefficient is that the result of the calculation may be ambiguous because the ratio of the number of objects in both components plays a strong role.[24]

2.5.5.3. The Manders colocalisation coefficients. To cancel out the large effect played by the number of objects, the Manders overlap coefficient may be divided into two new coefficients, known as the "split" coefficients:[24]

$$r_M^2 = k_1 \times k_2$$

Equation 2.12

Here, k_1 and k_2 are respectively defined by the equations below:

$$k_1 = \frac{\sum_i A_i \times B_i}{\sum_i A_i^2}$$

Equation 2.13

$$k_2 = \frac{\sum_i A_i \times B_i}{\sum_i B_i^2}$$

Equation 2.14

Using these coefficients, the degree of colocalisation is expressed as two separate parameters. In these equations, k_1 and k_2 depend on the sum of the products of the intensities of A and B. Therefore k_1 is sensitive to differences in intensity of the signal from B while, analogously, k_2 depends linearly on the intensity of A.[24] In the case of perfect colocalisation, k_1 will approach α and k_2 will reach $1/\alpha$, where α is the slope of the mean line in the cytofluorogram (related but not equal to the stoichiometry of the two molecules).

However, if one channel is corrupted by noise or background, the denominator of the corresponding coefficient will increase and consequently its value will decrease. Looking at both coefficients is therefore useful to identify the source of the problem if the overlap coefficient is close to zero.[24]

Based on the split overlap coefficients, two final coefficients are defined that are not dependent on the intensities of the signals. These are referred to as the Manders *colocalisation* coefficients (different from the Manders *overlap* coefficient defined above) and are defined below:[24]

$$M_1 = \frac{\sum_i A_{i,\mathrm{coloc}}}{\sum_i A_i}$$

Equation 2.15

$$M_2 = \frac{\sum_i B_{i,\mathrm{coloc}}}{\sum_i B_i}$$

Equation 2.16

Here, $A_{i,\mathrm{coloc}} = A_i$ if $B_i > 0$ and $B_{i,\mathrm{coloc}} = B_i$ if $A_i > 0$. Again, M_1 and M_2 can take any values between zero and one where the latter indicates complete colocalisation. The sum of the intensities of colocalising pixels from one channel is divided by the integrated density, i.e. a pixel from A is colocalised with B if it has a non-zero intensity counterpart in B. M_1 and M_2 have therefore been

defined so that colocalisation can be determined even when the signal intensities of the two components differ strongly.

A summary of the Pearson correlation coefficient and various Manders coefficients (overlap, split and colocalisation) is presented in Table 2.1.[25] Taken together, they are most useful when compared over several sets of images. The Pearson correlation coefficient (r_P) provides a value for the correlation between the intensity distributions of the components, but the overlap of the signals is better represented by the Manders overlap coefficient (r_M). In cases where there are an equal number of objects in each component of an image, the overlap coefficient exactly reflects the fraction of colocalising objects in the images. When the numbers of objects in the two components of the image differ significantly, the Manders colocalisation coefficients M_1 and M_2 should be used. M_1 and M_2 have been shown to be sensitive for uniform and non-uniform background and crosstalk, providing confidence that the result of these calculations reflects the biological reality of the image.[24]

Table 2.1. *A summary of the colocalisation coefficients used in this study.*[25]

Coefficient	Interpretation	Values indicating colocalisation	Values indicating no colocalisation
Pearson correlation coefficient, r_P	r_P describes the correlation between the intensity distributions of two channels	From 0.5 to 1.0	From -1.0 to 0.5
Manders overlap coefficient, r_M	r_M indicates an actual overlap of the signals and is considered to represent the true degree of colocalisation	From 0.6 to 1.0	From 0 to 0.6
Manders split coefficients, k_1 and k_2	k_1 and k_2 divide colocalisation into two separate parameters, allowing determination of the contribution of each channel to the areas of colocalisation	Any close values, such as 0.5 and 0.6 or 0.8 and 0.9	Any distant values, such as 0.5 and 0.9 or 0.2 and 0.7
Manders colocalisation coefficients, M_1 and M_2	M_1 and M_2 describe the contributions of the two channels to the pixels of interest	More than 0.5	Less than 0.5

2.5.5.4. Van Steensel's cross-correlation coefficient. A different approach, described by Van Steensel and co-workers, helps to distinguish between positive correlation and partial colocalisation. The latter might arise from the occasional overlap of randomly-distributed objects.[26]

The authors applied a cross-correlation analysis by shifting one image pixel-by-pixel in the *x*-direction relative to the other image (Figure 2.13). For each shifted set, they calculated the respective Pearson correlation coefficient (r_P). Finally, the retrieved values of the Pearson correlation coefficient (r_P) were plotted as a function of the pixel shift (δx).[26]

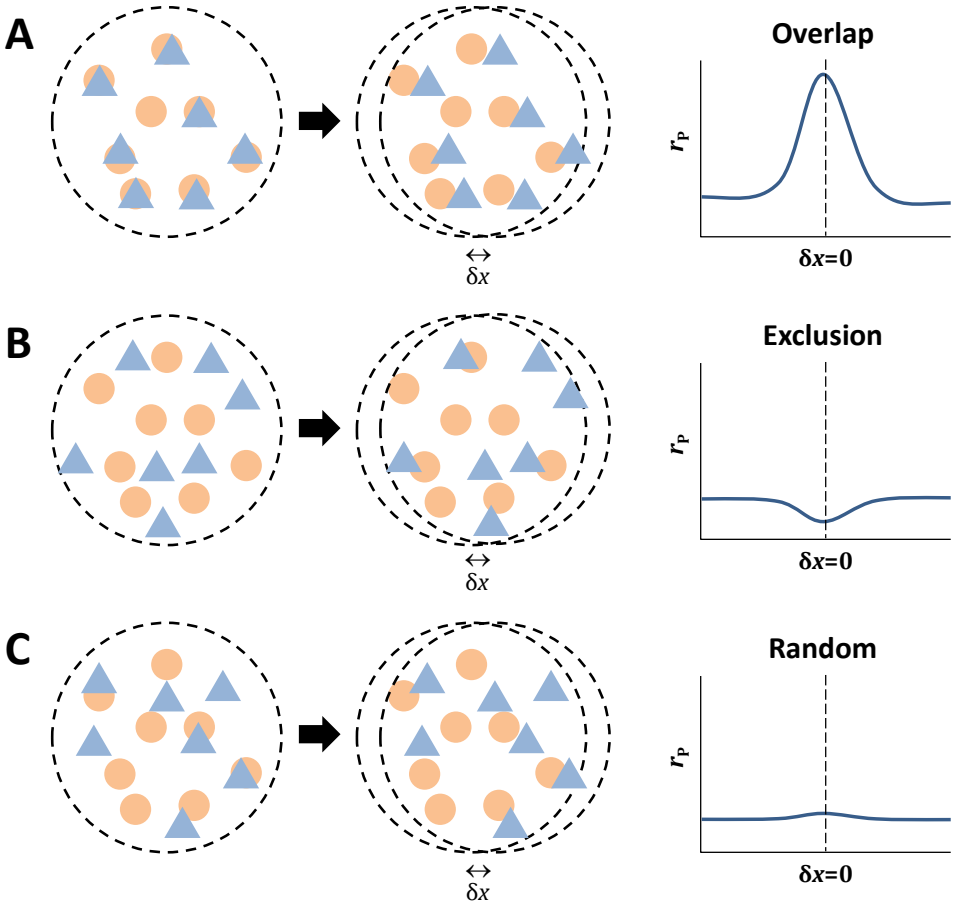

Figure 2.13. *An illustration of Van Steensel's cross-correlation analysis. Three different scenarios contain overlapping (A), mutually exclusive (B) and non-correlated (C) blue and orange elements.*

In a true colocalisation situation, the correlation is lost after the displacement. Consequently there is a peak in the Pearson correlation coefficient at δx=0 and the trace exhibits a bell-shaped curve as the coefficient decreases as the objects move further away from another. Structures

that are mutually excluded from one another show a dip at $\delta x=0$ as shifting either image over a small distance leads to an increase in the amount of overlap. For objects that are partially overlapping or those which are randomly-distributed with respect to each other, a small shift has no effect on the amount of overlap.

Van Steensel's cross-correlation analysis works well for signals that are located in punctate clusters. While this cross-correlation function allows ready discrimination between the different colocalisation situations, its major drawback is that it is only valuable for small, isotropic particles as it may vary depending on the orientation of the objects relative to the shift axis.

2.5.6. A brief overview of fluorescence reporters

As described above, fluorescence is an invaluable tool for probing biology at many levels, from cellular dynamics to complete organisms. Originally, fluorescence was observed from small organic dyes attached to antibodies which display high specificity for the protein of interest. However, antibody targeting of intracellular proteins normally requires cell fixation and permeabilisation which perturbs the biological system and may introduce artefacts.

Later, fluorophores were developed to recognise directly organelles, nucleic acids and ions in living cells. Over the past few decades, fluorescent proteins have enabled non-invasive imaging of reporter gene expression, protein trafficking and dynamic biochemical signals. Meanwhile, semiconductor nanocrystals (quantum dots) have been developed with superior brightness and photostability compared to previous fluorophores, but their use in cells and tissues remains challenging.[27]

Despite these advances, organic dyes remain the most common fluorescence reporters. The benefits of these dyes are that they are usually inexpensive, readily available and are often small compared to their substrates. Many possess superior photostability and brightness, but most important is their versatility. There is immense variation in their chemical, photophysical and spectroscopic properties meaning that their use can be adapted to almost any system. Unsurprisingly, a one-size-fits-all or "ideal" fluorescent dye does not exist so compromises have to be made depending on the role of the fluorescent reporter and the system in question. Microscopy, and especially live-cell imaging, is usually more challenging than spectroscopic studies in a cuvette. These considerations were kept in mind for the selection of an appropriate reporter fluorophore, as described in Chapter 3.

2.6. References

1. B. Valeur and J. Brochon, *New Trends in Fluorescence Spectroscopy*, Springer-Verlag GmbH, Heidelberg, 2001.
2. J. F. W. Herschel, *Phil. Trans.*, 1845, **135**, 143.
3. J. F. W. Herschel, *Phil. Trans.*, 1845, **135**, 147.
4. B. Valeur, *Molecular Fluorescence: Principles and Applications*, Wiley-VCH Verlag GmbH, Federal Republic of Germany, 2001.
5. G. G. Stokes, *Phil. Trans.*, 1852, **142**, 463.
6. G. G. Stokes, *Phil. Trans.*, 1853, **143**, 385.
7. J. R. Lakowicz, *Principles of Fluorescence Spectroscopy*, Springer, New York, 2010.
8. S. Udenfriend, *Protein Sci.*, 1995, **4**, 542.
9. Basic Concepts in Fluorescence, Florida State University, micro.magnet.fsu.edu/primer/techniques/fluorescence/fluorescenceintro.html (accessed January 2016).
10. John Daintith, *A Dictionary of Chemistry*, Oxford University Press, Oxford, 2008.
11. D. A. Skoog, F. J. Holler, S. R. Crouch, *Principles of Instrumental Analysis*, Sixth Edition, Thomson Brooks/Cole, Canada, 2007.
12. T. Förster, *Ann. Phys. (Berlin)*, 1948, **437**, 55.
13. R. M. Clegg, in *Fluorescence Imaging Spectroscopy and Microscopy*, ed. X. F. Wang and B. Herman, John Wiley & Sons, New York, 1996, pp. 179-252.
14. Q. Gu and J. E. Kenny, *Anal. Chem.*, 2009, **81**, 420.
15. K. Wilson and J. Walker, *Principles and Techniques of Practical Biochemistry*, Cambridge University Press, Cambridge, 2004.
16. M. van de Weert and L. Stella, *J. Mol. Struct.*, 2011, **998**, 144.
17. A. P. Demchenko, *Introduction to Fluorescence Sensing*, Springer, New York, 2010,
18. E. Abbe, *Arch. Mikrosk. Anat.*, 1873, **9**, 413.
19. L. Rayleigh, *Philos. Mag.*, 1896, **42**, 167.
20. B. Huang, H. Babcock and X. Zhuang, *Cell*, 2010, **143**, 1047.
21. M. G. L. Gustafsson, *J. Microsc.*, 2000, **198**, 82.
22. K. W. Dunn, M. M. Kamocka and J. H. McDonald, *Am. J. Physiol. Cell Physiol.*, 2011, **300**, C723.
23. S. Bolte and F. P. Cordelières, *J. Microsc.*, 2006, **224**, 213.
24. E. M. M. Manders, F. J. Verbeek and J. A. Aten, *J. Microsc.*, 1993, **169**, 375.
25. V. Zinchuk and O. Grossenbacher-Zinchuk, *Curr. Protoc. Cell Biol.*, 2011, **52**, 4.19.1.
26. B. van Steensel, E. P. van Binnendijk, C. D. Hornsby, H. T. M. van der Voort, Z. S. Krozowski, E. R. de Kloet and R. van Driel, *J. Cell Sci.*, 1996, **109**, 787.
27. B. Giepmans, S. R. Adams, M. H. Ellisman and R. Y. Tsien, *Science*, 2006, **312**, 217.

Chapter Three

The Design and Synthesis of Novel Fluorescent Quinoline Antimalarials

3.1. Introduction

For centuries, quinoline-based molecules have formed the cornerstone of chemotherapeutic resources to tackle the scourge of malaria. Given the prevalent use of these drugs, it is surprising that crucial details of the mechanism of action of these antimalarials against the most virulent malaria parasite, *Plasmodium falciparum*, remain elusive. While recent work has provided some clarity into the mode of action of the prototypical 4-aminoquinoline chloroquine,[1] its quinoline methanol counterparts, the diastereomeric *Cinchona* alkaloids quinine and quinidine, remain less well understood.

It has been extensively demonstrated that these antimalarials accumulate in the acidic digestive vacuole of the malaria parasite *P. falciparum* and that this property is a key aspect of their efficacies (Section 1.6.1).[2,3] However, their propensities to associate with other subcellular compartments have not been thoroughly evaluated. It was anticipated that a systematic survey of their subcellular localisation within *P. falciparum* would reveal deeper insights into their mechanism of action and might suggest potential secondary targets within the parasite to account for their potencies, particularly in the case of the *Cinchona* alkaloids.

Although fluorescence microscopy is an ideal tool with which to probe subcellular distributions of suitable molecules, various limitations described below suggest that the intrinsic fluorescence of the quinoline antimalarials cannot be exploited directly; hence, it was necessary to design and synthesise derivatives of these drugs labelled with an extrinsic fluorophore. As intimate association with Fe(III)PPIX is an important property of these antimalarials, structure-activity relationships of these interactions were evaluated to decide where suitable modifications to the parent compounds should be made. For the quinoline methanols, a number of fluorescent analogues were prepared in order to vary the length of the spacer chain between the quinoline core and the extrinsic fluorophore. By contrast, only a single novel fluorescent derivative of chloroquine was prepared.

In this chapter, design aspects relating to the synthesis of these novel fluorescent antimalarials will first be presented. The necessity of incorporating an extrinsic fluorophore into the parent quinolines and the choices of fluorophores will be defended. Structure-activity relationships between these antimalarials and Fe(III)PPIX will be presented, justifying the sites identified for covalent modification. For both classes of antimalarials, retrosynthetic analyses will be presented and key synthetic intermediates identified. Finally, appropriate mechanistic details relating to methods of synthesis will be discussed and relevant details pertaining to spectroscopic characterisation will be given. Photophysical and physicochemical characterisation of these fluorescent derivatives are described in Chapter 4.

Thus the specific objectives relating to design aspects described in this chapter were:

i. To identify a suitable reporter fluorophore and to evaluate current structure-activity models of the two classes of quinoline antimalarials in order to propose suitable sites of covalent modification to retain key physicochemical properties of the parent molecules;
ii. To propose the structures of suitable derivatives followed by appropriate retrosynthetic and forward analyses to generate efficient syntheses of these derivatives;

With these considerations in mind, the synthetic objectives described in this chapter were:

iii. To derivatise the quinoline methanol antimalarials via a thiol-ene 'click' reaction in order to provide convenient access to functionalised derivatives of the *Cinchona* alkaloids;
iv. To prepare various fluorescent derivatives of these alkaloids by varying the length of the spacer chain, requiring the application of various coupling methodologies;
v. To prepare a novel synthetic derivative of chloroquine via *N*-desethylation of chloroquine as an important intermediate;
vi. To fully characterise these novel fluorescent derivatives and their intermediates using a range of spectroscopic and analytical techniques.

3.2. Design aspects of novel fluorescent quinoline antimalarials

3.2.1. Identification of NBD as a suitable extrinsic fluorophore

The intrinsic fluorescence of the *Cinchona* alkaloids conferred by the 6-methoxyquinoline heterocycle is well established and has led to the use of quinine as a common fluorescence standard.[4] This inherent fluorescence also provides an intuitive starting point for fluorescence microscopy. Although a previous study successfully utilised the intrinsic fluorescence of quinine to investigate its distribution within *P. falciparum*,[5] in our hands it was not possible to observe any localisation using either widefield or confocal microscopy without causing significant photodamage to the cells, thus limiting the utility of this method.

There are several reasons that might account for this. Firstly, quinine has a poor extinction coefficient at its absorbance maximum which lies in the ultraviolet region of the spectrum, making this an undesirable combination for the direct excitation of live cells. Two-photon excitation also proved to be inefficient. Furthermore, fluorescence emission from quinine may be quenched by strongly-absorbing chromophores such as Fe(III)PPIX which is an important metabolic species in *P. falciparum*.

Most importantly, and somewhat surprisingly, quinine fluorescence is quenched in polar aprotic solvents with $E_T(30)$ values between 40-50 kcal/mol (Figure 3.1). It is not obvious what photophysical properties might account for this unexpected behaviour. These solvents have $E_T(30)$ values similar to those of phospholipid bilayers (49-50 kcal/mol)[6] as well as neutral lipid components (45 ± 4 kcal/mol for the synthetic neutral lipid blend described in Section 1.3.2),[7] both of which are essential and important subcellular components of *P. falciparum*. Hence, the value of quinine autofluorescence to evaluate thoroughly the subcellular localisation of the molecule is limited. By contrast, the 7-chloro-4-aminoquinoline heterocycle of chloroquine is only minimally fluorescent due to quenching caused by the chlorine atom, a manifestation of the internal heavy-atom effect (Section 2.3.2). This renders its autofluorescence unsuitable for live-cell microscopy as well.

Taken together, these obstacles suggested the attachment of an extrinsic fluorophore to these antimalarials. The *Cinchona* alkaloids have not yet been modified to incorporate an extrinsic fluorophore suitable for live-cell imaging. While several fluorescently-labelled derivatives of chloroquine have previously been prepared, it was anticipated that an improved design, more closely related to the physicochemical properties of the parent molecule, could be proposed.

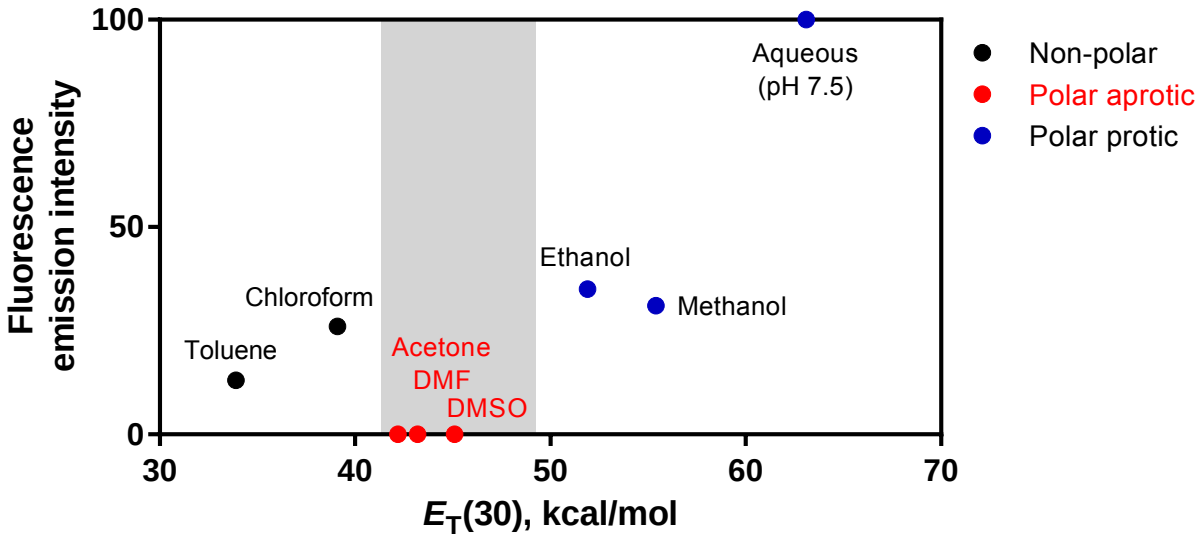

Figure 3.1. *Relative fluorescence emission intensities of quinine in eight common solvents. 20 μM solutions of quinine were excited at 333 nm at 25°C. Emission intensities were calculated relative to water (20 mM Hepes, pH 7.5) which was set at 100%.* E_T*(30) values taken from Reichardt.*[8] *Red points indicate polar aprotic solvents in which quinine fluorescence is quenched. The grey shaded region indicates the approximate range of* E_T*(30) values over which the quinine fluorescence is quenched corresponding to polarity values of phospholipid bilayers*[6] *and neutral lipid bodies.*[7]

With the recent growth of fluorescence microscopy, dozens of small-molecule fluorophores are now commercially available. 7-Nitrobenz-2-oxa-1,3-diazole (NBD, Figure 3.2) was selected as a suitable fluorescence reporter for several reasons. It is one of the smallest fluorophores and was thus expected to cause the least perturbation of biological activity upon conjugation to the drugs.[9] Although the fluorophore exhibits solvatochromism, typical excitation and emission maxima in aqueous media are approximately 470 nm and 540 nm, respectively. Hence these bands overlap only minimally with the prominent Soret region of Fe(III)PPIX. The NBD fluorophore also has a secondary excitation maximum at 350 nm. While the fluorescence of NBD is stable over a biologically-relevant pH range,[9] it is enhanced in non-aqueous environments which directly compensates for the quenching of native alkaloid fluorescence in these regions.

Finally, NBD was favoured for its modest aqueous fluorescence quantum yield. As the weakly-basic quinoline antimalarials in this study have been measured to accumulate several hundred- or thousand-fold in the digestive vacuole of *P. falciparum* (Section 1.6.1), this photophysical feature of the fluorophore was deliberately selected to avoid the fluorescence from this compartment overwhelming weaker signals from elsewhere within the cell.

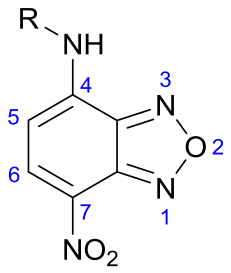

Figure 3.2. *The structure and conventional numbering of the 7-nitrobenz-2-oxa-1,3-diazole (NBD) fluorophore when substituted by an amine at the 4-position.*

NBD has been used extensively as an attachment to biomolecules, especially for the preparation of NBD-labelled lipids.[10,11] Given these applications, the fluorophore is readily available as an inexpensive 4-chloro derivative (NBD-Cl). An electron-withdrawing nitro group situated *para* to the chlorine atom makes this derivative susceptible to nucleophilic aromatic substitution. This suggested that it might be useful to introduce a terminal amine functionality into the quinoline antimalarials, a feature that was later judged to be a crucial consideration in the design of the novel fluorescent derivatives.

3.2.2. Retention of key physicochemical features of the parent molecules

The three quinoline antimalarials investigated in this study, quinine, quinidine and chloroquine, all associate appreciably with Fe(III)PPIX and this is presumed to be important for their activities. Consequently, retaining this strong association was deemed likely to assist in the retention of the biological activities of fluorescent derivatives of the parent molecules. This was to be an important factor in the evaluation of these compounds as suitable analogues of the parent molecules, as described in Chapter 4.

The solution-state interactions of the quinoline methanol antimalarials, quinine and quinidine, with Fe(III)PPIX have been extensively evaluated and were described in Section 1.5.2.[12] Most recently, it has been shown that coordination to the iron centre of Fe(III)PPIX via their benzylic alkoxide group is a key interaction.[13] This is also an important interaction in the solid state as identified by single-crystal analysis of the complexes between these alkaloids and Fe(III)PPIX.[14] This study also confirmed the importance of several other interactions. As described in Section 1.5.3, the electron-rich quinoline ring system has been shown to π-stack with the porphyrin ring of Fe(III)PPIX. The weakly-basic tertiary nitrogen is important for accumulation and for forming a salt bridge with one of the carboxylate groups of Fe(III)PPIX.[14] Additionally, the rigid quinuclidyl group is necessary for biological activity as its replacement with a less rigid tertiary

amine led to an increase in its IC_{50} value against *P. falciparum*.[15] Thus, functionalising the vinyl group of these alkaloids was an obvious choice since this was unlikely to interfere with Fe(III)PPIX association and hence the activity of their NBD-labelled derivatives.

Proposed derivatives of the *Cinchona* alkaloids, with retention of the key physicochemical interactions described above, are depicted in Scheme 3.1. These diastereomers have a crucial and opposite configurational attachment to the rigid bicyclic quinuclidine template, resulting in the different topologies indicated in the scheme. A single fluorescent derivative of quinine was proposed while several fluorescent derivatives of quinidine allowed the length of the spacer chain between the quinoline core and the NBD fluorophore to be varied.

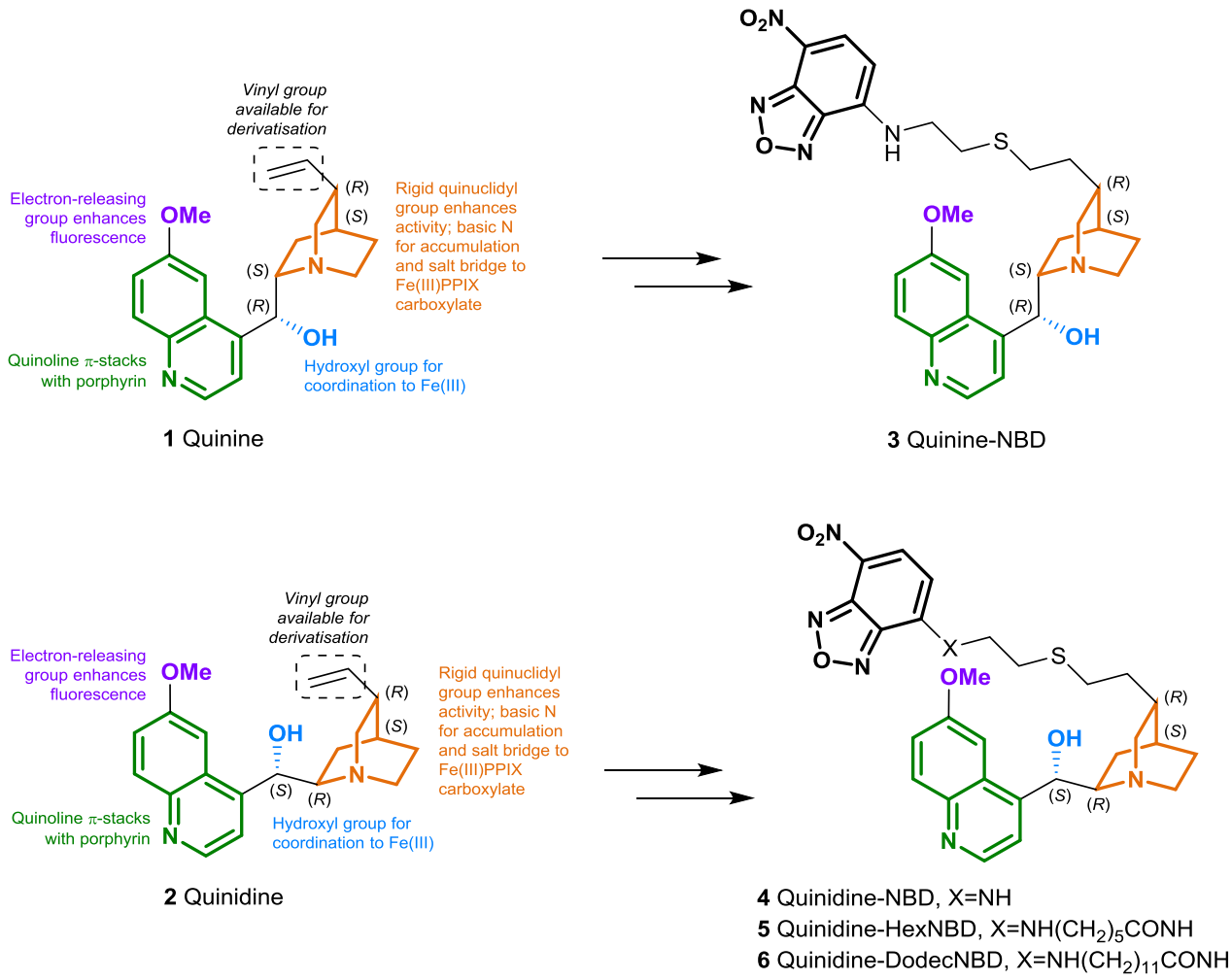

Scheme 3.1. *Key aspects of the structure-activity relationships between Fe(III)PPIX and the* Cinchona *alkaloids quinine (**1**) and quinidine (**2**), emphasising topological differences arising from their stereochemical configurations. Proposed NBD-labelled fluorescent derivatives (**3-6**) are shown in which key characteristics of the parent molecules are retained. Incorporation of the NBD fluorophore in the fluorescent derivatives is indicated by thickened black bond widths.*

As terminal double bonds are amenable to thiol-ene 'click' reactions, which are favoured for their efficacy, versatility and green chemistry properties, the introduction of a thioether linker was considered to be a crucial part of the design of fluorescent derivatives. As mentioned in Section 3.2.1, the introduction of a terminal amine functionality would provide a useful handle for the direct attachment of the NBD fluorophore or for the introduction of NBD-labelled alkyl chains of various lengths.

Finally, although these novel derivatives were prepared as new tools for investigations into malaria parasite biology for this study, quinine and quinidine have also been used as a muscle relaxant and as a cardiac depressant, respectively, and so it was anticipated that these new compounds might also be useful probes in applications beyond malaria research.[16]

By comparison, the interaction of the prototypical 4-aminoquinoline chloroquine with Fe(III)PPIX is fundamentally different from that of the quinoline methanols. Whereas the interaction between the quinoline methanols and Fe(III)PPIX is monomeric, chloroquine induces μ-oxo dimerisation of the porphyrin (Section 1.5.2). Hence, this drug contains a number of physicochemical motifs that are distinct from those of the quinoline methanols.

The quinoline ring of chloroquine is less electron-rich than the corresponding heterocycle of the quinoline methanols due to the deactivating effect of the chlorine atom as a result of its electron-withdrawing inductive effect. This promotes π-stacking with the π-excessive porphyrin. It has also been found that halogen-hydrogen interactions with Fe(III)PPIX are favoured by electronegative substituents such as chlorine (Scheme 3.2).[17] On the other hand, the electron-releasing 4-amino group increases the pK_a of the quinolinium ion, improving its capacity as a hydrogen-bond donor for strong binding to the μ-oxo bridge of the Fe(III)PPIX dimer.[15] Crucially, chloroquine also contains a basic aliphatic tertiary amine which is important for accumulation in the acidic digestive vacuole of *P. falciparum*.

Consequently, chloroquine has no obvious sites suitable for synthetic modification. The diethyl side chains offer the best opportunity for modification as these are situated furthest away from the quinoline core of the molecule. Thus, in order to introduce an additional primary amine functionality for facile attachment of the NBD fluorophore by nucleophilic aromatic substitution, a suitable *N*-dealkylated key intermediate was identified by retrosynthetic analysis as detailed later in this chapter (Section 3.4.1).

Unlike the *Cinchona* alkaloids, fluorescent analogues of chloroquine have previously been prepared and evaluated.[18-20] Indeed, one such derivative has already incorporated an extrinsic NBD fluorophore connected by a lengthy (six-carbon) linker chain.[18] We anticipated that a more suitable analogue of the parent molecule would require a shorter linker chain and this was taken into account in the design of target molecule **8**.

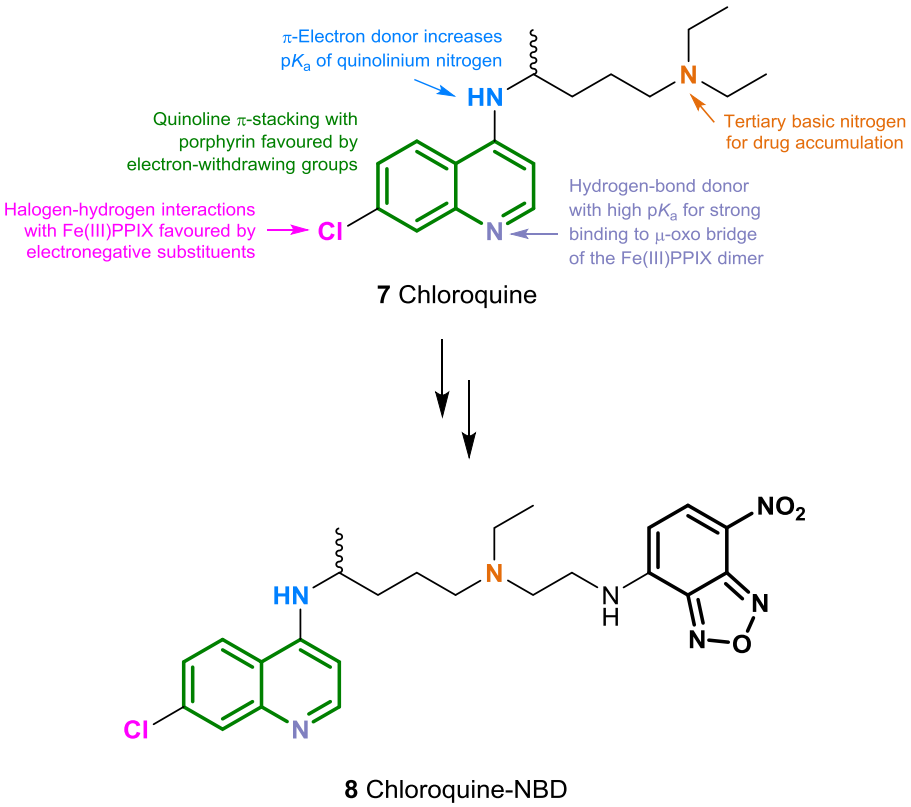

Scheme 3.2. *Key aspects of the structure-activity relationships between chloroquine (**7**) and Fe(III)PPIX are indicated, leading to a proposed novel NBD-labelled fluorescent derivative (**8**) which exhibits retention of the key characteristics of the parent molecule. Incorporation of the NBD fluorophore is indicated by thickened black bond widths.*

3.3. Synthesis of novel fluorescent quinoline methanol antimalarials

3.3.1. Retrosynthetic analysis and forward synthesis

First, an overview of the considerations relating to the synthesis and characterisation of the *Cinchona* alkaloid derivatives will be presented in the following two sections before commencing a discussion of the synthesis in detail (covered in Sections 3.3.3-3.3.6). In order to prepare the novel fluorescent quinoline methanols presented in Scheme 3.2, a retrosynthetic analysis of the target compounds (**3-6**) was conducted as depicted in Scheme 3.3. Disconnection of the N-C bond between the spacer chain and the fluorophore generated terminal amine-containing alkaloids that were identified as appropriate key intermediates (**9**, **10**). Subsequent cleavage of the S-C bond of the thioether linker yielded the parent alkaloids.

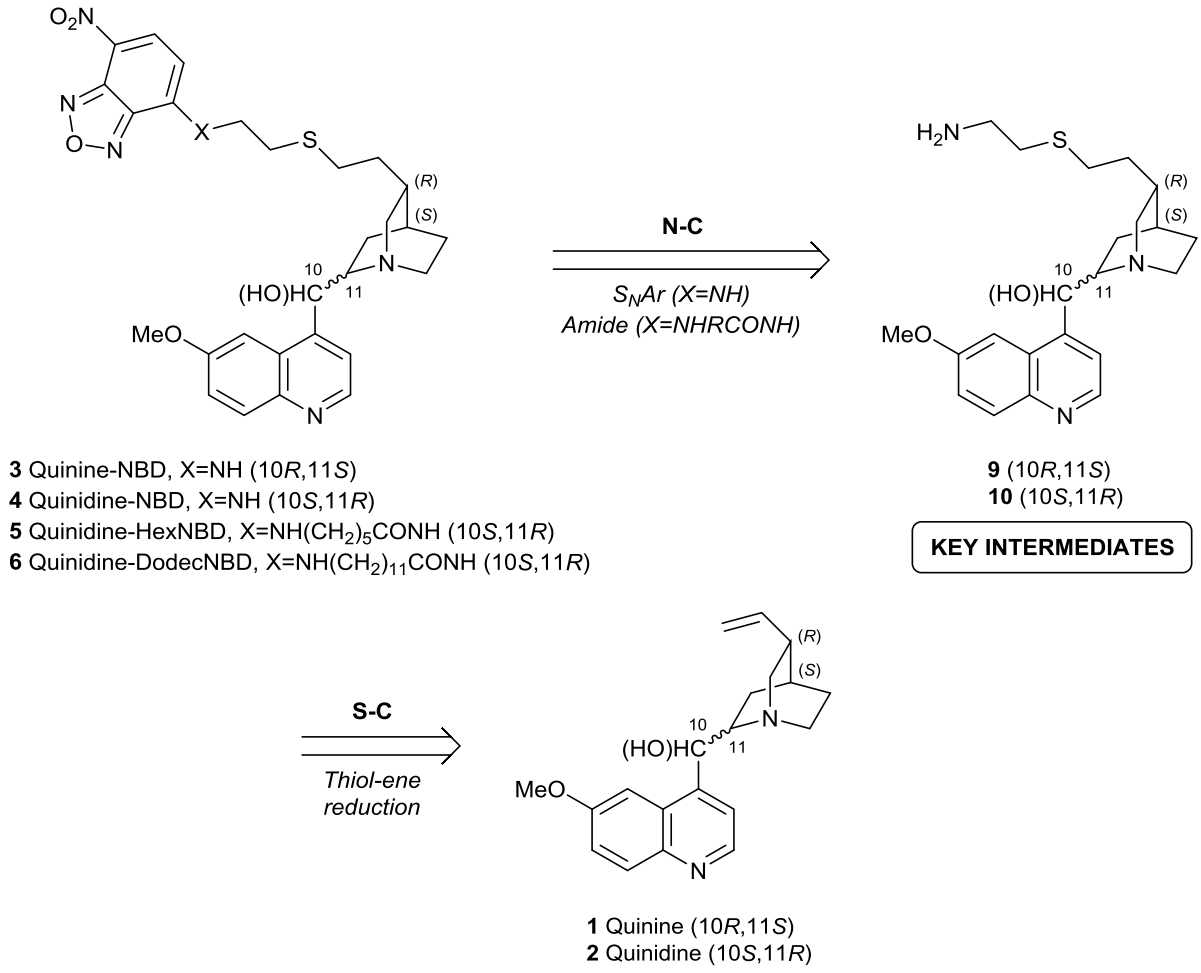

Scheme 3.3. *Retrosynthetic analysis reveals key intermediates* ***9*** *and* ***10*** *which provide access to a host of fluorescent derivatives of the* Cinchona *alkaloids.*

The full synthesis of the fluorescent derivatives of the *Cinchona* alkaloids is detailed below in Scheme 3.4. A regioselective thiol-ene 'click' reaction was chosen involving a bifunctional amino thiol in order to introduce an additional amine functional group to the alkaloids via a short thioether spacer, opening up the possibility of a variety of derivatives easily obtainable from the starting alkaloids. In this respect, there was a single report of such a modification of the vinyl group of quinine using a photoinitiated radical reaction.[21] For this reaction, it was necessary to use an *N*-Boc-protected amine instead of a primary amine directly but the extra protection step was mitigated by the short reaction time required for complete reduction and facile purification steps of this 'click' reaction. Subsequent cleavage of the *N*-Boc groups of **11** and **12** yielded the primary amines **9** and **10** which provided convenient handles for direct attachment of the NBD fluorophore via nucleophilic aromatic substitution of its 4-chloro derivative. As a result, the NBD-labelled alkaloids **3** and **4** with the shortest spacer chains were prepared over three steps in an overall yield of 10% each.

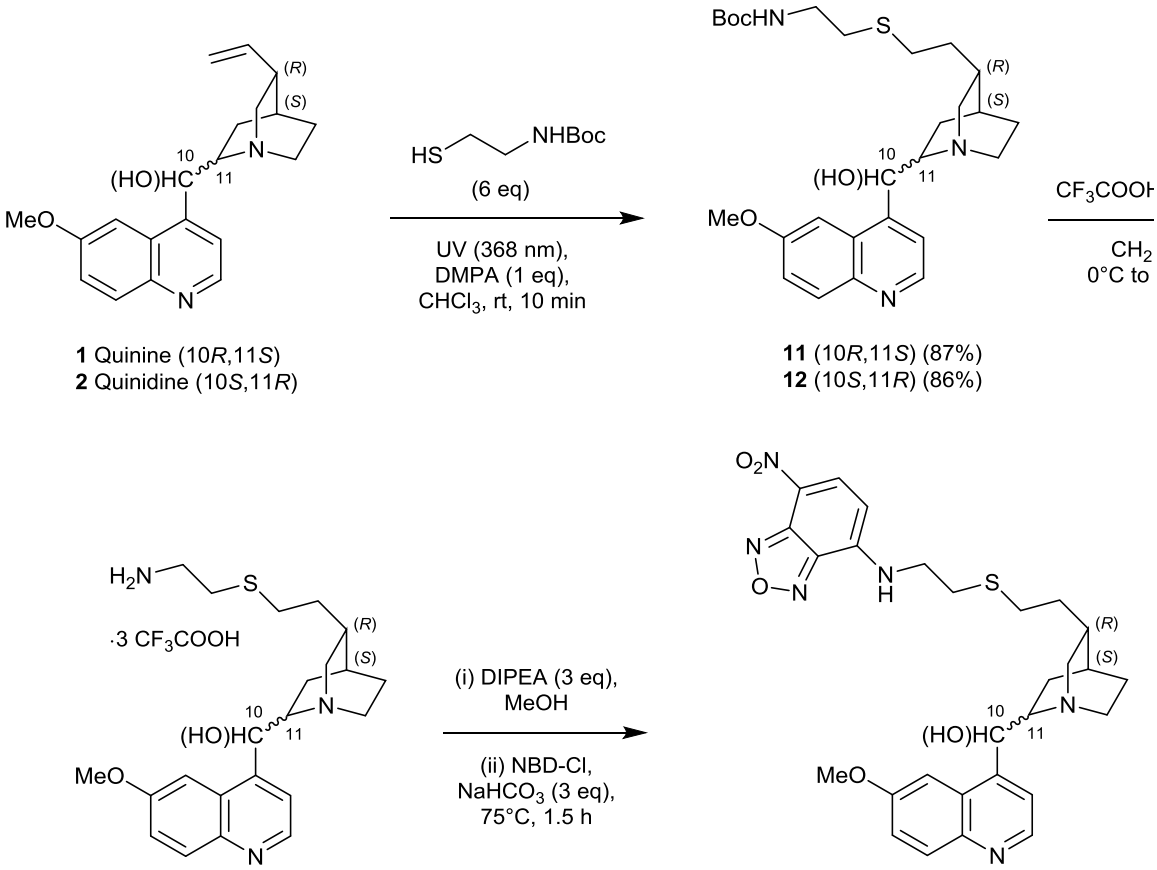

Scheme 3.4. *The forward synthesis of two novel 'short-chain' fluorescent derivatives **3** and **4** of the quinoline methanol antimalarials quinine (**1**) and quinidine (**2**), respectively.*

In order to vary the length of the spacer chain, NBD-labelled succinimidyl ester amino acids were prepared as depicted in Scheme 3.5. The latter were generated from nucleophilic aromatic substitution reactions of the NBD 4-chloro derivative with amino acids of different chain lengths (two versions) after which a DCC-mediated Steglich esterification introduced the succinimidyl ester leaving group for amide bond formation with the primary amine of the alkaloid derivative.

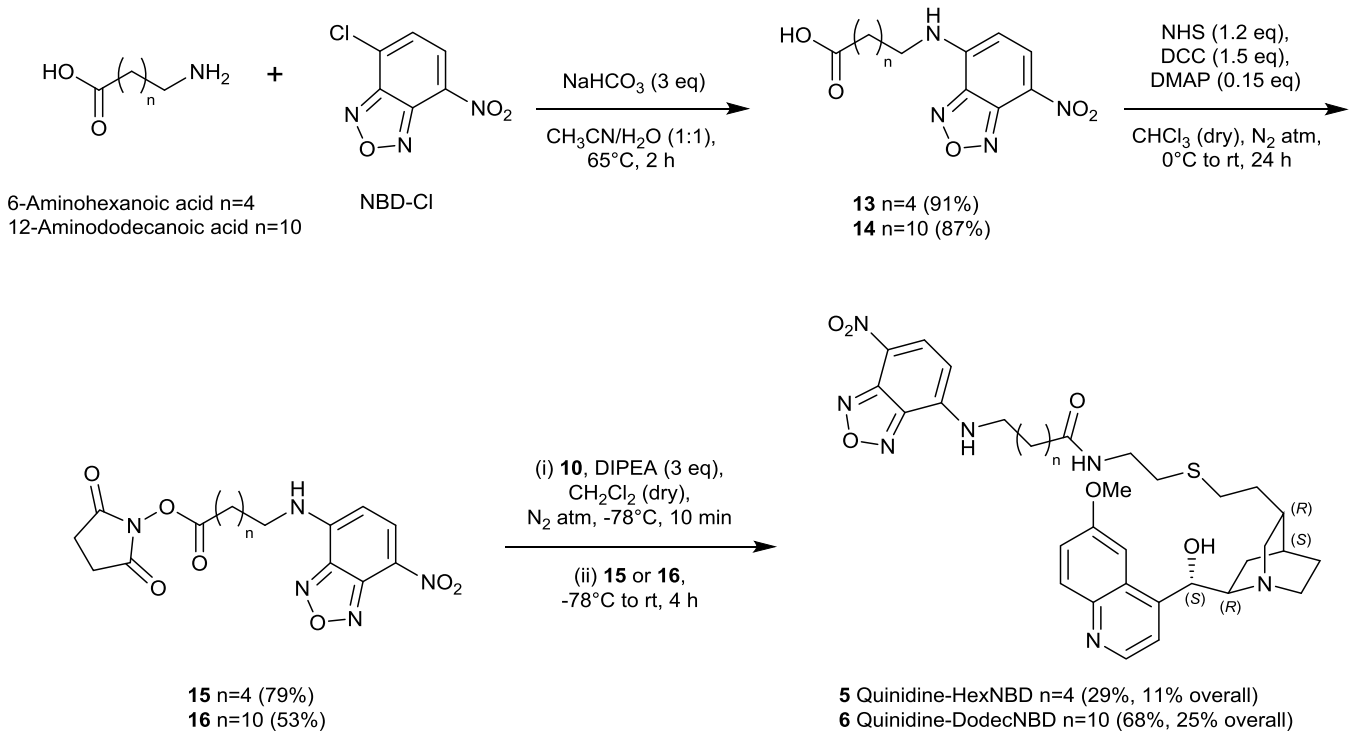

Scheme 3.5. *The synthesis of intermediate- and long-chain fluorescent derivatives* ***5*** *and* ***6*** *of quinidine (**2**). This required the preparation of two NBD-labelled amino acids and their respective succinimidyl esters.*

3.3.2. General considerations for NMR characterisation of modified alkaloids

Since quinine was first isolated in 1820, the alkaloid and its diastereomer, quinidine, have been of great interest to organic chemists. In 1853, Louis Pasteur exploited the unique stereochemical properties of these molecules as agents for chiral resolution. Today, these alkaloids are commonly found as chiral auxiliaries in catalytic asymmetric synthesis and as chiral selectors in stereoselective stationary phases. Despite the intense interest in these alkaloids, the first stereoselective total synthesis of quinine was only accomplished in 2001.[22]

The general structures of quinine and quinidine are characterised by an aromatic quinoline ring connected to an aliphatic quinuclidine bicyclic system through a chiral hydroxymethine carbon

linkage (Figure 3.3). The vinyl and methoxy substituents appear at C-18 of the quinuclidine ring and at C-6 of the quinoline ring, respectively. These alkaloids possess four chiral carbon centres of which two have the same absolute configuration in both alkaloids, i.e. (13*S*,18*R*). The other two chiral centres give rise to the diastereomeric relationship; (10*R*,11*S*) and (10*S*,11*R*) for quinine and quinidine, respectively.

Consequently, the ^{1}H and ^{13}C NMR spectra of the *Cinchona* alkaloids are relatively complex. The carbon atoms of the four quinuclidine ring methylene groups are all prochiral and hence their hydrogen atoms are diastereotopic and magnetically non-equivalent in their ^{1}H NMR spectra. Additional considerations for the NMR analysis of these alkaloids and their derivatives are summarised in Figures 3.3 and 3.4, for which quinine is given as a representative case.

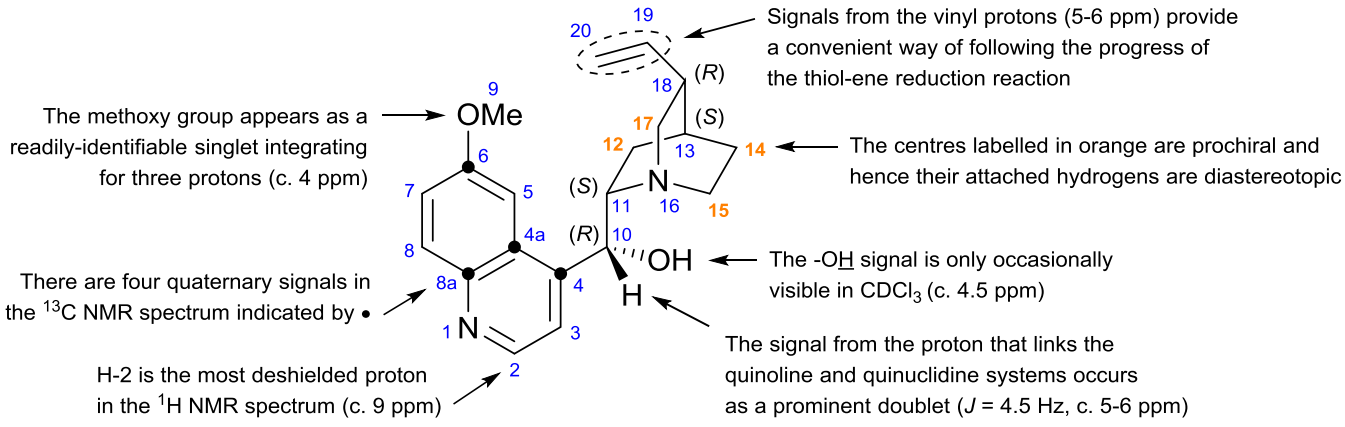

Figure 3.3. *General considerations for the characterisation of quinine (**1**) using NMR spectroscopy.*

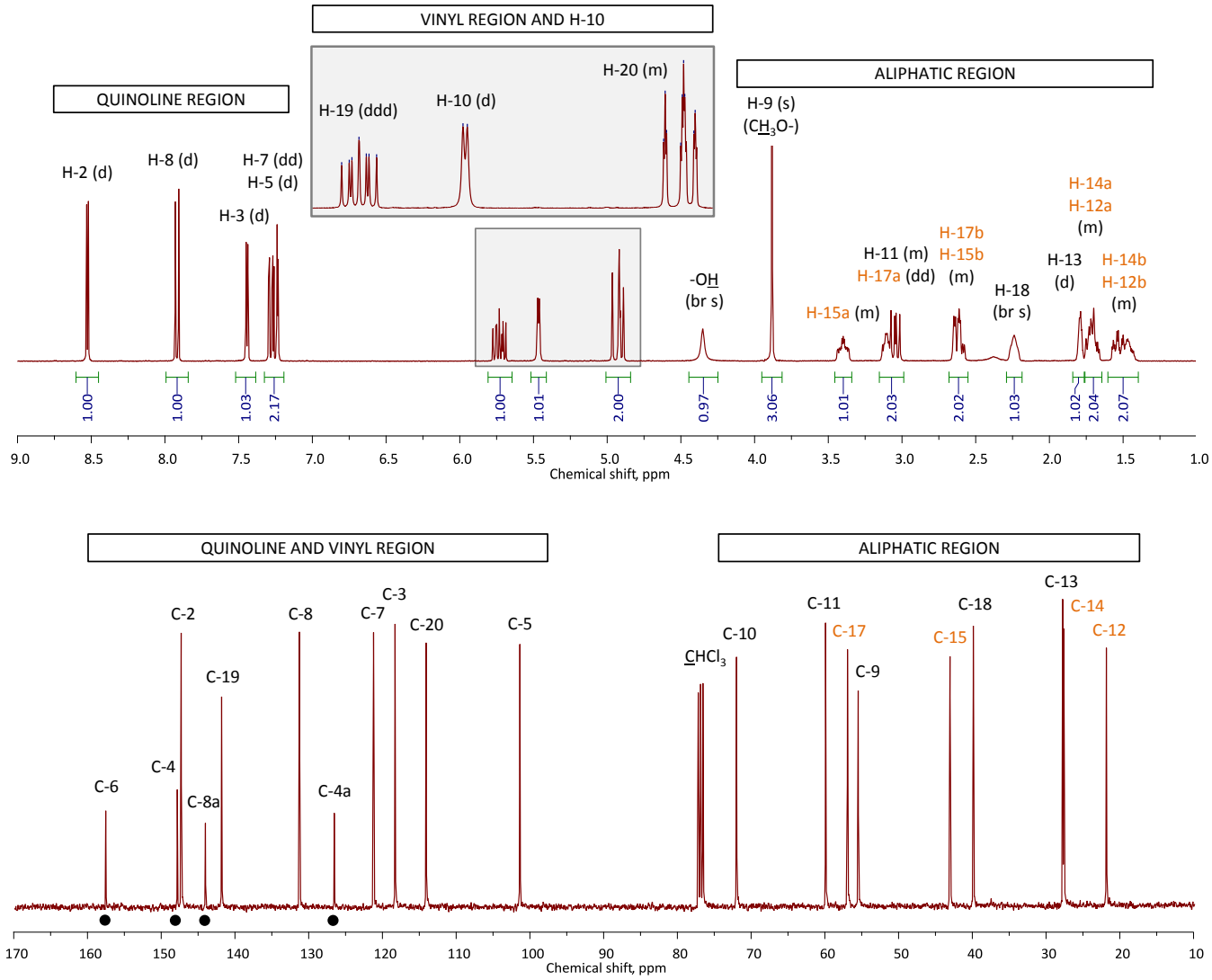

Figure 3.4. *^{1}H and ^{13}C NMR spectra of quinine (**1**) recorded in $CDCl_3$ at 400 MHz and 100 MHz, respectively. Assignments were confirmed using two-dimensional correlation NMR spectroscopy. Diastereotopic proton signals and their corresponding carbon atoms are labelled in orange. The spectra of quinidine (**2**) are almost identical except for small differences in the chemical shifts of the aliphatic proton signals. The numbering refers to the structure given in Figure 3.3.*

By contrast, the NMR properties of the NBD fluorophore are much simpler. The proton signals corresponding to H-a and H-b appear in the ^{1}H NMR as an AB doublet pair (J = 9 Hz) due to vicinal coupling (Figure 3.5). The proton signal for H-a is more shielded than the one for H-b owing to delocalisation of the amine lone pair into the six-membered ring. There are four quaternary carbon centres (indicated by ● in Figure 3.5) that relax very slowly and are typically difficult to detect in the ^{13}C NMR spectrum. This may be corrected by adding a paramagnetic spin-relaxation agent.

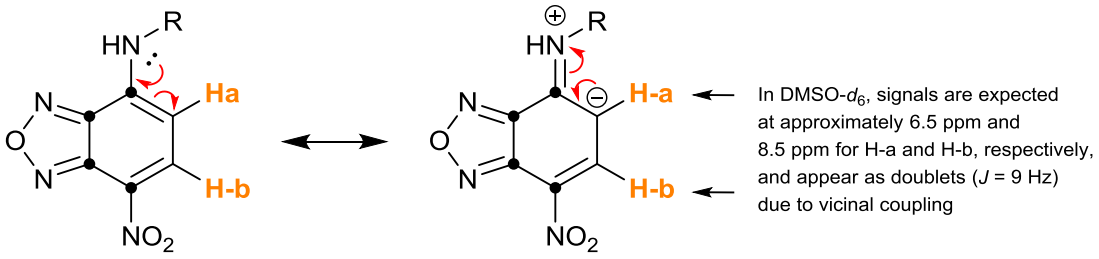

Figure 3.5. *Resonance structures of the NBD fluorophore when conjugated to an amine. Shielding by the lone pair of the amine results in a 2 ppm difference in chemical shift between the signals for H-a and H-b.*

3.3.3. Modifying the *Cinchona* alkaloids with the thiol-ene 'click' reaction

The term 'click' chemistry was introduced by K. B. Sharpless in 2001 to describe reactions that generate heteroatom-linked systems with high efficiency under a variety of mild conditions by joining small units together.[23,24] Such reactions also display characteristics such as being wide in scope, high-yielding and stereoselective. They usually require readily-available starting materials and employ simple reaction conditions that should be insensitive to atmospheric oxygen and trace amounts of water. Furthermore, such reactions should take place in no solvent, or one that is benign or easily removed, and generate only inoffensive by-products that can be removed non-chromatographically.[23,24]

One such example is the radical-mediated reduction of an alkene by a thiol which has become known as the "thiol-ene" reaction. Many examples exist which proceed with near-quantitative formation of the corresponding thioether in a regioselective fashion.[25] A wide-range of alkenes and thiols can be used. The mechanism of the thiol-ene reduction is depicted in Scheme 3.6 and follows a typical three-step radical sequence. The reaction is initiated by irradiating the thiol in the presence of a photoinitiator, which generates the thiyl radical (RS·) and other byproducts. A common, inexpensive photoinitiator is 2,2-dimethoxy-2-phenylacetophenone (DMPA), which is cleaved homolytically upon radiation with low-energy ultraviolet light. Propagation is a two-step process involving the direct addition of the thiyl radical at the less hindered (less substituted) carbon of the double bond so as to form the more substituted and more stable radical intermediate in what qualifies as an anti-Markovnikov addition. Hydrogen transfer from the thiol to this radical then generates the desired addition product with formation of a thiyl radical for further propagation.[23] Termination, which leads to incomplete conversion of the starting material, can result via radical homo-coupling such as the formation of a disulfide from two thiyl radicals.

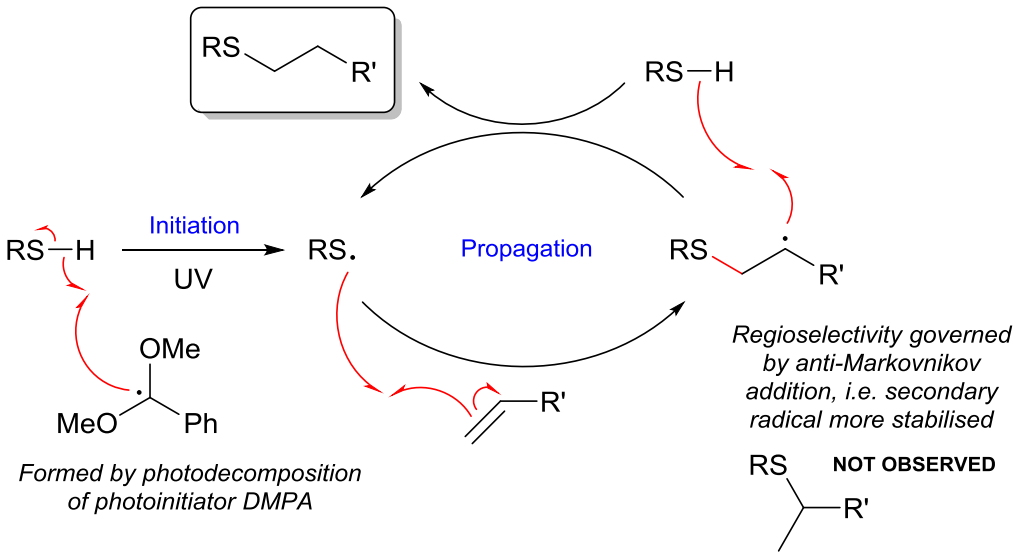

Scheme 3.6. *The mechanism of the thiol-ene 'click' reaction.*

Prior to this work quinine was reported as a substrate for the thiol-ene 'click' reaction using 3-mercaptopropyltriethoxysilane as reagent in which investigators recorded a high yield for conversion (98%) using DMPA as a radical initator.[21] While no chromatographic purification was required, a lengthy reaction time of 27 hours was reported. In order to generate key amino sulfide intermediates **9** and **10**, it was hoped to 'click' quinine with the bifunctional thiol-amine cysteamine directly (Scheme 3.7). However, thin-layer chromatography (TLC) revealed no or negligible reaction, even when the amounts of the reagents and the photoinitiator were systematically increased to ten equivalents in turn (Table 3.1).

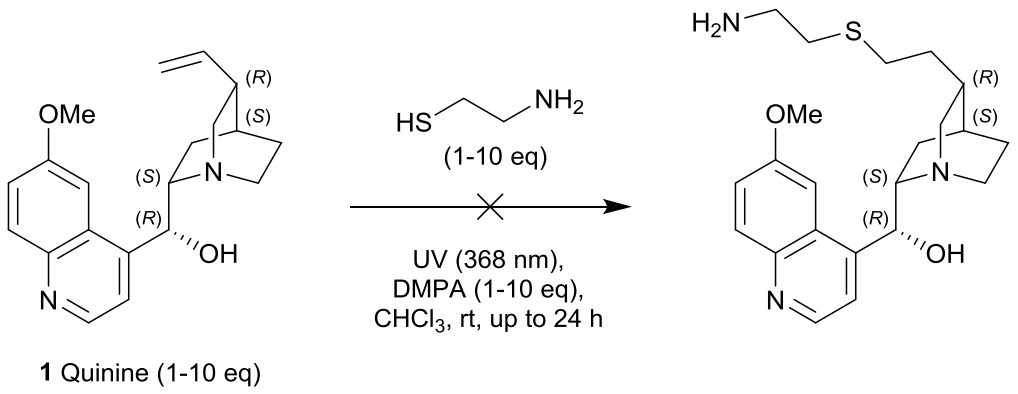

Scheme 3.7. *A first direct attempt at the thiol-ene 'click' reaction was unsuccessful as judged by TLC.*

Consequently, a number of model systems were exploited to probe the reaction conditions and these are further listed in Table 3.1. Firstly, a "proof-of-concept" reaction between styrene, the simplest UV-active alkene, and 1-butanethiol, a prototypical thiol, was explored. Fortunately, this appeared to be successful as evidenced by spot-to-spot conversion from the reagent (styrene) to the putative product on the TLC plate. A subsequent experiment using quinine itself and 1-butanethiol was also judged by TLC to be successful, suggesting that the problem in the reaction in Scheme 3.7 lay with the specific character of the thiol. This view was supported by a simple qualitative experiment between quinine and the thiol-containing amino acid L-cysteine, which did not proceed to any appreciable extent either.

Table 3.1. *Systematic investigation into the conditions required for the thiol-ene 'click' reaction. Reactions were performed at ambient conditions in $CHCl_3$. The reaction flask was illuminated at 368 nm for one hour.*

Entry	Alkene	Thiol	Photoinitiator	Success of reaction as evaluated by TLC
1	Quinine (1 eq)	Cysteamine (1 eq)	DMPA (10 eq)	No reaction
2	Quinine (1 eq)	Cysteamine (10 eq)	DMPA (1 eq)	No reaction
3	Quinine (10 eq)	Cysteamine (1 eq)	DMPA (1 eq)	No reaction
4	Styrene (1 eq)	1-Butanethiol (1 eq)	DMPA (1 eq)	Complete reaction
5	Quinine (1 eq)	1-Butanethiol (1 eq)	DMPA (1 eq)	Complete reaction
6	Quinine (1 eq)	L-Cysteine (1 eq)	DMPA (1 eq)	No reaction
7	Quinine (1 eq)	*N*-Boc-cysteamine (1 eq)	DMPA (1 eq)	Incomplete reaction
8	Quinine (1 eq)	*N*-Boc-cysteamine (6 eq)	DMPA (1 eq)	Complete reaction

As it is well-known that primary amines undergo facile one-electron oxidation involving the *N*-lone pair to form an aminium radical cation under the influence of ultraviolet light, this was suspected to have been the complicating factor with cysteamine.[26] Hence, it was decided to carry out the reaction using *N*-Boc-cysteamine instead, with the amino group protected as a carbamate. It was anticipated that this would also improve the solubility of the thiol, which might facilitate the reaction, as cysteamine is poorly soluble in $CHCl_3$. Upon reacting *N*-Boc-cysteamine with quinine under thiol-ene conditions, TLC indicated that the thiol reagent was completely consumed, corroborating the view that the primary amino group was the problem. By increasing the number of equivalents of the thiol it was possible to achieve complete reaction of the alkaloid.

As mentioned above, *Cinchona* alkaloids are well known for their fluorescent properties but this also makes these molecules susceptible to photodestruction when exposed to ultraviolet

radiation due to constant population of the 6-methoxyquinoline excited state. As a result, the ultraviolet radiation required for radical photoinitiation during the thiol-ene 'click' reaction (λ_{max} 368 nm) can damage the methoxyquinoline ring in the substrate and the product (λ_{max} 333 nm) if the illumination time of the reaction is not carefully monitored. Hence, this was investigated using ^{1}H NMR spectroscopy.

A trial thiol-ene reaction was conducted on a small scale with quinidine (**2**) as the limiting reagent (20 mg, 0.062 mmol) in $CDCl_3$ (2.5 mL). 0.35 mL aliquots were removed at 0, 2, 5, 10 and 30 minutes and diluted using $CDCl_3$. These were transferred to NMR tubes and their spectra recorded. Disappearance of the signals for the vinyl protons H-19 suggested that the thiol-ene reaction was complete after just five minutes (Figure 3.6). However, it was ultimately decided to expose the reaction to ten minutes' illumination to ensure complete reaction, as photodestruction of the heterocycle was only evident after 30 minutes.

Although introducing a primary amine directly into the alkaloid would have been more useful for our purposes, the versatility and rapid reaction time of these optimised reaction conditions mitigated the extra deprotection step that was required to liberate the primary amine. Consequently, a range of derivatised alkaloids were prepared according to Scheme 3.8.

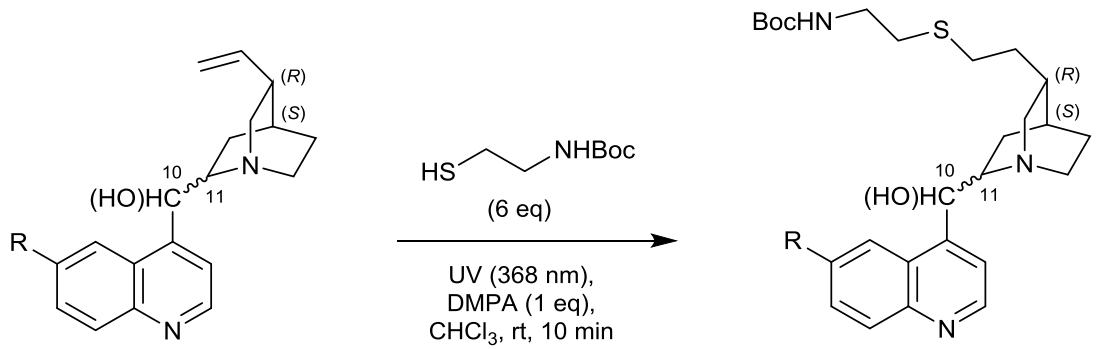

1 Quinine (10*R*,11*S*) R=OMe
2 Quinidine (10*S*,11*R*) R=OMe
17 Cinchonine (10*S*,11*R*) R=H

11 (10*R*,11*S*) R=OMe (87%)
12 (10*S*,11*R*) R=OMe (86%)
18 (10*S*,11*R*) R=H (97%)

Scheme 3.8. *A series of reactions showcasing the versatility of the thiol-ene 'click' reaction applied to various* Cinchona *alkaloids.*

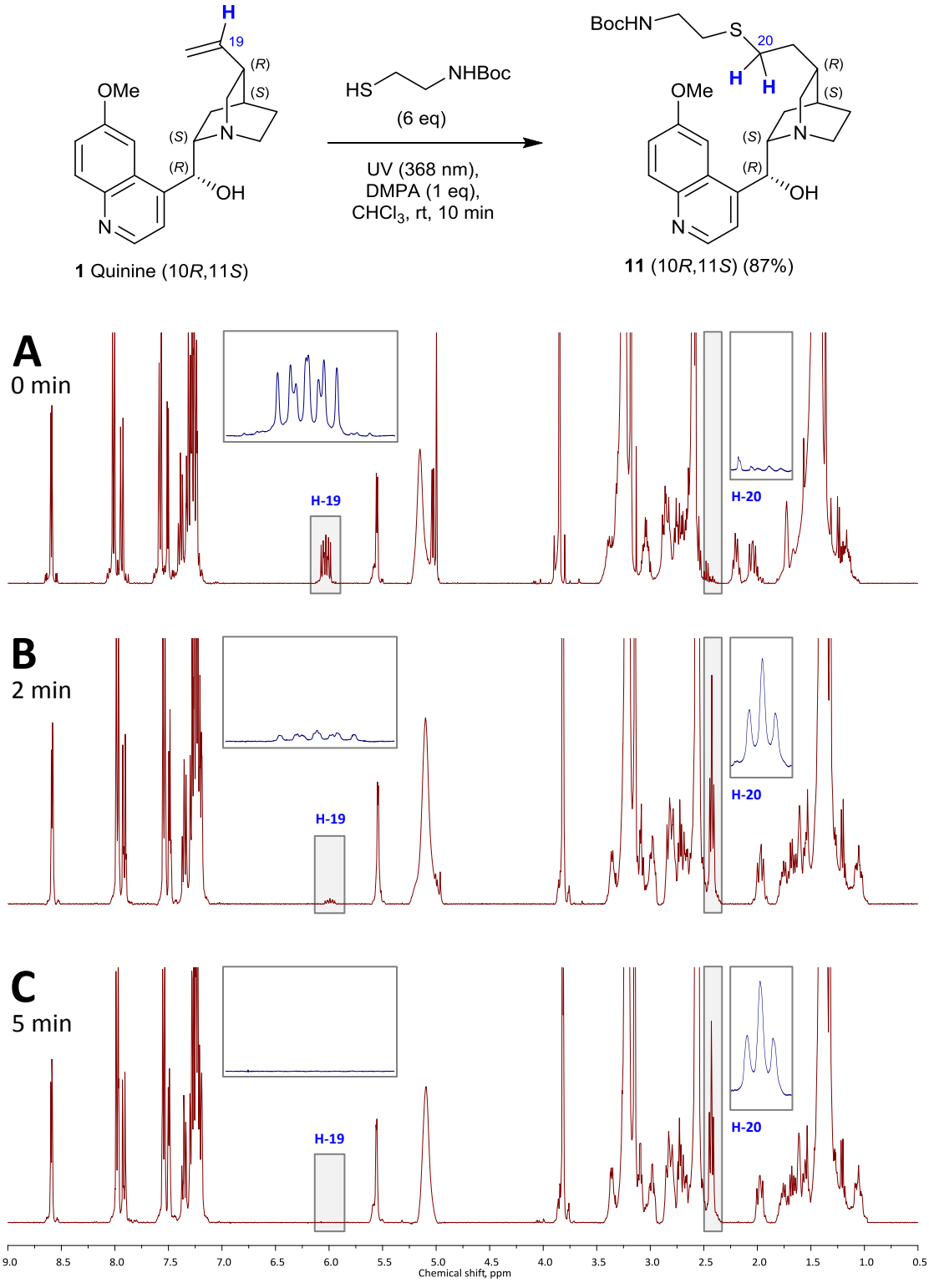

Figure 3.6. *A time-lapse experiment using ^{1}H NMR spectroscopy to determine the optimum illumination time required for the photoinitiated thiol-ene 'click' reaction. Spectra were recorded in $CDCl_3$ (300 MHz) (A) before illumination, i.e. at zero minutes, (B) after two minutes' illumination and (C) after five minutes' illumination. The proton signals corresponding to the disappearance of the H-19 multiplet (approx. 6 ppm) and the appearance of the H-20 triplet (approx. 2.5 ppm) have been enlarged.*

Hence the desired amine derivatives **11** and **12** of quinine and quinidine, respectively, were generated. Cinchonine (**17**), another *Cinchona* alkaloid related to quinidine, was also found to be a suitable substrate for amine derivatisation yielding **18**. It was also possible to introduce a primary hydroxyl group by using 2-mercaptoethanol as the thiol in the click reaction, generating the expected target and thus proving that the problem with the initial reaction conditions lay with the primary amine.

All three derivatised alkaloids were obtained in high yields (> 85%) by acid-base extraction and crystallisation from aqueous alcohol. Analytical purity was confirmed by elemental analysis. The presence of trace water in the reaction did not appear to affect the outcome of the reactions. Thus these reactions fulfil the criteria necessary for a successful 'click' reaction.[23]

As these thiol-ene derivatives are novel versions of the parent alkaloids, their optical properties were an important aspect of their characterisation. Specific rotations were measured in ethanol at the same concentrations for the parent alkaloids and their derivatives (Table 3.2). A correlation between the polarisation of light induced by each parent alkaloid and its derivatised product was observed, indicating retention of absolute stereochemistry in the product.

Table 3.2. *Specific rotations measured for the parent alkaloids and their thiol-ene derivatives measured using the D-line of a sodium lamp (λ = 589 nm) in ethanol at 20°C.*

Compound	Specific rotation, $[\alpha]_D^{20}$	Conditions (g/100 mL)
1 (Quinine)	-80°	*c.* 0.515
11	-83°	*c.* 0.797
2 (Quinidine)	+136°	*c.* 0.515
12	+138°	*c.* 0.797
17 (Cinchonine)	+107°	*c.* 0.468
18	+111°	*c.* 0.749

3.3.4. *N*-Boc deprotection and substitution of the NBD fluorophore

In order to render the amine-derivatised alkaloids **11** and **12** suitable for nucleophilic aromatic substitution reactions, the *N*-Boc protecting group needed to be removed. This was achieved using an excess of trifluoroacetic acid (TFA) in CH_2Cl_2 in which the mixture was stirred in an ice-bath for two hours to allow the reaction to proceed in a controlled manner, after which it was allowed to warm to room temperature. Surprisingly, the trifluoroacetate product was amenable to column chromatography, albeit using high concentrations of methanol in the mobile phase

(25% MeOH:CH_2Cl_2). These trifluoroacetate salts **9** and **10** were obtained in moderate yields (40-50%).

N-Boc deprotection follows a four-step mechanism represented in Scheme 3.9. Protonation of the *t*-butyl carbamate of the *N*-Boc protecting group (i) is followed by loss of the *t*-butyl cation which gives carbamic acid as an intermediate (ii). The *t*-butyl cation is quenched or deprotonated to give isobutylene. Decarboxylation of the acid generates the free amine (iii) and subsequent protonation of the amine under acidic conditions generates the trifluoroacetate salt of the product (iv).[27]

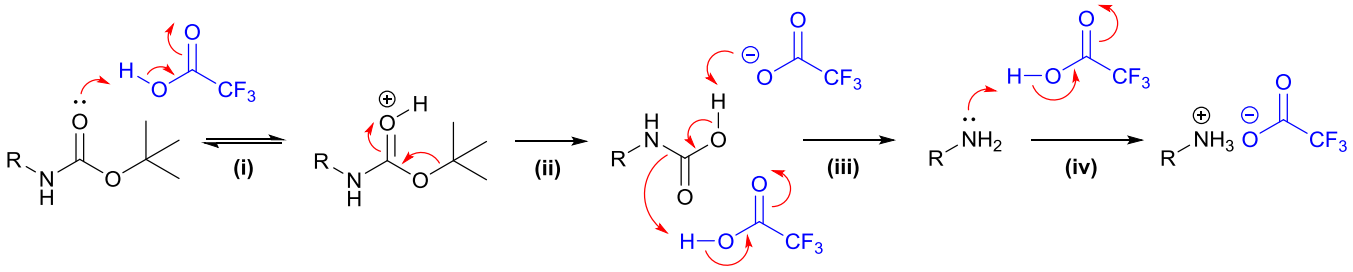

Scheme 3.9. *The general mechanism for the TFA-mediated deprotection of* N*-Boc-protected amines. TFA and the trifluoroacetate anion are depicted in blue.*

In the absence of a basic work-up, *N*-Boc deprotection of an amine generates a trifluoroacetate salt. Although it was possible to liberate the free base by dissolving the salts in MeOH and stirring with K_2CO_3, followed by filtration and rotary evaporation, some difficulties were encountered with the isolation of the free base. Hence, in order to continue using the salts in subsequent reactions, it was necessary to calculate the stoichiometry of the trifluoroacetate anion(s) associated with these molecules.

The pK_a values of the quinoline, quinuclidine and terminal amines of **9** and **10** are predicted to be 4.06, 8.85 and 9.78, respectively (MarvinSketch 14.8.25.0, ChemAxon Ltd, 2014). Since the pK_a of trifluoroacetic acid is 0.23, it was reasonable to expect that all three nitrogen atoms would be protonated, resulting in the coordination of three trifluoroacetate ions. This was confirmed by determining the molecular weights of **9** and **10** independently using two different techniques; namely, ^{1}H NMR and UV-Vis spectroscopy.

For the ^{1}H NMR study, 6-methoxyquinoline was used as an internal standard. The masses of two samples of **9** and **10** were accurately determined and the material transferred to vials containing accurately-determined masses of the internal standard. The mixture was then

dissolved in deuterated methanol (CD_3OD), transferred to an NMR tube and the ^1H NMR spectrum was recorded (300 MHz). The ratios of the integrals of aromatic and methoxy proton signals generated by the two compounds allowed the calculation of their molecular weights.

In the UV-Vis spectroscopy study, solutions containing accurately-determined masses of the salt were prepared in methanol. The molar absorption coefficient of the starting alkaloids is well known (λ_{max} 333 nm; ε = 5 000 M^{-1} cm^{-1} in EtOH) and the salts **9** and **10** exhibit the same absorption profile. As it is unlikely that chemical derivatisation of the vinyl group affects the chromophoric quinoline ring, it was reasonable to use the molar absorption coefficients of the starting alkaloids to calculate the concentrations of the salt solutions from the Beer-Lambert law. From this, the molecular weights of **9** and **10** could then be computed.

Two independent samples were examined for each molecule using each technique and, in both cases, the results were consistent and reproducible. The average molecular weight was determined to be 742 ± 8 g/mol, while the calculated molecular weight with three molecules of trifluoroacetate coordinated was predicted to be 743.64 g/mol. Thus the results corresponded to **9** and **10** each associating with three equivalents of trifluoroacetate, as initially expected.

With these salts in hand, the 4-chloro derivative of the NBD fluorophore could be linked to the derivatised alkaloid via nucleophilic aromatic substitution. Thus, the salts **9** and **10** were stirred in methanol at room temperature and three equivalents of *N*,*N*-diisopropylethylamine (Hünig's base), a moderately strong, non-nucleophilic base suitable for liberating the free amines, were added. Subsequently, the mixture was heated in the presence of NBD-chloride with an excess of sodium bicarbonate to neutralise the HCl released.[28]

The mechanism of this nucleophilic aromatic substitution (S_NAr) reaction is depicted in Scheme 3.10. It commences with the nucleophilic addition (A_N) of the liberated primary amine to the NBD heterocycle at the position of the chlorine. This is the slow, rate-determining step which forms a high-energy intermediate called a Meisenheimer complex. This anionic intermediate is resonance-stabilised by the electron-withdrawing nitro group that is situated *para* to the leaving group. This is followed by a rapid elimination step (E) to generate the NBD-labelled alkaloid, which effectively "switches on" the fluorescence of the NBD group as it removes the internal heavy-atom fluorescence quenching effect of the chlorine atom, making this reaction convenient to follow on the TLC plate.

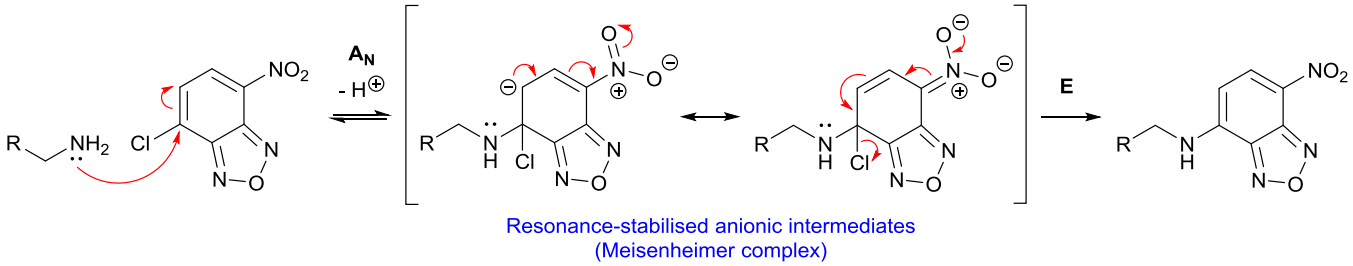

Scheme 3.10. *The general mechanism for the nucleophilic aromatic substitution (S_NAr) reaction of the NBD 4-chloro derivative and a primary amine.*

Column chromatography followed by recrystallisation in aqueous methanol yielded the 'short-chain' NBD-labelled alkaloids **3** and **4** in 26% and 27% yield, respectively. This resulted in a 10% overall yield for each compound over three steps.

By way of illustration, the ^{1}H NMR spectrum of NBD-labelled quinidine **4** is shown in Figure 3.7. The characteristic AB doublet pair due to the NBD signals H-a and H-b (6.5 ppm and 8.5 ppm, respectively, both with J = 8.9 Hz), as well as the doublet associated with the new secondary aryl amine peak (J = 4.0 Hz), are highlighted.

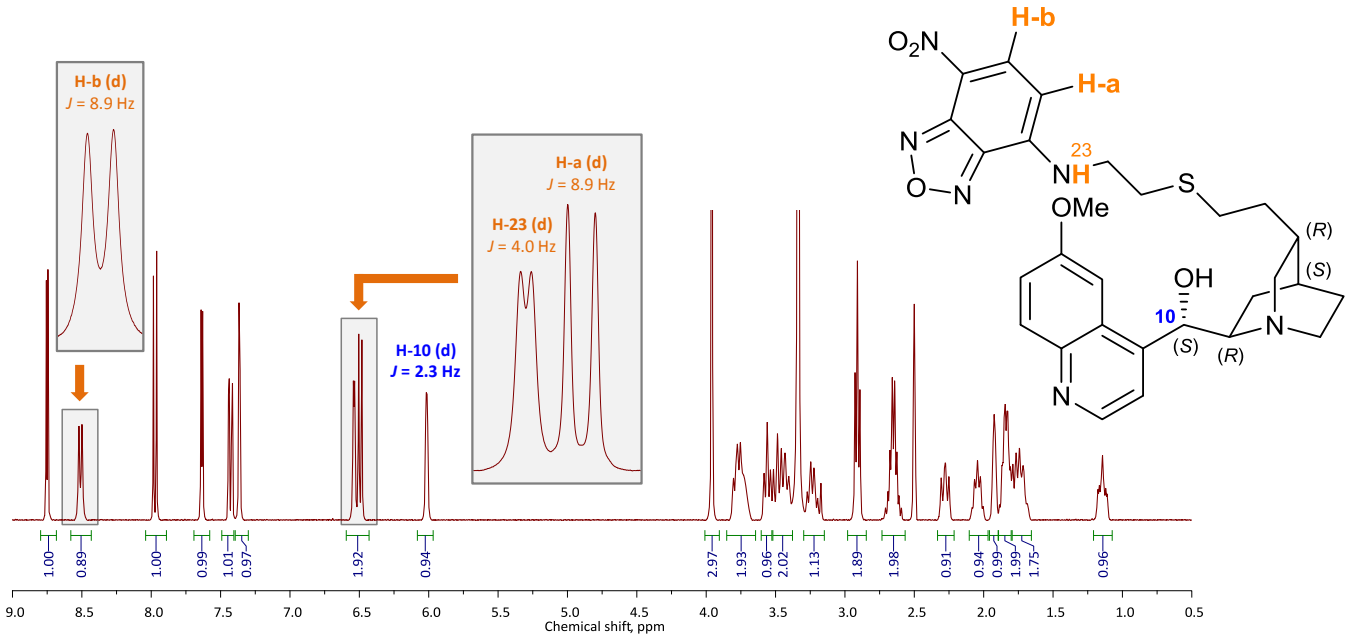

Figure 3.7. *^{1}H NMR spectrum of NBD-labelled quinidine (**4**) acquired in DMSO-d_6 (400 MHz). Important hydrogen atoms on the NBD fluorophore are displayed in orange and correspond to the proton signals in the enlarged boxes. H-10, which connects the quinoline and quinuclidine ring systems, is visible as a characteristic doublet (approx. 6 ppm) which confirms the integrity of the alkaloid core.*

3.3.5. Preparation and substitution of NBD-labelled amino acid succinimidyl esters to vary the length of the spacer chain

With the amine derivatives **8** and **9** of the alkaloids in hand and, in order to probe the effect of varying the length of the spacer chain between the quinoline core and the NBD fluorophore, it was necessary to derivatise the NBD fluorophore to make it suitable for amide linkage to the derivatised alkaloids.

A bifunctional linear amino acid with a variable tether provided an ideal linker between alkaloid and fluorophore in which it was elected to vary the tether length as six carbon atoms (6-aminohexanoic acid) and as twelve carbon atoms (12-aminododecanoic acid). In each case the amino group of the amino acid was coupled to the NBD fluorophore using the same reaction conditions for the nucleophilic aromatic substitution as described above. Following an acidic work-up to remove unreacted amino acid, recrystallisation in aqueous methanol generated the two NBD-labelled acids **13** and **14** in excellent yields (Scheme 3.11).[28,29]

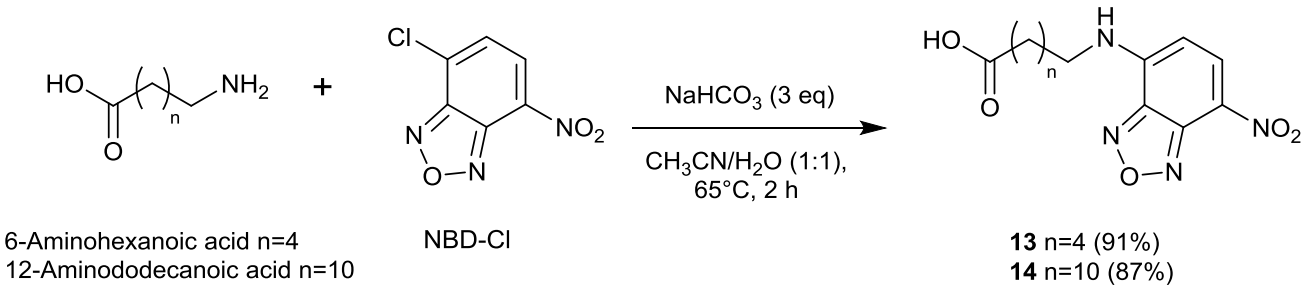

Scheme 3.11. *The preparation of two NBD-labelled amino acids with different chain lengths.*

The NBD-labelled amino acids **13** and **14** were characterised by NMR spectroscopy. However, the signals corresponding to the quaternary carbons in the NBD heterocycle were not clearly visible in the ^{13}C NMR spectrum (Figure 3.8A). Consequently, a spin-relaxation agent was used in order to visualise these poorly-relaxing nuclei by improving the sensitivity of the spectrum. Chromium(III) acetylacetonate, $Cr(acac)_3$, is an octahedral complex with three unpaired electrons that is typically used as a spin-relaxation agent. As the magnetogyric ratio of an unpaired electron is about 1 000 times larger than that of a proton, carbon will relax much faster in the presence of $Cr(acac)_3$ (Figure 3.8B). Although only a small mass of compound was available for this analysis, compounding the problem as the signal-to-noise ratio in these spectra was already low, addition of $Cr(acac)_3$ permitted assignment of the quaternary signals.

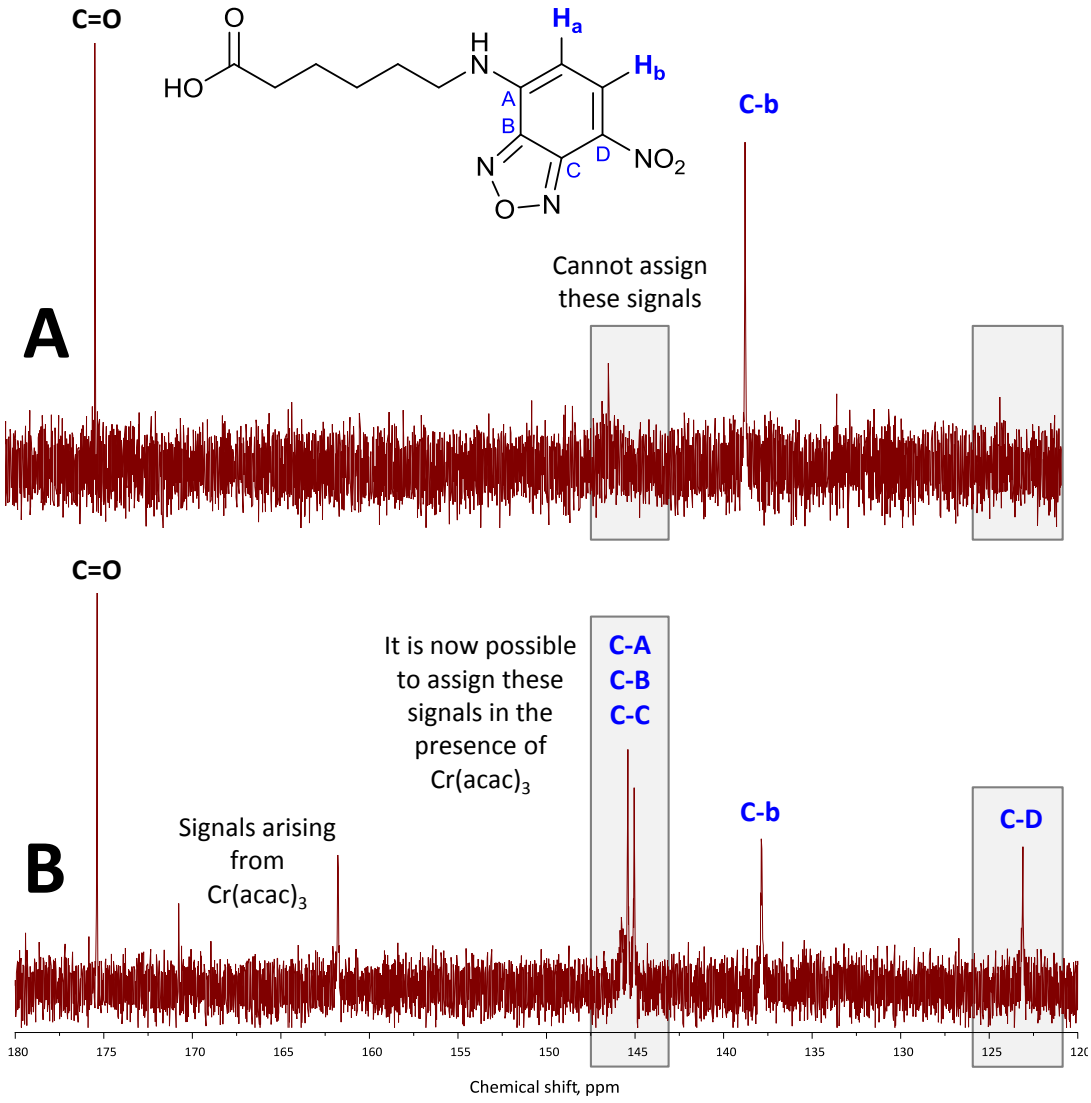

Figure 3.8. *^{13}C NMR spectra of NBD-labelled amino acid **13** in the absence (A) and presence (B) of spin-relaxation agent $Cr(acac)_3$. Spectra were collected in $CDCl_3$ (400 MHz).*

Linking these NBD-labelled amino acids **13** and **14** to the amine-derivatised alkaloids required the formation of an amide bond. In its simplest form, this involves direct condensation between an amine and a carboxylic acid, a reaction that requires high temperatures that are not always compatible with diverse functionalities. Instead, activating the hydroxyl moiety in the carboxylic acid by transforming it into a good leaving group allows for amine attack at a lower activation energy and hence milder reaction conditions may be used.[30-32] The premier methodology is based on activating the acid towards nucleophilic acyl substitution (S_NAc) using amide coupling agents such as the carbodiimides DCC or EDC. This is also the easiest methodology as activation of the carboxylic acid is conducted in situ.

Alternatively, one may activate the carboxylic acid via prior activation and then follow it with a nucleophilic acyl substitution reaction. There are various possibilities of which the simplest, in principle, is the activation of the carboxylic acid by conversion to its corresponding acid halide. A mixed anhydride methodology may be employed whereby a second carboxylic moiety is coupled onto the carboxylic acid; however, regioselectivity of the appropriate carbon centre may present a challenge when using this methodology. A variation on this method exploits chloroformates. In the presence of a base, the reaction between a carboxylate and a chloroformate yields a mixed carbonic anhydride which reacts rapidly with amines to form amides.

In this project, it was elected to exploit an active ester methodology by activating the carboxylic acid with the excellent leaving group, *N*-hydroxysuccinimide (NHS). A nucleophilic acyl substitution reaction then links the amine to the acyl centre of the active ester via an amide bond (Scheme 3.12). NHS esters are highly reactive and easily prepared. They react cleanly and rapidly and do not have the purification problems associated with carbodiimides or the regioselectivity challenges associated with mixed anhydride methodologies.

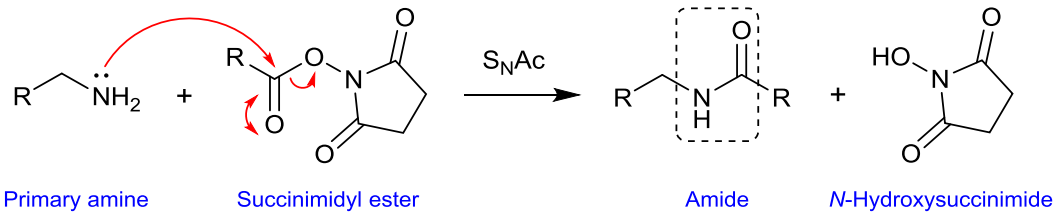

Scheme 3.12. *Nucleophilic acyl substitution (S_NAc) of a succinimidyl ester by a primary amine to generate an amide bond.*

It was first necessary to activate the NBD-labelled amino acids by esterification of the carboxylic acids with NHS. Two different methods were briefly screened.

The Yamaguchi esterification was first reported in 1979 and allows the mild synthesis of highly functionalised esters.[33] The carboxylic acid and 2,4,6-trichlorobenzoyl chloride form a mixed anhydride, which is then attacked regioselectively by 4-dimethylaminopyridine (DMAP) at the less hindered and more electrophilic carbon of the anhydride, producing acyl-substituted DMAP. This electrophilic centre is then intercepted by the hydroxyl group of the NHS to form the ester. Carrying out this reaction according to Scheme 3.13 generated the NBD-labelled succinimidyl ester **16** in a modest yield (43%) following column chromatography.

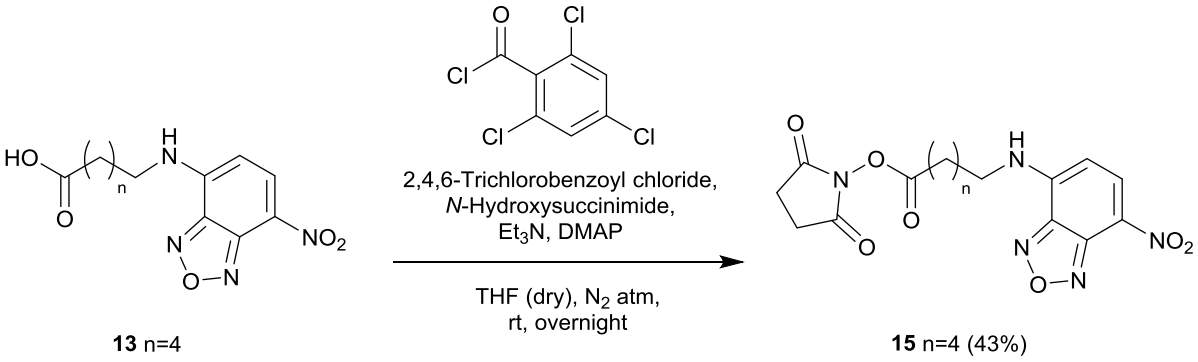

Scheme 3.13. *Preparation of NBD-labelled succinimidyl ester* ***15*** *under Yamaguchi esterification conditions.*

The second method that was screened was a Steglich esterification using DCC as the coupling reagent facilitated by catalytic amounts of DMAP.[34] Applying the Steglich conditions improved the yield of the NHS-labelled NBD-substituted esters which were prepared according to Scheme 3.14 with optimised reaction conditions indicated. The lability of the succinimidyl groups made isolation by column chromatography challenging in which the yield of **15** was markedly better than that of the longer-chain ester **16**.

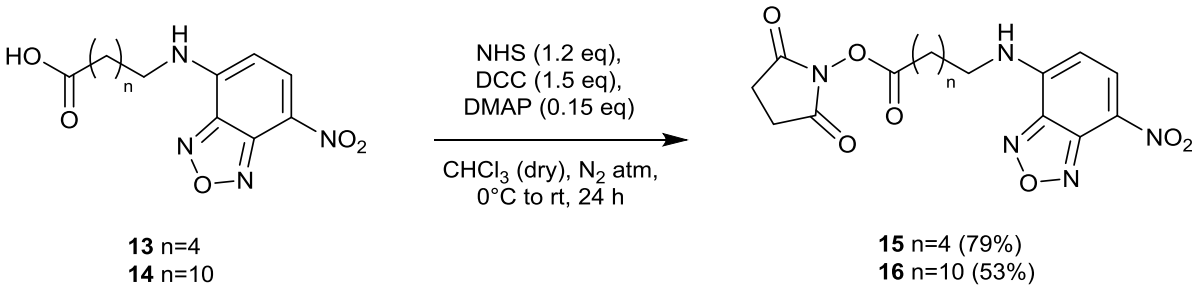

Scheme 3.14. *The preparation of NBD-labelled succinimidyl esters under Steglich esterification conditions.*

This esterification reaction was first described by Steglich in 1978.[34] The carboxylic acid reacts with DCC to form an *O*-acylurea that is then substituted by DMAP to form the reactive *N*-acyl pyridinium transfer agent that reacts with the hydroxyl group of the alcohol. The presence of DMAP is crucial as, without it, *O*-rearrangement of the *O*-acylurea intermediate to an *N*-acylurea "dead end" product competes with interception by the poorly nucleophilic alcohol. These ideas are depicted in the mechanism shown in Scheme 3.15, the first step of which involves proton transfer of the carboxyl proton to the basic imide nitrogen. This facilitates reaction of both partners by increasing both the nucleophilicity and electrophilicity of the carboxylate and imide,

respectively. Thereafter, the nucleophilic addition step is addition of a carboxylate ion onto a protonated imide.

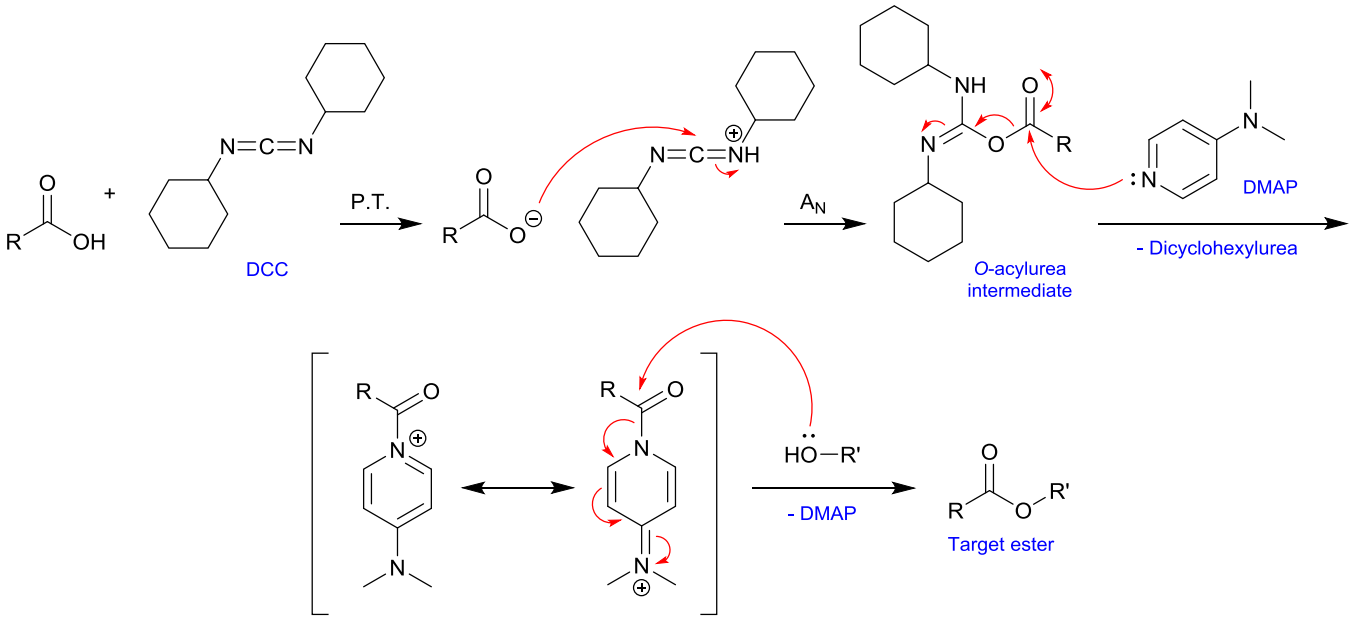

Scheme 3.15. *The general mechanism of the DCC-mediated Steglich esterification and the role of DMAP as an acyl transfer agent in this esterification.*

For characterisation of the NBD-labelled NHS esters, infrared spectroscopy was valuable. In Figure 3.9, the 4-chloro derivative of NBD (A) is contrasted with its amino acid substitute **13** (B) and NHS-labelled ester **15** (C). The spectra revealed two imide carbonyl stretches at 1785 cm^{-1} and 1815 cm^{-1}, and one at 1730 cm^{-1} for the succinimidyl ester carbonyl group.

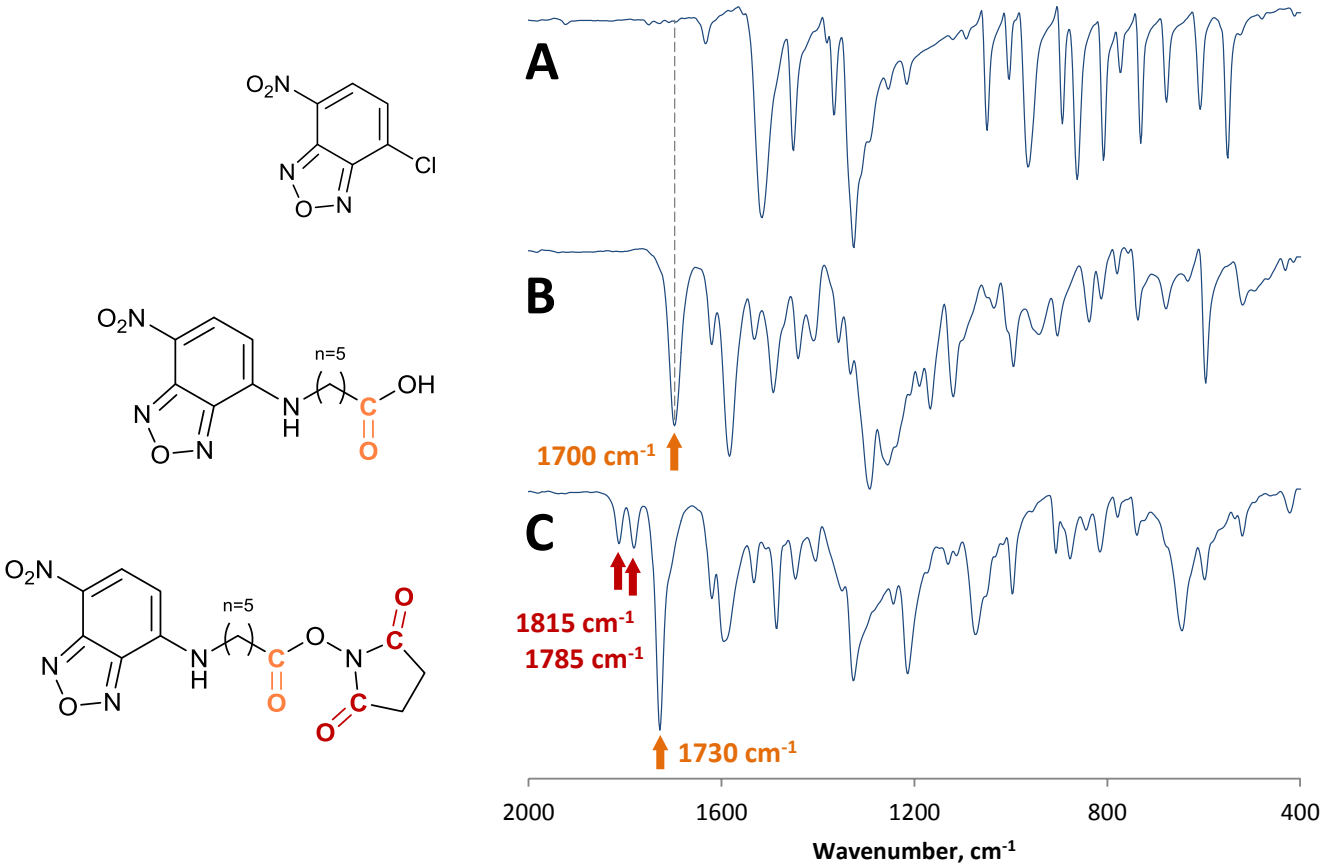

Figure 3.9. *Infrared spectra of the NBD 4-chloro derivative (A), the NBD-labelled amino acid* ***13*** *(B) and the NBD-labelled succinimidyl ester* ***15*** *(C). In (C), stretching vibrations of the carbonyl group of the amino acid (orange) and the imide bonds (red) indicate successful activation of the carboxylic acid.*

These NBD-labelled succinimidyl esters were then reacted with the primary amine quinidine substrate **10** in CH_2Cl_2 (Scheme 3.16) in which DIPEA (3 eq) was first added to neutralise the trifluoroacetate salt and to liberate the primary amine. To ensure that the reaction progressed in a controlled manner the neutralization reaction was first conducted at -78°C. Thereafter, the succinimidyl ester was added and the reaction allowed to warm slowly to room temperature over about four hours. This protocol resulted in higher overall yields and, following an aqueous work-up, the products were isolated by column chromatography in yields of 29% and 68% for **5** and **6**, respectively.

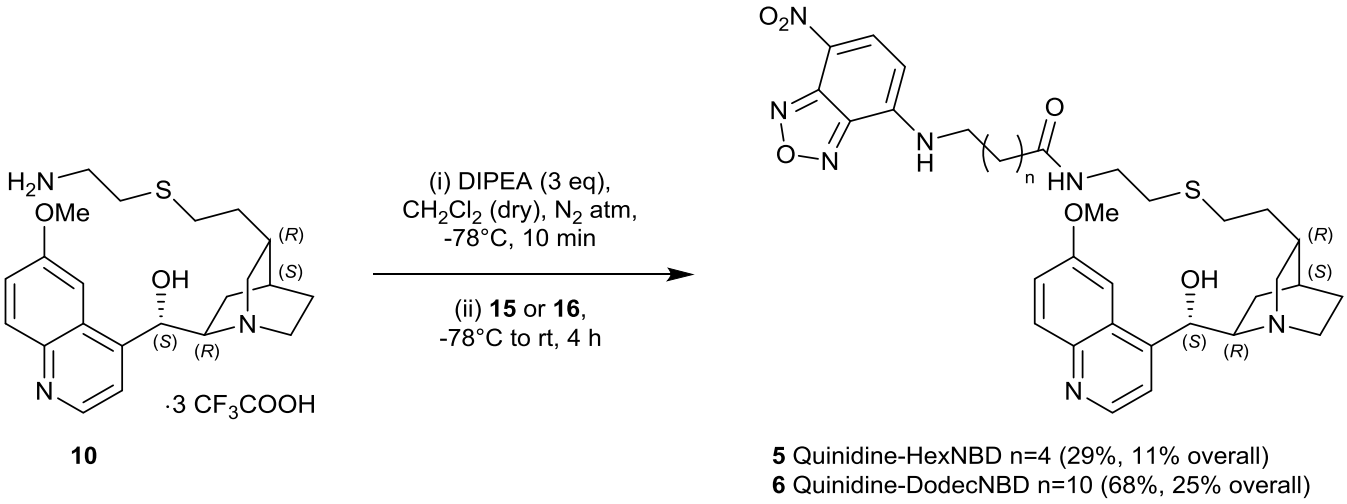

Scheme 3.16. *The preparation of two NBD-labelled quinidine molecules **5** and **6** with varying lengths of the spacer chain between the quinoline core and the NDB fluorophore.*

Figure 3.10 shows the ^{1}H NMR spectrum of the NBD-labelled quinidine derivative of intermediate chain-length (**5**) in which characteristic signals arising from the quinoline and NBD motifs are labelled. The new -NH signal (H-23), indicating formation of the amide bond, is observed as a broad singlet at approximately 5.5 ppm. Furthermore, the carbonyl group of the amide (C-i) was observed by HMBC to correlate to H-22, H-ii and H-iii, confirming the successful tethering of the two precursor molecules.

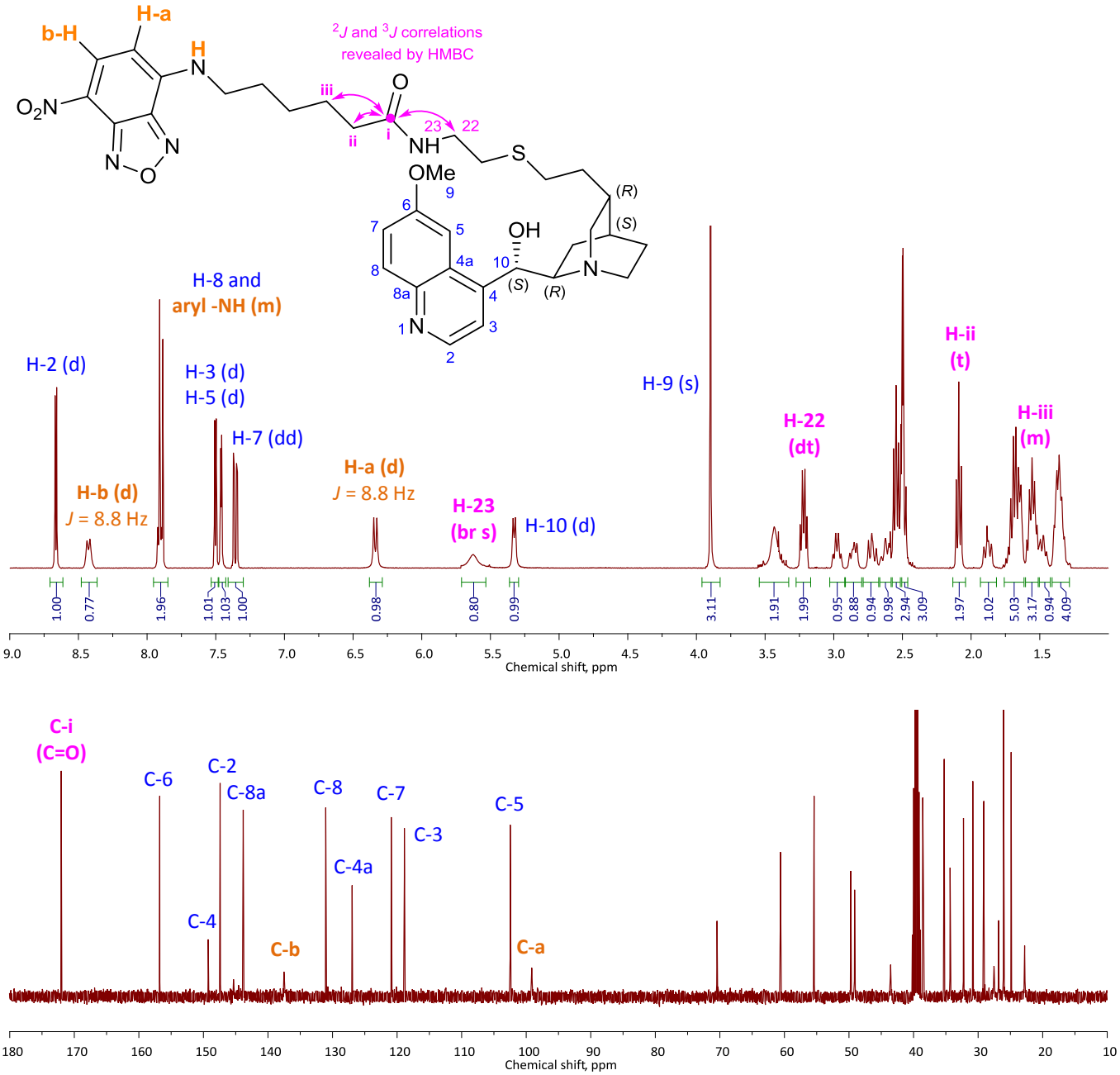

Figure 3.10. *^{1}H and ^{13}C NMR spectra of the NBD-labelled quinidine derivative of intermediate chain-length (**5**) in DMSO-d_6 (400 MHz). Signals relating the NBD fluorophore are indicated in orange while those corresponding to the quinoline core are shown in blue. Signals in pink indicate those corresponding to the ^{2}J and ^{3}J correlations revealed by HMBC.*

3.3.6. Preparation of a quinine derivative incorporating the bimane fluorophore

In order to increase the scope of the fluorophore-labelled alkaloid preparations, another small bicyclic heterocyclic fluorophore was identified: 1,5-diazabicyclo[3.3.0]octa-3,6-diene-2,8-dione or "bimane" (*bi*, two; *manus*, hand). Bimane fluoresces in the blue region of the visible spectrum and is typically available as its bromine derivative, monobromobimane (mBBr), which is susceptible to S_N2 alkylation by an amine nucleophile (Figure 3.11).

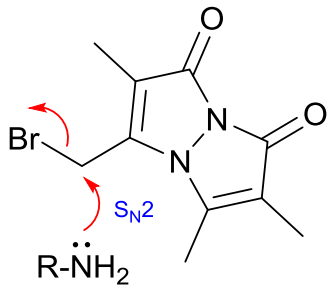

Figure 3.11. *The structure of monobromobimane (mBBr) indicating its susceptibility to S_N2 reactions.*

The synthesis and fluorescent properties of this family of heterocycles was first described by Kosower et al. in a series of articles from the early 1980s.[35,36] Bimane has suitable photophysical properties for live-cell microscopy and, like NBD, a major advantage is its small size. Its absorption maximum is located at 385 nm and it fluoresces in the blue region of the visible spectrum (460 nm). Hence, unlike NBD, it may be used in conjunction with other green-emitting cellular markers or dyes.

In order to prepare an additional bimane-labelled alkaloid, mBBr was reacted with the primary amine derivative of quinine (**9**) in dry CH_2Cl_2 (Scheme 3.17). As dry Et_3N is easier to distil than DIPEA, given the lower boiling point of the former, several equivalents of this base were added to neutralise the trifluoroacetate salt **9** and liberate the primary amine. Following addition of mBBr, the S_N2 reaction proceeded with stirring at room temperature overnight (18 hours). Scrupulous care was taken to ensure that water was eliminated from the system in order to avoid hydrolysis of the alkyl-bromide bond prior to substitution by the amine.

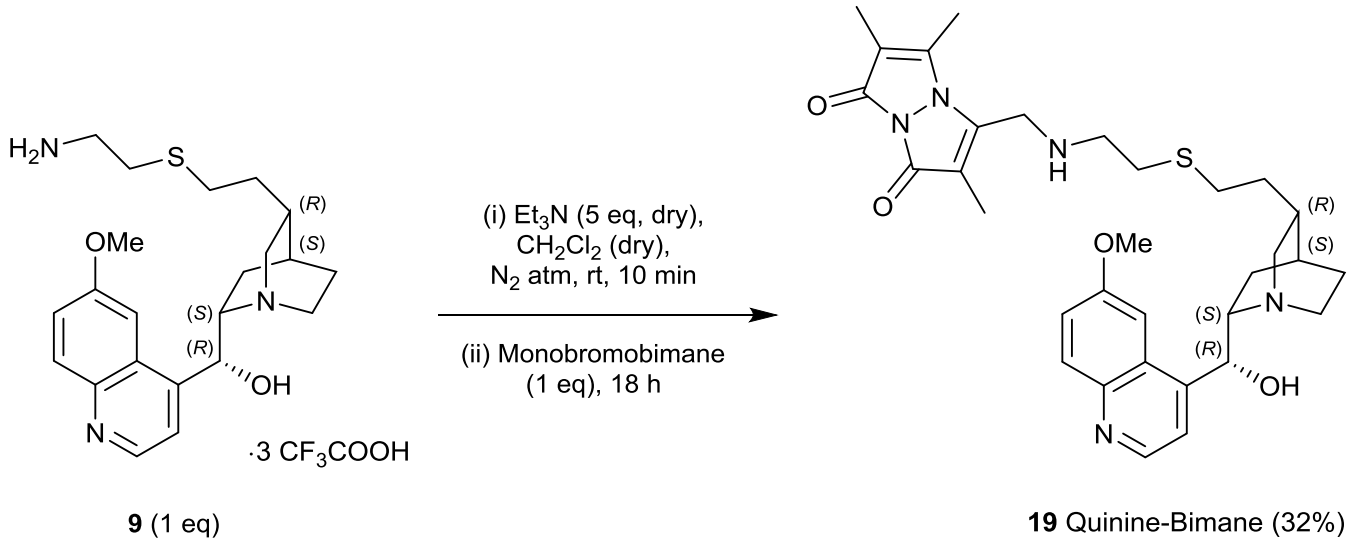

Scheme 3.17. *The synthesis of a bimane-labelled fluorescent derivative of quinine (**19**).*

Column chromatography yielded the quinine-bimane conjugate (**19**) as a pale-yellow solid in 32% yield. A portion of the ^{13}C NMR spectrum is presented in Figure 3.12 with assignments of the sp^2-hybridised carbon signals. Infrared spectra provided additional evidence of incorporation of the bimane group into the quinoline scaffold (Figure 3.13).

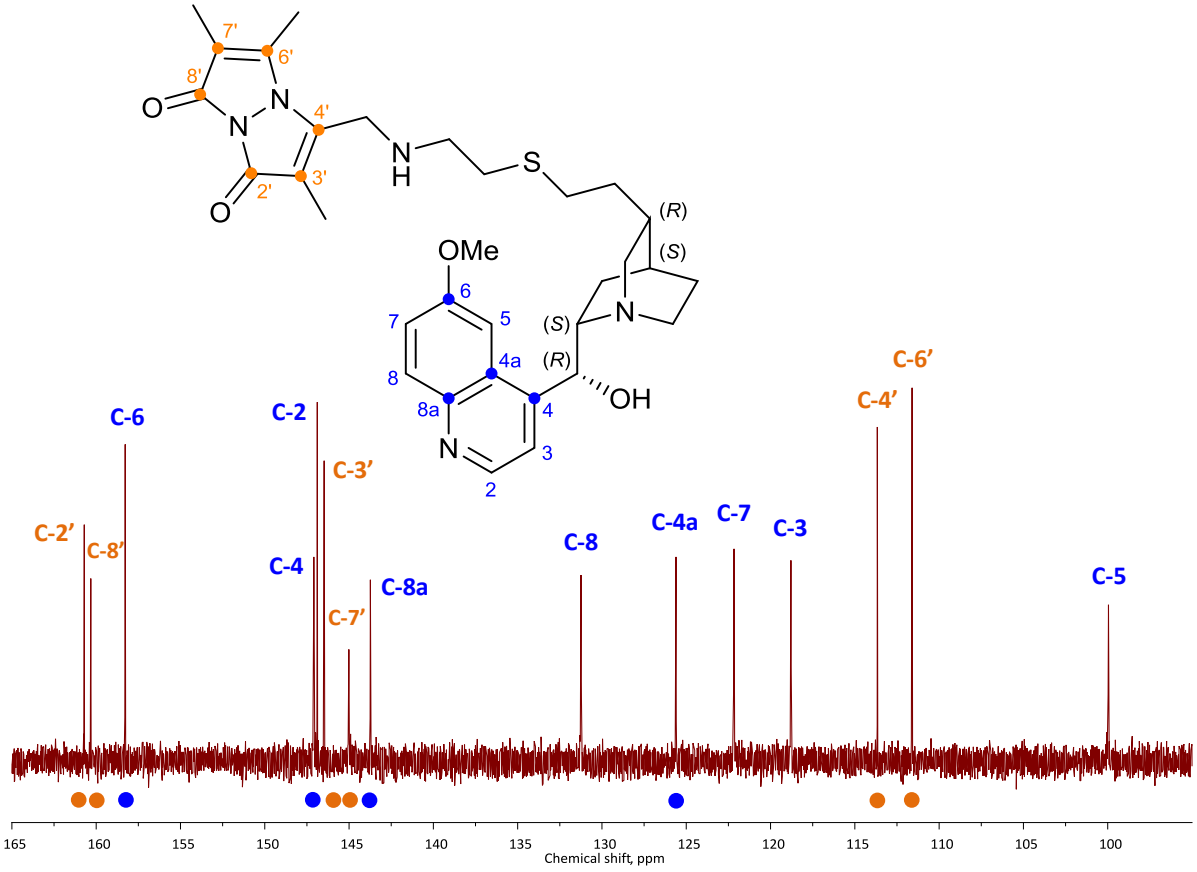

Figure 3.12. *A portion of the ^{13}C NMR spectrum of the quinine-bimane conjugate (**19**) in $CDCl_3$ (100 MHz). Signals corresponding to bimane are labelled in orange while those corresponding to the quinoline core are labelled in blue. Quaternary carbons are indicated in the structure with filled circles at the carbon atom and also below the corresponding signal in the ^{13}C NMR spectrum.*

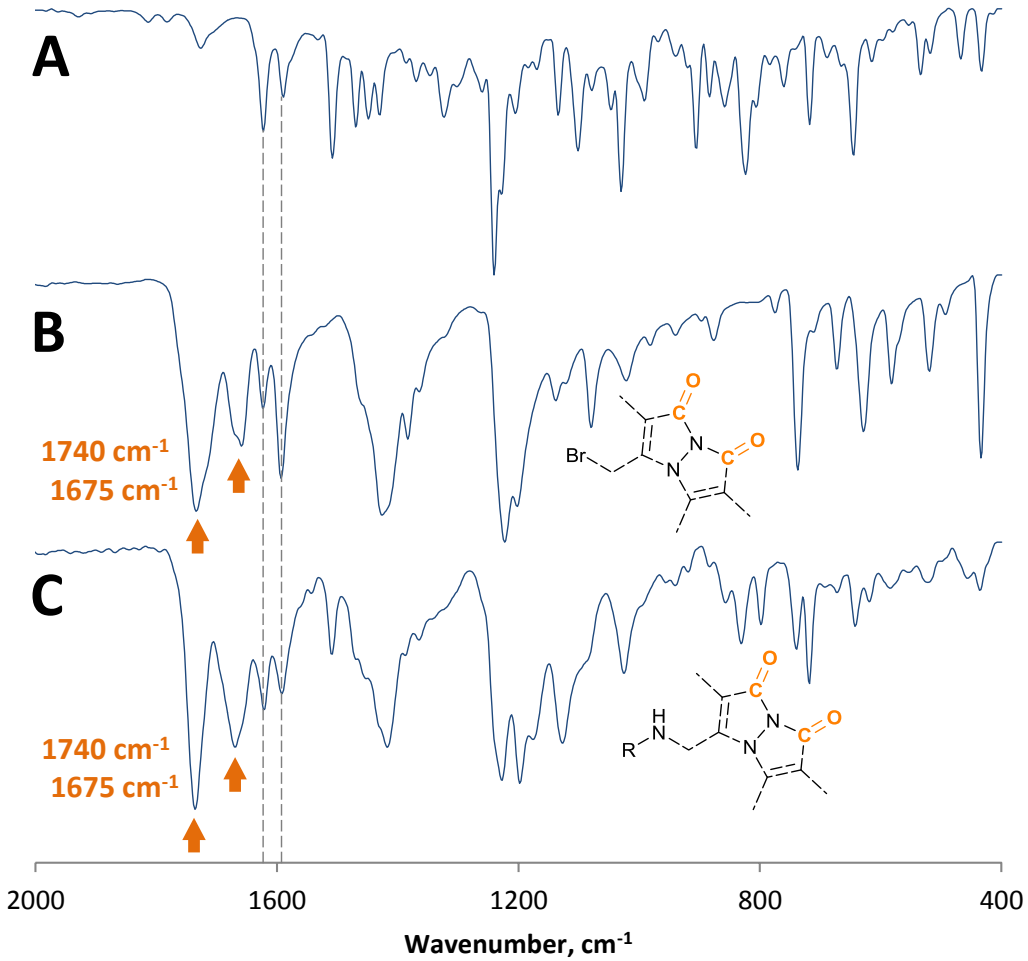

Figure 3.13. *Infrared spectra of quinine intermediate* ***9*** *(A), monobromobimane (B) and quinine-bimane conjugate* ***19*** *(C). Dashed lines show two stretching vibrations common amongst all three molecules. More importantly, the carbonyl stretches of the bimane functional group are indicated in orange in (B) and indicate incorporation of the bimane group into the alkaloid structure in (C).*

3.4. Synthesis of a novel fluorescently-tagged chloroquine derivative

3.4.1. Synthetic planning and *N*-desethylation of chloroquine

The prototypical 4-aminoquinoline, chloroquine, possesses three amino functionalities. The 4-amino nitrogen was considered to be insufficiently nucleophilic to partake in nucleophilic aromatic substitution with the fluorophore in view of resonance donation into the pyridine ring. Although the quinoline sp^2 ring nitrogen is DMAP-like and thus quite nucleophilic due to the aforementioned resonance effect of the 4-amino substituent, any substitution activity would only serve to act as a transfer site as in the case of DMAP. The remaining nitrogen in the side chain is a much stronger basic tertiary amine that is important for accumulation of the drug in the digestive vacuole of *P. falciparum* and, as such, was an unsuitable point of attachment for an extrinsic fluorophore.

Thus, in order to exploit similar methodology as used above, it was deemed necessary to introduce an additional aliphatic amine functionality into the molecules as a connection site for the fluorophore, and for this it was investigated whether one of the terminal ethyl groups connected to the tertiary amine could be selectively removed. Fortunately, there is precedent for this modification as there has been much interest in the *N*-dealkylated derivative of chloroquine (known as desethylchloroquine) as it is the major human metabolite of the antimalarial.[37] This led to the identification of **8** as a target for fluorophore attachment as proposed in Scheme 3.2 previously.

The synthesis thinking for accessing **8** is illustrated by way of a retrosynthetic analysis shown in Scheme 3.18 in which disconnection of the fluorophore produced the key intermediate primary amine **23**. Subsequent disconnection of a C-N bond on the tertiary amine generated desethylchloroquine (**21**). Importantly, the synthetic chemistry required to generate this *N*-dealkylated derivative of chloroquine was already available.[37]

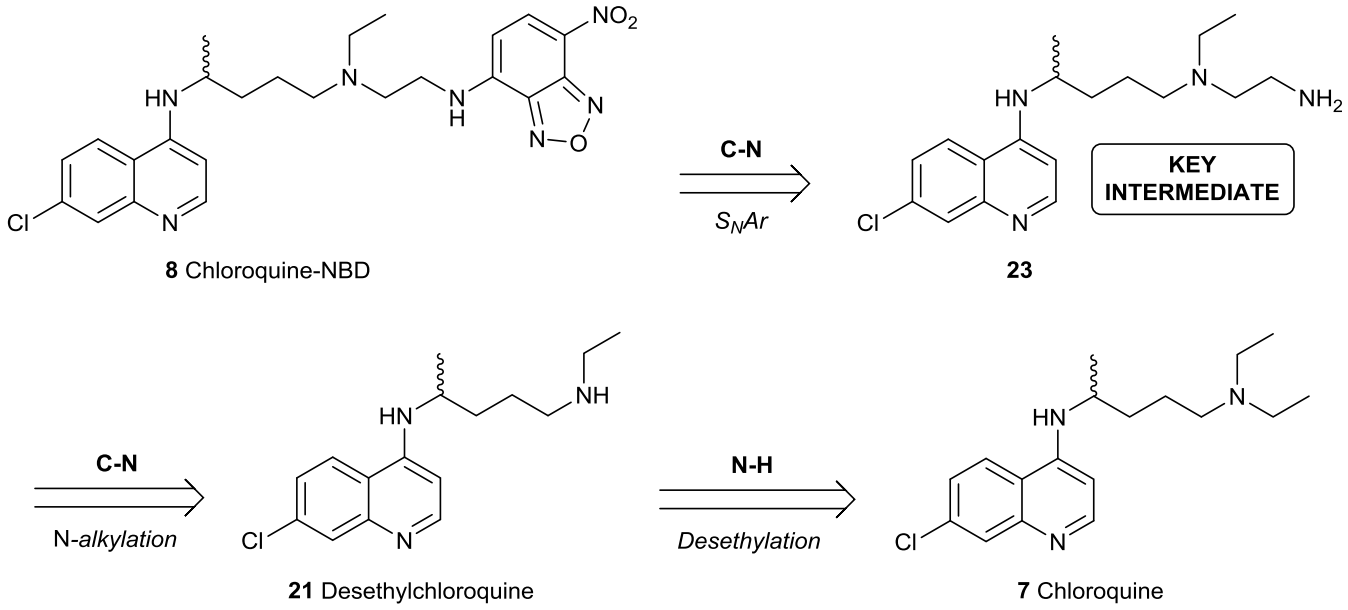

Scheme 3.18. *Retrosynthetic analysis of the target compound* ***8*** *via key intermediate* ***23*** *and desethylchloroquine* ***21****.*

The forward synthesis of the novel fluorescent derivative of chloroquine **8** is depicted in Scheme 3.19. First, an overview of the reactions involved follows: In the first step, selective *N*-dealkylation of chloroquine was achieved via formation of a chloroformate ester **20** followed by subsequent reduction by zinc in acetic acid to give **21**.[37,38] The latter was then condensed with *N*-Boc-glycinal under reductive amination conditions using $NaBH_3CN$ to generate *N*-Boc-protected amine **22**. This was followed by *N*-Boc deprotection of **22** to generate primary amine **23**, which could then be used in a nucleophilic aromatic substitution reaction with the 4-chloro derivative of the NBD fluorophore, using similar conditions to those described for preparing the fluorescently-labelled alkaloids above, to afford the NBD-labelled chloroquine derivative **8**.

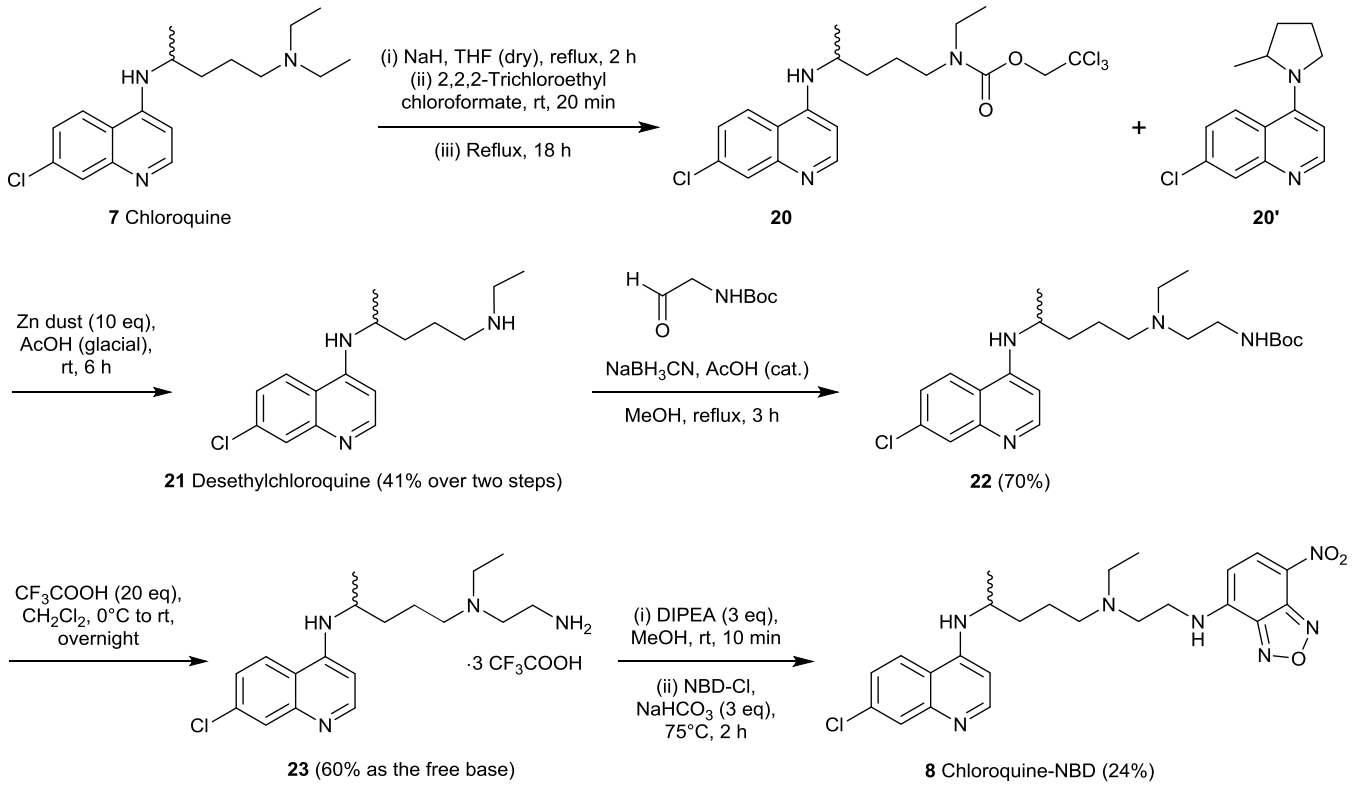

Scheme 3.19. *The forward synthesis of NBD-labelled chloroquine derivative* ***8****.*

The various steps of the synthesis of the NBD-labelled chloroquine derivative will now be described in detail. The first step involved desethylation of chloroquine via a chloroformate which was generated using sodium hydride and 2,2,2-trichloroethyl chloroformate in refluxing THF. Work-up and subsequent purification yielded two quinoline derivatives that could not be separated by column chromatography. Combined analysis via ^{1}H NMR, infrared spectroscopy and mass spectrometry suggested that this mixture comprised the desired carbamate **20** and pyrrolidine **20'** (Scheme 3.19). Integration of peaks in the ^{1}H NMR spectrum suggested that **20** and **20'** were present in approximate proportions of 2:1 respectively. This was also reflected in the relative intensities of the ion peaks in the mass spectrum. In the infrared spectrum, a prominent stretching band at 1715 cm^{-1} was observed for the carbamate while, in the mass spectrum, major peaks corresponding to the molecular weights of these two products were observed.

The formation of the two products **20** and **20'** may be rationalised as follows. Treatment of chloroquine with sodium hydride deprotonates the relatively acidic aromatic secondary 4-amino group, while the tertiary amine of the side chain becomes *N*-acylated by the chloroformate to afford a charged carbamate intermediate (depicted in square brackets in Scheme 3.20 below). One may speculate about the order of these chemical events in which it

makes sense that the *N*-acylation proceeds faster than the deprotonation. The amino anion can then reduce the energy of the molecule in two ways, either by a β-elimination on a relatively unhindered ethyl group (red arrows), or alternatively acting as a nucleophile at the α-methylene in the chain (blue arrows), the latter being dictated primarily by the distance between the two centres in the bond-forming step. While the former process affords the desired desethyl product **20** as its protected trichloroethyl carbamate, the latter affords pyrrolidine **20'** in a *5-exo-tet* cyclisation.

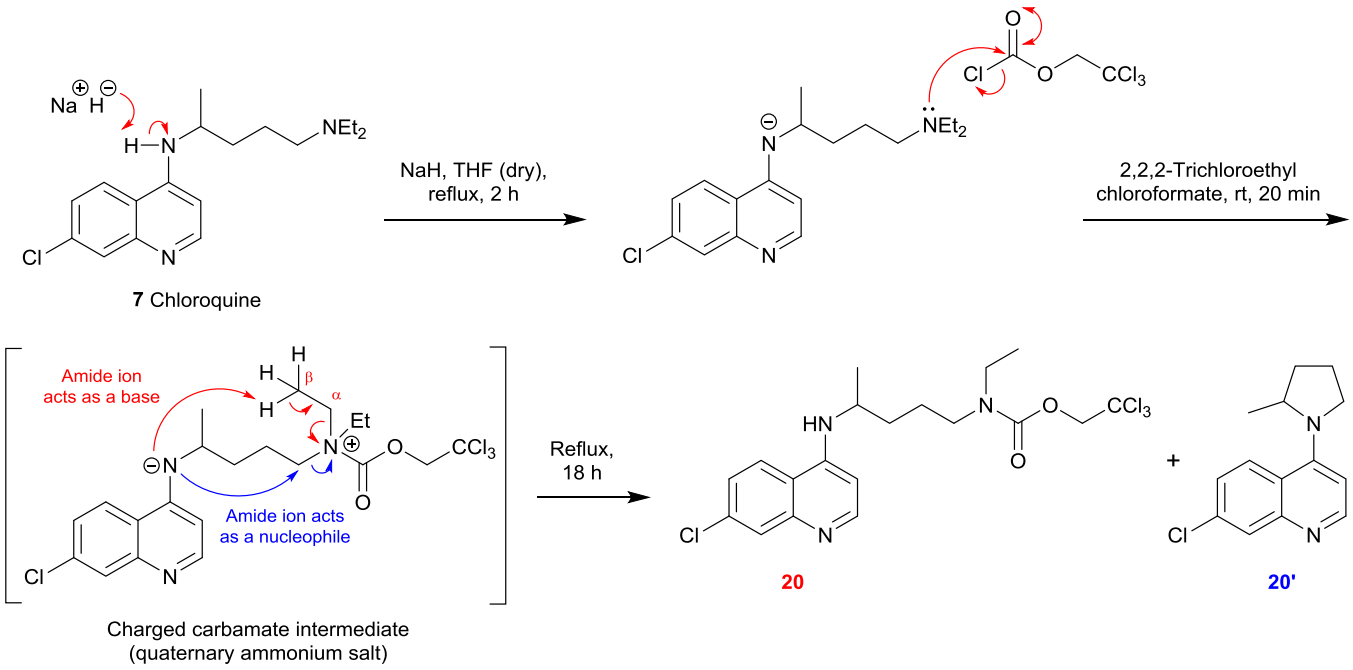

Scheme 3.20. *Preparation of carbamate **20** and pyrrolidine **20'** via a charged carbamate intermediate. In the second line of the scheme, the formation of **20** and **20'** are indicated by red and blue arrows, respectively.*

Treating the mixture of **20** and **20'** with zinc dust in acetic acid at room temperature, followed by column chromatography, gave the target compound desethylchloroquine (**21**) in 41% yield over the two steps.[37] Integration of the aliphatic proton signals of **21** using ^{1}H NMR spectroscopy confirmed that one of the diethyl groups had been removed. The decrease in intensity of the corresponding carbon signal in the ^{13}C spectrum confirmed the same. In addition, a broad singlet at approximately 4 ppm was exchanged upon washing with D_2O, confirming the presence of an additional secondary amine (Figure 3.14). Finally, the infrared spectrum of desethylchloroquine was indistinguishable from the infrared spectrum of the starting material.

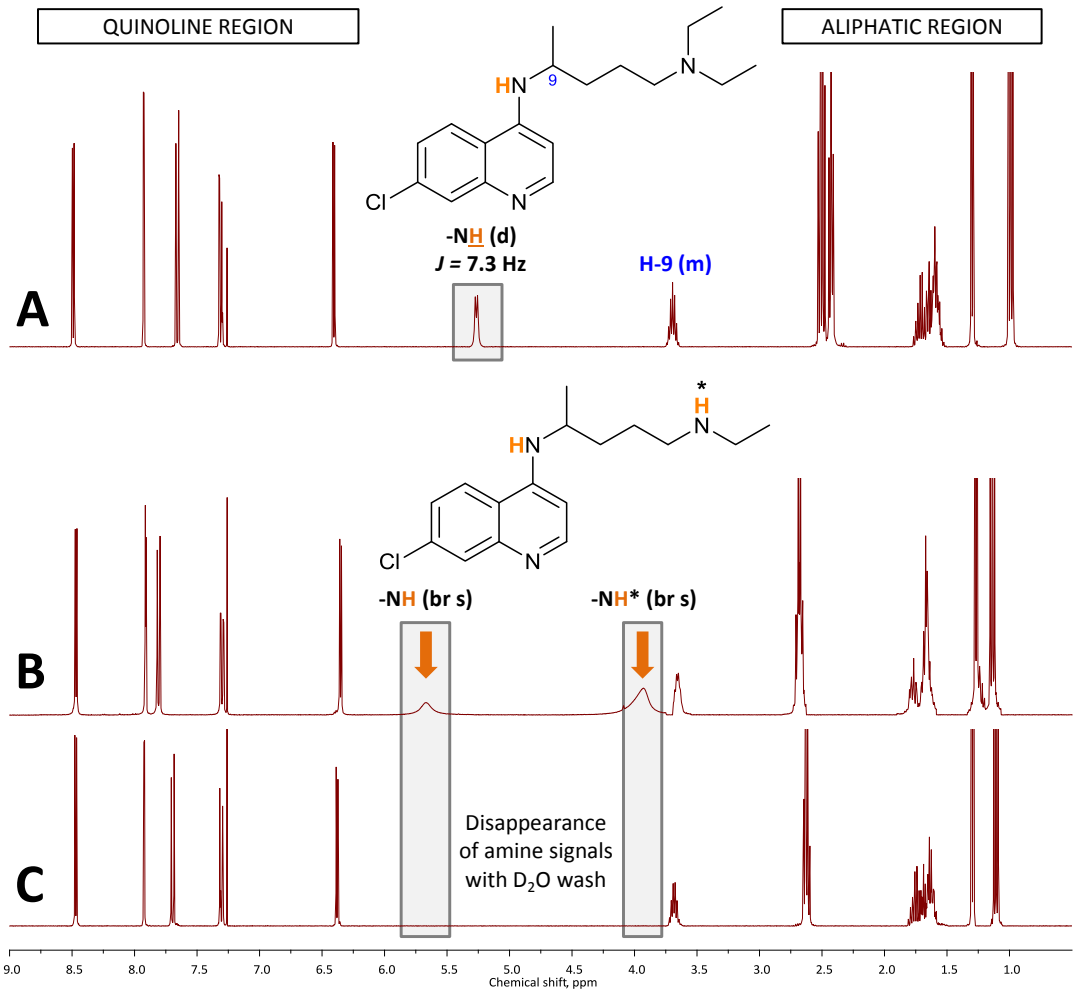

Figure 3.14. *A comparison of the ^{1}H NMR spectra of chloroquine* ***7*** *(A), desethylchloroquine* ***21*** *(B) and desethylchloroquine* ***21*** *with D_2O wash to confirm amine signals (C). All spectra were acquired in $CDCl_3$ at 400 MHz.*

3.4.2. *N*-Alkylation, *N*-Boc deprotection and fluorophore substitution

With desethylchloroquine **21** in hand, an additional (protected) amine was introduced by *N*-alkylation of the secondary aliphatic amine using reductive amination with *N*-Boc-glycinal, which could be prepared by $LiAlH_4$ reduction of a Weinreb amide as shown in Scheme 3.21. TLC analysis of the latter suggested that the crude product (99% yield) was sufficiently pure for use in the subsequent *N*-alkylation reaction. The ^{1}H NMR spectrum in $CDCl_3$ revealed a singlet at approximately 9.7 ppm corresponding to the aldehyde hydrogen (indicated in red in Scheme 3.21) which was not present in the starting material. Concomitant disappearance of the methyl and methoxy signals corresponding to the reduction of the Weinreb amide starting material was also observed.

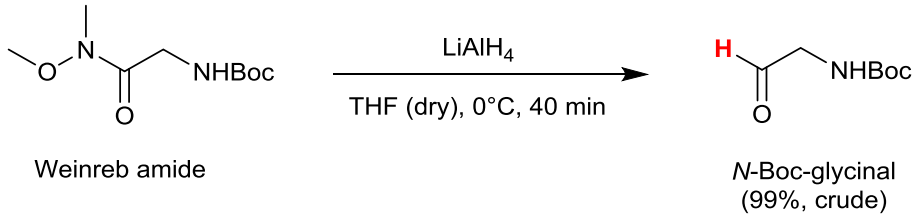

Scheme 3.21. *Reduction of a Weinreb amide to form* N*-Boc-glycinal. The hydrogen atom (red) was detected in the* ^{1}*H NMR spectrum (*$CDCl_3$*, 300 MHz) at approximately 9.7 ppm.*

Weinreb amides are *N*-methoxy-*N*-methylamides that are readily reduced with hydrides to afford aldehydes. This conversion proceeds through a stable lithium-chelated intermediate (Scheme 3.22), which avoids over-reduction to an alcohol.[39,40]

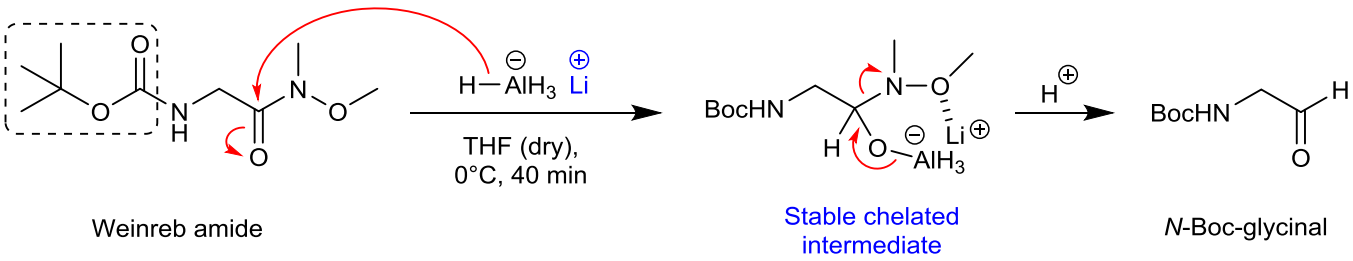

Scheme 3.22. *Mechanism of the Weinreb amide reduction which forms* N*-Boc-glycinal via a lithium-chelated intermediate.*

The *N*-alkylation reaction between desethylchloroquine **21** and *N*-Boc-glycinal was conducted in the presence of a catalytic amount of acetic acid, as shown in Scheme 3.23.[18] Quenching of the reaction, extraction and column chromatography of the residue gave **22** in 70% yield.

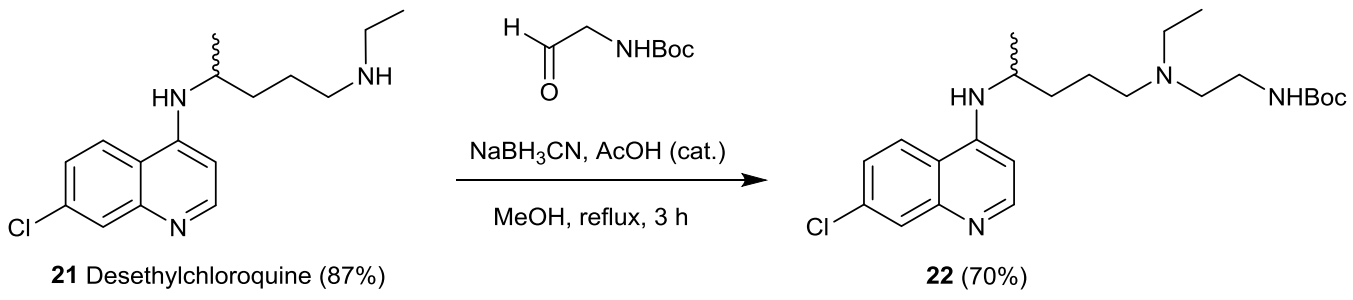

Scheme 3.23. *N-alkylation of desethylchloroquine **21** to afford reductively* N*-alkylated **22**.*

The ^{1}H and ^{13}C NMR spectra of **22** are depicted in Figure 3.15. A new singlet integrating for 9H at approximately 1.5 ppm corresponds to introduction of the *t*-butyl group, as well as a new C=O signal in the ^{13}C NMR spectrum (approximately 155 ppm). HMBC analysis confirmed the ^{3}J correlation relationship between the proton and carbon signals labelled 13, 14 and 16 (highlighted in pink). The new amine signal at approximately 5 ppm corresponds to the incorporation of the carbamate and is shown relative to the 4-amino group adjacent to the quinoline ring which gives a doublet at approximately 5.25 ppm.

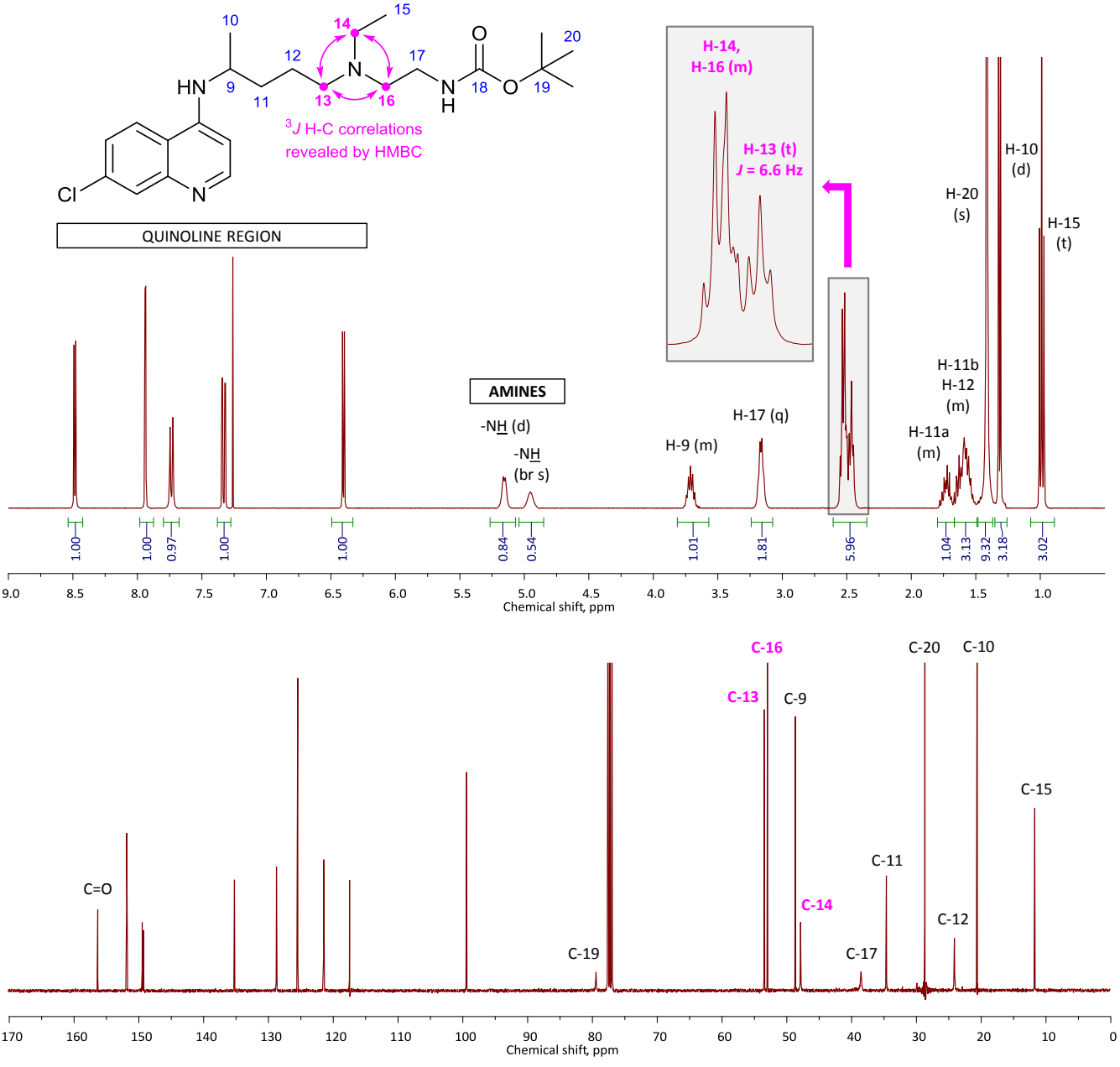

Figure 3.15. *^{1}H and ^{13}C NMR spectra of **22** (400 MHz and 100 MHz, $CDCl_3$) highlighting the aliphatic proton signals. The important methylene signals around the tertiary amine are highlighted in orange and enlarged.*

The general mechanism for the reductive amination in question proceeds via an intermediate iminium ion as depicted in a generalised form in Scheme 3.24. The iminium salt is formed when a secondary aliphatic amine reacts with an aldehyde under acid-catalysed conditions to produce a hydroxylamine intermediate. Proton transfer followed by elimination of water generates the iminium salt. Sodium cyanoborohydride ($NaBH_3CN$) was used as a mild reducing agent. Owing to the presence of the electron-withdrawing cyanide substituent group, it is less reactive than sodium borohydride and more stable in methanol.

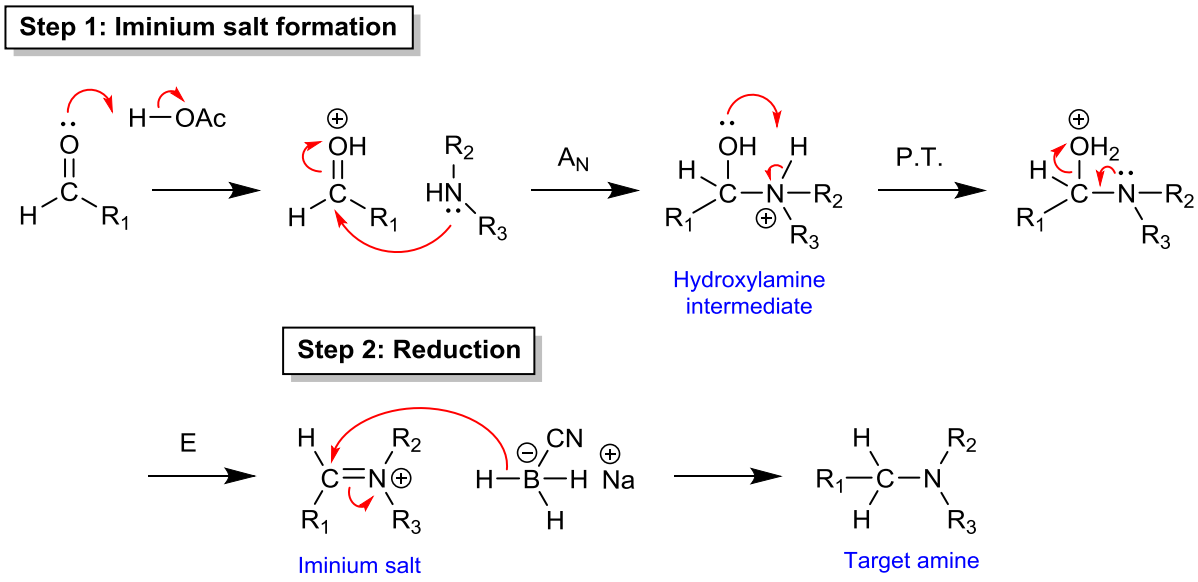

Scheme 3.24. *General mechanism for acid-catalysed reductive alkylation via iminium salt formation.*

In order to liberate the primary amine of compound **22** to render it suitable for nucleophilic aromatic substitution, it was necessary to cleave the *N*-Boc protecting group. This proceeded as described above for the *Cinchona* alkaloids, using an excess of TFA in CH_2Cl_2 to furnish the tris-trifluoroacetate salt of **23** (Scheme 3.25). Unlike its alkaloid counterparts, it was not possible to retrieve this salt from the stationary phase of the chromatographic column. This is probably due to the more polar nature of the chloroquine derivatives as a result of the higher pK_a values of its nitrogen atoms compared to those of the alkaloids. Hence, for characterisation purposes, a base extraction with 1 M NaOH and CH_2Cl_2 was employed followed by column chromatography, requiring the presence of 5% Et_3N in the 100% MeOH mobile phase, to afford the free base of **23** in 60% yield. Removal of the *N*-Boc protecting group in **23** was evident on TLC with concomitant disappearance of the carbamate and *t*-butyl signals in the NMR and infrared spectra.

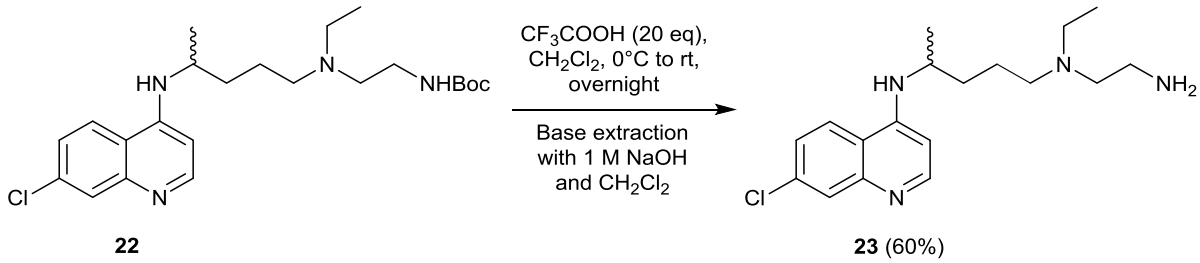

Scheme 3.25. N-*Boc deprotection of* ***22*** *and subsequent base extraction yielded the free base of* ***23****.*

For coupling purposes though, a similar methodology as described for the incorporation of the NBD fluorophore into the *Cinchona* alkaloids described previously was adopted using Hünig's base for deprotonation of the salt (of **23**) in which the latter was deemed pure enough via ^{1}H NMR for proceeding with reaction with the NBD fluorophore. Hence, as illustrated in Scheme 3.26, three equivalents of Hünig's base were added to liberate the amines from their salts, this time at room temperature, and this was followed by heating with NBD-chloride in methanol as solvent, with an excess of sodium bicarbonate to neutralise the HCl formed. Column chromatography yielded the NBD-labelled chloroquine derivative **8** in 24% yield.

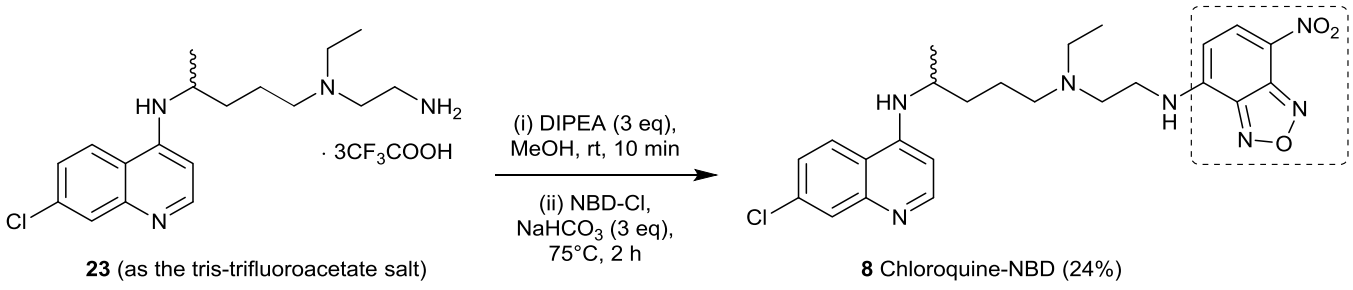

Scheme 3.26. *Neutralisation of the tris-trifluoroacetate salt* ***23*** *and* S_NAr *with NBD-Cl to generate fluorescent chloroquine derivative* ***8****. Incorporation of the NBD fluorophore is indicated in the dashed box.*

The ^{1}H and ^{13}C NMR spectra of the NBD-labelled chloroquine **8** are shown in Figure 3.16. Characteristic signals relating to the quinoline heterocycle are labelled in blue. The AB doublet pair due to the NBD signals H-a and H-b is highlighted in orange at 6.5 ppm and 8.5 ppm, respectively (J = 9.5 Hz). Surprisingly, the signal corresponding to the 4-amino hydrogen was not observed. Quaternary signals arising from the NBD heterocycle in the ^{13}C NMR spectrum were also observed, also highlighted in orange. The identity of product **8** was further corroborated using HRMS.

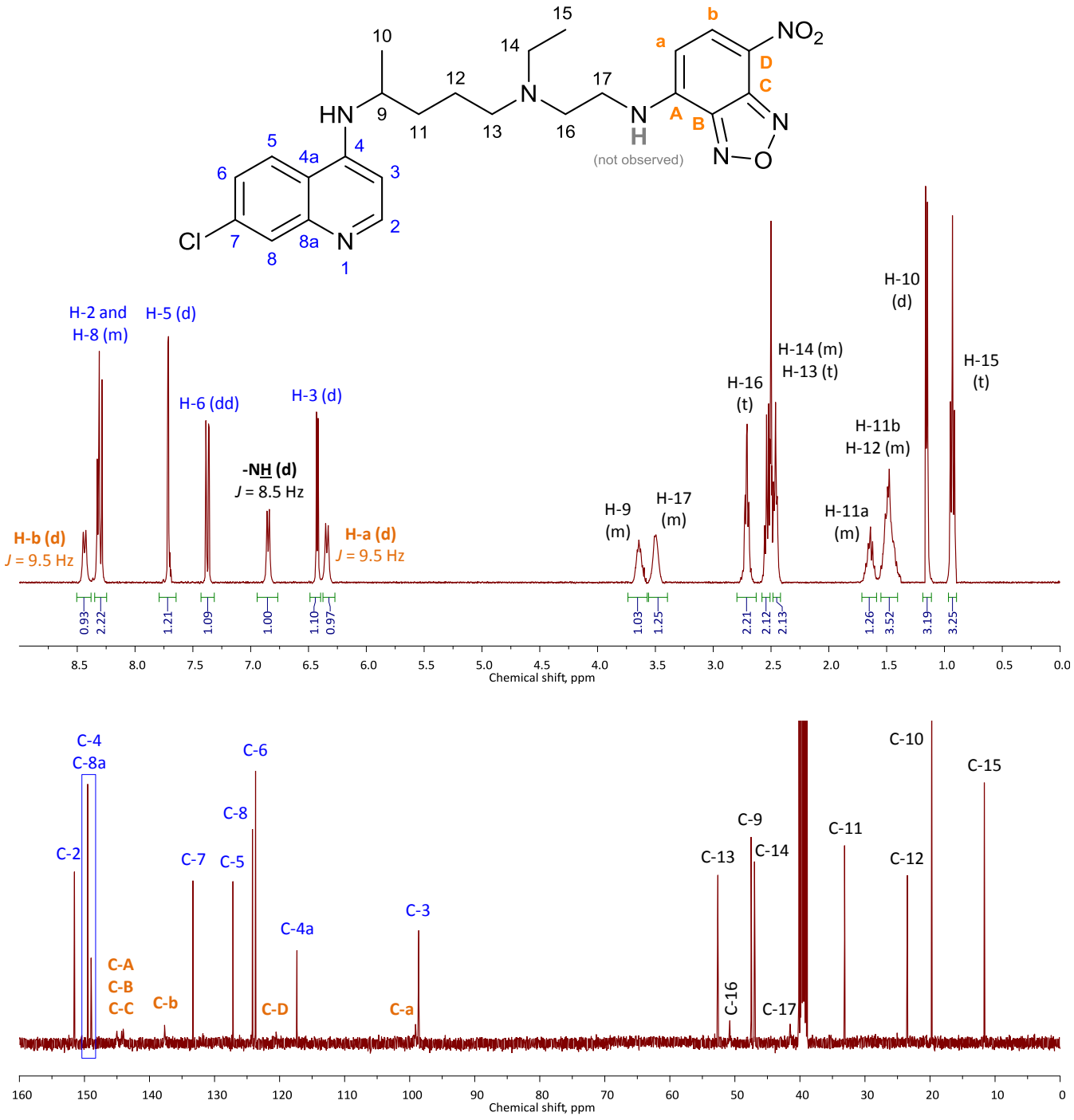

Figure 3.16. *^{1}H NMR spectrum of NBD-labelled chloroquine **8** in DMSO-d_6 (400 MHz). Proton signals relating to the hydrogen atoms in the NBD fluorophore are displayed in orange while those corresponding to the quinoline ring are shown in blue. Two-dimensional NMR correlation analysis proved covalent connectivity of the two precursor molecules.*

3.5. Summary and conclusions

This chapter describes the design and synthesis of a series of novel fluorescent antimalarials. Specifically, five fluorescent derivatives of the *Cinchona* alkaloids were prepared as representative probes for the class of quinoline methanol antimalarials; two were derivatives of quinine and three were derivatives of its diastereomer, quinidine. Three of these were 'short-chain' derivatives containing a minimum number of atoms between the pharmacophore and the fluorophore (**3**, **4** and **19** in Figure 3.17). The length of the spacer chain was varied by preparing quinidine derivatives with an intermediate (**5**) and longer (**6**) chain length. All derivatives were linked to the small green-emitting NBD fluorophore except for one which was linked to the blue-emitting bimane fluorophore (**19**). A single novel NBD-labelled chloroquine derivative was prepared (**8**) to represent the 4-aminoquinoline class of antimalarials.

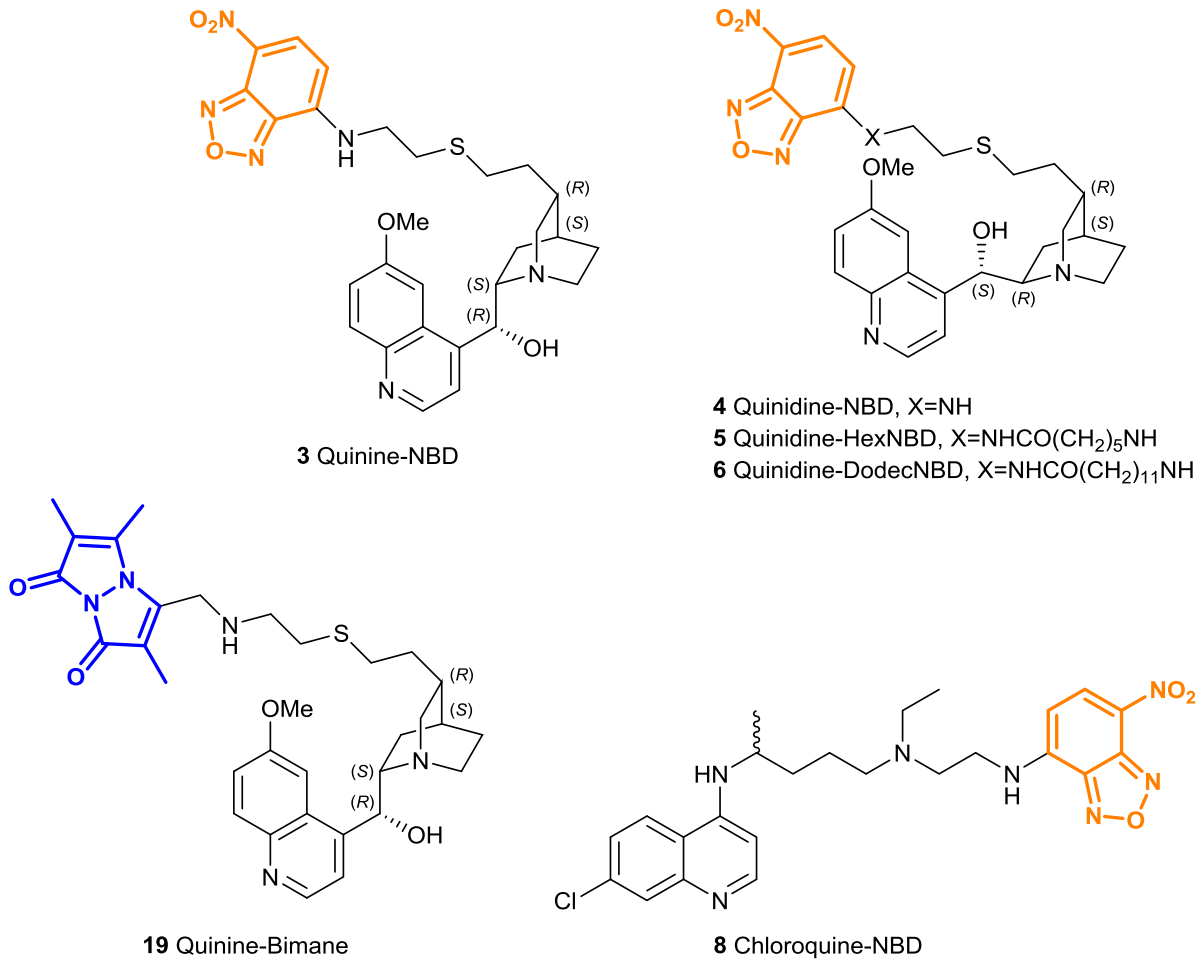

Figure 3.17. *The suite of six novel fluorescent antimalarials prepared in this chapter. Fluorophores are highlighted in colour.*

Design aspects of these novel fluorescent derivatives were described above. Briefly, in order to retain the distinctive interactions of the parent molecules with their putative target in *P. falciparum*, Fe(III)PPIX, it was important to preserve key physicochemical properties of the parent molecules as elucidated by recent structure-activity relationship studies. Retention of these properties was evident in all proposed derivatives. The primary choice of fluorophore, 7-nitrobenz-2-oxa-1,3-diazole (NBD), was explained.

A retrosynthetic analysis of the target quinoline methanols was provided, identifying a key intermediate containing a primary amine functionality. Versatile and convenient derivatisation of the parent alkaloids was enabled by a regioselective radical-mediated thiol-ene 'click' reduction. Following *N*-Boc deprotection of these reduced derivatives, the NBD fluorophore was attached by means of a nucleophilic aromatic substitution to generate two 'short-chain' derivatives (**3**, **4**). In order to vary the length of the spacer chain between the quinoline core and the fluorophore, NBD-labelled amino acids and their corresponding succinimidyl esters were prepared in order to facilitate amide bond formation between the two molecules (**5**, **6**). In addition, a final novel derivative was prepared using the blue-emitting bimane fluorophore (**19**). Together, these are the first derivatives of the *Cinchona* alkaloids that have been prepared for live-cell fluorescence microscopy.

For comparison purposes, an analogous single novel derivative of chloroquine was prepared. Retrosynthetic analysis of this derivative suggested utilising its *N*-dealkylated analogue, desethylchloroquine, as a key intermediate. *N*-Alkylation of this intermediate with *N*-Boc-glycinal, prepared from the reduction of a Weinreb amide, enabled introduction of an additional amine functionality in the molecule which, following *N*-Boc deprotection, was reacted with NBD in a manner similar to the quinoline methanols to form a novel fluorescent probe **8**.

All six novel fluorescent derivatives were characterised using a full range of spectroscopic and analytical techniques. Photophysical characterisation of these derivatives, and hence their evaluation as suitable analogues of the parent quinoline antimalarials, will be described in Chapter 4.

3.6. References

1. J. M. Combrinck, T. E. Mabotha, K. K. Ncokazi, M. A. Ambele, D. Taylor, P. J. Smith, H. C. Hoppe and T. J. Egan, *ACS Chem. Biol.*, 2013, **8**, 133.
2. D. J. Sullivan, I. Y. Gluzman, D. G. Russell and D. E. Goldberg, *Proc. Nat. Acad. Sci. USA*, 1996, **93**, 11865.
3. C. Sanchez, W. D. Stein and M. Lanzer, *Mol. Microbiol.*, 2008, **67**, 1081.
4. W. H. Melhuish, *J. Phys. Chem.*, 1961, **65**, 229.
5. E. B. Bohórquez, M. Chua and S. R. Meshnick, *Malaria J.*, 2012, **11**, 350.
6. K. A. Zacharlasse, N. V. Phuc and B. Kozanklewicz, *J. Phys. Chem.*, 1981, **85**, 2676.
7. A. N. Hoang, R. D. Sandlin, A. Omar, T. J. Egan and D. W. Wright, *Biochemistry*, 2010, **49**, 10107.
8. C. Reichardt, *Chem. Rev.*, 1994, **94**, 2319.
9. L. D. Lavis and R. T. Raines, *ACS Chem. Biol.*, 2008, **3**, 142.
10. A. Chattopadhyay, *Chem. Phys. Lipids*, 1990, **53**, 1.
11. O. Maier, V. Oberle and D. Hoekstra, *Chem. Phys. Lipids*, 2002, **116**, 18.
12. T. J. Egan, *J. Inorg. Biochem.*, 2006, **100**, 916.
13. J. Gildenhuys, C. J. Sammy, R. Muller, V. A. Streltsov, T. le Roux, D. Kuter and K. A. de Villiers, *Dalton Trans.*, 2015, **44**, 16767.
14. K. A. de Villiers, J. Gildenhuys and T. le Roux, *ACS Chem. Biol.*, 2012, **7**, 666.
15. J. N. Alumasa, A. P. Gorka, L. B. Casabianca, E. Comstock, A. C. de Dios and P. D. Roepe, *J. Inorg. Biochem.*, 2011, **105**, 467.
16. *Cinchona Alkaloids in Synthesis & Catalysis*, ed. C. E. Song, Wiley-VCH, Germany, 2009.
17. D. Kuter, V. Streltsov, N. Davydova, G. A. Venter, K. J. Naidoo and T. J. Egan, *J. Inorg. Biochem.*, 2016, **154**, 114.
18. M. Cabrera, J. Natarajan, M. F. Paguio, C. Wolf, J. S. Urbach and P. D. Roepe, *Biochemistry*, 2009, **48**, 9471.
19. L. M. Alcantara, J. Kim, C. B. Moraes, C. H. Franco, K. D. Franzoi, S. Lee, L. H. Freitas-Junior and L. S. Ayong, *Exp. Parasitol.*, 2013, **134**, 235.
20. C. C. Y. Loh, R. Suwanarusk, Y. Q. Lee, K. W. K. Chan, K. Choy, L. Rénia, B. Russell, M. J. Lear, F. H. Nosten, K. S. W. Tan and L. M. C. Chow, *PLOS ONE*, 2014, **9**, e110800.
21. A. K. Tucker-Schwartz, R. Farrell and R. Garrell, *J. Am. Chem. Soc.*, 2011, **133**, 11026.
22. G. Stork, D. Niu, A. Fujimoto, E. R. Koft, J. M. Balkovec, J. R. Tata and G. R. Dake, *J. Am. Chem. Soc.*, 2001, **123**, 3239.
23. H. C. Kolb, M. G. Finn and K. B. Sharpless, *Angew. Chem. Int. Ed.*, 2001, **40**, 2004.
24. C. E. Hoyle and C. N. Bowman, *Angew. Chem. Int. Ed.*, 2010, **49**, 1540.
25. B. Lowe, *Polym. Chem.*, 2010, **1**, 17.

26. A. J. Musacchio, L. Q. Nguyen, G. H. Beard and R. R. Knowles, *J. Am. Chem. Soc.*, 2014, **136**, 12217.
27. *Organic Chemistry*, J. Clayden, N. Greeves, S. Warren and P. Wothers, Oxford University Press, Oxford, 2001.
28. S. Haldar, S. Kumar, S. P. Kolet, H. S. Patil, D. Kumar, G. C. Kunda and H. V. Thulasarim, *J. Org. Chem.*, 2013, **78**, 10192.
29. J. Novotný, K. Pospěchová, A. Hrabálek, R. Čáp and K. Vávrová, *Bioorg. Med. Chem. Lett.*, 2009, **19**, 6975.
30. C. A. G. N. Montalbetti and V. Falque, *Tetrahedron*, 2005, **61**, 10827.
31. M. M. Joullié and K. M. Lassen, *Arkivoc*, 2010, **viii**, 189.
32. E. Valeur and M. Bradley, *Chem. Soc. Rev.*, 2009, 3**8**, 606.
33. I. Dhimitruka and J. SantaLucia, *Org. Lett.*, 2006, **8**, 47.
34. B. Neises and W. Steglich, *Ang. Chem. Int. Ed.*, 1978, **17**, 522.
35. E. M. Kosower and B. Pazhenchevsky, *J. Am. Chem. Soc.*, 1980, **102**, 4983.
36. E. M. Kosower, B. Pazhenchevsky, H. Dodiuk, H. Kanety and D. Faust, *J. Org. Chem.*, 1981, **46**, 1666.
37. M. Ansari and J. C. Craig, *Synthesis*, 1995, 147.
38. T. A. Montzka, J. D. Matiskella and R. A. Partyka, *Tet. Lett.*, 1974, **14**, 1325.
39. S. Nahm and S. M. Weinreb, *Tet. Lett.*, 1981, **22**, 3815.
40. M. Myers, J. Pokorski and D. H. Appella, *Org. Lett.*, 2004, **6**, 4699.

Chapter Four

Photophysical and Physicochemical Characterisation of Novel Fluorescent Derivatives

4.1. Introduction

The intimate mechanistic details describing the action of the quinoline antimalarials against the most virulent malaria parasite, *Plasmodium falciparum*, remain unclear. Furthermore, the two major classes of these antimalarials, the quinoline methanols and 4-aminoquinolines, generate differential ultrastructural and morphological effects on the parasite.[1-3] Thus, in order to generate deeper insights into the mechanism of action of these two classes of antimalarials, six novel fluorescent derivatives of these drugs were designed and synthesised for the purpose of live-cell imaging studies (Chapter 3).

Although these novel derivatives were expected to possess suitable photophysical properties for fluorescence microscopy, it was necessary to characterise and evaluate these derivatives thoroughly to ensure that key physicochemical properties of the parent drugs were retained. As the solution-state interactions of these quinoline antimalarials with Fe(III)PPIX have been well-characterised with respect to their binding modes and strengths of association,[4,5] these were used as benchmarks to determine whether the fluorescent derivatives were suitable analogues of the parent molecules. These derivatives were also evaluated for their activities against β-haematin formation and, crucially, against *P. falciparum* in vitro.

This chapter first describes the photophysical characterisation of the six novel fluorescent derivatives prepared in Chapter 3. Their absorption and fluorescence spectra are discussed as well as other photophysical aspects such as fluorescence quantum yields, solvatochromism, Förster resonance energy transfer and stability. Thereafter, the derivatives are directly compared to their parent compounds by evaluating their physicochemical interactions with Fe(III)PPIX. As described in Section 1.5.2, the solution-state interactions between the two classes of quinoline antimalarials with Fe(III)PPIX are fundamentally different. The quinoline methanols, represented in this work by the diastereomeric alkaloids quinine and quinidine, bind to Fe(III)PPIX with a 1:1 stoichiometry.[4] On the other hand, chloroquine, which represents the 4-aminoquinolines, induces μ-oxo dimerisation of Fe(III)PPIX in aqueous solution.[5]

To further determine which fluorescent derivatives were the most suitable analogues of their parent compounds, their aqueous solubilities and diffusion coefficients were measured and these observations were rationalised. The activities of the novel fluorescent derivatives were measured against β-haematin formation using a biomimetic detergent-mediated assay. Most importantly, their in vitro activities against *P. falciparum* were evaluated. Taken together, these measurements were used to decide which of the fluorescently-labelled derivatives prepared in Chapter 3 were most suitable for live-cell microscopy studies.

Thus the specific objectives described in this chapter were:

i. To fully characterise the photophysical properties of the six novel fluorescent derivatives prepared in Chapter 3 by interpreting their absorption and fluorescence spectra and establishing relevant photophysical aspects;
ii. To evaluate the physicochemical behaviour of these fluorescent derivatives by measuring their binding stoichiometries and association constants with Fe(III)PPIX and comparing these directly to the parent quinoline antimalarials;
iii. To measure the activities of these derivatives against β-haematin formation and the malaria parasite, *P. falciparum*, in vitro;
iv. To determine which of these six fluorescent derivatives are the most suitable analogues of the parent quinoline antimalarials for use in live-cell microscopy.

4.2. Photophysical evaluation of novel fluorescent derivatives

4.2.1. Absorption and fluorescence emission spectra

As described in Chapter 3, six novel fluorescent derivatives of the antimalarials quinine, quinidine and chloroquine were designed, synthesised and characterised. NBD was identified as a suitable reporter fluorophore and hence this dye was incorporated in most of these derivatives (Figure 4.1). A single NBD-labelled derivative of quinine was prepared (**3**) while three derivatives of its diastereomer, quinidine, were synthesised with varying chain lengths between the quinoline core and the reporter fluorophore and classified as short- (**4**), intermediate- (**5**) or long-chain (**6**) derivatives. In addition, another derivative of quinine with an alternative reporter fluorophore, bimane, was prepared (**19**). Finally, a novel NBD-labelled derivative of chloroquine was also synthesised (**8**).

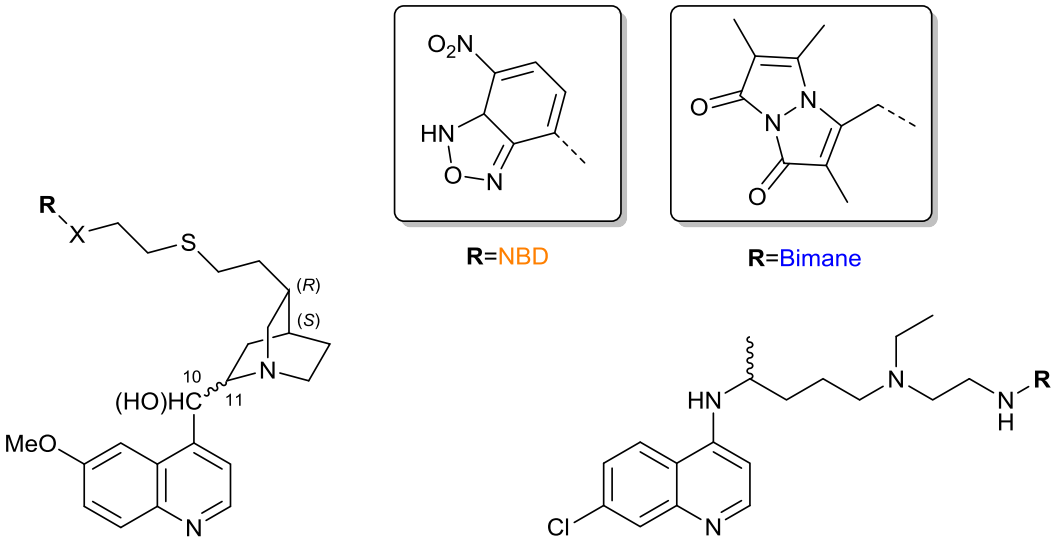

3 Quinine-NBD, X=NH, **R**=NBD (10*S*,11*R*)
4 Quinidine-NBD, X=NH, **R**=NBD (10*R*,11*S*)
5 Quinidine-HexNBD, X=NHCO$(CH_2)_5$NH, **R**=NBD (10*R*,11*S*)
6 Quinidine-DodecNBD, X=NHCO$(CH_2)_{11}$NH, **R**=NBD (10*R*,11*S*)
19 Quinine-Bimane, **R**=Bimane (10*S*,11*R*)

8 Chloroquine-NBD, **R**=NBD

Figure 4.1. *The suite of six fluorescent derivatives of the quinoline antimalarials prepared in this study.*

The absorption and fluorescence profiles of these novel fluorescent derivatives were measured in ethanol. Table 4.1 lists the absorption maxima (λ_{max}) and molar absorption coefficients (ε) at those wavelengths for each compound, as well as their fluorescence emission maxima following excitation at their absorption maxima.

Table 4.1. *Absorption maxima (λ_{max}) and molar absorption coefficients (ε) at those wavelengths of novel fluorescent derivatives measured in ethanol, as well as their corresponding fluorescence emission maxima.*

Fluorescent derivative	λ_{max}, nm (ε, M^{-1} cm^{-1})	Fluorescence emission maximum at λ_{max}, nm
Quinine-NBD (3)	335 (11 500), 465 (18 500)	545 (excitation at 465 nm)
Quinidine-NBD (4)	335 (11 000), 465 (17 000)	545 (excitation at 465 nm)
Quinidine-HexNBD (5)	335 (10 500), 465 (15 500)	530 (excitation at 465 nm)
Quinidine-DodecNBD (6)	335 (6 000), 465 (10 000)	530 (excitation at 465 nm)
Quinine-Bimane (19)	335 (10 000), 385 (8 500)	455 (excitation at 385 nm)
Chloroquine-NBD (8)	330 (18 000), 465 (15 000)	370, 520 (excitation at 330 nm); 530 (excitation at 465 nm)

All fluorescent derivatives possess two absorption maxima. The shorter-wavelength band at 330-335 nm corresponds to the absorption band of the quinoline core and also, in the case of the NBD-labelled derivatives, to the secondary absorption band of the NBD fluorophore. The longer-wavelength band corresponds to the absorption maximum of the extrinsic fluorophore. Generally, the NBD-labelled derivatives are characterised by strong absorption bands (ε > 10 000 M^{-1} cm^{-1}) except for the longest-chain quinidine derivative (**6**). The bimane derivative of quinine (**19**) has the lowest molar absorption coefficient at its primary absorption band and thus was expected to be less bright compared to the NBD-labelled derivatives.

Fluorescence emission was recorded following excitation at both absorption maxima. All compounds exhibited a single emission maximum in ethanol (that is, no fluorescence emission was observed from the quinoline core) except in the case of the NBD-labelled chloroquine (**8**) for which fluorescence emission following excitation at 330 nm resulted in a strong band in the ultraviolet range centred at 370 nm.

Despite their stereochemical differences, quinine and quinidine are photophysically identical. Primary and secondary absorption bands are observed at approximately 335 nm and 320 nm (Figure 4.2A) and correspond to electronic transitions to the first and second excited singlet states, respectively. The alkaloids exhibit fluorescence maxima at approximately 383 nm in their free base or monocationic species. While the dicationic forms of these alkaloids fluoresce more brightly at longer wavelengths (approximately 460 nm), this species is unlikely to be physiologically significant. Taking the lower limit of the pH of the acidic digestive vacuole of *P. falciparum* (Section 1.3.4)[6] and incorporating a pK_a value of 4.42 for the quinolinic nitrogen,[7] the Henderson-Hasselbalch equation predicts that this species is not likely to be present at more than 17% of the drug concentration in the digestive vacuole of the parasite.

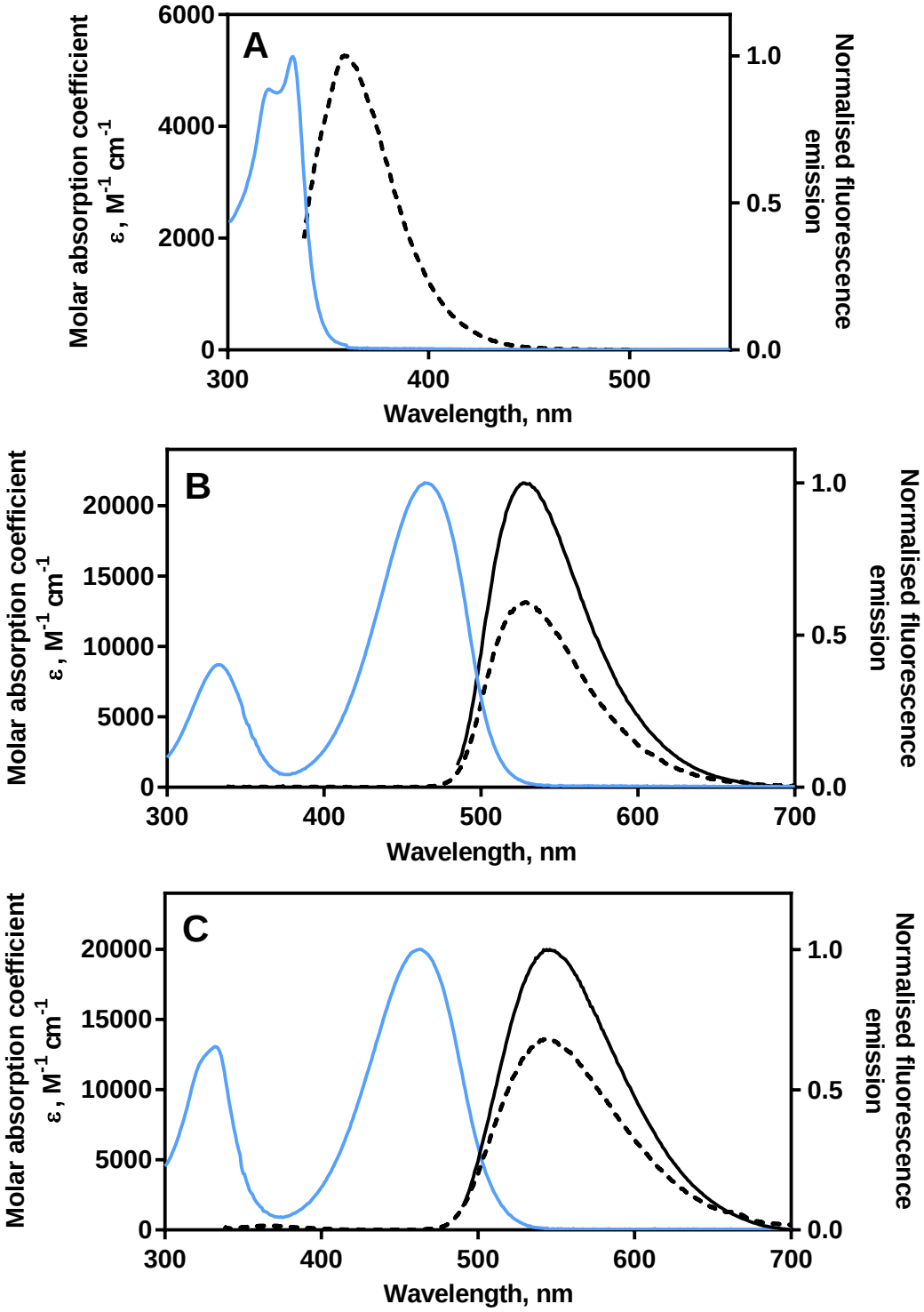

Figure 4.2. *The absorption and fluorescence emission spectra of (A) quinine, (B) NBD-labelled 6-aminohexanoic acid and (C) the NBD-labelled quinine derivative (**3**). Absorption spectra (blue) and fluorescence emission spectra (black) were recorded in ethanol. The dashed black line indicates fluorescence emission from excitation at 335 nm and the solid black line indicates an emission spectrum following excitation at 485 nm. The weak emission peak at approximately 380 nm in (C) is evidence for Förster resonance energy transfer from the quinoline core to the NBD fluorophore (Section 4.2.3).*

The NBD fluorophore, on the other hand, has a primary absorption band at approximately 460 nm and a secondary absorption band centred at 350 nm (Figure 4.2B). The molar absorption coefficient of the former band is particularly high ($\varepsilon \approx 20\ 000\ M^{-1}\ cm^{-1}$). As this coefficient is related to the brightness of a dye, NBD fluorescence is more suitable for microscopy compared to the autofluorescence of the *Cinchona* alkaloids ($\varepsilon \approx 5\ 000\ M^{-1}\ cm^{-1}$). Excitation of either band of the NBD fluorophore generates fluorescence in the green region of the visible spectrum (approximately 545 nm in ethanol) but this fluorescence is always greater following excitation of the primary absorption band. The NBD fluorophore is strongly solvatochromic and thus its emission maximum and intensity depend on the solvent.

The NBD-labelled alkaloids all display similar photophysical properties and are exemplified in this discussion by the NBD-labelled quinine derivative (**3**, Figure 4.2C). Its absorption spectrum is essentially the sum of the absorption spectra of its constituent chromophores. Consequently, the secondary absorption band in the ultraviolet region exhibits the structure of the alkaloid absorption band but with a higher molar absorption coefficient than either of the starting materials. Whilst either band can be excited to generate fluorescence, a brighter emission profile is always observed from direct excitation of the NBD fluorophore. The very weak emission peak at approximately 380 nm is evidence for efficient Förster resonance energy transfer from the quinoline core to the NBD fluorophore (Section 4.2.3).

The absorption and emission spectra of the bimane derivative of quinine (**19**) are depicted in Figure 4.3. Again, the absorption spectrum of this derivative resembles the sum of the absorption spectra of its two constituent chromophores. The absorption band of quinine is preserved (λ_{max} 333 nm) while a secondary, broader absorption band corresponding to the bimane fluorophore (λ_{max} 383 nm) overlaps closely with the emission maximum of quinine. Excitation of either band results in fluorescence emission in the blue region (approximately 460 nm) although the fluorescence intensity arising from excitation at the absorption maximum of quinine (λ_{max} 333 nm) is greater. Once again, a weak emission peak at approximately 380 nm is evidence that much of the energy from excitation of the quinoline core is transferred non-radiatively to the bimane fluorophore via a Förster resonance energy transfer mechanism.

In the case of the NBD-labelled chloroquine derivative (**8**, Figure 4.4), the high molar extinction coefficient of the 4-amino-7-chloroquinoline heterocycle means that the ultraviolet absorption band (λ_{max} 330 nm) is more strongly absorbing than the primary absorption band of the NBD fluorophore (λ_{max} 465 nm). It is somewhat surprising that the primary fluorescence emission band results from excitation of the quinoline directly with its fluorescence maximum in the ultraviolet region (approximately 385 nm) while fluorescence arising from direct excitation of

the NBD fluorophore is very much weaker. This is counterintuitive as one might expect reduced quinoline fluorescence as a result of spin-orbit coupling of the chlorine atom. Nevertheless, it is possible that an intramolecular arrangement might bring the NBD fluorophore in close proximity to the chlorine atom thus reducing the intensity of its fluorescence. In contrast to the derivatives described above, the significant emission of fluorescence from the quinoline core suggests that Förster resonance energy transfer between the quinoline core and the NBD fluorophore in this molecule is not an efficient process.

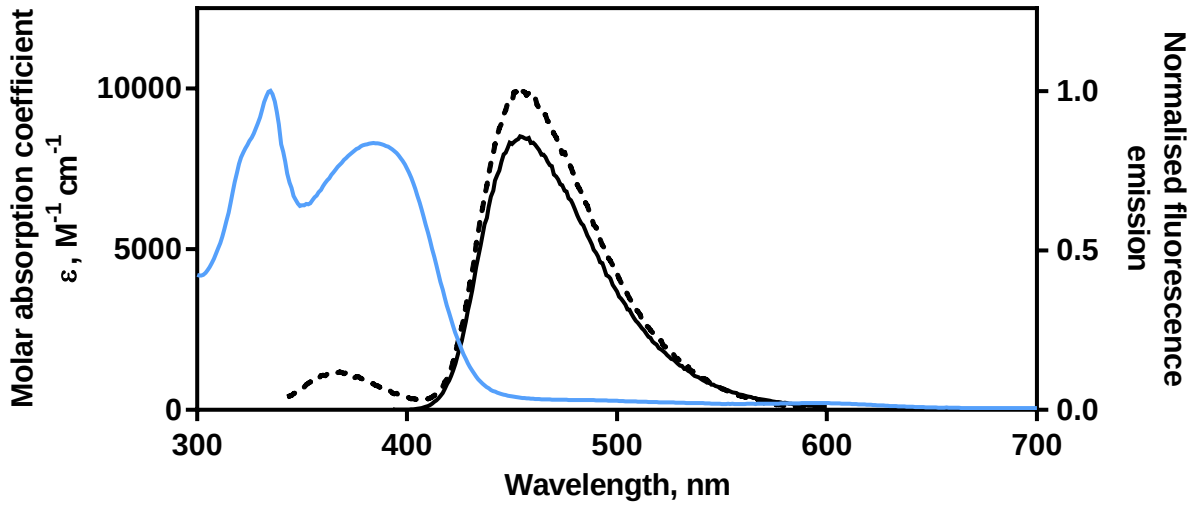

Figure 4.3. *The absorption and fluorescence emission spectra of the quinine-bimane conjugate (**19**) in ethanol. The dashed black line indicates fluorescence emission arising from excitation at 335 nm and the solid black line indicates the emission spectrum following excitation at 385 nm.*

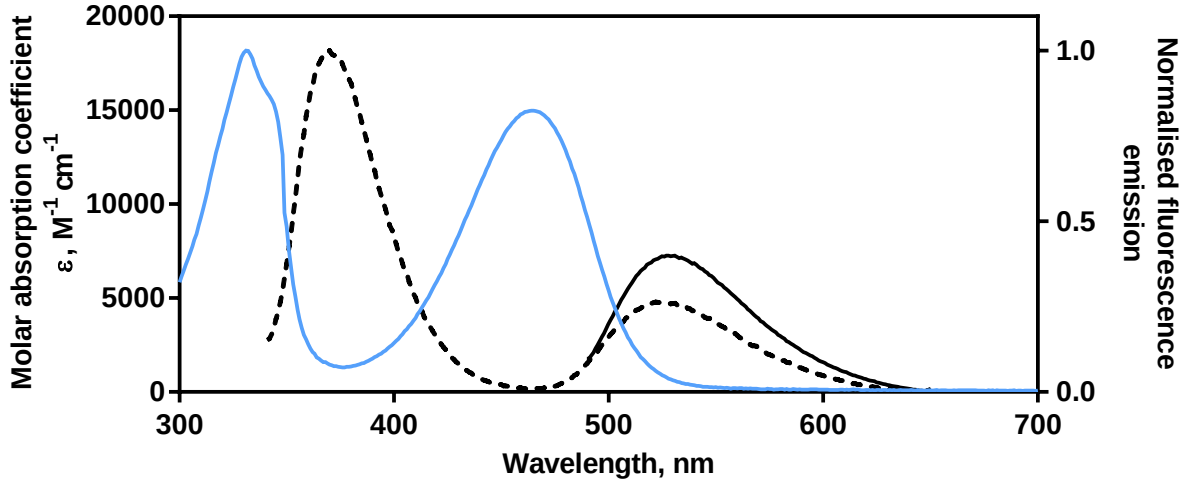

Figure 4.4. *The absorption and fluorescence emission spectra of the NBD-labelled chloroquine derivative (**8**) in ethanol. The dashed black line indicates fluorescence emission arising from excitation at 335 nm and the solid black line indicates the emission spectrum following excitation at 480 nm.*

As described in Section 2.3.3, the fluorescence quantum yield (Φ) of a fluorophore is defined as the ratio of the number of photons emitted as fluorescence to the number of photons absorbed. Bright fluorophores are efficient fluorescence emitters and thus have quantum yields approaching unity. Relative fluorescence quantum yields may be determined experimentally by comparing a fluorophore of known fluorescence quantum yield to a fluorophore of unknown fluorescence quantum yield while keeping the experimental parameters constant.

Fluorescence quantum yields were measured in both organic and mixed aqueous solvents. These were ethanol and 40% (v/v) DMSO in 20 mM Hepes, pH 7.5 (Table 4.2). The latter solvent was used in anticipation of subsequent binding studies. Quinine was used as the reference fluorophore for which a fluorescence quantum yield of Φ = 0.546 in 0.5 M sulfuric acid has been measured.[8] While the NBD fluorophore has a high fluorescence quantum yield in ethanol (Φ ≈ 0.2), its fluorescence is much weaker in mixed aqueous solution (Φ ≈ 0.04) and is weaker still in pure aqueous solution. The opposite is observed for the parent alkaloids quinine and quinidine which have much larger fluorescence quantum yields in aqueous solution compared to ethanol.

Consequently, the NBD-labelled alkaloids are all relatively bright in ethanol but less so in the mixed aqueous medium. The intermediate- (**5**) and long-chain (**6**) derivatives are brighter compared to their short-chain counterparts (**3**, **4**) in both solvents, possibly because of the formation of an hydrophobic environment facilitated by intramolecular folding arrangements accessible to derivatives with longer chain lengths. While the bimane derivative (**19**) is not very bright in ethanol, it is reasonably bright in aqueous solution. Of all the derivatives, the NBD-labelled chloroquine (**8**) exhibited the lowest quantum yield in both organic and mixed aqueous media, most likely due to the internal heavy-atom quenching effect of the chlorine substituent.

Table 4.2. *Fluorescence quantum yields evaluated relative to quinine in 0.5 M sulfuric acid (Φ = 0.546).[8] Two independent measurements were made and uncertainties represent standard errors of the mean.*

Compound	Fluorescence quantum yield (Φ) in ethanol	Fluorescence quantum yield (Φ) in 40% (v/v) DMSO in 20 mM Hepes, pH 7.5
Quinine/quinidine	0.064 ± 0.002	0.242 ± 0.012
Quinine-NBD (3)	0.111 ± 0.002	0.018 ± 0.003
Quinidine-NBD (4)	0.086 ± 0.008	0.017 ± 0.002
Quinidine-HexNBD (5)	0.227 ± 0.040	0.039 ± 0.002
Quinidine-DodecNBD (6)	0.391 ± 0.027	0.033 ± 0.003
Quinine-Bimane (19)	0.049 ± 0.006	0.018 ± 0.002
Chloroquine	0.003 ± 0.001	0.018 ± 0.003
Chloroquine-NBD (8)	0.004 ± 0.001	0.017 ± 0.004

4.2.2. Solvent effects on NBD-labelled derivatives

Solvent molecules assist in lowering the energy of the excited state by rearranging around the excited fluorophores in a process termed solvent relaxation. This may affect the absorption and fluorescence profiles of the molecules. Solvatochromism is the shift in the fluorescence emission maximum resulting from changes in solvent polarity (Section 2.3.6). A more polar solvent produces a larger reduction in the energy level of the excited state while a less polar solvent reduces the stabilisation effects of the solvent; consequently, a larger Stokes shift is seen in more polar solvents compared to less polar solvents.

The fluorescence emission spectrum of the NBD fluorophore is susceptible to this solvatochromic shift. For the NBD-labelled quinidine derivative, a shift in the fluorescence emission maximum from approximately 525 nm to 550 nm was observed across ten common solvents. Plotting the emission maximum against solvent polarity, as measured by the solvent polarity parameter $E_T(30)$, produced an excellent linear correlation (R^2 = 0.980, Figure 4.5). This relatively small shift in emission maximum is unlikely to have any implications for fluorescence microscopy.

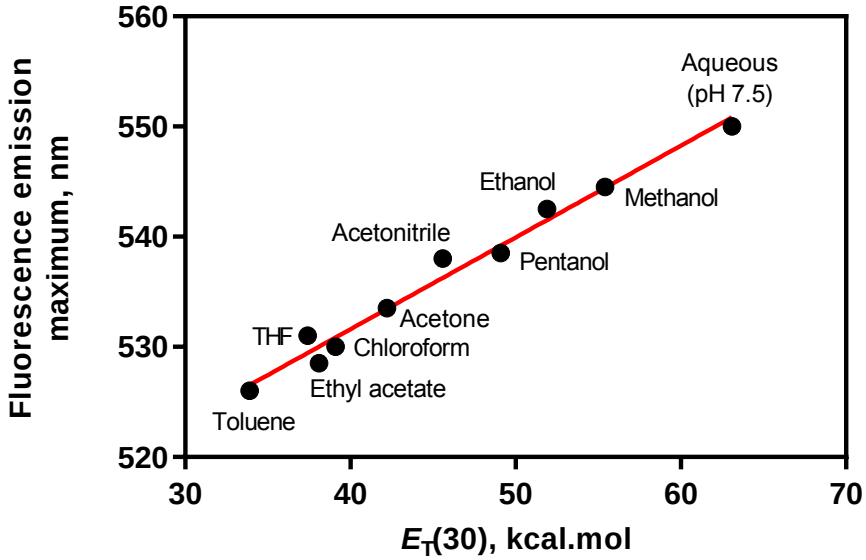

Figure 4.5. *The relationship between the fluorescence emission maximum of the NBD fluorophore and solvent polarity in ten common solvents.* $E_T(30)$ *values taken from Reichardt.*[9] *The short-chain NBD-labelled quinidine derivative (**4**) was excited at 480 nm at a concentration of 20 μM at 25°C.*

The intensity of fluorescence emission was also measured across a variety of different solvents. Again, this generated a good correlation with the $E_T(30)$ solvent polarity parameter (R^2 = 0.906,

Figure 4.6). As expected, the fluorescence of the NBD fluorophore was brightest in non-polar environments but was fairly weak in aqueous solution. Hence, association of these derivatives with cellular components with $E_T(30)$ values similar to those of phospholipid bilayers (49-50 kcal/mol)[10] and neutral lipid components (45 ± 4 kcal/mol for the synthetic neutral lipid blend described in Section 1.3.2)[11] should be easily detectable. On the other hand, their modest aqueous fluorescence quantum yield means that the signal arising from the digestive vacuole – their preferred site of accumulation – will not overwhelm the detector of the microscope at the expense of other subcellular signals.

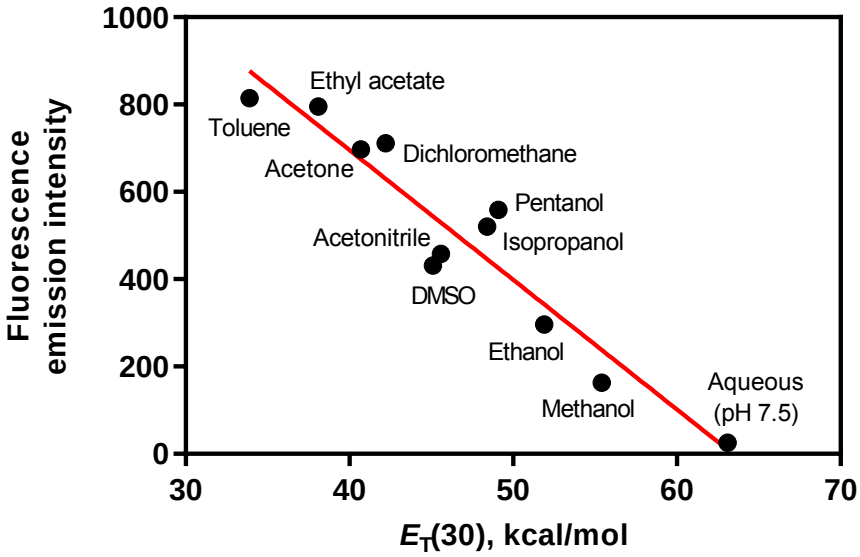

Figure 4.6. *The relationship between fluorescence intensity and solvent polarity for eleven common solvents.* $E_T(30)$ *values taken from Reichardt.*[9] *The short-chain NBD-labelled quinidine derivative (**4**) was excited at 480 nm at a concentration of 20 μM at 25°C.*

Despite the rapid nature of the absorption process, solvent-dependent effects may still be observed in absorption spectra. Absorption spectra for the NBD-labelled quinine derivative were compared between ethanol and 20 mM Hepes, pH 7.5, for which there is an $E_T(30)$ difference of approximately 11.2 kcal/mol. For the NBD-labelled quinine derivative (**3**), a hypochromic shift of approximately of 2 500 M^{-1} cm^{-1} with an increase in solvent polarity, was observed for the ultraviolet absorption band (Figure 4.7). A bathochromic shift of approximately 15 nm (460 to 475 nm) was detected for the primary absorption band, again with an increase in solvent polarity.

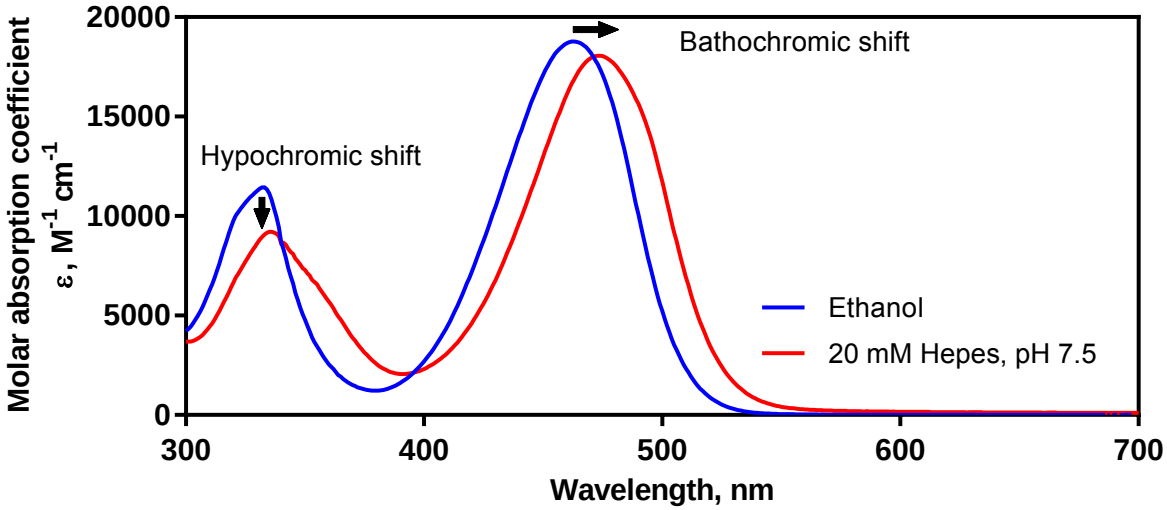

Figure 4.7. *Solvent-dependent shifts in the absorption spectra of the NBD-labelled quinine derivative (**3**) in two different solvents.*

4.2.3. Förster resonance energy transfer

Förster resonance energy transfer is a long-range electrodynamic phenomenon that results from dipole-dipole interactions between two fluorophores. As described in Section 2.3.5, the rate of energy transfer depends on the spectral overlap of the emission spectrum of the donor and the absorption spectrum of the acceptor, the quantum yield of the donor (Φ_D), the relative orientation of donor and acceptor transition dipoles (κ) and the distance between the two fluorophores (R). The important equations associated with quantifying these parameters are reprinted in this section for convenience:

$$J = \int \varepsilon_A(\lambda)\, I_D(\lambda)\, \lambda^4\, d\lambda \Big/ \int I_D(\lambda)\, d\lambda$$

Equation 4.1

$$R_0 = 9.79 \times 10^{-5}\, (J\, \kappa^2\, n^{-4}\, \Phi_D)^{1/6}$$

Equation 4.2

$$E = 1/[1 + (R/R_0)^6]$$

Equation 4.3

In Equation 4.1, J is a measure of the spectral overlap between the donor fluorescence emission and acceptor absorption while R_0, the characteristic Förster distance for which energy transfer

is 50% efficient, is given by Equation 4.2. If the distance between a donor and acceptor pair is known, the efficiency of energy transfer (E) given by Equation 4.3 can be calculated.

There are three donor-acceptor pairs amongst the six fluorescent derivatives prepared in this work. The 6-methoxyquinoline core of the quinine and quinidine alkaloids may function as a donor fluorophore with either the NBD or bimane fluorophores as the acceptor. In the case of the NBD-labelled chloroquine derivative (**8**), the 4-amino-7-chloroquinoline core of chloroquine is the donor and the NBD fluorophore is the acceptor. In these calculations, the donor fluorophores will be exemplified by the substituted quinoline rings of quinine and chloroquine.

In order to determine the potentials of these donor-acceptor pairs for non-radiative energy transfer via Förster resonance energy transfer, the spectral overlap J for each donor-acceptor pair was calculated using Equation 4.1. From these values, the characteristic Förster distance for each donor-acceptor pair was calculated from Equation 4.2. In order to be biologically relevant, absorption and fluorescence emission spectra were collected in 20 mM Hepes at pH 7.5. For the orientation factor κ a value of 0.67 was used as it was assumed that both probes can undergo unrestricted isotropic motion. A value of 1.33, the refractive index of aqueous solution, was used for n.

The results of these calculations are listed in Table 4.3. The Förster distance R_0 is the largest for the quinine-NBD donor-acceptor pair indicating that energy transfer is most efficient between this pair of fluorophores. In contrast, the overlap integral J and R_0 are smaller for the quinine-bimane pair. This is likely a result of the smaller molar extinction coefficient of bimane at its λ_{max}. While the overlap integral J of the chloroquine-NBD pair is larger than the overlap integral of the quinine-bimane pair, its R_0 value is much smaller than the other two pairs. This is because the donor (chloroquine) has a very weak fluorescence quantum yield due to the internal heavy-atom effect previously mentioned.

Table 4.3. *Calculated overlap integrals (J) and characteristic Förster distances (R_0) for the three donor-acceptor pairs described in this work in 20 mM Hepes, pH 7.5.*

	Donor	Acceptor	Overlap integral J, M^{-1} cm^{-1} nm^4	Characteristic Förster distance R_0	Efficiency of energy transfer (R = 13 Å)
1	**Quinine**	**NBD**	1.55×10^{-14}	28.7 Å	99%
2	**Quinine**	**Bimane**	9.59×10^{-15}	16.1 Å	78%
3	**Chloroquine**	**NBD**	1.11×10^{-14}	11.5 Å	33%

A model of the short-chain NBD-labelled quinine derivative (**3**) was energy-minimised using the Marvin Sketch software package (Version 14.8.25.0, ChemAxon Ltd, 2014). The minimum distance measured between the two fluorophores (R = 13 Å) was used in Equation 4.3 to determine an approximate efficiency of energy transfer (Table 4.3). As this distance is very much smaller than the Förster distance between the quinine-NBD donor-acceptor pair, this fluorophore pair exhibited the greatest efficiency of energy transfer (99%). This efficiency was also reasonably high for the quinine-bimane pair (78%) but much lower for the chloroquine-NBD pair (33%).

These calculations rationalise the profiles of the fluorescence emission spectra of the fluorescently-labelled derivatives. For the NBD-labelled alkaloids (Figure 4.2C), there is a very small emission peak arising from the quinoline core in the ultraviolet region suggesting that Förster resonance energy transfer is very efficient (almost 100%). For the quinine-bimane derivative (Figure 4.3), this band is more pronounced suggesting that energy transfer is less efficient (approximately 80%). Finally, for the chloroquine-NBD pair (Figure 4.4), excitation of the quinoline core generates fluorescence that is very much greater than the fluorescence emitted by the NBD fluorophore, suggesting that Förster resonance energy transfer between these two fluorophores is much less favoured in accordance with predicted behaviour.

4.2.4. Sensitivity of NBD-labelled derivatives to light and temperature

Exposure of fluorescent molecules to ambient light leads to constant population of the excited state which may eventually result in photobleaching and loss of fluorescence. In the presence of solvent, the enhanced reactivity of the excited-state can lead to reactions with the solvent. Thus, in order to probe the propensities of the NBD-labelled alkaloids to photo- and thermal degradation, a quantitative stability study was conducted.

The intermediate-chain NBD-labelled quinidine derivative (**5**) was selected as a representative molecule. Approximately 1 mg of this derivative was weighed out in several glass vials which was either left as a solid or dissolved in acetonitrile and subjected to the conditions listed in Table 4.4. This included storage in a freezer (-4°C), in an oven (70°C) or on the laboratory benchtop at ambient temperature (23°C). Two sets of the latter samples were prepared, one which was exposed to ambient light and one which was not. After three months at these conditions, quantitative analysis was performed using HPLC.

No decomposition of the samples stored in the freezer or in the dark on the benchtop, either in the solid phase or in solution, was recorded (Table 4.4). While some decomposition was

observed at the high temperature of the oven (16%) or upon exposure to light on the benchtop (9%), the combination of ambient light in the solution phase caused the most degradation (96%). The results indicate that it is important to protect the NBD-labelled derivatives from light, especially when they are in the solution state.

Table 4.4. *Decomposition of the intermediate-chain NBD-labelled quinidine derivative (**5**) after three months as a solid or solution and exposed to various conditions.*

Entry	Temperature	Exposure to ambient light	Decomposition in the solid state	Decomposition in the solution state
1	-4°C	No	0%	0%
2	23°C	No	0%	0%
3	23°C	Yes	9%	96%
4	70°C	No	16%	N/A

4.3. Physicochemical evaluation of novel fluorescent derivatives

4.3.1. Binding stoichiometries and association constants of complexes with Fe(III)PPIX

A common feature amongst the quinoline antimalarials is the thermodynamic stabilities of their complexes with Fe(III)PPIX. Since it was first proposed that Fe(III)PPIX is the molecular target of various quinoline antimalarials,[12,13] increasing evidence has shown that the interactions of these drugs with Fe(III)PPIX are central to their antimalarial activity.[4] This direct interaction appears to involve inhibition of the incorporation of Fe(III)PPIX into haemozoin, either by adsorption of the drug onto the surface of the crystal and inhibiting further biocrystallation[14] or by sequestering free Fe(III)PPPIX via complexation and thus making the porphyrin unavailable for biocrystallisation.[15] Accumulation of free Fe(III)PPIX following drug treatment has been observed for chloroquine and quinine, verifying that the haemozoin biocrystallisation pathway is indeed the likely target of these drugs within *P. falciparum* (Section 1.5.1).[16]

As the binding stoichiometries and association constants with Fe(III)PPIX in solution of the three quinoline antimalarials in this study have been thoroughly characterised (Section 1.5.2),[4,5] these measurements were used as benchmarks to determine whether the fluorescently-labelled derivatives prepared in the previous chapter were suitable analogues of the parent molecules. As Fe(III)PPIX exhibits complex speciation in solution, it was elected to use a mixed aqueous solution of 40% DMSO (v/v) in 20 mM Hepes, pH 7.5, in which Fe(III)PPIX is predominantly monomeric, to simplify the comparison.[17] This also allowed direct comparison of results with previous measurements.[18,19]

In order to determine the binding stoichiometries of these complexes, the method of continuous variation, also known as Job's method, was employed.[20] In this approach, two equimolar stock solutions of Fe(III)PPIX and quinoline are mixed in a manner such that the total concentration of the two components is kept constant while the Fe(III)PPIX to quinoline ratio varies from sample to sample. The absorbance is plotted as a function of the mole fraction of Fe(III)PPIX.

As stoichiometric ratios give rise to the greatest deviation in absorbance from the expected absorbance of Fe(III)PPIX, the position corresponding to the ratio of the complex is observed at the intersection of two lines fitted to the points originating from either side of the mole fraction scale. For example, a point of intersection corresponding to a 0.5 mole fraction of Fe(III)PPIX suggests a complex of 1:1 composition while an intersection corresponding to a mole fraction of 0.67 indicates a complex with a 2:1 ratio of Fe(III)PPIX to quinoline compound.

In these experiments, it is important to ensure (i) that the system conforms to the Beer-Lambert law, (ii) that a single complex predominates under the conditions of the experiment, (iii) that the total concentration of Fe(III)PPIX plus quinoline compound is kept constant and (iv) that pH is maintained constant.[20]

A typical Job plot obtained from these experiments is depicted in Figure 4.8. In this case, the stoichiometry of the complex between Fe(III)PPIX and quinine was measured. The dashed red line indicates the absorbance of Fe(III)PPIX alone at 400 nm. Blue lines represent regression analyses through the two sets of circular data points. In this example, the intersection of the two solid blue lines corresponded to a mole fraction of Fe(III)PPIX of 0.499 and hence a 1:1 binding stoichiometry.

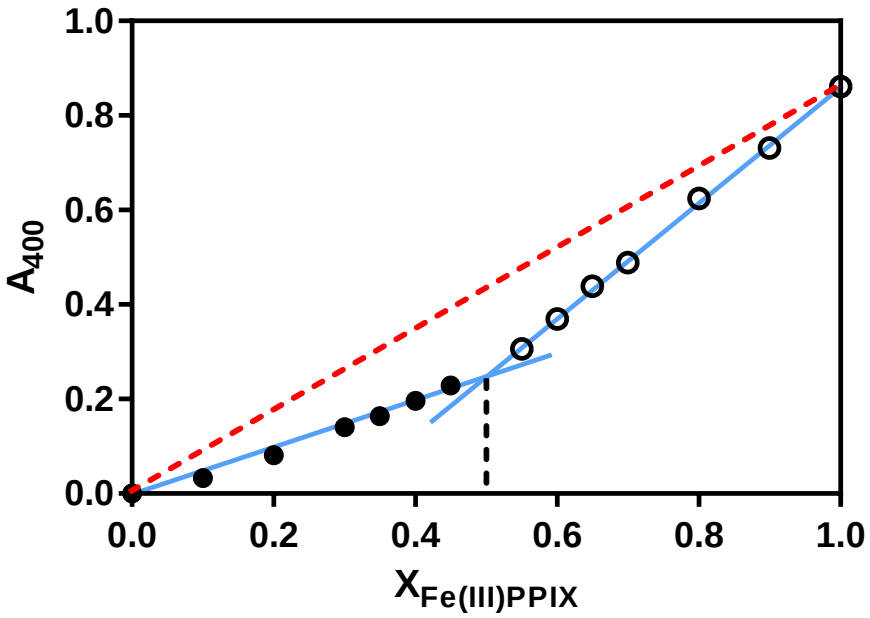

Figure 4.8. *Example of a typical Job plot to determine the stoichiometry of the Fe(III)PPIX-quinoline complexes; in this case, quinine was used. The dashed red line represents the absorbance of Fe(III)PPIX at 400 nm in the absence of a binding partner. Blue lines represent the lines of best fit through the two sets of circular data points. The intersection of the two blue lines corresponds to a Fe(III)PPIX mole fraction of 0.5 and hence to a 1:1 binding stoichiometry.*

These measurements were made for the fluorescently-labelled derivatives as well as the parent quinoline antimalarials. The results are tabulated in Table 4.5. As expected, the parent alkaloids quinine and quinidine formed complexes with Fe(III)PPIX with an unambiguous 1:1 ratio.[18,19] Their NBD-labelled derivatives retained the same clear binding stoichiometry, except for the longest-chain quinidine derivative (**6**) which could not be measured due to insolubility at the

necessary concentrations and the quinine-bimane derivative (**19**) for which a point of intersection of 0.455 ± 0.009 was observed. Nevertheless, a 1:1 binding ratio for this derivative is still likely as any other stoichiometric ratio corresponding to this mole fraction of Fe(III)PPIX would lead to an unusual, and hence unlikely, aggregation state of the two components.

Table 4.5. *Stoichiometries and association constants (log* K*) for complexes of the quinoline antimalarials and their fluorescently-labelled derivatives with Fe(III)PPIX determined via Job's method and spectrophotometric titrations, respectively. Experiments were conducted in 40% (v/v) DMSO in 20 mM Hepes, pH 7.5, at 25°C. Measurements were performed in triplicate and uncertainties represent standard errors of the mean. ND = Not determined due to insolubility at the required concentrations.*

Entry	Compound	Point of intersection from Job plot	Stoichiometry of Fe(III)PPIX to quinoline	Log *K*
1	Quinine (**1**)	0.499 ± 0.019	1 : 1	4.49 ± 0.03
2	Quinine-NBD (**3**)	0.480 ± 0.009	1 : 1	4.92 ± 0.02
3	Quinine-Bimane (**19**)	0.455 ± 0.009	1 : 1	4.26 ± 0.02
4	Quinidine (**2**)	0.499 ± 0.007	1 : 1	4.95 ± 0.06
5	Quinidine-NBD (**4**)	0.471 ± 0.009	1 : 1	5.22 ± 0.07
6	Quinidine-HexNBD (**5**)	0.539 ± 0.019	1 : 1	5.17 ± 0.03
7	Quinidine-DodecNBD (**6**)	ND	ND	ND
8	Chloroquine (**7**)	0.686 ± 0.003	2 : 1	10.11 ± 0.04
9	Chloroquine-NBD (**8**)	0.606 ± 0.009	2 : 1	10.56 ± 0.09

An unambiguous ratio of 2:1 was obtained for the Fe(III)PPIX-chloroquine complex, in agreement with experimental observations in aqueous solution.[5] Although the stoichiometry of the Fe(III)PPIX complex with the NBD-labelled chloroquine derivative (**8**) was less definitive (0.606 ± 0.009), this most likely corresponds to a 2:1 ratio for the reasons given above.

Having determined the stoichiometries of the Fe(III)PPIX-quinoline complexes, the strength of this interaction was measured by spectrophotometric titration. In the mixed aqueous system of 40% DMSO (v/v) in 20 mM Hepes at pH 7.5, the strong quenching of the Soret band was used to determine association constants in accordance with methods used previously (Section 1.5.2).[18] All spectrophotometric titration data were fitted over the entire spectrum using the HypSpec software package (Version 1.1.33, HyperQuad, 2008). The association constants (log *K*) fitted using the binding ratios determined from the Job plots are listed in the final column of Table 4.5. A representative example of a spectrophotometric titration of quinidine with Fe(III)PPIX is shown in Figure 4.9.

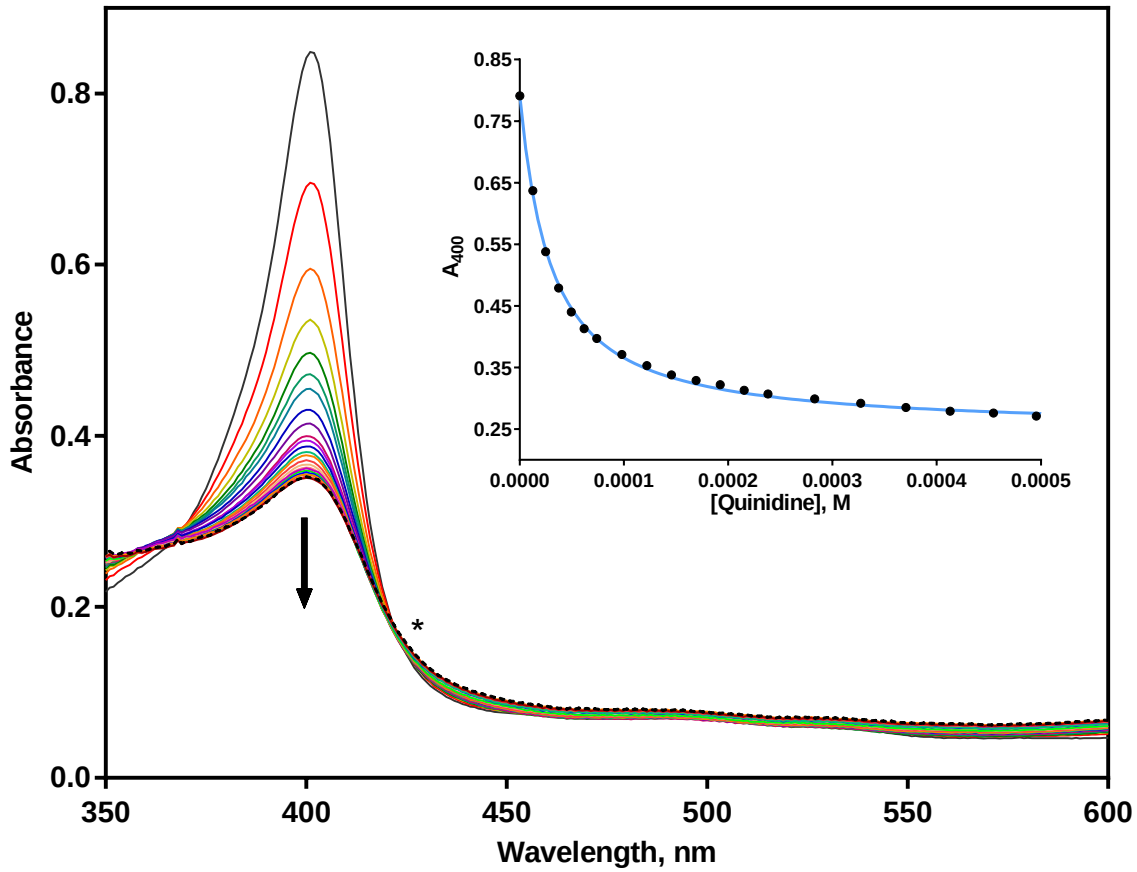

Figure 4.9. *Spectrophotometric changes observed upon the addition of quinidine to Fe(III)PPIX in 40% DMSO (v/v) in 20 mM Hepes, pH 7.5, at 25°C. The initial spectrum with no compound added is shown as a continuous black line and the final spectrum is shown as a black dashed line. Intermediate spectra are coloured. The direction of change at 400 nm is indicated by an arrow and an isosbestic point is indicated by an asterisk. All spectra are corrected for dilution.* ***Inset:*** *Absorbance values at 400 nm fitted to a 1:1 association model using non-linear least squares fitting are represented by a continuous blue line.*

Fe(III)PPIX has previously been shown to bind more strongly to quinidine than to quinine, corroborating the current measurements.[18,19] As described earlier (Section 1.5.3), it has been shown in the solid state that there are three cooperative interactions responsible for the association between Fe(III)PPIX and the *Cinchona* alkaloids.[21] This three-point binding mode of the alkaloids to Fe(III)PPIX comprises π-π stacking interactions, coordination to the iron centre of Fe(III)PPIX and a charge-assisted intramolecular hydrogen bond between the Fe(III)PPIX propionate group and the hydrogen of the (protonated) quinuclidine nitrogen of the alkaloid.[21] These observations corroborate previous computational predictions.[22] Molecular mechanics modelling revealed that quinine and quinidine possess low-energy conformers that facilitate the formation of this charge-assisted hydrogen bond. Indeed, quinidine exhibits a lower strain energy of complex formation than quinine as a result of the "pre-organisation" afforded by its

absolute stereochemistry.[22] This might explain its more favourable association constant and hence superior activity against *P. falciparum* compared to quinine.[7]

The NBD-labelled derivatives of the *Cinchona* alkaloids all exhibit somewhat stronger binding to Fe(III)PPIX compared to the parent compounds. For example, log *K* values of 4.49 ± 0.03 and 4.92 ± 0.02 were found for quinine and its NBD-labelled derivative (**3**), respectively. It is likely that the three cooperative interactions with Fe(III)PPIX described above are retained by the NBD-labelled derivatives but with enhancement of the π-stacking effect facilitated by the heteroaromatic NBD fluorophore. Once again, the association constant for the longest-chain quinidine derivative (**6**) could not be measured due to its insolubility at the necessary concentrations indicating its unsuitability for live-cell imaging studies. The association constant for the quinine-bimane derivative (**19**) was somewhat reduced (log *K* = 4.26 ± 0.01) compared to quinine itself.

For chloroquine, the binding model was adjusted to account for complex formation with a 2:1 ratio of Fe(III)PPIX to chloroquine. In this case, the binding of the NBD-labelled derivative was also somewhat stronger (log *K* 10.56 ± 0.09) compared to chloroquine on its own (log *K* 10.11 ± 0.04), most likely because of enhanced π-stacking interactions due to the NBD fluorophore.

In order to verify the speciation of Fe(III)PPIX in the complex with the NBD-labelled chloroquine, magnetic circular dichroism spectra were collected. This technique offers better resolution than conventional absorption spectroscopy and thus can indicate, unambiguously, the species of Fe(III)PPIX present. It has been definitively shown that chloroquine induces μ-oxo dimerisation of Fe(III)PPIX.[5] This complex exhibits a characteristic magnetic circular dichroism spectrum (Figure 4.10A).[5] A magnetic circular dichroism spectrum obtained for the complex between Fe(III)PPIX and the NBD-labelled chloroquine closely resembles this spectrum (Figure 4.10B). This "fingerprint" technique shows that the NBD-labelled chloroquine derivative very likely also induces μ-oxo dimerisation of Fe(III)PPIX, corroborating the 2:1 stoichiometric measurements and similar association constants obtained.

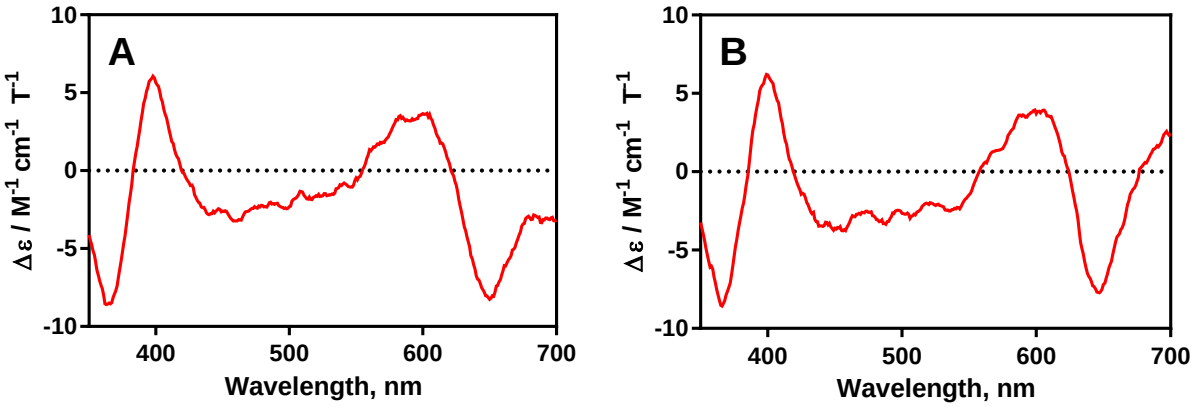

Figure 4.10. *Magnetic circular dichroism spectra of (A) the Fe(III)PPIX-chloroquine complex and (B) the complex between Fe(III)PPIX and the NBD-labelled chloroquine derivative. The spectra resemble closely those previously reported for the Fe(III)PPIX-chloroquine μ-oxo dimer complex.*[2]

All of the novel fluorescent derivatives retained the binding stoichiometry and reasonably similar association constants to their parent compounds with Fe(III)PPIX, their likely target within the malaria parasite, except for the long-chain NBD-labelled quinidine derivative (**6**) for which the necessary measurements could not be performed. These results suggest that, with the exception of **6**, the derivatives are largely unaffected by the tethering of the fluorescent tag. These results also vindicate the design choice in Chapter 3 to functionalise the vinyl group of the *Cinchona* alkaloids as covalently modifying this part of the parent molecule does not appear to impact binding with Fe(III)PPIX. Similarly, for chloroquine, introducing a fourth amino functionality by selective *N*-dealkylation of a terminal diethyl group does not affect the capacity of the labelled derivative to induce μ-oxo dimerisation of Fe(III)PPIX.

4.3.2. Solubility, aggregation and quenching studies of NBD-labelled derivatives

As described previously, several NBD-labelled derivatives of quinidine were prepared by varying the length of the spacer chain between the alkaloid core and the reporter NBD fluorophore to generate derivatives of short (**4**), intermediate (**5**) and long (**6**) chain lengths. These three derivatives possess similar photophysical properties to one another (Table 4.1) although the latter two derivatives possess a higher fluorescence quantum yield than the short-chain derivative (Table 4.2). However, only the short- (**4**) and intermediate-chain (**5**) derivatives were shown to retain their binding stoichiometries and association constants upon complexation with Fe(III)PPIX. These properties could not be measured for the long-chain quinidine derivative (**6**) due to the insolubility of this derivative at the necessary concentrations. Thus, to distinguish between these derivatives in order to determine the most suitable analogue, further physicochemical properties were probed.

To determine the aqueous solubility ranges of the NBD-labelled alkaloids compared to their parent alkaloids, a turbidimetric solubility assay was employed. In this assay, absorbance was measured at 620 nm to detect light scattering arising from insolubility. (The quinolines themselves do not absorb at this wavelength.) Table 4.6 demonstrates that the parent alkaloids quinine and quinidine are soluble in aqueous solution (pH 7.5) at concentrations greater than 200 μM. However, their NBD-labelled derivatives are all less soluble in aqueous solution. While the short-chain derivatives (**3**, **4**) are soluble between 150-200 μM, the longer chain derivatives are even less soluble. The long-chain derivative (**6**) was particularly insoluble, accounting for the difficulties associated with measuring its stoichiometry or association constant with Fe(III)PPIX, even in the presence of 40% (v/v) DMSO.

Table 4.6. *The aqueous solubility ranges of the* Cinchona *alkaloids and their NBD-labelled derivatives measured by turbidimetry in 20 mM Hepes, pH 7.5.*

Entry	Compound	Solubility range
1	Quinine (**1**)	> 200 μM
2	Quinine-NBD (**3**)	150-200 μM
3	Quinidine (**2**)	> 200 μM
4	Quinidine-NBD (**4**)	150-200 μM
5	Quinidine-HexNBD (**5**)	100-150 μM
6	Quinidine-DodecNBD (**6**)	20-40 μM

The reduced solubility of the NBD-labelled derivatives indicates an increased hydrophobicity which most likely results from the incorporation of the heteroaromatic NBD fluorophore. This hydrophobicity may encourage aggregation of these derivatives in aqueous solution which would be detrimental to live-cell imaging studies. Hence, diffusion measurements were conducted to determine whether there was evidence of aggregation as a result of reduced aqueous solubility.

To measure the diffusion coefficients of the NBD-labelled quinidine derivatives, a diffusion cell method was used in which a concentrated solution of the alkaloid was loaded into a lower chamber of the apparatus and allowed to diffuse into the corresponding upper chamber at ambient temperature.[23] The upper chamber was then isolated, its absorbance measured and the concentration of the diffused molecule determined. Diffusion constants were calculated from Equation 4.4 which is derived from Fick's laws of diffusion.[23] In this expression, D is the diffusion coefficient ($m^2\ s^{-1}$), h is the height of the diffusing column (m), t is the length of time (s), c_0 the initial concentration (M) and c the final concentration in the upper well (M).

$$D = \left(\frac{ch}{c_0}\right)^2 \frac{\pi}{t}$$

Equation 4.4

The hydrodynamic radius of the molecule *R*, which is the apparent radius of the solvated molecule, can be calculated from its diffusion coefficient using the Stokes-Einstein equation (Equation 4.5). In this expression, k is the Boltzmann constant (J K^{-1}), T is the absolute temperature (K), η is the viscosity (Pa s) and *R* is the hydrodynamic radius (m).

$$R = \frac{kT}{6\pi\eta D}$$

Equation 4.5

Diffusion coefficients were determined for quinidine and its NBD-labelled derivatives in both aqueous solution and 40% DMSO (v/v) in 20 mM Hepes, pH 7.5 (Table 4.7). In aqueous solution, the diffusion coefficients of the short- (**4**) and intermediate-chain (**5**) NBD-labelled derivatives were much smaller than the diffusion coefficient of the parent alkaloid quinidine, reflecting the reduced hydrophilicity of these derivatives. Their corresponding hydrodynamic radii were much larger to reflect their slower rates of diffusion; this was particularly large for the intermediate-chain derivative (102 Å) compared to the short-chain derivative (20 Å). The large hydrodynamic radius of the former molecule suggests aggregation in aqueous solution.

Table 4.7 *Diffusion parameters for quinidine and its NBD-labelled derivatives measured in aqueous and mixed aqueous solutions. ND = Not determined due to insolubility at the required concentrations.*

Entry	Compound	Diffusion coefficient *D* and hydrodynamic radius *R* in 20 mM Hepes, pH 7.5	Diffusion coefficient *D* and hydrodynamic radius *R* in 40% DMSO (v/v) in 20 mM Hepes at pH 7.5
1	Quinidine	10.5 x 10^{-10} m^2 s^{-1} (2.37 Å)	2.87 x 10^{-10} m^2 s^{-1} (3.55 Å)
2	Quinidine-NBD (**3**)	1.27 x 10^{-10} m^2 s^{-1} (19.5 Å)	1.59 x 10^{-10} m^2 s^{-1} (6.41 Å)
3	Quinidine-HexNBD (**4**)	0.245 x 10^{-10} m^2 s^{-1} (101.7 Å)	1.58 x 10^{-10} m^2 s^{-1} (6.44 Å)
4	Quinidine-DodecNBD (**5**)	ND	ND

In mixed aqueous solution, the hydrodynamic radii of the short- (**4**) and intermediate-chain (**5**) NBD-labelled derivatives were very much smaller than in aqueous solution at approximately 6.5

It is most likely that DMSO prevents aggregation due to its capacity as an efficient hydrogen-bond acceptor and its lower dielectric constant. In both systems, the diffusion coefficients for the long-chain NBD-labelled quinidine derivative (**6**) could not be measured due to insolubility at the required concentrations, indicating again the unsuitability of this derivative for live imaging studies.

To investigate whether these diffusion coefficients were indeed evidence of aggregation rather than increased molecular volume, especially in the case of the intermediate-chain derivative (**5**), an empirical relationship was exploited that relates the logarithm of the diffusion coefficient (log *D*) to molar volume (log V_m). A deviation from this relationship is evidence of aggregation.[25]

The molar volume is calculated by dividing the molar mass of a substance by its density, which was predicted using the ChemSketch software package (Version 12.01, Advanced Chemistry Development Inc., 2010). Although this relationship holds strongly for polycyclic aromatic organic molecules, it can also be used to estimate the degree of aggregation of more complex organic molecules.[25] Hence a number of known diffusion coefficients of polycyclic aromatic organic molecules (filled circles) were incorporated into the plot (Figure 4.11) along with the values from Table 4.7 (unfilled circles).[25,26] The linear regression fitted to this data set (excluding the point in blue) is indicated by the red line and shows a very good correlation between the two parameters (R^2 = 0.949).

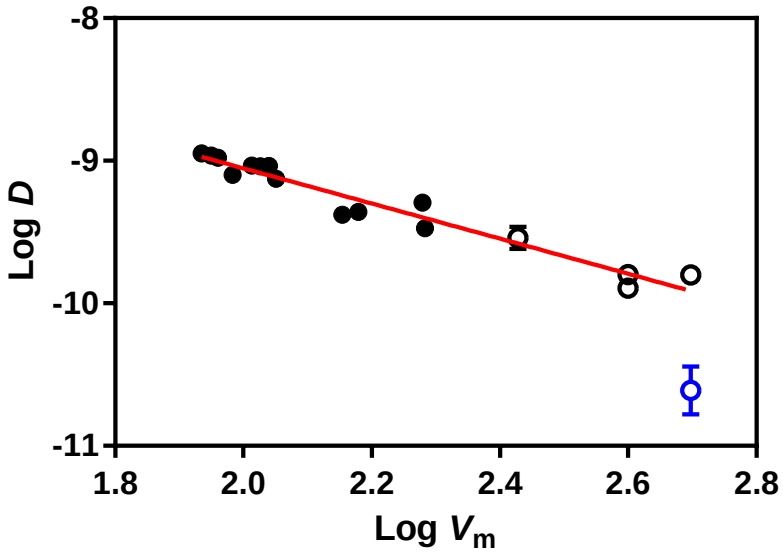

Figure 4.11. *Plot of the dependence of log* D *on log* V_m *at 298 K (R^2 = 0.949). Regression analysis excluded the point indicated in blue. Previously-measured values are indicated by filled circles[25,26] while unfilled circles represent values measured in this work and listed in Table 4.7. The blue point corresponds to the intermediate-chain NBD-labelled quinidine derivative (**5**) in aqueous solution (20 mM Hepes, pH 7.5).*

All the values measured in this work, which are represented by unfilled circles in Figure 4.11 but exclude the point in blue, obey the relationship between log D on log V_m at 298 K. This suggests that the NBD-labelled derivatives do not display behaviour associated with aggregation in aqueous solution, the only exception of which is the intermediate-chain NBD-labelled quinidine derivative (**5**) whose values fall far outside the regression line (indicated by the blue point in Figure 4.11). This deviation suggests that the molecular weight of this complex is far larger than expected, consistent with behaviour arising from aggregation. These observations also show that the short-chain NBD-labelled derivatives (**3**, **4**) are more closely related to the physicochemical properties of the parent molecules and are therefore more suitable analogues of the parent alkaloids.

To probe the nature of the aggregation phenomenon exhibited by the intermediate-chain NBD-labelled quinidine derivative (**5**), its fluorescence emission spectrum was monitored in the presence of Fe(III)PPIX. Fe(III)PPIX is a strongly-absorbing chromophore and so exerts a substantial inner-filter effect on fluorescence spectra in which the exciting radiation and/or fluorescence emission is attenuated, giving a lower signal than expected (Section 2.4.2). Furthermore, Fe(III)PPIX quenches fluorescence due to spin-orbit coupling of the heavy Fe(III) atom, especially with molecules with which it associates such as the intermediate-chain NBD-labelled derivative (**5**, Log K = 5.17 ± 0.03 from Table 4.5).

An example of the conspicuous inner-filter effect caused by Fe(III)PPIX is demonstrated by measuring the fluorescence emission of NBD-labelled 6-aminohexanoic acid which may be excited at either 465 nm or 350 nm to generate fluorescence at λ_{max} 545 nm. (The absorption and fluorescence spectra of this molecule were depicted above in Figure 4.2B.) This molecule has been measured to interact negligibly with Fe(III)PPIX and so one would not, initially, expect a decrease in its fluorescence emission in the presence of Fe(III)PPIX. However, attenuation of the fluorescence signal following excitation at both wavelengths is observed (represented by filled circles in Figure 4.12). This apparent quenching may be corrected by applying the inner-filter factor that was presented in Equation 2.8 which takes into account the attenuation of the signal as a result of the strong absorption spectrum of Fe(III)PPIX. Consequently, there is no *actual* quenching of the fluorescence emission that takes place (unfilled circles in Figure 4.12).

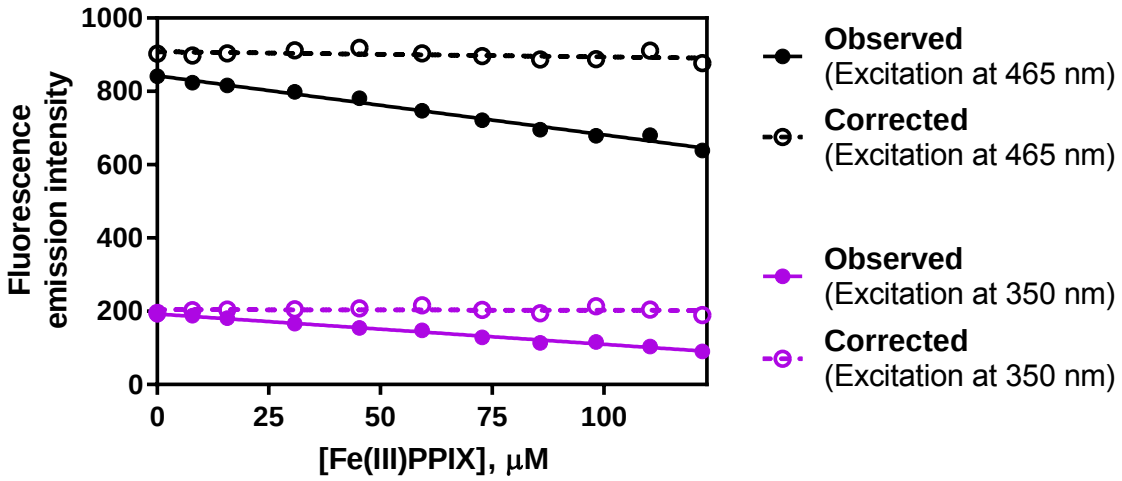

Figure 4.12. *An illustration of the inner-filter effect when Fe(III)PPIX is titrated with NBD-labelled 6-aminohexanoic acid (20 μM) in 20 mM Hepes, pH 7.5. Filled circles indicate attenuation of fluorescence in the presence of Fe(III)PPIX when excited at two different wavelengths, while unfilled circles indicate the correction applied by Equation 2.8. This reveals that there is no* actual *attenuation of the fluorescence signal caused by Fe(III)PPIX quenching. In both cases emission was monitored at 545 nm.*

In the case of quenching studies with the intermediate-chain NBD-labelled quinidine derivative (**5**) in the presence of Fe(III)PPIX, all fluorescence spectra were corrected for the inner-filter effect. It is worth pointing out that the aqueous absorption and emission spectra of this derivative (Figure 4.13) are somewhat different from its spectra in ethanol (Figure 4.2C) in which this molecule did not display an appreciable fluorescence emission at 385 nm. However, in the aqueous environment emission *is* observed at 385 nm, most likely due to reduced efficiency of Förster resonance energy transfer. Hence, fluorescence may be monitored at this emission wavelength to generate additional insights into its local chemical environment.

Upon titrating Fe(III)PPIX into an aqueous solution of the intermediate-chain NBD-labelled quinidine derivative (**5**) and monitoring the fluorescence emission at both excitation and emission wavelengths, two different fluorescence emission profiles were observed (Figure 4.14). Fluorescence emission following excitation at the wavelength corresponding to the NBD fluorophore (485 nm) indicates a rapidly diminishing fluorescence profile, while fluorescence emission following excitation at the wavelength corresponding to the quinoline core (335 nm) shows that fluorescence is quenched more gradually. This differential quenching profile suggests the presence of different chemical environments inhabited by the two fluorophores of the intermediate-chain quinidine derivative (**5**).

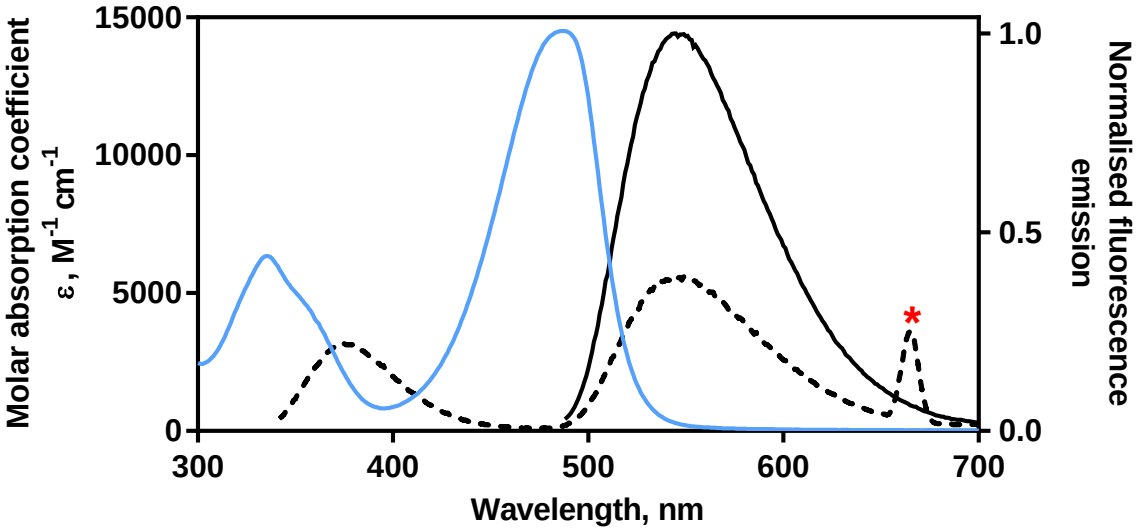

Figure 4.13. *The absorption and fluorescence emission spectra of the intermediate-chain NBD-labelled quinidine derivative (**5**) in 20 mM Hepes, pH 7.5. The dashed black line indicates fluorescence emission arising from excitation at 335 nm while the solid black line indicates the emission spectrum following excitation at 480 nm. The red asterisk indicates stray light from second-order excitation that occurs at exactly double the excitation wavelength, i.e. 670 nm.*

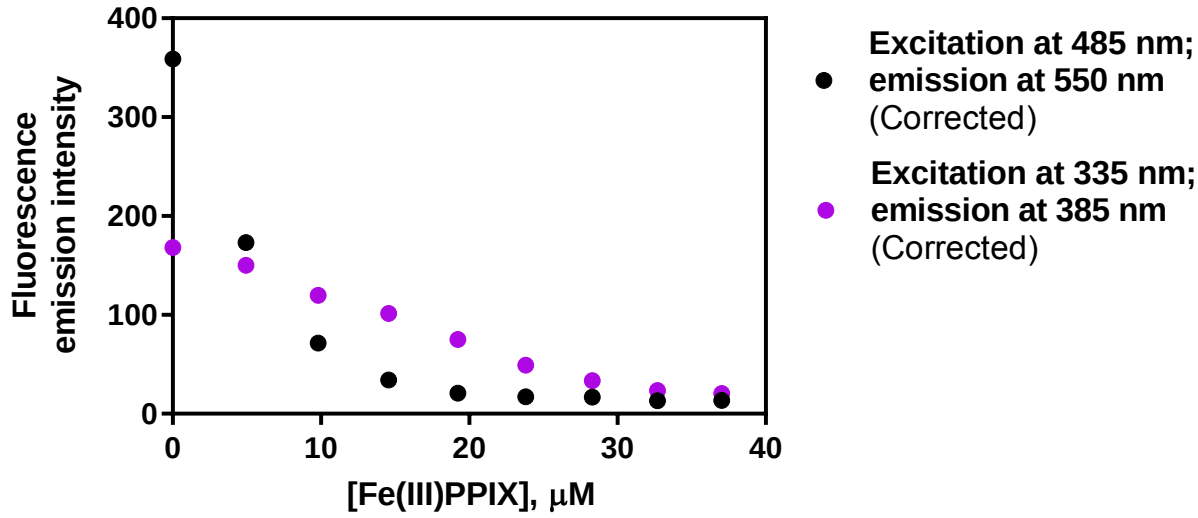

Figure 4.14. *Quenching behaviour of the intermediate-chain NBD-labelled derivative (**5**) in 20 mM Hepes pH 7.5 after the addition of Fe(III)PPIX. Excitation at 485 and 335 nm were monitored at 550 and 385 nm, respectively. Data points were corrected for the inner-filter effect by applying Equation 2.8.*

The differential quenching effect of the intermediate-chain NBD-labelled quinidine derivative (**5**) may be qualitatively explained by an equilibrium process. As diffusion measurements suggest that this molecule aggregates in solution, it is not unreasonable to expect that these

molecules are packed to form micelles in which hydrophilic groups are in contact with the surrounding solvent while hydrophobic groups are sequestered together in the micelle centre (Figure 4.15A). In the case of the intermediate-chain NBD-labelled quinidine derivative (**5**), the quinidine groups, which are monocationic at pH 7.5, are exposed to the aqueous medium on account of their hydrophilic character (represented in blue in Figure 4.15). On the other hand, the NBD fluorophore is hydrophobic in character and prefers the interior of the micelle (represented in orange in Figure 4.15).

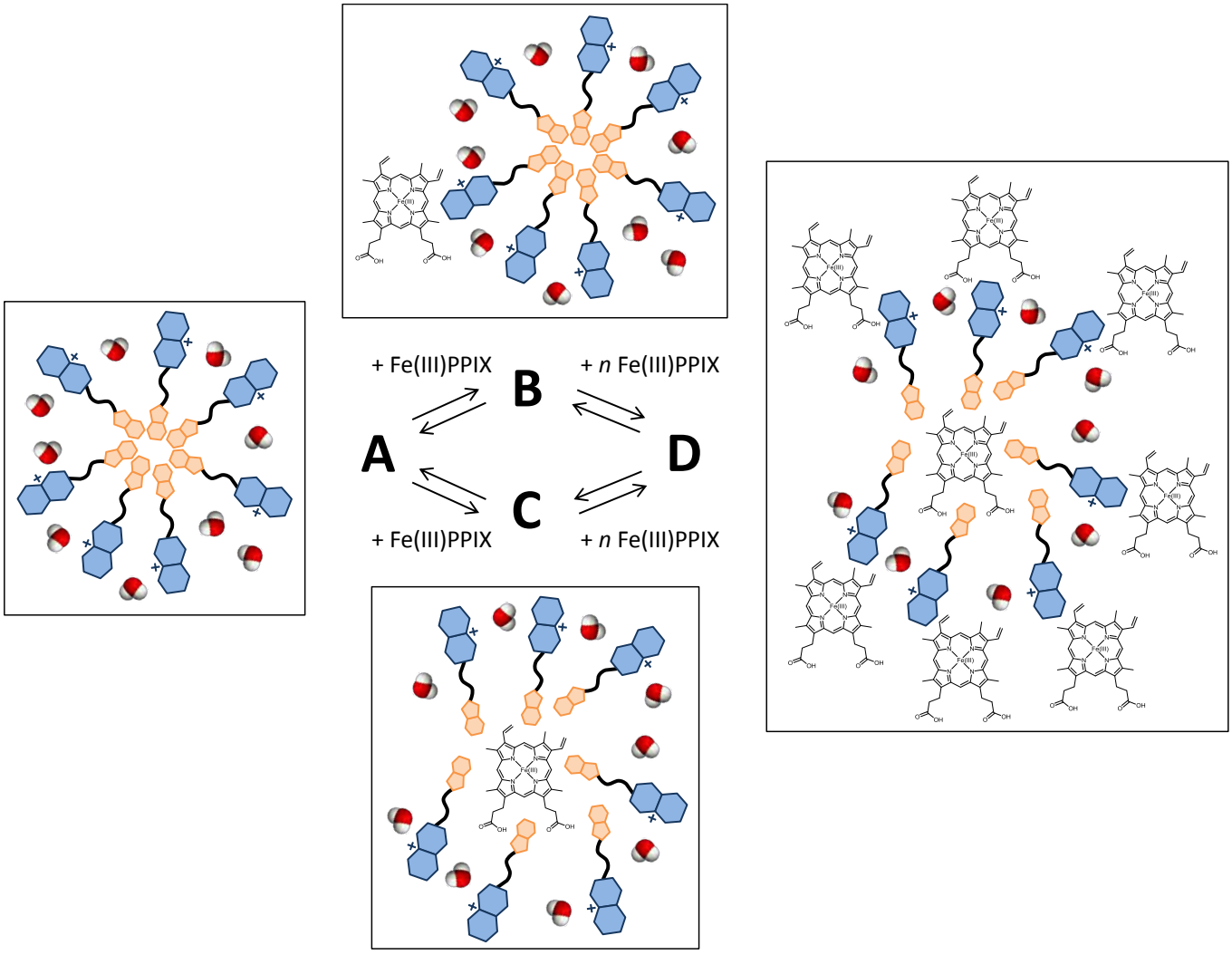

Figure 4.15. *A qualitative equilibrium model rationalising the differential quenching observed for the quinoline and NBD fluorophores of the intermediate-chain NBD-labelled quinidine derivative (**5**) in aqueous solution in the presence of Fe(III)PPIX. The quinoline and NBD fluorophores are represented in blue and orange, respectively. Water molecules are also indicated. Addition of Fe(III)PPIX gives rise to three different arrangements of Fe(III)PPIX (**B-D**) in relation to the micelle (**A**). Addition of a large amount of Fe(III)PPIX* (n) *results in complete quenching of the quinoline and NBD fluorophores.*

In the absence of Fe(III)PPIX, the intermediate-chain NBD-labelled quinidine derivative (**5**) likely forms the micelle arrangement represented in Figure 4.15A. Upon addition of a small amount of Fe(III)PPIX, some quenching of the quinoline may be observed on account of the 1:1 association of the quinoline with Fe(III)PPIX (Figure 4.15B). On the other hand, due to its amphipathic nature, Fe(III)PPIX may prefer to partition within the micelle and hence a small amount of Fe(III)PPIX may quench a larger number of the NBD fluorophores simultaneously (Figure 4.15C). This gives rise to the differential quenching profile observed in Figure 4.14 where the NBD fluorescence appears to be disproportionately quenched at low concentrations of Fe(III)PPIX compared to the quinoline. After a large amount of Fe(III)PPIX is added (*n* equivalents), complete quenching of both the quinoline and NBD fluorophores is observed. This occurs because all of the quinoline groups have been quenched in a 1:1 manner and Fe(III)PPIX has also partitioned within the micelle (Figure 4.15D), quenching all the NBD fluorescence.

As live-cell microscopy is conducted in an aqueous medium, these observations suggest that the intermediate-chain NBD-labelled quinidine derivative (**5**) is a less suitable analogue of the parent molecule compared to its short-chain derivative (**4**). However, in order to conclude definitively which of the derivatives is the most suitable analogue of the parent molecule, it was necessary to test these derivatives against β-haematin inhibition and, most importantly, *P. falciparum*, as described in the subsequent section.

4.4. Evaluation of the activities of novel fluorescent derivatives

The mechanism of haemozoin formation in the malaria parasite implicates neutral lipid bodies as sites of nucleation and crystal growth (Section 1.3.2).[27-29] However, the relatively high cost of lipids and the handling times required to prepare a suitable lipid blend are not amenable to initial laboratory screening. Instead, an assay to monitor synthetic haemozoin (β-haematin) formation based on the low-cost, commercially-available detergent NP-40 has been developed (Section 1.4.4).[30,31] This detergent acts as a surrogate for neutral lipid droplets to promote crystallisation under physiologically-relevant conditions. β-Haematin inhibition is quantified by means of the colourimetric pyridine-ferrichrome method in which pyridine forms a low-spin complex with Fe(III)PPIX but not with β-haematin.[32] Monitoring the absorbance at the Soret band of the pyridine-Fe(III)PPIX complex (405 nm) provides a rapid quantification of β-haematin inhibition.

The parent quinoline antimalarials as well as their fluorescent derivatives were tested using this assay, the results of which are listed in Table 4.8. These are presented as IC_{50} values, i.e. the concentration of compound needed to inhibit β-haematin formation by 50%. Representative examples of sigmoidal dose-response curves obtained for quinine, its bimane-labelled derivative (**19**) and the monobromobimane starting material (Figure 3.11) are presented in Figure 4.16.

IC_{50} values of 52.3 ± 1.3 μM and 24.7 ± 0.6 μM were obtained for quinine and quinidine, respectively. The result is consistent with previous assays in which quinidine is a more potent β-haematin inhibitor than quinine.[19] Chloroquine (22.0 ± 0.8 μM) was found to have similar activity to quinidine.

Significantly, all fluorescent derivatives were found to be more active than their parent compounds. The NBD-labelled derivative of quinine (**3**) was a more potent β-haematin inhibitor than its bimane analogue (**19**). Both of these derivatives were more active than quinine itself. The short-chain derivative of quinidine (**4**) was the most active of all the tested compounds (5.2 ± 0.07 μM), although only slightly more active that its intermediate-chain counterpart (**5**) at 6.5 ± 0.1 μM. The long-chain derivative of quinidine was the least active of the three NBD-labelled quinidine derivatives (**6**) most likely because of its poor aqueous solubility; however, it was still more active than its parent compound. The NBD-labelled chloroquine (**8**) was also more active than its parent antimalarial with an IC_{50} value of almost half that of chloroquine.

Table 4.8. *50% inhibitory activities (IC_{50}) of quinoline antimalarials and their fluorescently-labelled derivatives measured using the NP-40 detergent-mediated assay for β-haematin inhibition and an in vitro assay against* P. falciparum*. Measurements were performed in triplicate and uncertainties represent standard errors of the mean.*

Entry	Compound	β-Haematin inhibition IC_{50}, μM	*P. falciparum* IC_{50}, nM (NF54 strain)	*P. falciparum* IC_{50}, nM (Dd2 strain)
1	Quinine	52.3 ± 1.3	62 ± ND	//
2	Quinine-NBD (**3**)	12.1 ± 0.01	100 ± 2	//
3	Quinine-Bimane (**19**)	30.4 ± 1.6	721 ± 17	//
4	Quinidine	24.7 ± 0.6	43 ± 7	//
5	Quinidine-NBD (**4**)	5.2 ± 0.07	109 ± 4	//
6	Quinidine-HexNBD (**5**)	6.5 ± 0.1	190 ± 30	//
7	Quinidine-DodecNBD (**6**)	12.1 ± 2.2	39 ± 18	//
8	Chloroquine	22.0 ± 0.8	14 ± 3	179 ± 14
9	Chloroquine-NBD (**8**)	14.3 ± 0.8	10 ± 0.3	22 ± 7

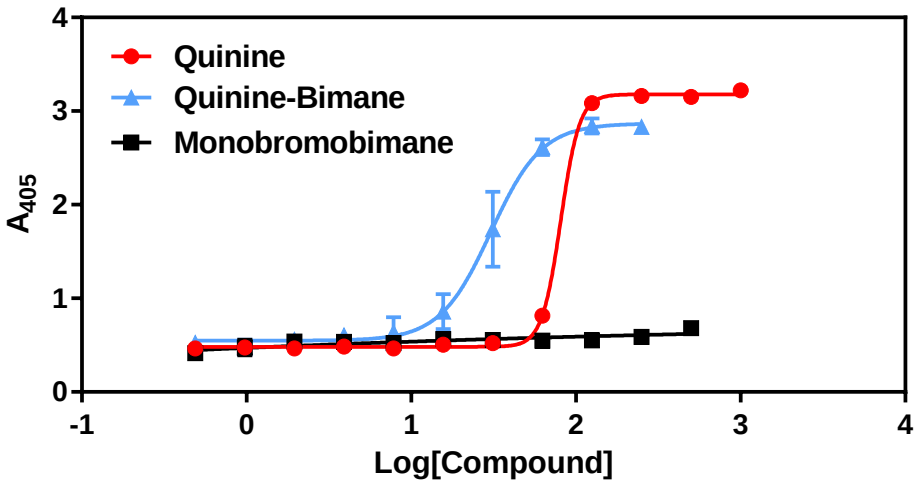

Figure 4.16. *Representative examples of sigmoidal dose-response curves obtained using the NP-40 detergent-mediated assay for quinine (red) and quinine-bimane derivative (blue), both of which showed activity against β-haematin formation. Monobromobimane (black) was inactive.*

Compounds were also tested for antiplasmodial activity in vitro against *P. falciparum* and quantified via the lactate dehydrogenase method developed by Makler et al.[33] The results are also reported as IC_{50} values in Table 4.8. For the parent alkaloids and their fluorescent derivatives, activity was only tested against the chloroquine-sensitive NF54 strain. Quinidine was again found to be a more potent antimalarial than quinine, corroborating previous

observations.[7] Intriguingly, the opposite relationship was observed between their respective short-chain derivatives whereby the NBD-labelled quinidine derivative (**4**, 109 ± 4 nM) was less active than the NBD-labelled quinine derivative (**3**, 100 ± 2 nM). In contrast to the results for β-haematin formation, both of these derivatives were only about half as potent as their parent alkaloids. The long-chain NBD-labelled quinidine derivative (**6**) was the most potent of all three NBD-labelled quinidine derivatives. Presumably its enhanced lipophilicity allows it to cross bilayers or embed itself in biological membranes more efficiently, increasing its potency against *P. falciparum*.

Despite favourable physicochemical interactions with Fe(III)PPIX and its capacity to inhibit β-haematin formation, the bimane-labelled quinine derivative (**19**) was found to be much less active against *P. falciparum* (721 ± 17 nM). This indicates that this derivative is not, in fact, a suitable analogue of its parent alkaloid. Hence the short-chain NBD-labelled quinine derivative (**3**) is a more suitable fluorescent analogue of quinine than its bimane-labelled counterpart (**19**). While further work will be needed to ascertain the reason(s) for the reduced activity of the quinine-bimane conjugate (**19**) against *P. falciparum*, one does not expect the trends of the NP-40 assay to directly parallel the results of the biological testing. While the conditions of the β-haematin formation assay closely mimic biological conditions, other factors such as lipophilicity become important when considering, for example, permeability through membranes in a biological system.

Chloroquine and its NBD-labelled derivatives were tested against the chloroquine-sensitive and chloroquine-resistant NF54 and Dd2 strains, respectively (Table 4.8). The NBD-labelled chloroquine derivative (**8**) exhibited improved activity compared to its parent compound in both strains. In the resistant Dd2 strain, a two-fold reduction in the activity of the chloroquine derivative was observed compared to a 12-fold reduction in the activity of its parent. The large increase in the IC_{50} value of chloroquine against this strain is genuine evidence of resistance while, on the other hand, the small two-fold change in the IC_{50} value of the fluorescent derivative shows that its activity against the resistant strain was, in fact, largely retained. This is consistent with previous observations that modifications to the chloroquine side-chain are sufficient to overcome resistance mechanisms and hence are major determinants in cross-resistance.[34,35]

4.5. Summary and conclusions

Six novel fluorescent derivatives of the quinoline antimalarials were synthesised as described in Chapter 3 and as depicted in Figure 4.1. The broad aim of this chapter was to evaluate these derivatives using a suite of photophysical and physicochemical techniques in order to determine which of these derivatives were the most suitable analogues of the parent antimalarials for use in live-cell microscopy. The most important component of this evaluation was the measurement of their biological activities against *P. falciparum*.

Photophysical characterisation indicated that the NBD-labelled derivatives possess a lower-energy absorption band (λ_{max} approximately 480 nm) corresponding to the primary absorption band of the NBD fluorophore and a higher-energy band in the ultraviolet region corresponding to the superposition of the secondary absorption band of the NBD fluorophore and the absorption band of the quinoline core. Fluorescence emission following excitation at either of these wavelengths was observed at approximately 540 nm. This fluorescence exhibited a small solvatochromic shift from 525-550 nm over ten common solvents which showed excellent correlation with the $E_T(30)$ polarity parameter (R^2 = 0.980). Fluorescence emission of the NBD-labelled derivatives was enhanced in non-polar media but modest in aqueous solution, suggesting that this fluorophore was particularly suitable for evaluating the association of these derivatives with non-aqueous or lipid components of *P. falciparum*.

Fluorescence quantum yields of all derivatives were higher in ethanol than in mixed aqueous solution, except for the NBD-labelled chloroquine derivative (**8**) for which the aqueous fluorescence quantum yield was higher than in ethanol. While substantial fluorescence was observed from the 4-amino-7-chloroquinoline heterocycle (approximately 380 nm), the corresponding fluorescence from the 6-methoxyquinoline heterocycle was greatly diminished in the bimane-labelled quinine derivative (**19**) and was absent in the NBD-labelled alkaloids (**3-6**). This suggests that non-radiative energy transfer between the two fluorophores in the latter cases may be efficiently facilitated by a Förster resonance energy transfer mechanism. This observation was rationalised by quantitative predictions of spectral overlap and evaluation of the characteristic Förster distances R_0 between the donor-acceptor pairs.

As the binding stoichiometries and association constants of these antimalarials with Fe(III)PPIX have been well characterised,[4,5] these measurements were used as benchmarks to determine whether the fluorescently-labelled derivatives had retained key physicochemical properties that were likely to be important for their in vitro activities. Spectrophotometric titrations revealed that a 1:1 binding stoichiometry to Fe(III)PPIX was conserved for the NBD-labelled

alkaloids, vindicating the design choice to functionalise the vinyl group of these molecules. The strength of association with Fe(III)PPIX was also retained, albeit slightly enhanced in the NBD-labelled derivatives and most likely due to improved π-stacking interactions with the heterocyclic NBD fluorophore. Unfortunately these values could not be measured for the long-chain NBD-labelled alkaloid (**6**) as suitably high concentrations could not be reached. A 2:1 binding stoichiometry to chloroquine and its NBD-labelled derivative (**8**) was observed and μ-oxo dimerisation of Fe(III)PPIX in aqueous solution was confirmed by magnetic circular dichroism, indicating that addition of the NBD fluorophore does not affect the capacity of this derivative to induce μ-oxo dimerisation of Fe(III)PPIX.

In order to evaluate further the physicochemical properties of the three NBD-labelled quinidine derivatives with varying chain lengths (**4-6**), their aqueous solubilities and diffusion coefficients were measured. Their aqueous solubilities were reduced compared to the parent molecules, most likely as a result of the incorporation of the hydrophobic NBD fluorophore. The long-chain NBD-labelled quinidine derivative (**6**) was particularly insoluble, indicating its unsuitability for microscopy. Furthermore, the intermediate-chain quinidine derivative (**5**) aggregates in aqueous solution. This may result from micelle formation in which the hydrophobic fluorophore is screened from the aqueous milieu, also indicating the unsuitability of this derivative.

A detergent-mediated assay indicated that all of these derivatives retained their abilities to inhibit β-haematin formation and, indeed, were more active β-haematin inhibitors than the drugs. Crucially, the NBD-labelled derivatives were all active against the chloroquine-sensitive NF54 strain of *P. falciparum* with IC_{50} values in the nanomolar range. Surprisingly, the bimane-labelled derivative of quinine (**19**) was much less active against this strain (IC_{50} > 700 nM) indicating that, despite an otherwise-favourable physicochemical profile, it was unsuitable as an analogue of quinine. The NBD-labelled chloroquine derivative (**8**) was active against the NF54 strain and somewhat less active against the chloroquine-resistant Dd2 strain. The two-fold reduction in the activity of this derivative compared to the 12-fold reduction in the activity of chloroquine in the resistant strain is consistent with previous observations that modifying the chloroquine side-chain may overcome mechanisms of resistance in resistant strains.

Taken together, these results indicate that the short-chain NBD-labelled alkaloids (**3**, **4**) are the most suitable analogues of quinine and quinidine, respectively, by virtue of the retention of their interactions with Fe(III)PPIX and their potent activities against β-haematin formation in *P. falciparum*. For the same reasons, the NBD-labelled chloroquine derivative (**8**) is a suitable analogue of its parent molecule. Hence, these novel fluorescent derivatives were exploited in live-cell fluorescence microscopy studies of *P. falciparum* as described in Chapter 5.

4.6. References

1. G. H. Jacobs, A. Oduola, D. E. Kyle, W. K. Milhous, S. K. Martin and M. Aikawa, *Am. J. Trop. Med. Hyg.*, 1988, **39**, 87.
2. N. Sachanonta, K. Chotivanich, U. Chaisri, G. D. H. Turner, D. J. P. Ferguson, N. P. J. Day and E. Pongponratn, *Ultrastruct. Pathol.*, 2011, **35**, 214.
3. L. Roberts, T. J. Egan, K. A. Joiner and H. C. Hoppe, *Antimicrob. Agents Chemother.*, 2008, **52**, 1840.
4. T. J. Egan, *J. Inorg. Biochem.*, 2006, **100**, 916.
5. D. Kuter, S. Benjamin and T. J. Egan, *J. Inorg. Biochem.*, 2014, **133**, 40.
6. Y. Kuhn, P. Rohrbach and M. Lanzer, *Cell. Microbiol.*, 2007, **9**, 1004.
7. D. C. Warhurst, J. C. Craig, I. S. Adagu, D. J. Meyer and S. Y. Lee, *Malar. J.*, 2003, **2**, 26.
8. W. H. Melhuish, *J. Phys. Chem.*, 1961, **65**, 229.
9. C. Reichardt, *Chem. Rev.*, 1994, **94**, 2319.
10. K. A. Zacharlasse, N. V. Phuc and B. Kozanklewicz, *J. Phys. Chem.*, 1981, **85**, 2676.
11. A. N. Hoang, R. D. Sandlin, A. Omar, T. J. Egan and D. W. Wright, *Biochemistry*, 2010, **49**, 10107.
12. P. B Macomber, H. Sprinz and A. J. Tousimis, *Nature*, 1967, **214**, 937.
13. A. C. Chou, R. Chevli and C. D. Fitch, *Biochemistry*, 1980, **19**, 1543.
14. J. Gildenhuys, T. le Roux, T. J. Egan and K. A. de Villiers, *J. Am. Chem. Soc.*, 2013, **135**, 1037.
15. J. Gildenhuys, C. J. Sammy, R. Muller, V. A. Streltsov, T. le Roux, D. Kuter and K. A. de Villiers, *Dalton Trans.*, 2015, **44**, 16767.
16. J. M. Combrinck, T. E. Mabotha, K. K. Ncokazi, M. A. Ambele, D. Taylor, P. J. Smith, H. C. Hoppe and T. J. Egan, *ACS Chem. Biol.*, 2013, **8**, 133.
17. G. S. Collier, J. M. Pratt, C. R. de Wet and C. F. Tshabalala, *Biochem. J.*, 1979, **179**, 281.
18. T. J. Egan, W. W. Mavuso, D. C. Ross, H. M. Marques, 1997, *J. Inorg. Biochem*., 1997, **68**, 137.
19. T. J. Egan, E. Hempelmann and W. W. Mavuso, *J. Inorg. Biochem.*, 1999, **73**, 101.
20. Z. D. Hill and P. MacCarthy, *J. Chem. Ed.*, 1986, **63**, 62.
21. K. A. de Villiers, J. Gildenhuys and T. le Roux, *ACS Chem. Biol.*, 2012, **7**, 666.
22. K. A. de Villiers, H. M. Marques and T. J. Egan, *J. Inorg. Biochem.*, 2008, **102**, 1660.
23. P. W. Linder, L. R. Nassimbeni, A. Polson and A. L. Rodgers, *J. Chem. Ed.*, 1976, **53**, 330.
24. T. M. Aminabhavi and B. Gopalakrishna, *J. Chem. Eng. Data*, 1995, **40**, 856.
25. K. E. Gustafson and R. M. Dickhut, *J. Chem. Eng. Data*, 1994, **39**, 281.
26. R. Niesner and A. Heintz, *J. Chem. Eng. Data*, 2000, **45**, 1121.
27. K. E. Jackson, N. Klonis, D. J. P. Ferguson, A. Andisa, C. Dogovski and L. Tilley, *Mol. Microbiol.*, 2004, **54**, 109.
28. I. Coppens and O. Vielemeyer, *Int. J. Parasitol.*, 2005, **35**, 597.

29. J. M. Pisciotta, I. Coppens, A. K. Tripathi, P. F. Scholl, J. Shuman, S. Bajad, V. Shulaev and D. J. Sullivan, *Biochem. J.*, 2007, **402**, 197.
30. M. D. Carter, V. V. Phelan, R. D. Sandlin, B. O. Bachmann and D. W. Wright, *Comb. Chem. High Throughput Screen.*, 2010, **13**, 205.
31. R. D. Sandlin, M. D. Carter, P. J. Lee, J. M. Auschwitz, S. E. Leed, J. D. Johnson and D. W. Wright, *Antimicrob. Agents Chemother.*, 2011, **55**, 3363.
32. K. K. Ncokazi and T. J. Egan, *Anal. Biochem.*, 2005, **338**, 306.
33. M. T. Makler, J. M. Ries, J. A. Williams, J. E. Bancroft, R. C. Piper, B. L. Gibbins and D. J. Hinrichs, *Am. J. Trop. Med. Hyg.*, 1993, **48**, 739.
34. R. G. Ridley, W. Hofheinz, H. Matile, C. Jaquet, A. Dorn, R. Masciadri, S. Jolidon, W. F. Richter, A. Guenzi, M. A. Girometta, H. Urwyler, W. Huber, S. Thaithong and W. Peters, *Antimicrob. Agents Chemother.*, 1996, **40**, 1846.
35. D. De, F. M. Krogstad, L. D. Byers and D. J. Krogstad, *J. Med. Chem.*, 1998, **41**, 4918.

Chapter Five

Live-Cell Fluorescence Microscopy of Novel Analogues of the Quinoline Antimalarials

5.1. Introduction

Although quinoline-based drugs are regarded by many as the archetypal antimalarials, the intimate details of their mechanism of action against *Plasmodium falciparum* remain unclear. While most investigations have focused on the inhibition of haemozoin formation as their primary target and hence on the accumulation of these drugs within the digestive vacuole, these molecules may exert additional effects on the parasite. For example, the ultrastructure of several organelles in addition to the digestive vacuole is altered following drug treatment (Section 1.6.2).[1,2] Furthermore, quinine (representing the quinoline methanols) and chloroquine (representing the 4-aminoquinolines) generate differential morphological effects on the parasite.[3,4] While these effects may merely reflect the physicochemical differences between these two classes of antimalarials, they also suggest possible secondary targets within *P. falciparum*.

Investigating the subcellular localisation of these antimalarials in *P. falciparum*, with emphasis on organelles other than the digestive vacuole, may reveal deeper insights into their mode(s) of action. Hence, novel fluorescent derivatives representing the two major classes of these quinoline drugs were designed and synthesised (Chapter 3). These fluorescent derivatives were thoroughly evaluated in order to determine which of these were the most suitable analogues of

the parent compounds (Chapter 4). These experiments identified the short-chain NBD-labelled derivatives of quinine and quinidine (**3** and **4**, respectively) and the NBD-labelled chloroquine derivative (**8**) as suitable analogues of their parent antimalarials. These analogues were therefore exploited in the live imaging studies described in this chapter.

Several challenges associated with live imaging of the malaria parasite, notably its sensitivity to light and the restrictions posed by the diffraction limit of light, will be discussed. Several commercially-available tracker dyes used to co-stain organelles and other subcellular structures in this work will be described. Using confocal microscopy, a comprehensive survey of the accumulation and distribution of these analogues in *P. falciparum*-infected erythrocytes will be presented. Accumulation relative to co-illuminated organelles including the nucleus, endoplasmic reticulum (ER), mitochondrion and membranes will be illustrated. Quantitative colocalisation analysis was used to add rigour to these qualitative observations and a time-lapse study to investigate accumulation of the NBD-labelled quinine analogue across the 48-hour intraerythrocytic life cycle of the parasite was also conducted.

In order to address some of the limitations associated with the small size of the parasite, super-resolution structured-illumination microscopy (SR-SIM), which offers a two-fold improvement in resolution over confocal imaging, was employed. Once again, the colocalisation of the analogues was investigated relative to the ER, mitochondrion and membranes using the lipid-specific stains LysoTracker and Nile Red. Observations regarding the prevalence and size distribution of haemozoin-associated neutral lipid bodies in the presence and absence of drug treatment will be presented. Finally, a critical discussion of all the major points arising from the live-cell imaging experiments in this chapter will be given.

Thus the specific objectives described in this chapter were:

i. To establish conditions suitable for live-cell imaging of *P. falciparum*;
ii. To observe accumulation of the novel fluorescent analogues of the quinoline antimalarials within *P. falciparum*-infected erythrocytes;
iii. To investigate general patterns of distribution, qualitatively and quantitatively, of these analogues relative to tracker dyes for organelles such as the nucleus, ER, mitochondrion and membranous structures using both confocal and super-resolution microscopies;
iv. To generate new insights into the stage-specificity and size distribution of neutral lipid bodies in *P. falciparum* in the presence and absence of the NBD-labelled analogues;

5.2. General considerations for live-cell imaging of *P. falciparum*

5.2.1. Photosensitivity and endogenous fluorescence

While live-cell fluorescence microscopy provides exceptional insights into structural and functional details of the intraerythrocytic malaria parasite, an important consideration for *P. falciparum* is that the parasite is extremely light-sensitive.[5] Moderate exposure to light causes irreversible acidification of the parasite cytosol by as much as a whole pH unit, probably due to disruption of the digestive vacuole membrane (Figure 5.1).[5]

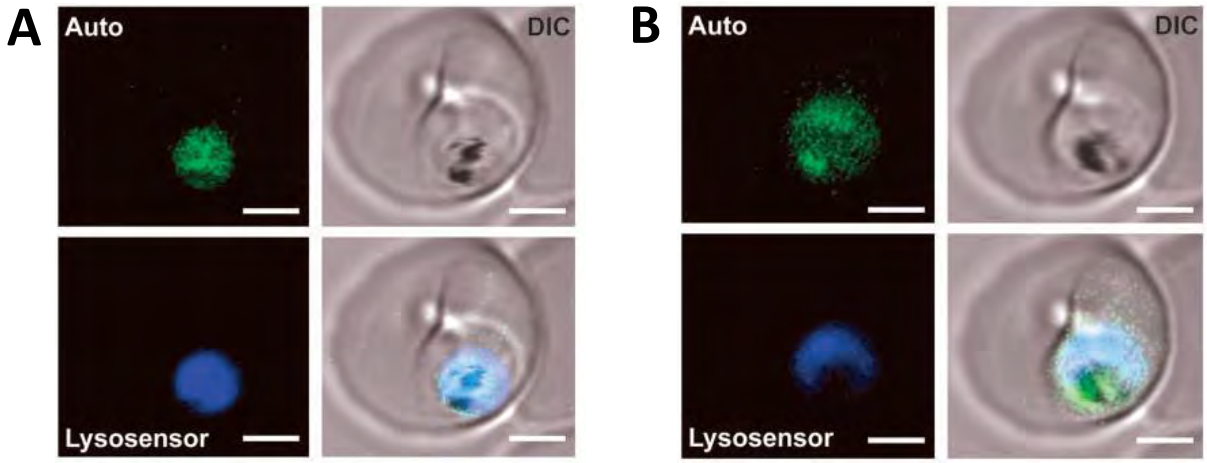

Figure 5.1. *An illustration of the susceptibility of* P. falciparum *to photodamage via rupture of the digestive vacuole upon strong illumination. Panel A represents an infected erythrocyte stained with LysoSensor Blue DND-192 ("Lysosensor") which colocalises with a weak autofluorescence arising from the cell ("Auto"). In Panel B, after 40 exposures at five-second intervals, both the autofluorescence and LysoSensor staining are found throughout the cytosol, indicating its acidification. Scale bars represent 2 μm. Reproduced from Wissing et al.,* J. Biol. Chem.*, 2002, **277**, 37747 with permission from the American Society of Biochemistry and Molecular Biology.*

The authors hypothesise that the digestive vacuole membrane is highly susceptible to photodamage as a result of ferriprotoporphyrin IX, Fe(III)PPIX, which acts as a photosensitiser. A rapid increase in hydroxyl radicals is observed during irradiation.[5] These are believed to be produced by a Fenton reaction with hydrogen peroxide which is produced during autoxidation of Fe(II)PPIX to Fe(III)PPIX, catalysed in turn by ferrous iron, viz.

$$Fe^{2+} + H_2O_2 \rightarrow Fe^{3+} + HO^{\bullet} + HO^{-}$$

The hydroxyl radicals result in peroxidation of polyunsaturated fatty acids which are enriched in the digestive vacuole membrane, resulting in disruption of the membrane and acidification of the cytosol.[5] Furthermore, hydrogen peroxide released during haemoglobin degradation has been shown to inhibit the digestive vacuolar H^+-ATPase directly (Section 1.3.4), disrupting pH regulation in the parasite by loss of the pH gradient rather than by loss of integrity of the digestive vacuole membrane.[6] This has been confirmed by ultrastructural studies.[6]

In order to reduce artefacts arising from photodamage of *P. falciparum* in this work, exposure of cells to light was kept at a minimum. Nevertheless, exposure to high-energy illumination was sometimes unavoidable, particularly in confocal microscopy for which high excitation energies are often required. Thus, in order to ensure that irreversible acidification of the parasite had not occurred over the course of an experiment, the autofluorescence of the digestive vacuole was monitored before and after each acquisition to ensure that membrane integrity had been maintained.

Autofluorescence in *P. falciparum* arises from the haemozoin pigment and is also observed from its synthetic equivalent, β-haematin (Figure 5.2).[7] Both species of crystalline Fe(III)PPIX exhibit a solid-state exciton fluorescence characterised by excitation and emission maxima of 555 and 577 nm, respectively.[7] This excitation maximum corresponds to the Q-band in the absorption spectrum which represents the lowest-energy singlet state of the material. The quantum yield of this autofluorescence is very low which makes it unsuitable for extensive imaging, but this is in fact advantageous as the signal is unlikely to interfere with the fluorescence of the much brighter fluorescent dyes used in this work.

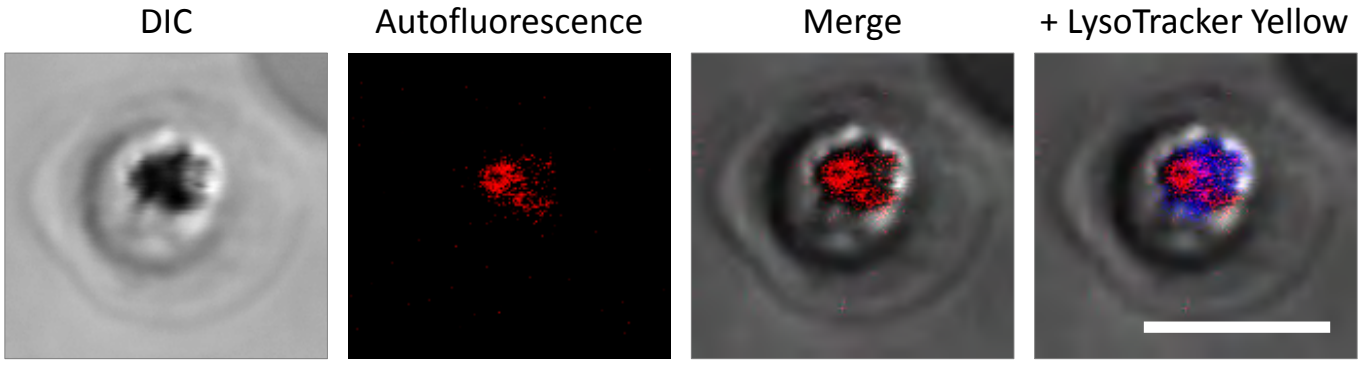

Figure 5.2. *Haemozoin autofluorescence (red) originating from the digestive vacuole of* P. falciparum*, detected following excitation with the 561 nm laser and emission from the 575-630 nm filter. This autofluorescence colocalises with the signal from LysoTracker Yellow (false-coloured blue) which is specific for the digestive vacuole of the parasite. The scale bar represents 5 μm.*

5.2.2. Stage-dependent sensitivity of *P. falciparum* to quinoline antimalarials

Although the intraerythrocytic life cycle of *P. falciparum* may be conveniently divided into the ring, trophozoite and schizont stages based on morphology and metabolism (Section 1.2.2.), considerable variation is demonstrated amongst these stages in their sensitivities to the quinoline antimalarials. In order to address this, Yayon et al. monitored the effects of clinically-relevant doses of chloroquine on *P. falciparum* by three different techniques and found that the trophozoite and schizont-stage were considerably more sensitive to chloroquine than ring-stage parasites.[8] Furthermore, chloroquine sensitivity decreased as nuclear division neared completion.[8] These findings were identical in chloroquine-sensitive and -resistant strains.[8]

The authors commented that this stage-specificity in chloroquine sensitivity may be related to changes exhibited by later-stage parasites with respect to the rate of uptake of the drug, the presence of intracellular factors, changes in the chloroquine receptor site or changes in a metabolic process that is specifically inhibited by the drug.[8] These comments from over three decades ago are insightful in the light of recent work which confirms the primary role of chloroquine as a haemozoin inhibitor and shows that a concomitant dose-dependent increase in free Fe(III)PPIX is correlated with a decrease in parasite growth.[9]

For quinine, stage-specific experiments indicated that its primary mode of action is exerted on mature-stage parasites, producing 80% growth inhibition in schizonts within two hours of drug exposure and 100% growth inhibition of trophozoites over the same period.[10] More recently, a flow cytometry-based approach for assessing the stages of the parasite life cycle showed that quinine and chloroquine both cause parasite death during the trophozoite stage.[11] Wilson et al. found it unlikely that either of these drugs exert additional antimalarial efficacy through inhibition of merozoite invasion, ring development or schizont rupture.[11] (It should be noted here that a single study found that ring-stage parasites are more susceptible to chloroquine than trophozoites, and that chloroquine in therapeutic concentrations prevented the transformation of rings to trophozoites.[12])

Consequently, in this work, only trophozoite- or schizont-stage parasites were examined as these stages of the intraerythrocytic life cycle are most sensitive to the quinoline antimalarials under investigation. Furthermore, this period is characterised by intense metabolic activity and parasite growth, alleviating some of the problems associated with the small size of the cells and the practical challenges posed by resolution.

5.2.3. Overcoming the challenges of resolution for imaging *P. falciparum*

Erythrocytes are already amongst the smallest of mammalian cells; *P. falciparum* is smaller still. Depending on the stage of its intraerythrocytic life cycle, the parasite varies in size from 1 μm to 6 μm. Consequently, organelles such as the nucleus and digestive vacuole are even smaller and make the quantification of signals from these structures using widefield or confocal microscopy challenging.

Furthermore, large amounts of haemoglobin and free Fe(III)PPIX within the infected host cell and *P. falciparum* present further complicating factors.[13] Fe(III)PPIX is highly photoactive and may interfere with fluorescence excitation and emission signals. While isolating the parasites from the host cell via detergent lysis may provide some relief, this practice introduces problems of its own and most likely perturbs the natural metabolic processes of the parasite.

Despite its obvious value in providing high-resolution images, electron microscopy is limited in its usefulness for investigating *P. falciparum* for several reasons. Firstly, membrane preservation in parasites is generally poor following sample preparation and this creates problems with identifying organelles in micrograph sections. Furthermore, serial sectioning is laborious, making it difficult to analyse the large number of cells necessary to obtain an overall picture of an organism's organisation. Imaging live cells, on the other hand, offers the possibility of observing organelle morphology dynamically with minimal perturbation. However, light microscopy suffers from the so-called "diffraction limit" and traditional microscopy is fundamentally limited in its ability to resolve small cellular structures (Section 2.5.3).

Thus, in order to overcome these limitations, a "super-resolution" technique was employed in the latter part of this work. Super-resolution structured-illumination microscopy (SR-SIM) is the simplest but also the most versatile of these techniques, offering an improvement in confocal resolution of up to two-fold without any special fluorophores or unusual sample preparation. This technique uses patterned illumination to reveal new information about the sample and was described fully in Section 2.5.4.

A comparison between widefield (epifluorescence) imaging and SR-SIM is shown in Figure 5.3. The resolution enhancement in the lower panel is clearly visible. Colocalisation, in which the fluorescent molecules exhibit spatial overlap due to association with the same cellular structures, is clearly visible between the red and the green channels and manifests as yellow in the merged images. These channels represent LysoTracker Red, which illuminates the membranes of acidic compartments, and the NBD-labelled quinine derivative, respectively.

Neither channel colocalises with the blue signal which represents the nucleus. Preliminary qualitative analysis of Figure 5.3 reveals a preference of the red and green signals for the region surrounding the haemozoin (labelled "Hz") and hence the digestive vacuole.

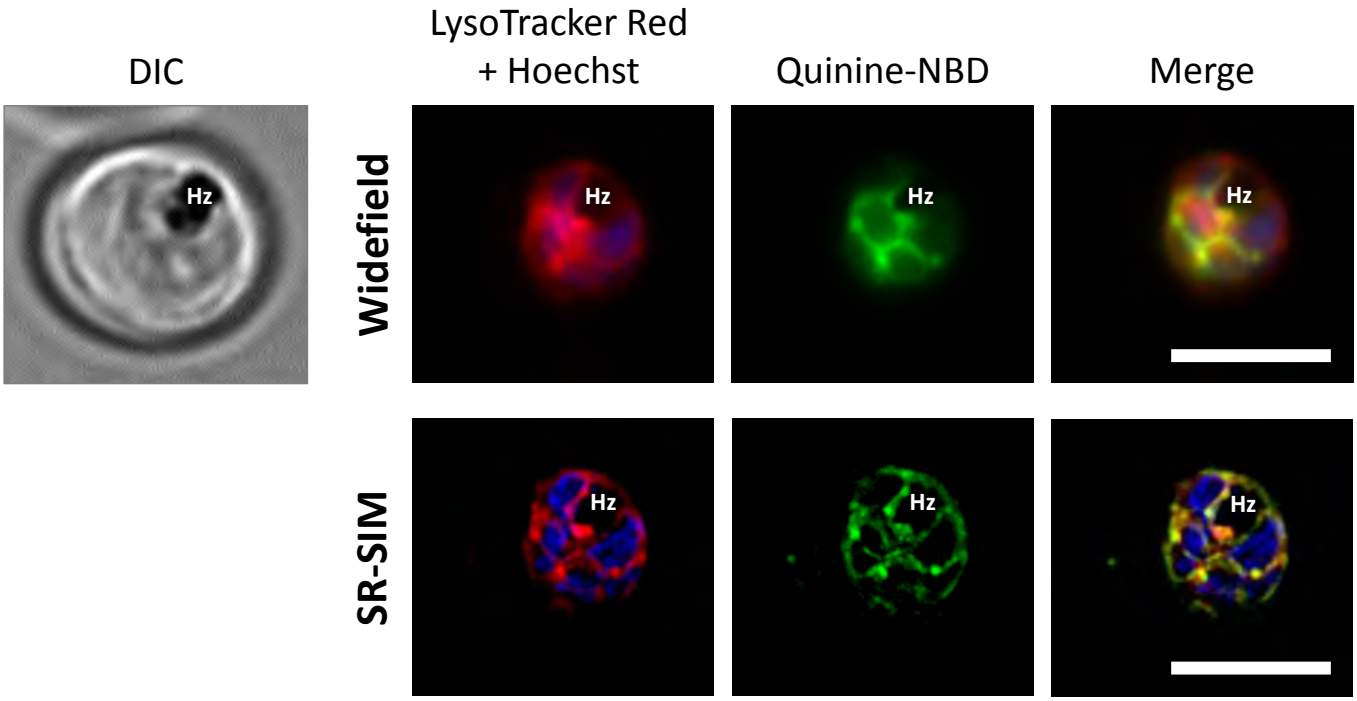

Figure 5.3. *A comparison of widefield and SR-SIM imaging modalities. The upper panel represents a three-colour experiment in widefield mode. The lower panel represents the same experiment using SR-SIM with a concomitant improvement in resolution. Colocalisation between the red and green channels is visible as yellow in the merged images. Haemozoin is labelled "Hz". Scale bars represent 5 µm.*

In order to ensure that multicolour imaging using SR-SIM is reliable, especially for colocalisation analysis, it was necessary to ensure that all fluorescence channels were properly aligned. Hence, the microscope software was carefully calibrated with a channel alignment algorithm for the correction of lateral and axial drift and for chromatic aberration between the different fluorescent channels. For this purpose, multicolour fluorescent beads supplied by the microscope manufacturer were used. The results of the channel alignment algorithm are seen in Figure 5.4. The multicolour beads appear as three separate objects before the alignment; after the alignment algorithm, all three colours overlap precisely with one another. The coefficients obtained from this channel alignment algorithm were then applied to every image set post-acquisition to ensure correct alignment of the fluorescence channels.

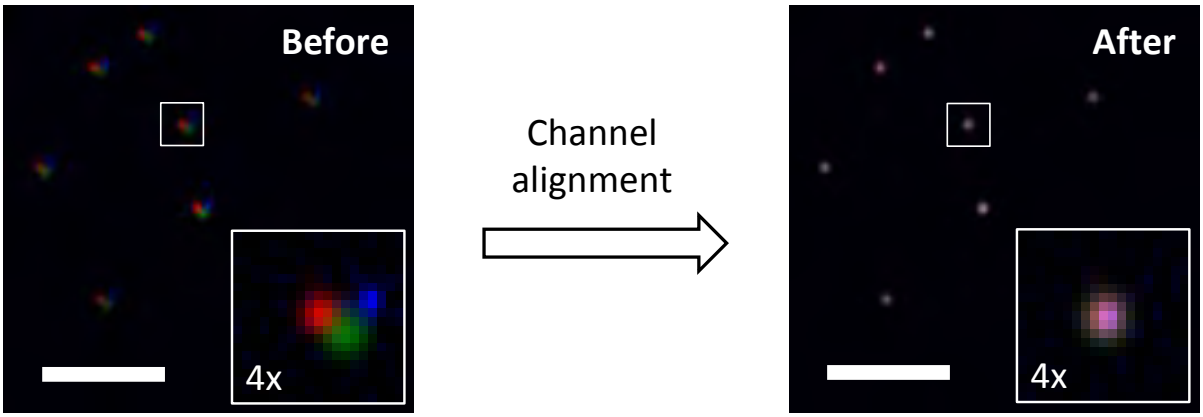

Figure 5.4. *An illustration of the alignment of fluorescence channels before and after the alignment algorithm using multicoloured fluorescent beads. Scale bars represent 0.25 μm but the insets represent a four-fold magnification of the single bead in the small white box.*

All images were acquired over a range of 2 μm which is approximately the thickness of an erythrocyte. This "z-stack" comprises a number of slices approximately 0.1 μm thick in the axial (vertical) direction. Unless otherwise stated, all images presented in this chapter are maximum intensity projections of this acquired stack. Care was taken to evaluate each image stack on its own merits but, usually, maximum intensity projections were high-contrast, fair representations of the three-dimensional organisation of the cells.

5.2.4. Commercially-available tracker dyes used in this work

Several commercially-available tracker dyes were used to co-illuminate cellular compartments or subcellular structures in *P. falciparum*. As described below, these dyes have all been used previously in live imaging of the parasite hence justifying their use in this work. The chemical structures of these trackers are illustrated in Figure 5.5.[14]

Hoechst 33342, hereafter referred to as "Hoechst", is a cell-permeable bis-benzimidazole dye that is widely used to stain DNA in live or fixed cells. In *P. falciparum*, this gives a useful indication of the developmental stages of the asexual parasite. This dye binds to the minor groove of double-stranded DNA with AT-rich regions appearing the most fluorescent[14] and thus is particularly well suited to this study as the genome of *P. falciparum* is AT-rich (82%).[15] Although Hoechst is excited in the ultraviolet region, in this study it was mostly used in conjunction with two-photon excitation (Section 2.5.2).

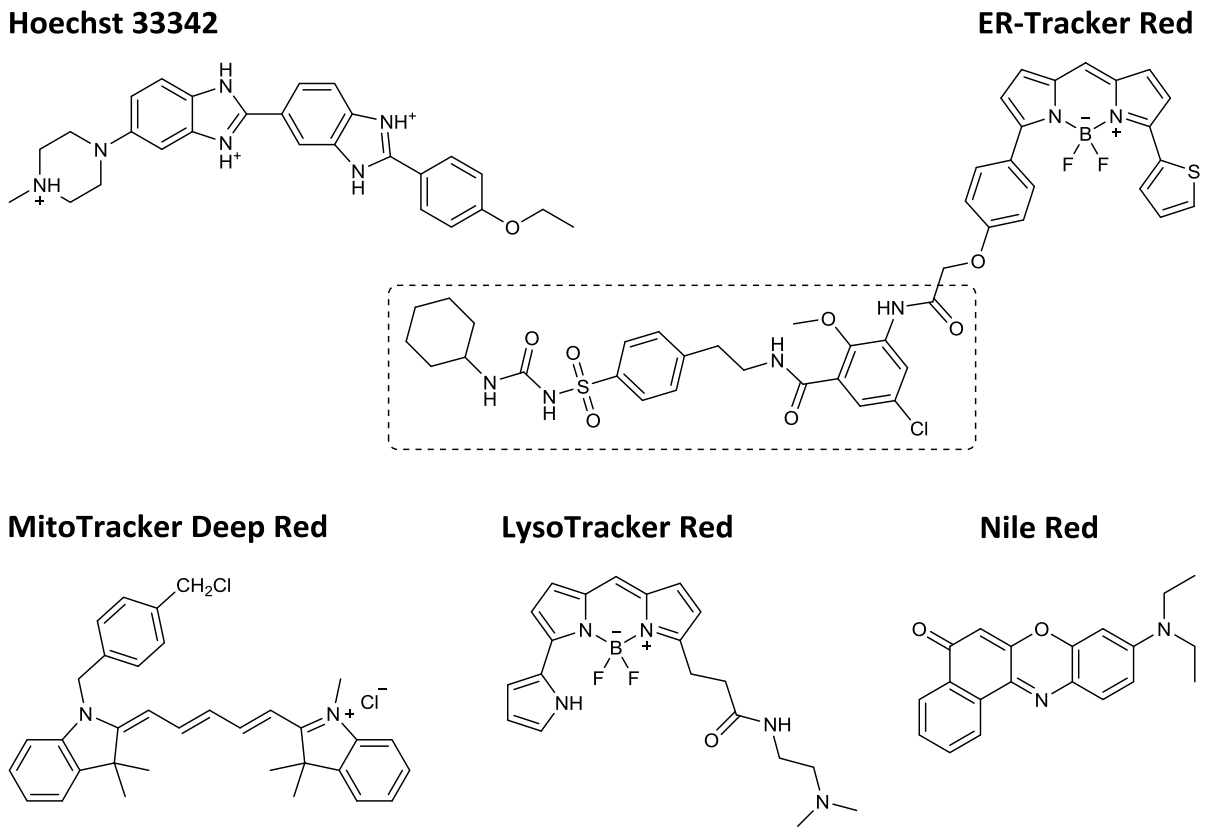

Figure 5.5. *The chemical structures of the commercially-available tracker dyes used in this study. The sulfonylurea drug glibenclamide is shown in the dashed box in its derivatised amide form.*

ER-Tracker Red (Figure 5.5) is a cell-permeable stain that comprises glibenclamide, a sulfonylurea antidiabetic drug, covalently tethered to a BODIPY (boron-dipyrromethane) reporter dye. The manufacturer indicates that glibenclamide binds to the sulfonylurea receptors of ATP-sensitive K^+ channels which are prominent on the ER.[14] However, quinine has also been found to inhibit the binding of a [^{3}H]-glibenclamide derivative to the inner mitochondrial membrane, most likely by binding to its sulfonylurea receptors.[16] Hence the NBD-labelled quinine analogue in this work may compete with ER-Tracker Red for binding to these sulfonylurea receptors. Furthermore, as sulfonylurea receptors may be present on other organelles such as the mitochondrion, non-specific staining may also be observed. Although the localisation of ER-Tracker to the ER has previously been verified in *P. falciparum*,[17] for super-resolution imaging in the latter part of this work care was taken to compare the signal received from the ER-Tracker to the expected morphology of the ER as previously described. This is discussed further in Section 5.4.1.

MitoTracker Deep Red (Figure 5.5) is a far-red carbocyanine dye that passively diffuses across membranes and accumulates in active mitochondria. Its chloromethyl moiety reacts with thiol-

containing cysteine residues in the mitochondria.[14] Thereafter, if the membrane potential in the mitochondrion is lost, the dye is still covalently bound in place. Hence, in order to generate reliable signals from this tracker dye which may be confounded by drug treatment, parasites were incubated first with MitoTracker to ensure covalent accumulation of the dye prior to treatment with the NBD-labelled analogues. MitoTracker Deep Red has previously been used to illuminate mitochondria in *P. falciparum* in combination with the SYBR nuclear dye to develop a medium-throughput flow cytometry-based assay to determine death-inducing compounds.[18]

LysoTracker Red (Figure 5.5) is an acidotropic dye that illuminates acidic organelles in live cells, such as the digestive vacuole in *P. falciparum*. The dye consists of an *N*,*N*-dimethylethylamine motif which, like ER-Tracker Red, is linked to a BODIPY reporter dye.[14] The fluorophore and weak base are together only partially protonated at neutral pH and the dye is thus freely permeable to cell membranes. The weakly basic amine selectively accumulates in low pH compartments due to the weak base effect.[14] LysoTracker Red has previously been used for distinguishing the digestive vacuole of the parasite.[19]

Finally, Nile Red (Figure 5.5) is a lipophilic dye that has been well-characterised and is commonly used to illuminate lipids in cells.[20] It is highly solvatochromic in non-polar environments but is almost entirely quenched in water.[20] Nile Red has previously been used to identify neutral lipid bodies within *P. falciparum* which have been implicated in haemozoin formation (Section 1.3.2).[21] An advantage of Nile Red is that it has very broad excitation and emission spectra, allowing one to distinguish between different chemical environments as described below. A disadvantage of this property is that cross-talk is frequently observed when Nile Red is used in conjunction with other green dyes for which high-energy excitation is required.

When excited using a 561 nm laser and monitored for fluorescence in the red region of the visible spectrum (650-710 nm), Nile Red emits a signal that corresponds to fluorescence from a phospholipid-rich environment.[20] However, if the dye is excited with the same laser but emission is monitored at lower wavelengths (575-630 nm), the resulting signal corresponds to an environment characterised by uncharged or neutral lipids. Thus neutral lipid bodies in *P. falciparum* may be clearly identified using these settings (indicated by white arrows in Figure 5.6).[20] However, if Nile Red is excited with a high-energy laser at 488 nm and emission is measured between 500-550 nm, wavelengths typically used for the detection of fluorophores emitting in the green region of the visible spectrum, cross-talk in the green channel from low-wavelength emission of Nile Red may be detected. This problem may be circumvented by using a narrower filter for green fluorescence to exclude this interfering signal. Recording emission

from 500-520 nm, for example, eliminates the cross-talk but also reduces the amount of light that is collected from the green fluorophore itself.

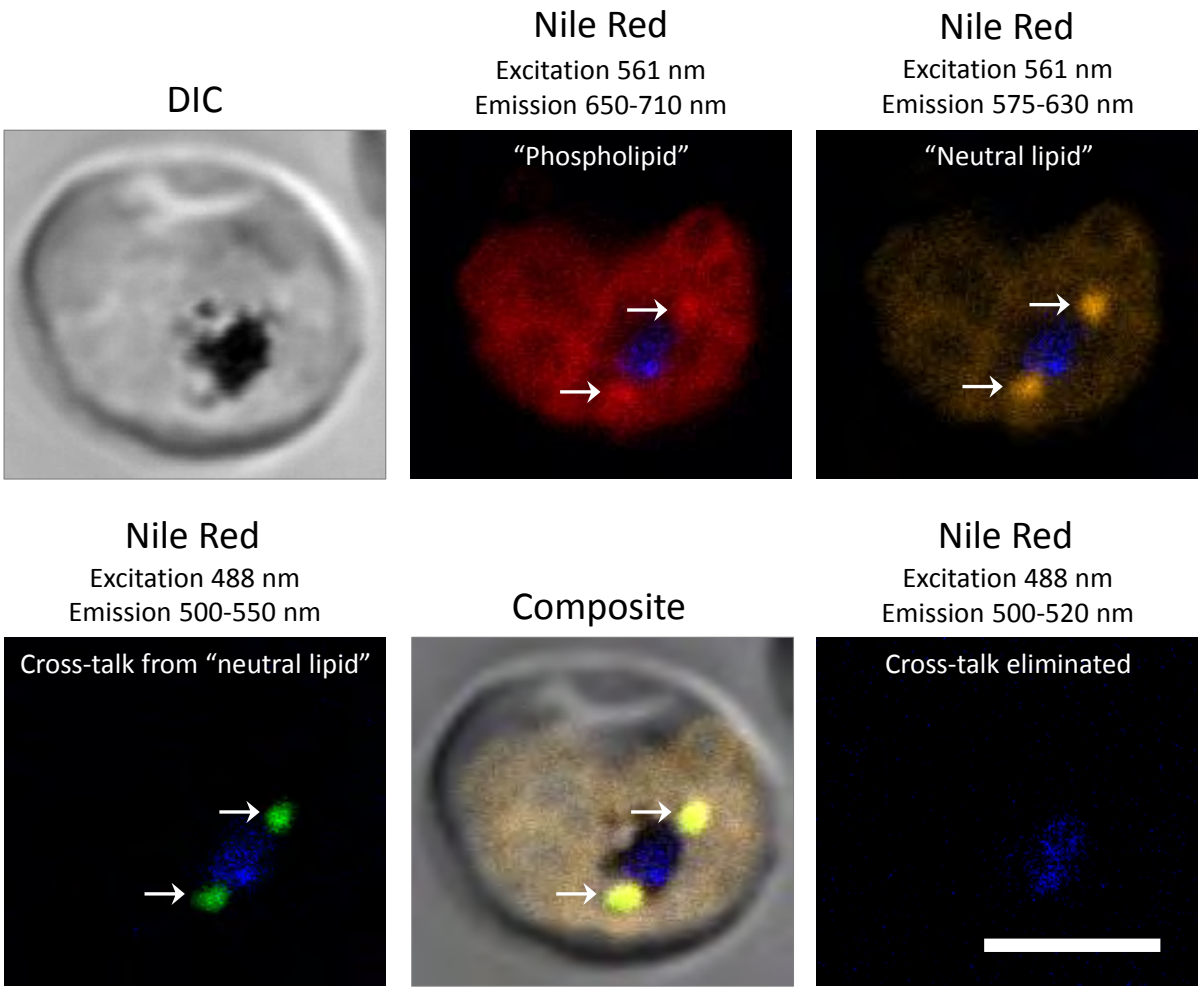

Figure 5.6. *An erythrocyte infected with a mature* P. falciparum *parasite and the staining pattern of Nile Red at various excitation and emission wavelengths. Blue represents the haemozoin autofluorescence previously described. Neutral lipid bodies are indicated by white arrows. Nile Red cross-talk from these neutral lipid bodies may be detected in what is typically the "green" region. The final panel represents excitation at 488 nm and the collection of green fluorescence over a reduced range (500-520 nm). With these collection parameters, the cross-talk corresponding to the neutral lipid bodies is no longer visible in the green channel. The scale bar represents 5 µm.*

5.3. Distribution of novel fluorescent analogues in *P. falciparum*

5.3.1. Detection of novel fluorescent analogues in infected erythrocytes

Confocal fluorescence microscopy was used for the initial examination of erythrocytes infected with the chloroquine-sensitive NF54 strain of *P. falciparum*. Infected erythrocytes were resuspended in Ringer's solution and incubated at 37°C for imaging.[22] Infected erythrocytes were readily identified under transmitted light by the haemozoin pigment. Detection of the novel NBD-labelled analogues within these cells was systematically investigated.

Figure 5.7 illustrates selective accumulation of the NBD-labelled analogues of quinine and quinidine in infected erythrocytes. Although these analogues were observed to distribute throughout the parasite, there was a discernible structure to these patterns which was likely to correspond to accumulation within different organelles. For example, the diffuse signal corresponding to the parasite's cytosol might indicate accumulation in the ER while, on the other hand, the tube-like structures that are seemingly in contact with the parasite plasma membrane may correspond to the mitochondrion (indicated by white arrows in Panels A and B in Figure 5.7). These analogues show a preference for localisation near the haemozoin ("Hz") which most likely indicates accumulation within the digestive vacuole.

For the NBD-labelled quinidine analogue, some cytoplasmic or plasma membrane staining in the infected host cell is observed (Panel B in Figure 5.7). This was present to a lesser extent in erythrocytes incubated with the NBD-labelled quinine analogue but was not observed at all in uninfected erythrocytes. Indeed, no accumulation of any of the NBD-labelled analogues, including the chloroquine analogue, was observed in uninfected erythrocytes (Panel C in Figure 5.7). Although there are some differences in the host cell plasma membrane composition between infected and uninfected erythrocytes,[23] this alone is probably not responsible for the selectivity of the analogues for the plasma membrane of infected host cells. It is possible that macromolecular remodelling of the host cell membrane, possibly through proteins exported to the host cell from *P. falciparum*, may provide additional binding sites on the surface of the host cell for these analogues.[24]

The reversibility of accumulation and specificity of binding of these analogues in *P. falciparum* was investigated via competition experiments. There was negligible attenuation of the green signal when imaging medium containing the NBD-labelled analogues was removed and replaced with fresh medium containing no analogue or an equivalent amount of the parent antimalarial, suggesting that accumulation of the analogues within *P. falciparum* was irreversible or non-

specific. This was confirmed when cells, after initial loading with the parent quinoline, were washed in fresh medium and then incubated with the respective NBD-labelled analogue. Typical accumulation patterns of the NBD-labelled analogues were still observed, suggesting that the association was non-specific or that they had displaced the parent antimalarials despite the fact that the reverse did not occur. This is probably indicative of non-specific binding of the analogues. This is unsurprising given their enhanced lipophilicities over the parent compounds resulting from the tethered fluorescent tag.

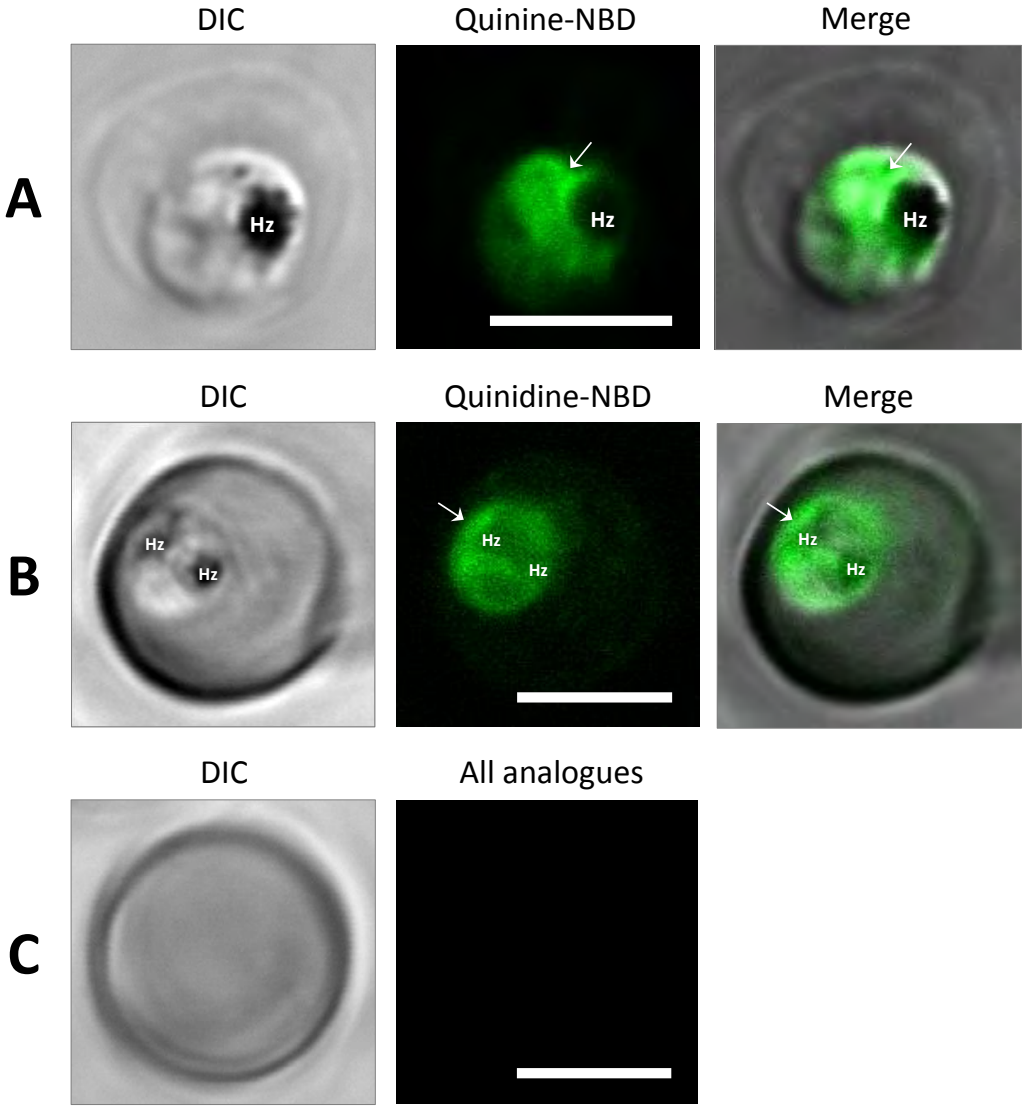

Figure 5.7. *Panels A and B represent* P. falciparum*-infected erythrocytes incubated with the NBD-labelled analogues of quinine and quinidine, respectively. White arrows indicate patterns of accumulation in close association with the parasite plasma membrane and resembling the morphology of the mitochondrion. In Panel B, cytoplasmic or plasma membrane staining of the infected host cell is observed. Panel C represents an uninfected erythrocyte variously incubated with all fluorescent analogues, including the NBD-labelled chloroquine derivative. Scale bars represent 5 μm.*

Figure 5.8 indicates a z-stack over a vertical displacement of approximately 2 µm. In the upper two layers, corresponding to the plane of the host cell, binding of the quinidine analogue to the erythrocyte membrane is evident. Punctate clusters in the host cell cytosol likely correspond to parasite-derived transport vesicles. As one moves deeper through the infected cell and through the various planes of the parasite, more structural detail within the parasite is visible. Accumulation patterns within the parasite are similar to those described above with the most prominent signal arising from the region corresponding to the digestive vacuole. There is a reduction in green signal at the site of the haemozoin itself; this is to be expected as it is unlikely that the drug analogue penetrates the tightly-packed crystal.

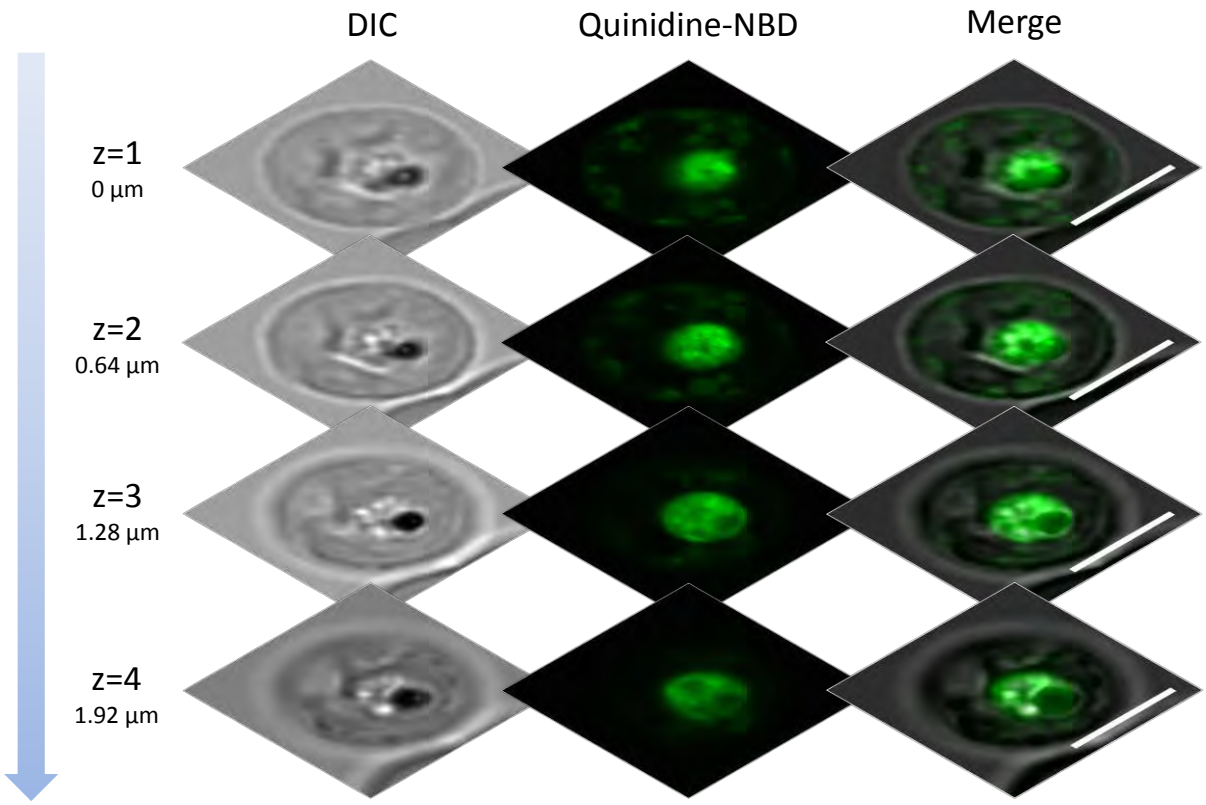

Figure 5.8. *A z-stack over an axial displacement of approximately 2 µm. Staining of the host cell membrane and cytosol is evident in the upper two layers. Regions of accumulation of the quinidine analogue corresponding to various structures within the parasite can be seen in all layers. Scale bars represent 5 µm.*

Selective accumulation in infected erythrocytes, almost entirely within *P. falciparum*, was also observed for the NBD-labelled chloroquine analogue (Figure 5.9). Accumulation was most significant around the haemozoin and hence within the digestive vacuole of the parasite. This is indicated by "Hz" in Figure 5.9 with arrows showing regions of most intense accumulation.

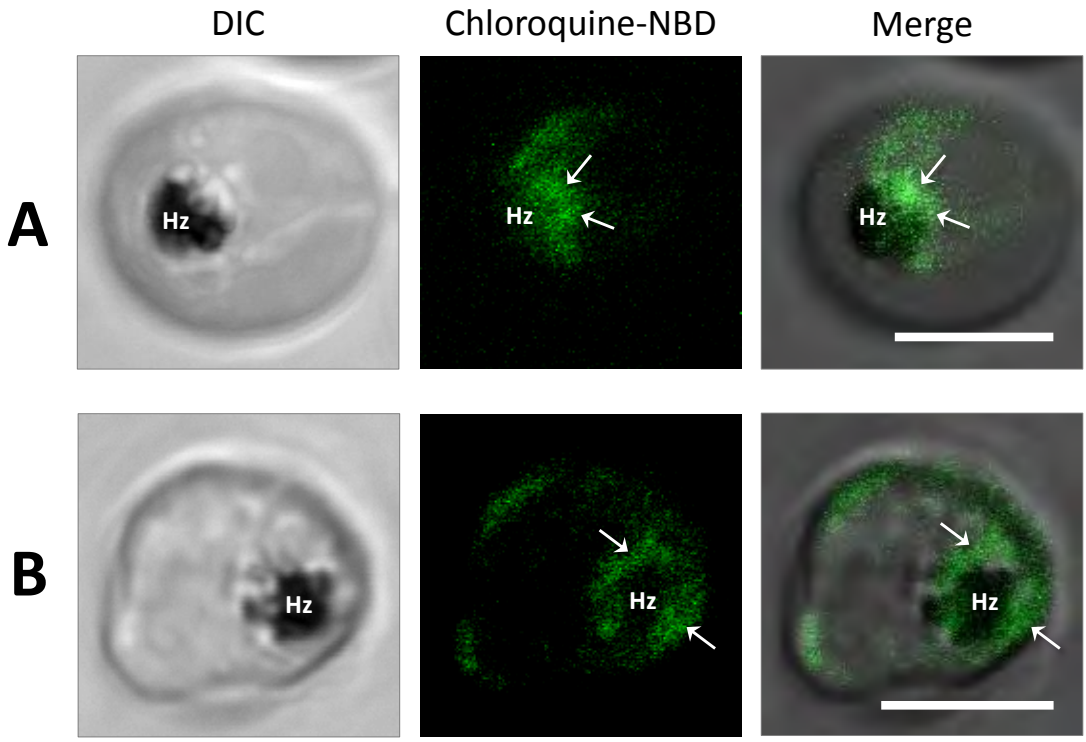

Figure 5.9. *The distribution of the NBD-labelled chloroquine analogue in* P. falciparum*. The regions of brightest fluorescence from this analogue were closely associated with haemozoin ("Hz") and hence the digestive vacuole as indicated by white arrows. Scale bars represent 5 μm.*

Generally, the signal observed from the NBD-labelled chloroquine was weaker than the signal from the NBD-alkaloids. While this may be due to the lower quantum yield of the chloroquine analogue (Table 4.2), it may also indicate enhanced accumulation of this analogue in aqueous compartments such as the digestive vacuole. This is not surprising as the chloroquine analogue is more hydrophilic than its alkaloid counterparts. Indeed, chloroquine may be expected to accumulate over a hundred-fold in the digestive vacuole compared to the alkaloids (Section 1.6.1). Furthermore, the NBD fluorescence is weakest in aqueous medium compared to non-polar environments (Figure 4.6). This was deliberately chosen to avoid the signal from this compartment overwhelming signals from elsewhere in the cell.

Alternatively, the weaker signal of the chloroquine analogue might also be explained by the fact that it binds more strongly to Fe(III)PPIX compared to the alkaloid analogues. Consequently, its fluorescence is more readily quenched via the heavy-atom effect. Hence, any fluorescence signal observed from the chloroquine analogue originates from molecules which are not complexed to Fe(III)PPIX. Indeed, at doses of the NBD-labelled chloroquine analogue close to its IC_{50} value (< 50 nM), negligible signal was observed suggesting that all accumulated analogue within *P. falciparum* at this concentration had been quenched.

Taken together, these observations support the hypothesis that Fe(III)PPIX is the molecular target of chloroquine within *P. falciparum* and hence that haemozoin inhibition is its primary mode of the action against the parasite. While quinine and quinidine are also likely to share this target and mechanism of action, localisation studies suggest additional effects against the parasite insofar as their fluorescent analogues are suitable representations of the parent antimalarials.

Although not shown here, the other NBD-labelled derivatives of quinidine that were prepared in Chapter 3 (that is, those with varying chain lengths between the quinoline core and the NBD fluorophore) also accumulated selectively within *P. falciparum*. However, following the process of evaluation as described in Chapter 4, these fluorescent derivatives were not considered suitable analogues of the parent molecules and hence their localisation was not considered in detail. Nevertheless, these derivatives might yet prove to be useful tools in the future as membrane-specific probes due to their hydrophobic character and are mentioned here for completeness.

It was also shown in Chapter 3 that the bimane-labelled quinine derivative was not a suitable analogue of the parent alkaloid. This was primarily because its activity against the parasite was significantly reduced (IC_{50} > 700 nM) compared to quinine (IC_{50} ≈ 60 nM). Despite this, cells were incubated with this derivative but no signal was detected in *P. falciparum*-infected erythrocytes. This suggests two possible explanations which may be related to its reduced activity in vitro. Either this derivative does not accumulate within infected erythrocytes, which may explain its reduced activity against *P. falciparum*, or its fluorescence is completely quenched within the infected erythrocyte even at the high concentrations required for imaging (300 nM).

Intriguingly, at the excitation and emission settings at which fluorescence from the bimane-labelled quinine derivative was expected, an endogenous signal was observed originating from the digestive vacuole. This most likely corresponds to autofluorescence originating from the haemozoin as it was present even in control (untreated) cells. It was detected following irradiation with a two-photon laser at approximately 750 nm (corresponding to an excitation wavelength of 375 nm) with emission between 415-500 nm. This autofluorescence is more prominent than the autofluorescence previously discussed above in Section 5.2.1.[17] Furthermore, this new endogenous signal is compatible with other dyes such as LysoTracker and Nile Red which would typically overwhelm the characteristic autofluorescence arising from haemozoin in the red region. This previously-unreported autofluorescence signal is depicted in Figure 5.10.

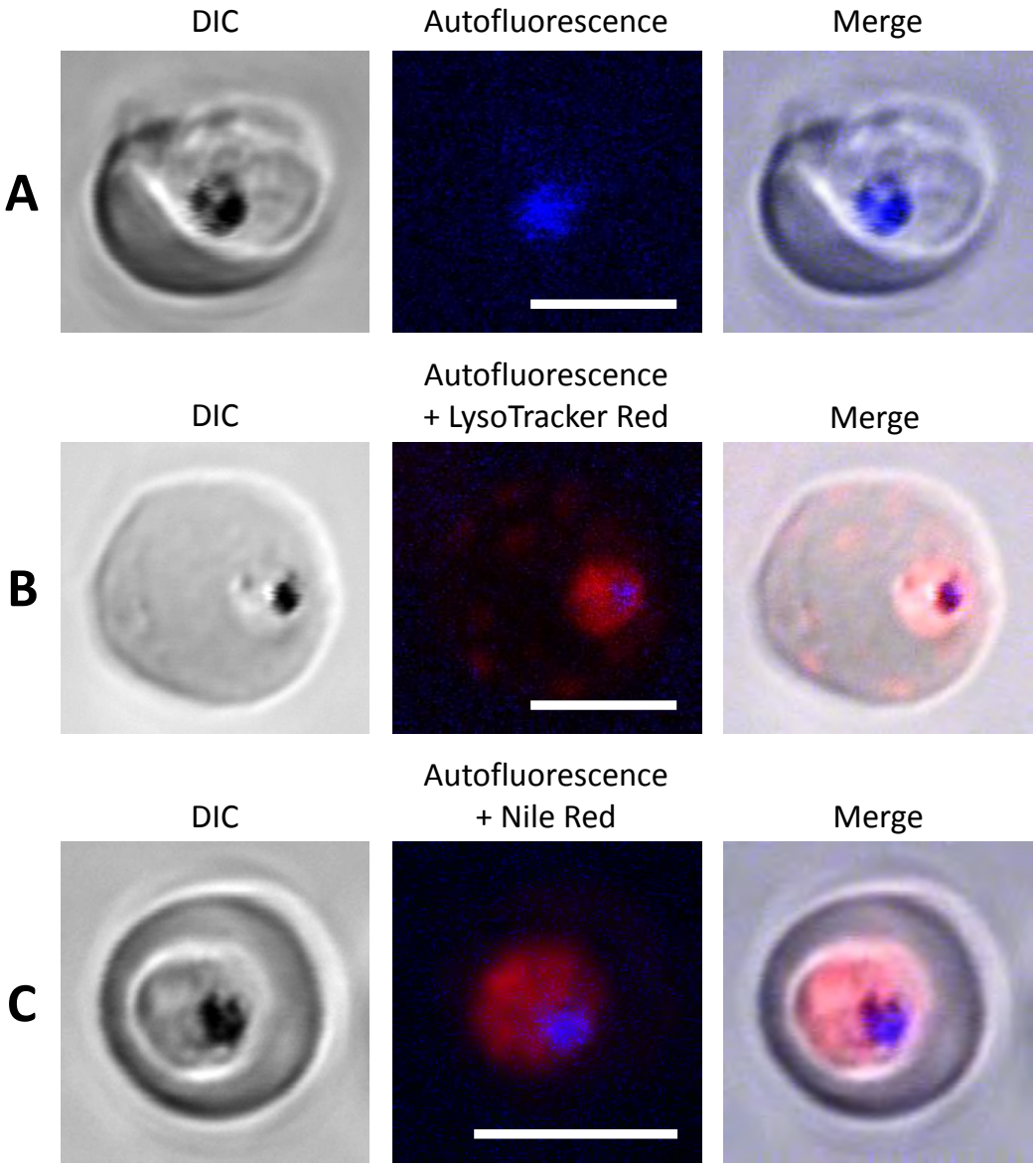

Figure 5.10. *Erythrocytes infected with* P. falciparum*. A strong haemozoin autofluorescence (blue) corresponded to two-photon excitation at 750 nm and emission between 415-500 nm observed in (A) untreated cells and also cells treated with (B) LysoTracker Red and (C) Nile Red. Scale bars represent 5 μm.*

This new autofluorescence phenomenon may correspond to the autofluorescence reported by Bohórquez et al. which these investigators observed from a "non-acidic compartment adjacent to the digestive vacuole".[19] They claimed to detect the autofluorescence of quinine following excitation at 405 nm with emission from 410-455 nm. Their images are reproduced in Panel A of Figure 5.11. These excitation and emission wavelengths are a surprising choice as the absorption maximum of quinine is centred in the ultraviolet region at approximately 335 nm. Indeed, its molar extinction coefficient at 405 nm is negligible (Figure 4.2A). Furthermore, quinine has a very weak fluorescence emission spectrum in the detection range used by

Bohórquez et al. (Figure 4.2A). Although it is possible that some of the dicationic species of quinine, which does fluoresce between 410-455 nm, may be present in the parasite, the authors specifically claimed that the alkaloid accumulated in a *non-acidic* compartment. It is very unlikely that the monocationic species would predominate in non-acidic conditions. They inferred the non-acidic nature of this compartment from the fact that the autofluorescence signal did not colocalise with LysoTracker Red (Panel B in Figure 5.11).

It is more likely that the autofluorescence signal arises from haemozoin autofluorescence rather than quinine. The authors do not present any untreated cells in their work, in which the quinine autofluorescence signal would be absent, to support their claim. Indeed, as described in Section 3.2.1, the autofluorescence of quinine could not be detected to any appreciable extent using direct or two-photon excitation.

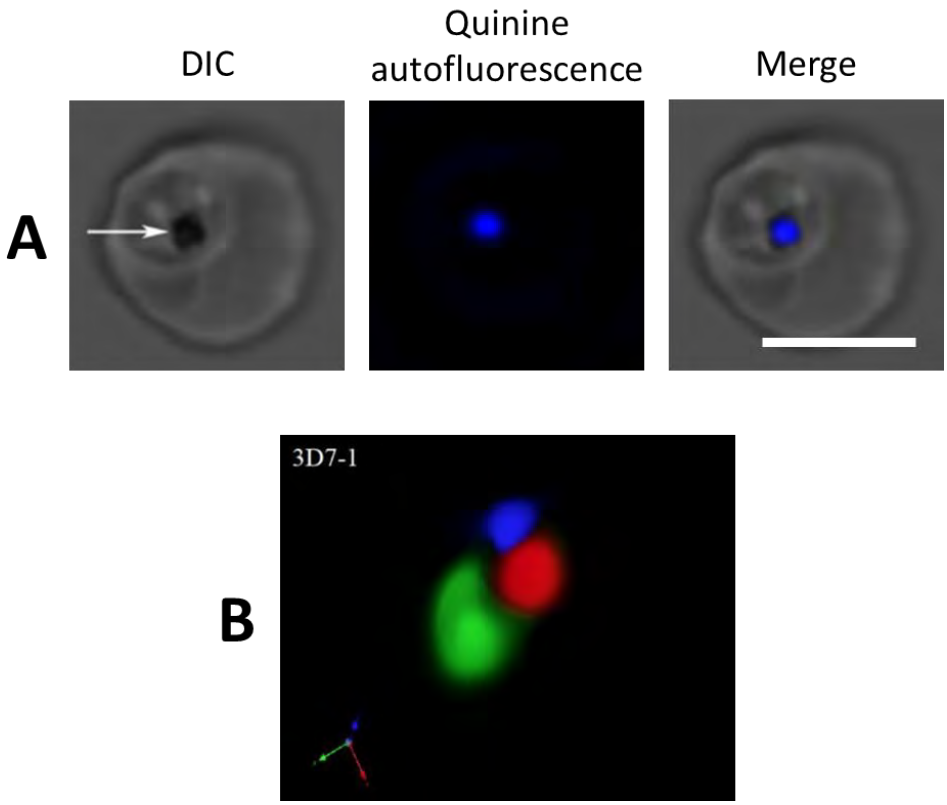

Figure 5.11. *Panel A represents a* P. falciparum *trophozoite (3D7 strain) incubated with quinine (blue). A white arrow points to haemozoin crystals in the digestive vacuole. The authors claim that "quinine overlapped with haemozoin … and thus localised to the food vacuole". The scale bar represents 5 µm. Panel B represents a reconstruction of a* P. falciparum *parasite indicating the different regions in space occupied by quinine (blue), LysoTracker Red (red) and a nuclear stain in green. Reproduced with minor modifications from E. B. Bohórquez et al.,* Malaria J.*, 2012, **11**, 350. Licensed by BioMed Central Ltd. 2012.*

Besides the digestive vacuole, *P. falciparum* possesses several organelles that also play important roles during the intraerythrocytic cycle such as the endoplasmic reticulum (ER), the mitochondrion and the plastid (apicoplast). Unlike the digestive vacuole, these organelles persist in all stages of the intraerythrocytic cycle of *P. falciparum* and cannot be formed de novo. Furthermore, these organelles are becoming increasingly important as targets for drugs. For example, the clinically-relevant antimalarial atovaquone is a *P. falciparum* mitochondrial electron transport inhibitor. Consequently, the ER and the mitochondrion were examined in conjunction with the NBD-labelled analogues of the quinoline antimalarials. As described in Section 5.2.4, these organelles were illuminated using ER-Tracker Red and MitoTracker Deep Red, respectively.

When incubated with ER-Tracker Red and Hoechst, infected erythrocytes displayed a diffuse, featureless red signal that appeared to represent the parasite cytosol but did not overlap with the highly-localised blue nuclear dye (Figure 5.12). The signal representing ER-Tracker colocalised broadly with the NBD-labelled analogues of quinine and quinidine. While suitable images in the presence of the NBD-labelled chloroquine analogue were more challenging to obtain, broad colocalisation was also observed between this analogue and the ER-Tracker. In contrast, overlap in signals was not observed between the green and blue channels, providing a first indication that the NBD-labelled quinolines do not localise to the nuclear compartment(s) of the parasite.

It was found that incubating the cells with both ER-Tracker and the NBD-labelled analogues simultaneously resulted in a weak signal from the tracker dye. This situation was improved by treating the cells first with the ER-Tracker and then, after some time, the drug analogues. This suggests competitive binding which was not unexpected given that quinine binds to the sulfonylurea receptors which are prominent on the ER.[16] That similar "competition" was noted for all three drug analogues may be as a result of structural similarities amongst the three quinoline antimalarials. Indeed, this observation serves as further evidence that the ER is an important site of accumulation of these drugs.

On the other hand, the signal obtained from MitoTracker Deep Red corresponded to a more localised, tube-like structure within the parasite (Figure 5.13). This structure was typically found in close juxtaposition with the parasite plasma membrane and colocalised with regions of high signal intensity from all three NBD-labelled analogues, indicating that there was some extent of colocalisation between the mitochondrion and these analogues.

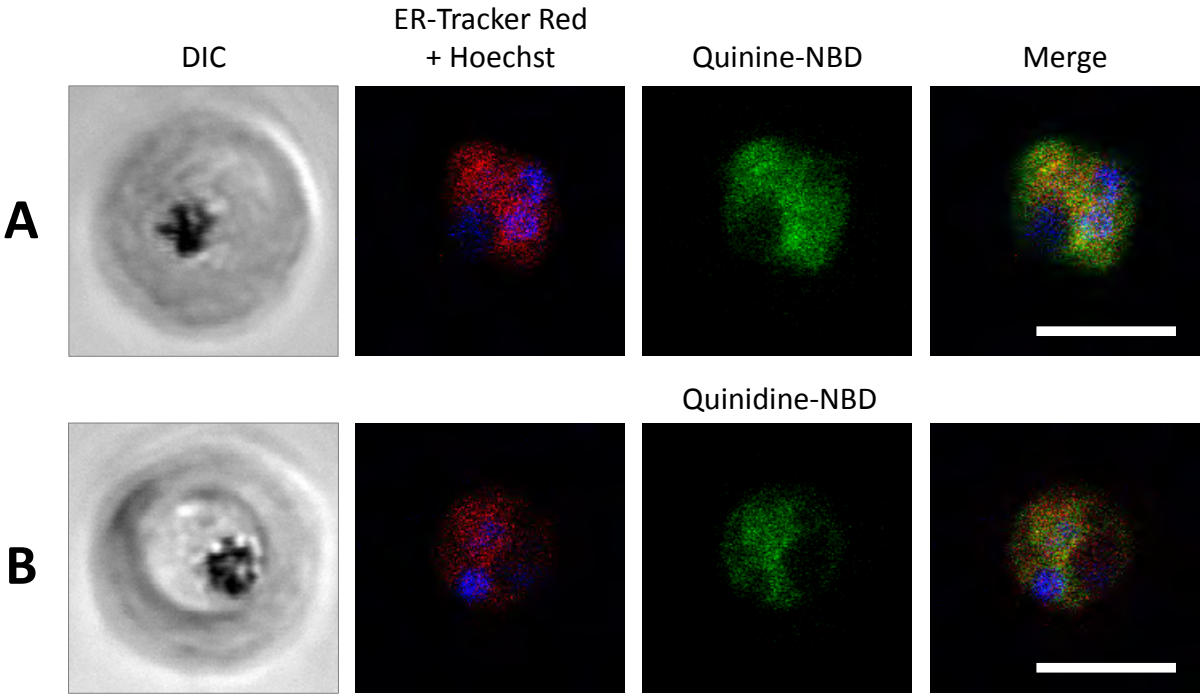

Figure 5.12. P. falciparum-*infected erythrocytes incubated with (A) quinine and (B) quinidine analogues (green) and co-stained with ER-Tracker Red (red) and Hoechst (blue). Broad colocalisation was observed between the analogues and the ER dye, but not with the nuclear dye. Scale bars represent 5 µm.*

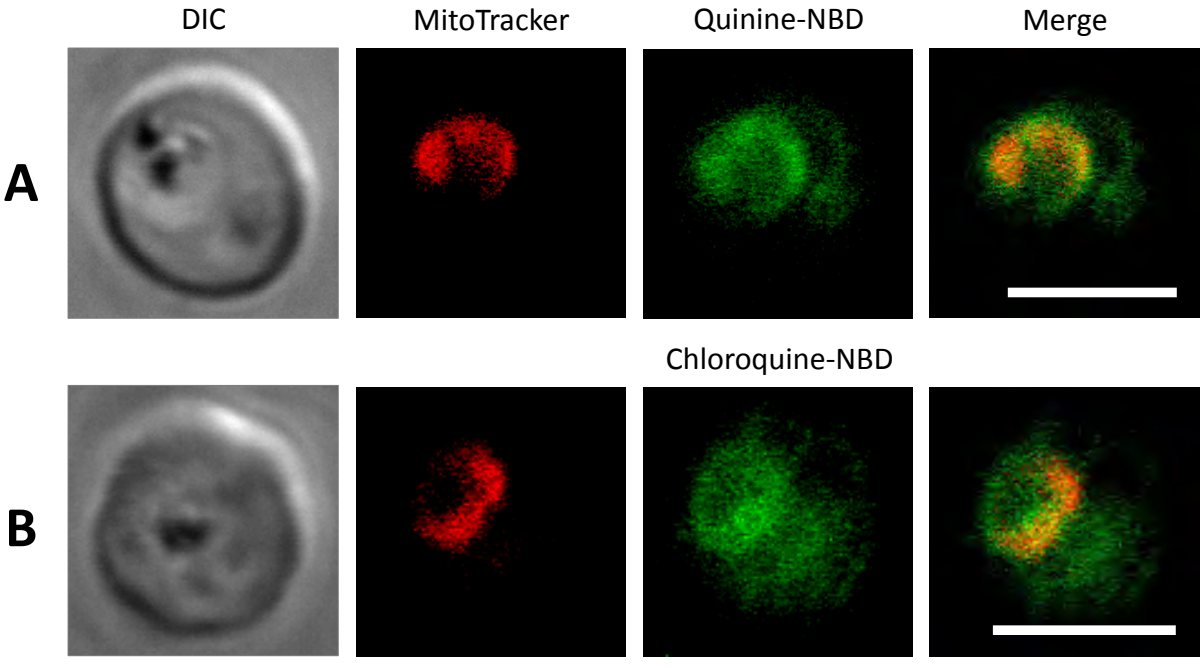

Figure 5.13. P. falciparum-*infected erythrocytes incubated with (A) quinine and (B) chloroquine analogues (green) in addition to MitoTracker Deep Red (red). Although diffuse signals were observed for the drug analogues, a highly localised signal was observed for MitoTracker which colocalised with prominent green signals from the NBD-labelled analogues. Scale bars represent 5 µm.*

The ER and mitochondrion have previously been implicated in ultrastructural studies of drug-treated *P. falciparum*. In quinine-exposed *P. falciparum*, mitochondria showed marked swelling with a more electron-lucent matrix.[2] In *P. falciparum* treated with chloroquine, the mitochondrion also appeared swollen.[1] It was also noted that the ER became difficult to identify following treatment with chloroquine.[1] The "disintegration" of the ER may also explain why it was difficult to acquire suitable images dual-stained with the chloroquine analogue and ER-Tracker. Indeed, images of cells acquired with the tracker dyes on their own and without analogue treatment provided better signal corresponding to ER-Tracker. These colocalisation observations may also be related to the remark by Combrinck et al. that liberated Fe(III)PPIX in chloroquine-treated parasites was observed in a region outside the digestive vacuole, possibly corresponding to be the ER.[9]

It is tantalising to imagine that accumulation of the quinoline antimalarials in either of these organelles may interfere with essential metabolic processes of *P. falciparum*. However, it may not be entirely surprising that the NBD-labelled analogues accumulate in the ER of the parasite. It is well-established that lipophilic xenobiotics tend to accumulate in the ER, where many of the enzymes responsible for their catabolism reside.[25] Xenobiotics refer to foreign molecules not normally produced in an organism or expected to be found there, or substances that are present in much higher concentrations than usual.[25] These definitions both apply to the NBD-labelled drug analogues. It is thus difficult to distinguish whether the quinoline antimalarials play a specifically-disruptive metabolic role within the ER or whether their accumulation there is simply the consequence of a natural detoxification system that cells have developed to deal with foreign substances.

5.3.2. Quantitative colocalisation analysis

As demonstrated above, qualitative image analysis is useful for identifying patterns of signal distribution in a small number of cells, especially relative to other subcellular structures such as haemozoin or co-stained organelles. It is also useful for giving a first impression of the extent of signal overlap. However, qualitative analysis is inherently subjective and becomes impractical as the number of images becomes large. Thus, analysing images *quantitatively* to measure the amount of overlap between different signals is more efficient and less subjective. Quantitative analysis is particularly helpful in distinguishing between the distributions of closely-related fluorophores such as the diastereomeric NBD-labelled alkaloids.

As described in Section 2.5.5, quantitative methods involve global statistical analysis of the pixel intensity distribution. Correlations between the intensity values of the pixels in a dual-channel

image are examined and this is done using a variety of coefficients that measure the strength of the relationship between these two values. For the colocalisation analysis described below, "Just Another Colocalisation Plugin" (JACoP) for ImageJ (Version 1.48) was used.[26]

As many of the colocalisation coefficients defined in Section 2.5.5 are sensitive to background noise, it is useful to define a threshold or cut-off value below which pixel intensities are discarded. However, deciding which pixels count as signal and which pixels count as noise by visual estimation is tedious and subjective. Instead, a robust way to determine thresholds has been proposed by Costes et al.[27] On a cytofluorogram, the expected location of pixels representing noise is close to the origin and takes the shape of a formless cloud. When isolated, this population has a Pearson correlation coefficient of zero. Appropriate thresholds will therefore have been determined when all pixels carrying intensities below the thresholds have a Pearson correlation coefficient equal to or below zero.[27] These values are computed incrementally, avoiding user input. The only drawback is that automatic thresholding is limited to images with a good signal-to-noise ratio. In the case of poor signal-to-noise ratio, the cloud formed by pixels contributing to noise encompasses part of the cloud formed by pixels contributing to the fluorescence signal.[27]

Table 5.1 presents the correlation coefficients computed by quantitative analysis of at least ten different single-cell images for each pair of channels. The Pearson correlation coefficient was calculated with and without the automatic thresholding algorithm. All other coefficients were calculated with the automatically-generated threshold values taken into account. The signal of the NBD-labelled quinine analogue was directly compared to that of LysoTracker Red and Hoechst. In order to compare the NBD-labelled alkaloids against one another, the signal of the NBD-labelled quinidine analogue was also analysed against LysoTracker Red. As one would not expect LysoTracker Red (which labels the membranes of acidic compartments) to colocalise with Hoechst (which represents the nucleus), these correlation coefficients served as negative controls. To aid interpretation of Table 5.1, a sample dataset is provided in Figure 5.14.

In the absence of automatic thresholding, the Pearson correlation coefficient shows that there is good overlap between the signals of the NBD-labelled alkaloids and LysoTracker Red ($r_P > 0.5$) but that the overlap between either of these signals with Hoechst is poor ($r_P < 0.5$). According to Figure 5.14, this is an accurate reflection of qualitative impressions of the images, i.e. the signals from the NBD-labelled alkaloids share very many more pixels with LysoTracker than with Hoechst. When automatic thresholding is applied, the negative correlations are somewhat stronger ($r_P < 0$) but the positive correlations become weaker. This reflects pixels of noise in the images which are discarded by the thresholding algorithm. The Pearson coefficients determined

in the presence of automatic thresholding are more reliable but they make the case of positive colocalisation more ambiguous.

Table 5.1. *Quantitative colocalisation analysis of at least ten different single-cell images per dataset generated a range of correlation coefficients in the presence or absence of automatic thresholding. Average values are given and uncertainties represent standard errors of the mean, except in the case of Van Steensel's cross-correlation coefficient (CCF) for which the values are the modes of the datasets.*

		No thresholds	Automatic thresholds applied					Van Steensel's CCF	
Channel 1	**Channel 2**	r_P	r_P	r_M	$\lvert k_1 - k_2 \rvert$	M_1	M_2	**Min. δx**	**Max. δx**
Quinine-NBD	**LysoTracker**	0.772 ± 0.068	0.662 ± 0.036	0.870 ± 0.015	0.192 ± 0.058	0.897 ± 0.012	0.910 ± 0.024	-20	0
Quinidine-NBD	**LysoTracker**	0.895 ± 0.019	0.684 ± 0.065	0.910 ± 0.016	0.194 ± 0.058	0.818 ± 0.122	0.957 ± 0.006	20	-1
Quinine-NBD	**Hoechst**	0.241 ± 0.028	-0.122 ± 0.017	0.716 ± 0.024	0.582 ± 0.212	0.217 ± 0.026	0.558 ± 0.096	-20	10
LysoTracker	**Hoechst**	0.214 ± 0.020	-0.130 ± 0.034	0.755 ± 0.027	0.983 ± 0.143	0.335 ± 0.166	0.316 ± 0.120	-20	11

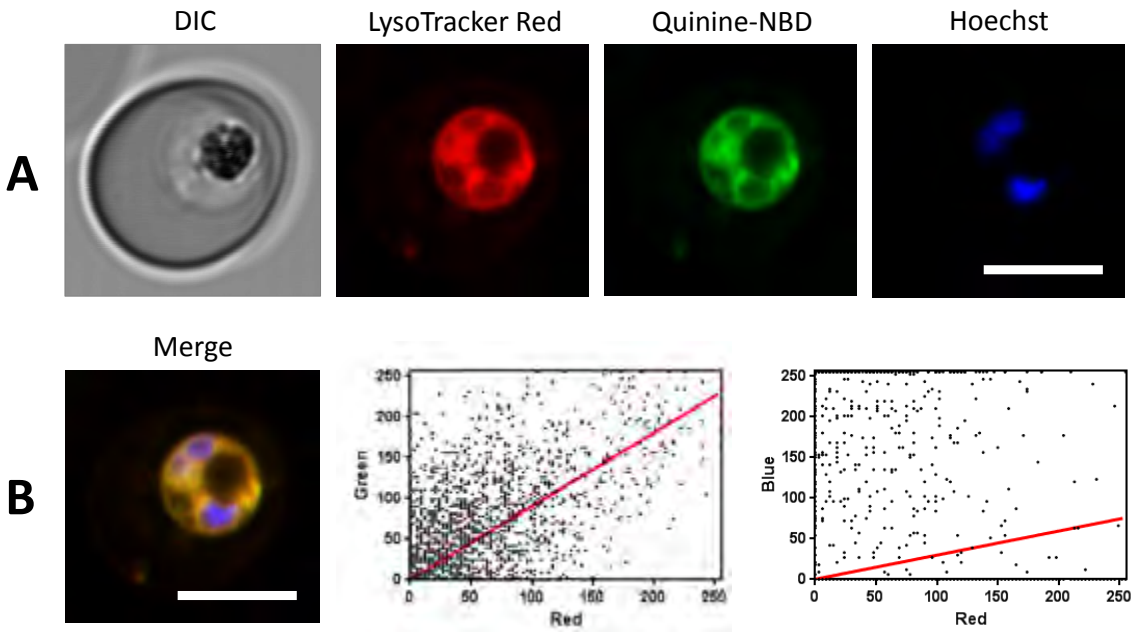

Figure 5.14. *Panel A represents an erythrocyte infected with* P. falciparum *and treated with LysoTracker Red (red), NBD-labelled quinine (green) and Hoechst (blue). Panel B represents the merged image where yellow indicates areas of overlap. Cytofluorograms show first estimates of colocalisation between red and green channels and between red and blue channels, respectively. Scale bars represent 5 μm.*

If the average intensity values of the pixels are not subtracted from the original intensity values (Section 2.5.5), the Manders overlap coefficient (r_M) can be generated which ranges from zero to one. The advantage of this coefficient is that it is less sensitive to differences in signal intensity between channels that might arise from labelling with different fluorophores, photobleaching and differences in gain settings during image acquisitions.[26] All of these factors are relevant to the images in question. In the case of the Manders overlap coefficient, there is a stronger correlation obtained between the red and green channels ($r_M >> 0.5$). However, it is surprising that a positive correlation is also observed for the blue signals with either the red or green channels ($r_M > 0.6$). While the Manders overlap coefficient is regarded as more reliable than the Pearson correlation coefficient, it is not good practice to rely on these two coefficients alone; hence, other colocalisation coefficients were evaluated as well.

As described in Section 2.5.5, the extent of colocalisation may be further examined by "splitting" the Manders overlap coefficient into two separate parameters (k) to determine the contributions of either signal to the extent of colocalisation. In the case of good colocalisation k_1 will approach α (the line of best fit through the cytofluorogram). This is indeed the case for the dataset in Figure 5.14 in which $k_1 = 0.683$ for the red-green channel combination. The mean slope of the cytofluorogram is α = 0.657, which is close to the value of k_1, suggesting very good colocalisation. Because k_1 is sensitive to differences in intensity from channel B, and vice versa, the difference between these split coefficients ($|k_1 - k_2|$) gives a further indication of colocalisation as it is typically small for true colocalisation. This is the case for the red and green channel pairs in Table 5.1 ($|k_1 - k_2| \approx 0.1$). This relationship also shows that there is an equal contribution to colocalisation from both channels. In contrast, this value is high for the red-blue channels ($|k_1 - k_2| > 0.3$) indicating an absence of colocalisation.

The Manders colocalisation coefficients M_1 and M_2 both approach unity in the case of the red-green channels, suggesting excellent colocalisation between these channels. These values are much lower (M_1, $M_2 < 0.5$) for the green-blue and red-blue channel combinations which, when taken in conjunction with the other coefficients above, show conclusively that there is no colocalisation between these channels.

Finally, van Steensel's cross-correlation coefficient (CCF) can be used as an alternative approach to distinguish between positive correlation and partial colocalisation. The images are shifted pixel-by-pixel in the x-direction relative to one image and for each shifted set the Pearson correlation coefficient is calculated (Section 2.5.5). In a true colocalisation scenario, the correlation is lost after the displacement and is reflected by small δx values for the NBD-labelled alkaloids compared to LysoTracker Red ($\delta x = 0$ and $\delta x = -1$). In the case of the blue dye, a larger

Pearson correlation coefficient is obtained only after the shift process (δx = 10 and δx = 11). In this case, an improvement in colocalisation is achieved only after shifting the images relative to one another, suggesting that they were not colocalised to begin with.

These various colocalisation coefficients show that, in general, colocalisation of the quinidine analogue with LysoTracker Red is higher than with the quinine analogue. None of these three signals overlap significantly with the nucleus. The implications of these observations are discussed critically in Section 5.5. Further verification of these quantitative colocalisation results may be obtained by considering a three-dimensional rendering of a sample image set. Although the qualitative analysis above has been performed on images acquired by confocal microscopy, better three-dimensional renderings may be constructed from super-resolution datasets as the axial slices are much thinner (z = 0.1 μm) hence there is less interpolation required. In Figure 5.15, which is a three-dimensional rendering of the data set acquired in Figure 5.3, it can be seen that red and green regions are closely apposed and often overlap, especially on the surface of the parasite. The blue signal does not overlap with either the red or green signals. The "hole" or absence of signal in the top right-hand corner corresponds to the haemozoin in this schizont-stage parasite. Some binding of the analogue can also be seen in the infected host cell.

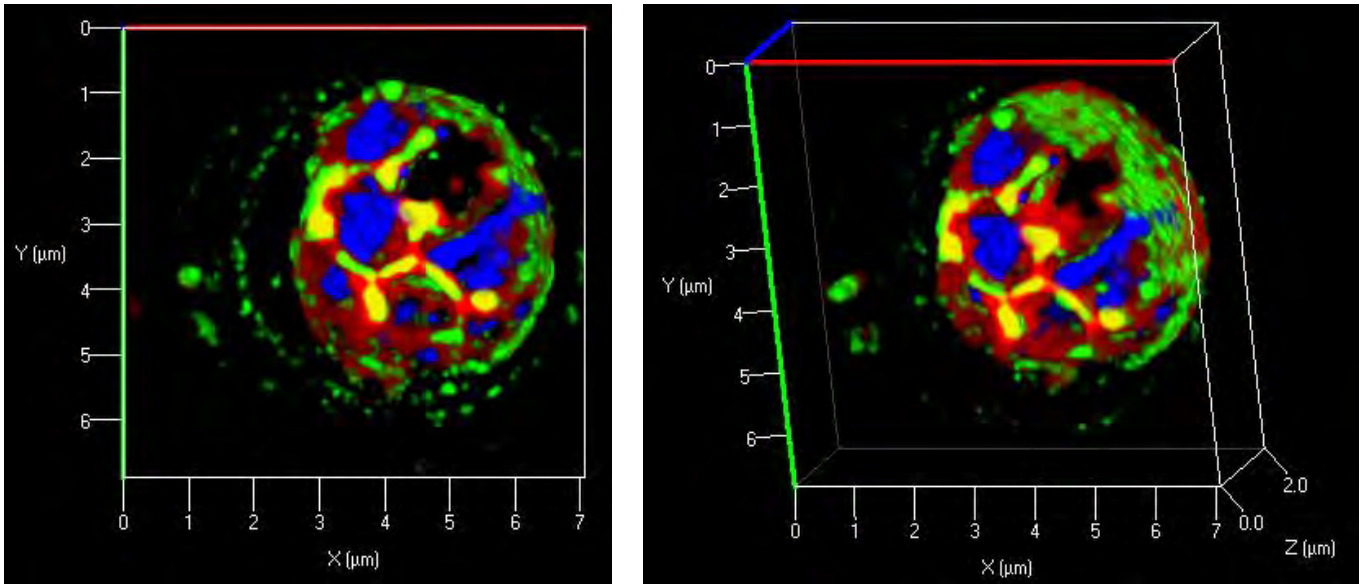

Figure 5.15. *Two different views of a three-dimensional rendering of the schizont in Figure 5.3 incubated with LysoTracker Red (red), Hoechst (blue) and the NBD-labelled quinine analogue (green).*

To understand better the spatial distribution of the NBD-labelled analogues relative to the ER and mitochondrion, quantitative analysis was carried out between the confocal image pairs in the presence of these trackers. Because the quinine and quinidine analogues have very similar distributions (Table 5.1), these analogues were pooled when considering their colocalisation relative to the ER. Additionally, because suitable images of NBD-labelled chloroquine and ER-Tracker could not be obtained, these were not included in the quantitative analysis. All coefficients in Table 5.2 were obtained in the presence of automatically-determined threshold values.

The Pearson correlation coefficient (r_P) is high in the case of the NBD-labelled analogues and ER-Tracker, but it is lower in the case of MitoTracker. This reflects initial qualitative impressions of the images in which the ER-Tracker is generally diffuse, overlapping with the entire signal from the NBD-labelled analogues (Figure 5.12). On the other hand, the MitoTracker dye is more tightly localised relative to the green signal and this is reflected by a lower Pearson correlation coefficient as there are large areas of green signal that do not correspond to a signal in the red channel (Figure 5.13). The more reliable Manders overlap coefficient (r_M) indicates excellent overlap ($r_M > 0.8$) for all three channels which is somewhat surprising given that the fraction of overlap between the green and red channels differs between the ER and mitochondrial signals.

Table 5.2. *Quantitative colocalisation analysis of at least five different single-cell images per dataset generated a range of correlation coefficients in the presence of automatic thresholding. Average values are given and uncertainties represent standard errors of the mean, except in the case of Van Steensel's cross-correlation coefficient (CCF) for which the values are the modes of the datasets.*

		Automatic thresholds applied					Van Steensel's CCF	
Channel 1	**Channel 2**	r_P	r_M	$\lvert k_1 - k_2 \rvert$	M_1	M_2	**Min. δx**	**Max. δx**
NBD-labelled alkaloid	**ER-Tracker**	0.730 ± 0.052	0.840 ± 0.023	0.135 ± 0.013	0.801 ± 0.045	0.532 ± 0.126	-20	0
NBD-labelled alkaloid	**MitoTracker**	0.378 ± 0.034	0.855 ± 0.008	0.104 ± 0.013	0.771 ± 0.122	0.996 ± 0.003	-20	2
NBD-labelled chloroquine	**MitoTracker**	0.541 ± 0.042	0.836 ± 0.005	0.127 ± 0.038	0.627 ± 0.187	0.995 ± 0.003	20	1

The difference between the "split" k coefficients between green and red channel pairs is once again small and indicates a positive colocalisation between all dye pairs. The Manders

coefficients are most useful where there are clear structural features in the images;[26] hence, in the case of a very diffuse signal such as ER-Tracker, the value is fairly low ($M_2 \approx 0.5$). These same coefficients are very high for the NBD-labelled probes when compared with Mito-Tracker ($M_2 > 0.5$), showing excellent colocalisation. Van Steensel's CCF also shows that these results represent a true colocalisation situation as the magnitude of the Pearson correlation coefficient does not improve after shifting the channels relative to one another; on the other hand, the Pearson correlation coefficient can be minimised by shifting the channels further away from one another in the *x*-direction (min. $\delta x = 20$ or -20).

Some of the coefficients presented in Table 5.2 have large uncertainties compared to those in Table 5.1. This is probably due to noise in these signals, particularly from the ER-Tracker for which the signal was weak and relatively featureless. Nevertheless, these results corroborate the qualitative observations that there is broad overlap between the ER and the NBD-labelled alkaloids, and between the mitochondrion and the NBD-labelled analogues.

5.3.3. NBD-labelled quinine distribution over the life cycle of *P. falciparum*

P. falciparum undergoes a 48-hour life cycle of asexual replication in human erythrocytes which causes the clinical symptoms of malaria. This cycle commences when extracellular merozoites invade erythrocytes. Upon entry into the erythrocyte, ring-stage parasites actively modify the host cell and begin ingesting the abundant haemoglobin from the erythrocyte (Section 1.2.3). To avoid the toxic effects of Fe(III)PPIX, this molecule is biocrystallised to haemozoin within the parasite's digestive vacuole. The mechanism of this biocrystallisation process is still unclear but neutral lipid bodies[28] and, more recently, phospholipid membranes[29,30] have been implicated in its formation (Section 1.3.2). After almost complete consumption of the erythrocyte cytoplasm, trophozoites undergo a series of nuclear divisions to form multinucleated schizonts. These eventually form many daughter merozoites which burst out of the remnant host cell and invade fresh erythrocytes.

Despite diminished use due to decreased efficacy and undesirable side effects, quinine remains the frontline drug for severe malaria and malaria in pregnancy.[31] Due to its clinical relevance, the accumulation of its NBD-labelled analogue over the course of the intraerythrocytic life cycle was monitored at six time points (Figure 5.16). Besides live-cell fluorescence imaging, slides of fixed cells were prepared in which parasitised erythrocytes were detected using a Giemsa stain to tell most reliably the size and extent of the nucleus and thus the life cycle stage of the parasite. As mentioned in Section 5.2.4, Nile Red can be monitored using different emission filters to differentiate between phospholipid and neutral lipid structures within *P. falciparum*.

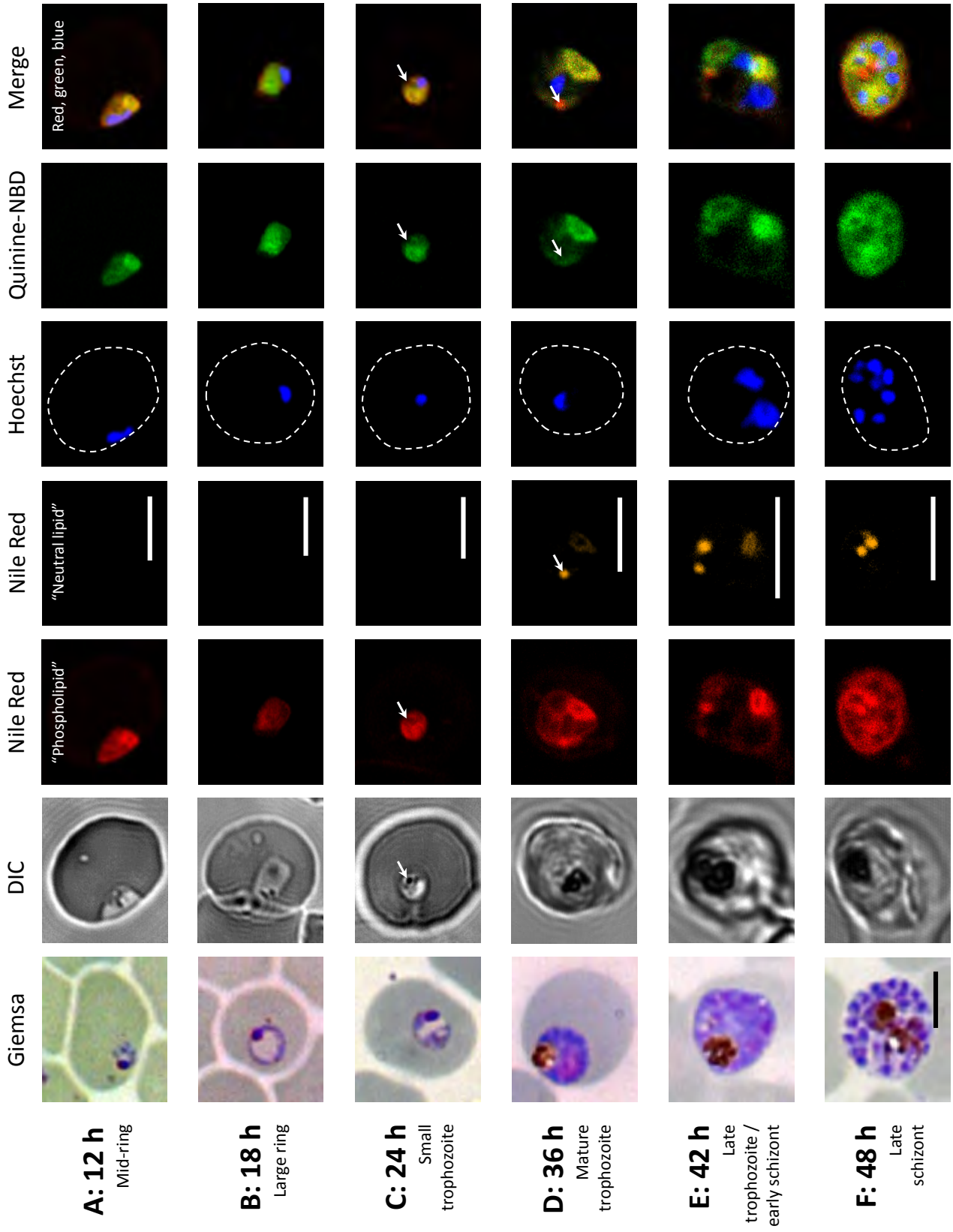

Figure 5.16. *Time-lapse experiment of* P. falciparum*. Giemsa-stained slides of fixed cells and fluorescence channels of live cells were recorded at six time intervals. At each time point, parasites were incubated with Nile Red (red, gold), Hoechst (blue) and NBD-labelled quinine (green). Scale bars represent 5 μm.*

The earliest time point that was investigated was the mid-ring stage approximately 12 h into the intraerythrocytic life cycle (Figure 5.16A). At this stage, parasites were small (1-2 μm) and were often in close proximity to the plasma membrane of the host cell following invasion. The nucleus (blue) was elongated and was found alongside the plasma membrane of the host cell. Nile Red revealed large amounts of phospholipid (red) but no emission in the region corresponding to neutral lipid (gold). The pattern of red emission resembled the pattern of fluorescence from the quinine analogue (green) resulting in large overlap between these signals.

At approximately 18 h, similar features were observed but the parasite had positioned itself in the centre of the erythrocyte (Figure 5.16B). There was still prominent overlap between the phospholipid region of Nile Red (red) and the NBD-labelled quinine (green). The nucleus was rounder in shape and fluorescence from both red and green channels was reduced in the region corresponding to the nucleus (blue).

After the first day of the *P. falciparum* life cycle (24 h), haemozoin was detectable both in the Giemsa-stained slides and in the transmitted light channel of the fluorescence microscope (indicated by a white arrow in Figure 5.16C). The appearance of haemozoin corresponded to the formation of a small digestive vacuole. However, at this stage there was still no indication of neutral lipid bodies, consistent with other studies that implicate these structures only later in the parasite life cycle.[32] The appearance of more structure in the red channels, corresponding to phospholipid regions, indicated the development of organelles such as the ER and a juvenile mitochondrion. Overlap with the green channel was still prominent, especially near the haemozoin and hence indicative of association with the young digestive vacuole.

Upon maturation of the trophozoite at approximately 36 h, the parasite increased at least two-fold in size (Figure 5.16D). Extensive haemoglobin catabolism was evident from the large haemozoin pigment and individual clumps of crystals were discernible, especially in the Giemsa-stained slide. Also prominent was the appearance of a spherical neutral lipid body (approximately 0.5 μm in diameter) indicated by a white star in Figure 5.16D. There was some evidence of overlap between the quinine analogue and the neutral lipid body but not an increase in signal as might be expected from accumulation within this neutral lipid environment and in which the brightness of the NBD fluorophore is enhanced.

At this time point, the signals of the phospholipid region of Nile Red and the quinine analogue still overlapped extensively. Maturation of organelles corresponded to distinct shapes with their signals. The tube-like structure which appeared adjacent to the plasma membrane was likely to be the mitochondrion (Figure 5.16D). This structure also appeared faintly in the neutral lipid

region of the Nile Red spectrum. A significant amount of green signal was seen in the region corresponding to the digestive vacuole which may be significant given that this is also the period in the life cycle in which quinine has been found to be most active against *P. falciparum* (Section 5.2.2).

At 42 h, corresponding to the late trophozoite or early schizont stage, the nucleus was enlarged and irregular. In most cells examined, several nuclei were often present indicating that the parasite had commenced nuclear division (Figure 5.16E). The parasite took up almost the entire erythrocyte and the haemozoin pigment was very prominent. The number and size of neutral lipid bodies increased. In this example, one lipid body showed partial colocalisation with the NBD-labelled quinine analogue. There was still extensive overlap between the phospholipid region of Nile Red and the quinine analogue while the signal from Hoechst (nucleus) was clearly excluded from both channels. Once again, a small circular structure was faintly visible in the neutral lipid region of the Nile Red signal which corresponded to a similar signal in the phospholipid and NBD-labelled quinine channels.

At 48 h, corresponding to the late schizont phase of the intraerythrocytic life cycle, many daughter merozoites, each with its own nucleus, were almost fully formed (Figure 5.16F). At this stage, the haemozoin was usually found in the centre of the host cell and often in intimate association with several neutral lipid bodies. In this example, the lipid bodies displayed little if any colocalisation with the NBD-labelled quinine. Nevertheless, there was high lipid content in this mature cell and this phospholipid emission overlapped strongly with the quinine analogue. Eventually the host cell burst, releasing many merozoites each of which took some of the quinine analogue fluorescence with them (not shown).

Although quinine is known to be most active in mature-stage parasites (Section 5.2.2),[10,11] these data show that quinine accumulates in all stages of the intraerythrocytic *P. falciparum* life cycle. At all six points of this time-lapse experiment, the quinine analogue showed an affinity for membranous regions within the parasite by overlapping with the Nile Red emission corresponding to phospholipid signal. This corroborates the quantitative measurements in which the quinine analogue localised strongly with LysoTracker Red. Despite this, the quinine analogue did not readily associate with the neutral lipid bodies even though the quinine analogue is somewhat lipophilic due to its tethered fluorescent tag. Hence it is more likely that this alkaloid may interact with phospholipid rather than neutral lipid components within *P. falciparum*.

5.4. Colocalisation studies with super-resolution microscopy

5.4.1. Colocalisation of NBD-labelled analogues with the ER and mitochondrion

In order to overcome the limitations of resolution and to generate deeper insights into the localisation and distribution of the NBD-labelled analogues of the quinoline antimalarials in *P. falciparum*, super-resolution structured-illumination microscopy (SR-SIM) was employed. This modality offers a two-fold enhancement in resolution compared to confocal microscopy (Section 2.5.4). Importantly, it is a live-cell imaging technique and does not require special sample preparation or fluorophores. Imaging conditions are also less harsh, preserving the integrity of the cells. As SR-SIM has not previously been used to investigate drug localisation in *P. falciparum*, the tracker dyes used to co-stain organelles were first validated in the absence of the NBD-labelled analogues. These images were compared to images obtained in previous studies in which their morphologies were fully characterised using organelle-specific fluorescent proteins.

In the case of the ER and the mitochondrion, van Dooren et al. have produced transfected lines of *P. falciparum* that allow specific illumination of these organelles.[33] For the ER, they used an ER-specific marker PfBiP to encode a fluorescent fusion protein BIP(s)–GFP–SDEL.[33] This comprised the BiP signal sequence (BiP)s followed by a green fluorescent protein (GFP) reporter and finally the SDEL motif of PfBiP which was postulated to mediate retention of BiP in the ER. They confirmed the localisation of this construct using immunofluorescence, demonstrating that it is retained in the ER and that it reliably depicts the structure of the organelle.[33] In a separate experiment, they prepared a double transfectant line in which both mitochondrial and apicoplast proteins were tagged with the fluorescent proteins eYFP and dsRed, respectively.[33]

In early intraerythrocytic parasites, the ER has a simple morphology and comprises a crescent shape that subsequently develops into a ring of fluorescence, presumably around the nuclear envelope, from which extensions emerge into the cytosol (Panel A in Figure 5.17).[33] Van Dooren et al. reported occasional “horn-like” extensions emerging from the nuclear envelope which often extend around the digestive vacuole.[33] Whether this indicates trafficking of substrates between these organelles still remains to be seen. In later stages, the ER appears to branch extensively through the cytosol, creating a complicated network. These changes in morphology probably reflect the increase in the number of functions of the ER as the parasite becomes more metabolically active.

Panel B in Figure 5.17 represents SR-SIM images of ER-Tracker Red (red) and Hoechst (blue). There are various similarities to the images of Van Dooren et al. such as the ER encircling the nucleus and even the presence of the "horn-like" structures making contact with the digestive vacuole, indicated by white arrows in both panels. Thus it may be concluded that ER-Tracker Red is a suitable tracker molecule for the ER in SR-SIM studies of *P. falciparum*.

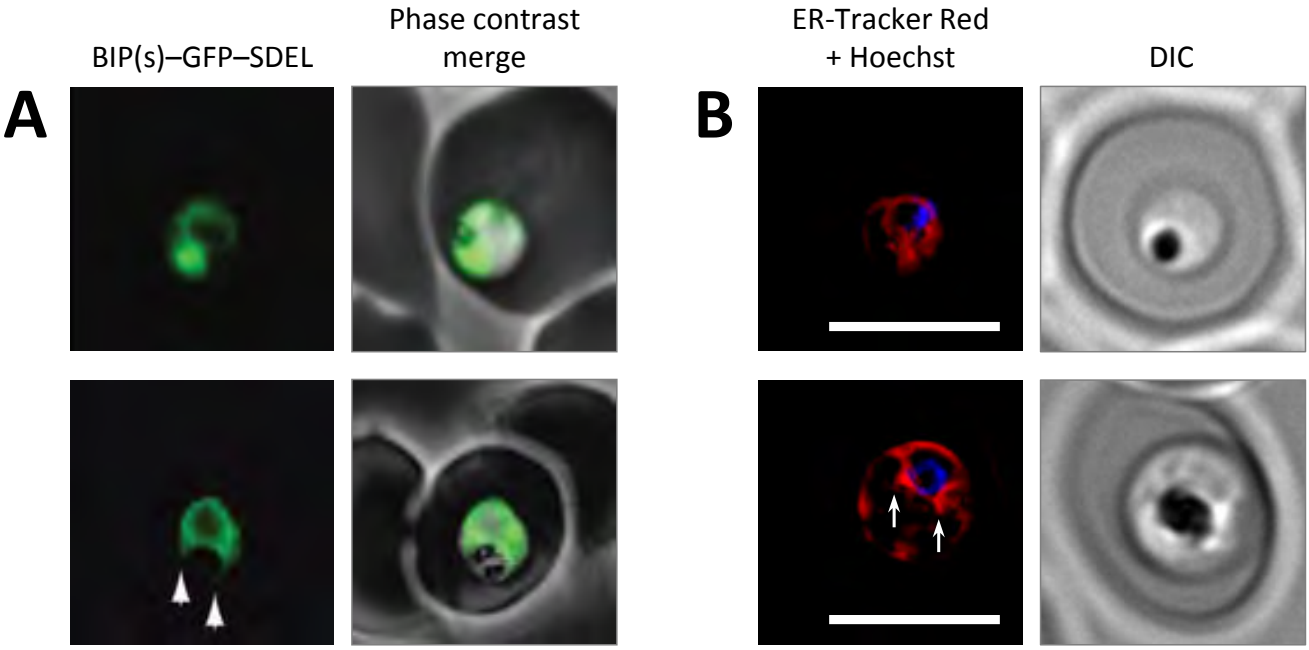

Figure 5.17. *Comparison of ER morphology in* P. falciparum *using (A) fluorescent proteins and (B) ER-Tracker Red. Panel A represents confocal images of a GFP-labelled protein that is specifically localised to the ER.*[33] *Panel B represents SR-SIM images of ER-Tracker Red (red) and Hoechst (blue). Scale bars represent 5 μm. Panel A is reproduced with permission from G. G. van Dooren et al.,* Mol. Microbiol.*, 2005, **57**, 405.*

Figure 5.18 depicts several SR-SIM images of ER-Tracker Red in the presence of the three NBD-labelled antimalarials. It is immediately clear that there is an improvement in signal from the ER-Tracker in the confocal studies which was previously diffuse and featureless. In Figure 5.18, the structure of the ER is complex and becomes more reticulate in more mature cells. All three NBD-labelled analogues showed colocalisation with at least some regions of the ER. The regions with most prominent colocalisation between red and green channels are indicated with white arrows in Figure 5.18. In the case of the NBD-labelled alkaloids, staining of the plasma membrane of the host erythrocyte was also frequently observed. This is particularly evident in Figure 5.18B.

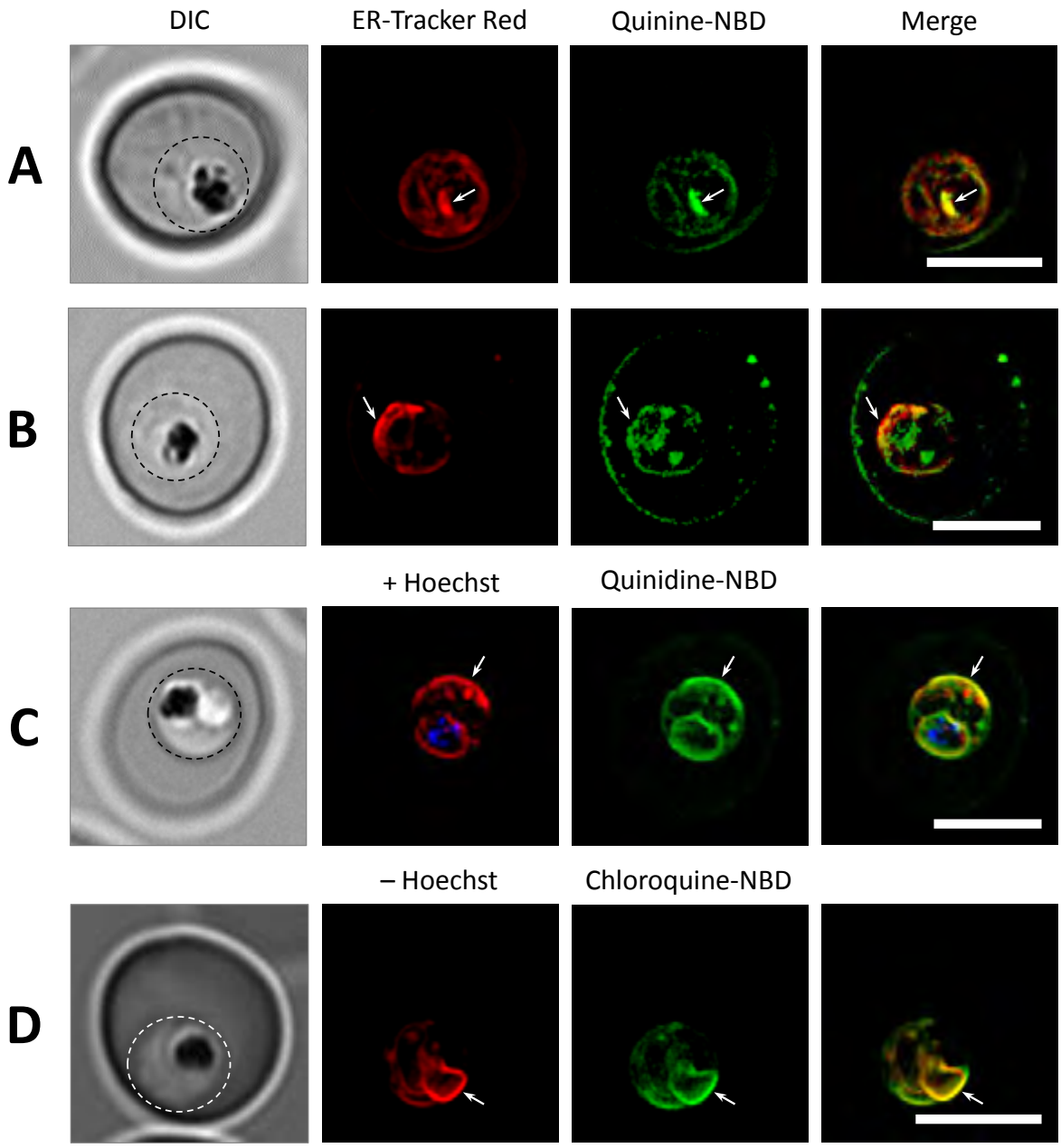

Figure 5.18. *Erythrocytes infected with mature* P. falciparum *and incubated with ER-Tracker Red (red) and the NBD-labelled analogues (green). Yellow indicates regions of overlap with areas of most intense overlap indicated by a white arrow. Scale bars represent 5 μm.*

The signal for the NBD-labelled chloroquine analogue is very weak and, once transformed by the SR-SIM post-acquisition processing algorithm, it emerges as discrete punctate clusters. It is not possible to say whether this punctate clustering reflects the actual distribution of this molecule within *P. falciparum* or whether it is merely an artefact of SR-SIM processing. The ER is often closely juxtaposed with the haemozoin, and hence the digestive vacuole, and these regions were occasionally observed to colocalise with the analogues (Figure 5.18A). In almost

each case, there is signal corresponding to the analogues that does not colocalise with the ER-Tracker. This could refer to alternative sites of localisation such as the mitochondrion, or accumulation within the digestive vacuole as is likely the case in Figure 5.18B.

The mitochondrion of *P. falciparum* presents a different morphological profile from the ER. Ultrastructural studies have identified the mitochondrion as a single crescent-shaped organelle in merozoites that branches out to form a tubular structure in trophozoites, before segregating along with the nucleus into daughter merozoites.[33] In mature parasites it frequently appears to fuse upon itself and is often seen in close association with the plasma membrane (Panel A in Figure 5.19, white arrows).[33] A similar profile was also observed for the SR-SIM images of the mitochondrion acquired using MitoTracker Deep Red, validating the use of this organelle indicator (Panel B in Figure 5.19). Panel C in Figure 5.19 represents a particularly clear confocal image of MitoTracker (blue) and LysoTracker Red (red) showing the morphology of a branched mitochondrion often closely associated with the parasite plasma membrane (white arrows).

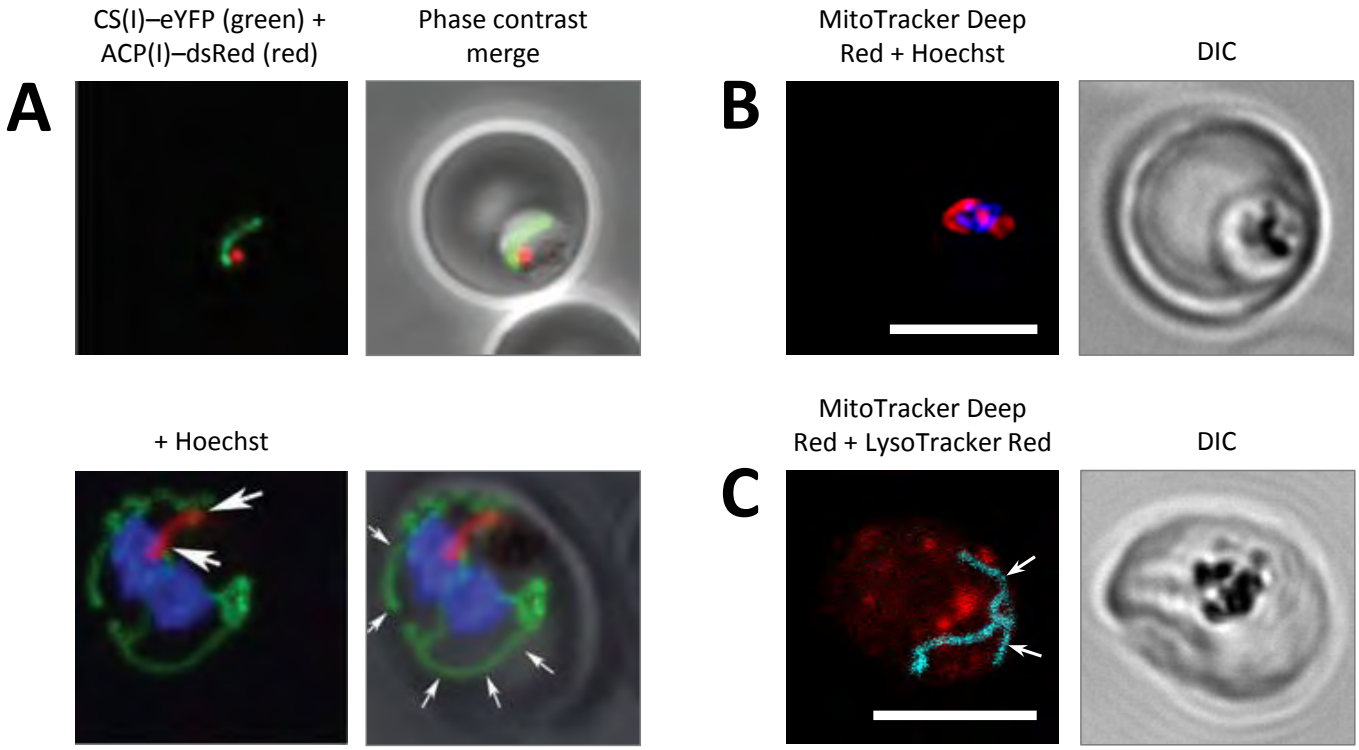

Figure 5.19. *Comparison of mitochondrial morphology in* P. falciparum*. Panel A represents confocal images of eYFP-labelled mitochondrial protein CS(I) (green). The apicoplast protein ACP(1) has been tagged with fluorescent protein dsRed (red). In some panels, Hoechst (blue) has been added as a co-stain. Panel B represents SR-SIM images of ER-Tracker Red (red) and Hoechst (blue). Panel C represents a confocal image of MitoTracker Deep Red (blue) and LysoTracker Red (red). Scale bars represent 5 µm. Panel A is reproduced with permission from G. G. van Dooren et al.,* Mol. Microbiol.*, 2005, **57**, 405.*

Although the apicoplast was not investigated in this study, it is mentioned here for completeness. Van Dooren et al. noted that the apicoplast (indicated in red in Panel A of Figure 5.19) is a small, cylindrical structure which lengthens during the trophozoite stage.[33] Electron microscopy studies revealed a close association between the apicoplast and mitochondrion at various stages during the intraerythrocytic cycle. This has been postulated to allow transfer of metabolites between these two organelles.[33]

Figure 5.20 shows SR-SIM images of MitoTracker Deep Red in the presence of the three NBD-labelled quinoline analogues. Regions of colocalisation were mostly in close association with the plasma membrane of the parasite and sometimes with the haemozoin-containing digestive vacuole (white arrows in Figure 5.20). Once again, an apparently punctate distribution of the NBD-labelled chloroquine derivative probably results from a weak signal from this fluorophore. As was the case in Figure 5.20, there are often regions of green fluorescence from the analogues that do not overlap with the MitoTracker dye, suggesting accumulation within other subcellular compartments such as the ER or the digestive vacuole (Figure 5.20A). For that matter, there are also regions illuminated by MitoTracker that do not overlap with signal from the analogues, suggesting only partial accumulation of the analogues within this organelle (Figure 5.20B).

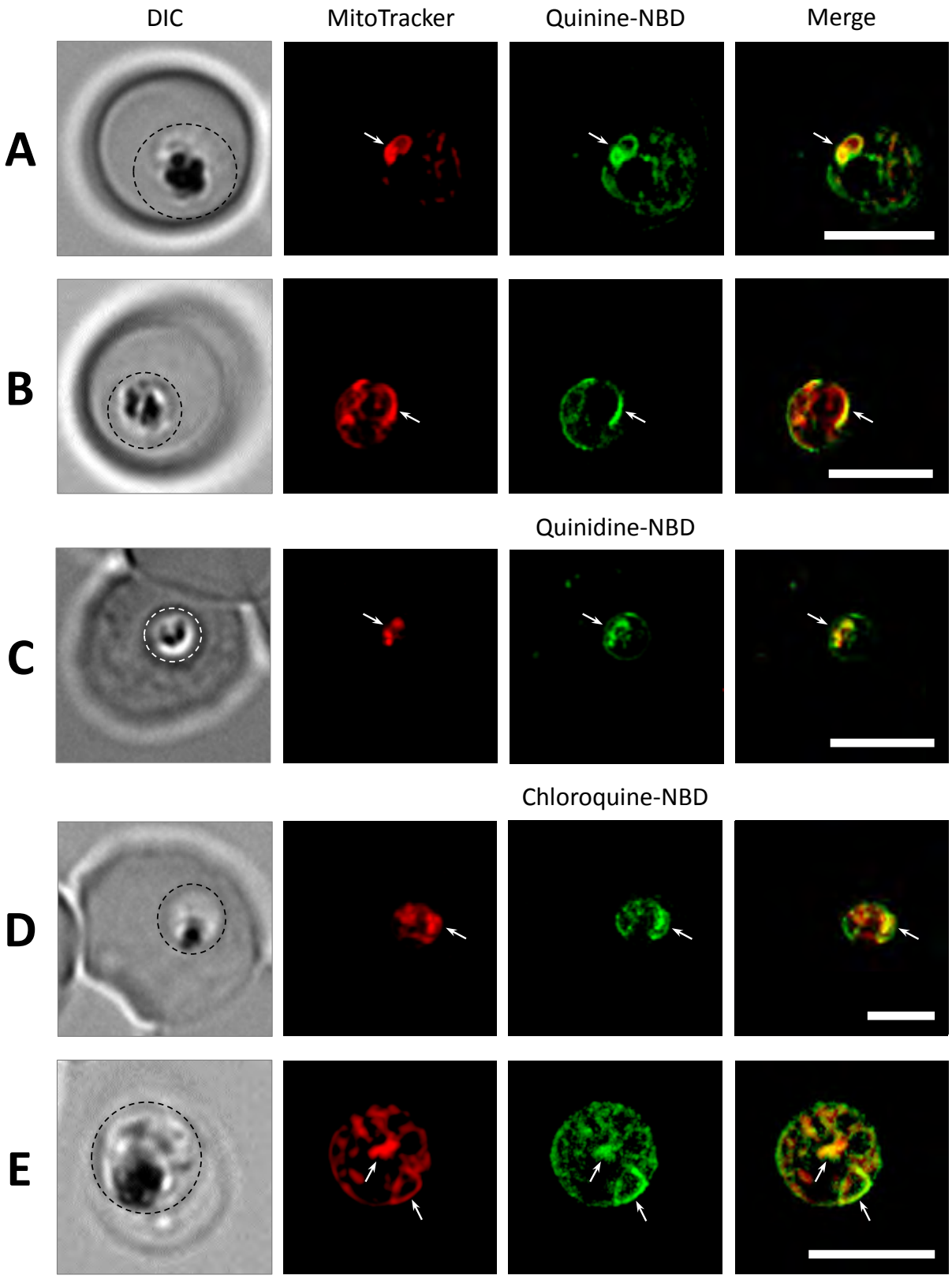

Figure 5.20. *Erythrocytes infected with mature* P. falciparum *and incubated with MitoTracker Deep Red (red) and the NBD-labelled analogues (green). Yellow indicates regions of overlap. Areas of most intense overlap are indicated with a white arrow. Scale bars represent 5 μm.*

5.4.2. Colocalisation studies with lipid probes LysoTracker Red and Nile Red

To further investigate the affinity of the fluorescent analogues of the quinoline antimalarials for lipid and membranous structures within *P. falciparum*, infected erythrocytes were stained with either LysoTracker Red or Nile Red and examined using SR-SIM.

LysoTracker Red, which comprises a weakly basic aminoalkyl chain tethered to a BODIPY reporter, stains the membranes of acidic organelles. When infected erythrocytes were stained with this dye, the regions of greatest fluorescence intensity corresponded to the parasite digestive vacuole (white arrows in Panel A, Figure 5.21). Some punctate structures, possibly acidic transport vesicles, were also illuminated. LysoTracker Red also weakly stained the parasite plasma membrane, presumably because the cytoplasmic pH of *P. falciparum* is somewhat lower than that of the host cell. Occasional cross-talk in the green channel was observed due to photo-conversion of LysoTracker Red to a green fluorescent molecule,[34] but this signal was weak compared to the analogues and so could be ignored.

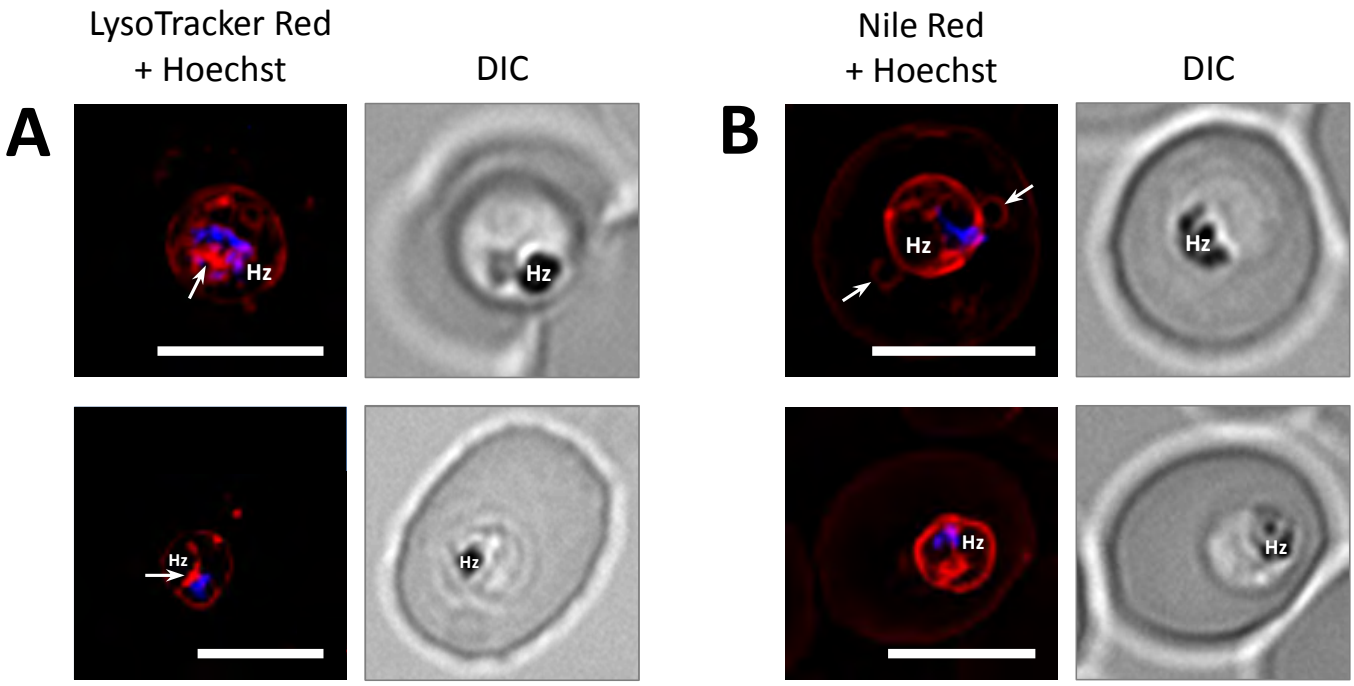

Figure 5.21. *Erythrocytes infected with* P. falciparum *and illuminated by (A) LysoTracker Red or (B) Nile Red and co-stained with Hoechst (blue). Haemozoin is labelled "Hz". Scale bars represent 5 μm.*

Nile Red (Panel B in Figure 5.21) stains membranes brightly. It revealed the membrane network within *P. falciparum* in which the digestive vacuole and parasite plasma membranes were often particularly clear. Nile Red also illuminated the host cell plasma membrane weakly and small,

vesicle-like structures within the erythrocyte cytosol (white arrows in Figure 5.21B). As described in Section 5.2.4, Nile Red is useful for differentiating between structures of phospholipid and neutral lipid composition, especially neutral lipid bodies in very mature parasites, but this property comes at the cost of its broad excitation and emission spectra which make co-staining with other dyes challenging.

As colocalisation between LysoTracker Red and the analogues of quinine and quinidine was discussed quantitatively above (Section 5.3.2), observations will now focus on colocalisation between this lipid dye and the NBD-labelled chloroquine analogue.

Figure 5.22 illustrates once again the selective accumulation of the chloroquine analogue within infected erythrocytes. Panel A shows two erythrocytes alongside one another, infected (left) and uninfected (right). Fluorescence corresponding to the chloroquine analogue was only detected from the infected erythrocyte and specifically from *P. falciparum*. Closer inspection of this cell reveals partial colocalisation of the chloroquine analogue with LysoTracker Red but not with Hoechst. The green signal that does not colocalise with the LysoTracker Red probably arises from accumulation in the aqueous compartment of the digestive vacuole rather than from the membranes, an observation which was previously difficult to resolve using the confocal microscope. This indicates a preference of the chloroquine analogue for hydrophilic environments rather than for membranes which is probably a fundamental difference between this class of antimalarial and the quinoline methanols. Although some colocalisation seems to be present between LysoTracker Red, chloroquine and the Hoechst dye, this is probably a misleading result from the maximum intensity projection which has placed these organelles “on top” of one another in the two-dimensional representation.

Panel B of Figure 5.22 represents a magnified region of Panel A. The green signal corresponding to the chloroquine analogue appears to be grouped into two distinct patterns. One part of the signal is closely associated with the haemozoin, which presumably indicates accumulation within the digestive vacuole (“DV”), while the other originates from the other side of the cell and appears to be in close association with the plasma membrane. This signal, coupled with its distinctive worm-like shape and apposition to the parasite plasma membrane, is highly suggestive of accumulation within the mitochondrion. That LysoTracker Red stains the mitochondrion might be explained by the pH gradient maintained between the intermembrane space and the matrix of this organelle. Studies on mammalian mitochondria have found that the difference in pH between these two compartments of the mitochondrion may be as much as a whole pH unit, which is probably sufficient to account for the accumulation of the LysoTracker Red dye within this organelle.[35]

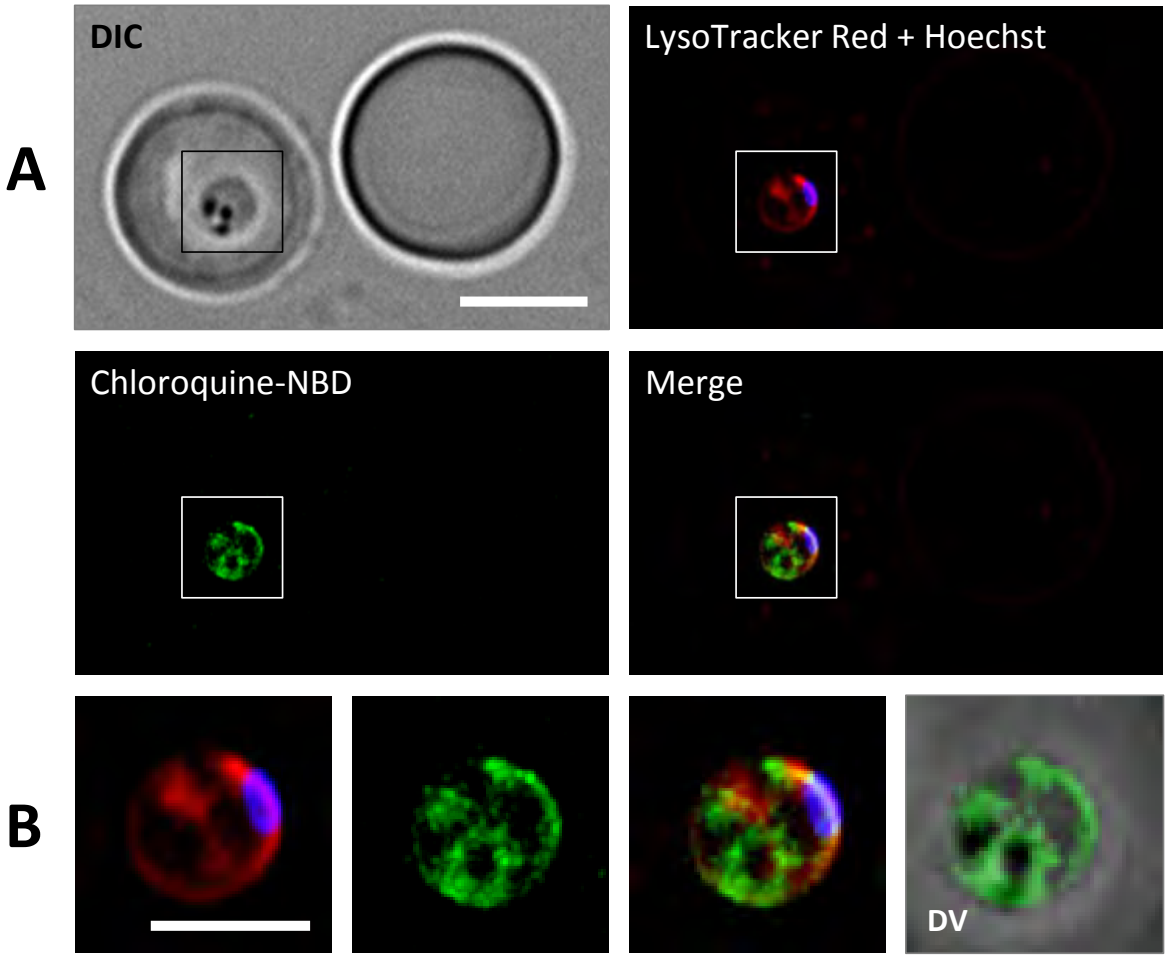

Figure 5.22. *Panel A shows infected (left) and uninfected (right) erythrocytes alongside one another. Green fluorescence is detected from* P. falciparum *only. Some colocalisation with LysoTracker Red is observed. Panel B represents a magnification of the boxed region in Panel A and indicates two main regions of green fluorescence corresponding to the chloroquine analogue. One region is clearly haemozoin-associated and is likely to represent the digestive vacuole ("DV") while the other region appears to represent what one might expect for accumulation within the mitochondrion. Scale bars represent 5 µm.*

Both lipid dyes often revealed small vesicle-like structures within the host cell and sometimes in neighbouring uninfected erythrocytes. These are illustrated in Figure 5.23 which represents the same erythrocytes as those in Figure 5.22. In Panel B of Figure 5.23, the contrast was enhanced to reveal all staining features of LysoTracker Red as indicated by white arrowheads. These vesicle-like structures have recently been characterised and it is now known that they are exported from *P. falciparum* and may enter other erythrocytes, even uninfected ones. That they are illuminated with LysoTracker Red does not necessarily mean that they are very acidic in nature, as they exhibit about the same intensity of fluorescence as the plasma membranes of infected and uninfected erythrocytes. It has recently been determined that these structures, so-

called "exosome-like vesicles", enable direct communication between parasites within a population and are even capable of delivering genes.[36] Communication via these exosome-like vesicles also appears to promote differentiation to the sexual forms of *P. falciparum*.[36]

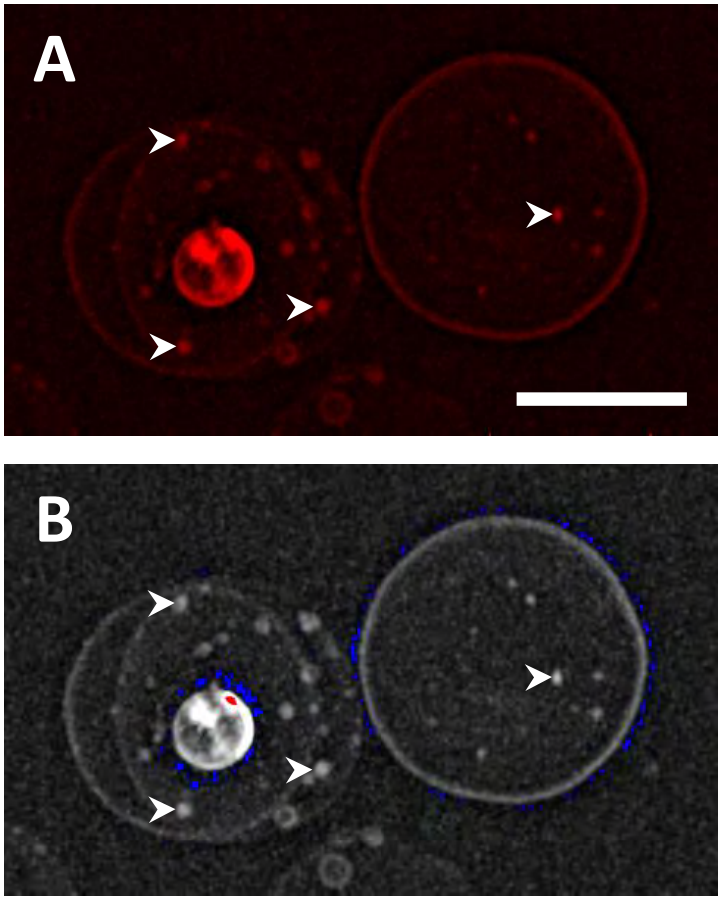

Figure 5.23. *Panel A shows infected (left) and uninfected (right) erythrocytes side-by-side that are stained with LysoTracker Red. There are many extra-parasitic vesicles, some of which are indicated by white arrowheads. In Panel B, the same image has been converted to greyscale to enhance the contrast. Blue indicates empty pixels. The scale bar represents 5 μm.*

Infected erythrocytes treated with the chloroquine analogue were also incubated with Nile Red. This time, the intimate association between membranous components of *P. falciparum* and the chloroquine analogue is more obvious in the mature trophozoite represented in Figure 5.24. In this image sequence, the chloroquine analogue exhibits an affinity for the parasite plasma membrane ("PPM") and, especially, the internal membrane of the digestive vacuole ("DV"). The two prominent lipid bodies, indicated by white arrowheads, probably do not correspond to signal from the chloroquine derivative but instead represent cross-talk from Nile Red due to the high excitation energies used to excite the former fluorophore. However, it is difficult to say

where the signal arising from the lipid bodies "starts" and where the signal from the chloroquine analogue "ends"; hence, there might be some overlap between the spatial localisation of the signals.

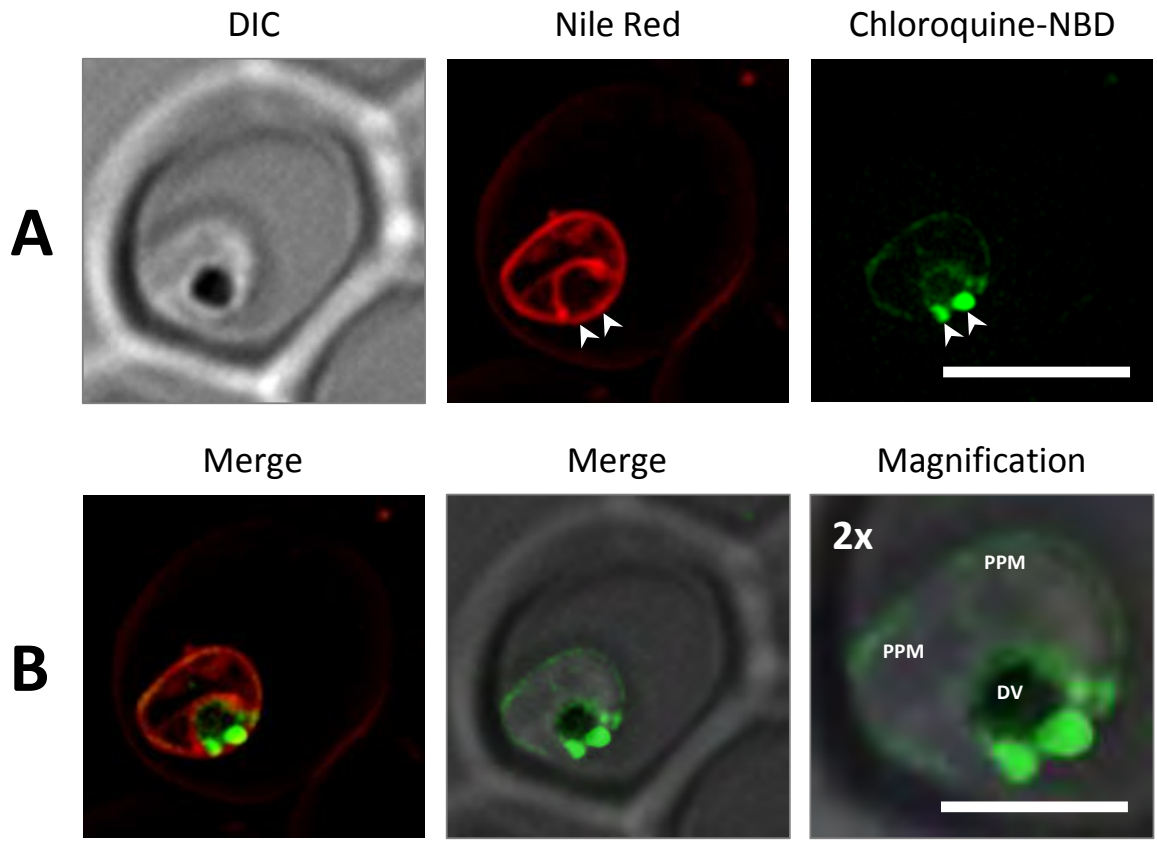

Figure 5.24. *An infected erythrocyte stained with Nile Red (red) which clearly indicates the parasite plasma membrane ("PPM") and the digestive vacuole ("DV") in the presence of the NBD-labelled chloroquine analogue (green). White arrowheads indicate two neutral lipid bodies, the signals of which likely originate from the Nile Red dye. Scale bars represent 5 μm.*

Figure 5.24 presents intriguing evidence in light of recent work by Kapishnikov et al. which shows that haemozoin crystals nucleate at the inner surface of the digestive vacuole with biocrystallisation occurring in the aqueous rather than in the lipid phase.[29,30] With respect to the inhibition of haemozoin formation, Figure 5.24 suggests that this may occur from adsorption of chloroquine to haemozoin crystals positioned in or adjacent to the inner membrane of the digestive vacuole. One might usually expect the signal from the analogue to be quenched in this case; however, as the chloroquine analogue is present at much higher levels than its IC_{50} value, there may well be an over-abundance of probe to compensate for the quenching effect.

Intimate association between the alkaloid analogues with membranous structures of acidic compartments has been shown via quantitative analysis with LysoTracker Red (Section 5.3.2) and a similar affinity of the chloroquine analogue for phospholipid components is demonstrated in Figure 5.24 above. The discussion will now turn to colocalisation of the fluorescent analogues with neutral lipid components. For these experiments, the analogues were administered in somewhat higher concentrations than usual (2 μM compared to 300 nM) to generate sufficient signal such that lower excitation energies could be used to ensure that there was no cross-talk from the Nile Red channel in the full green collection range (500-550 nm). It was not possible to eliminate cross-talk in the presence of the NBD-labelled chloroquine derivative; hence, these colocalisation studies were only performed with the analogues of quinine and quinidine. Figure 5.25 illustrates two representative images of infected cells at different stages of the intraerythrocytic life cycle treated with Nile Red and the NBD-labelled quinidine analogue.

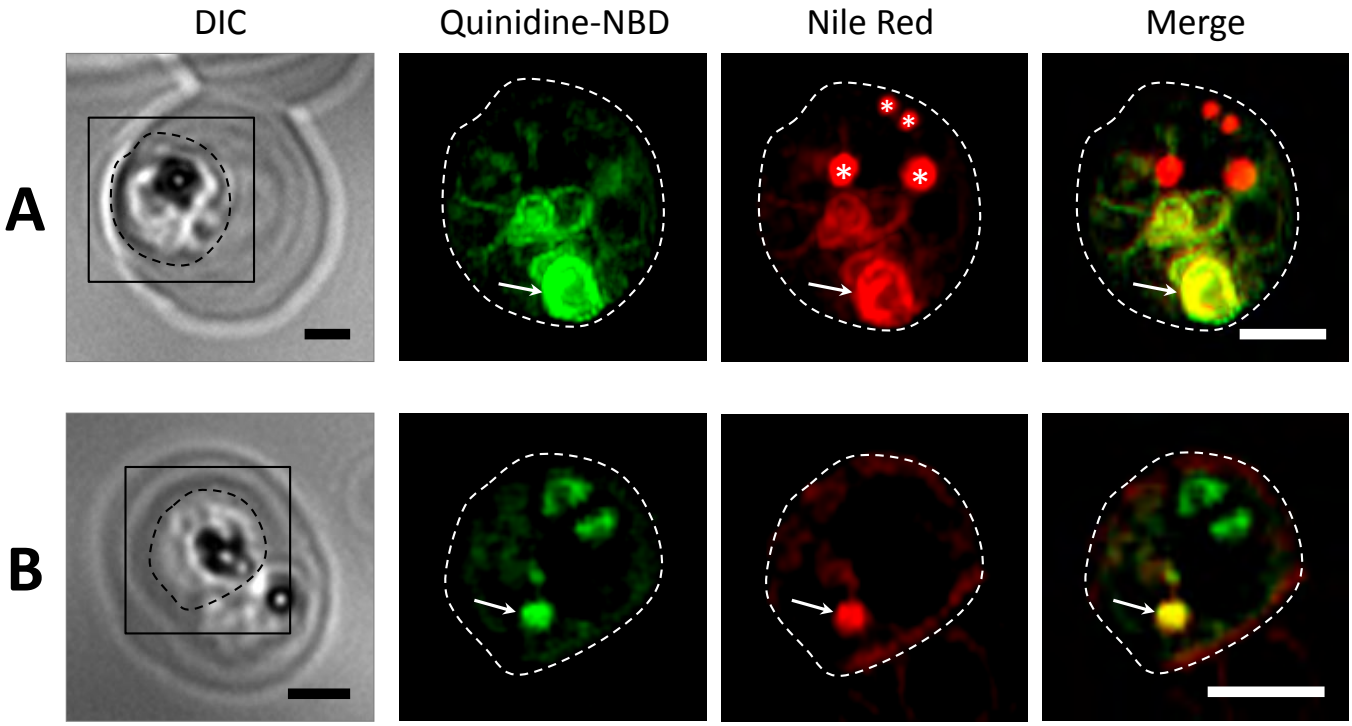

Figure 5.25. P. falciparum*-infected erythrocytes stained with a high concentration of the NBD-labelled quinidine analogue (green) to eliminate any cross-talk from the Nile Red dye (red). Neutral lipid bodies are indicated by white asterisks. The arrow in Panel A refers to colocalisation within a densely-reticulated structure, possibly the ER or the mitochondrion. The arrow in Panel B indicates a lipid body-like structure that does not match the intensity profile of a typical neutral lipid body. Scale bars represent 2 μm.*

Panel A in Figure 5.25 represents a schizont. This is indicated by nuclear division that has occurred at the periphery of the cell in the compartments not illuminated by any signal. Four

spherical neutral lipid bodies are evident and are indicated by white asterisks. These vary in size from 0.3 μm to 0.7 μm and appear to be in intimate association with the haemozoin, although one cannot tell whether they are placed within or outside the digestive vacuole. These neutral lipid bodies do not show colocalisation with the quinidine analogue, except for the large lipid body on the right-hand side for which partial colocalisation may be observed. There is broad colocalisation between the quinidine analogue and Nile Red across the rest of the cell, especially within a densely-reticulated structure in the lower half of the cell (indicated by a white arrow) which represents the ER or the mitochondrion, or both.

On the other hand, Panel B in Figure 5.25 represents a mature trophozoite. The white arrow indicates a region of intense colocalisation of the two dyes which, although resembling a haemozoin-associated lipid body, does not match the spherical shape or the deep fluorescence profile typical of neutral lipid bodies. Furthermore, as will be discussed below, neutral lipid bodies are only observed in later trophozoites and schizonts.[32] Thus this structure is more likely to be one of the organelles in which colocalisation was previously observed and thus may be the ER or the mitochondrion. As this structure lies in close association with the digestive vacuole, it may be the former. Additionally, there is a region of NBD-labelled quinidine accumulation at the top of the cell that is clearly haemozoin-associated but does not overlap with the Nile Red. This is most likely evidence of accumulation of the quinidine analogue within the digestive vacuole.

Of all the cells examined (n = 15), approximately half of the neutral lipid bodies that were identified colocalised only partially with the quinine and quinidine analogues such as the example in Figure 5.25A. For the other half of the neutral lipid bodies identified, no colocalisation was observed. Thus it is unlikely that the quinoline methanol antimalarials exert a significant portion of their mechanism of action via accumulating within neutral lipid bodies; nevertheless, it is still possible that partial accumulation on the surface of the lipid body may be sufficient to exert an important biological effect.

It is interesting that the NBD-labelled alkaloids do not merely sequester within the lipid bodies on account of their high lipophilicities compared to the parent compounds. It has previously been hypothesised that these lipid bodies may sequester free Fe(III)PPIX to promote haemozoin biocrystallisation,[28] but this was not observed as any such sequestration would result in quenching of the Nile Red signal as has previously been shown in synthetic lipid bodies.[37] Such quenching does not appear to occur endogenously as the Nile Red signal from these bodies is always deeply intense and shows no evidence of internal quenching. However, that does not rule out accumulation of Fe(III)PPIX, or the Fe(III)PPIX-quinoline complex, on the surface of the neutral lipid bodies where fluorescence quenching would render these species unobservable.

In order to investigate whether the NBD-labelled alkaloids exert any effects on the population or size distribution of haemozoin-associated neutral lipid bodies, cells were examined in the absence and presence of the alkaloid analogues and the number of neutral lipid bodies per cell was enumerated. In each case, the cells were classed according to their developmental stage. The size of haemozoin-associated lipid bodies, if present, were recorded. To facilitate this process, the mature stages of intraerythrocytic development were divided into six stages based on morphological considerations (Table 5.3). It was thought that identifying specific morphological features for developmental classification was a more reliable system than using time points which may vary owing to imperfect synchronisation. Neutral lipid bodies were assumed to be spherical and classified as small (< 0.5 μm), medium (0.5-1 μm) or large (> 1 μm). In total, 51 cells were examined. 29 of these were untreated while the remaining 22 were treated with either of the NBD-labelled alkaloids.

Table 5.3. *Classification of cells over six stages from early trophozoite to late schizont.*

Stage	Size of cell relative to host erythrocyte	Presence of haemozoin	Appearance and number of nuclei
Early trophozoite	Small and spherical	Light brown pigment visible	1, inside cytoplasm (not on edge of cell)
Mid-trophozoite	Medium-sized and spherical	Clump of pigment	1, enlarged
Late trophozoite	Enlarged; not necessarily spherical	Large clump(s) of pigment	1 or 2, irregularly-shaped
Early schizont	Irregular shape	Large clump(s) of pigment	2-5, irregularly-shaped
Mid-schizont	Irregular shape; parasite fills most of the host cell	Large clump(s) of pigment	> 5, mostly oval in shape
Late schizont	Parasite fills the entire host cell; about to burst	Large clump(s) of pigment	>> 5, all round or oval in shape

Neutral lipid bodies were only found in late trophozoite-stage parasites as has been previously observed.[32] The vast majority of these were digestive vacuole-associated; of the 84 neutral lipid bodies examined, only 15 (18%) were not in clear proximity to the haemozoin. Figure 5.26 illustrates the average number and size distribution of haemozoin-associated lipid bodies per cell from late trophozoites to late schizonts. In untreated cells, small to medium-sized lipid bodies were the most common. Medium-sized lipid bodies occurred more frequently in treated cells. This trend may be rationalised if the NBD-labelled alkaloids are considered to behave in a detergent-like manner, with the charged quinoline group at one end tethered to a hydrophobic fluorophore at the other end which may encourage the aggregation of smaller lipid bodies.

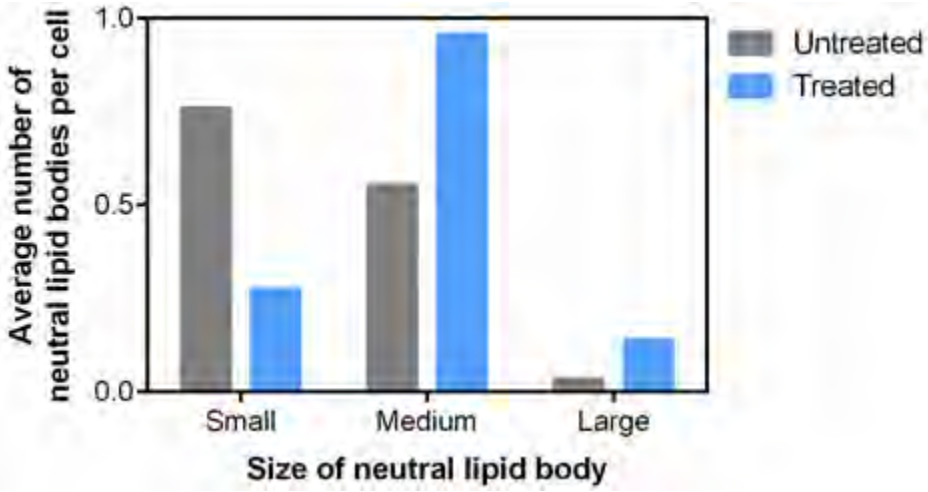

Figure 5.26. *The average number and size distribution of haemozoin-associated neutral lipid bodies per cell across all phases of the life cycle of* P. falciparum *in the absence or presence of the NBD-labelled alkaloids. Neutral lipid bodies were classified as small (< 0.5 μm), medium (0.5-1 μm) or large (> 1 μm).*

Figure 5.27 depicts the average number and size distribution of haemozoin-associated neutral lipid bodies per cell across the four major stages in which they appear. Similar trends are observed for both untreated and treated cells. There is an increase in the average number of lipid bodies per cell from the late trophozoite phase, peaking in the mid-schizont phase. Thereafter the average number of lipid bodies per cell decreases, possibly through aggregation.

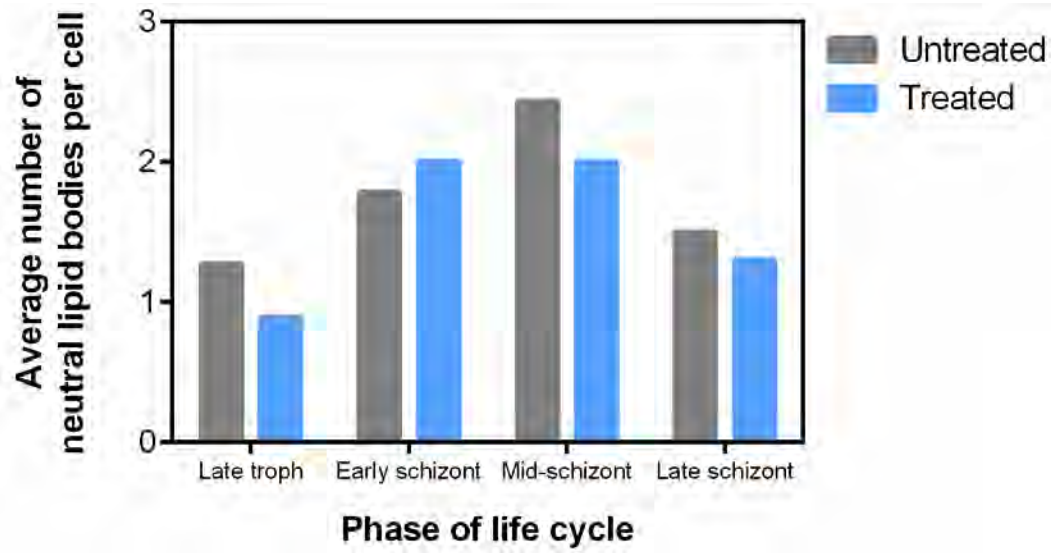

Figure 5.27. *The average number and size distribution of haemozoin-associated neutral lipid bodies per cell across the four life cycle stages of* P. falciparum *in which they appear in the absence or presence of the NBD-labelled alkaloids.*

This increase in the average number of lipid bodies from the trophozoite to the schizont stage corresponds to the increase in diacylglycerol and triacylglycerol seen over the final 16 hours of the parasite's life cycle.[38] In particular, this profile matches closely the abundance profile of triacylglycerol in *P. falciparum* which peaks in the early- to mid-schizont phase but diminishes just before host cell rupture.[38]

Figure 5.28 illustrates the average number of neutral lipid bodies per cell as a fraction of the total. This indicates that the small lipid bodies form a smaller proportion of the total in the later-stage parasites while the proportion of medium-sized lipid bodies increases as the parasite matures. This suggests that aggregation of smaller lipid bodies may be responsible for the decrease in number of lipid bodies reported in the late schizont phase. The final few hours of the *P. falciparum* life cycle are characterised by an increase in diacylglycerol abundance,[38] suggesting that hydrolysis of triacylglycerol to diacylglycerol may be related to such aggregation of neutral lipid bodies.

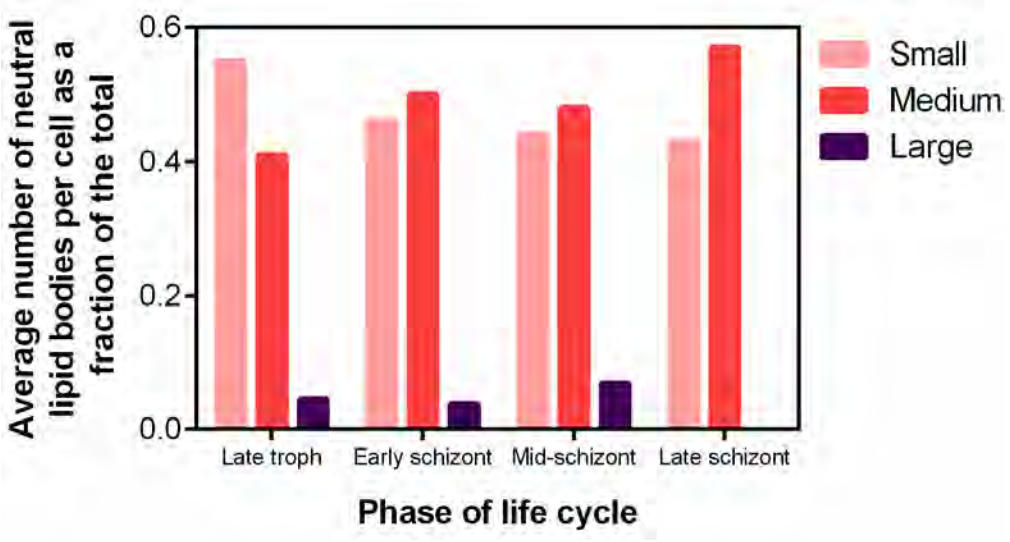

Figure 5.28. *The size distribution of haemozoin-associated neutral lipid bodies in untreated cells, measured across the late phases of the life cycle of* P. falciparum *in which they appear.*

A drawback of this study is the high concentrations of the NBD-labelled alkaloids that were used to increase their fluorescence signal in order to eliminate cross-talk from the Nile Red (2.0 μM). It is undesirable to use such high concentrations as it has been found that micromolar levels of lysosomotropic compounds induce apoptotic hallmarks. This has led investigators to establish a programmed cell death pathway for *P. falciparum*, analogous to mammalian apoptosis.[39,40] It has been found that micromolar levels of chloroquine (> 3 μM) resulted in the permeabilisation of

the digestive vacuole membrane with an abrupt and rapid redistribution of calcium ions.[39,40] However, there was no visible rupture of the digestive vacuole membrane by transmission electron microscopy.[40] Digestive vacuole permeabilisation is trigged by any lysosomotropic compound, suggesting that the NBD-labelled alkaloids may have the same effect. However, it is unlikely that neutral lipid metabolism was deleteriously affected over the short exposure time of the high concentrations of these analogues to the cells (1-2 hours). The investigators claim that digestive vacuole permeabilisation and other apoptotic indicators only occur approximately three hours after drug treatment at high concentrations.[41]

5.5. Critical discussion of live-cell microscopy observations

For decades it has been believed that the prototypical quinoline antimalarials, quinine and chloroquine, exert their mechanism of action on *P. falciparum* by inhibiting haemozoin biocrystallisation. Not only do these molecules interact directly with Fe(III)PPIX[42] and probably with haemozoin itself,[43] but they have been shown to inhibit the formation of β-haematin.[44] Most recently, it has been shown that treatment of *P. falciparum* with both chloroquine and quinine leads to a decrease in haemozoin formation and a concomitant increase in free Fe(III)PPIX, lending support to this hypothesis.[9]

Such inhibition requires large quantities of the inhibitor to be present in the digestive vacuole of the parasite, the main site of haemoglobin catabolism and haemozoin biocrystallisation. While mechanisms of accumulation due to a "non-saturable" weak base effect and "saturable" Fe(III)PPIX binding have been described in Section 1.6.1, visual evidence of accumulation in the digestive vacuole has been provided by autoradiography of tritiated chloroquine and quinidine[45] and the detection of chloroquine derivatives using fluorescence microscopy.[46,47] Additional evidence supporting haemozoin inhibition as the primary mechanism of action of these quinoline antimalarials has now been provided by the detailed live-cell studies described herein.

Mature-stage *P. falciparum* were treated with the novel fluorescent analogues of quinine, quinidine and chloroquine that were synthesised earlier in this work. These analogues accumulated selectively in infected erythrocytes and almost entirely in the parasite, although some staining of the host cell cytoplasm or plasma membrane by the alkaloid analogues was observed. The analogues of quinine and quinidine were distributed more diffusely throughout the parasite than the chloroquine analogue which was prominently localised to fewer regions within the parasite. Significantly, all three analogues accumulated near the haemozoin in a region corresponding to the digestive vacuole (Figures 5.7 and 5.9). This was particularly notable for the chloroquine analogue for which super-resolution imaging revealed areas of intense accumulation near the haemozoin (Figure 5.22). These observations are in accordance with expectations for haemozoin formation as the mechanism of action of these antimalarials. The observations also account for the swelling of the digestive vacuole that is evident in ultrastructural studies.[1,2] Additionally, this is the first time that visual evidence of accumulation within *P. falciparum* of a labelled quinine derivative has been provided.

Treatment with the fluorescent analogues at their respective IC_{50} values generated no detectable signal. This was most likely due to fluorescent quenching by the putative target of

these molecules, Fe(III)PPIX, further supporting haemozoin inhibition as their mechanism of action. As a result, cells were treated with concentrations of probes at several times their IC_{50} values to generate a detectable signal. It should be noted that the fluorescence emission of the NBD reporter fluorophore is at least 15-fold brighter in environments corresponding to the polarities of neutral lipid and phospholipid, respectively, compared to aqueous solution (Figure 4.6). Hence, the fact that prominent signals were detected from the aqueous interior of the digestive vacuole shows that this is a site of significant accumulation of the analogues.

The NBD-labelled analogues of quinine and quinidine exhibited colocalisation with LysoTracker Red, a dye which partitions into the membranes of acidic organelles, but not with the nuclear stain, Hoechst. This was corroborated by quantitative measurements which showed that these analogues have a strong affinity for membranous structures, especially the quinidine analogue. Whether this is related to their relative lipophilicities may be examined by comparing the acid dissociation constants and partition coefficients of the parent alkaloids (Table 5.4). Considering that these alkaloids are diastereomers of one another, these values are very similar. Although quinidine is less hydrophobic than quinine in its uncharged form or at a neutral pH, it is more lipophilic at an acidic pH (log *D* = 0.40 compared to log *D* = 0.30 for quinine) which may explain why it is more likely to colocalise to a greater extent with LysoTracker. This observation may also be related to the fact that quinidine is more active against the malaria parasite in vitro than its diastereomer quinine (Table 4.8), although it should be noted that the activities of the two analogues of these alkaloids against *P. falciparum* were very similar to one another.

Table 5.4. *Acid dissociation constants (pK_a) and partition coefficients of the diastereomeric alkaloids quinine and quinidine cited from Warhurst et al.*[48]

	pK_{a1}	pK_{a2}	Log *P*	Log *D* (pH 7.4)	Log *D* (pH 5.2)
Quinine	8.58	4.12	3.17	1.97	0.30
Quinidine	8.58	4.42	2.84	1.66	0.40

Quantitative analysis of the NBD-labelled alkaloids supports qualitative observations that all three analogues do not accumulate in the nucleus of the *P. falciparum*. It is still widely reported that these quinolines disrupt DNA replication by intercalating with the nucleic acid base pairs, a mechanism which requires high concentrations of drug in the nucleus and for which there is little evidence (Section 1.5.4).[49-51] It has now been possible to show, using qualitative and quantitative image analysis of these fluorescent analogues, that an absence of accumulation of

these analogues in the nucleus makes this mode of action of the quinoline antimalarials extremely unlikely.

With respect to other organelles, it is very likely that the quinoline antimalarials associate with the ER of the parasite. Although confocal imaging of ER-Tracker Red gave a featureless signal throughout the cytoplasm of *P. falciparum* which broadly colocalised with the alkaloid analogues, super-resolution microscopy indicated clear colocalisation of all three analogues with the ER marker (Figure 5.18). In addition, the signal of this marker was attenuated if administered simultaneously with the analogues, suggesting competitive binding to the sulfonylurea receptors on the surface of the ER to which ER-Tracker and quinine are known to bind.[16] This provides further evidence for an interaction between the drug analogues and this organelle. Furthermore, these observations corroborate a previous ultrastructural study of *P. falciparum* which noted disintegration of the ER following treatment with chloroquine.[1] This may be enhanced by the lytic effect of Fe(III)PPIX which was observed to localise to a region corresponding to the ER following chloroquine treatment.[9] Indeed, the ER is implicated in phospholipid biosynthesis, calcium storage and trafficking of proteins in *P. falciparum* and has been shown to lie in close proximity to the digestive vacuole, an observation which was corroborated by the imaging described herein (Figure 5.18A).[33] Consequently, association of the quinoline antimalarials with the ER, either in their native form or as a complex with Fe(III)PPIX, may disrupt crucial metabolic processes within the ER or interrupt intracellular transport between this compartment and the digestive vacuole.

It is also possible that the quinoline antimalarials localise to the mitochondrion of *P. falciparum* (Figure 5.20). The organelle signal provided by MitoTracker Deep Red was clear and represented the tube-like structure described by previous morphological studies.[33] However, colocalisation with this organelle was less clear than in the case of the ER. Despite this, colocalisation with all three NBD-labelled analogues was supported by quantitative analysis. The intermembrane space in the mitochondrion might account for accumulation of the quinoline antimalarials due to the weak base effect, which may also explain labelling of the mitochondrion by LysoTracker Red. Accumulation of the analogues is consistent with the swelling of the mitochondrion that is observed by electron microscopy after treatment with both quinine and chloroquine.[1,2] It is thought that the mitochondrion may associate with the plasma membrane of *P. falciparum* to serve as a conduit for plasma membrane phospholipids.[33] Given the lipophilic nature of the quinoline antimalarials, especially the *Cinchona* alkaloids, it is possible that high concentrations of these drugs may interfere with this aspect of lipid metabolism. The mitochondrion has also been implicated in a programmed cell death pathway

after treatment with high concentrations of lysosomotropic molecules;[41] hence, it would not be surprising if this were due in part to an accumulation of the quinoline antimalarials there.

To investigate the affinity of the quinoline analogues for lipid components within *P. falciparum*, cells were co-stained with either LysoTracker Red or Nile Red and investigated with SR-SIM. There is evidence that haemozoin formation is mediated by neutral lipid bodies or phospholipid membranes (Section 1.3.2).[21,28-30] Pisciotta et al. have suggested that neutral lipid bodies provide transient repositories of free Fe(III)PPIX, concentrating the metalloporphyrin while promoting haemozoin formation at the surface where the acidic conditions of the digestive vacuole favour lipid-mediated biocrystallisation.[28] If this hypothesis is correct, it is plausible that the quinoline antimalarials might themselves accumulate in the neutral lipid bodies and sequester free Fe(III)PPIX by complexation, reducing the availability of Fe(III)PPIX for biocrystallisation. However, quenching of the Nile Red-labelled lipid bodies, which would be expected in the case of Fe(III)PPIX sequestration in these bodies, was not observed.[37] Furthermore, only very partial colocalisation, if any, between neutral lipid bodies and the NBD-labelled alkaloids was observed in mature parasites. Despite being implicated in haemozoin formation, neutral lipid bodies are only observed from the late trophozoite stage, well after biocrystallisation has commenced. It is, however, possible that Fe(III)PPIX accumulates in lipid bodies in earlier stages of the life cycle to promote haemozoin biocrystallisation, quenching the signal from Nile Red and hence preventing their detection in these early stages.

Phospholipid components have also been implicated in haemozoin formation and hence are of interest in elucidating the mechanism of action of the quinoline antimalarials. Kapishnikov et al. recently reported that haemozoin nucleation occurs at the inner membrane of the digestive vacuole, with biocrystallisation occurring in the aqueous rather than the lipid phase.[29] The authors argue that their data rule out the possibility of haemozoin crystals being nucleated within, or on the surfaces of, lipid nanospheres.[29] This is supported by a striking observation in Figure 5.24 in which the chloroquine analogue was closely associated with the inner membrane of the digestive vacuole as well as the parasite plasma membrane. Close association of this analogue with the inner surface of the digestive vacuole membrane suggests an affinity for this membrane or even for adsorption to haemozoin, as these crystals have previously been shown to line the inner membrane of the digestive vacuole.[29] Adsorption to haemozoin as a mechanism of action for chloroquine is somewhat more plausible, stoichiometrically and chemically, than sequestration of Fe(III)PPIX in solution or in neutral lipid bodies. Alternatively, differential association with phospholipid membranes may also be responsible for the differential morphological effects exhibited by these antimalarials.[3,4]

There are several limitations to the fluorescence microscopy approach carried out in this work. Although live-cell imaging conditions imply that *P. falciparum* has been imaged with as few disturbances to its natural metabolic processes as possible, all three analogues of the quinoline antimalarials have been labelled by a hydrophobic fluorophore that is structurally-distinct from the parent molecules. Hopefully, the incorporation of this smallest-possible organic fluorophore has been mitigated by thorough evaluation against the parent antimalarials as carried out in Chapter 4. Nevertheless, the presence of the fluorophore reduces its aqueous solubility (Table 4.6), increasing its hydrophobicity and this may be responsible for the striking preference of the analogues for membranous and lipid components demonstrated above. Furthermore, these labelled probes are quenched upon complexation with Fe(III)PPIX and possibly by haemozoin as well. Despite the utility of fluorescence exhibited in this chapter, alternative techniques or fluorophores to probe solution- or solid-state interactions of these quinoline antimalarials with Fe(III)PPIX will be required.

5.6. Summary and conclusions

Live-cell fluorescence microscopy provides exceptional insights into structural and functional minutiae of intraerythrocytic *P. falciparum*. Although ultrastructural studies provide excellent resolution, these samples suffer from extensive preparation procedures and poor contrast. Most especially, structural and functional information cannot easily be related to one another. Light microscopy, on the other hand, lends itself to live-cell studies with minimal sample preparation, allowing the acquisition of reliable and dynamic information about the system at hand.

In this chapter, the novel fluorescent analogues of the quinoline antimalarials that were prepared in Chapter 3, and subsequently validated in Chapter 4, were investigated using live-cell imaging methods. Although *P. falciparum* presents a number of challenges for light microscopy, especially the photosensitivity of the cells and their small size, these may be overcome to generate valuable insights. In this work a number of commercially-available tracker dyes were selected to co-stain structures within live parasites.

The NBD-labelled derivatives of quinine, quinidine and chloroquine that were identified as suitable analogues of their parent antimalarials were all found to accumulate selectively within *P. falciparum*-infected erythrocytes. No accumulation was observed in uninfected erythrocytes. All three analogues, but especially the NBD-labelled chloroquine analogue, were frequently found in close association with the haemozoin pigment and hence with the digestive vacuole. This is consistent with its well-established primary mode of action as a haemozoin inhibitor. In addition to digestive vacuole accumulation, the analogues of quinine and quinidine were more diffusely spread throughout the cell and were also observed to accumulate in the plasma membranes of the parasite and the host cell.

By contrast, the bimane-labelled derivative of quinine was not observed at all, suggesting a quenching effect or a lack of accumulation within *P. falciparum* that may be responsible for its diminished activity against the parasite. Intriguingly, a bright autofluorescence signal corresponding to the haemozoin was detected in the blue region of the visible spectrum where such fluorescence has not previously been observed. This is likely to correspond to the supposed autofluorescence of quinine as claimed in previous work by Bohórquez et al.[19]

Quantitative colocalisation analysis indicated excellent correlation between the distributions of the two NBD-labelled alkaloids and LysoTracker Red, confirming the qualitative observations that these molecules show preferential accumulation in membranous structures within the parasite. Quinidine showed superior colocalisation with LysoTracker Red, indicating a high

affinity for membranes, which may be partly responsible for its more potent activity against *P. falciparum* compared to its diastereomer quinine. A negative correlation was found between all three of these signals and Hoechst, representing the parasite nucleus, indicating that it is extremely unlikely that these molecules exert their action by interfering with DNA replication as is still occasionally reported.

All three NBD-labelled quinoline antimalarials exhibited colocalisation with the ER and the mitochondrion following co-staining with the organelle-specific dyes ER-Tracker Red and MitoTracker Deep Red, respectively. Furthermore, the signal of the ER-Tracker Red was attenuated if the NBD-labelled quinolines and the dyes were administered simultaneously, suggesting competition for binding sites or changes in organelle morphology as a result of drug-treatment. This corroborates previous ultrastructural studies of *P. falciparum* which implicate both of these organelles in the mechanism of action of the quinoline antimalarials, as previous investigators have reported swelling of the mitochondrion and disintegration of the ER following treatment with these drugs.[1,2] Using super-resolution structured-illumination microscopy (SR-SIM), convincing colocalisation was again observed between all three NBD-labelled analogues and the ER and mitochondrion, but with much greater precision. It was again shown that the NBD-labelled chloroquine analogue possesses a strong affinity for the digestive vacuole, a characteristic shared by the NBD-labelled alkaloids in addition to their accumulation within membranous structures.

These NBD-labelled alkaloids did not accumulate significantly within haemozoin-associated neutral lipid bodies. Although the size distribution of these lipid bodies shifted from small to medium size after treatment (< 0.5 μm to 0.5-1.0 μm), and the average number of neutral lipid bodies per cell decreased after treatment, in both cases the mid-schizont phase of the life cycle exhibited the highest number of neutral lipid bodies per cell, corroborating previous studies[32] and matching the abundance profiles of neutral lipids during this stage of the life cycle.[38]

Taken together, these results support haemozoin inhibition through accumulation in the digestive vacuole as the primary mechanism of action of these quinoline antimalarials. Secondary effects due to association with the ER, mitochondrion and phospholipid membranes may cause deleterious metabolic disruption to the parasite. Whether these regions of accumulation within the parasite are the result of binding of these quinoline antimalarials to specific protein targets within *P. falciparum* is investigated in the subsequent chapter.

5.7. References

1. G. H. Jacobs, A. Oduola, D. E. Kyle, W. K. Milhous, S. K. Martin and M. Aikawa, *Am. J. Trop. Med. Hyg.*, 1988, **39**, 87.
2. N. Sachanonta, K. Chotivanich, U. Chaisri, G. D. H. Turner, D. J. P. Ferguson, N. P. J. Day and E. Pongponratn, *Ultrastruct. Pathol.*, 2011, **35**, 214.
3. O. Famin and H. Ginsburg, *Biochem. Pharmacol*., 2002, **63**, 393.
4. L. Roberts, T. J. Egan, K. A. Joiner and H. C. Hoppe, *Antimicrob. Agents Chemother.*, 2008, **52**, 1840.
5. F. Wissing, C. Sanchez, P. Rohrbach, S. Ricken and M. Lanzer, *J. Biol. Chem.*, 2002, **277**, 37747.
6. D. A. van Schalkwyk, K. J. Saliba, G. A. Biagini, P. G. Bray and K. Kirk, *PLOS ONE*, 2013, **8**, e58933.
7. M. Bellemare, D. S. Bohle, C. Brosseau, E. Georges, M. Godbout, J. Kelly, M. L. Leimanis, R. Leonelli, M. Olivier and M. Smilkstein, *J. Phys. Chem. B*, 2009, **113**, 8391.
8. A. Yayon, J. A. Vande Waa, M. Yayon, T. G. Geary and J. B. Jensen, *J. Protozool.*, 1983, **30**, 642.
9. J. M. Combrinck, T. E. Mabotha, K. K. Ncokazi, M. A. Ambele, D. Taylor, P. J. Smith, H. C. Hoppe and T. J. Egan, *ACS Chem. Biol.*, 2013, **8**, 133.
10. T. S. Skinner, L. S. Manning, W. A. Johnston and T. M. E. Davis, *Int. J. Parasitol.*, 1996, **26**, 519.
11. D. W. Wilson, C. Langer, C. D. Goodman, G. I. McFadden and J. G. Beeson, *Antimicrob. Agents Chemother.*, 2013, **57**, 1455.
12. Y. Zhang, K. S. O. Asante and A. Jung, *J. Parasit.*, 1986, **72**, 830.
13. M. Lanzer and P. Rohrbach, *Curr. Sci.*, 2007, **92**, 1561.
14. I. Johnson and M. T. Z. Spence, *The Molecular Probes Handbook: A Guide to Fluorescent Probes and Labelling Technologies*, Life Technologies Corporation, 2010.
15. J. L. Weber, *Gene*, 1987, **52**, 103.
16. P. Bednarczyk, A. Kicińska, V. Kominkova, K. Ondrias, K. Dolowy and A. Szewczyk, *J. Membrane Biol.*, 2004, **199**, 63.
17. P. Gratraud, E. Huws, B.Falkard, S. Adjalley, D. A. Fidock, L. Berry, W. R. Jacobs, M. S. Baird, H. Vial and L. Kremer, *PLOS ONE*, 2009, **4**, e6889.
18. E. H. Ekland, J. Schneider and D. A. Fidock, *FASEB J.*, 2011, **25**, 3583.
19. E. B. Bohórquez, M. Chua and S. R. Meshnick, *Malaria J.*, 2012, **11**, 350.
20. P. Greenspan, E. P. Mayer and S. D. Fowler, *J. Cell Biol.*, 1985, **100**, 965.
21. K. E. Jackson, N. Klonis, D. J. P. Ferguson, A. Andisa, C. Dogovski and L. Tilley, *Mol. Microbiol.*, 2004, **54**, 109.

22. Y. Kuhn, P. Rohrbach and M. Lanzer, *Cell. Microbiol.*, 2007, **9**, 1004.
23. L. L. Hsiao, R. J. Howard, M. Aikawa and T. F. Taraschi, *Biochem. J.*, 1991, **274**, 121.
24. K. W. Deitsch and T. E. Wellems, *Mol. Biochem. Parasitol.*, 1996, **76**, 1.
25. C. H. Walker, R. M. Sibly, S. P. Hopkin and D. B. Peakall, *Principles of Ecotoxicology (Fourth Edition)*, CRC Press, 2012.
26. S. Bolte and F. P. Cordelières, *J. Microsc.*, 2006, **224**, 213.
27. S. V. Costes, D. Daelemans, E. H. Cho, Z. Dobbin, G. Pavlakis and S. Lockett, *Biophys. J.*, 2004, **86**, 3993.
28. J. M. Pisciotta, I. Coppens, A. K. Tripathi, P. F. Scholl, J. Shuman, S. Bajad, V. Shulaev and D. J. Sullivan, *Biochem. J.*, 2007, **402**, 197.
29. S. Kapishnikov, T. Berthing, L. Hviid, M. Dierolf, A. Menzel, F. Pfeiffer, J. Als-Nielsen and L. Leiserowitz, *Proc. Natl. Acad. Sci. USA*, 2012, **109**, 11184.
30. S. Kapishnikov, A. Weiner, E. Shimoni, P. Guttmann, G. Schneider, N. Dahan-Pasternak, R. Dzikowski, L. Leiserowitz and M. Elbaum, *Proc. Natl. Acad. Sci. USA*, 2012, **109**, 11188.
31. J. Achan, A. O. Talisuna, A. Erhart, A. Yeka, J. K. Tibenderana, F. N. Baliraine, P. J. Rosenthal and U. D'Alessandro, *Malaria J.*, 2011, **10**, 144.
32. N. M. Q. Palacpac, Y. Hiramine, F. Mi-ichi, M. Torii, K. Kita, R. Hiramatsu, T. Horii and T. Mitamura, *J. Cell Sci.*, 2004, **117**, 1469.
33. G. G. van Dooren, M. Marti, C. J. Tonkin, L. M. Stimmler, A. F. Cowman and G. I. McFadden, *Mol. Microbiol.*, 2005, **57**, 405.
34. E. C. Freundt, M. Czapiga and M. J. Lenardo, *Cell Res.*, 2007, **17**, 956.
35. J. Santo-Domingo and N. Demaurex, *J. Gen. Physiol.*, 2012, **139**, 415.
36. N. Regev-Rudzki, D. W. Wilson, T. G. Carvalho, X. Sisquella, B. M. Coleman, M. Rug, D. Bursac, F. Angrisano, M. Gee, A. F. Hill, J. Baum and A. F. Cowman, *Cell*, 2013, **153**, 1120.
37. A. N. Hoang, R. D. Sandlin, A. Omar, T. J. Egan and D. W. Wright, *Biochemistry*, 2010, **49**, 10107.
38. S. Gulati, E. H. Ekland, K. V. Ruggles, R. B. Chan, B. Jayabalasingham, B. Zhou, P. Mantel, M. C. S. Lee, N. Spottiswoode, O. Coburn-Flynn, D. Hjelmqvist, T. S. Worgall, M. Marti, G. D. Paolo and D. A. Fidock, *Cell Host Microbe*, 2015, **18**, 371.
39. J. H. Ch'ng, S. R. Kotturi, A. G. L. Chong, M. J. Lear and K. S. W. Tan, *Cell Death Dis.*, 2010, **1**, e26.
40. J. H. Ch'ng, K. Liew, A. S. P. Goh, E. Sidhartha and K. S. W. Tan, *Cell Death Dis.*, 2011, **2**, e216.
41. J. H. Ch'ng, L. Renia, F. Nosten and K. S. W. Tan, *Trends Parasitol.*, 2012, **28**, 220.
42. T. J. Egan, *J. Inorg. Biochem.*, 2006, **100**, 916.
43. J. Gildenhuys, T. le Roux, T. J. Egan and K. A. de Villiers, *J. Am. Chem. Soc.*, 2013, **135**, 1037.
44. T. J. Egan, D. C. Ross and P. A. Adams, *FEBS Lett.*, 1994, **352**, 54.

45. D. J. Sullivan, I. Y. Gluzman, D. G. Russell and D. E. Goldberg, *Proc. Natl. Acad. Sci. USA*, 1996, **93**, 11865.
46. M. Cabrera, J. Natarajan, M. F. Paguio, C. Wolf, J. S. Urbach and P. D. Roepe, *Biochemistry*, 2009, **48**, 9471.
47. C. C. Y. Loh, R. Suwanarusk, Y. Q. Lee, K. W. K. Chan, K. Choy, L. Rénia, B. Russell, M. J. Lear, F. H. Nosten, K. S. W. Tan and L. M. C. Chow, *PLOS ONE*, 2014, **9**, e110800.
48. D. C. Warhurst, J. C. Craig, I. S. Adagu, D. J. Meyer and S. Y. Lee, *Malar. J.*, 2003, **2**, 26.
49. *Antimicrobial Drug Resistance*, ed. L. Bryan, Academic Press Inc., London, 1984.
50. *Principles of Pharmacology: The Pathophysiological Basis of Drug Therapy*, ed. D. E. Golan, Lippincott Williams & Wilkins, China, 2012.
51. S. Percario, D. R. Moreira, B. A. Q. Gomes, M. E. S. Ferreira, C. M. Goncalves, P. S. O. C. Laurindo, T. C. Vilhena, M. F. Dolabela and M. D. Green, *Int. J. Mol. Sci.*, 2012, **13**, 16346.

Chapter Six

Affinity Detection and Identification of Quinoline Antimalarial Binding Targets

6.1. Introduction

There is considerable evidence to suggest that the quinoline antimalarials quinine, quinidine and chloroquine interact with the haemozoin biocrystallisation pathway in *P. falciparum* by inhibiting the incorporation of Fe(III)PPIX into the growing crystal (Section 1.5).[1-3] In spite of this, ultrastructural investigations suggest that organelles other than the digestive vacuole may be implicated in the mode of action of these antimalarials.[4,5] It has also been shown that quinine and chloroquine exhibit morphological effects on the parasite that are seemingly unrelated to their roles as haemozoin inhibitors (Section 1.6.2).[6,7] Intriguingly, these two drugs, representing the two major structural classes of the quinoline antimalarials, were found to modulate endocytosis in a differential manner.[6,7] These observations suggest that these drugs may have secondary targets against the parasite in addition to their primary role as haemozoin inhibitors.

Previous investigations to determine whether these molecules have additional targets against *P. falciparum* have exploited photoaffinity-labelling strategies (Section 1.6.3). While this tends to label proteins with high specificity, it requires covalent modification of the drug in order to introduce photoreactive and radiolabelled components for binding to the target and for detection, respectively. Many of these derivatives modified the quinoline heterocycle directly which is likely to be an essential part of the pharmacophore and hence may interfere with

important binding interactions.[8,9] Although a single matrix-based affinity chromatography study has been carried out, these investigators were unable to identify any protein binding targets of quinoline antimalarials in *P. falciparum*.[10] A reason for this might be that a hydroxychloroquine-labelled matrix was used as a substitute for chloroquine itself.[10] With respect to the quinoline methanol antimalarials, alkaloid-labelled matrices have not yet been exploited in affinity chromatography studies to probe the binding targets of these molecules in *P. falciparum*.

Hence, this chapter describes a thorough investigation into the binding targets of the quinoline antimalarials in uninfected human erythrocytes and *P. falciparum* using a chemical proteomics approach. Using a matrix-based affinity detection methodology, agarose beads linked to quinine, quinidine and chloroquine were prepared using the novel derivatives of these drugs described in Chapter 3 of this work. These matrices were used to probe the erythrocyte and *P. falciparum* proteomes for binding targets of these antimalarials. In the latter case, this was followed by mass spectrometric analysis of these sub-proteomes in conjunction with SDS-Page to identify protein targets.

Thus the specific objectives described in this chapter were:

i. To prepare cell lysate from uninfected human erythrocytes and *P. falciparum* trophozoites in a manner suitable for use in these experiments;
ii. To prepare quinoline antimalarial-labelled affinity matrices using the novel derivatives of the quinoline antimalarials prepared in Chapter 3;
iii. To use these drug-labelled matrices to extract quinoline antimalarial-binding proteins in uninfected erythrocytes and to detect these via SDS-Page;
iv. To use these drug-labelled matrices to capture drug-binding sub-proteomes of quinoline antimalarial binding targets from *P. falciparum* and to identify target proteins, if any, using SDS-Page and mass spectrometry.

6.2. Background to the techniques employed in this chapter

It is surprising that approximately 18% of approved drugs have a poorly-defined mechanism of action and that as many as 7% do not have a well-defined primary target.[11] Despite recent work that directly implicates chloroquine, quinine and quinidine as haemozoin inhibitors,[1-3] the online database DrugBank describes the mechanism of action of these prototypical antimalarials as "not well understood".[12]

Drug target identification methods typically include affinity-based methods and phenotypic methods. In the former approach, direct binding of the drug to its target(s) is probed while, in phenotypic methods, targets are inferred from physiological or biochemical responses induced by the drugs.[13] Affinity-based target identification methods are typically divided into matrix-based and matrix-free affinity detection methods.[13] Matrix-based affinity methods usually take the form of affinity chromatography where the "pull-down" of a target protein is achieved by covalently attaching the small molecule to a solid support such as a bead or a capturable group such as biotin. On the other hand, matrix-free affinity detection relies on labelling methods such as the incorporation of a radioisotope or a photoreactive/fluorescent label into the ligand of interest.[13] A critically significant point is that both of these methods are limited to molecules containing derivitisable functionalities. These methods require that the binding of the ligand to its target, and hence the biological activity of the ligand, is not affected by the modification.

6.2.1. Affinity chromatography as a matrix-based affinity detection method

Affinity chromatography is used to separate complex mixtures by exploiting specific receptor-ligand interactions. This is done by immobilising the ligand on an insoluble matrix (stationary phase) and exposing the matrix to a mixture containing the putative receptor (mobile phase). The protein target may be recovered from the stationary phase by displacement with a mobile phase containing a high concentration of the unbound ligand or by elution under denaturing conditions. In this work, the ligands of interest were small-molecule drugs and the receptors, if any, were expected to be proteins.

Matrix-based affinity chromatography typically requires at least three conditions: (1) the ligand must contain a reactive functionality, (2) the biological activity and binding specificity of the small molecule should not be affected by derivatisation and (3) the matrix must not hinder binding of the target protein to the drug. The primary limitation of this method is usually the synthetic chemistry required to derivatise the ligand to make it amenable to covalent linkage to the solid support, especially in the case of complex natural products. Usually, structure-activity

relationship studies are carried out to identify functional groups that are dispensable for ligand activity which are then used as points of attachment to the affinity scaffold.

This matrix is then exposed to all the possible binding targets. This is usually a complex mixture such as cell lysate or protein extract. This is followed by extensive washing to remove non-specific binding partners. Retained proteins are then eluted under denaturing conditions that disrupt intermolecular interactions ("solid-phase elution", Figure 6.1A) or with an excess of free ligand ("competition elution", Figure 6.1B). Proteins may then be separated and identified by SDS-Page or by mass spectrometry directly. Often there are many more non-specific binders than actual targets and so negative control experiments using an inactive analogue or a non-specific binding matrix are important ("comparison variant", Figure 6.1C).

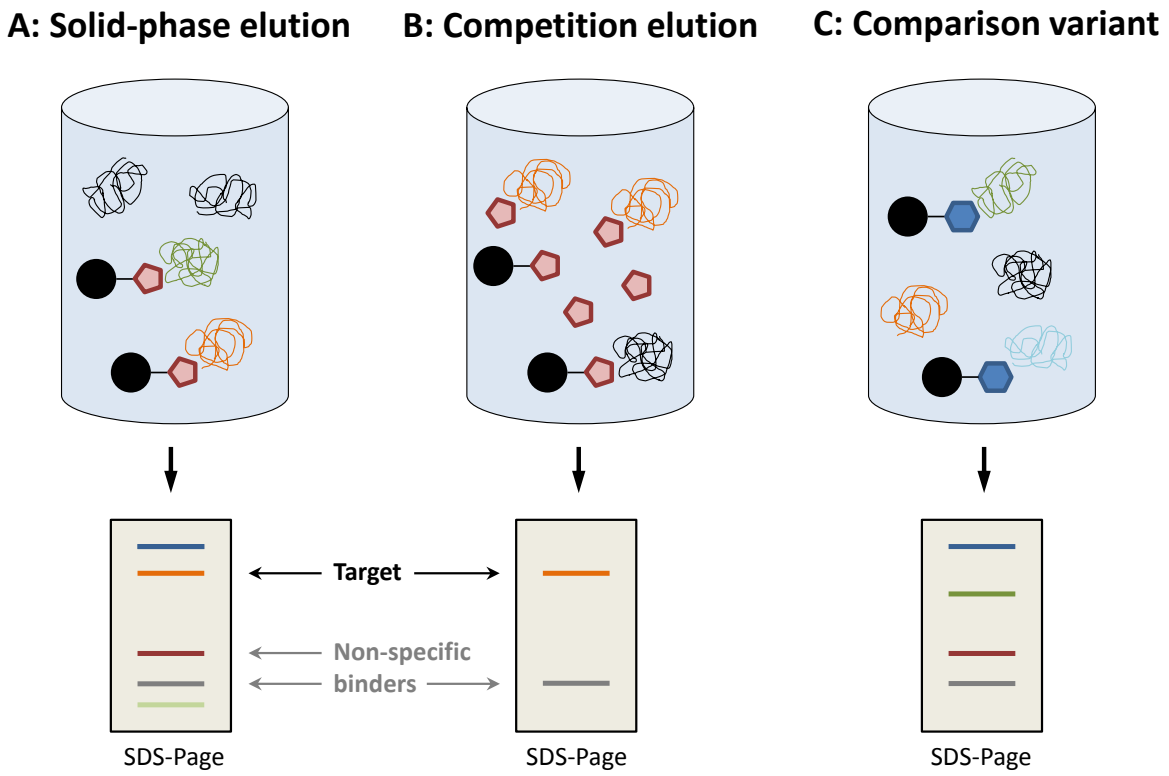

Figure 6.1. *Detection of protein targets using matrix-based affinity chromatography. A ligand (red pentagon) is tethered to a matrix (black circle) and incubated with protein extract. After non-binding proteins have been removed by a series of washing steps, any ligand-bound proteins are eluted using (A) denaturing buffer conditions or (B) an excess of free ligand and then investigated by SDS-Page. To minimise the identification of non-specific binders, the proteins that are obtained with an inactive ligand analogue or non-specific matrix is also determined (C) and the two outcomes are compared.*[13]

6.2.2. Preparation of biological material for affinity experiments

Evidence has shown that the trophozoite and schizont stages of *P. falciparum* are most sensitive to the quinoline antimalarials investigated in this work (Section 5.2.2).[14-16] Hence, mature cultures of *P. falciparum* were harvested for this study. The workflow for the preparation of parasite material for these experiments is illustrated in Figure 6.2. During cell lysis, samples were placed on ice to maintain their integrity, protease inhibitors were used to prevent premature proteolysis and gentle mixing helped to minimise protein aggregation.

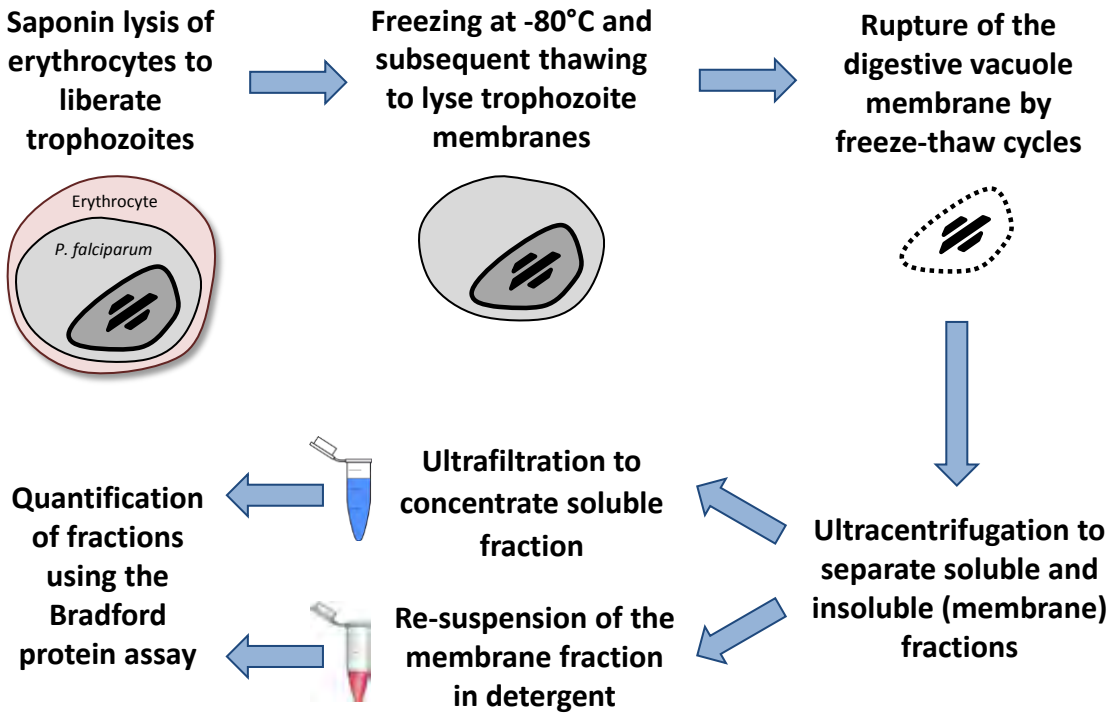

Figure 6.2. *Workflow to prepare material from* P. falciparum *for this study.*

In order to liberate the trophozoite from the erythrocyte, the infected cultures were lysed using saponin. The resultant pellet was washed several times to remove extraneous erythrocyte material but especially excess haemoglobin which might obscure detection of proteins of lower abundance. Saponin-lysed parasites were then stored for several days at -80°C. Subsequent thawing of this sample ruptured the parasitophorous vacuolar and plasma membranes of the parasite. However, the tougher digestive vacuole membranes remained intact as evidenced by the small assemblies of haemozoin crystals. In order to lyse this membrane, a freeze-thaw cycle was commenced over several days. Digestive vacuole lysis was judged to be complete when a wet mount showed no distinct shapes under high magnification.

Ultracentrifugation was performed to separate soluble proteins from the membrane-associated insoluble fraction. Afterwards, the soluble fraction was concentrated via ultrafiltration using 3 kDa molecular weight cut-off tubes. The membrane fraction was resuspended with a minimum volume of 1% (w/v) CHAPS detergent and triturated to promote mixing. Finally, the protein concentrations of all fractions were quantified using the Bradford assay. This assay measures the binding of Coomassie Brilliant Blue G-250 dye to proteins.[17] Under acidic conditions, the dye is predominantly in the doubly-protonated red cationic form (λ_{max} 470 nm); however, when the dye binds to protein, it is converted to a stable unprotonated blue form (λ_{max} 595 nm). Hence, measuring the absorbance at this latter wavelength is used to determine the protein concentration with the use of a standard curve.[18] In this assay, bovine serum albumin was used for calibration purposes.

Material from uninfected human erythrocytes was also prepared. These cells were lysed at 4°C for an hour in the presence of a buffer previously formulated by Graves et al.[10] To promote cell lysis, this buffer contained 0.1% CHAPS detergent. Centrifugation of lysed material permitted insoluble residue to be removed. Lysate was quantified using the Bradford protein assay.

6.2.3. Separation of bound proteins by SDS-Page and detection by staining

Electrophoresis refers to the movement of charged molecules in response to an electric field, resulting in their separation. When electrophoresis is performed in polyacrylamide, the gel serves as a size-exclusion sieve during separation; hence, smaller proteins travel faster than larger proteins. In this work a discontinuous buffer system was used in which the gel is divided into a large-pore “stacking gel” above a smaller-pore “resolving gel”. In this system, proteins first migrate quickly through the stacking gel and are slowed down as they enter the resolving gel. As they slow down, the proteins stack on top of one another to form a tight band which improves resolution. Discontinuous systems also have glycinate and chloride ions in the electrophoresis buffer which sandwich the proteins as they migrate through the gel, tightening the bands even more.[19]

SDS-Page, the most popular format of electrophoresis, incorporates the detergent sodium dodecyl sulfate (SDS) into the discontinuous buffer system. When proteins are separated in the presence of SDS, they are fully denatured and dissociate from one another. SDS binds non-covalently to proteins in a manner that imparts (i) an overall negative charge on the proteins, (ii) a similar mass-to-charge ratio for all proteins and (iii) a long rod-like shape on the proteins instead of their complex tertiary confirmations.[19] Consequently, the rate at which SDS-bound

proteins migrate in a gel depends predominantly on their sizes, enabling molecular weight estimation.

Following electrophoresis, detection of the protein bands is carried out by staining the gel. The most popular stain is the Coomassie Brilliant Blue series of anionic dyes but this stain is only moderately sensitive. For example, the detection limit of Coomassie Brilliant Blue R-250 is 36-47 ng protein/mm^2.[19] However, silver-based stains have a much lower detection limit of approximately 0.1 ng protein/mm^2.[20] Furthermore, staining a gel first with Coomassie Brilliant Blue, followed by de-staining and subsequent treatment with a silver stain enhances sensitivity four-fold allowing extremely low-abundance proteins to be identified (0.025 ng/mm^2).[20]

6.2.4. Mass spectrometry-based proteomics

Once a sample has been identified for mass spectrometric analysis, the proteins must be enzymatically cleaved into smaller fragments. These may be “in-solution” or “in-gel” digestions depending on whether the source is a protein mixture or a band from a protein electrophoresis gel, respectively. In both cases, digestion is preceded by several modifications to the proteins. Proteins are usually reduced and cysteine residues are thiomethylated.[21] They are then digested by a suitable protease such as trypsin. Following the removal of residual components from the digestion, liquid chromatography separates out the trypsin-digested peptides by hydrophobicity. These peptides are then delivered to a tandem mass spectrometer. In this work, peptides were eluted onto an electrospray ionisation source where they were nebulised in small, highly-charged droplets.[22] The first spectrometer separates peptides according to their mass-to-charge ratio (m/z). Ions of a particular m/z ratio are then selected and fragmentation occurs, after which the resulting fragment ions are separated and then detected in a second stage of mass spectrometry. Following detection of these fragment ions, the resultant spectra are compared to databases in order to identify the original proteins corresponding to the fragment ions.

6.3. Affinity chromatography and identification of binding targets

6.3.1. Preparation of the quinoline antimalarial-labelled stationary phase

As described in Section 6.2.1 above, affinity chromatography requires the small molecule ligand to be attached to a stationary phase. In this study, *N*-hydroxysuccinimide-activated Sepharose 4 Fast Flow (GE Healthcare) was selected as a suitable scaffold (Figure 6.3). This is a highly cross-linked agarose matrix containing pre-activated *N*-hydroxysuccinimide (NHS) end-groups which form stable amide bonds when reacted with amine-containing ligands. This activated scaffold was anticipated to be compatible with the derivatives of the quinoline antimalarials prepared earlier in this work.

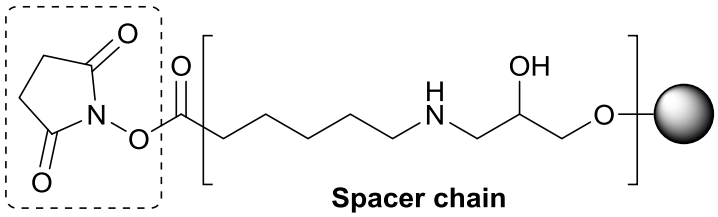

Figure 6.3. *Sepharose 4 Fast Flow beads activated with an* N*-hydroxysuccinimide (NHS) leaving group indicated in the dashed box. The spacer chain is indicated in brackets.*[23]

The identity of the spacer chain between the bead and the activated end-group is important as there should be enough space for binding to take place. A short spacer chain may generate steric hindrance which will obstruct the ligand-target interaction. On the other hand, if the spacer chain is too hydrophobic, different linkers may interact with one another or promote unspecific target binding with macromolecules.[24] For these reasons, an optimal chemical spacer should be mildly hydrophilic and lengthy enough to avoid steric hindrance. This was judged to be the case for the spacer chain depicted in Figure 6.3.

The ligands used in this work were the primary amine-containing derivatives of quinine, quinidine and chloroquine prepared in Chapter 3. These derivatives were prepared by taking into account the structure-activity relationships of the parent molecules with Fe(III)PPIX. Hence, key structural motifs were retained, an approach that was validated in Chapter 4. These derivatives lend themselves to a facile coupling reaction with NHS-activated beads through nucleophilic acyl substitution (S_NAc) as illustrated in Figure 6.4. This results in the departure of the NHS group and the formation of an amide bond between the quinoline pharmacophore and the matrix.

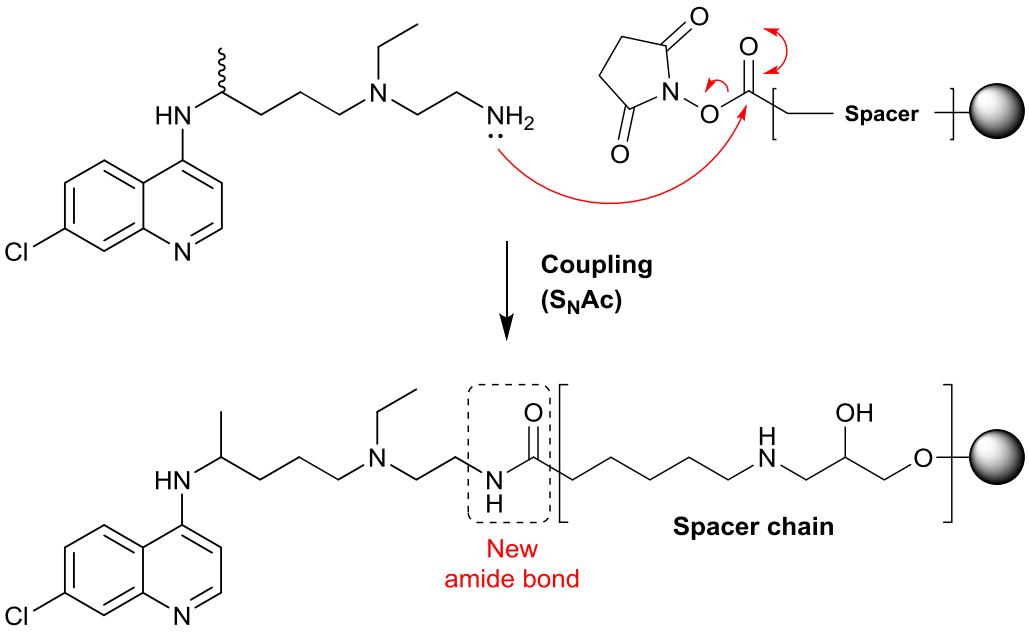

Figure 6.4. *The coupling reaction to the beads via nucleophilic acyl substitution (S_NAc) of the* N*-hydroxysuccinimidyl ester, exemplified by the chloroquine derivative prepared in Chapter 3.*

A workflow for preparing the drug-labelled beads is presented in Figure 6.5. Briefly, the beads were washed with 1 mM HCl to remove the isopropanol solution in which they were supplied. Thereafter, the beads were incubated with a solution comprising the number of moles of the derivatised drug necessary for the desired loading capacity, dissolved in 100 mM Hepes at pH 8.3. This was rotated at room temperature for one hour after which the beads were washed three times with the fresh buffer that did not contain any ligand.

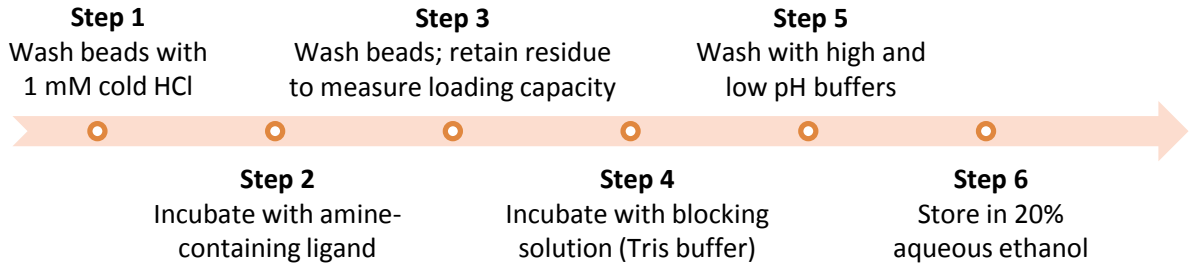

Figure 6.5. *Workflow to prepare the drug-labelled beads for this study.*

In order to quantify the amount of ligand that had coupled to the beads, the washings were collected, made up to a known volume and quantified by spectrophotometry. Thereafter, the beads were incubated in "blocking solution" comprising 100 mM Tris at pH 8.5. As the structure of Tris contains a primary amine (aminomethane) linked to three hydroxymethyl groups, the amine reacted with the remaining NHS-activated end-groups to give "Tris-blocked" end-groups that were hydrophilic in nature. After this step, the beads were alternately washed with high and low pH buffers and were stored in 20% aqueous ethanol to avoid microbial contamination.

Depending on the sizes of the ligand and the putative target(s), it is important to avoid over-loading the derivatised ligand onto the beads as this may result in steric hindrance between the binding targets. It has previously been reported that 3 μmol ligand/mL matrix is an optimal concentration.[24] The manufacturer's specifications indicate that there are 19.5 μmol/mL NHS binding sites available on the NHS-activated Sepharose 4 Fast Flow beads.[23] Hence, incubating 1 mL of beads with 19.5 μmol ligand results in 100% loading capacity. Differences in loading capacity can be seen in Figure 6.6A below, where 100% loading results in overloading of the matrix and hence encourages non-specific interactions, probably due to auto-aggregation of proteins as a result of hydrophobic interactions. When only 3 μmol/mL ligand was applied to the beads, spectrophotometry indicated that almost all of this ligand (> 95%) was linked to the framework within an hour. The lane corresponding to this loading capacity in Figure 6.6A showed a better elution profile where only those proteins that are likely to interact directly with the ligand were retained.

In order to establish an appropriate buffer system for the affinity chromatography experiments, samples of chloroquine-labelled beads (loaded at 3 μmol chloroquine/mL) were exposed to the soluble fraction recovered from *P. falciparum* lysate in the presence of two different buffers. Protein binders were removed by solid-phase elution (Figure 6.6B). One sample was prepared in the presence of a Tris-based buffer at pH 8.3 while the other was a Hepes-based buffer previously used by Graves et al. at pH 7.5.[10] The latter buffer contained 0.1% CHAPS detergent. Despite this, it can be seen from Figure 6.6B that elution profiles for both buffers are very similar. Hence, binding interactions do not appear to be affected by the presence of the small amount of detergent in the affinity buffer which might have been suspected to weaken intermolecular interactions. Hence, this buffer was used for subsequent affinity chromatography experiments and is hereafter referred to as "affinity buffer".

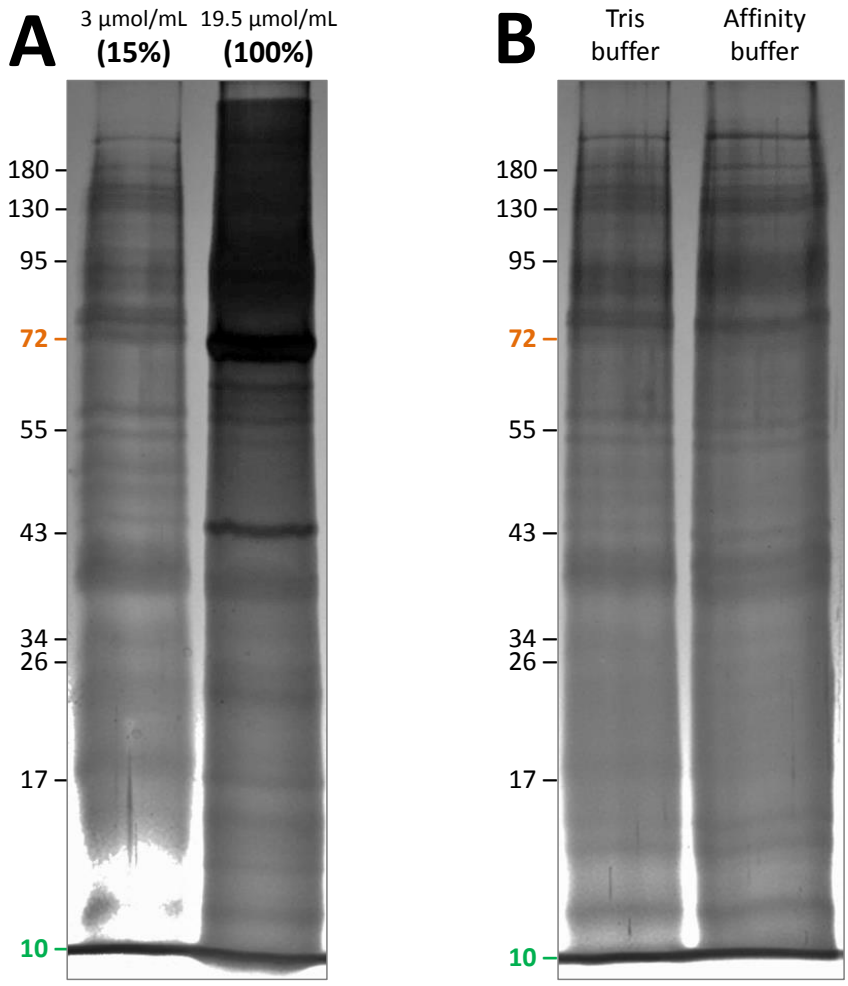

Figure 6.6. *SDS-Page (14% acrylamide) visualised with a silver stain. In both panels, beads were exposed to the soluble fraction recovered from* P. falciparum*. Bound proteins were removed by solid-phase elution. Panel A demonstrates the difference between two different loading capacities of quinine-labelled beads. 3 µmol/mL corresponds to 15% of the available loading capacity and 19.5 µmol/mL corresponds to a fully-loaded matrix (100%). In the latter case, non-specific binding is evident as a result of overloading of the beads. Panel B demonstrates beads labelled with chloroquine (3 µmol/mL) that were washed extensively with either a Tris-based buffer or "affinity buffer". Both elution profiles are almost identical; hence, binding was not affected by the presence of a small amount of detergent (0.1% CHAPS) in the affinity buffer.*

6.3.2. Matrix-based affinity chromatography of uninfected human erythrocytes

Matrix-based affinity chromatography was conducted in microcentrifuge tubes. An aliquot of labelled beads was equilibrated in affinity buffer. To this was added a suitable amount of cell lysate from uninfected human erythrocytes and the mixture was gently rocked at 4°C for half an hour. Afterwards, the mixture was centrifuged to separate the beads from non-specific binders in the supernatant. The beads were resuspended in fresh affinity buffer and washed several

times to ensure that all non-specifically bound proteins were removed. At this stage, solid-phase elution was carried out to compare the binding proteomes of all three of the drug-labelled beads as well as the "blocked" Tris-labelled beads. Hence, sample application buffer was added directly to the microfuge tubes. Following dry-boiling and centrifugation, the supernatants of the four samples were separated on SDS-Page and stained.

Figure 6.7 indicates the erythrocyte binding proteomes of the labelled beads after solid-phase elution. The elution profiles show that chloroquine retained the most material. Despite not being labelled with a drug, the Tris-labelled beads still retained protein material indicating non-specific binding of proteins either to the Tris motif, to the spacer or to the beads themselves. These bands are mostly also present in the lanes corresponding to the drug-labelled beads as well, suggesting that these bands arise from the binding of proteins to the beads themselves. The diastereomers quinine and quinidine showed very similar elution profiles to one another.

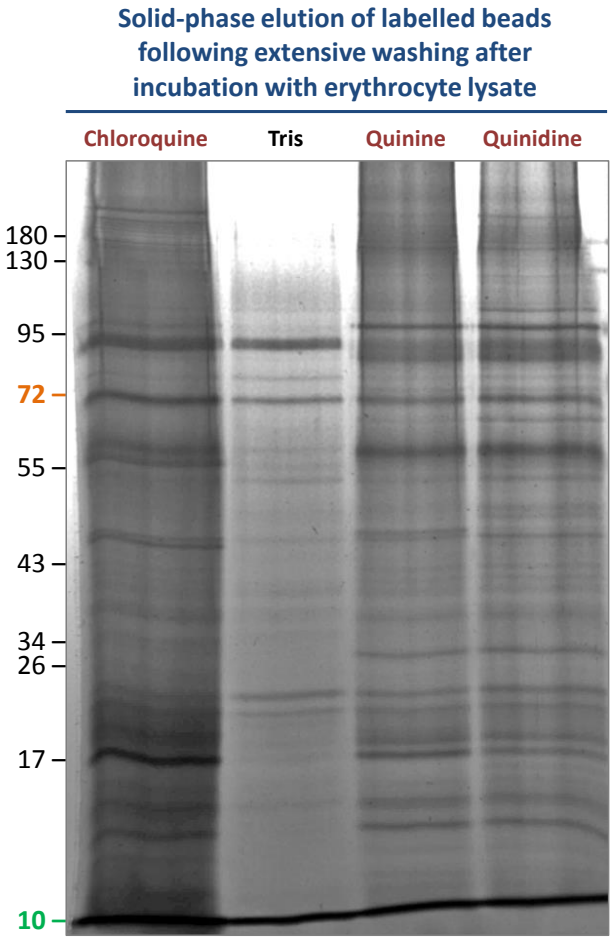

Figure 6.7. *SDS-Page (14% acrylamide) treated with a silver stain. Labelled beads were exposed to human erythrocyte lysate after which they were thoroughly washed with affinity buffer. Bound proteins were removed directly by the denaturing conditions of solid-phase elution.*

An alternative approach to solid-phase elution is competition elution which is carried out by incubating the beads with a high concentration of the free ligand after they have been exposed to a protein mixture. Rather than eluting all the proteins bound to the beads, competition elution removes only those proteins which interact specifically with the free ligand and hence are competed off the ligand-labelled beads. Thus, a high concentration of free ligand was added to the tubes and this mixture was incubated at 4°C for a further 20 minutes. Following centrifugation, sample application buffer was added to the supernatants. These were dry-boiled and proteins were separated by SDS-Page and stained.

Figure 6.8 indicates the major bands eluted from chloroquine- and Tris-labelled beads after two consecutive elutions with a high concentration of chloroquine (5 mM). The elution profiles were identical for both the first and second elutions, indicating that not all chloroquine-binding proteins were eluted after the first incubation with free ligand.

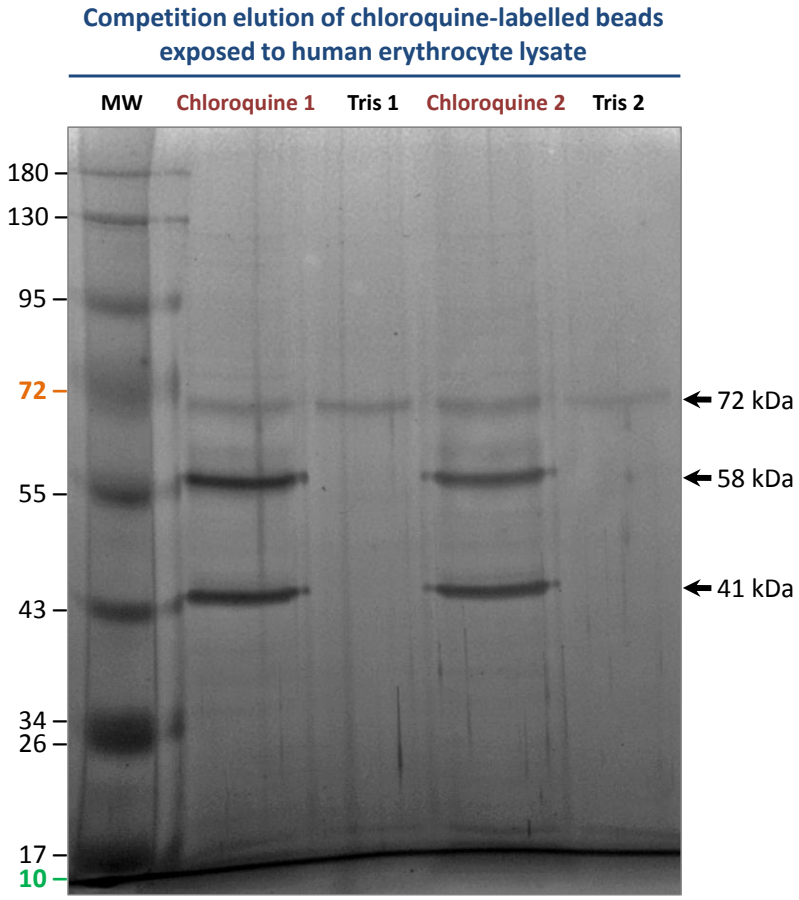

Figure 6.8. *SDS-Page (12% acrylamide) treated with silver stain. Chloroquine- and Tris-labelled beads were exposed to erythrocyte lysate. Two consecutive competition elutions were performed using a high concentration of free chloroquine (5 mM). Three major bands were identified and their approximate molecular weights are indicated.*

The several dominant bands that eluted corresponded to three molecular weights. Two bands, of approximately 41 and 58 kDa, were specific for the chloroquine-labelled beads. However, these bands did not present themselves tightly on the gel suggesting that other proteins with similar molecular weights may be present, possibly isoforms of these proteins. The third band corresponded to a non-specific binding protein which also eluted from the Tris-labelled beads in the presence of chloroquine (72 kDa).

The 58 kDa protein that was specifically eluted from the chloroquine-labelled beads corresponds closely to a 55 kDa protein isolated by Graves et al.[10] Those investigators identified this protein as human aldehyde dehydrogenase 1 (ALDH1) after screening the human erythrocyte purine-binding proteome by using γ-ATP-linked Sepharose affinity matrix. ALDH1 was also captured on hydroxychloroquine-labelled beads by screening uninfected erythrocyte lysate directly. The mouse homologue of this protein was also detected by passing lysate from a mouse over the same beads. However, in vitro assays of ALDH1 in the presence of chloroquine revealed that it was a weak inhibitor of ALDH1 at physiological levels of NAD^+, indicating that ALDH1 was unlikely to be a direct target of chloroquine unless chloroquine accumulates to high levels in the tissues, which is unlikely in the case of the unparasitised erythrocyte.[10] However, ALDH1 may be involved in the side-effects observed for chloroquine, such as retinopathy which results from an accumulation of retinaldehyde in the retina.[10]

As several incubations with the free drug were required to competitively elute all of the binding proteins from the beads, it was decided to pool the elutions and concentrate them by ultrafiltration using microfuge tubes with a low molecular weight cut-off (3 kDa). Hence, this would allow more sensitive detection of all binding proteins.

Figure 6.9 represents such a competition elution experiment performed for all the labelled beads. Fractions were combined and concentrated after three competitive elutions. It can be seen that there are several more chloroquine-specific binding partners than originally illustrated by Figure 6.8. The major bands from the chloroquine-labelled beads were still present at approximately 74, 58 and 43 kDa which almost certainly correspond to the 72, 58 and 41 kDa proteins observed in Figure 6.8. These bands are also indicated with red arrows in the inset in Figure 6.9.

Once again, Tris-labelled beads were eluted with a high concentration of the corresponding free ligand to identify non-specific binders corresponding to that ligand. Indeed, a non-specific band corresponding to all the labelled beads across all six lanes was observed at 74 kDa, although this was less clear for the Tris-labelled beads eluted with quinidine. The band at 61 kDa appears to

be specific for the drug-labelled beads, although there may be a trace of this band in the corresponding Tris-labelled lanes. This 61 kDa band does not correspond to the dominant band previously observed at approximately 58 kDa in the lane corresponding to the chloroquine-labelled beads. Instead, there is a cluster of bands around this molecular weight suggesting a host of possible binding targets.

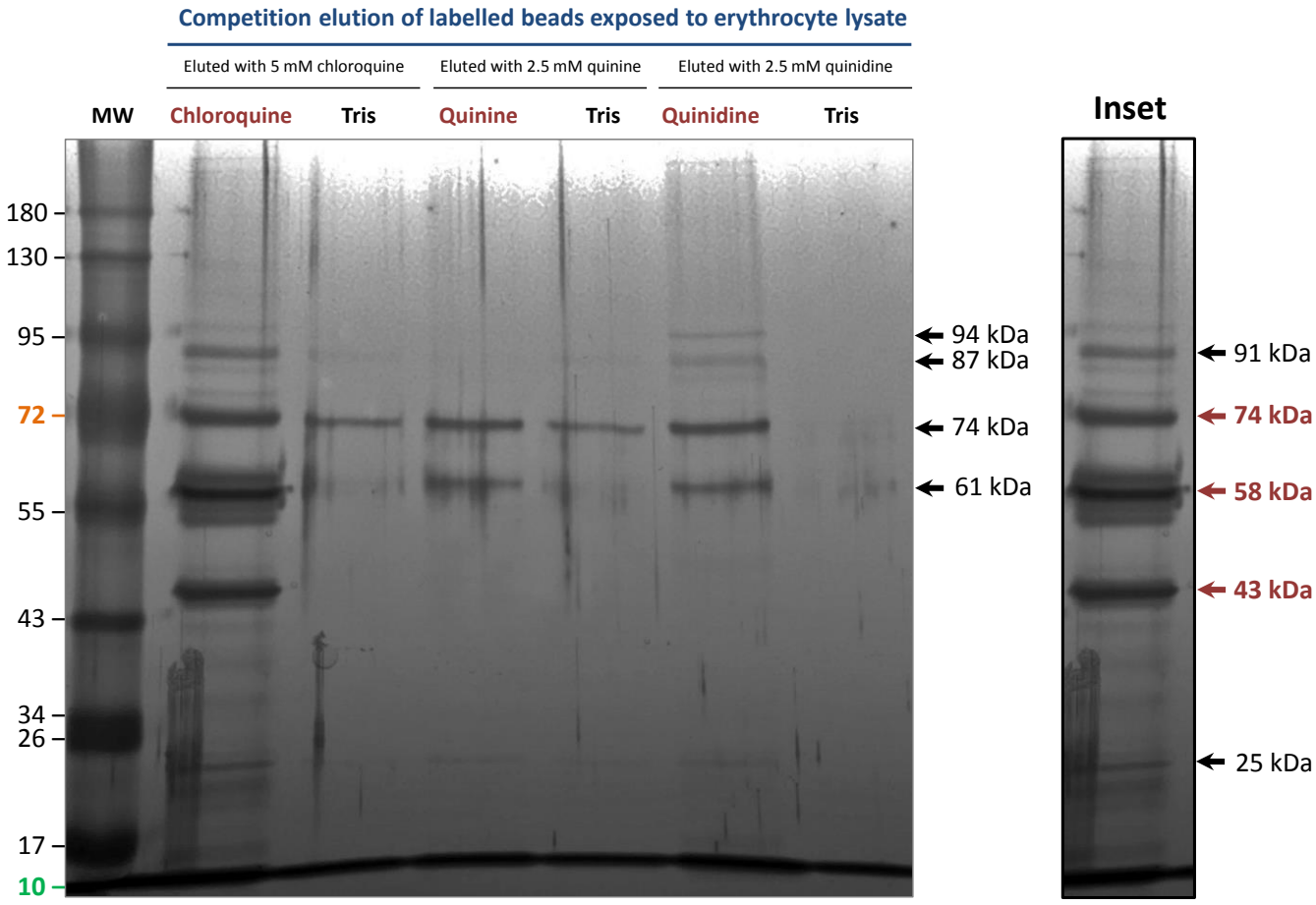

Figure 6.9. *SDS-Page (12% acrylamide) treated with silver stain. Competition elution of labelled beads reveals specific and non-specific binding interactions after exposure to human erythrocyte lysate. The inset represents elution of the chloroquine-labelled beads (second lane from the left). The three bands indicated by the molecular weights in red correspond to the dominant bands identified previously in Figure 6.8.*

Higher molecular-weight bands were also observed from chloroquine- and quinidine-labelled beads (87 and 94 kDa, respectively), but not for the quinine-labelled beads. Bands corresponding to a higher molecular weight were not observed. Conversely, another tight cluster of bands of lower molecular weight corresponding to the chloroquine-labelled beads centred at around 43 kDa. Finally, a low molecular weight band at approximately 25 kDa was observed for chloroquine with only faint traces in the other lanes. Further work will be required

to identify these specifically-eluting proteins in order to determine whether they play a mechanistic role in the action of these quinoline antimalarials.

6.3.3. Matrix-based affinity chromatography of *P. falciparum*

As material isolated from *P. falciparum* was in somewhat limited supply, the limit of detection of binding targets that could be revealed by staining on SDS-Page was determined. In a typical affinity experiment, approximately 40 μg of protein isolated from *P. falciparum* was loaded onto the labelled beads. The average protein abundance in *P. falciparum* is approximately 200 ppm.[25] Assuming that all of this "average" protein is successfully retained on the beads and then eluted, 8 ng of this protein will be retrieved. If this material is spread over a band with dimensions 0.5 mm x 10 mm on SDS-Page, the band will have a local concentration of 1.6 ng protein/mm^2. The detection limit of silver staining is 0.1 ng/mm^2. Double staining, on the other hand, increases sensitivity to 25 pg/mm^2. These limits are 16- and 64-fold above the concentration of this "average" protein, respectively.

This implies that proteins with abundances higher than 3 ppm may be detected on a gel by double staining. Of the approximately 5 000 proteins in *P. falciparum* proteome, more than 80% have abundances greater than 3 ppm.[25] However, proteins which are known targets of small molecules tend to have abundances very much higher than this. For example, atovaquone disrupts mitochondrial electron transport by inhibiting the cytochrome bc_1 complex[26] while pyrimethamine inhibits bifunctional dihydrofolate reductase-thymidylate synthase. Plasmepsin is a putative target for halofantrine.[27] These three proteins have abundances of 90, 765 and 242 ppm, respectively.[25] Hence, the small amount of *P. falciparum* lysate available was not considered to be a limiting factor in these experiments.

Labelled beads were exposed to both the soluble and membrane fractions of lysate recovered from mature *P. falciparum* cultures. After incubation, the labelled beads were eluted with an excess of the respective free ligand. As before, for each drug-labelled bead a corresponding Tris-labelled fraction was eluted with the same concentration of free ligand to determine any non-specific binders. For each fraction, three competitive elutions were performed. These were pooled and concentrated by ultrafiltration.

Figure 6.10 depicts a silver-stained gel of samples after competition elution of the membrane fraction recovered from *P. falciparum* lysate. There are several faint bands in the lanes corresponding to the drug-labelled beads between 72-180 kDa; however, the gel reveals a prominent band in the high molecular weight region above 180 kDa (indicated by an arrow on

the right-hand side of the gel). As this band lies above the highest marker in the molecular weight ladder (180 kDa), an approximate molecular weight for this band could not be calculated. The band appears to be specific for the drug-labelled beads compared to Tris-labelled beads eluted with chloroquine (central lane in Figure 6.10). The same band was also detected in the drug-labelled lanes incubated with the soluble fraction recovered from the *P. falciparum* lysate, albeit to a much lesser extent.

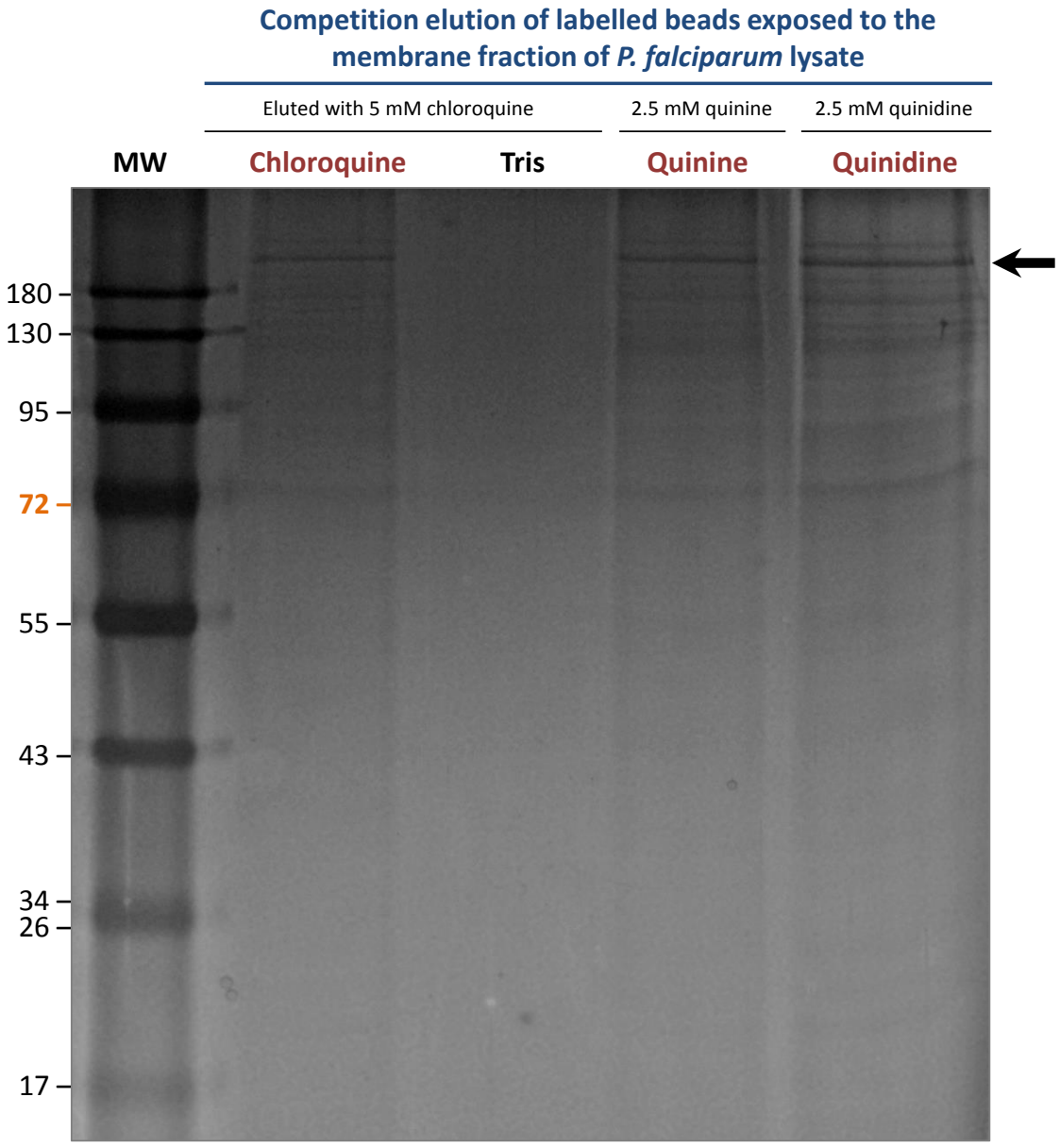

Figure 6.10. *SDS-Page (15% acrylamide) treated with a silver stain. Beads were incubated with the membrane fraction recovered from* P. falciparum*. Lanes represent samples following three successive competitive elutions of labelled beads with an excess of free ligand and subsequent concentration. A high molecular weight band was observed for the drug-labelled lanes as indicated by the black arrow.*

In order to further investigate this prominent band, the same samples were separated using a gel with a lower concentration of acrylamide to emphasise the higher molecular weight bands. The gel was first stained with Coomassie Brilliant Blue, followed by silver staining, to give the highest sensitivity of detection. In Figure 6.11, the same high molecular weight band as before was observed in the lanes corresponding to the drug-labelled beads. A faint band corresponding to the same molecular weight was also identified in the Tris-labelled lane eluted with chloroquine. This suggested that it was likely that some of this protein had been retained non-specifically on the Tris-labelled beads but was eluted upon exposure to a high concentration of chloroquine.

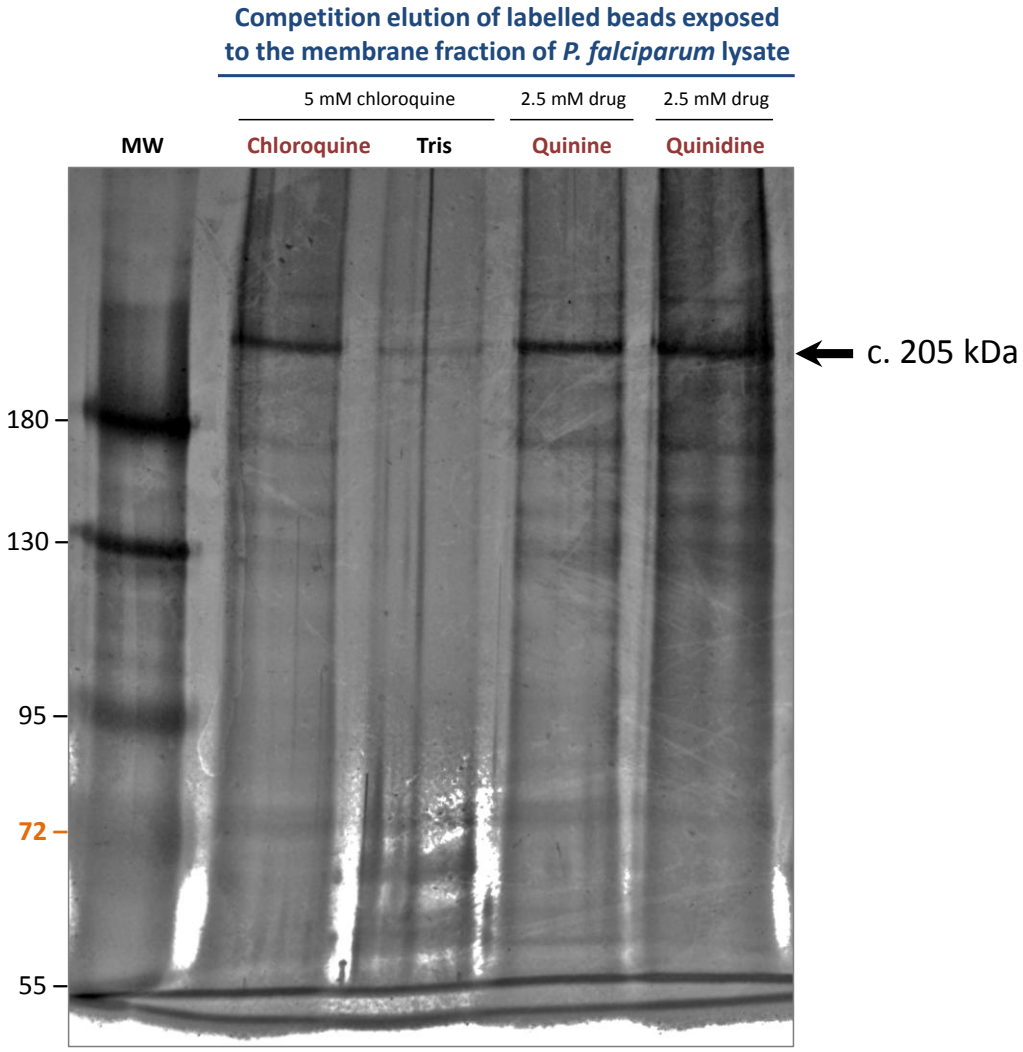

Figure 6.11. *SDS-Page (8% acrylamide) treated with Coomassie Brilliant Blue followed by silver staining. A prominent band in the region 200-250 kDa is indicated by the black arrow.*

Although an accurate molecular weight could not be determined, this band was estimated to lie in the molecular weight range 200-250 kDa. In order to identify a possible protein corresponding to this band, all proteins in the *P. falciparum* proteome within this molecular weight range were listed (Table 6.1).[25,28] All proteins in this range have abundances greater than 5 ppm, almost double the limit of detection afforded by double staining. Many of the proteins in this molecular weight range are so-called "hypothetical proteins" meaning that their functions cannot be readily assigned. Only a few proteins in this molecular weight range have had their functions characterised while several of these proteins have only putative functions which have been assumed from their gene sequences.

Table 6.1. *List of proteins from the* P. falciparum *proteome with molecular weights between 200-250 kDa.*

PaxDb ID	Protein name	Abundance	Molecular weight
MAL7P1.102	Hypothetical protein, conserved	37 ppm	206 kDa
PF11_0091	Hypothetical protein	6 ppm	207 kDa
PFF1260c	Hypothetical protein, conserved	5 ppm	210 kDa
PFL1530w	Asparagine-rich protein, putative	28 ppm	213 kDa
PFL1865w	Hypothetical protein, conserved	21 ppm	213 kDa
PfMRP1	Multidrug resistance-associated protein (ABC transporter)	11 ppm	214 kDa
PF11_0317	Structural maintenance of chromosome protein, putative	168 ppm	215 kDa
PFB0540w	Hypothetical protein	14 ppm	215 kDa
PFC0325c	Hypothetical protein, conserved	21 ppm	216 kDa
PF07_0016	Hypothetical protein, conserved	9 ppm	218 kDa
PF07_0115	Cation-transporting ATPase	32 ppm	225 kDa
PFL1800w	Hypothetical protein, conserved	23 ppm	231 kDa
PFL2335w	Hypothetical protein, conserved	42 ppm	231 kDa
PFL0930w	Clathrin heavy chain, putative	292 ppm	233 kDa
PFF0410w	Hypothetical protein, conserved	29 ppm	233 kDa
M26-32-14	Hypothetical protein, conserved	12 ppm	235 kDa
PFI0250c	Hypothetical protein, conserved	9 ppm	235 kDa
PF14_0454	Hypothetical protein	14 ppm	238 kDa
MAL7P1.171	Hypothetical protein	22 ppm	244 kDa
MAL7P1.109	Hypothetical protein, conserved	15 ppm	246 kDa
PF10_0320	Leucine-rich repeat protein 8, LRR8	9 ppm	247 kDa
PfRON2	Hypothetical protein	17 ppm	249 kDa

Only three proteins in this molecular weight range have been characterised; namely, multidrug resistance-associated protein (PfMRP1, 214 kDa), a cation-transporting ATPase (225 kDa) and

leucine-rich repeat protein 8 (247 kDa). The 225 kDa cation-transporting ATPase may be involved in binding to small molecules such as the quinoline antimalarials which are cations at physiological pH. On the other hand, leucine-rich repeat motifs are frequently involved in the formation of protein-protein interactions and hence are unlikely to interact with the quinoline antimalarials. A more likely candidate for this protein is PfMRP1. This protein has been associated with decreased susceptibility to antimalarials including chloroquine and quinine (Section 1.4.3).[29] The fact that it is a membrane-associated transporter explains why it was prominently observed in the membrane fraction recovered from *P. falciparum* compared to the corresponding soluble fraction.

In order to identify this protein, these samples were analysed using mass spectrometry-based proteomics. To increase the number of hits while limiting the amount of interference that might be generated from gel bands, samples from each set of labelled beads from both soluble and membrane fractions were pooled and analysed in-solution. Following digestion, separation and tandem mass spectrometry, peptide fragments were screened against databases for *H. sapiens* and *P. falciparum*.

When screened against the human proteome, no hits in the range 200-250 kDa were retrieved. Indeed, no hits were expected from *H. sapiens* as there were no bands corresponding to this molecular weight range detected from affinity chromatography of the erythrocyte lysate (Figure 6.9). When screened against the *P. falciparum* proteome, several proteins across a broad molecular weight range were identified. Table 6.2 lists only those proteins that were present in all the samples as reflected by the gel in Figure 6.11. These are listed in order of decreasing probability of identification.

Table 6.2. *List of* P. falciparum *proteins identified across all labelled beads, in order of decreasing probability.*

Entry	Protein name	Molecular weight
1	Multidrug resistance-associated protein (PfMRP1)	214 kDa
2	Hypothetical protein	21 kDa
3	Hypothetical protein	12 kDa
4	Hypothetical protein	349 kDa
5	Fructose-bisphosphate aldolase	42 kDa
6	Hypothetical protein	12 kDa
7	Hypothetical protein	103 kDa

Once again, many of the proteins identified in this list are hypothetical proteins. Only two of these proteins have been characterised. The first is fructose-bisphosphate aldolase, an enzyme important in glycolysis. This has a much lower molecular weight (42 kDa) than the observed band (200-250 kDa). Furthermore, this is one of the most abundant proteins in the *P. falciparum* proteome (> 8 000 ppm) and hence is more likely to be a contaminant. Thus, the only protein in the molecular weight range corresponding to the 200-250 kDa gel bands in Figure 6.11 is PfMRP1 (214 kDa). This was also the protein with the highest probability of identification, suggesting it is extremely likely that this was the protein competitively eluted from the chloroquine-, quinine- and quinidine-labelled beads and in much lower quantity from the Tris-labelled beads.

As described in Section 1.4.3, PfMRP1 is one of many ATP-binding cassette transporters in *P. falciparum*. Although only identified just over a decade ago,[30] it has subsequently been shown to localise to the parasite plasma membrane and to membrane-bound vesicles during the intraerythrocytic stages.[31,32] Disrupting PfMRP1 expression in *P. falciparum* under normal culture conditions resulted in parasites that could not grow to a parasitaemia higher than 5%, possibly because of lower efficiency in removing toxic metabolites.[32] These parasites also accumulated more radiolabelled glutathione, chloroquine and quinine and became more sensitive to several antimalarials, including chloroquine, quinine and artemisinin.[32] This indicates that PfMRP1 most likely plays a role in the efflux of glutathione, chloroquine and quinine from the parasite.[34] Expression of PfMRP1 also increased in the presence of chloroquine and mefloquine.[33] Although PfMRP1 is expressed in all stages of the life cycle, Noguiera et al. showed that this expression peaks at the late trophozoite and early schizont stages.[33] Interestingly, this is exactly when the quinoline antimalarials have been shown to be most potent against the parasite (Section 5.2.2).[14-16]

PfMRP1 has not previously been identified to bind directly to these drugs. Although photoaffinity-based techniques label substrates with high specificity and have previously been exploited to probe for binding targets of these drugs in *P. falciparum*, the rapid nature of photolabelling means that it labels substrates promiscuously; that is, molecules in higher abundance are more likely to be labelled. This may explain why the photoreactive derivative of chloroquine designed by Foley et al. detected lactate dehydrogenase enzyme (PfLDH) as it is an extremely abundant protein in *P. falciparum* (> 9 000 ppm).[8,25] The activity of this enzyme was later shown not to be significantly affected by the presence of chloroquine.

PfMRP1 is a low abundance protein in the *P. falciparum* proteome (11 ppm).[25] Hence, the matrix-based study of Graves et al. may not have been sensitive enough to detect this protein.[10]

Alternatively, these authors' use of a hydroxychloroquine-labelled matrix as a substitute for chloroquine itself might also have contributed to a reduced specificity of the matrix for PfMRP1.

It is probably unsurprising that other membrane transporters associated with the quinoline antimalarials, such as PfCRT and PfMDR1, were not detected at all in this study which only investigated a chloroquine-sensitive strain of *P. falciparum*. PfCRT associates more strongly with the quinoline antimalarials in resistant strains in which polymorphic mutations allow these drugs to bind more readily to the transporter.[29] PfMDR1, on the other hand, is typically expressed at low levels in sensitive strains. Amplification in resistant strains is one of its key characteristics.[29] As PfMRP1 is itself a low abundance protein in sensitive strains, this means PfMRP1 must bind these quinoline antimalarials in a strong and specific manner.[29] That the drug-labelled beads in this study were selective for PfMRP1 is evidence of a dynamic binding process between these ligands and the protein receptor. The fact that only a single, dominant band was detected on SDS-Page, coupled with the relatively small number of proteins retrieved from in-solution proteomic analysis, suggests that these matrix-based scaffolds were exquisitely selective in detecting binding targets in *P. falciparum*.

6.4. Summary and conclusions

Although chloroquine, quinine and quinidine are generally accepted to function primarily as haemozoin inhibitors, these quinoline antimalarials exert other effects on *P. falciparum* which may not be related to this primary role. For example, quinine and chloroquine appear to modulate endocytosis in a differential manner.[6] This suggests that these antimalarials may have alternative targets within the parasite. Thus the aim of this chapter was to isolate and identify protein binding targets, if any, of the quinoline antimalarials in uninfected erythrocytes and *P. falciparum* using chemical proteomics.

Biological material from both uninfected human erythrocytes and *P. falciparum* trophozoites was prepared in a manner suitable for use in these experiments. Quinoline antimalarial-labelled matrices were prepared by reacting *N*-hydroxysuccinimide-activated beads with the primary amine-containing derivatives prepared in Chapter 3 of this work. A deliberate reduction in coupling capacity of these matrices (3 μmol/mL) prevented overloading of the beads.

These drug-labelled matrices were used to capture quinoline antimalarial-binding proteins in uninfected erythrocytes. Binding sub-proteomes were separated and visualised using SDS-Page. Two dominant, specific human binding targets were detected for chloroquine (41 kDa and 58 kDa). The latter corresponds closely in molecular weight to that of human aldehyde dehydrogenase 1 (ALDH1), a 55 kDa protein that was previously isolated by Graves et al. using hydroxychloroquine-labelled beads.[10] A host of less dominant bands were detected for chloroquine with fewer bands generally observed for the alkaloids, but a specific band at approximately 61 kDa was detected for all three quinoline antimalarials. Further work will be required to identify these bands.

The drug-labelled matrices were also used to extract quinoline antimalarial-binding proteins from *P. falciparum*. SDS-Page revealed a single band between 200-250 kDa that was prominent in the membrane-associated fraction recovered from the parasite. Screening the *P. falciparum* proteome in this molecular weight range suggested that PfMRP1 might be a suitable candidate (214 kDa). This was confirmed by in-solution proteomics that identified PfMRP1 as the only protein in the appropriate molecular weight range across samples from all the labelled beads. No human proteins in this molecular weight range were identified. This is an intriguing result as PfMRP1 has been implicated in resistance mechanisms of chloroquine and quinine.

6.5. References

1. J. M. Combrinck, T. E. Mabotha, K. K. Ncokazi, M. A. Ambele, D. Taylor, P. J. Smith, H. C. Hoppe and T. J. Egan, *ACS Chem. Biol.*, 2013, **8**, 133.
2. J. Gildenhuys, T. le Roux, T. J. Egan and K. A. de Villiers, *J. Am. Chem. Soc.*, 2013, **135**, 1037.
3. T. J. Egan and K. K. Ncokazi, *J. Inorg. Biochem.*, 2004, **98**, 144.
4. G. H. Jacobs, A. Oduola, D. E. Kyle, W. K. Milhous, S. K. Martin and M. Aikawa, *Am. J. Trop. Med. Hyg.*, 1988, **39**, 87.
5. N. Sachanonta, K. Chotivanich, U. Chaisri, G. D. H. Turner, D. J. P. Ferguson, N. P. J. Day and E. Pongponratn, *Ultrastruct. Pathol.*, 2011, **35**, 214.
6. L. Roberts, T. J. Egan, K. A. Joiner and H. C. Hoppe, *Antimicrob. Agents Chemother.*, 2008, **52**, 1840.
7. O. Famin and H. Ginsburg, *Biochem. Pharmacol*., 2002, **63**, 393.
8. M. Foley, L. W. Deady, K. Ng, A. F. Cowman and L. Tilley, *J. Biol. Chem.*, 1994, **269**, 6955.
9. J. Desneves, G. Thorn, A. Berman, D. Galatis, N. La Greca, J. Sinding, M. Foley, L. W. Deady, A. F. Cowman and L. Tilley, *Mol. Biochem. Parasitol.*, 1996, **82**, 181.
10. P. R. Graves, J. J. Kwiek, P. Fadden, R. Ray, K. Hardeman, A. M. Coley, M. Foley and T. A. J. Haystead, *Mol. Pharm.*, 2002, **62**, 1364.
11. E. Gregori-Puigjané, V. Setola, J. Hert, B. A. Crews, J. J. Irwin, E. Lounkine, L. Marnett, B. L. Roth and B. K. Shoichet, *Proc. Natl. Acad. Sci. USA*, 2012, **109**, 11178.
12. DrugBank, http://www.drugbank.ca (accessed July 2016).
13. G. C. Terstappen, C. Schülpen, R. Raggiaschi and G. Gaviraghi, *Nat. Rev. Drug Discov.*, 2007, **6**, 891.
14. A. Yayon, J. A. Vande Waa, M. Yayon, T. G. Geary and J. B. Jensen, *J. Protozool.*, 1983, **30**, 642.
15. T. S. Skinner, L. S. Manning, W. A. Johnston and T. M. E. Davis, *Int. J. Parasitol.*, 1996, **26**, 519.
16. D. W. Wilson, C. Langer, C. D. Goodman, G. I. McFadden and J. G. Beeson, *Antimicrob. Agents Chemother.*, 2013, 57, 1455.
17. M. M. Bradford, *Anal. Biochem.*, 1976, **72**, 248.
18. Quick Start Bradford Protein Assay Instruction Manual, Bio-Rad Laboratories, Inc.
19. A Guide to Polyacrylamide Gel Electrophoresis and Detection, Bio-Rad Laboratories, Inc.
20. ProteoSilver Plus Silver Stain Kit Technical Bulletin, Sigma-Aldrich.
21. R. Aebersold and M. Mann, *Nature*, 2003, **422**, 198.
22. U. Rix and G. Superti-Furga, *Nat. Chem. Biol.*, 2009, **5**, 616.
23. *Affinity Chromatography: Principles and Methods*, Amersham Biosciences, 2002.

24. D. Guiffant, D. Tribouillard, F. Gug, H. Galons, L. Meijer, M. Blondel and S. Bach, *Biotechnol. J.*, 2007, **2**, 68.
25. PaxDB, http://pax-db.org (accessed August 2016).
26. A. L. Baggish and D. R. Hill, *Antimicrob. Agents Chemother.*, 2002, **46**, 1163.
27. R. Friedman and A. Caflisch, *ChemMedChem*, 2009, **4**, 1317.
28. D. Tao, C. Ubaida-Mohien, D. K. Mathias, J. G. King, R. Pastrana-Mena, A. Tripathi, I. Goldowitz, D. R. Graham, E. Moss, M. Marti and R. R. Dinglasan, *Mol. Cell. Proteomics*, 2014, 13, 2705.
29. C. P. Sanchez, A. Dave, W. D. Stein and M. Lanzer, *Int. J. Parasitol.*, 2010, **40**, 1109.
30. A. Klokouzas, T. Tiffert, D. van Schalkwyk, C. Wu, H. W. van Veen, M. A. Barrand and S. B. Hladky, *Biochem. Biophys. Res. Commun.*, 2004, **321**, 197.
31. R. A. Kavishe, J. M. W. van den Heuvel, M. van de Vegte-Bolmer, A. J. F. Luty, F. G. M. Russel and J. B. Koenderink, *Malaria J.*, 2009, **8**, 205.
32. D. K. Raj, J. Mu, H. Jiang, J. Kabat, S. Singh, M. Sullivan, M. P. Fay, T. F. McCutchan and X. Su, *J. Biol. Chem.*, 2009, **284**, 7686.
33. F. Nogueira, D. Lopes, A. C. Alves and V. E. do Rosário, *J. Cell Anim. Biol.*, 2008, **2**, 10.
34. J. B. Koenderink, R. A. Kavishe, S. R. Rijpma and F. G. M. Russel, *Trends Parasitol.*, 2010, **26**, 440.

Chapter Seven

Overall Conclusions and Further Work

7.1. Overall conclusions

Malaria is the most serious parasitic disease occurring in man and places an intolerable burden on global health. Quinoline-based antimalarials have provided the foundation of malaria treatment for centuries and remain of great interest. Despite recent challenges posed by resistance, these antimalarials continue to be used widely, especially in cases of severe malaria and malaria in pregnancy.[1] In addition, the quinoline motif persists as an important template in drug discovery.[2,3] However, the mechanistic details of the modes of action of these antimalarials against the intraerythrocytic cycle of the most virulent malaria parasite, *Plasmodium falciparum*, remain incompletely resolved. Hence the broad aim of this work was to develop new tools with which to investigate these antimalarials, and to use these tools to generate deeper insights into their mechanism of action against *P. falciparum*. In this work, the two major classes of these antimalarials, the quinoline methanols and 4-aminoquinolines, were represented by the diastereomeric *Cinchona* alkaloids, quinine and quinidine, and chloroquine, respectively.

Recent evidence continues to support the inhibition of haemozoin biocrystallisation as a primary mode of action of these quinoline antimalarials.[4,5] Accordingly, most studies have focused on the parasite digestive vacuole as the sole site of action of these drugs. However, ultrastructural analyses implicate other regions of the parasitic cell following treatment with

these drugs.[6-8] In addition, previous work to identify protein binding targets of these antimalarials suggests that alternative modes of action against *P. falciparum* may exist.[9,10] Hence, in order to conduct a systematic investigation into the localisation of these antimalarials within *P. falciparum*, fluorescently-labelled derivatives were prepared from which the most suitable analogues for microscopy were selected. These were then imaged in *P. falciparum* using live-cell confocal and super-resolution microscopy. Finally, in a chemical proteomics approach, agarose beads were functionalised with the drugs and these were used to identify protein binding targets of these antimalarials in *P. falciparum*. These ideas are depicted in Figure 7.1.

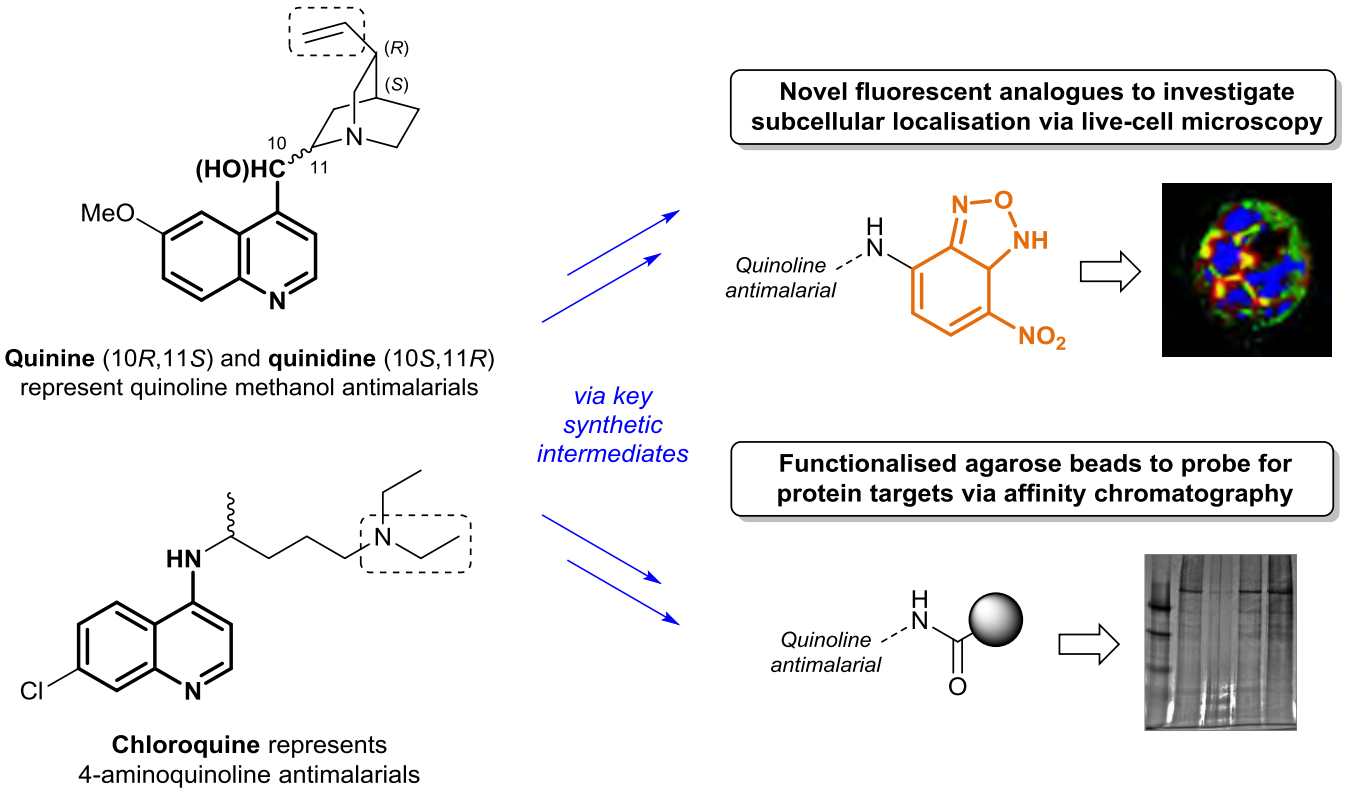

Figure 7.1. *A summary of the two major approaches taken in this study. Dashed boxes represent the regions of synthetic modification of the parent compounds.*

For the preparation of fluorescent derivatives, NBD was selected as a suitable reporter on account of its appropriate photophysical properties and small size. Structure-activity relationships between Fe(III)PPIX and the quinoline antimalarials were evaluated which suggested that the vinyl group of the alkaloids and the *N*-diethyl side chain of chloroquine were suitable sites for structural modification (dashed boxes in Figure 7.1). A general synthetic strategy was the introduction of an additional amino group for attachment of the NBD fluorophore via nucleophilic aromatic substitution. For the alkaloids, this was enabled by a

regioselective radical-mediated thiol-ene click reduction which provided facile access to derivatives in high yield. Additional derivatives were prepared in which the length of the spacer chain between the quinoline core and the fluorophore was varied by preparing NBD-labelled amino acids and their corresponding succinimidyl esters. In contrast, only a single fluorescent derivative of chloroquine was prepared for which an *N*-dealkylated analogue of the drug was exploited as a key intermediate.

In order to determine which of these derivatives were the most suitable analogues of the parent antimalarials for live-cell imaging, their physicochemical interactions with Fe(III)PPIX were evaluated. Spectrophotometric titrations revealed that distinctive features of association were retained for most NBD-labelled alkaloids, vindicating the design choice to functionalise the vinyl group. Aqueous solubility and diffusion measurements suggested that the most suitable analogues of the alkaloids were those in which the chain length between the quinoline core and the reporter fluorophore was the shortest. Longer-chain derivatives were either insufficiently soluble or exhibited behaviour analogous to micelles, excluding these derivatives from use in microscopy studies. Crucially, all derivatives exhibited low to moderate nanomolar activities against a chloroquine-sensitive strain of *P. falciparum*. These results confirmed that the labelled alkaloids with the shortest spacer chain were the most suitable analogues of the quinoline methanol antimalarials. Indeed, these are the first derivatives of these antimalarials suitable for live-cell imaging that have been prepared. For chloroquine and its NBD-labelled derivative, μ-oxo dimerisation of Fe(III)PPIX and activity against *P. falciparum* were conserved, indicating the suitability of this derivative as a representative 4-aminoquinoline for microscopy.

Live-cell imaging demonstrated selective accumulation of these fluorescently-labelled analogues within *P. falciparum*-infected erythrocytes. The chloroquine analogue was invariably found in close association with the haemozoin and hence the region corresponding to the digestive vacuole. This is in accordance with its established role as a haemozoin inhibitor, corroborating previous imaging studies[11,12] and vindicating the approach taken in this work. Analogues of the quinoline methanols were also found near the haemozoin although this did not always correspond to the regions of most intense fluorescence. Intriguingly, an autofluorescence signal that had been previously reported to originate from quinine was instead found to correspond to the haemozoin in untreated cells. This casts doubt on the claim made by earlier investigators that quinine localises to a non-acidic compartment adjacent to the digestive vacuole.[13] Instead, the analogues of quinine and quinidine were found to have an affinity for membranous structures within the parasitic cell. Quantitative analysis of cells co-stained with the lipophilic dye LysoTracker Red demonstrated extensive colocalisation between these two signals, indicating a preference for phospholipid bilayers of acidic organelles. The

distribution of the quinidine analogue colocalised with membranes to a larger extent than its quinine counterpart which may explain the more potent activity of quinidine against *P. falciparum*. Significantly, qualitative and quantitative analysis revealed that the analogues of the alkaloids did not accumulate in the nucleus. This makes the persistent claims that these molecules disrupt DNA replication in *P. falciparum* very unlikely.

In order to overcome the resolution limitations of the confocal microscope, a super-resolution technique (SR-SIM) was employed. Extensive colocalisation was observed between analogues of all three quinoline antimalarials and the ER. Colocalisation between these analogues and the mitochondrion was also evident but less conclusive. These observations are consistent with ultrastructural studies in which swelling of the mitochondrion and disintegration of the ER following drug treatment were observed.[6,7] Furthermore, a shared receptor between the quinine analogue and ER-Tracker Red on the surface of the ER gave rise to behaviour consistent with competitive binding between these two ligands, strengthening the case for colocalisation with this organelle.[14]

Whether the regions of accumulation in *P. falciparum* corresponded to binding of these antimalarials to protein targets within the parasite was investigated using chemical proteomics. Drug-labelled matrices captured quinoline antimalarial-binding proteins in human erythrocytes and *P. falciparum*. In uninfected erythrocytes, two dominant binding targets were detected for chloroquine, one of which corresponded closely in molecular weight to that of human aldehyde dehydrogenase 1 (ALDH1, 55 kDa) which was previously isolated using hydroxychloroquine-labelled beads.[15] In *P. falciparum*, SDS-Page revealed a prominent band between 200-250 kDa from the membrane-associated fraction. Proteomics analysis revealed that this band corresponded to *P. falciparum* multidrug resistance-associated protein (PfMRP1, 214 kDa). This is intriguing as PfMRP1 has been implicated in resistance mechanisms of chloroquine and quinine.[16] Disrupting this gene makes cells more susceptible to these drugs, indicating that this protein plays a role in transport and hence must bind these substrates.[17] That PfMRP1 was detected in binding sub-proteomes corresponding to all drug-labelled matrices shows that PfMRP1 dynamically binds to all three of the quinoline antimalarials investigated in this study.

PfMRP1 has previously been shown to localise to the parasite plasma membrane.[17] The analogues of all three quinoline antimalarials illuminated this membrane, suggesting that binding to PfMRP1 might be partly responsible for this localisation pattern. It is believed that this protein extrudes these drugs from the parasite cytoplasm to the parasitophorous vacuolar lumen.[17] Hence PfMRP1 is likely to have a high affinity for the quinoline antimalarials as this protein is found in relatively low abundance and, furthermore, the quinoline antimalarials are

unlikely to be present in high concentrations in the parasite cytoplasm. That PfMRP1 is a low-abundance protein but was still identified by affinity chromatography strengthens the findings that additional protein targets in *P. falciparum* were not detected. Thus it is likely that these antimalarials do not bind appreciably to protein targets within organelles such as the ER, the digestive vacuole and the mitochondrion, despite evidence of accumulation of the fluorescent analogues within or on the surface of these organelles. Although quinine has been shown to bind to the surface of mammalian sulfonylurea receptors which are prominent on the ER and mitochondrial membranes,[14] these receptors were not detected in any of the affinity experiments performed in this work.

Besides Fe(III)PPIX and the single protein PfMRP1, what other targets could possibly play a role in the mechanism of action of the quinoline antimalarials or in modulating their activity against a chloroquine-sensitive strain of *P. falciparum*? As proteins form the vast majority of known drug targets,[18] interaction of these antimalarials with a further non-protein target in addition to Fe(III)PPIX within *P. falciparum* would be extremely unusual. As described before, interaction with DNA is very unlikely as the analogues were not observed to localise to the nucleus, let alone at the high concentrations required for the inhibition of DNA replication. Interaction with RNA in the cytoplasm cannot be ruled out but is unlikely. Molecules targeting RNA are typically antisense oligonucleotides or anti-ribosomal antibiotics; presumably, interaction of the quinoline antimalarials with ribosomes would have been detected by the sensitive proteomic analysis of the drug-binding sub-proteomes isolated by affinity chromatography. Carbohydrates are also unlikely targets. Although glucose consumption of infected erythrocytes increases nearly 100-fold compared to uninfected erythrocytes,[19] *P. falciparum* possesses a conserved and efficient glycolytic pathway and targeting carbohydrates is unlikely to yield the specificity or potency exhibited by the quinoline antimalarials.

On the other hand, direct interaction with lipids is more likely. These antimalarials are all somewhat lipophilic, especially the *Cinchona* alkaloids, and association with membranes and membranous organelles was a prominent feature of the analogues as revealed by microscopy. Although these analogues are indeed more lipophilic than their parent molecules and more brightly fluorescent in low rather than high dielectric media, it has previously been shown that these antimalarials interact appreciably with bilayers. Indeed, quinine causes more disruption of the phospholipid bilayers than chloroquine.[20,21] Hence, it may be speculated that secondary effects due to association with membranous organelles such as the ER, the mitochondrion and other membranous structures might be responsible for deleterious metabolic disruption caused by the quinoline antimalarials, especially the quinoline methanols, in addition to their primary roles as haemozoin inhibitors.

Taken together, these results support haemozoin inhibition by accumulation in the digestive vacuole as the primary mechanism of action of the quinoline antimalarials, with Fe(III)PPIX as the primary target of these antimalarials. This was in agreement with live-cell localisation studies in which the digestive vacuole was a primary site of accumulation of the drug analogues, particularly in the case of chloroquine. Only a single protein binding target was identified which most likely plays a role as a transporter responsible for modulating the activity of these compounds but is not a drug target as such. While live-cell imaging and affinity chromatography did not reveal significant differences between the two major classes of these antimalarials that might be responsible for their differential effects against *P. falciparum*,[8] one may speculate that their fundamentally different interactions with Fe(III)PPIX may be responsible for these differential effects. Free Fe(III)PPIX itself is deleterious to cells and the complex between chloroquine and Fe(III)PPIX enhances the lytic effects on cells that have been observed with Fe(III)PPIX alone.[22,23] Quinine, quinidine and chloroquine all form stable complexes with Fe(III)PPIX, lending support to this hypothesis.

Overall, this study has generated and evaluated new tools to investigate the mechanism of action of the quinoline antimalarials against *P. falciparum*. A systematic approach has confirmed that Fe(III)PPIX, and hence haemozoin inhibition, is the primary target of these molecules with room for a secondary role resulting from direct interaction with lipid components such as phospholipid bilayers and/or membranous organelles. These quinoline antimalarials bind to PfMRP1 which is unlikely to be a drug target but probably modulates their activity within *P. falciparum*.

It is remarkable that, despite decades or even centuries of use, the mechanistic details relating to the action of the quinoline antimalarials against *P. falciparum* has remained elusive. The insights generated in this study have made some progress in addressing this matter. Nevertheless, the historical value of the *Cinchona* alkaloids and the impact of their synthetic derivative, chloroquine, cannot be understated. It is likely that these molecules will continue to play a valuable role in the future, especially as mechanistic probes. These investigations may still lead to hitherto undiscovered insights into the metabolism of this pathogen and hopefully improved chemotherapeutic resources to eliminate this devastating infectious disease.

7.2. Further work

In this work, PfMRP1 was identified as a binding target of the quinoline antimalarials using SDS-Page and proteomic analysis. In order to confirm unequivocally the identity of this protein band, Western blotting using an anti-PfMRP1 antibody should be performed. Similarly, binding relationships between the quinoline antimalarials and this protein may also be verified using antibodies that are specific for these drugs. For this, it is necessary that the free drug which was used to elute PfMRP1 is still bound to the protein in its denatured form on the SDS-Page gel. Proteomic analysis should also be carried out to identify the bands corresponding to the proteins pulled down from uninfected erythrocytes. Of particular importance are the two bands corresponding to putative chloroquine-binding proteins (41 kDa and 58 kDa), the latter of which is expected to correspond to human ALDH1 as identified by Graves et al.[15] A further band at approximately 61 kDa that was detected for all three quinoline antimalarials should also be identified and may provide insights into binding targets within the uninfected host cell.

PfMRP1 was identified from the chloroquine-sensitive NF54 strain of *P. falciparum*. Resistant strains of *P. falciparum* have mutations in the genes corresponding to other known quinoline transporters such as PfCRT.[16] Mutations in this gene confers resistance by actively extruding these quinoline antimalarials from the digestive vacuole.[16] As this mutation results in more efficient transport of these quinoline antimalarials, the mutated protein is likely to bind more strongly to these drugs. Hence, it would be interesting to investigate whether PfCRT may be identified by affinity chromatography using these resistant strains. It would also be interesting to investigate how the patterns of accumulation of the fluorescent analogues prepared in this work differ in resistant strains, especially under the super-resolution microscope.

Of particular interest is the interaction of the quinoline antimalarials with lipid or membranous components within *P. falciparum*. In order to investigate whether these drugs cause deleterious effects to the organelles in which their analogues accumulate, such as the ER, mitochondrion and membrane bilayers, further experiments should be performed. If treatment with the quinoline antimalarials leads to generation of reactive oxygen species within these organelles, for example, this could be probed using fluorescent indicators developed for this purpose. The ER is a calcium store in *P. falciparum*; thus, calcium redistribution in the parasitic cell following treatment with the drugs could be probed with suitable fluorescent dyes and may be an indication of disruption of this organelle caused by an accumulation of the drug.[24] Cytoskeletal components such as actin are involved in endocytosis in *P. falciparum*[25] and this may be related to the effects of quinine and chloroquine to modulate endocytosis in *P. falciparum* in a differential manner.[8] Morphological changes in actin could be monitored using a suitable actin-

specific dye such as SiR-actin.[26] While the chloroquine complex with Fe(III)PPIX is known to have a deleterious effect on cells,[22,23] the effects of the complexes of Fe(III)PPIX with the *Cinchona* alkaloids should be investigated to determine whether these may in some way be responsible for the differential effects against *P. falciparum* exhibited by the two major classes of these drugs.

As demonstrated in this study, fluorescently-labelled analogues provide useful tools with which to probe the localisation of drugs in cells. Although NBD was selected for this study on account of the specific properties described above, namely, its small size and photophysical attributes, alternative reporter dyes may be used in the preparation of additional novel derivatives of the quinoline antimalarials. Boron-dipyrromethane (BODIPY) dyes, for example, offer superior photochemical stability, high fluorescence quantum yields and good solubility[27,28] and, if these drug conjugates are validated as suitable analogues of the parent molecules, they may generate further insights into the localisation of the quinoline antimalarials within *P. falciparum*. While it was anticipated that these novel derivatives would provide new tools for investigations into malaria parasite biology, quinine and quinidine have also been used as a muscle relaxant and as a cardiac depressant, respectively, and so these new compounds might also be useful in applications beyond malaria research.[29] Although this study made use of SR-SIM, more sophisticated super-resolution techniques are likely to reveal deeper insights into the patterns of localisation of the drug analogues within *P. falciparum*. However, these techniques, of which STORM and STED are likely to be the most suitable, usually require fluorescence reporters with distinctive photophysical properties. On the other hand, transmission electron microscopy could also be harnessed to improve resolution with a correlative light and electron microscopy (CLEM) approach bridging the gap between these two imaging paradigms.

While this work has developed new tools for generating novel insights into the modes of action of the quinoline antimalarials, further mechanistic details still remain unresolved. In order to generate additional insights, other representative antimalarials from the two major structural classes of quinoline antimalarials should be investigated. For example, mefloquine might be a suitable representative quinoline methanol and amodiaquine a suitable 4-aminoquinoline. This work has also shown the value of taking a holistic approach to investigating a problem by exploiting different tools and techniques in a complementary manner. A cross-disciplinary approach such as this is arguably more powerful than single techniques in isolation and should be exploited in the future to generate further insights at the interface of chemistry and biology.

7.3. References

1. J. Achan, A. O. Talisuna, A. Erhart, A. Yeka, J. K. Tibenderana, F. N. Baliraine, P. J. Rosenthal and U. D'Alessandro, *Malaria J.*, 2011, **10**, 144.
2. D. A. Fidock, P. J. Rosenthal, S. L. Croft, R. Brun and S. Nwaka, *Nat. Rev. Drug Discov.*, 2004, **3**, 509.
3. J. N. Burrows, K. Chibale and T. N. C. Wells, *Curr. Top. Med. Chem.*, 2011, **11**, 1226.
4. J. M. Combrinck, T. E. Mabotha, K. K. Ncokazi, M. A. Ambele, D. Taylor, P. J. Smith, H. C. Hoppe and T. J. Egan, *ACS Chem. Biol.*, 2013, **8**, 133.
5. J. Gildenhuys, T. le Roux, T. J. Egan and K. A. de Villiers, *J. Am. Chem. Soc.*, 2013, **135**, 1037.
6. G. H. Jacobs, A. Oduola, D. E. Kyle, W. K. Milhous, S. K. Martin and M. Aikawa, *Am. J. Trop. Med. Hyg.*, 1988, **39**, 87.
7. N. Sachanonta, K. Chotivanich, U. Chaisri, G. D. H. Turner, D. J. P. Ferguson, N. P. J. Day and E. Pongponratn, *Ultrastruct. Pathol.*, 2011, **35**, 214.
8. L. Roberts, T. J. Egan, K. A. Joiner and H. C. Hoppe, *Antimicrob. Agents Chemother.*, 2008, **52**, 1840.
9. M. Foley, L. W. Deady, K. Ng, A. F. Cowman and L. Tilley, *J. Biol. Chem.*, 1994, **269**, 6955.
10. J. Desneves, G. Thorn, A. Berman, D. Galatis, N. La Greca, J. Sinding, M. Foley, L. W. Deady, A. F. Cowman and L. Tilley, *Mol. Biochem. Parasitol.*, 1996, **82**, 181.
11. M. Cabrera, J. Natarajan, M. F. Paguio, C. Wolf, J. S. Urbach and P. D. Roepe, *Biochemistry*, 2009, **48**, 9471.
12. C. C. Y. Loh, R. Suwanarusk, Y. Q. Lee, K. W. K. Chan, K. Choy, L. Rénia, B. Russell, M. J. Lear, F. H. Nosten, K. S. W. Tan and L. M. C. Chow, *PLOS ONE*, 2014, **9**, e110800.
13. E. B. Bohórquez, M. Chua and S. R. Meshnick, *Malaria J.*, 2012, **11**, 350.
14. P. Bednarczyk, A. Kicińska, V. Kominkova, K. Ondrias, K. Dolowy and A. Szewczyk, *J. Membrane Biol.*, 2004, **199**, 63.
15. P. R. Graves, J. J. Kwiek, P. Fadden, R. Ray, K. Hardeman, A. M. Coley, M. Foley and T. A. J. Haystead, *Mol. Pharm.*, 2002, **62**, 1364.
16. C. P. Sanchez, A. Dave, W. D. Stein and M. Lanzer, *Int. J. Parasitol.*, 2010, **40**, 1109.
17. D. K. Raj, J. Mu, H. Jiang, J. Kabat, S. Singh, M. Sullivan, M. P. Fay, T. F. McCutchan and X. Su, *J. Biol. Chem.*, 2009, **284**, 7686.
18. J. P. Overington, B. Al-Lazikani and A. L. Hopkins, *Nat. Rev. Drug Discov.*, 2006, **5**, 993.
19. D. L. Vander Jagt, L. A. Hunsaker, N. M. Campos and B. R. Baack, *Mol. Biochem. Parasitol.*, 1990, **42,** 277.
20. R. Zidovetzki, I. W. Sherman, A. Atiya and H. De Boeck, *Mol. Biochem. Parasitol.*, 1989, **35**, 199.

21. R. Zidovetzki, I. W. Sherman, P. A. Maguire and H. De Boeck, *Mol. Biochem. Parasitol.*, 1990, **38**, 33.
22. C. D. Fitch, R. Chevli, H. S. Banyal, G. Phillips, M. A. Pfaller and D. J. Krogstad, *Antimicrob. Agents Chemother.*, 1982, **21**, 819.
23. A. C. Chou and C. D. Fitch, *J. Clin. Invest.*, 1980, **66**, 856.
24. P. Rohrbach, O. Friedrich, J. Hentschel, H. Plattner, R. H. A. Fink and M. Lanzer, *J. Biol. Chem.*, 2005, **280**, 27960.
25. W. A. Smythe, K. A. Joiner and H. C. Hoppe, *Cell. Microbiol.*, 2008, **10**, 452.
26. G. Lukinavičius, L. Reymond, E. D'Este, A. Masharina, F. Göttfert, H. Ta, A. Güther, M. Fournier, S. Rizzo, H. Waldmann, C. Blaukopf, C. Sommer, D. W. Gerlich, H. Arndt, S. W. Hell and K. Johnsson, *Nat. Methods*, 2014, **11**, 731.
27. G. Ulrich, R. Ziessel and A. Harriman, *Angew. Chem. Int. Ed.*, 2008, **47**, 1184.
28. A. Loudet and K. Burgess, *Chem. Rev*., 2007, **107**, 4891.
29. *Cinchona Alkaloids in Synthesis & Catalysis*, ed. C. E. Song, Wiley-VCH, Germany, 2009.

Appendix

Experimental Methods and Characterisation of Organic Compounds

8.1. Synthetic organic chemistry

8.1.1. General synthetic methods

Unless otherwise stated, all reagents were purchased from Sigma-Aldrich and used without further purification. Monobromobimane was procured from Synchem UG & Co. KG. Solvents were generally purchased from Kimix Chemicals. Anhydrous $CHCl_3$ and CH_2Cl_2 were freshly distilled over $CaCl_2$ and P_4O_{10}, respectively. THF was distilled from sodium wire and benzophenone. Double-distilled deionised water (dH_2O) was provided by a Millipore Direct-Q3 water purification system.

For photoinitatied reactions, a Philips Actinic BL TL-D 15 W/10 1SL tubular low-pressure mercury vapour lamp with an emission maximum of 368 nm was used. Photosensitive reactions were protected from ambient light by aluminium foil. All purifications were performed under dim light. Thin-layer chromatography (TLC) was carried out on aluminium-backed silica gel 60 F_{254} plates (Merck). Compounds were visualised under short-wavelength UV light (254 nm) or long-wavelength UV light for fluorescence detection (365 nm). Plates were sprayed with a 2.5% solution of anisaldehyde in a mixture of sulfuric acid and ethanol (1:10 v/v) or with a 0.3% solution of ninhydrin in absolute ethanol acidified with 3% glacial acetic acid.[1]

For column chromatography, silica gel with pore size 60 Å and particle size 35-70 μm was used. Occasionally, flash chromatography was performed using a Biotage Isolera (silica gel with pore size 60 Å and particle size 63-200 μm).

Nuclear magnetic resonance (NMR) spectra were recorded on a Bruker 400 MHz spectrometer. Chemical shifts were recorded relative to residual chloroform in $CDCl_3$ (δ7.26 ppm in ^{1}H NMR and δ77.16 ppm in ^{13}C NMR), residual DMSO in DMSO-d_6 (δ2.50 ppm in ^{1}H NMR and δ39.52 in ^{13}C NMR) or residual methanol in CD_3OD (δ3.31 ppm in ^{1}H NMR and δ49.00 in ^{13}C NMR).[2]

Melting points were determined on a Reichert-Jung Thermovar hot-stage microscope. Optical rotation measurements were taken on a PerkinElmer Model 343 Polarimeter. Infrared (IR) spectra were recorded using either a PerkinElmer Spectrum Two FT-IR spectrometer with a PerkinElmer UATR attachment or a Bruker Tensor 27 FT-IR spectrometer with a Bruker Platinum ATR attachment. Absorption spectra were recorded at 25°C on a Varian Cary 100 UV-Vis or a Shimadzu UV-1800 spectrophotometer and were baseline-corrected.

Electron ionisation (EI) mass spectrometry was executed on a JEOL GCmate II. High-resolution mass spectrometry (HRMS) was performed at the Central Analytical Facility at Stellenbosch University using a Waters Synapt G2 with an electrospray ionisation (ESI) positive source. CHNS analysis was performed using a Thermo Flash EA 1112 series combustion analyser. High-performance liquid chromatography (HPLC) was performed using an Agilent 1220 LC System VL equipped with an Agilent ZORBAX Eclipse Plus C18 column (5 μm, 4.6 mm x 150 mm). Compounds dissolved in acetonitrile (0.3 mg/mL) were run at a flow rate of 1 mL/min with UV detection at 254 nm.

Systematic names were generated using ChemBioDraw (Version 13.0.2.3021, CambridgeSoft, 2013). The systematic numbering differs from the numbering indicated in blue on the structures which has been selected to aid NMR assignments. Overall percentage yields were calculated from the lowest-yielding route to a final product.

8.1.2. General procedure for the thiol-ene 'click' reduction of *Cinchona* alkaloids

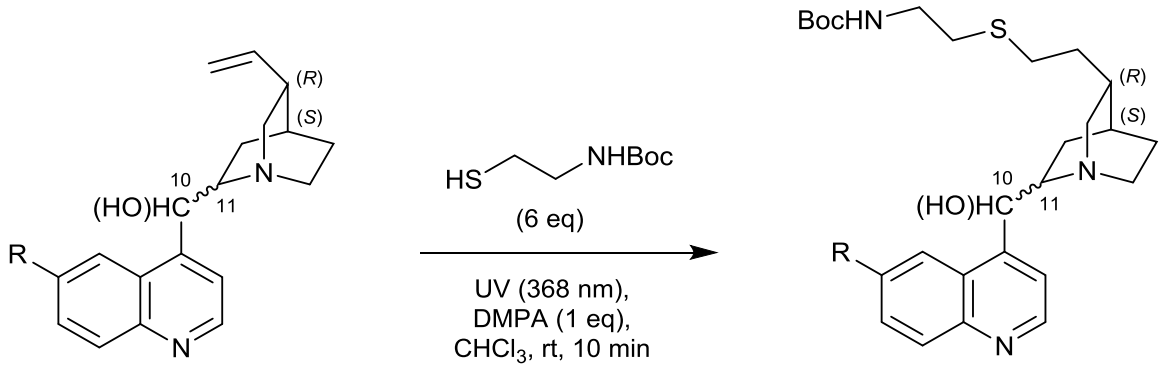

1 Quinine (10*R*,11*S*) R=OMe
2 Quinidine (10*S*,11*R*) R=OMe
17 Cinchonine (10*S*,11*R*) R=H

11 (10*R*,11*S*) R=OMe (87%)
12 (10*S*,11*R*) R=OMe (86%)
18 (10*S*,11*R*) R=H (97%)

This method was adapted from a previously-reported procedure.[3] The reaction was found not to be sensitive to oxygen or trace water; it is therefore unnecessary to use an inert atmosphere or anhydrous solvent. The reaction can be performed on a large scale (up to 2 g) enabling large amounts of thiolated derivatives to be easily prepared. Progress of the reaction is difficult to visualise using TLC due to 'smearing' of the amines across the silica substrate. Furthermore, the R_f values of the alkaloid starting materials and their products were often identical.

Alkaloid **1**, **2** or **17** (1 eq) and radical photoinitiator 2,2-dimethoxy-2-phenyl-acetophenone (DMPA, 1 eq) were both dissolved in $CHCl_3$ in a round-bottomed flask equipped with a stirrer bar. The thiol *tert*-butyl (2-mercaptoethyl)carbamate (6 eq) was added via syringe and the mixture was stirred thoroughly for several minutes. The flask was covered with a septum and placed on a stirrer plate against the centre of a Philips Actinic BL TL-D 15 W/10 1SL tubular low-pressure mercury vapour lamp. The entire apparatus was wrapped in aluminium foil and irradiated for ten minutes while stirring. During irradiation, the reaction mixture changed from colourless to light yellow.

The solvent was removed on a rotary evaporator and the reaction mixture was taken up in ethyl acetate (25 mL). This was transferred into a separating funnel and the organic component was washed with ice-cold 0.5 M citric acid (4 x 25 mL) to move the (protonated) product to the aqueous phase (pH 2-3). (The concentration, identity and temperature of the acid are important to avoid cleaving the *N*-Boc protecting group.)

Afterwards, the organic phase containing unreacted DMPA, the degradation products of DMPA and remaining thiol reactant was discarded. The aqueous phase was then basified to pH 11-12 with approximately ice-cold 5 M NaOH (40 mL). The neutral organic product was then extracted with ethyl acetate (3 x 25 mL). The extracts were combined and this was then washed with citric acid, basified and extracted as before to remove further impurities.

After a final wash with brine, magnesium sulfate was added to remove trace water. Following filtration, the solvent was removed under reduced pressure and the product **11**, **12** or **18** was dried on a vacuum pump. While ^{1}H NMR analysis indicated sufficient purity for subsequent reactions (> 95%), for combustion analysis these compounds were recrystallised from aqueous ethanol or methanol as described below.

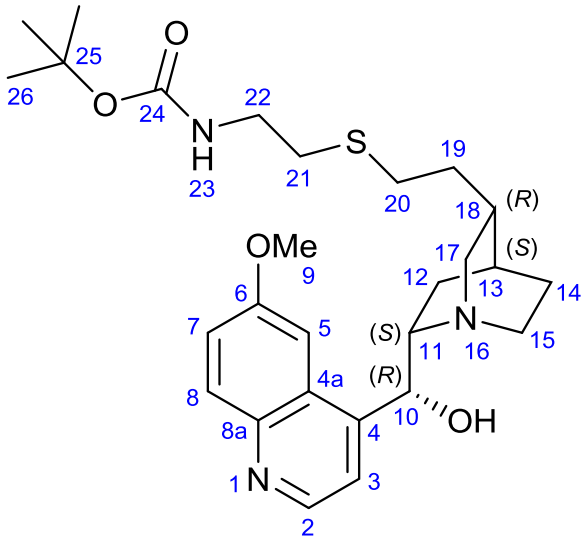

tert-Butyl (2-((2-((1*S*,3*R*,4*S*,6*S*)-6-((*R*)-hydroxy(6-methoxyquinolin-4-yl)methyl)quinuclidin-3-yl)ethyl)thio)ethyl)carbamate (11).

The general procedure above was followed. The alkaloid quinine (**1**, 1.000 g, 3.08 mmol), DMPA (790 mg, 3.08 mmol) and the thiol *tert*-butyl (2-mercaptoethyl)carbamate (3.12 mL, 18.48 mmol) were mixed in $CHCl_3$ (10 mL) and irradiated for ten minutes. Subsequent acid-base extraction yielded **11** as a white powder (1.340 g, 2.67 mmol, 87%). **11** was then further recrystallised from aqueous ethanol (1.084 g, 2.16 mmol, 70%). MP 69-71°C. $[\alpha]_D^{20}$ -82.6° (*c.* 0.797, EtOH). UV (EtOH) λ_{max}, nm (ε, M^{-1} cm^{-1}): 333 (5 000). ATR-FTIR ν_{max}/cm^{-1} 1705 (strong, sharp C=O stretching vibration in the region expected for a secondary carbamate).[4] ^{1}H NMR (400 MHz, $CDCl_3$) δ_H 8.57 (1H, d, *J* 4.6 Hz, H-2), 7.8 (1H, d, *J* 9.2 Hz, H-8), 7.49 (1H, d, *J* 4.6 Hz, H-3), 7.20 (1H, dd, *J* 9.2, 2.7 Hz, H-7), 7.15 (1H, d, *J* 2.7 Hz, H-5), 5.71 (1H, br s, H-10), 4.88 (2H, br s, -N<u>H</u>- secondary amide H-23 and hydroxyl -O<u>H</u>), 3.80 (3H, s, H-9), 3.65 (1H, m, H-15a), 3.21 (2H, q, *J* 6.1 Hz, H-22), 3.10 (2H, m, H-11 and H-17a), 2.68 (1H, m, H15-b), 2.53 (2H, t, *J* 6.7 Hz, H-21), 2.39 (3H, m, H-20 and H-17b), 1.78 (4H, m, H-18, H-14a, H-12a and H-13), 1.46 (3H, m, H-19 and H-14b), 1.38 (10H, m, H-26 and H-12b). ^{13}C NMR (100 MHz, $CDCl_3$) δ_C 158.0 (C-6), 155.9 (C-24), 147.4 (C-2), 147.1 (C-4), 144.2 (C-8a), 131.5 (C-8), 126.5 (C-4a), 121.7 (C-7), 118.6 (C-3), 101.3 (C-5), 79.6 (C-25), 70.6 (C-10), 60.0 (C-11), 57.9 (C-17), 56.1 (C-9), 43.4 (C-15), 39.9 (C-22), 34.4 (C-19), 34.3 (C-18), 32.5 (C-21), 29.8 (C-20), 28.5 (C-26), 27.4 (C-14), 25.6 (C-13), 20.8 (C-12). HRMS (ESI-TOF) *m/z*: $[M+H]^+$ calculated for $C_{27}H_{40}N_3O_4S$ 502.2740, found 502.2752. Anal. Calcd for $C_{27}H_{39}N_3O_4S$: C, 64.64; H, 7.84; N, 8.38; S, 6.39. Found: C, 64.72; H, 7.71; N, 8.52; S, 6.04.

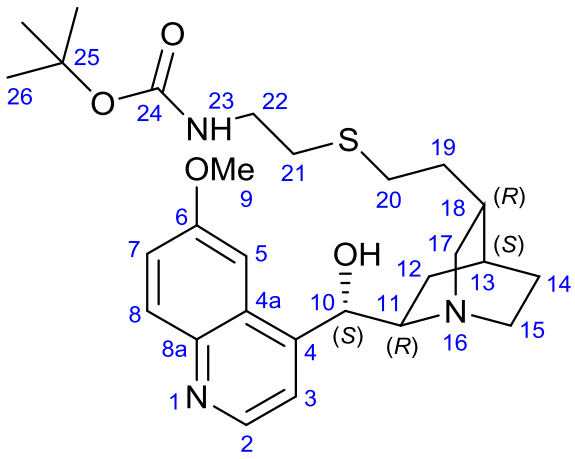

***tert*-Butyl (2-((2-((1*S*,3*R*,4*S*,6*R*)-6-((*S*)-hydroxy(6-methoxyquinolin-4-yl)methyl)quinuclidin-3-yl)ethyl)thio)ethyl)carbamate (12).**

The general procedure above was followed. The alkaloid quinidine (**2**, 500 mg, 1.54 mmol), DMPA (395 mg, 1.54 mmol) and the thiol *tert*-butyl (2-mercaptoethyl)carbamate (1.56 mL, 9.23 mmol) were mixed in $CHCl_3$ (5 mL) and irradiated for ten minutes. Subsequent acid-base extraction yielded **12** as a white powder (668 mg, 1.32 mmol, 86%). **12** was then recrystallised from aqueous ethanol (556 mg, 1.11 mmol, 72%). MP 168-170°C. $[\alpha]_D^{20}$ +137.5° (*c.* 0.797, EtOH). UV (EtOH) λ_{max}, nm (ε, M^{-1} cm^{-1}): 333 (5 000). ATR-FTIR ν_{max}/cm^{-1} 1705 (strong, sharp C=O stretching vibration in the region expected for a secondary carbamate).[4] ^{1}H NMR (400 MHz, $CDCl_3$) δ_H 8.64 (1H, d, *J* 4.6 Hz, H-2), 7.95 (1H, d, *J* 9.2 Hz, H-8), 7.51 (1H, d, *J* 4.6 Hz, H-3), 7.29 (1H, dd, *J* 9.2, 2.6 Hz, H-7), 7.18 (1H, d, *J* 2.6 Hz, H-5), 5.59 (1H, d, *J* 3.9 Hz, H-10), 5.01 (1H, br s, -N<u>H</u>- secondary amide H-23), 3.85 (3H, s, H-9), 3.29 (2H, q, *J* 6.4 Hz, H-22), 3.14 (1H, dq, *J* 7.3, 2.4 Hz, H-15a), 3.02 (1H, td, *J* 9.3, 4.0 Hz, H-11), 2.86 (2H, m, H-17a and H15-b), 2.74 (1H, m, H-17b), 2.61 (2H, m, H-21), 2.46 (2H, t, *J* 7.7 Hz, H-20), 2.00 (1H, m, H-12a), 1.81 (1H, m, H-19a), 1.70 (1H, m, H-19b), 1.66 (1H, m, H-13), 1.59 (1H, t, *J* 8.0 Hz, H-18), 1.47 (2H, m, H-14), 1.41 (9H, s, H-26), 1.08 (1H, m, H-12b). ^{13}C NMR (100 MHz, $CDCl_3$) δ_C 157.8 (C-6), 156.1 (C-24), 148.0 (C-4), 147.7 (C-2), 144.3 (C-8a), 131.7 (C-8), 126.7 (C-4a), 121.6 (C-7), 118.5 (C-3), 101.5 (C-5), 79.7 (C-25), 72.1 (C-10), 59.9 (C-11), 55.7 (C-9), 50.8 (C-15), 50.3 (C-17), 40.2 (C-22), 34.9 (C-18), 32.8 (C-19), 32.1 (C-21), 29.8 (C-20), 28.5 (C-26), 27.2 (C-13), 26.8 (C-14), 20.7 (C-12). HRMS (ESI-TOF) *m/z*: $[M+H]^+$ calculated for $C_{27}H_{40}N_3O_4S$ 502.2740, found 502.2750. Anal. Calcd for $C_{27}H_{39}N_3O_4S$: C, 64.64; H, 7.84; N, 8.38; S, 6.39. Found: C, 64.38; H, 7.79; N, 8.52; S, 6.35.

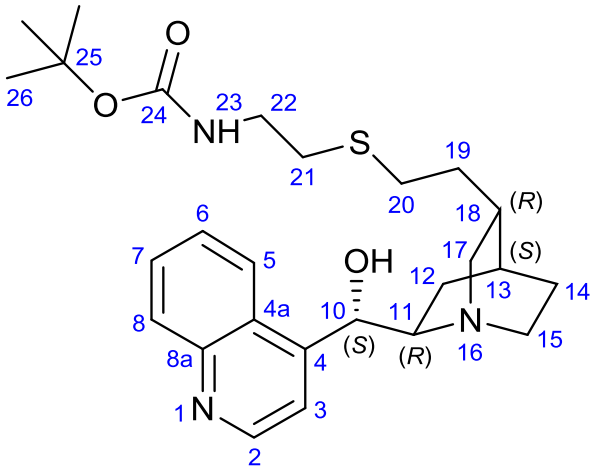

***tert*-Butyl (2-((2-((1*S*,3*R*,4*S*,6*R*)-6-((*S*)-hydroxy(quinolin-4-yl)methyl)quinuclidin-3-yl)ethyl)thio)ethyl)carbamate (18).**

The general procedure above was followed. The alkaloid cinchonine (**17**, 908 mg, 3.08 mmol), DMPA (790 mg, 3.08 mmol) and the thiol *tert*-butyl (2-mercaptoethyl)carbamate (3.12 mL, 18.48 mmol) were dissolved in a 1:1 mixture of $CHCl_3$:MeOH (v/v, 10 mL) and irradiated for ten minutes. Subsequent acid-base extraction yielded **18** as a white powder (1.490 g, 2.99 mmol, 97%). **18** was then further recrystallised from aqueous ethanol (1.002 g, 2.13 mmol, 69%). MP 151-153°C $[\alpha]_D^{20}$ +110.8° (*c.* 0.749, EtOH). UV (EtOH) λ_{max}, nm (ε, M^{-1} cm^{-1}): 315 (3 500). ATR-FTIR ν_{max}/cm^{-1} 1710 (strong, sharp C=O stretching vibration in the region expected for a secondary carbamate).[4] ^1H NMR (400 MHz, $CDCl_3$) δ_H 8.81 (1H, d, *J* 4.5 Hz, H-2), 8.08 (1H, dd, *J* 8.4, 1.2 Hz, H-8), 7.94 (1H, dd, *J* 8.4, 1.2 Hz, H-5), 7.64 (1H, ddd, *J* 8.4, 7.0, 1.2 Hz, H-7), 7.60 (1H, d, *J* 4.5 Hz, H-3), 7.40 (1H, ddd, *J* 8.4, 7.0, 1.2 Hz, H-6), 5.70 (1H, d, *J* 3.5 Hz, H-10), 5.00 (1H, br s, -N<u>H</u>- secondary amide H-23), 4.76 (1H, br s, secondary hydroxyl -O<u>H</u>), 3.27 (2H, dt, *J* 13.3, 6.9 Hz, H-22), 3.15 (1H, ddd, *J* 13.5, 7.6, 2.0 Hz, H-15a), 2.98 (1H, td, *J* 9.1 Hz, H-11), 2.81 (2H, m, H-17a and H-15b), 2.61 (3H, m, H-17b and H-21), 2.45 (2H, t, *J* 7.8 Hz, H-20), 2.01 (1H, dd, *J* 12.7 Hz, H-12a), 1.82 (1H, m, H-19a), 1.70 (1H, dt, *J* 14.2, 7.1 Hz, H-19b), 1.64 (1H, br s, H-13), 1.56 (1H, quin, *J* 2.9 Hz, H-18), 1.41 (11H, m, H-14 and H-26), 1.06 (1H, m, H-12b). ^{13}C NMR (100 MHz, $CDCl_3$) δ_C 156.1 (C-24), 150.2 (C-2), 149.7 (C-4), 148.3 (C-8a), 130.4 (C-8), 129.1 (C-7), 126.7 (C-6), 125.8 (C-4a), 123.2 (C-5), 118.3 (C-3), 79.7 (C-25), 72.1 (C-10), 60.2 (C-11), 50.8 (C-15), 50.3 (C-17), 40.1 (C-22), 35.0 (C-18), 32.9 (C-19), 32.1 (C-21), 29.8 (C-20), 28.5 (C-26), 27.3 (C-14), 26.8 (C-13), 20.6 (C-12). HRMS (ESI-TOF) *m/z*: $[M+H]^+$ calculated for $C_{26}H_{38}N_3O_3S$ 472.2634, found 472.2630. Anal. Calcd for $C_{26}H_{37}N_3O_3S$: C, 66.21; H, 7.91; N, 8.91; S, 6.80. Found: C, 66.01; H, 8.20; N, 8.90; S, 6.78.

8.1.3. General procedure for the cleavage of *N*-Boc-protected amines

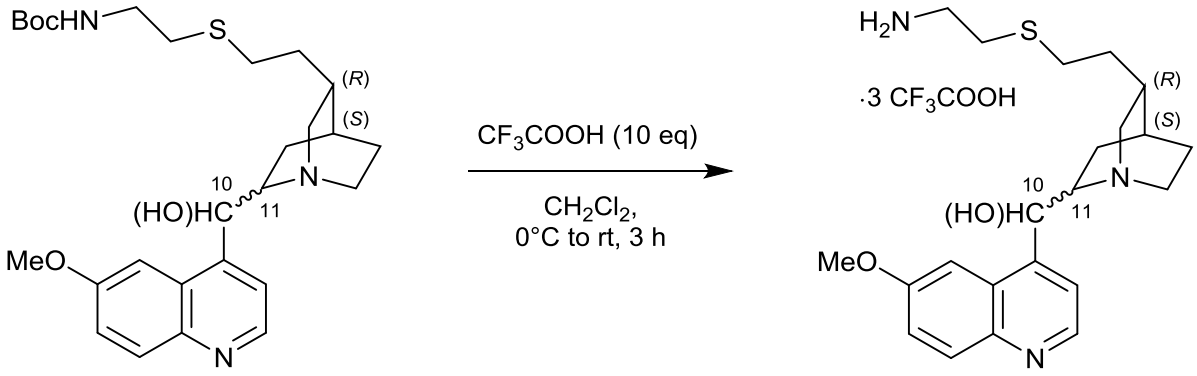

11 (10*R*,11*S*)
12 (10*S*,11*R*)

9 (10*R*,11*S*) (45%)
10 (10*S*,11*R*) (43%)

The *N*-Boc protected amine **11** or **12** (1 eq) was dissolved in CH_2Cl_2 in a round-bottomed flask equipped with a stirrer bar and cooled in an ice-bath to 0°C. Trifluoroacetic acid (TFA, 10 eq) was added dropwise over ten minutes during which time the reaction mixture changed from colourless to bright yellow. After two hours no further change was observed by TLC. During this time the ice-bath was not replenished, allowing the reaction mixture to warm slowly to room temperature. Excess TFA was removed under reduced pressure and the resulting oil was purified by column chromatography over an elution gradient of 0-25% MeOH:CH_2Cl_2. The appropriate fractions were collected, the volume was reduced and the product was dried on a vacuum pump to afford pure **9** or **10** as a trifluoroacetate salt.

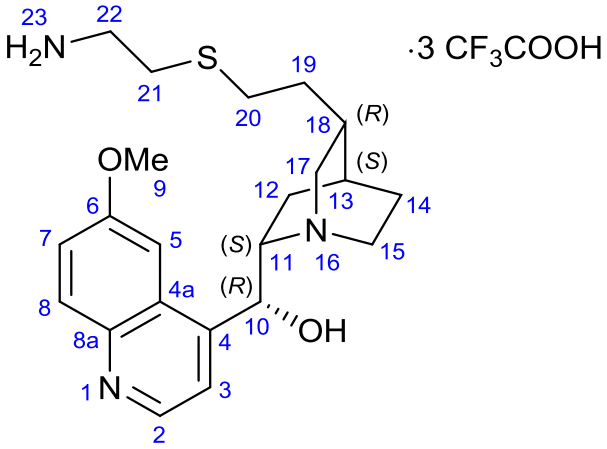

Tris(trifluoroacetate) (1*S*,2*S*,4*S*,5*R*)-5-(2-((2-ammonioethyl)thio)ethyl)-2-((*R*)-hydroxy(6-methoxyquinolin-1-ium-4-yl)methyl)quinuclidin-1-ium (9).

Following the general method above, **11** (0.885 g, 1.76 mmol) was dissolved in CH_2Cl_2 (10 mL) and cooled to 0°C. TFA (1.35 mL, 2.007 g, 17.6 mmol) was added dropwise. After two hours the excess solvent was evaporated and column chromatography yielded the salt **9** (0.589 g, 0.79 mmol, 45%) as a sticky white amorphous solid. UV (EtOH) λ_{max}, nm (ε, M^{-1} cm^{-1}): 333 (5 000). R_f 0.36 (MeOH:CH_2Cl_2 15:85). ATR-FTIR ν_{max}/cm^{-1} 1675 (strong, sharp C=O stretching vibration). ^{1}H NMR (400 MHz, CD_3OD) δ_H 8.87 (1H, d, *J* 5.1 Hz, H-2), 8.11 (1H, d, *J* 9.3 Hz, H-8), 8.06 (1H, d, *J* 5.1 Hz, H-3), 7.64 (1H, dd, *J* 9.3, 2.7 Hz, H-7), 7.56 (1H, d, *J* 2.7 Hz, H-5), 6.19 (1H, s, H-10), 4.25 (1H, m, H-15a), 4.05 (3H, s, H-9), 3.71 (1H, m, H-11), 3.64 (1H, dd, *J* 13.0, 10.8 Hz, H-17a), 3.31 (1H, m, H-15b), 3.06 (3H, m, H-22 and H-17b), 2.74 (2H, t, *J* 6.8 Hz, H-21), 2.54 (2H, t, *J* 7.5 Hz, H-20), 2.26 (3H, m, H-18, H-14a and H-12a), 2.11 (1H, m, H-13), 1.91 (1H, m, H-14b), 1.63 (3H, m, H-19 and H-12b). ^{13}C NMR (100 MHz, CD_3OD) δ_C 163.3 (C=O TFA anion), 161.2 (C-6), 151.6 (C-4), 145.6 (C-2), 140.9 (C-8a), 128.6 (C-8), 128.2 (C-4a), 129.9 (C-7), 120.9 (C-3), CF_3 from TFA anion not observed, 102.5 (C-5), 68.3 (C-10), 61.2 (C-11), 57.14 (C-17), 57.05 (C-9), 45.2 (C-15), 39.8 (C-22), 33.90 (C-19), 33.86 (C-18), 29.72 (C-21), 29.69 (C-20), 26.1 (C-13), 25.6 (C-14), 19.0 (C-12). HRMS (ESI-TOF) *m*/*z*: $[M+H]^+$ Calculated for $C_{22}H_{32}N_3O_2S$ 402.2215; found 402.2208. HPLC: 99.0%.

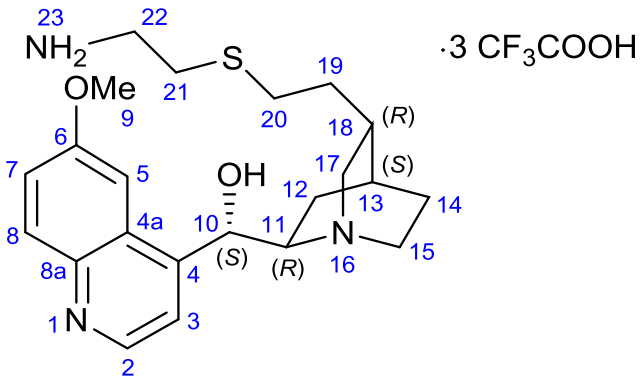

Tris(trifluoroacetate) (1*S*,2*R*,4*S*,5*R*)-5-(2-((2-ammonioethyl)thio)ethyl)-2-((*S*)-hydroxy(6-methoxyquinolin-1-ium-4-yl)methyl)quinuclidin-1-ium (10).

Following the general method above, **12** (0.963 g, 1.92 mmol) was dissolved in CH_2Cl_2 (10 mL) and cooled to 0°C. TFA (1.48 mL, 2.190 g, 19.2 mmol) was added dropwise. After two hours the excess solvent was evaporated and column chromatography yielded the salt **10** (0.617 g, 0.83 mmol, 43%) as a clear gum. UV (EtOH) λ_{max}, nm (ε, M^{-1} cm^{-1}): 333 (5 000). R_f 0.36 (MeOH:CH_2Cl_2 15:85). ATR-FTIR ν_{max}/cm^{-1} 1675 (strong, sharp C=O stretching vibration). ^{1}H NMR (400 MHz, CD_3OD) δ_H 8.87 (1H, d, *J* 5.1 Hz, H-2), 8.10 (1H, d, *J* 9.3 Hz, H-8), 8.07 (1H, d, *J* 5.1 Hz, H-3), 7.63 (1H, dd, *J* 9.3, 2.7 Hz, H-7), 7.56 (1H, d, *J* 2.7 Hz, H-5), 6.31 (1H, s, H-10), 4.05 (4H, m, H-9 and H-15a), 3.69 (1H, t, *J* 9.4 Hz, H-11), 3.54 (2H, m, H-15b and H-17a), 3.34 (1H, m, H-17b), 3.19 (2H, t, *J* 6.8 Hz, H-22), 2.87 (2H, t, *J* 6.8 Hz, H-21), 2.67 (2H, m, H-20), 2.48 (1H, m, H-12a), 2.21 (1H, m, H-18), 2.04 (1H, br s, H-13), 1.94 (4H, m, H-19 and H-14), 1.27 (1H, m, H-12b). ^{13}C NMR (100 MHz, CD_3OD) δ_C 163.4 (C=O TFA anion), 160.5 (C-6), 148.1 (C-4), 147.4 (C-2), 143.7 (C-8a), 130.8 (C-8), 127.6 (C-4a), 124.4 (C-7), 120.4 (C-3), CF_3 from TFA anion not observed, 102.0 (C-5), 68.6 (C-10), 61.2 (C-11), 56.8 (C-9), 51.1 (C-15), 50.5 (C-17), 39.9 (C-22), 33.6 (C-18), 32.3 (C-19), 29.9 (C-20 and C-21), 26.6 (C-13), 24.5 (C-14), 18.8 (C-12). HRMS (ESI-TOF) *m/z*: $[M+H]^+$ Calculated for $C_{22}H_{32}N_3O_2S$ 402.2215; found 402.2217. HPLC: 99.3%.

8.1.4. General procedure for the nucleophilic substitution of NBD-Cl by amino-functionalised alkaloids

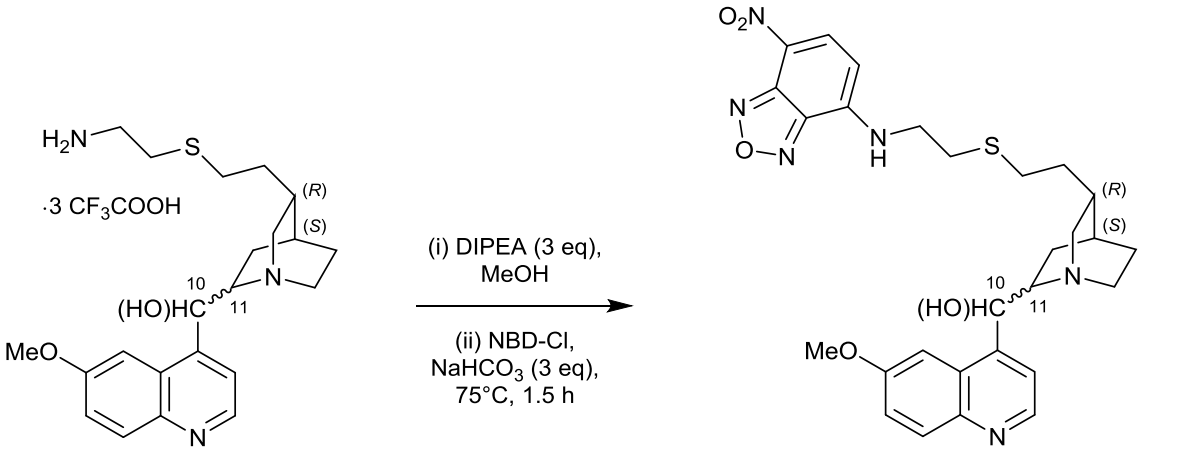

9 (10*R*,11*S*)
10 (10*S*,11*R*)

3 Quinine-NBD (10*R*,11*S*) (26%, 10% overall)
4 Quinidine-NBD (10*S*,11*R*) (27%, 10% overall)

The trifluoroacetate salt **9** or **10** (1 eq) was dissolved in MeOH in a two-necked round-bottomed flask equipped with a stirrer bar. *N*,*N*-Diisopropylethylamine (DIPEA, 3 eq) was added and the mixture was stirred for ten minutes to liberate the amines from the trifluoroacetate anions. A septum was attached to one neck of the flask while a reflux condenser was attached to the other neck and the mixture was heated to 75°C. Solid $NaHCO_3$ (3 eq) was added. 4-Chloro-7-nitrobenzo[*c*][1,2,5]oxadiazole (NBD-Cl, 1 eq) was dissolved in CH_3CN (10 mL) and added dropwise. The mixture was incubated for two hours, during which time the colour changed from bright yellow to deep brown which indicated successful displacement of the chlorine by the terminal amine of the alkaloid to form the fluorescent NBD adduct. After this time TLC indicated that all NBD-Cl was consumed. The reaction mixture was cooled and filtered through a pad of Celite. The volume was reduced on the rotary evaporator and the mixture was purified using column chromatography (0-20% MeOH:CH_2Cl_2 elution gradient). The appropriate fractions were selected, the volume was reduced and the resultant product **3** or **4** was recrystallised from aqueous MeOH.

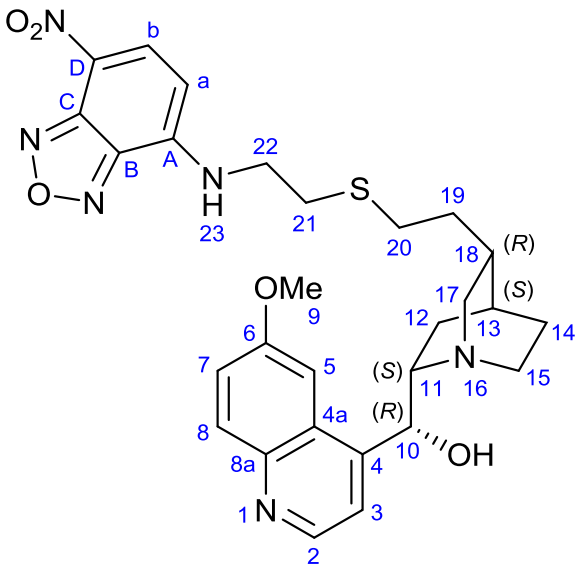

(*R*)-(6-methoxyquinolin-4-yl)((1*S*,2*S*,4*S*,5*R*)-5-(2-((2-((7-nitrobenzo[*c*][1,2,5]oxadiazol-4-yl)amino)ethyl)thio)ethyl)quinuclidin-2-yl)methanol, "Quinine-NBD" (3).

Following the general method above, **9** (1.497 g, 2.01 mmol) was dissolved in MeOH (20 mL) and neutralised with DIPEA (1.05 mL, 6.03 mmol). $NaHCO_3$ (507 mg, 6.03 mmol) was added and the mixture heated to 75°C, after which NBD-Cl (401 mg, 2.01 mmol) was added. The product **3** was isolated by column chromatography and purified by recrystallisation from aqueous MeOH (294 mg, 0.52 mmol, 26%, 10% overall). UV (EtOH) λ_{max}, nm (ε, M^{-1} cm^{-1}): 333 (11 500), 464 (18 500); UV (20 mM Hepes, pH 7.5) λ_{max}, nm (ε, M^{-1} cm^{-1}): 335 (8 500), 473 (17 500). R_f 0.61 (MeOH:CH_2Cl_2 10:90). ATR-FTIR ν_{max}/cm^{-1} 1295 (strong, sharp NO_2 symmetric stretching vibration). ^{1}H NMR (400 MHz, DMSO-d_6) δ_H 8.74 (1H, d, *J* 4.5 Hz, H-2), 8.45 (1H, d, *J* 8.9 Hz, H-b), 7.95 (1H, d, *J* 9.2 Hz, H-8), 7.63 (1H, d, *J* 4.5 Hz, H-3), 7.51 (1H, d, *J* 2.8 Hz, H-5), 7.41 (1H, dd, *J* 9.2, 2.8 Hz, H-7), 6.41 (2H, m, H-a and aryl -N<u>H</u>-), 6.04 (1H, d, *J* 2.6 Hz, H-10), 3.99 (4H, m, H-9 and H-15a), 3.60 (3H, m, H-22 and H-11), 3.47 (1H, t, *J* 11.6 Hz, H-17a), 3.20 (1H, m, H-15b), 2.94 (1H, dd, *J* 12.1, 5.6 Hz, H-17b), 2.79 (2H, t, *J* 7.0 Hz, H-21), 2.59 (2H, m, H-20), 2.05 (3H, m, H-18, H-14a and H-12a), 1.96 (1H, br s, H-13), 1.73 (1H, m, H-14b), 1.57 (2H, m, H-19), 1.47 (1H, m, H-12b). ^{13}C NMR (100 MHz, DMSO-d_6) δ_C 157.7 (C-6), 147.3 (C-2), 145.1 (C-4), 144.7, 144.2, 143.9 (C-A, C-B and C-C), 143.7 (C-8a), 137.6 (C-b), 131.3 (C-8), 125.6 (C-4a), 121.5 (C-7), 120.8 (C-D), 119.0 (C-3), 101.9 (C-5), 99.3 (C-a), 65.9 (C-10), 59.0 (C-11), 56.4 (C-9), 54.5 (C-17), 43.2 (C-22), 42.8 (C-15), 32.3 (C-19), 32.1 (C-18), 29.3 (C-21), 28.6 (C-20), 24.3 (C-14 and C-13), 17.6 (C-12). HRMS (ESI-TOF) *m*/*z*: $[M+H]^+$ Calculated for $C_{28}H_{33}N_6O_5S$ 565.2233; found 565.2229. HPLC: 96.1%.

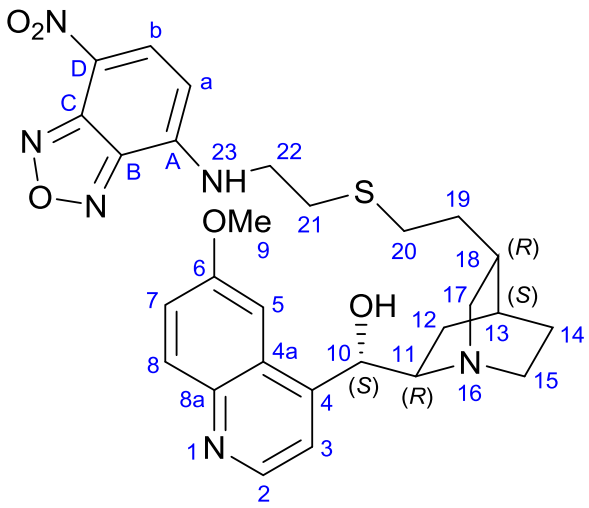

(*S*)-(6-methoxyquinolin-4-yl)((1*S*,2*R*,4*S*,5*R*)-5-(2-((2-((7-nitrobenzo[*c*][1,2,5]oxadiazol-4-yl)amino)ethyl)thio)ethyl)quinuclidin-2-yl)methanol, "Quinidine-NBD" (4).

Following the general method above, **10** (1.542 g, 2.02 mmol) was dissolved in MeOH (20 mL) and neutralised with DIPEA (1.06 mL, 6.06 mmol). $NaHCO_3$ (509 mg, 6.06 mmol) was added and the mixture heated to 75°C, after which NBD-Cl (403 mg, 2.02 mmol) was added. The product **4** was isolated by column chromatography and purified by recrystallisation from aqueous MeOH (311 mg, 0.55 mmol, 27%, 10% overall). UV (EtOH) λ_{max}, nm (ε, M^{-1} cm^{-1}): 332 (11 000), 463 (17 000); UV (20 mM Hepes, pH 7.5) λ_{max}, nm (ε, M^{-1} cm^{-1}): 335 (9 000), 479 (19 000). R_f 0.61 (MeOH:CH_2Cl_2 10:90). ATR-FTIR ν_{max}/cm^{-1} 1300 (strong, sharp NO_2 symmetric stretching vibration). ^1H NMR (400 MHz, DMSO-d_6) δ_H 8.75 (1H, d, *J* 4.5 Hz, H-2), 8.51 (1H, d, *J* 8.9 Hz, H-b), 7.97 (1H, d, *J* 9.3 Hz, H-8), 7.64 (1H, d, *J* 4.5 Hz, H-3), 7.43 (1H, dd, *J* 9.3, 2.9 Hz, H-7), 7.37 (1H, d, *J* 2.9 Hz, H-5), 6.54 (1H, d, *J* 4.0 Hz, aryl -N<u>H</u>-), 6.50 (1H, d, *J* 8.9 Hz, H-a), 6.02 (1H, d, *J* 2.3 Hz, H-10), 3.96 (3H, s, H-9), 3.76 (3H, m, H-22 and H-15a), 3.56 (1H, t, *J* 9.2 Hz, H-11), 3.45 (2H, m, H-17a and H-15b), 3.22 (1H, m, H-17b), 2.91 (2H, t, *J* 6.9 Hz, H-21), 2.65 (2H, m, H-20), 2.28 (1H, t, *J* 11.2 Hz, H-12a), 2.04 (1H, quin, *J* 8.2 Hz, H-18), 1.92 (1H, br s, H-13), 1.80 (4H, m, H-19 and H-14), 1.15 (1H, m, H-12b). ^{13}C NMR (100 MHz, DMSO-d_6) δ_C 157.7 (C-6), 147.4 (C-2), 144.7 (C-4), 144.3, 144.2, 144.1 (C-A, C-B and C-C), 143.7 (C-8a), 137.7 (C-b), 131.4 (C-8), 125.4 (C-4a), 121.6 (C-7), 121.0 (C-D), 118.8 (C-3), 101.2 (C-5), 99.4 (C-a), 66.4 (C-10), 59.0 (C-11), 55.8 (C-9), 48.9 (C-15), 48.3 (C-17), 43.3 (C-22), 31.7 (C-18), 31.1 (C-19), 29.4 (C-21), 28.7 (C-22), 24.5 (C-13), 23.0 (C-14), 17.2 (C-12). HRMS (ESI-TOF) *m/z*: $[M+H]^+$ Calculated for $C_{28}H_{33}N_6O_5S$ 565.2233; found 565.2247. HPLC: 98.0%.

8.1.5. General procedure for the preparation of NBD-labelled amino acids

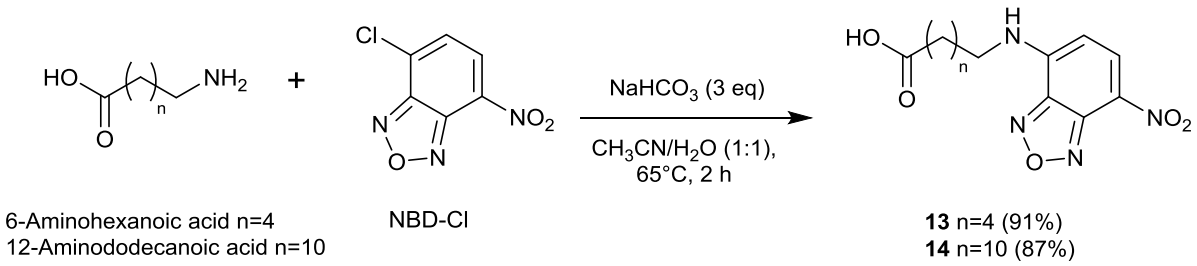

6-Aminohexanoic acid n=4
12-Aminododecanoic acid n=10

NBD-Cl

13 n=4 (91%)
14 n=10 (87%)

The procedures of Novotný et al. and Haldar et al. were followed for the preparation of the NBD-labelled amino acids of **13** and **14**.[5,6] Briefly, the amino acid (1.2 eq) and $NaHCO_3$ (3 eq) were dissolved in dH_2O (10 mL) in a two-necked round-bottomed flask equipped with a stirrer bar. A septum was attached to one neck and a reflux condenser was attached to the other. The mixture was heated to 65°C. 4-Chloro-7-nitrobenzo[*c*][1,2,5]oxadiazole (NBD-Cl, 1 eq) was dissolved in CH_3CN (10 mL) and added dropwise via syringe. The mixture was incubated for two hours, during which time the colour changed from bright yellow to deep brown. After two hours, TLC indicated that all the NBD-Cl had been consumed. The mixture was cooled and the CH_3CN was removed on the rotary evaporator. The remaining aqueous phase was acidified to approximately pH 2 with 1 M HCl. Thereafter it was extracted three times with EtOAc (20 mL), washed with brine, dried with $MgSO_4$, filtered and the solvent removed. The resultant NBD-labelled amino acid **13** or **14** was then recrystallised from aqueous MeOH.

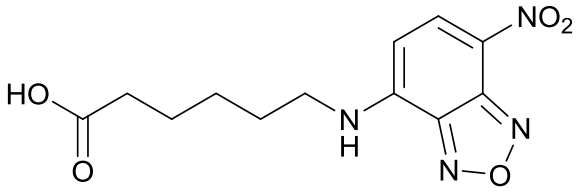

6-((7-nitrobenzo[*c*][1,2,5]oxadiazol-4-yl)amino)hexanoic acid (13).[5]

The NBD-labelled amino acid **13** was prepared from 6-aminohexanoic acid (679.7 mg, 4.81 mmol) as described above and recrystallised from aqueous MeOH to yield bright orange crystals (1.077 g, 3.66 mmol, 91%). MP 153-155°C (lit.[5] MP 158-159°C). UV (EtOH) λ_{max}, nm (ε, M^{-1} cm^{-1}): 333 (8 500), 456 (19 500). ATR-FTIR ν_{max}/cm^{-1} 1700 (strong, sharp C=O stretching vibration indicates saturated carboxylic acid). MS (EI+) *m*/*z*: $[M]^+$ 294.

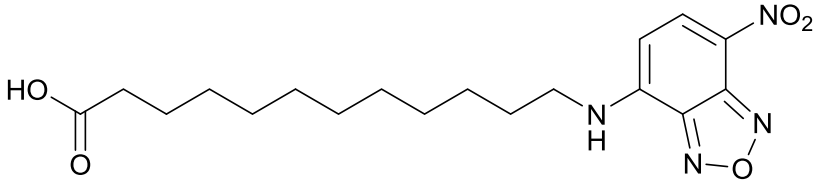

12-((7-nitrobenzo[*c*][1,2,5]oxadiazol-4-yl)amino)dodecanoic acid (14).[5]

The NBD-labelled amino acid **14** was prepared from 12-aminododecanoic acid (327 mg, 1.52 mmol) as described above and recrystallised from aqueous MeOH to yield dark orange crystals (501 mg, 1.32 mmol, 87%). MP 92-94°C (lit.[5] MP 94-96°C). UV (EtOH) λ_{max}, nm (ε, M^{-1} cm^{-1}): 333 (8 000), 464 (19 000). ATR-FTIR ν_{max}/cm^{-1} 1720 (strong, sharp C=O stretching vibration indicates saturated carboxylic acid). MS (EI+) *m*/*z*: $[M]^+$ 378.

8.1.6. General procedure for the preparation of NBD-labelled amino acid succinimidyl esters

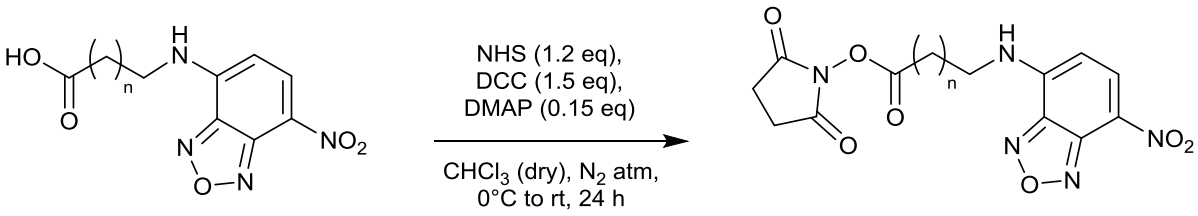

13 n=4
14 n=10

15 n=4 (79%)
16 n=10 (53%)

A procedure previously described for the preparation of the NBD-labelled amino acid succinimidyl esters was followed.[5] Briefly, dry $CHCl_3$ (10 mL) was added to a two-necked round-bottomed flask equipped with a stirrer bar under an inert atmosphere (N_2) to which the NBD-labelled amino acid **13** or **14** (1 eq), *N*-hydroxysuccinimide (NHS, 1.2 eq) and catalytic 4-dimethylaminopyridine (DMAP, 0.15 eq) had already been added. This was cooled in an ice-bath to 0°C. *N*,*N*′-Dicyclohexylcarbodiimide (DCC, 1.5 eq) was dissolved in dry $CHCl_3$ (2 mL) and added dropwise. If necessary, additional dry CH_3CN (5 mL) was added to ensure that the NBD-labelled amino acid was completely dissolved.

The flask was left to stir overnight and was gradually allowed to reach room temperature. After 24 hours, TLC indicated that the NBD-labelled amino acid was completed consumed. Solvents were evaporated and the residue was resuspended in a half-brine/half-water mixture to remove the urea by-product. The desired product was extracted three times with EtOAc, dried with brine and Na_2SO_4, filtered and the solvent removed. NBD-labelled amino acid succinimidyl esters **15** and **16** were labile but flash chromatography (100% EtOAc) could be used to furnish the product in a form suitable for further use (judged to be > 95% pure from ^{1}H NMR).

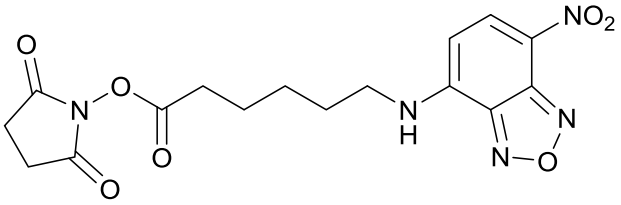

2,5-dioxopyrrolidin-1-yl 6-((7-nitrobenzo[*c*][1,2,5]oxadiazol-4-yl)amino)hexanoate (15).[5]

The NBD-labelled succinimidyl ester **15** was prepared from **13** (221 mg, 0.75 mmol) as described above and purified by column chromatography to yield bright orange crystals (232 mg, 0.59 mmol, 79%). MP 177-179°C (lit.[5] MP 189-191°C). UV (EtOH) λ_{max}, nm (ε, M^{-1} cm^{-1}): 333 (8 500), 456 (19 500). ATR-FTIR ν_{max}/cm^{-1} 1815 and 1785 (medium, sharp C=O stretching vibrations typical of succinimidyl carbonyls), 1730 (strong, sharp C=O stretching vibration typical of succinimidyl ester). MS (EI+) *m*/*z*: $[M]^+$ 391.

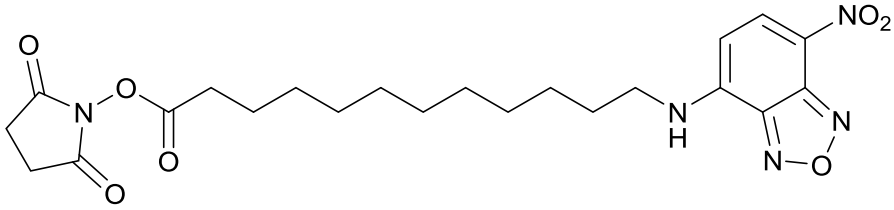

2,5-dioxopyrrolidin-1-yl 12-((7-nitrobenzo[*c*][1,2,5]oxadiazol-4-yl)amino)dodecanoate (16).[5]

The NBD-labelled succinimidyl ester **16** was prepared from **14** (504 mg, 1.06 mmol) as described above and purified by column chromatography to yield bright orange crystals (264 mg, 0.56 mmol, 53%). MP 160-162°C (lit.[5] MP 162-164°C). UV (EtOH) λ_{max}, nm (ε, M^{-1} cm^{-1}): 333 (8 000), 464 (19 000). ATR-FTIR ν_{max}/cm^{-1} 1815 and 1785 (medium, sharp C=O stretching vibrations typical of succinimidyl carbonyls), 1730 (strong, sharp C=O stretching vibration typical of succinimidyl ester). MS (EI+) *m*/*z*: $[M]^+$ 475.

8.1.7. General procedure for the nucleophilic substitution of succinimidyl esters by the functionalised alkaloid

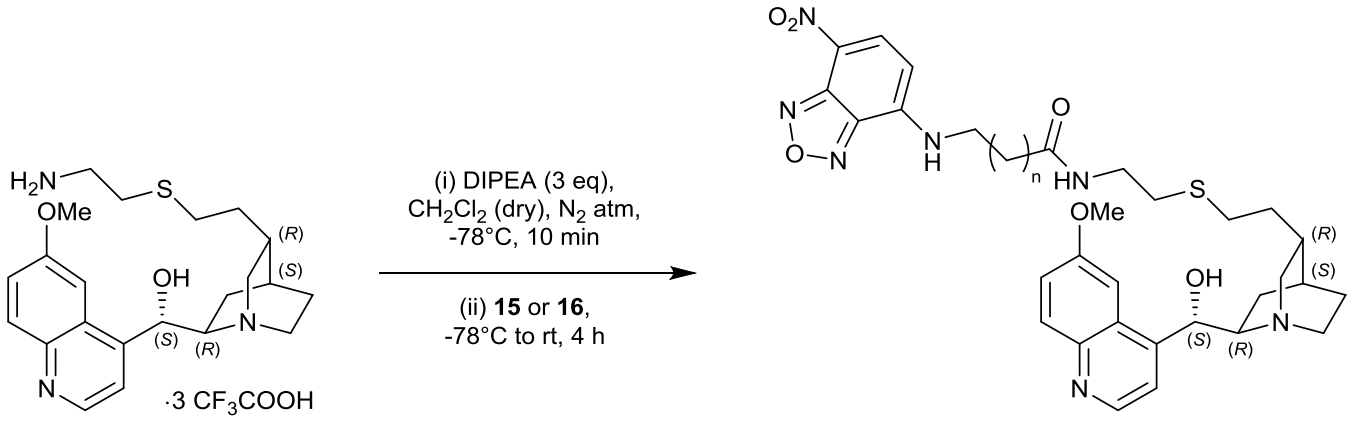

10

5 Quinidine-HexNBD n=4 (29%, 11% overall)
6 Quinidine-DodecNBD n=10 (68%, 25% overall)

To a round-bottomed flask equipped with a stirrer under an inert atmosphere (N_2) charged with the salt **10** (1 eq) was added dry CH_2Cl_2. This was cooled to -78°C, to which DIPEA (3 eq) was added dropwise. This was stirred for ten minutes to ensure neutralisation of the salt. Then the NBD-labelled amino acid succinimidyl ester **15** or **16** (1 eq) in dry CH_2Cl_2 was added dropwise. After three hours of continuous stirring the mixture was allowed to warm to room temperature. TLC indicated that the succinimidyl ester starting material had been completely consumed. The mixture was diluted with CH_2Cl_2 (10 mL) and washed three times with water to remove the NHS by-product. The volume was reduced. Column chromatography was performed (0-25% MeOH:CH_2Cl_2 elution gradient), the appropriate fractions collected, the volume reduced and the pure NBD-labelled alkaloid **5** or **6** was dried on the vacuum pump.

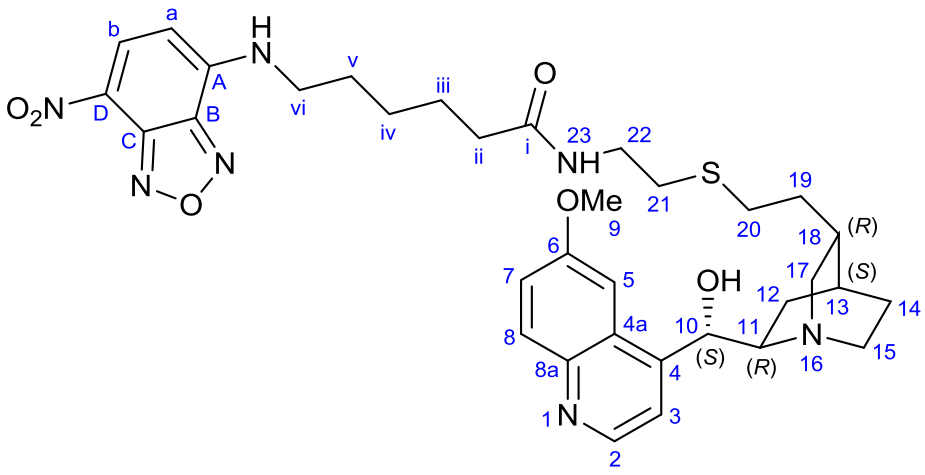

***N*-(2-((2-((1*S*,3*R*,4*S*,6*R*)-6-((*S*)-hydroxy(6-methoxyquinolin-4-yl)methyl)quinuclidin-3-yl)ethyl)thio)ethyl)-6-((7-nitrobenzo[*c*][1,2,5]oxadiazol-4-yl)amino)hexanamide, "Quinidine-HexNBD" (5)**.

Following the general method above, **10** (410 mg, 0.55 mmol) was dissolved in dry CH_2Cl_2 (10 mL) and cooled to -78°C. DIPEA (0.29 mL, 1.65 mmol) was added dropwise. **15** (215 mg, 0.55 mmol) in dry CH_2Cl_2 (5 mL) was added. After three hours of stirring, excess solvent was evaporated and, following dilution and extraction, column chromatography yielded **5** (110 mg, 0.16 mmol, 29%, 11% overall) as an orange solid. UV (EtOH) λ_{max}, nm (ε, M^{-1} cm^{-1}): 332 (10 500), 464 (15 500); UV (20 mM Hepes, pH 7.5) λ_{max}, nm (ε, M^{-1} cm^{-1}): 335 (6 500), 487 (14 500). R_f 0.40 (MeOH:CH_2Cl_2 10:90). ATR-FTIR ν_{max}/cm^{-1} 1625 (medium, sharp C=O stretching vibration for amide). ^{1}H NMR (400 MHz, DMSO-d_6) δ_H 8.66 (1H, d, *J* 4.6 Hz, H-2), 8.43 (1H, d, *J* 8.8 Hz, H-b), 7.90 (2H, m, aryl -NH- and H-8), 7.50 (1H, d, *J* 4.6 Hz, H-3), 7.46 (1H, d, *J* 2.8 Hz, H-5), 7.36 (1H, dd, *J* 9.3, 2.8 Hz, H-7), 6.34 (1H, d, *J* 8.8 Hz, H-a), 5.63 (1H, br s, amide -NH-), 5.53 (1H, d, *J* 6.6 Hz, H-10), 3.90 (3H, s, H-9), 3.43 (2H, br s, H-vi), 3.22 (2H, dt, *J* 7.8, 6.1 Hz, H-22), 2.98 (1H, m, H-11), 2.86 (1H, m, H-15a), 2.72 (1H, dd, *J* 13.0, 7.2 Hz, H-15b), 2.62 (1H, m, *J* 10.1 Hz, H-17a), 2.55 (3H, t, *J* 7.2 Hz, H-21 and H-17b), 2.50 (2H, m, H-20), 2.09 (2H, t, *J* 7.3 Hz, H-ii), 1.88 (1H, t, *J* 11.7 Hz, H-12a), 1.68 (5H, m, H-13, H-19 and H-v), 1.56 (3H, m, H-18 and H-iii), 1.47 (1H, m, H-14a), 1.36 (4H, m, H-iv, H-14b and H-12b). ^{13}C NMR (100 MHz, DMSO-d_6) δ_C 172.0 (C-i), 156.7 (C-6), 149.2 (C-4), 147.4 (C-2), 143.3, 144.5, 144.2 (C-A, C-B and C-C), 143.8 (C-8a), 137.5 (C-b), 131.0 (C-8), 126.9 (C-4a), 120.9 (C-7), 120.0 (C-D), 118.8 (C-3), 102.4 (C-4), 99.1 (C-a), 70.4 (C-10), 60.6 (C-11), 55.4 (C-9), 49.7 (C-15), 49.1 (C-17), 43.5 (C-iv), 38.5 (C-22), 35.2 (C-ii), 34.3 (C-18), 32.2 (C-19), 30.8 (C-21), 29.1 (C-20), 27.5 (C-v), 26.8 (C-14), 26.0 (C-iv), 26.0 (C-13), 24.8 (C-iii), 22.9 (C-12). HRMS (ESI-TOF) *m*/*z*: $[M+H]^+$ Calculated for $C_{34}H_{44}N_7O_6S$ 678.3074; found 678.3082. HPLC: 96.4%.

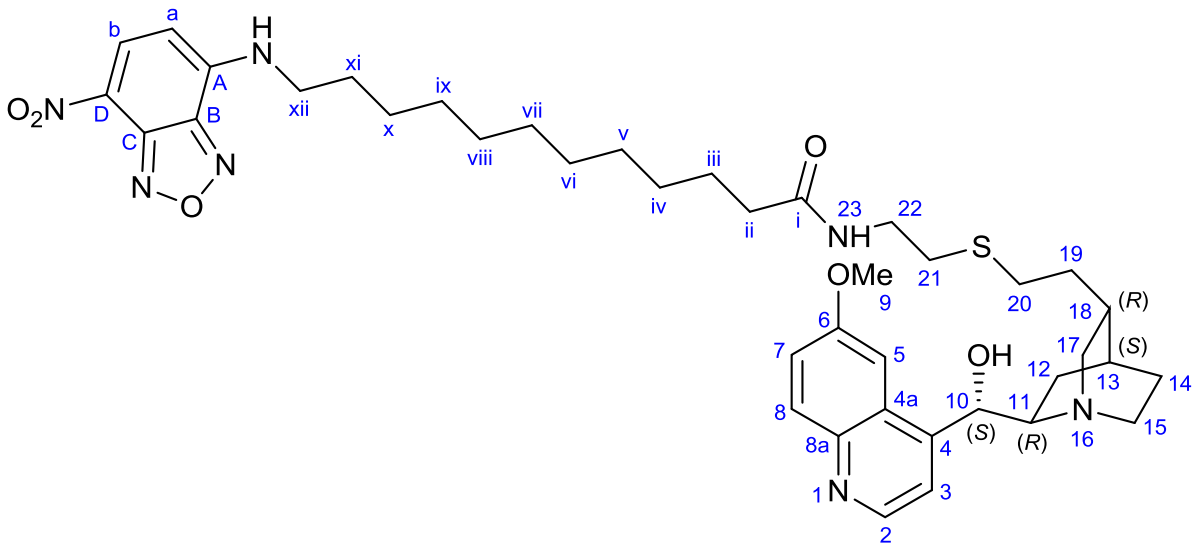

***N*-(2-((2-((1*S*,3*R*,4*S*,6*R*)-6-((*S*)-hydroxy(6-methoxyquinolin-4-yl)methyl)quinuclidin-3-yl)ethyl)thio)ethyl)-12-((7-nitrobenzo[*c*][1,2,5]oxadiazol-4-yl)amino)dodecanamide, "Quinidine-DodecNBD" (6).**

Following the general method above, **10** (404 mg, 0.53 mmol) was dissolved in dry CH_2Cl_2 (10 mL) and cooled to -78°C. DIPEA (0.28 mL, 1.59 mmol) was added dropwise. **16** (252 mg, 0.53 mmol) in dry CH_2Cl_2 (5 mL) was added. After three hours of stirring, excess solvent was evaporated and, following dilution and extraction, column chromatography yielded **6** (271 mg, 0.36 mmol, 68%, 25% overall) as an orange solid. UV (EtOH) λ_{max}, nm (ε, M^{-1} cm^{-1}): 333 (6 000), 466 (10 000); UV (20 mM Hepes, pH 7.5) λ_{max}, nm (ε, M^{-1} cm^{-1}): 339 (3 000), 485 (4 000). R_f 0.31 (MeOH:CH_2Cl_2 10:90). ATR-FTIR ν_{max}/cm^{-1} 1625 (medium, sharp C=O stretching vibration for amide). ^{1}H NMR (400 MHz, DMSO-d_6) δ_H 8.73 (1H, d, *J* 4.6 Hz, H-2), 8.47 (1H, d, *J* 9.2 Hz, H-b), 7.93 (2H, m, aryl -NH- and H-8), 7.64 (1H, d, *J* 4.6 Hz, H-3), 7.55 (1H, d, *J* 2.6 Hz, H-5), 7.40 (1H, dd, *J* 9.2, 2.6 Hz, H-7), 6.46 (1H, br s, amide -NH-), 6.38 (1H, d, *J* 9.2 Hz, H-a), 6.29 (1H, br s, H-10), 4.00 (3H, s, H-9), 3.74 (1H, m, H-15a), 3.46 (4H, m, H-11, H-15b and H-xii), 3.32 (1H, m, H-17a), 3.24 (2H, dt, *J* 7.8, 6.1, H-22), 3.16 (1H, m, H-17b), 2.56 (4H, m, H-20 and H-21), 2.29 (1H, t, *J* 11.4 Hz, H-12a), 2.03 (3H, m, H-18 and H-ii), 1.91 (1H, br s, H-13), 1.80 (3H, m, H-19 and H-14a), 1.68 (3H, m, H-xi and H-14b), 1.48 (2H, t, *J* 7.5 Hz, H-iii), 1.34 (2H, m, H-x), 1.22 (12H, m, H-iv, H-v, H-vi, H-vii, H-viii and H-ix), 1.15 (1H, m, H-12b). ^{13}C NMR (100 MHz, DMSO-d_6) δ_C 172.1 (C-i), 157.7 (C-6), 147.3 (C-2), 145.2 (C-4), 145.1, 144.3, 144.1 (C-A, C-B and C-C), 143.7 (C-8a), 137.8 (C-b), 131.2 (C-8), 125.6 (C-4a), 121.7 (C-7), 120.5 (C-D), 118.8 (C-3), 101.7 (C-5), 99.0 (C-a),66.1 (C-10), 59.0 (C-11), 56.5 (C-9), 48.6 (C-15), 48.1 (C-17), 43.3 (C-xii), 38.4 (C-22), 35.4 (C-ii), 31.8 (C-18), 31.1 (C-19), 30.7 (C-21), 28.9 (C-20), 28.9, 28.9, 28.7, 28.6, 28.6, 28.5 (C-iv, C-v, C-vi, C-vii, C-viii and C-ix), 27.6 (C-xi), 26.3 (C-x), 25.2 (C-iii), 24.6 (C-13), 23.2 (C-14), 17.2 (C-12). HRMS (ESI-TOF) *m/z*: $[M+H]^+$ Calculated for $C_{40}H_{56}N_7O_6S$ 762.4013; found 762.4017. HPLC: 95.2%.

8.1.8. Preparation of bimane-labelled quinine

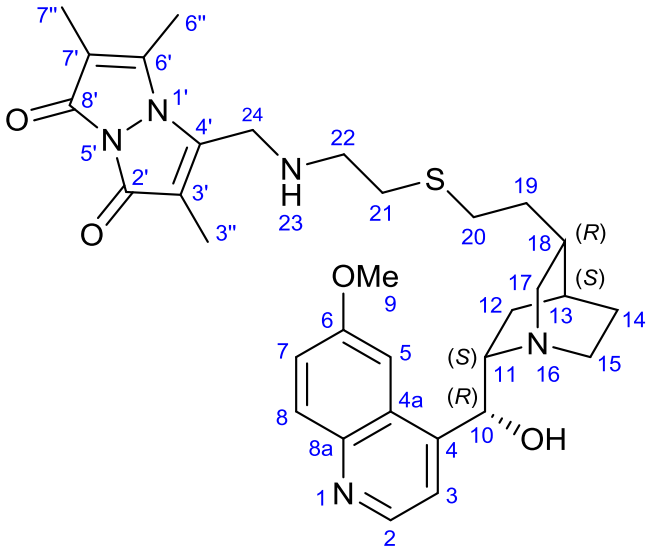

3-(((2-((2-((1*S*,3*R*,4*S*,6*S*)-6-((*R*)-hydroxy(6-methoxyquinolin-4-yl)methyl)quinuclidin-3-yl)ethyl)thio)ethyl)amino)methyl)-2,5,6-trimethyl-1*H*,7*H*-pyrazolo[1,2-*a*]pyrazole-1,7-dione, "Quinine-Bimane" (19).

To a stirring solution of **9** (345 mg, 0.46 mmol) in dry CH_2Cl_2 under N_2 at room temperature was added dry triethylamine (0.25 mL, 1.79 mmol) dropwise. After ten minutes, monobromobimane (91 mg, 0.34 mmol) which had been dissolved in a minimum volume of dry CH_2Cl_2 was added dropwise. This was stirred in the dark for 18 hours, after which TLC analysis indicated that the monobromobimane had been completely consumed. The solvent was removed and the residue was taken up in ethyl acetate (20 mL), to which half an equivalent volume of brine (10 mL) was added to encourage retention of the polar product in the organic phase. A second extraction was performed and the extracts were combined and dried with sodium sulfate, which was subsequently washed with methanol during filtration to remove any adsorbed product. Following removal of the solvent, the residue was adsorbed onto silica and column chromatography was performed over an elution gradient of 0-15% MeOH:CH_2Cl_2. The appropriate fractions were combined and the volume was reduced to isolate pure product **19** as a pale yellow crystalline solid (64 mg, 0.11 mmol, 32%). UV (EtOH) λ_{max}, nm (ε, M^{-1} cm^{-1}): 335 (10 000), 387 (8 500); UV (20 mM Hepes, pH 7.5) λ_{max}, nm (ε, M^{-1} cm^{-1}): 333 (5 500), 388 (4 000). R_f 0.50 (MeOH:CH_2Cl_2 12:88). MP 116-118°C. ATR-FTIR ν_{max}/cm^{-1} 1740, 1675 (strong C=O stretches). ^{1}H NMR (400 MHz, $CDCl_3$) δ_H 8.55 (1H, d, *J* 4.4 Hz, H-2), 7.71 (1H, d, *J* 9.2 Hz, H-8), 7.55 (1H, d, *J* 4.4 Hz, H-3), 7.05 (1H, dd, *J* 9.2, 2.4 Hz, H-7), 6.95 (1H, d, *J* 2.4 Hz, H-5), 6.12 (1H, s, H-10), 4.20 (1H, m, H-15a), 3.70 (3H, s, H-9), 3.62 (2H, s, H-24), 3.42 (1H, t, *J* 11.6 Hz, H-17a), 3.25 (1H, t, *J* 9.2 Hz, H-11), 2.99 (1H, m, H-15b), 2.71 (3H, m, H-22 and H-17b), 2.55 (2H, t, *J* 6.2

Hz, H-21), 2.36 (2H, t, *J* 7.2 Hz, H-20), 2.31 (3H, s, H-6''), 2.13 (2H, m H-14a and H-12a), 2.03 (1H, m, H-18), 1.94 (1H, br s, H-13), 1.71 (3H, s, H-3''), 1.66 (4H, m, H-14b and H-7''), 1.47 (2H, q, *J* 7.2 Hz, H-19), 1.38 (1H, m, H-12b); -O<u>H</u> and -N<u>H</u>- not observed. ^{13}C NMR (100 MHz, $CDCl_3$) δ_C 160.7 (C-2'), 160.3 (C-8'), 158.3 (C-6), 147.1 (C-4), 146.9 (C-2), 146.5 (C-3'), 145.0 (C-7'), 143.7 (C-8a), 131.2 (C-8), 125.6 (C-4a), 122.2 (C-7), 118.8 (C-3), 113.7 (C-4'), 111.6 (C-6'), 100.0 (C-5), 66.9 (C-10), 60.2 (C-11), 56.6 (C-17), 56.2 (C-9), 47.9 (C-22), 43.8 (C-15), 42.7 (C-24), 33.6 (C-19), 33.1 (C-18), 32.3 (C-21), 29.5 (C-20), 25.2 (C-13), 25.1 (C-14), 18.3 (C-12), 11.3 (C-6''), 6.9 (C-3''), 6.7 (C-7''). HRMS (ESI-TOF) *m/z*: $[M+H]^+$ calculated for $C_{32}H_{42}N_5O_4S$ 592.2958, found 592.2958. HPLC: 97.2%.

8.1.9. Synthesis of an NBD-labelled derivative of chloroquine

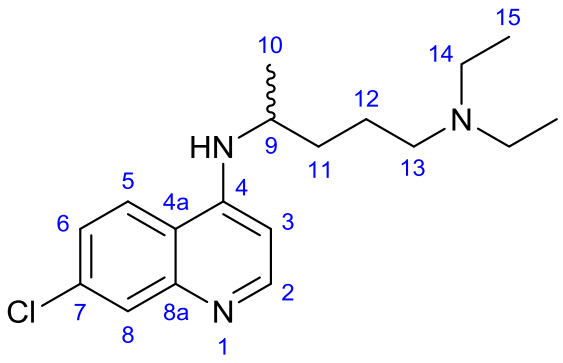

***N*⁴-(7-chloroquinolin-4-yl)-*N*¹,*N*¹-diethylpentane-1,4-diamine, chloroquine free base (7).** Chloroquine diphosphate was converted to the free base as previously described, with minor modifications.[7] Briefly, chloroquine diphosphate (5.000 g, 9.69 mmol) was dissolved in 100 mL H_2O to which 5 M NaOH (100 mL) was slowly added. After three successive extractions with CH_2Cl_2 (100 mL each), the organic fractions were combined and dried with $MgSO_4$. Following filtration and removal of the solvent, the residue was washed with diethyl ether (20 mL) and the solvent removed once more. Drying on the vacuum pump yielded chloroquine free base **1** as a white crystalline solid (2.964 g, 9.27 mmol, 96%). ^{1}H NMR (400 MHz, $CDCl_3$) δ_H 8.49 (1H, d, *J* 5.4 Hz, H-2), 7.93 (1H, d, *J* 2.2 Hz, H-8), 7.66 (1H, d, *J* 9.0 Hz, H-5), 7.31 (1H, dd, *J* 9.0, 2.2 Hz, H-6), 6.41 (1H, d, *J* 5.4 Hz, H-3), 5.26 (1H, d, *J* 6.4 Hz, -NH-), 3.70 (1H, m, H-9), 2.50 (4H, q, *J* 7.2 Hz, H-14), 2.43 (2H, t, *J* 6.8 Hz, H-13), 1.62 (4H, m, H-11 and H-12), 1.30 (3H, d, *J* 6.4 Hz, H-10), 0.99 (6H, t, *J* 7.2 Hz, H-15). ^{13}C NMR (100 MHz, $CDCl_3$) δ_C 152.1 (C-2), 149.4 (C-4 and C-8a), 134.9 (C-7), 129.0 (C-8), 125.1 (C-6), 121.3 (C-5), 117.5 (C-4a), 99.4 (C-3), 52.7 (C-13), 48.4 (C-9), 47.0 (C-14), 34.7 (C-12), 24.0 (C-11), 20.3 (C-10), 11.6 (C-15).

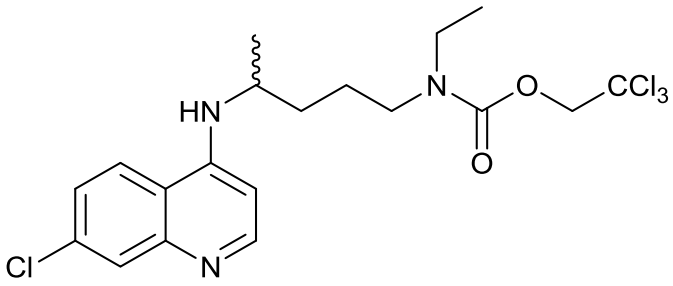

20

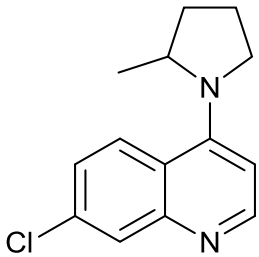

20'

2,2,2-Trichloroethyl (4-((7-chloroquinolin-4-yl)amino)pentyl)(ethyl)carbamate (20) and 7-chloro-4-(2-methylpyrrolidin-1-yl)quinoline (20').

A previously-reported procedure was followed with slight modifications.[8] To a clear solution of chloroquine **7** (2 964 mg, 9.27 mmol, 1 eq) in anhydrous THF (40 mL) under N_2 was added NaH (60% oil dispersion, 444 mg, 11.1 mmol, 1.2 eq) at room temperature. The solution was heated to 70°C and refluxed for two hours. The resulting cloudy yellow mixture was then cooled to room temperature and 2,2,2-trichchoroethyl chloroformate (1.53 mL, 11.1 mmol, 1.2 eq) was added dropwise. The mixture was stirred for 20 minutes at room temperature and then refluxed for 18 hours, during which time it turned brown. After cooling, the reaction was quenched with H_2O dropwise. THF was removed and the residue was treated with additional H_2O (80 mL) and extracted with diethyl ether (3 x 80 mL). Combined extracts were washed (H_2O, brine), dried (Na_2SO_4), filtered and reduced. Column chromatography (0-100% EtOAc) gave a mixture of the chloroformate **20** and pyrrolidine **20'** as a yellow gum (1 802 mg) which did not yield to separation. Unreacted chloroquine starting material was recovered from the column (109 mg, 0.34 mmol, 4%). ATR-FTIR ν_{max}/cm^{-1} 1715 (strong, sharp C=O stretching vibration for carbamate **20**; lit.[8] 1710). MS (EI+) *m*/*z*: $[M]^+$ 467 (**20**), 247 (**20'**).

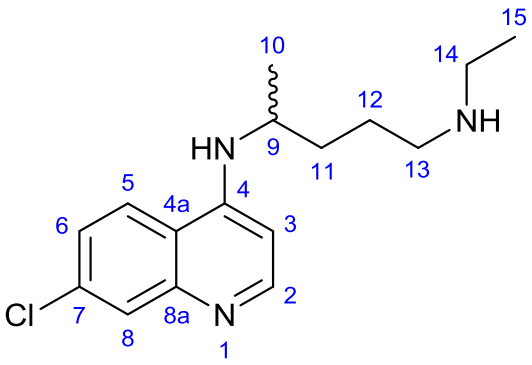

***N*⁴-(7-chloroquinolin-4-yl)-*N*¹-ethylpentane-1,4-diamine, desethylchloroquine (21).**

A previously-reported procedure was followed with slight modifications.[8] To a flask containing a mixture of **20** and **20'** (overall mass 1.532 g) was added glacial acetic acid (10 mL) and a small volume of CH_2Cl_2 (3 mL) to dissolve the starting material. Zinc dust (2 079 mg, 33.33 mmol) was added in small portions and the mixture was stirred at room temperature for six hours. The contents were filtered through Celite, which was subsequently washed with hot MeOH. The volume was reduced and cold 5 M NH_4OH (100 mL) was added. The mixture was extracted with CH_2Cl_2 (3 x 100 mL) and the combined extracts were washed (H_2O, brine), dried ($MgSO_4$), filtered and reduced. The residue was dissolved in a minimum amount of CH_2Cl_2, and purified using column chromatography using 0-40% MeOH:CH_2Cl_2 followed by increasing additions of Et_3N (0-4%) to the 40% MeOH:CH_2Cl_2 mobile phase for the elution of **21**. The removal of solvent yielded **21** as a sticky yellow-brown gum (678 mg, 2.15 mmol, 41% over two steps), whose ATR-FTIR spectrum was indistinguishable from that of chloroquine **1**. ^{1}H NMR (400 MHz, $CDCl_3$) δ_H 8.47 (1H, d, *J* 5.4 Hz, H-2), 7.91 (1H, d, *J* 2.2 Hz, H-8), 7.81 (1H, d, *J* 9.0 Hz, H-5), 7.31 (1H, dd, *J* 9.0, 2.2 Hz, H-6), 6.35 (1H, d, *J* 5.4 Hz, H-3), 5.67 (1H, br s, -N<u>H</u>-, exchanged with D_2O), 3.93 (1H, br s, -N<u>H</u>-, exchanged with D_2O), 3.66 (1H, m, H-9), 2.68 (4H, m, H-13 and H-14), 1.78 (1H, m, H-11a), 1.66 (3H, m, H-11b and H-12), 1.27 (3H, t, *J* 6.4 Hz, H-10), 1.14 (3H, t, *J* 7.1 Hz, H-15). ^{13}C NMR (100 MHz, $CDCl_3$) δ_C 152.0 (C-2), 149.4 (C-4 and C-8a), 134.9 (C-7), 128.7 (C-8), 125.1 (C-6), 121.5 (C-5), 117.6 (C-4a), 99.2 (C-3), 48.8, 48.5, 43.9 (C-14, C-13, C-9; cannot assign), 34.0 (C-12), 25.8 (C-11), 20.3 (C-10), 14.3 (C-15). MS (EI+) *m*/*z*: $[M-H]^+$ 291.

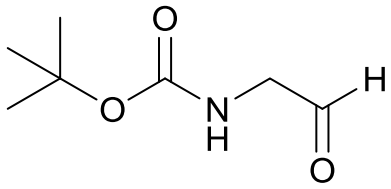

***tert*-Butyl (2-oxoethyl)carbamate, *N*-Boc-glycinal.**

A previously-reported procedure was followed with slight modifications.[9] Freshly-distilled THF (40 mL) was added to a two-necked round-bottomed flask under N_2. The flask was cooled to 0°C in an ice bath and $LiAlH_4$ (217 mg, 5.73 mmol), which had been carefully weighed into a dry sample vial, was added in small portions over several minutes. Weinreb amide *tert*-butyl (2-(methoxy(methyl)amino)-2-oxoethyl)carbamate (1 000 mg, 4.58 mmol) was dissolved in dry THF (10 mL) and added dropwise to the $LiAlH_4$ slurry via syringe. The mixture was stirred for one hour after which the TLC spot corresponding to the starting material, visualised using an anisaldehyde stain, disappeared. The reaction was quenched by slow dropwise addition of ice-cold saturated Na_2SO_4 and the mixture was allowed to warm to room temperature. The mixture was transferred to a separating funnel, diluted with H_2O (25 mL) and extracted with EtOAc (3 x 25 mL). The organic layers were combined and washed with 1 M HCl (3 x 25 mL), saturated $NaHCO_3$ (2 x 25 mL) and brine (2 x 25 mL). The solution was dried with Na_2SO_4, filtered and the solvent was reduced. The crude *N*-Boc-glycinal (724 mg, 99% crude) was used immediately in the subsequent reaction. MS (EI+) *m*/*z*: $[M]^+$ 159.

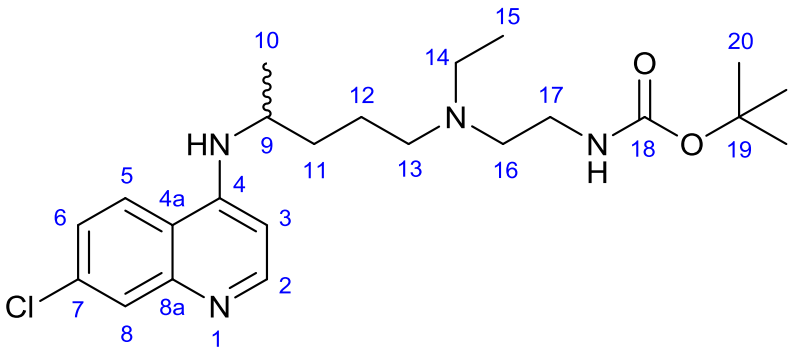

tert-Butyl (2-((4-((7-chloroquinolin-4-yl)amino)pentyl)(ethyl)amino)ethyl)carbamate (22).

A previously-reported procedure was followed with slight modifications.[10] To a flask containing desethylchloroquine **21** (918 mg, 3.15 mmol) and *N*-Boc-glycinal (752 mg, 4.73 mmol) in MeOH (20 mL) was added a catalytic amount of glacial acetic acid (five drops). This was stirred at room temperature for 15 minutes. Thereafter, $NaBH_3CN$ (594 mg, 9.45 mmol) was added in small portions and the mixture was refluxed at 80°C for four hours. The mixture was then cooled and quenched dropwise with H_2O. The solvent was removed, saturated $NaHCO_3$ (30 mL) added and the organic material extracted into CH_2Cl_2 (3 x 30 mL). The organic fractions were combined, dried (Na_2SO_4) and reduced. Column chromatography was performed with an elution gradient of 0-40% MeOH:CH_2Cl_2 to afford product **22** (941 mg, 2.20 mmol, 70%) as a light-brown oil. ATR-FTIR ν_{max}/cm^{-1} 1700 (strong, sharp C=O stretching vibration indicates carbamate). ^1H NMR (400 MHz, $CDCl_3$) δ_H 8.48 (1H, d, *J* 5.4 Hz, H-2), 7.94 (1H, d, *J* 2.2 Hz, H-8), 7.74 (1H, d, *J* 8.8 Hz, H-5), 7.33 (1H, dd, *J* 8.8, 2.2 Hz, H-6), 6.40 (1H, d, *J* 5.4 Hz, H-3), 5.15 (1H, d, *J* 7.8 Hz, NH), 4.95 (1H, br s, carbamate -NH-) 3.71 (1H, m, H-9), 3.17 (2H, q, *J* 6.0 Hz, H-17), 2.52 (4H, m, H-14 and H-16), 2.46 (2H, t, *J* 6.8 Hz, H-13), 1.72 (1H, m, H-11a), 1.59 (3H, m, H-11b and H-12), 1.41 (9H, s, H-20), 1.32 (3H, d, *J* 6.4 Hz, H-10), 0.99 (3H, t, *J* 7.0, H-15). ^{13}C NMR (100 MHz, $CDCl_3$) δ_C 156.2 (C-18), 151.8 (C-2), 149.4, 149.2 (C-4, C-8a), 135.1 (C-7), 128.6 (C-8), 125.6 (C-6), 121.3 (C-5), 117.4 (C-4a), 99.3 (C-3), 79.3 (C-19), 55.4 (C-13), 52.9 (C-14 or C-16), 48.6 (C-9), 47.8 (C-14 or C-16), 38.4 (C-17), 34.5 (C-11), 28.6 (C-20), 24.0 (C-12), 20.5 (C-10), 11.6 (C-15). MS (EI+) *m/z*: $[M]^+$ 435.

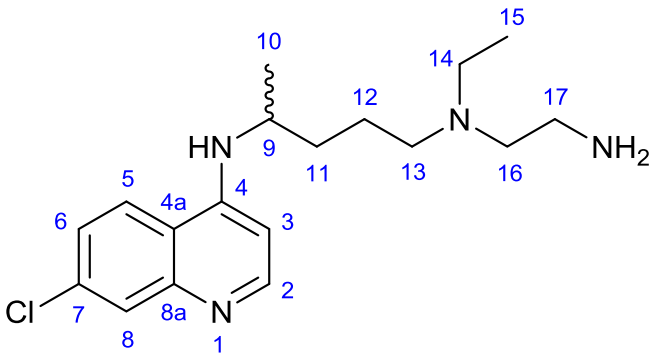

***N*¹-(2-aminoethyl)-*N*⁴-(7-chloroquinolin-4-yl)-*N*¹-methylpentane-1,4-diamine (23).**

A previously-reported procedure was followed with slight modifications.[10] To a stirring solution of **22** (586 mg, 1.35 mmol, 1 eq) in CH_2Cl_2 at 0°C was added dropwise trifluoroacetic acid (TFA, 2.1 mL, 27 mmol, 20 eq). The mixture was left to stir for eight hours while coming gradually to room temperature, after which TLC analysis indicated the reaction was complete. Excess solvent and TFA was removed. At this stage the product was considered pure enough by TLC to use in the subsequent step as a tris-trifluoroacetate salt. To isolate the free base, the residue was dissolved in 1 M NaOH and extracted with CH_2Cl_2 (3 x 50 mL). The organic layers were combined, washed with brine, dried (Na_2SO_4), filtered and reduced. Purification was achieved by column chromatography using an eluent of 0-100% MeOH:CH_2Cl_2 followed by the addition of 0-5% Et_3N, after which product **23** was isolated as a light-yellow oil (271 mg, 0.81 mmol, 60%). ^{1}H NMR (400 MHz, $CDCl_3$) δ_H 8.50 (1H, d, *J* 5.4 Hz, H-2), 7.93 (1H, d, *J* 2.2 Hz, H-8), 7.71 (1H, d, *J* 9.0 Hz, H-5), 7.33 (1H, dd, *J* 9.0, 2.2 Hz, H-6), 6.40 (1H, d, *J* 5.4 Hz, H-3), 5.07 (1H, d, *J* 7.6 Hz, -N<u>H</u>-, exchangeable in D_2O), 3.70 (1H, m, H-9), 2.72 (2H, m, H-17), 2.48 (6H, m, H-13, H-14 and H-16), 1.73 (3H, m, H-11a and N<u>H</u>$_2$, the latter exchangeable in D_2O), 1.59 (3H, m, H-11b and H-12), 1.31 (3H, d, *J* 6.4 Hz, H-10), 0.99 (3H, t, *J* 7.0, H-15). ^{13}C NMR (100 MHz, $CDCl_3$) δ_C 152.2 (C-2), 149.9, 149.2 (C-4, C-8a; cannot assign), 134.9 (C-7), 129.1 (C-8), 125.2 (C-6), 121.2 (C-5), 117.5 (C-4a), 99.4 (C-3), 56.5, 53.6, 47.9 (C-13, C-14, C-16; cannot assign), 48.5 (C-9), 39.9 (C-17), 34.5 (C-11), 24.2 (C-12), 20.5 (C-10), 11.9 (C-15). MS (EI+) *m*/*z*: $[M]^+$ 335.

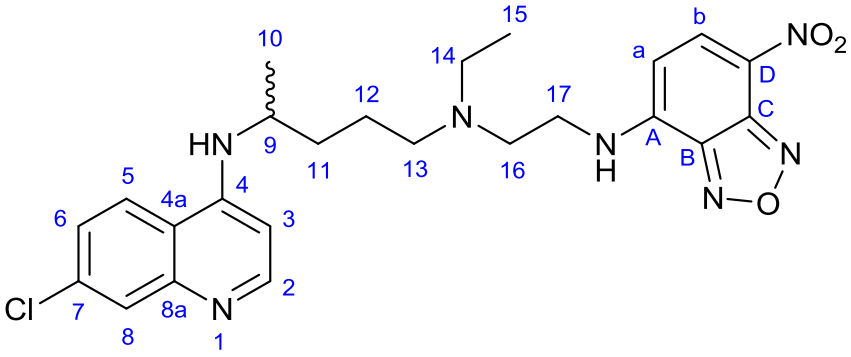

N^4-(7-chloroquinolin-4-yl)-N^1-ethyl-N^1-(2-((7-nitrobenzo[*c*][1,2,5]oxadiazol-4-yl)amino)ethyl)pentane-1,4-diamine, "Chloroquine-NBD" (8).

The crude tris-trifluoroacetate salt of **20** (400 mg, 0.59 mmol) was dissolved in methanol (10 mL) in a round-bottomed flask charged with a stirrer bar. *N*,*N*-Diisopropylethylamine (0.31 mL, 1.77 mmol) was added dropwise and stirred for ten minutes after which $NaHCO_3$ (150 mg, 1.77 mmol) was added and the temperature raised to 75°C. NBD-Cl (120 mg, 0.59 mmol) in MeOH (5 mL) was added dropwise. After 2.5 hours, the TLC indicated consumption of both starting materials. The reaction mixture was cooled and the methanol was removed. Water (30 mL) was added and the residue was extracted using CH_2Cl_2 (3 x 30 mL). The combined extracts were dried (Na_2SO_4), filtered and reduced. The residue was then adsorbed onto silica and column chromatography was performed with an elution gradient of 0-30% MeOH:CH_2Cl_2. The appropriate fractions were combined and the volume was reduced to isolate product **8** as a dark-red crystalline solid (71 mg, 0.14 mmol, 24%). MP 61-63°C. ATR-FTIR ν_{max}/cm^{-1} 1450 (medium, -NO_2 asymmetric stretch lowered by conjugation), 1300 (strong, -NO_2 symmetric stretch lowered by conjugation).[11] ^{1}H NMR (400 MHz, DMSO-d_6) δ_H 8.44 (1H, d, *J* 9.5 Hz, H-b), 8.31 (2H, m, H-2 and H-8), 7.71 (1H, d, *J* 2.2 Hz, H-5), 7.37 (1H, dd, *J* 9.0, 2.2 Hz, H-6), 6.85 (1H, d, *J* 8.5 Hz, aryl -N<u>H</u>-), 6.42 (1H, d, *J* 6.0 Hz, H-3), 6.34 (1H, d, *J* 9.5 Hz, H-a), -N<u>H</u>- adjacent to NBD heterocycle not observed, 3.62 (1H, m, H-9), 3.48 (2H, m, H-17), 2.71 (2H, t, *J* 6.6 Hz, H-16), 2.55 (2H, m, H-14), 2.46 (2H, t, *J* 6.8 Hz, H-13), 1.65 (1H, m, H-11a), 1.48 (3H, m, H-11b and H-12), 1.16 (3H, d, *J* 6.4 Hz, H-10), 0.93 (3H, t, *J* 7.0, H-15). ^{13}C NMR (100 MHz, DMSO-d_6) δ_C 151.5 (C-2), 149.5, 149.0 (C-4, C-8a; cannot assign), 145.0, 144.3, 144.0 (C-A, C-B and C-C; cannot assign), 137.7 (C-b), 133.3 (C-7), 127.2 (C-5), 124.2 (C-8), 123.7 (C-6), 120.5 (C-D), 117.3 (C-4a), 99.1 (C-a), 98.6 (C-3), 52.4 (C-13), 50.8 (C-16), 47.5 (C-9), 47.0 (C-14), 41.5 (C-17), 33.1 (C-11), 23.5 (C-12), 19.7 (C-10), 11.7 (C-15). HRMS (ESI-TOF) *m*/*z*: $[M+H]^+$ calculated for $C_{24}H_{29}ClN_7O_3$ 498.2020, found 498.2022. HPLC: 96.3%.

8.2. Physicochemical and in vitro evaluation of fluorescent derivatives

8.2.1. General physicochemical methods

Unless otherwise stated, all compounds were purchased from Sigma-Aldrich and used without further purification. Solvents were generally purchased from Kimix Chemicals. Bovine haemin (Fe(III)PPIX-Cl) was obtained from Fluka. NP-40 was obtained from Pierce Biotechnology, Rockford, IL, USA. Double-distilled deionised water (dH_2O) was provided by a Millipore Direct-Q3 water purification system. Hoechst 33342, LysoTracker Red, ER-Tracker Red and MitoTracker Deep Red were all obtained from Molecular Probes (Oregon, USA) and later Thermo Fisher Scientific. Nile Red was obtained from Sigma-Aldrich.

Absorption spectra were recorded on a Varian Cary 100 UV-Vis or a Shimadzu UV-1800 spectrophotometer and were baseline-corrected. Fluorescence spectra were measured using a Varian Cary Eclipse spectrofluorimeter. Assay plates were read using a SpectraMax 340 PC 384 Absorbance Microplate Reader (Molecular Devices). Magnetic circular dichroism (MCD) spectra were recorded on a ChiraScan-Plus CD spectrophotometer with an MCD attachment (0.997 T) at 22°C.

All stock solutions were stored in the dark and working solutions were made up immediately prior to use. Unless otherwise stated, the temperature was maintained at 25.0 ± 0.2°C by means of a thermostatted water bath. Aliquots of solutions were delivered into quartz cuvettes (1.00 mm or 10.00 mm) using a Hamilton syringe. Cuvettes were scrupulously washed with 0.2 M NaOH, followed by several rinsings with water, then addition of 1 M HNO_3 and several final rinsings with water to remove adsorbed Fe(III)PPIX.[12]

Titration curves were analysed using a non-linear least squares fitting in HypSpec (Version 1.1.33, Protonic Software). Sigmoidal dose-response curves were fitted to absorbance data using GraphPad Prism (Version 6.05, GraphPad Software). All measurements were performed in triplicate.

8.2.2. Relative fluorescence quantum yields

Relative fluorescence quantum yields were calculated according to Equation 8.1 in which Φ represents the relative fluorescence quantum yield, A is the absorbance of the sample at the excitation wavelength, F is the area under the fluorescence emission curve and n is the refractive index of the solvent system. The subscripts S and X refer to the standard and to the

unknown samples, respectively.[13] The reported measurement by Melhuish of Φ = 0.546 for quinine sulfate in 0.5 M sulfuric acid was used as a standard value.[14]

$$\Phi_X = \left(\frac{A_S}{A_X}\right)\left(\frac{F_X}{F_S}\right)\left(\frac{n_X}{n_S}\right)^2 \Phi_S$$

Equation 8.1

Absorbance values were kept below 0.1 in order to minimise inner filter-effects. In each case, the area under the fluorescence emission curve was determined by summing the fluorescence intensities across the entire emission range. Refractive indices of 1.346, 1.3614 and 1.3885 were used for sulfuric acid, ethanol and 40% DMSO (v/v) in 20 mM Hepes, pH 7.5, respectively. The final value was calculated by interpolation.[15]

8.2.3. Quantitative measurements of thermal and photodecomposition

Approximately 1 mg of the NBD-labelled quinoline (> 95% pure) was deposited in a small glass vial. This was either left as a solid or dissolved in HPLC-grade acetonitrile (1 mL). The vials were then closed and sealed before being left for three months under the test conditions described in Section 4.2.4. After three months, the vials were opened and each sample was made up to a total of 2 mL HPLC-grade acetonitrile and filtered through a 0.22 μm nylon membrane. Quantitative analysis was performed using HPLC in which each sample was run for 15 minutes on a 5-100% acetonitrile gradient in 0.1% trifluoroacetic acid at a flow rate of 1 mL/min. In each case, the decomposition was measured by expressing the area under the peak corresponding to the retention time of the original sample as a fraction of the total signal recorded for the sample.

8.2.4. Job plots to determine binding stoichiometries with Fe(III)PPIX

To construct Job plots to determine the binding stoichiometries of complexes with Fe(III)PPIX, the absorption spectra of solutions of varying ligand and Fe(III)PPIX mole fractions were recorded in 40% DMSO (v/v) in 20 mM Hepes, pH 7.5, according to a method previously described.[16] The total concentration of the system was constrained to 0.75 mM and absorbance was measured at 400 nm in a 1.00 mm path length cuvette. Depending on expected binding, fifteen working solutions were prepared with mole fractions of Fe(III)PPIX between 0 and 1. Spectrophotometric data were analysed at 400 nm.

8.2.5. Spectrophotometric titrations to determine association constants with Fe(III)PPIX

Thermodynamic association constants were measured in 40% DMSO (v/v) in 20 mM Hepes, pH 7.5, according to a method previously described.[17] Stock solutions of quinolines were prepared at concentrations of 0.5 mM or 1 mM depending on the strength of association with Fe(III)PPIX. Each stock compound was titrated into a 5 μM Fe(III)PPIX working solution. The resulting spectrophotometric data were analysed using an appropriate complexation model with HypSpec.

8.2.6. Magnetic circular dichroism (MCD)

MCD spectra were recorded as previously described.[16] Solutions were prepared by diluting a stock solution of Fe(III)PPIX (1 mM in 0.1 M NaOH) to a final concentration of 7.5 μM. For the quinolines, stock solutions (20 mM in DMSO) were diluted to a final concentration of 15 μM.

8.2.7. Turbidimetric assay to assess aqueous solubility

Test compounds were prepared in a 96-well plate at concentrations ranging from 0-200 μM in DMSO and 20 mM Hepes, pH 7.5, diluted from a stock solution of 20 mM in DMSO. The final concentration of DMSO in 20 mM Hepes, pH 7.5, did not exceed 1% (v/v). After preparing the plate, it was covered and left to equilibrate for two hours at ambient temperature. Absorbances of the wells were then measured at 620 nm. Absorbance values were corrected by subtracting the absorbance of each DMSO sample from the absorbance of each aqueous sample.

8.2.8. Diffusion measurements

Diffusion measurements were performed using a diffusion cell approach.[12,18] The analyte, typically with a concentration between 100-400 μM, was loaded into the lower chamber of the diffusion apparatus and allowed to diffuse into the corresponding blank solution in an adjacent upper chamber for several hours at ambient temperature. The absorbance of the solution isolated from the upper chamber was measured and its concentration determined. Diffusion coefficients and hydrodynamic radii were then calculated from Equations 4.4 and 4.5, respectively. If necessary, diffusion coefficients were corrected to 298 K using Equation 8.2 where D represents the diffusion coefficient (m^2/s), η is the viscosity (Pa s) and T is the temperature (K).

$$\frac{D_1\eta_1}{T_1} = \frac{D_2\eta_2}{T_2}$$

Equation 8.2

8.2.9. NP-40 detergent-mediated assay to measure β-haematin inhibition

The β-haematin formation inhibition assay method described by Carter et al. was modified for manual liquid delivery.[19,20] 20 mM stock solutions of the samples were prepared by dissolving the pre-weighed compounds in DMSO. These were delivered to a 96-well plate in triplicate to give concentrations ranging from 0 to 1000 μM (final well concentration) with a total DMSO volume of 10 μL in each well, after which deionised water (70 μL) and NP-40 (20 μL; 30.55 μM) were added. The absorbances of plate wells were pre-read at 405 nm on a SpectraMax 340 PC384 Absorbance Microplate Reader (Molecular Devices, Sunnyvale, CA, USA). A 25 mM haematin stock solution was prepared by sonicating haemin in DMSO for one minute and then suspending 178 μL of this in a 1 M acetate buffer (pH 4.8). The homogenous suspension (100 μL) was then added to the wells to give final buffer and haematin concentrations of 0.5 M and 100 μM, respectively. The plate was covered and incubated at 37°C for 5-6 hours. After incubation, free haem was detected using the pyridine-ferrichrome method developed by Ncokazi and Egan.[21] A solution of 50% (v/v) pyridine, 30% (v/v) water, 20% (v/v) acetone and 0.2 M Hepes was prepared and 32 μL added to each well to give a final pyridine concentration of 5% (v/v). Acetone (60 μL) was then added to assist with haematin dispersion. The absorbances of plate wells were again read at 405 nm, from which the pre-read values were subtracted. Sigmoidal dose-response curves with variable slopes were fitted to the absorbance data using GraphPad Prism v6.05 to obtain a 50% inhibitory concentration (IC_{50}) for each compound. Data were fitted to Equation 8.3 where the IC_{50} is the midpoint of the curve and H is the Hill slope which describes the steepness of the curve. T and B are the lower and upper baselines of the curve, respectively.

$$Y = B + \frac{(T - B)}{1 + 10^{(\mathrm{LogIC_{50}} - X)H}}$$

Equation 8.3

8.2.10. *Plasmodium falciparum* culturing

Continuous *in vitro* cultures of asexual erythrocyte stages of chloroquine-sensitive *Plasmodium falciparum* (NF54 strain) were maintained using a modified method of Trager and Jensen.[22] The

cultures were maintained between 4-8% parasitaemia and 3-6% haematocrit. The culture was synchronised at the ring stage by incubating with D-sorbitol.

8.2.11. In vitro activity testing against *P. falciparum*

Samples were tested in triplicate on separate occasions at the Division of Pharmacology, Department of Medicine, University of Cape Town. Quantitative assessment of antiplasmodial activity in vitro was determined via the parasite lactate dehydrogenase assay using a modified method described by Makler.[23] The test samples were prepared to a 20 mg/mL stock solution in DMSO and were tested as a suspension if not completely dissolved. A full dose-response was performed for all compounds to determine the concentration inhibiting 50% of parasite growth (IC_{50}). A starting concentration (100 μg/mL) was serially diluted two-fold in complete medium to give ten concentrations, the lowest of which was 0.2 μg/mL. Reference drugs were tested at a starting concentration of 1000 ng/mL. Active compounds were re-tested at a starting concentration of 1000 ng/mL. The highest concentration of solvent to which the parasites were exposed had no measurable effect on the parasite viability (data not shown). The IC_{50} values were obtained using a non-linear dose-response curve fitting analysis in GraphPad Prism.

8.3. Live-cell fluorescence microscopy

8.3.1. General methods

Nunc Lab-Tek II eight-well chamber slides (Thermo Fisher Scientific, Massachusetts, USA) with cover glass of No. 1.5 thickness were coated with 150 µL of 0.01% (w/v) poly-L-lysine solution. After ten minutes, the solution was removed and the plates were left to air-dry. Ringer's solution was prepared according to the recipe in Table 8.1, as previously described.[24] The pH was adjusted to 7.4 after which the solution was filtered through a 0.22 µm nylon syringe filter.

Table 8.1. *Constituents of Ringer's solution for live-cell imaging of* P. falciparum.[24]

Component	Molecular weight	Final concentration	Mass required for 100 mL
NaCl	58.44	122.5 mM	715.9 mg
KCl	74.56	5.4 mM	40.3 mg
$CaCl_2$ (dihydrate)	147.02	1.2 mM	17.6 mg
$MgCl_2$ (anhydrous)	95.21	0.8 mM	7.6 mg
D-Glucose	180.16	11 mM	198.2 mg
Hepes	238.30	25 mM	595.8 mg
NaH_2PO_4	119.98	1 mM	12.0 mg

Human erythrocytes infected with *P. falciparum* trophozoites (NF54 strain) were generously donated by colleagues at the Division of Pharmacology, Department of Medicine, University of Cape Town. After harvesting and centrifugation of the cells, 5 µL of the parasitised erythrocyte pellet were resuspended in 5 mL Ringer's solution and were vortexed to reduce clumping of the erythrocytes. 150 µL aliquots of suspended cells were placed in each well of the chamber slide and incubated for at least twenty minutes to allow the erythrocytes to adhere to the cover glass. After this, the Ringer's solution was removed and replaced with a fresh aliquot of Ringer's solution (150 µL) to remove non-adhered cells. This solution was then removed again and replaced with Ringer's solution (150 µL) containing appropriate concentration(s) of the fluorescent dye(s) as listed in Tables 8.2 and 8.3.

8.3.2. Live-cell confocal fluorescence microscopy

Confocal microscopy was performed using a Zeiss Axiovert 200 M LSM 150-META confocal microscope at the Confocal and Light Microscope Imaging Facility at the University of Cape

Town. A Plan-Apochromat 63×/1.40 Oil DIC M27 objective lens was used and the cells were incubated at 37°C. Images were captured and processed with ZEN 2011 (Carl Zeiss Microscopy GmbH). Laser transmission was kept as low as possible to minimise phototoxicity to the cells.[25] Dye concentrations with respective excitation and emission settings are listed in Table 8.2.

Table 8.2. *Concentrations of fluorescent dyes used for confocal imaging of* P. falciparum *with respective excitation lasers and emission filter settings.*

Dye	Concentration	Excitation laser	Emission filter
Hoechst 33342	2 µM	750 nm (two-photon)	Spectral 415-500
Novel fluorescent derivative	500 nM	488 nm	BP 500-550
LysoTracker Red	200 nM	561 nm	BP 575-630
Nile Red	200 nM	561 nm	BP 575-630
ER-Tracker Red	500 nM	561 nm	BP 575-630
MitoTracker Deep Red	200 nM	633 nm	BP 650-710 IR

8.3.3. Live-cell super-resolution structured-illumination microscopy (SR-SIM)

SR-SIM was performed using a Zeiss LSM 780 ELYRA S1 microscope at the CAF Fluorescence Microscopy Unit at Stellenbosch University. Thin (0.1 µm) z-stacks of high-resolution image frames were collected in three rotations by utilising an alpha Plan-Apochromat 63×/1.4 Oil DIC M27 ELYRA objective lens. Images were reconstructed using ZEN 2011 (Carl Zeiss Microscopy GmbH) based on a structured-illumination algorithm. To ensure accurate colocalisation analysis, a channel alignment procedure was followed using a slide of three-colour fluorescent beads #1783-455 Tool for Calibration Multi Spek (supplied by Carl Zeiss Microscopy GmbH). Dye concentrations with respective excitation and emission settings are listed in Table 8.3.

Table 8.3. *Concentrations of fluorescent dyes used for SR-SIM imaging of* P. falciparum *with respective excitation lasers and emission filter settings.*

Dye	Concentration	Grating	Excitation laser	Emission filter
Hoechst 33342	2 µM	35.0 µm	405 nm	BP 420-480 + LP 750
Novel fluorescent derivative	500 nM	42.0 µm	488 nm	BP 495-550 + LP 750
LysoTracker Red	200 nM	51.0 µm	561 nm	BP 570-620 + LP 750
Nile Red	200 nM	51.0 µm	561 nm	BP 570-620 + LP 750
ER-Tracker Red	500 nM	51.0 µm	561 nm	BP 570-620 + LP 750
MitoTracker Deep Red	200 nM	51.0 µm	642 nm	655 LP

8.4. Affinity detection and proteomic identification of binding targets

8.4.1. Preparation of biological material for affinity detection experiments

8.4.1.1. Saponin lysis of erythrocytes

Mature-stage *P. falciparum*-infected erythrocytes were harvested and generously donated by colleagues at the Division of Pharmacology, Department of Medicine, University of Cape Town. Parasites were liberated from the erythrocytes using a 1% saponin solution in 0.01 M phosphate-buffered saline (PBS) at pH 7.4. This was incubated at room temperature for 15 minutes and then centrifuged at 1 500 rcf for ten minutes. The supernatant was removed and the pellet was washed with 3 x 20 mL PBS to remove erythrocyte debris. Trophozoites were stored at -80°C.

8.4.1.2. Rupture of the digestive vacuole membrane by freeze-thaw lysis

Storage at -80°C and subsequent thawing resulted in lysis of the trophozoites but left the digestive vacuoles intact. This was confirmed by viewing a Giemsa-stained slide. A 10x protease inhibitor cocktail solution was prepared by dissolving one tablet of the SigmaFAST Protease Inhibitor Cocktail in 10 mL acidified dH_2O (pH 4.5-5.5). 500 µL of this 10x solution was added to the trophozoite pellet (approximately 5 mL in total). This mixture was split into six fractions of approximately 1 mL each. Each fraction was centrifuged at 10 900 rpm for five minutes and the supernatants were collected, pooled and stored at -20°C. To the pellet of each fraction was added approximately 1 mL of the 1x protease inhibitor solution followed by thorough mixing. Fractions were frozen at -80°C for 20 minutes and then thawed at 37°C for ten minutes. Fractions were vortexed, centrifuged for two minutes at 10 900 rpm and the supernatants were removed and pooled. The freeze-thaw cycle was continued over several days. Digestive vacuole lysis was judged to be complete when a wet mount showed no distinct shapes or aggregates under 100-fold magnification. Following lysis, the haemozoin was washed and collected. The pooled lysate was stored at -20°C.

8.4.1.3. Ultracentrifugation, ultrafiltration and quantification

The pooled lysate was thawed and poured into Beckman polyallomer centrifuge tubes (#331 374, 14 mm x 95 mm, 15 mL) and filled with acidified water. In order to separate soluble and insoluble (membrane) fractions, a Beckman centrifuge model L7-65 ultracentrifuge with a SW40-TI rotor was used. The samples were centrifuged at 31 000 rpm (120 000 x *g*) for one hour at 4°C to pellet out the insoluble membrane material. The supernatants were transferred to Merck Amicon Ultra-15 Centrifugal Filter Devices with a 3 kDa molecular weight cut-off (#UFC900308, 15 mL). These were spun using a Beckman J2-21M/E centrifuge with a JA-14

rotor at 7 000 rpm for 15 minutes at 4°C at least three times. The insoluble fraction was resuspended with a minimum volume of 1% (w/v) CHAPS detergent and triturated to promote mixing. Finally, the protein concentrations of all fractions were quantified using the Bio-Rad Quick Start Bradford Protein Assay using the instructions supplied by the manufacturer. Bovine serum albumin was used as a standard.

8.4.1.4. Lysis and quantification of human erythrocyte material

Uninfected human erythrocytes were lysed in the presence of the buffer previously described by Graves et al. with slight modifications.[26] The recipe is given in Table 8.4 and is hereafter referred to as "affinity buffer". 250 µL pelleted human erythrocytes were mixed with 250 µL affinity buffer (2x) and lysed by rocking gently for half an hour at 4°C with occasional single-second bursts of sonication. This was followed by centrifugation at 4°C for ten minutes at 13 500 x *g*. This lysate was quantified using the Bio-Rad Quick Start Bradford Protein Assay using the instructions supplied by the manufacturer.

Table 8.4. *Constituents of affinity buffer required for a 2x concentration in 100 mL.[26] To this was added one SigmaFAST Protease Inhibitor Cocktail tablet. The pH was adjusted to 7.5.*

Component	Molecular weight, g/mol	Final concentration for 2x	Mass required for 200 mL
NaCl	58.44	100 mM	0.584 g
$MgCl_2$	91.21	20 mM	0.190 g
Hepes	238.30	100 mM	2.383 g
CHAPS	614.88	0.2% (w/v)	200 mg

8.4.2. Preparation of drug-labelled agarose beads

Approximately 500 µL packed beads of NHS-activated Sepharose 4 Fast Flow (GE Healthcare) were washed three times with 1 mM cold HCl (1 mL). Thereafter, the beads were incubated with a coupling solution which comprised a sufficient number of moles of the derivatised ligand necessary for a 3 µmol/mL loading capacity dissolved in 100 mM Hepes at pH 8.3. This was rotated at room temperature for one hour after which the sample was washed three times with 100 mM Hepes at pH 8.3, this time containing no ligand. The supernatant from each wash step was collected and made up to a known volume for quantification by spectrophotometry to determine the amount of derivatised ligand remaining. The beads were then incubated in "blocking solution", comprising 100 mM Tris at pH 8.5, and rotated at room temperature for one

hour. Following centrifugation, the blocking solution was removed and the beads were washed with Hepes buffer (100 mM, pH 8.3) followed by acetate buffer (100 mM, pH 4.5). This wash routine, alternating between high and low pH values, was repeated three times. The beads were stored in 20% aqueous ethanol to avoid microbial contamination.

8.4.3. Matrix-based affinity chromatography

An aliquot of 150 µL suspended beads (approximately 100 µL packed beads) was equilibrated by washing three times with 1x affinity buffer (1 mL). For erythrocyte experiments, up to 3 mg of erythrocyte lysate was added to the beads and the total volume was made up to 1 mL with affinity buffer (1x). Alternatively, 40 µg of *P. falciparum* lysate was added to the beads and the total volume was made up to 500 µL. This mixture was gently rocked at 4°C for half an hour. The beads were centrifuged at 4°C for two minutes at 13 500 x *g* and the supernatant was removed. The beads were then resuspended in 800 µL affinity buffer (1x) and washed six times in total.

For solid-phase elution, 40 µL sample application buffer (4x) was added to the samples followed by mixing, centrifugation and dry-boiling at 95°C for five minutes. Samples were then loaded onto the gel directly. Alternatively, for competition elution, 450 µL of a concentrated solution of the drug in affinity buffer (1x) was added to the beads and this was rotated at 4°C for 20 minutes. Concentrations were 5 mM for chloroquine and 2.5 mM for quinine and quinidine. Following centrifugation, the supernatant was loaded onto a Pall Nanosep Centrifugal Device with Omega Membrane with a 3 kDa molecular weight cut-off. This was concentrated at 13 500 x *g* at 4°C for about six minutes until approximately 40-50 µL of each sample remained. The remaining supernatant was removed and placed in a new microfuge tube. To this was added 15 µL sample application buffer (4x) followed by mixing, centrifugation and dry boiling at 95°C for five minutes. Samples were then loaded onto the SDS-Page gel directly.

8.4.4. SDS-polyacrylamide gel electrophoresis (SDS-Page)

8.4.4.1. Recipes

- For the **separating (resolving) gel buffer**, 18.2 g Tris and 0.4 g SDS were made up to 100 mL and adjusted to pH 8.8. This gave concentrations of 150 mM Tris and 0.4% SDS.
- For the **stacking gel buffer**, 6.05 g Tris and 0.4 g SDS were made up to 100 mL and adjusted to pH 6.8. This gave concentrations of 50 mM Tris and 0.4% SDS.
- For the **running buffer (5x)**, 15.1 g Tris, 72 g glycine and 5 g SDS were made up to 1 L. The pH was not adjusted. When diluted to 1x, this gave concentrations of 25 mM Tris, 200 mM glycine and 0.1% SDS.

- To make approximately 20 mL of the **sample application buffer (4x)**, 10 mL of the stacking buffer was added to 8 mL glycerol, 0.8 g SDS, 0.8 mL β-mercaptoethanol, 0.2 mg bromophenol blue indicator and 1.2 mL dH_2O.

The relative proportions of reagents required to cast the separating and stacking gels, at acrylamide concentrations of 15% and 5% (w/v), respectively, are listed in Table 8.5. APS was stored in the freezer and re-prepared weekly. 40% (w/v) acrylamide was prepared using a 29:1 (w/v) monomer:crosslinker ratio. The monomer was acrylamide and the crosslinker was *N*,*N*'-methylenebisacrylamide. TEMED refers to tetramethylethylenediamine.

Table 8.5. *Components required to make separating and stacking gels at acrylamide concentrations of 15% and 5% (w/v), respectively. These amounts are sufficient for casting two gels.*

	Separating gel (15%)	**Stacking gel (5%)**
Water	7.1 mL	2.96 mL
40% (w/v) acrylamide	7.5 mL	500 µL
Buffer	5.2 mL (Separating buffer)	540 µL (Stacking buffer)
10% (w/v) APS	200 µL	40 µL
TEMED	12 µL	8 µL
Total	20 mL	4.048 mL

8.4.4.2. Casting the gels; electrophoresis

Equipment was thoroughly cleaned with 70% (v/v) aqueous ethanol. 1.0 mm gels were cast as per standard procedure. Briefly, the solution for the separating gel was prepared and inserted into the casting apparatus. Isopropanol was used to level out the gel surface. After polymerisation, the isopropanol was removed and the stacking gel was prepared. This was added to the casting apparatus and a ten-lane comb was gently inserted. Once the stacking gel had set, the apparatus was placed in the running chamber of a Bio-Rad Mini-PROTEAN Tetra System. The comb was removed and running buffer (1x) was added. Samples were prepared by diluting an appropriate volume of sample application buffer (4x) followed by dry-boiling for five minutes at 95°C using a Thermo Scientific Reacti-Therm I #TS-18822 heating mantle with a Reacti-Block #TS-18819 attachment for microfuge tubes. 15 µL of sample was loaded on the gel. 5 µL of the PageRuler Pre-Stained Protein Ladder 10 to 180 kDa (Thermo Fischer Scientific #26616) was also loaded on each gel. 5 µL sample application buffer (1x) was added to empty wells. For electrophoresis, a Bio-Rad PowerPac Basic was used. Single gels were run at 20 mA for 70 minutes and double gels were run at 30 mA for 85 minutes. After the run, the plates were gently prised apart and placed in dH_2O.

8.4.4.3. Staining

For Coomassie staining, the gel was incubated with Coomassie Brilliant Blue R-250 Staining Solution (Bio-Rad #1610436) and gently rocked at room temperature overnight. This staining solution was also prepared in-house by dissolving 0.1% Coomassie Brilliant Blue R-250 (w/v) in 50:40:10 (v/v/v) methanol:water:acetic acid. Following staining, gels were destained using Coomassie Brilliant Blue R-250 Destaining Solution (Bio-Rad #1610438) by washing the gel with water and then covering the gel with destaining solution. This was gently rocked at room temperature for several hours, during which the destaining solution was changed at least three times. The destaining solution was also prepared in-house by mixing 50:40:10 (v/v/v) water:methanol:acetic acid. Alternatively, gels were silver-stained using the procedure described in the Sigma-Aldrich ProteoSilver Plus Silver Stain Kit. Gels were imaged using a Bio-Rad ChemiDoc XRS+ with ImageLab software (Version 5.2.1, Bio-Rad Laboratories, Inc.).

8.4.5. Proteomic analysis

Proteomic analysis was carried out at the CAF Proteomics Unit at Stellenbosch University. All reagents were analytical grade or equivalent and were supplied as indicated.

8.4.5.1. Sample preparation

Protein solutions were precipitated overnight at -20°C with five volumes of ice-cold acetone. The pellets were solubilised by dissolving them in 100 mM triethylammonium bicarbonate (TEAB; Sigma).

8.4.5.2. In-solution digestion

Samples were reduced by adding 50 mM tris(2-carboxyethyl)phosphine (TCEP; Fluka) in 100 mM TEAB (final concentration 5 mM TCEP) followed by incubation at room temperature for 30 minutes. Following reduction, cysteine residues were modified to methylthio using 200 mM methane methylthiosulfonate (MMTS; Sigma) in 100 mM TEAB (final concentration 20 mM) for 30 minutes. After modification, the samples were diluted to 98 µL with 100 mM TEAB. Proteins were digested by adding 5 µL trypsin (1 µg/µL; Promega) and incubating for 18 hours at 37°C. Samples were dried down and resuspended in 100 µL 2% acetonitrile (Fluka):0.1% formic acid (FA; Sigma).

8.4.5.3. Desalting

Residual digest reagents were removed using an in-house manufactured C18 stage tip (Empore C18 extraction discs; Supelco). The 20 µL sample was loaded onto the stage tip after activating the C18 membrane with 30 µL methanol (Sigma) and equilibration with 30 µL 2%

acetonitrile:0.05% FA. The bound sample was washed with 30 µL 2% acetonitrile:0.1% FA before elution with 30 µL 50% acetonitrile:0.1% FA. The eluate was evaporated to dryness. The dried peptides were dissolved in 20 µL 2% acetonitrile:0.1% FA for LC-MS analysis.

8.4.5.4. Liquid chromatography

Liquid chromatography was performed on a Thermo Scientific Dionex UltiMate 3000 RSLCnano equipped with a 0.5 cm x 300 µm C18 trap column and a 35 cm x 75 µm in-house manufactured C18 analytical column (Luna C18, 3.6 µm; Phenomenex). The solvent systems were:

Loading: 2% acetonitrile:0.1% FA
Solvent A: 2% acetonitrile:0.1% FA
Solvent B: 100% acetonitrile:water

The samples were loaded onto the trap column using loading solvent at a flow rate of 15 µL/min from a temperature-controlled autosampler. Loading was performed for five minutes before the sample was eluted onto the analytical column. The flow rate was set to 500 nL/min and the gradient generated as follows: 2%-10% Solvent B over five minutes; 5%-25% Solvent B from 5-50 minutes using Chromeleon non-linear gradient 6; 25%-45% Solvent B from 50-65 minutes, using Chromeleon non-linear gradient 6. Chromatography was performed at 50°C and the outflow was delivered to the mass spectrometer through a stainless steel nano-bore emitter.

8.4.5.5. Mass spectrometry

Mass spectrometry was performed using a Thermo Scientific Fusion mass spectrometer equipped with a Nanospray Flex ionisation source. The sample was introduced through a stainless steel emitter. Data were collected in positive mode with spray voltage set to 2 kV and ion transfer capillary set to 275°C. Spectra were internally calibrated using polysiloxane ions at m/z = 445.12003 and 371.10024. MS1 scans were performed using the orbitrap detector set at 120 000 resolution over the scan range 350-1650 with AGC target at 3E5 and maximum injection time of 40 ms. Data were acquired in profile mode. MS2 acquisitions were performed using monoisotopic precursor selection for ions with charges +2 to +6 with error tolerance set to ± 0.02 ppm. Precursor ions were excluded from fragmentation once for a period of 30 s. Precursor ions were selected for fragmentation in HCD mode using the quadrupole mass analyser with HCD energy set to 32.5%. Fragment ions were detected in the orbitrap mass analyser set to 15 000 resolution. The AGC target was set to 1E4 and the maximum injection time to 45 ms. These data were acquired in centroid mode.

8.4.5.6. Data analysis

The raw files generated by the mass spectrometer were imported into Proteome Discoverer (Version 1.4, Thermo Scientific) and processed using the SequestHT algorithm. Data analysis was structured to allow for methylthio as a fixed modification as well as deamidation and oxidation. Precursor tolerance was set to 10 ppm and fragment ion tolerance to 0.02 Da. Databases for *P. falciparum* and *H. sapiens* were obtained from UniProt (www.uniprot.org). The raw files generated were converted to Mascot generic format (mgf) and the files interrogated using the Myrimatch algorithm through SearchGUI. Search parameters were set as for the Sequest HT search. The results files were imported into Scaffold (Version 1.4.4, Proteome Software Inc.) and identified peptides validated using the X!Tandem search algorithm included in Scaffold. Peptide and Protein validation were done using the Peptide and Protein Prophet algorithms. Further analysis was performed using Scaffold Viewer (Version 4.5.3, Proteome Software Inc.).

8.5. References

1. E. Merck, in *Dyeing Reagents for Thin-Layer and Paper Chromatography*, Darmstadt, 1980.
2. H. E. Gottlieb, V. Kotlyar and A. Nudelman, *J. Org. Chem.*, 1997, **62**, 7512.
3. A. K. Tucker-Schwartz, R. Farrell and R. Garrell, *J. Am. Chem. Soc*., 2011, **133**, 11026.
4. S. Pinchas and D. Ben-Ishai, *J. Am. Chem. Soc.*, 1957, **79**, 4099.
5. J. Novotný, K. Pospěchová, A. Hrabálek, R. Čáp and K. Vávrová, *Bioorg. Med. Chem. Lett.*, 2009, **19**, 6975.
6. S. Haldar, S. Kumar, S. P. Kolet, H. S. Patil, D. Kumar, G. C. Kunda and H. V. Thulasarim, *J. Org. Chem.*, 2013, **78**, 10192.
7. W. I. Sundquist, D. P. Bancroft and J. Lippard, *J. Am. Chem. Soc.*, 1990, **112**, 1590.
8. M. Ansari and J. C. Craig, *Synthesis*, 1995, 147.
9. M. Myers, J. Pokorski and D. H. Appella, *Org. Lett.*, 2004, **6**, 4699.
10. M. Cabrera, J. Natarajan, M. Paguio, C. Wolf, J. Urbach and P. D. Roepe, *Biochemistry*, 2009, **48**, 9471.
11. M. Kurt, P. Chinna Babu, N. Sundaraganesan, M. Cinar and M. Karabacak, *Spectrochim. Acta Mol. Biomol. Spectrosc.*, 2011, **79**, 1162.
12. K. A. de Villiers, C. H. Kaschula, T. J Egan and H. M. Marques, *J. Biol. Inorg. Chem.*, 2007, **12**, 101.
13. S. Fery-Forgues and D. Lavabre, *J. Chem. Ed.*, 1999, **76**, 1260.
14. W. H. Melhuish, *J. Phys. Chem.*, 1961, **65**, 229.
15. T. Aminabhavi and B. Gopalakrishna, *J. Chem. Eng. Data*, 1995, **40**, 856.
16. D. Kuter, S. Benjamin and T. J. Egan, *J. Inorg. Biochem.*, 2014, **133**, 40.
17. T. J. Egan, W. M. Mavuso, D. C. Ross and H. M. Marques, *J. Inorg. Biochem.*, 1997, **68**, 137.
18. P. W. Linder, L. R. Nassimbeni, A. Polson and A. L. Rodgers, *J. Chem. Ed.*, 1976, **53**, 330.
19. M. D. Carter, V. V. Phelan, R. D. Sandlin, B. O. Bachmann and D. W. Wright, *Comb. Chem. High Throughput Screen.*, 2010, **13**, 205.
20. R. D. Sandlin, M. D. Carter, P. J. Lee, J. M. Auschwitz, S. E. Leed, J. D. Johnson and D. W. Wright, *Antimicrob. Agents Chemother.*, 2011, **55**, 3363.
21. K. K. Ncokazi and T. J. Egan, *Anal. Biochem.*, 2005, **338**, 306.
22. W. Trager and J. B. Jensen, *Science*, 1976, **193**, 673.
23. M. T. Makler, J. M. Ries, J. A. Williams, J. E. Bancroft, R. C. Piper, B. L. Gibbins and D. J. Hinrichs, *Am. J. Trop. Med. Hyg.*, 1993, **48**, 6.
24. Y. Kuhn, P. Rohrbach and M. Lanzer, *Cell. Microbiol.*, 2007, **9**, 1004.
25. F. Wissing, C. Sanchez, P. Rohrbach, S. Ricken and M. Lanzer, *J. Biol. Chem.*, 2002, **277**, 37747.
26. P. R. Graves, J. J. Kwiek, P. Fadden, R. Ray, K. Hardeman, A. M. Coley, M. Foley and T. A. J. Haystead, *Mol. Pharm.*, 2002, **62**, 1364.